Springer Series in Optical Sciences

Editorial Board: A. L. Schawlow K. Shimoda A. E. Siegman T. Tamir

Managing Editor: H. K. V. Lotsch

Volumes 1 - 41 are listed on the back inside cover

B. K. Agarwal

X-Ray Spectroscopy

An Introduction

Second Edition

With 239 Figures

Springer-Verlag
Berlin Heidelberg New York
London Paris Tokyo
Hong Kong Barcelona
Budapest

Professor BIPIN K. AGARWAL, Ph. D. (deceased)
Formerly Head of the Physics Department, Dean of the Faculty of Science
University of Allahabad, Allahabad 211001, India

ISBN 3-540-50719-1 2nd ed. Springer-Verlag Berlin Heidelberg New York
ISBN 0-387-50719-1 2nd ed. Springer-Verlag New York Berlin Heidelberg

ISBN 3-540-09268-4 1st ed. Springer-Verlag Berlin Heidelberg New York
ISBN 0-387-09268-4 1st ed. Springer-Verlag New York Berlin Heidelberg

Library of Congress Cataloging-in-Publication Data

Agarwal, B. K. (Bipin Kumar), 1931–
X-ray spectroscopy : an introduction / B.K. Agarwal. – 2nd ed.
p. cm. – (Springer series in optical sciences ; v. 15)
Bibliography: p.
Includes indexes.
ISBN 0-387-50719-1 (U.S.)
1. X-ray spectroscopy. I. Title. II. Series.
[DNLM: 1. Spectrum Analysis. 2. X-Rays. QC 482. S6 A261x]
QC482.S6A34 1991 537.5'352–dc19 DNLM/DLC
for Library of Congress

54/3020 – 54310 – Printed on acid-free paper

To my Mami Ji
in memory

Preface to the Second Edition

An attempt has been made in this edition of the book to retain the appeal of the first edition even after the addition of new material and the deletion of other matter which no longer appears essential.

Major revisions have been made in almost all the chapters to include new developments. The material on EXAFS has been updated and put in a separate chapter. The chapter on experimental methods has been considerably expanded to include energy dispersive techniques. New topics like heavy-ion bremsstrahlung, X-ray lasers, resonant emission, appearance potential spectroscopy, and EXAFS of high-T_C superconducting materials have been added. It is hoped that readers will find the new edition more useful and attractive.

I am grateful to Professor R. H. Pratt, University of Pittsburgh, for reading the revised version of the first chapter, to Dr. H. Lotsch, of Springer-Verlag, for encouraging me to revise the book, and to Prashant and Seema for helping me in preparing the manuscript.

Allahabad,
July 1989

B. K. Agarwal

Preface to the First Edition

Röntgen's discovery of X-rays in 1895 launched a subject which became central to the development of modern physics. The verification of many of the predictions of quantum theory by X-ray spectroscopy in the early part of the twentieth century stimulated great interest in this area, which has subsequently influenced fields as diverse as chemical physics, nuclear physics, and the study of the electronic properties of solids, and led to the development of techniques such as Auger, Raman, and X-ray photoelectron spectroscopy.

The improvement of the theoretical understanding of the physics underlying X-ray spectroscopy has been accompanied by advances in experimental techniques, and the subject provides an instructive example of how progress on both these fronts can be mutually beneficial. This book strikes a balance between historical description, which illustrates this symbiosis, and the discussion of new developments. The application of X-ray spectroscopic methods to the investigation of chemical bonding receives special attention, and an up-to-date account is given of the use of extended X-ray absorption fine structure (EXAFS) in determining interatomic distances, which has attracted much attention during the last decade.

This monograph is intended to be used as a basic text for a one-year course at postgraduate level, and aims to provide the general background that is essential to enable the reader to participate fruitfully in the growing research activity in this field.

Sri Arvind Agarwal and Dr. Chitra Dar have helped me in many ways in the preparation of the manuscript. My whole family joined me in preparing and checking the index.

Allahabad,
April 1979

B. K. Agarwal

Contents

1. Continuous X-Rays

X-rays are electromagnetic radiations in the wavelength region around 1Å. An X-ray tube is operated by accelerating electrons to high energy and then allowing them to strike a metallic target. Within the target, the motions of electrons are affected by the strong fields of the atomic nuclei, and the electrons are slowed or even stopped within small distances. In other words, the electrons are strongly decelerated. As a result *bremsstrahlung* (*deceleration radiation*) or *continuous radiation* (*white radiation*) is produced. It would therefore be useful to study the nature of the field of a charged particle that is in uniform motion and then decelerated.

1.1 Field of a Point Charge Moving with Uniform Velocity

Measurements of charge made from all reference frames give the same value. The charge Q is a scalar, an invariant number, with respect to the Lorentz transformations. This fact determines the nature of the field of a moving charge.

A point charge Q is at rest at the origin in the frame F (Fig. 1.1a). In this frame, the electric field $\boldsymbol{E}$ is radial, spherically symmetric and has the magnitude Q/r^2. In the xz plane its components are

$$E_x = \frac{Q}{r^2}\cos\theta = \frac{Qx}{(x^2+z^2)^{3/2}},$$

$$E_z = \frac{Q}{r^2}\sin\theta = \frac{Qz}{(x^2+z^2)^{3/2}}. \tag{1.1}$$

The field is radial as $E_z/E_x = z/x$.

Let the frame F' move with speed v toward the left (Fig. 1.1b). The Lorentz transformations with $\gamma = 1/(1-\beta^2)^{1/2}$, $\beta = v/c$, where c is the speed of light, are

$$x = \gamma(x' - vt'), \quad y = y', \quad z = z', \quad t = \gamma\left(t' - \frac{v}{c^2}x'\right). \tag{1.2}$$

The clocks read zero when $x = 0$ and $x' = 0$ coincide.

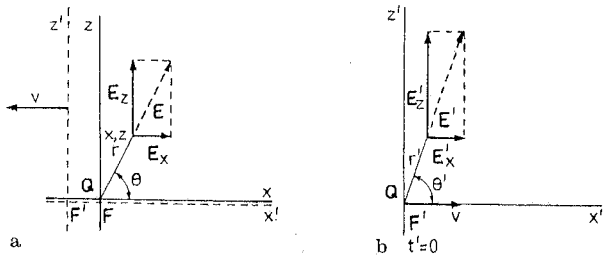

Fig. 1.1. The electric field of a point charge Q **a** in the rest frame F, and **b** in the frame F' in which Q moves with a given constant velocity v

At the instant $t' = 0$, when Q passes the origin in F',

$$E'_x = E_x = \frac{Q\gamma x'}{[(\gamma x')^2 + z'^2]^{3/2}},$$

$$E'_z = \gamma E_z = \frac{\gamma Q z'}{[(\gamma x')^2 + z'^2]^{3/2}}. \tag{1.3}$$

The field remains radial as $E'_z/E'_x = z'/x'$. Clearly

$$E'^2 = E'^2_x + E'^2_z = \frac{\gamma^2 Q^2 (x'^2 + z'^2)}{[(\gamma x')^2 + z'^2]^3} = \frac{Q^2 (x'^2 + z'^2)}{\gamma^4 (x'^2 + z'^2 - \beta^2 z'^2)^3}$$

$$= \frac{Q^2 (1-\beta^2)^2}{(x'^2 + z'^2)[1 - (\beta^2 z'^2/(x'^2 + z'^2))]^3}. \tag{1.4}$$

Using $r' = (x'^2 + z'^2)^{1/2}$ and $z' = r' \sin\theta'$ (Fig. 1.1b),

$$E'(\theta') = \frac{Q}{r'^2} \frac{1-\beta^2}{(1-\beta^2 \sin^2\theta')^{3/2}}; \tag{1.5}$$

$E'(90°) = (Q/r'^2)\gamma$ and $E'(0) = (Q/r'^2)/\gamma^2$, where $\gamma > 1$. For $\beta = 0$, we get $E'(\theta') = Q/r'^2$.

Thus, if β is not negligible, the field is stronger at right angles to the motion than in the direction of motion, at the same distance from Q. Let us indicate the intensity of the field by the density of lines of force. A two-dimensional picture would be as shown in Fig. 1.2. In a three-dimensional picture, the lines of force tend to concentrate in a slab perpendicular to the direction of motion.

The field strength due to a stationary or uniformly moving charge falls off as $1/r^2$ and is *nonradiating*. It does not contribute to the energy flux over a large sphere. The reason is as follows. The energy flux is given by a quadratic expression in field strengths. Therefore, in this case it will vary as $1/r^4$. The integral over a spherical surface, $\int(\text{energy flux}) r^2 \, d\Omega$, will then involve $1/r^2$ in the integrand. For larger r ($r \to \infty$), the contribution will become negligible.

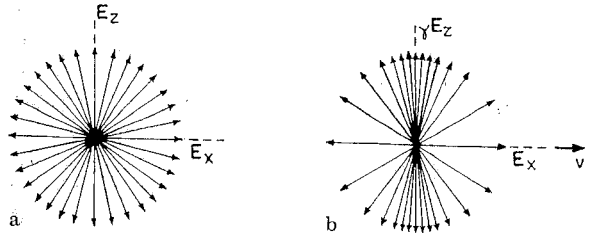

Fig. 1.2a, b. Lines of force of a positive charge **a** at rest, **b** moving, $\beta \sim 4/5$. The lines of force tend to concentrate in a slab perpendicular to the direction of motion, **b**, in a three-dimensional picture

1.2 Radiation from an Accelerated or Decelerated Charged Particle

Consider an electron that is initially at rest at $x = 0$ (Fig. 1.3). It is suddenly (in negligible time interval Δt) accelerated up to a high speed Δv, $\Delta\beta \sim 4/5$, at $t = 0$. The electron moves away along the x axis with this speed. We observe the situation after a time $t \gg \Delta t$ (Fig. 1.3). No signal can travel with a speed greater than c, and thus any observer at a point outside the sphere or radius $c(t + \Delta t)$ around the origin must see the field of a charge at rest at the origin (static field). The observer could not have received the information that the electron had started to move. Similarly, for all points inside the sphere of radius ct, the field at time t must be due to a uniformly moving electron (convective field). The lines have the appropriate Lorentz-contracted configuration of Fig. 1.2b, converging to the electron at a distance $\Delta v t$ from the origin.

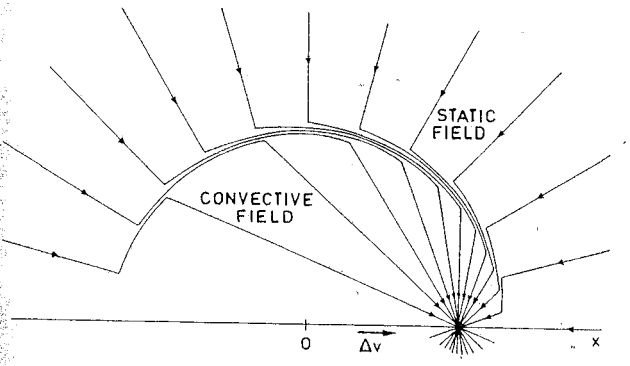

Fig. 1.3. Field at time t due to an electron, initially at rest at $x = 0$, that is suddenly accelerated at $t = 0$, and moves away with uniform velocity Δv, $\beta \sim 4/5$

There exists a thin spherical shell of width $c\Delta t$ within which the transition from the static field to the convective field occurs. The shell of adjustment expands with the velocity c around $x = 0$. Because lines of force cannot break, within this shell the lines of force will run so as to connect the outer (static) and inner (convective) field lines (Fig. 1.3).

For bremsstrahlung (braking radiation) we consider the case of an electron that has been moving with uniform velocity Δv until it reaches the origin ($x = 0$) at $t = 0$, where it is suddenly decelerated within a short interval of time Δt. It remains at rest thereafter. The resulting field after a time t is shown in Fig. 1.4. The static field is within a sphere of radius ct. The convective Lorentz-contracted field is outside a sphere of radius $c(t + \Delta t)$. The transition spherical shell of small width $c\Delta t$ moves out with the velocity c. The news that the electron has stopped cannot reach, by time t, any point farther than ct from the origin. The convective field therefore will continue to follow the charge as if it has continued to move at its original speed and will converge to the position where the electron would be if it had not stopped. From (1.1, 2)

$$\frac{E_z}{E_x} = \tan\theta, \quad \frac{E_z'}{E_x'} = \tan\theta' = \frac{\gamma E_z}{E_x} = \gamma\tan\theta, \quad \gamma = \frac{1}{\sqrt{1-\beta^2}}. \tag{1.6}$$

It is clear from this and the resulting construction (Fig. 1.4) that the field lines, connecting the inner field to the outer field, must have a transverse component. For $\beta \sim 4/5$, Fig. 1.4 shows that there exists an intense field within the transition shell, with field lines that run almost perpendicular to the radius vector from the origin. Thus *an outgoing wave of transverse electric field is radiated outward with velocity c by the decelerated electron.*

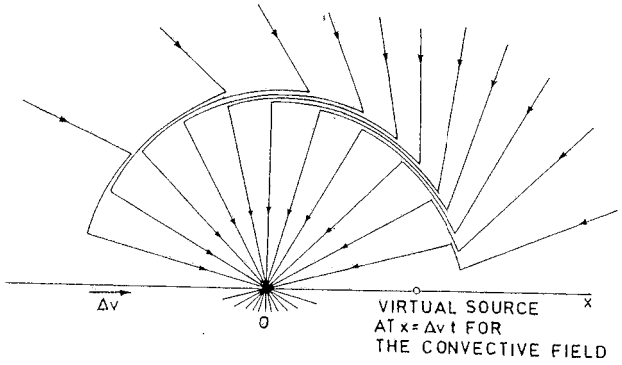

Fig. 1.4. Field at time t due to a decelerated electron which stopped at $x = 0$, $t = 0$

1.3 Transverse Radiation Field due to the Acceleration of an Electron to Low Velocity ($\beta < 1/3$)

For an electron initially at rest, accelerated suddenly within a short interval of time Δt to a velocity Δv, $\Delta\beta < 1/3$, we have $\theta' \simeq \theta$. Thus, after a time t, the field lines look like that shown in Fig. 1.5 (compare with Fig. 1.3). For low velocity, the lines of force will not be Lorentz-contracted in the inside region. They will simply move parallel to themselves a distance $t\Delta v \sin\theta$.

During the time Δt of the acceleration, the wave advances a distance $c\Delta t$. The part AB (kink) of the field line inside the shell is straight when the acceleration $a = \Delta v/\Delta t$ is uniform. Resolve the electric field E at any point on AB into a radial component E_r (parallel to $0B$) and a perpendicular or tangential component E_θ. Then E_θ/E_r is approximately (ratio of corresponding sides of similar triangles)

$$\frac{E_\theta}{E_r} = \frac{t\Delta v\sin\theta}{c\Delta t} = \frac{at}{c}\sin\theta. \tag{1.7}$$

Using $E_r = e/r^2$ and $t = r/c$,

$$E_\theta = \frac{ea}{c^2 r}\sin\theta. \tag{1.8}$$

Thus, within the transition shell, we have two components

$$E_r \propto 1/r^2 \quad \text{and} \quad E_\theta \propto 1/r. \tag{1.9}$$

For large r, E_r becomes negligible and only E_θ remains. At great distances, we shall be left with a pulse of a *transverse field* travelling outward with velocity c. Its energy flux will vary as $1/r^2$, making the integral over a spherical surface independent of r. A finite contribution will be obtained even for large r. Therefore, it is a *radiating field.*

The above simple calculation shows that an accelerated (or decelerated) electron generates a *transverse radiation field.* This result is of interest in connection with the theory of continuous X-rays.

In the spirit of the present simple calculation, *Ohanian* [1.1] has calculated the magnetic field H in the shell (kink) region. It is induced by the time-dependent electric field. By symmetry requirements, the magnetic field lines form closed loops about the direction of motion. The strength of H follows from the Maxwell–Ampère law

$$\int H\cdot dl = \frac{1}{c}\frac{d\Phi}{dt} \tag{1.10}$$

(in cgs units), where the electric flux Φ is determined by E_θ. The field $\boldsymbol{H} = (e/c)(\boldsymbol{v}\times\boldsymbol{r})/r^3$ of a moving charge due to E_r falls off as $1/r^2$ and so is of no interest. In the shell the magnetic field is everywhere perpendicular to the electric field (Fig. 1.6). Integrate along a circular path that follows a magnetic field line

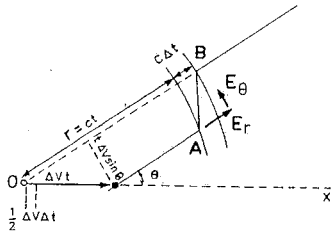

Fig. 1.5. Electron at rest is accelerated within a time Δt to a slow velocity Δv. The acceleration is $a = \Delta v/\Delta t$

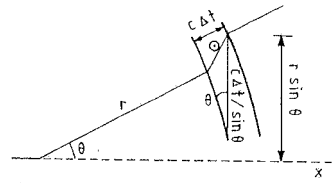

Fig. 1.6. Magnetic lines in the shell. The integration is along a circle of radius $r \sin\theta$ perpendicular to the plane of the paper.

to get

$$\int \boldsymbol{H} \cdot d\boldsymbol{l} = 2\pi r H \sin\theta. \tag{1.11}$$

To find Φ consider a flat circular surface. This area intercepts E_θ only in an annular region of radius $r \sin\theta$, width $c\Delta t/\sin\theta$, and area $2\pi c \Delta t r$ (Fig. 1.6). As E_θ makes an angle with the surface of the annulus, $\Delta\Phi = 2\pi c \Delta t r E_\theta \sin\theta$. In a time Δt the kink moves beyond the annular region and so this flux disappears. One gets

$$\frac{d\Phi}{dt} = \frac{\Delta\Phi}{\Delta t} = 2\pi c r E_\theta \sin\theta. \tag{1.12}$$

From (1.10–12), in magnitude,

$$H = E_\theta. \tag{1.13}$$

A general calculation of both $\boldsymbol{E}$ and $\boldsymbol{H}$ requires the use of Maxwell's equations.

1.4 Maxwell's Equations

For a charge that moves with velocity $\boldsymbol{v}$ at a given point and a given time, the current density is $\boldsymbol{j} = \rho \boldsymbol{v}$, where ρ is the *charge density*. If the electric and magnetic field strengths are $\boldsymbol{E}(x, y, z, t)$ and $\boldsymbol{H}(x, y, z, t)$, the *Maxwell equations* for a given distribution of charge and current are

$$\nabla \times \boldsymbol{E} + \frac{1}{c}\frac{\partial \boldsymbol{H}}{\partial t} = 0 \quad \textit{(Faraday's law)}, \tag{1.14a}$$

$$\nabla \cdot \boldsymbol{H} = 0 \quad \textit{(absence of free magnetic poles)}, \tag{1.14b}$$

$$\nabla \times \boldsymbol{H} - \frac{1}{c}\frac{\partial \boldsymbol{E}}{\partial t} = \frac{4\pi}{c}\boldsymbol{j} \quad \textit{(generalized Ampère's law)}, \tag{1.14c}$$

$$\nabla \cdot \boldsymbol{E} = 4\pi\rho \quad \textit{(Coulomb's law)}. \tag{1.14d}$$

In view of (1.14b), $\boldsymbol{H}$ can always be expressed as the curl of a vector potential $\boldsymbol{A}$

$$\boldsymbol{H} = \nabla \times \boldsymbol{A}. \tag{1.15a}$$

Then the homogeneous equation (1.14a) becomes $\nabla \times (\boldsymbol{E} + c^{-1}\partial \boldsymbol{A}/\partial t) = 0$, so we can introduce a *scalar potential* ϕ by

$$\boldsymbol{E} + \frac{1}{c}\frac{\partial \boldsymbol{A}}{\partial t} = -\nabla\phi. \tag{1.15b}$$

These definitions of $\boldsymbol{H}$ and $\boldsymbol{E}$ in terms of $\boldsymbol{A}$ and ϕ can now be substituted in the last two inhomogeneous Maxwell equations. Using curl curl = grad div $- \nabla^2$,

$$\frac{1}{c^2}\frac{\partial^2 \boldsymbol{A}}{\partial t^2} - \nabla^2 \boldsymbol{A} + \nabla\left(\nabla \cdot \boldsymbol{A} + \frac{1}{c}\frac{\partial\phi}{\partial t}\right) = \frac{4\pi}{c}\boldsymbol{j}, \tag{1.16a}$$

$$-\nabla^2\phi - \frac{1}{c}\nabla \cdot \frac{\partial \boldsymbol{A}}{\partial t} = 4\pi\rho. \tag{1.16b}$$

A vector is uniquely defined only when both its curl and divergence are specified. The curl of $\boldsymbol{A}$ is given in (1.15a). For div $\boldsymbol{A}$ introduce the *Lorentz condition*

$$\nabla \cdot \boldsymbol{A} = -\frac{1}{c}\frac{\partial\phi}{\partial t}. \tag{1.17}$$

It uncouples (1.16a, b),

$$\nabla^2\phi - \frac{1}{c^2}\frac{\partial^2\phi}{\partial t^2} = -4\pi\rho(\boldsymbol{x}, t), \tag{1.18a}$$

$$\nabla^2 \boldsymbol{A} - \frac{1}{c^2}\frac{\partial^2 \boldsymbol{A}}{\partial t^2} = -\frac{4\pi}{c}\boldsymbol{j}(\boldsymbol{x}, t). \tag{1.18b}$$

These two equations along with (1.17) are equivalent to Maxwell's equations. Therefore, it is enough to solve the inhomogeneous equations (1.18), which have the familiar form of wave equations with source terms on the right.

1.5 Coulomb Potential

For a static field (1.18a) reduces to the *Poisson equation*

$$\nabla^2\phi(\boldsymbol{x}) = -4\pi\rho(\boldsymbol{x}), \tag{1.19}$$

which has a solution

$$\phi(\boldsymbol{x}) = \int \frac{\rho(\boldsymbol{x}')}{|\boldsymbol{x} - \boldsymbol{x}'|}\, d^3x'. \tag{1.20}$$

To verify (1.20), operate with ∇^2 on both sides:

$$\nabla^2\phi = \nabla^2\int \frac{\rho(x')}{|x-x'|}\,d^3x' = \int \rho(x')\,\nabla^2\left(\frac{1}{|x-x'|}\right)d^3x'. \tag{1.21}$$

To evaluate $\nabla^2(1/|x-x'|)$, translate the origin to x'. Then consider $\nabla^2(1/R)$, where $R = |x|$,

$$\nabla^2\left(\frac{1}{R}\right) = \frac{1}{R}\frac{d^2}{dR^2}\left(R\frac{1}{R}\right) = \frac{1}{R}\frac{d^2}{dR^2}(1) = 0 \quad \text{for } R \neq 0. \tag{1.22}$$

At $R = 0$, the expression is undefined, so use a limiting process. Integrating $\nabla^2(1/R)$ over a small volume dV that contains the origin, and using the divergence theorem to obtain a surface integral, we have

$$\int_{dV} \nabla^2\left(\frac{1}{R}\right)d^3x = \int_S \boldsymbol{n}\cdot\nabla\left(\frac{1}{R}\right)dS$$

$$= \int_S \frac{\partial}{\partial R}\left(\frac{1}{R}\right)R^2\,d\Omega = -4\pi. \tag{1.23}$$

Results (1.22, 23) can be combined as

$$\nabla^2(1/R) = -4\pi\delta^3(x),$$

or

$$\nabla^2\left(\frac{1}{|x-x'|}\right) = -4\pi\delta^3(x-x'), \tag{1.24}$$

where $\delta^3(x)$ is the *Dirac delta function*. From (1.21, 24),

$$\nabla^2\phi = \int \rho(x')\,[-4\pi\delta^3(x-x')]\,d^3x' = -4\pi\rho(x).$$

For a point charge, $\rho = e\delta^3(x)$, (1.20) gives

$$\phi = e/R \quad (\textit{Coulomb potential}). \tag{1.25}$$

1.6 Retarded Potentials

To solve (1.18a) divide the whole space into infinitely small regions (cells), and determine the field produced by the *point* charge $de = \rho dV$ located in one of these cells of volume dV. Equation (1.18a) being linear in ϕ, the actual field will be the sum of the fields produced by all such charge elements.

We wish to solve (1.18a) for a moving point charge, $\partial^2\phi/\partial t^2 \neq 0$. The charge de in a given cell is, in general, a function of time. Choose the origin of coordinates in the cell under consideration, where the point charge $de(t)$ is located. Then (1.18a) becomes

$$\nabla^2\phi - \frac{1}{c^2}\frac{\partial^2\phi}{\partial t^2} = -4\pi\,de(t)\delta^3(\boldsymbol{R}), \tag{1.26}$$

where $\boldsymbol{R}$ is the distance from the origin. Everywhere, except at the origin, $\delta^3(\boldsymbol{R}) = 0$. Therefore, the equation

$$\nabla^2\phi - \frac{1}{c^2}\frac{\partial^2\phi}{\partial t^2} = 0 \quad (|\boldsymbol{R}| \neq 0), \tag{1.27}$$

is satisfied everywhere except at the origin, whereas in a small volume element dV that surrounds the origin

$$\int_{dV}\left[\nabla^2\phi - \frac{1}{c^2}\frac{\partial^2\phi}{\partial t^2}\right]dV = -4\pi\,de(t). \tag{1.28}$$

For de placed at the origin, ϕ has central symmetry, $\phi(\boldsymbol{R}, t) = \phi(R, t)$. Therefore, in spherical coordinates (1.27) becomes

$$\frac{1}{R^2}\frac{\partial}{\partial R}\left(R^2\frac{\partial\phi}{\partial R}\right) - \frac{1}{c^2}\frac{\partial^2\phi}{\partial t^2} = 0. \tag{1.29}$$

Putting $\phi(R, t) = \chi(R, t)/R$,

$$\frac{\partial^2\chi}{\partial R^2} - \frac{1}{c^2}\frac{\partial^2\chi}{\partial t^2} = 0. \tag{1.30}$$

This one-dimensional wave equation is solved by any function $f(T)$ of $T = t - R/c$ or $t + R/c$,

$$T = t - \frac{R}{c}, \tag{1.31}$$

$$\frac{\partial f}{\partial R} = -\frac{1}{c}\frac{\partial f}{\partial T}, \quad \frac{\partial^2 f}{\partial R^2} = \frac{1}{c^2}\frac{\partial^2 f}{\partial T^2},$$

$$\frac{\partial f}{\partial t} = \frac{\partial f}{\partial T}, \quad \frac{\partial^2 f}{\partial t^2} = \frac{\partial^2 f}{\partial T^2}.$$

The solution $f(t - R/c)$ represents a plane wave that is propagated *outward* along the polar axis R with a velocity c. The reason is that the field has the same value when $t - R/c = \text{const.}$, that is, $R = \text{const.} + \text{ct.}$, we can take the solution to be

$$\chi = \chi\left(t - \frac{R}{c}\right), \quad \text{or} \quad \phi = \frac{\chi(t - R/c)}{R}. \tag{1.32}$$

So far, the form of χ is arbitrary. It can be chosen so that (1.28), or (1.26), is satisfied for the potential at the origin. As $R \to 0$, the potential increases to infinity. Consequently, its derivatives with respect to the coordinates increase more rapidly than its time derivative. Then, as $R \to 0$ in (1.28), or (1.26), we can ignore the term $\partial^2\phi/\partial t^2$, and get a static field equation that leads to the Coulomb law (Sect. 1.5). Thus, near the origin, (1.32) must go over to the

Coulomb law and we should put $\chi(t) = de(t)$; that is

$$\phi = \frac{de(t - R/c)}{R}. \tag{1.33}$$

To find the solution of (1.18a) for an arbitrary distribution of charges $\rho(\boldsymbol{x}, t)$, write $de = \rho dV$ in (1.33) and sum over the whole space

$$\phi(\boldsymbol{x}, t) = \int \frac{\rho(\boldsymbol{x}', t - R/c)\, dV'}{R}, \tag{1.34}$$

$$R^2 = (x - x')^2 + (y - y')^2 + (z - z')^2, \quad dV' = dx'\, dy'\, dz',$$

where $R = |\boldsymbol{x} - \boldsymbol{x}'|$ is the distance from the volume element dV' to the point of observation. We can write the result briefly as

$$\phi(\boldsymbol{x}, t) = \int \frac{[\rho(\boldsymbol{x}', T)]_{\text{ret}}}{R}\, dV'. \tag{1.35a}$$

It is called the *retarded scalar potential.* $[\rho]_{\text{ret}}$ means that ρ is to be taken at the *retarded time* $T = t - R/c$.

An observer at the field point $\boldsymbol{x}$ is affected at a given time t only by what a source at $\boldsymbol{x}'$ was doing at an earlier time T. Because $t - T = R/c$, the earlier time T precedes the present time t by just the amount of time it takes the information to travel the distance R from the source point $\boldsymbol{x}'$ to the field point $\boldsymbol{x}$, namely R/c.

A retarded potential can be realized in the following way. Let an observer be situated at the point $\boldsymbol{x}$ (Fig. 1.7). Around this point, consider a sphere contracting with a radial velocity c. This news-collecting sphere converges on the point $\boldsymbol{x}$ at the time of observation t. Then this sphere must have passed the source of the electric field $\rho(\boldsymbol{x}')$ at $\boldsymbol{x}'$ at the earlier time $T = t - R/c$. Because $R = |\boldsymbol{x} - \boldsymbol{x}'|$, it is the retarded distance measured at the time of passage of the sphere at the source; $R = R(T) = c(T - t)$, where t is the time of observation.

A similar analysis of (1.18b) gives the *retarded vector potential*

$$\boldsymbol{A}(\boldsymbol{x}, t) = \frac{1}{c}\int_V \frac{\boldsymbol{j}(\boldsymbol{x}', t - |\boldsymbol{x} - \boldsymbol{x}'|/c)}{|\boldsymbol{x} - \boldsymbol{x}'|}\, dV' = \frac{1}{c}\int_V \frac{[\boldsymbol{j}(\boldsymbol{x}', T)]_{\text{ret}}}{R}\, dV' \tag{1.36b}$$

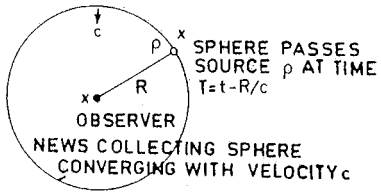

Fig. 1.7. Sphere collecting news for retarded potential at x. The time of observation is t

1.7 Lienard–Wiechert Potentials

Consider a situation in which all parts of a given charge distribution in any small volume element are moving systematically with a velocity $\boldsymbol{v}$ (Fig. 1.8). As the news-collecting sphere shrinks with velocity c, the charge distribution also moves with velocity $\boldsymbol{v}$. Therefore, the amount of charge crossed at the earlier time T by the sphere in time dT is

$$de = [\rho]_{\text{ret}}\, dS dR - [\rho]_{\text{ret}} \frac{\boldsymbol{v} \cdot \boldsymbol{R}}{R}\, dT dS. \tag{1.37}$$

Because $dS dR = dV'$ and $dT = dR/c$,

$$\frac{[\rho]_{\text{ret}}\, dV'}{R} = \frac{de}{s}, \tag{1.38}$$

$$s \equiv \left[R - \frac{\boldsymbol{v} \cdot \boldsymbol{R}}{c}\right]_{t - R/c} = \left[R\left(1 - \frac{\boldsymbol{v} \cdot \boldsymbol{n}}{c}\right)\right]_T.$$

The retarded potentials thus become

$$\phi = \int \frac{de}{s}, \quad \boldsymbol{A} = \frac{1}{c}\int \frac{\boldsymbol{v}\, de}{s}. \tag{1.39}$$

We can use (1.39) to calculate the potentials due to a moving *point* charge. When viewed from a large distance, the moving charge distribution in a small volume element will appear as a point charge. Clearly, in such a limit of a point charge the distance-dependent terms are slowly varying. In (1.39), we can take $1/s$ outside the integral sign and write $\int de = e$ as the known charge of a point electron. Thus,

$$\phi(\boldsymbol{x}, t) = \left[\frac{e}{s}\right]_{\text{ret}}, \quad \boldsymbol{A}(\boldsymbol{x}, t) = \frac{1}{c}\left[\frac{e\boldsymbol{v}}{s}\right]_{\text{ret}}. \tag{1.40}$$

These are called *Lienard–Wiechert potentials* of a single electron. For $\boldsymbol{v} = 0$, (1.40) reduces to $\phi = e/R$, $\boldsymbol{A} = 0$, as expected.

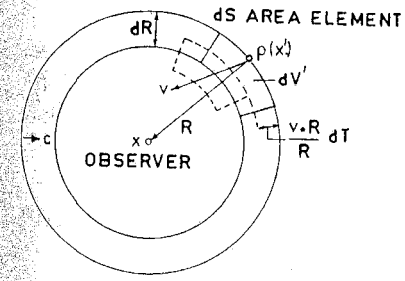

Fig. 1.8. Elements dS of sphere collecting news from the charge distribution in motion with velocity $\boldsymbol{v}$

1.8 Radiation from an Accelerated Charge

The field strengths $\boldsymbol{E}$, $\boldsymbol{H}$ can now be found from (1.40) and (1.15). It is necessary to express the derivatives of ϕ, $\boldsymbol{A}$ with respect to t in terms of the derivatives with respect to T. The retarded time T and the retarded distance R are related by the retardation condition

$$R[\boldsymbol{x}, \boldsymbol{x}'(T)] = f(\boldsymbol{x}, T) = [(x-x')^2 + (y-y')^2 + (z-z')^2]^{1/2} = c(t-T). \tag{1.41}$$

It connects the field- and source-point variables. We can use (1.41) to relate the partial derivative $\partial/\partial t$ to $\partial/\partial T$, keeping the point of observation x, y, z fixed.

Differentiate the identity $R^2 = \boldsymbol{R}\cdot\boldsymbol{R}$. Using $\partial \boldsymbol{R}(T)/\partial T = -\boldsymbol{v}(T)$, as $\boldsymbol{R}$ is from e to $\boldsymbol{x}$,

$$\left(\frac{\partial R}{\partial T}\right)_x = -\frac{\boldsymbol{R}\cdot\boldsymbol{v}}{R}, \tag{1.42}$$

where the suffix $\boldsymbol{x}$ indicates that $\boldsymbol{x}$ is fixed. Now differentiate the relation $R = c(t-T)$ with respect to t,

$$\frac{\partial R}{\partial t} = \frac{\partial R}{\partial T}\frac{\partial T}{\partial t} = -\frac{\boldsymbol{R}\cdot\boldsymbol{v}}{R}\frac{\partial T}{\partial t} = c\left(1 - \frac{\partial T}{\partial t}\right), \tag{1.43}$$

$$\frac{\partial T}{\partial t} = \frac{1}{1 - \boldsymbol{R}\cdot\boldsymbol{v}/Rc} = \frac{R}{s}, \quad \frac{\partial}{\partial t} = \frac{R}{s}\frac{\partial}{\partial T}. \tag{1.44}$$

Similarly, differentiating the same relation with respect to the coordinates and keeping t fixed,

$$\nabla R = (\nabla)_T R + \frac{\partial R}{\partial T}\nabla T = \frac{\boldsymbol{R}}{R} - \frac{\boldsymbol{R}\cdot\boldsymbol{v}}{R}\nabla T = -c\nabla T. \tag{1.45}$$

Here $(\nabla)_T$ represents differentiation with respect to the first argument of the function $f(\boldsymbol{x}, T)$ in (1.41) with T kept fixed, and we have used the rules

$$\left(\frac{\partial f}{\partial x}\right)_t = \left(\frac{\partial f}{\partial x}\right)_{t,T} + \left(\frac{\partial f}{\partial T}\right)_{x,t}\left(\frac{\partial T}{\partial x}\right)_t, \tag{1.46a}$$

$$(\nabla)_T R = \left(\boldsymbol{i}_x\frac{\partial}{\partial x} + \boldsymbol{i}_y\frac{\partial}{\partial y} + \boldsymbol{i}_z\frac{\partial}{\partial z}\right)[(x-x')^2 + (y-y')^2 + (z-z')^2]^{1/2} = \frac{\boldsymbol{R}}{R}. \tag{1.46b}$$

From (1.45)

$$\nabla T = -\frac{\boldsymbol{R}}{cs}, \quad \nabla = (\nabla)_T - \frac{\boldsymbol{R}}{cs}\frac{\partial}{\partial T}. \tag{1.47}$$

These relations transform the differential operators from the coordinates of the field point to those of the moving electron. For $s = R - \boldsymbol{v}\cdot\boldsymbol{R}/c$,

$$\frac{\partial s}{\partial t} = \frac{\partial s}{\partial T}\frac{\partial T}{\partial t} = \left(\frac{\partial R}{\partial T} - \frac{1}{c}\frac{\partial \boldsymbol{R}}{\partial T}\cdot\boldsymbol{v} - \frac{1}{c}\boldsymbol{R}\cdot\frac{\partial \boldsymbol{v}}{\partial T}\right)\frac{R}{s}$$

$$= \left(-\frac{\boldsymbol{R}\cdot\boldsymbol{v}}{R} + \frac{v^2}{c} - \frac{\boldsymbol{R}\cdot\dot{\boldsymbol{v}}}{cs}\right)\frac{\boldsymbol{R}}{s}, \tag{1.48}$$

$$\nabla s = (\nabla)_T\left(R - \frac{\boldsymbol{v}\cdot\boldsymbol{R}}{c}\right) - \frac{\boldsymbol{R}}{cs}\frac{\partial}{\partial T}\left(R - \frac{\boldsymbol{v}\cdot\boldsymbol{R}}{c}\right) = \left(\frac{\boldsymbol{R}}{R} - \frac{\boldsymbol{v}}{c}\right)$$

$$-\frac{\boldsymbol{R}}{cs}\left(-\frac{\boldsymbol{R}\cdot\boldsymbol{v}}{R} + \frac{v^2}{c} - \frac{\boldsymbol{R}\cdot\dot{\boldsymbol{v}}}{c}\right), \tag{1.49}$$

where $\boldsymbol{v}$ depends only on T and $\dot{\boldsymbol{v}} = \partial\boldsymbol{v}/\partial T$. Clearly

$$\frac{\partial \boldsymbol{v}}{\partial t} = \frac{\partial \boldsymbol{v}}{\partial T}\frac{\partial T}{\partial t} = \dot{\boldsymbol{v}}\frac{R}{s}, \tag{1.50}$$

$$\nabla\times\boldsymbol{v} = \left[(\nabla)_T - \frac{\boldsymbol{R}}{cs}\frac{\partial}{\partial T}\right]\times\boldsymbol{v} = -\frac{\boldsymbol{R}\times\dot{\boldsymbol{v}}}{cs}. \tag{1.51}$$

From (1.40) and (1.15), using $\nabla\times(\psi\boldsymbol{B}) = \psi(\nabla\times\boldsymbol{B} + (\nabla\psi)\times\boldsymbol{B}$,

$$\frac{1}{e}\boldsymbol{E} = -\nabla\frac{1}{s} - \frac{1}{c^2}\frac{\partial}{\partial t}\frac{\boldsymbol{v}}{s} = \frac{1}{s^2}\nabla s - \frac{1}{c^2 s}\frac{\partial \boldsymbol{v}}{\partial t} + \frac{\boldsymbol{v}}{c^2 s^2}\frac{\partial s}{\partial t}, \tag{1.52a}$$

$$\frac{1}{e}\boldsymbol{H} = \frac{1}{c}\nabla\times\frac{\boldsymbol{v}}{s} = \frac{1}{cs}\nabla\times\boldsymbol{v} - \frac{1}{cs^2}(\nabla s\times\boldsymbol{v}). \tag{1.52b}$$

Making suitable substitutions, we obtain

$$\frac{1}{e}\boldsymbol{E}(\boldsymbol{x}, t) = \frac{1}{s^2}\frac{1}{R}\left(\boldsymbol{R} - \frac{\boldsymbol{v}R}{c}\right) - \frac{\boldsymbol{R}}{cs^3}\left(-\frac{\boldsymbol{R}\cdot\boldsymbol{v}}{R} + \frac{v^2}{c} - \frac{\boldsymbol{R}\cdot\dot{\boldsymbol{v}}}{c}\right)$$

$$-\frac{1}{c^2 s}\frac{\boldsymbol{R}}{s}\dot{\boldsymbol{v}} + \frac{\boldsymbol{v}}{c^2 s^2}\frac{\boldsymbol{R}}{s}\left(-\frac{\boldsymbol{R}\cdot\boldsymbol{v}}{R} + \frac{v^2}{c} - \frac{\boldsymbol{R}\cdot\dot{\boldsymbol{v}}}{c}\right)$$

$$= \frac{1}{s^3}\left(\boldsymbol{R} - \frac{\boldsymbol{v}R}{c}\right)\left(1 - \frac{v^2}{c^2}\right) - \frac{R - \boldsymbol{v}\cdot\boldsymbol{R}/c}{c^2 s^3}R\dot{\boldsymbol{v}} + \frac{1}{c^2 s^3}\left(\boldsymbol{R} - \frac{\boldsymbol{v}R}{c}\right)\boldsymbol{R}\cdot\dot{\boldsymbol{v}}$$

$$= \frac{1}{s^3}\left(\boldsymbol{R} - \frac{\boldsymbol{v}R}{c}\right)\left(1 - \frac{v^2}{c^2}\right) + \frac{1}{c^2 s^3}\left\{\boldsymbol{R}\times\left[\left(\boldsymbol{R} - \frac{\boldsymbol{v}R}{c}\right)\times\dot{\boldsymbol{v}}\right]\right\}, \tag{1.53a}$$

where in the last step we have combined the two terms that contain $\dot{v}$ by using $A\times(B\times C)=B(A\cdot C)-C(A\cdot B)$. Similarly, from (1.52b),

$$\frac{1}{e}H(x,t)=\nabla\cdot\frac{v}{cs}=\frac{1}{c}\left(\nabla\frac{1}{s}\right)\times v+\frac{1}{cs}(\nabla\times v)$$
$$=-\frac{1}{cs^2}\left\{\left[\left(\frac{R}{R}-\frac{v}{c}\right)-\frac{R}{sc}\left(-\frac{R\cdot v}{R}+\frac{v^2}{c}-\frac{R\cdot\dot{v}}{c}\right)\right]\times v\right\}+\frac{1}{cs}\left(-\frac{R\times\dot{v}}{cs}\right)$$
$$=\frac{v\times R}{cs^3}\left(1-\frac{v^2}{c^2}\right)+\frac{1}{c^2s^3}\frac{R}{R}\times\left\{R\times\left[\left(R-\frac{Rv}{c}\right)\times\dot{v}\right]\right\}=\frac{R\times E}{R}. \tag{1.53b}$$

In (1.53), all quantities on the right side are understood to refer to the retarded time $T=t-R/c$. Clearly, the magnetic field H is perpendicular to E and to the retarded radius vector R.

The fields E and H given by (1.53) are composed of two separate parts. The *velocity fields*, independent of acceleration, vary as $1/R^2$ for large distances and so are nonradiating. The *acceleration fields* depend linearly upon the acceleration $\dot{v}$, vary as $1/R$ for large distances and so give rise to a finite energy flow through any large sphere, i.e., to an *emission of radiation* (*bremsstrahlung*).

1.9 Radiation at Low Velocities

If the charge is accelerated, but its velocity is small, $v/c\ll 1$,

$$R-\frac{v}{c}R\approx R,\quad s=R-\frac{R\cdot v}{c}\approx R. \tag{1.54}$$

If we consider only the radiation fields (E_{rad} and H_{rad}), which vary as $1/R$,

$$\frac{1}{e}E_{\text{rad}}=\frac{1}{c^2s^3}\left\{R\times\left[\left(R-\frac{vR}{c}\right)\times\dot{v}\right]\right\}\approx\frac{1}{c^2R^3}[R\times(R\times\dot{v})], \tag{1.55}$$

$$\frac{1}{e}H_{\text{rad}}=\frac{1}{c^2s^3}\frac{R}{R}\times\left\{R\times\left[\left(R-\frac{vR}{c}\right)\times\dot{v}\right]\right\}\approx\frac{1}{c^2R^4}\{R\times[R\times(R\times\dot{v})]\}$$
$$=\frac{1}{c^2R^4}\{R\times[(R\cdot\dot{v})R-(R\cdot R)\dot{v}]\}=\frac{1}{c^2R^4}(-R\times\dot{v}R^2)$$
$$=\frac{1}{c^2R^2}(\dot{v}\times R). \tag{1.56}$$

Clearly, as in (1.8),

$$|E_{\text{rad}}|=\frac{e}{c^2R^3}|R\times(R\times\dot{v})|=\frac{e}{c^2R^3}|R||R\times\dot{v}|\sin\frac{\pi}{2}$$
$$=\frac{e}{c^2R}\dot{v}\sin\Theta=|H_{\text{rad}}|\quad(v/c\ll 1), \tag{1.57}$$

where Θ is the angle between R and $\dot{v}$ (Fig. 1.9a). Here E is expressed in electrostatic and H in electromagnetic units to preserve the symmetry of our expression. We shall drop the suffix "rad" in the future. Vectors E and H are perpendicular to each other and both are perpendicular to R. The vector E lies in the plane of $\dot{v}$ and R, (1.55). In other words, the radiation is *polarized* in the plane of emission that contains $\dot{v}$ and R. If it is the xy plane (Fig. 1.9b), then $E_\Theta=(e\dot{v}/c^2R)\sin\Theta$, $E_r=E_z=0$, and $H_z=(e\dot{v}/c^2R)\sin\Theta$, $H_r=H_\Theta=0$. Equation (1.57) shows that E vanishes for $\Theta=0$ and has its maximum value for $\Theta=\pi/2$, when $v/c\lesssim 1/10$ (low velocity).

The intensity $I(\Theta)$ of this radiation is given by the magnitude of the Poynting vector[1] S

$$I(\Theta)=|S|=\frac{c}{4\pi}|E\times H|=\frac{c}{4\pi}E^2=\frac{e^2}{4\pi c^3R^2}\dot{v}^2\sin^2\Theta,\quad v/c\ll 1. \tag{1.58}$$

Equation (1.58) gives the well-known $\sin^2\Theta$ angular distribution shown in Fig. 1.10. A three-dimensional model of the distribution would look like a fat

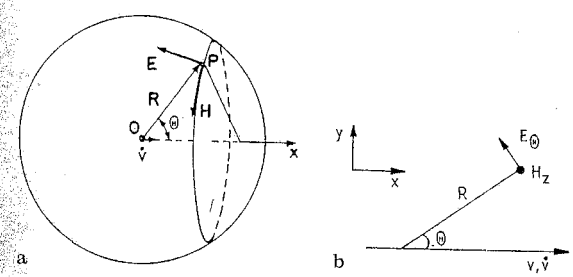

Fig. 1.9. **a** Radiation field at P due to an accelerated positive charge at 0. E is perpendicular to R and lies in the plane of $\dot{v}$ and R. H is normal to the plane of $\dot{v}$ and R. **b** Radiation is polarized in the xy plane containing $\dot{v}$ and R

[1] Multiply (1.14c) by E and (1.14a) by H and combine the results to get

$$\frac{1}{e}E\cdot\frac{\partial E}{\partial t}+\frac{1}{c}H\cdot\frac{\partial H}{\partial t}=-\frac{4\pi}{c}j\cdot E-[H\cdot(\nabla\times E)-E\cdot(\nabla\times H)]$$

Using $\nabla\cdot(A\times B)=B\cdot(\nabla\times A)-A\cdot(\nabla\times B)$,

$$\frac{\partial}{\partial t}\left(\frac{E^2+H^2}{8\pi}\right)=-j\cdot E-\frac{c}{4\pi}\nabla\cdot(E\times H).$$

The vector $S=(c/4\pi)E\times H$ is called the *Poynting vector*. Comparison with the equation of continuity suggests that $(E^2+H^2)/8\pi=E^2/4\pi$ is the energy per unit volume or *energy density*. Consequently, $(c/4\pi)E^2$ represents the energy that passes normally through unit area in unit time. Because $|S|=(c/4\pi)E^2$, it represents the *intensity* of the radiation at the instant under consideration.

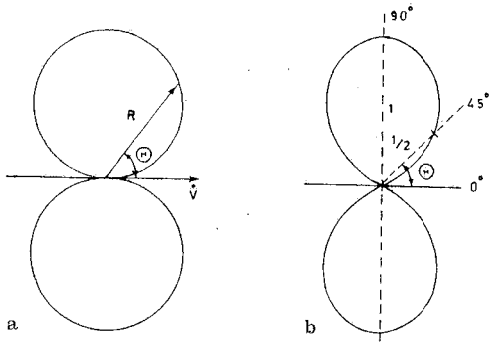

Fig. 1.10a, b. Angular distribution of radiation of an electron, $v \ll c$: **a** $E \propto \sin\Theta$; **b** $I(\Theta) \propto \sin^2\Theta$

tire with its axis parallel to $\dot{v}$. The rate at which an electron loses energy by radiation is obtained by integrating over a spherical surface around the electron. This is the *power*, or energy per unit time,

$$-\frac{dU}{dT}=P=\int_0^{\pi} I(\Theta)\cdot 2\pi R\sin\Theta\cdot R d\Theta$$

$$=\frac{e^2\dot{v}^2}{2c^3}\int_0^{\pi}\sin^3\Theta d\Theta=\frac{2}{3}\frac{e^2\dot{v}^2}{c^3} \quad \text{(in Gaussian units).} \tag{1.59}$$

This is called *Larmor's formula* for a nonrelativistic accelerated charge.

It is often useful to express (1.59) in terms of *electric dipole moment* instead of the electric charge of an electron. If an atom is neutral when the accelerated electron is at $x=0$, a dipole moment $D=ex$ is created when the electron moves to x. We can write $e\dot{v}=ed^2x/dt^2=\ddot{D}$. Then

$$E=H=\frac{\ddot{D}}{rc^2}\sin\Theta, \quad P=\frac{2}{3c^3}\ddot{D}^2. \tag{1.60}$$

1.10 Polarization of Continuous X-Rays

Polarization of X-rays was first demonstrated by *Barkla* [1.2]. The primary X-ray beam from the X-ray tube was scattered by a scattering block of graphite (Fig. 1.11). The scattered intensity of the X-ray beam was measured in two mutually perpendicular directions. The X-ray tube was first placed so that the flow of electrons in the tube was parallel to the x axis. Denoting the scattered intensity of the X-ray beam in a parallel direction to the tube axis by $I^s_{\parallel}$ (ionization in detector 1) and that at right angles (detector 2) by $I^s_{\perp}$, we can define the degree of the polarization for X-rays emitted at an angle Θ to the electron direction by

$$P_{\text{pol}(\Theta)}=\frac{I^s_{\perp}-I^s_{\parallel}}{I^s_{\perp}+I^s_{\parallel}}=\frac{I_{\parallel}-I_{\perp}}{I_{\parallel}+I_{\perp}}. \tag{1.61}$$

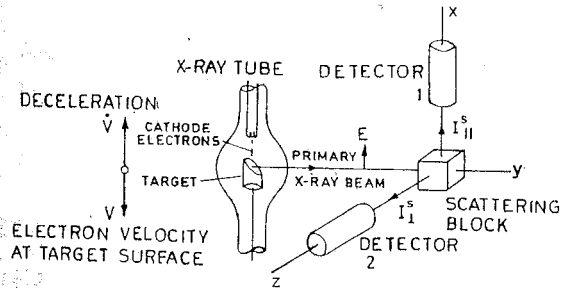

Fig. 1.11. Barkla's experiment for detecting polarization of primary X-rays ($\Theta=90°$)

Here $I_{\parallel}(I_{\perp})$ is the intensity of primary X-rays, emitted at an angle Θ, and polarized with electric vector parallel (perpendicular) to the plane of emission. Barkla found that $I_{\perp}$ was greater than $I_{\parallel}$ by about 20% for $\Theta=90°$. The same result was obtained with the tube axis parallel to x. Thus the primary beam was partly polarized. This proved that X-rays were transverse electromagnetic waves.

If the deceleration $\dot{v}$ of the electron inside the target is parallel to the x axis then the resulting primary X-ray beam at $\Theta=90°$ should be completely polarized with electric vector $\boldsymbol{E}$ parallel to the x axis. The electron bound to an atom in the scattering block will move with acceleration $\boldsymbol{a}$ in the same direction

$$\boldsymbol{a}=\frac{\text{Force}}{\text{mass}}=\frac{e\boldsymbol{E}}{m}. \tag{1.62}$$

This accelerated electron will in turn radiate a transverse electromagnetic wave (X-rays) according to (1.60), which at the point of observation P will be

$$E_p=\frac{e|\boldsymbol{a}|}{c^2R}\sin\Theta=\frac{e^2|\boldsymbol{E}|}{mc^2R}\sin\Theta=\begin{cases}0 & \text{for } \Theta=0,\\ e^2E/mc^2R & \text{for } \Theta=\pi/2.\end{cases} \tag{1.63}$$

Therefore, Barkla should have recorded $I^s_{\parallel}=0$, giving $P_{\text{pol}}=100\%$. The fact that he got $I^s_{\parallel}\neq 0$ and only $I^s_{\parallel}<I^s_{\perp}$ shows that some of the primary radiation is due to electrons that are not being decelerated parallel to the x axis in the thick target. After one collision with the target atom, the direction of $\dot{v}$ for the cathode electron changes. We can expect complete polarization for a very thin target in which the electrons do not have their direction of motion altered before they suffer a collision, resulting in deceleration and accompanying radiation. Thin aluminium foil targets in the X-ray tube have been used by *Kulenkampff* [1.3]. They have shown a strong polarization of primary X-rays in the predicted plane. *Dasannacharya* [1.4] extended this work for several thicknesses of Al foils and different tube voltages.

1.11 The Case of $\dot{v}$ Parallel to v (Relativistic)

This case is of special interest for the theory of the production of continuous X-rays. If $\dot{v}$ and v are along the *same* direction, $v \times \dot{v} = 0$, then for any v, small or large, the radiation fields are

$$E = \frac{e}{c^2 s^3}[R \times (R \times \dot{v})], \quad H = \frac{eR}{c^2 s^3}(\dot{v} \times R). \tag{1.64}$$

These results differ from (1.55, 56) only by the factor

$$\frac{R^3}{s^3} = \frac{R^3}{(R - R \cdot v/c)^3} = \frac{1}{\left(1 - \frac{v}{c}\cos\Theta\right)^3}, \tag{1.65}$$

where Θ is the angle between R and the common direction of $\dot{v}$ and v. The effect of this relativistic weighting factor due to retardation of the electromagnetic potential is to increase the radiation in the forward direction (Fig. 1.12). The lobes of Fig. 1.10 are tilted in the direction of v. From (1.57, 65),

$$E = H = \frac{R^3}{s^3}\frac{e\dot{v}}{c^2 R}\sin\Theta = \frac{e\dot{v}}{c^2 R}\frac{\sin\Theta}{(1-\beta\cos\Theta)^3}. \tag{1.66}$$

The corresponding instantaneous intensity for one decelerated electron is

$$I(\Theta) = \frac{c}{4\pi}E^2 = \frac{e^2\dot{v}^2}{4\pi c^3 R^2}\frac{\sin^2\Theta}{(1-\beta\cos\Theta)^6}. \tag{1.67}$$

For $v/c \ll 1$, it reduces to (1.58). The direction Θ_{max} of the propagation of the greatest intensity is determined by the condition $dI/d\Theta = 0$:

$$\Theta_{max} = \cos^{-1}\left[\frac{1}{4\beta}\sqrt{1+24\beta^2} - 1\right] \to \frac{1}{2\gamma}, \tag{1.68}$$

where the last form is the limiting value for $\beta \to 1$.

1.12 Sommerfeld's Theory for the Spatial Distribution of Continuous X-Rays

The incident electrons will be stopped by a succession of collisions with the target atoms in an X-ray tube. Each collision results in deceleration of the

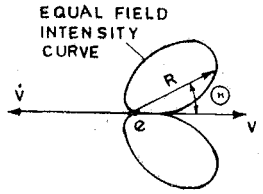

Fig. 1.12. Radiation pattern for a fast electron decelerated along its line of motion

electron and so emission of radiation. If the target is thick, such multiple collisions deflect the electrons irregularly. *Stokes* [1.5] assumed that continuous X-rays are produced in irregular electromagnetic pulses due to the irregular decelerations of the electrons in the target. *Thomson* [1.6] for purpose of calculation simply assumed that the cathode electron is brought to *rest* within a very short distance inside the target by a *uniform deceleration along its original line of motion.*

Sommerfeld [1.7] used Thomson's assumption to calculate the total radiated energy traversing unit area at the point of observation P, due to stopping of the electron:

$$I_{tot}(\Theta) = \int I(\Theta)dt.$$

The integration is over the entire time of the radiation pulse, that is, until the electron comes to rest. I is given by (1.67). If t is the observer time at which the radiation reaches P, which left the electron at the instant T, then $t = T + R/c$ and $dt = dT + dR/c$. From Fig. 1.13, $dR = -v dT\cos\Theta$ and so $dt = (1 - \beta\cos\Theta)dT = (1 - \beta\cos\Theta)dv/\dot{v}$. Then

$$I_{tot}(\Theta) = \int I(\Theta)dt = \int I(\Theta)(1-\beta\cos\Theta)\frac{cd\beta}{\dot{v}}$$

$$= \int \frac{e^2\dot{v}^2}{4\pi c^3 R^2}\frac{\sin^2\Theta}{(1-\beta\cos\Theta)^6}(1-\beta\cos\Theta)\frac{cd\beta}{\dot{v}}. \tag{1.69}$$

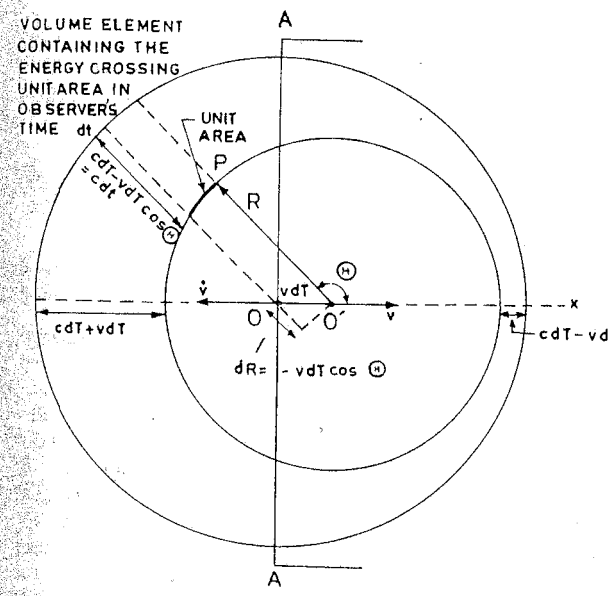

Fig. 1.13. Location of energy radiated by an electron incident on a target AA, as the electron moves from 0 to 0′ in time dT

The integral over dv (i.e. $cd\beta$) extends from the initial velocity $v_0 = c\beta_0$ of the electron to the final zero velocity. Assume that $\dot{v}$ is constant while the velocity decreases from v_0 to 0, then (as T increases, v decreases)

$$I_{\text{tot}}(\Theta) = \frac{e^2\dot{v}\sin^2\Theta}{4\pi c^3 R^2}\int_0^{\beta_0}\frac{c\,d\beta}{(1-\beta\cos\Theta)^5}$$

$$= \frac{e^2\dot{v}\sin^2\Theta}{16\pi c^2 R^2\cos\Theta}\left(\frac{1}{(1-\beta_0\cos\Theta)^4}-1\right), \tag{1.70}$$

$$I_{\text{tot}}(\Theta) = \frac{e^2\dot{v}\sin^2\Theta}{4\pi c^3 R^2}\int_0^{\beta_0} c\,d\beta = \frac{e^2\dot{v}v_0}{4\pi c^3 R^2}\sin^2\Theta, \quad \textit{small } \beta. \tag{1.71}$$

Thus, the classical theory predicts the energy-distribution polar diagram for radiation. In Fig. 1.14 we plot the intensity as a function of angle Θ, according to (1.70), for three values of v_0/c. The movement of the direction of maximum intensity toward the direction of incident-electron velocity (forward direction) with the increase of the incident velocity is easily seen. An X-ray tube is like a low-velocity linear accelerator ($v_0/c \lesssim 1/3$). For a high-velocity accelerator ($v_0/c \sim 1$), the radiation is confined to a very narrow cone in the direction of the motion (dotted curve in Fig. 1.14).

Sommerfeld's condition, that the bombarding electrons are decelerated along the direction of incident motion, is likely to be satisfied in two cases: 1) extremely thin target, and 2) thick target of very low atomic number.

The radiation loss from the electron while it is being accelerated between the cathode and the target of the X-ray tube is negligible, because this acceleration over a large distance is very slow in comparison with the rapid deceleration inside the solid target. From (1.59), for an *accelerated* electron

$$P = \frac{2}{3}\frac{e^2}{m^2c^3}\left(\frac{dp}{dt}\right)^2 = \frac{2}{3}\frac{e^2}{m^2c^3}\left(\frac{dE}{dx}\right)^2, \tag{1.72}$$

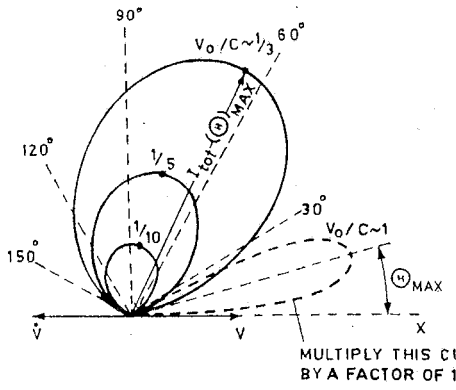

Fig. 1.14. Theoretical radiation pattern for an electron decelerated in its direction of motion, when the detector is placed at a given distance R. The solid dot represents the direction of maximum intensity $I_{\text{tot}}(\Theta)_{(\max)}$. The dashed curve is for $v_0/c \sim 1$ and has been reduced by a factor of about 100 for convenience. $v_0/c = 1/3$ corresponds to about 30 keV kinetic energy of the electron

where $p = mv$ and the rate of change of momentum is equal to the change of energy E of the particle per unit distance, dE/dx. The ratio of power radiated to power supplied by the tube voltage is

$$\frac{P}{dE/dt} = \frac{2}{3}\frac{e^2}{m^2c^3}\frac{1}{v}\frac{dE}{dx} \xrightarrow[\beta\to 1]{} \frac{2}{3}\frac{e^2/mc^2}{mc^2}\frac{dE}{dx}. \tag{1.73}$$

Thus, the radiation loss will be unimportant unless the gain of energy is of the order of $mc^2 = 0.51$ MeV in a distance of $e^2/mc^2 = 2.8\times10^{-13}$ cm, or $\sim 2\times10^{15}$ keV cm^{-1}. In an X-ray tube, the distance between the filament and the target is of the order of a centimetre and $V \sim 20$ kV. Therefore, radiation loss is negligible compared to the energy gain of the electron accelerated in the direction of and by the electric field eV. In the target, owing to rapid deceleration in collisions, dE/dx has a large value, which increases with Z. For circular accelerators, like the synchrotron, the radiation loss is greater. The Sommerfeld theory has been put in a useful form by *Weinstock* [1.8], *Scheer* and *Zeitler* [1.9] and *Kulenkampff* [1.10].

For the X-ray production the final velocity not zero but, say, β_1 in (1.70). Using the average value $\beta = (\beta_0+\beta_1)/2$, *Sommerfeld* [1.11] writes $I_\nu(\Theta) \propto \sin^2\Theta/(1-\beta\cos\Theta)^4$. The condition $dI/d\Theta = 0$ gives

$$\cos\Theta_{\text{m}} = \frac{1}{2\beta}[(1+8\beta^2)^{1/2}-1] \xrightarrow[v\ll c]{} 2\beta.$$

It is observed that Θ_{m} decreases with increasing energy [1.12].

1.13 Frequency Spectrum of Continuous X-Rays

The radiated energy is spread over a range of frequencies. This frequency spectrum can be obtained by Fourier analysis of the radiation field.

The radiation takes place when the incident electron suddenly changes its direction during a collision with one of the atoms in the target. Assume zero collision time and $v \ll c$. Then we can write the resulting acceleration and field as

$$\dot{v} = \delta(t_0 - t)\Delta v, \quad \int \dot{v}\,dt = \Delta v, \tag{1.74}$$

$$E(t) = \frac{e\sin\Theta}{c^2 R}\Delta v\,\delta(t_0 - t), \tag{1.75}$$

where t_0 is the instant at which the radiation takes place. In (1.75), the instantaneous field is expressed in the observer's time because we wish to consider a frequency spectrum in terms of the observer's frequencies ω.

Introduce the Fourier transform

$$E(t) = \int_0^{+\infty} E(\omega)e^{-i\omega t}d\omega, \tag{1.76}$$

where ω is the angular frequency, $\omega = 2\pi\nu$. It is customary to integrate only over

positive frequencies, because the sign of the frequency has no physical meaning. The inverse is

$$E(\omega)=\frac{1}{\pi}\int_{-\infty}^{+\infty}E(t)e^{i\omega t}dt. \tag{1.77}$$

From (1.75, 77),

$$E(\omega)=\frac{e\sin\Theta}{\pi c^2 R}\Delta v\, e^{i\omega t_0}. \tag{1.78}$$

The total energy radiated is given by the integral of the Poynting vector over the surface of a sphere and over the time during which the change of velocity takes place. For $v \ll c$

$$-U=\int\left(-\frac{dU}{dT}\right)dT=\frac{c}{4\pi}\int\int E^2\,dt d\sigma. \tag{1.79}$$

By Parseval's formula[2]

$$\int_{-\infty}^{+\infty}|E|^2\,dt=\pi\int_0^{\infty}|E(\omega)|^2 d\omega. \tag{1.80}$$

Therefore, for the energy radiated in a frequency interval $d\omega$,

$$\begin{aligned}-U(\omega)d\omega&=\pi\frac{c}{4\pi}\int_\sigma|E(\omega)|^2 d\sigma d\omega\\&=\frac{e^2(\Delta v)^2}{4\pi^2c^3R^2}d\omega\int_0^{2\pi}d\Phi\int_0^{\pi}\sin^2\Theta R^2\sin\Theta d\Theta=\frac{4e^2}{3c}\left(\frac{\Delta v}{c}\right)^2\frac{d\omega}{2\pi}.\end{aligned} \tag{1.81}$$

Equation (1.81) shows that the spectrum of radiation is independent of frequency ω (Fig. 1.15). The spectrum extends to high ω values, owing to the simplifying assumption of zero collision time. A Fourier analysis of a finite-collision-time process will damp the very-high-frequency components but *not* abruptly, as observed (see below).

---

[2] Parseval's formula is

$$\pi\int_0^{\infty}|g(\omega)|^2 d\omega=\int_{-\infty}^{+\infty}|f(t)|^2 dt, \quad \text{where}$$

$$f(t)=\int_0^{+\infty}g(\omega)e^{-i\omega t}d\omega, \quad g(\omega)=\frac{1}{\pi}\int_{-\infty}^{+\infty}f(t)e^{i\omega t}dt.$$

Proof:

$$\int_0^{+\infty}|g(\omega)|^2 d\omega=\int_0^{\infty}g^*(\omega)g(\omega)d\omega=\int_0^{+\infty}g^*(\omega)\frac{1}{\pi}\int_{-\infty}^{+\infty}f(t)e^{i\omega t}d\omega dt,$$

$$\int_{-\infty}^{+\infty}|f(t)|^2 dt=\int_{-\infty}^{+\infty}f(t)\int_0^{\infty}g^*(\omega)e^{i\omega t}d\omega dt=\pi\int_0^{\infty}|g(\omega)|^2 d\omega. \quad \text{QED}$$

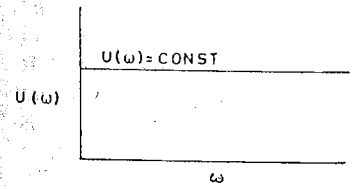

Fig. 1.15. Frequency spectrum of continuous X-rays, according to the classical theory

1.14 Experimental Spectral and Spatial Distributions

Nicholas [1.13] studied the spectral distribution of continuous X-rays from thin-foil targets. Foils were ^{13}Al 0.7 μm thick and ^{79}Au 0.99 μm thick. The voltage on the X-ray tube was 45 kV and angles were 40°, 90°, and 140° to the forward direction of the incident electrons. His results are shown in Fig. 1.16. The data are in agreement with the classical theory (Fig. 1.15). A new feature is the appearance of a *cutoff* at a frequency ν_{max} for a given voltage on the X-ray tube, which is not predicted by the classical theory.

The spectral and spatial distributions from thin foils have also been studied by *Kulenkampff* [1.3], *Bohm* [1.14], *Honerjäger* [1.15], and *Harworth* and *Kirkpatrick* [1.16]. *Kulenkampff* and *Bohm* used 0.6 μm (6000 Å) thick foil of ^{13}Al as target. *Honerjäger* used thinner ^{13}Al foils (100, 350 and 1000 Å) and ^{28}Ni foil of 150 Å thickness. *Harworth* and *Kirkpatrick* used 199 Å thick Ni foil. As the radiation from such thin foils is very weak, it is not possible to obtain reliable analysis of the spectrum with a crystal. These workers used selective absorbers to select out portions of the spectrum, and used ionization chambers as detectors. The Ross balanced-filter technique can be used to isolate portions of the spectrum. Ag-Pd metal sheets pass a band of 485 to 508 XU and Se-As pair of powdered metals pass the band 979–1044 XU. Note that 1 kXU = 1000 XU = 1.00208 Å.

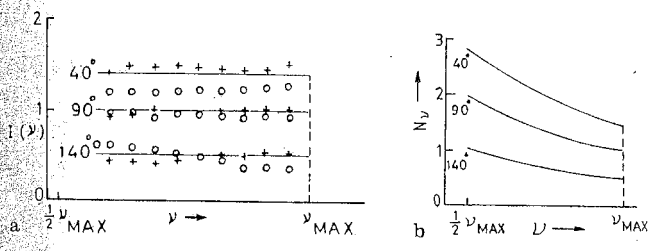

Fig. 1.16a,b. Thin-target spectra at different angles. o Al and + Au data are not on the same scale of intensity. **a** Intensity $I(\nu)$ in ergs per frequency interval ($h\nu \times$ no. of photons) is constant for all photon energies. **b** The number of photons per frequency interval N_ν varies as $1/h\nu$ when derived from **a**

In 1955, *Kerscher* and *Kulenkampff* [1.17] studied the spectral and spatial distribution of the intensity of the continuous spectrum from an ^{13}Al foil of thickness 250 Å for 34 keV electrons. Their apparatus is shown in Fig. 1.17. It consists of a flat, brass vacuum chamber placed between the poles of an electromagnet (not shown). The cathode C emits an electron beam that is accelerated by a voltage of 34 kV, exits through the slit S and moves along a circle that passes through the diaphragm D and the foil F under study. Finally, the electron beam is collected by the electrode E placed at the end of a curved leg so as to isolate the X-rays that may be emitted by it. The detector for the X-rays emitted by the foil F is a proportional counter that moves along an arc that extends from $-5°$ to $+185°$. X-rays from F come out of the box from a long slot on one side of the chamber to fall on the counter. The slot is covered by an Al foil to maintain the vacuum. The proportional counter, used with a single-channel pulse-height analyzer, measures the intensity (number of photons) as well as the energy (frequency) of the X-rays received by it. *Boersch* et al. [1.18] used a different setup.

The measured distribution of intensity along the spectrum is given in Fig. 1.18. These straight lines were obtained at various angles Θ to the forward direction of the bombarding electrons. The slopes of the lines nearly agree with the results of *Nicholas* in the range $40° < \Theta < 140°$. Outisde of this range, especially at smaller angles, the lines become slanting.

Kerscher and *Kulenkampff* obtained angular distribution (shape function) curves from Fig. 1.18 by reading intensities at chosen values of $\nu = \nu_{max}$, $0.7\ \nu_{max}$ and $0.4\ \nu_{max}$. The resulting curves are shown in Fig. 1.19 and are in agreement

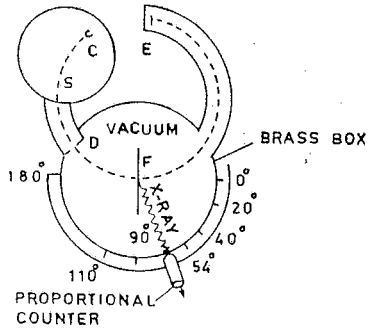

Fig. 1.17. Apparatus for the study of continuous X-ray spectrum of thin foils

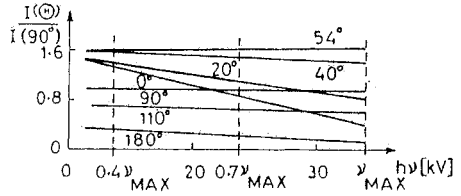

Fig. 1.18. The distribution of spectral intensity for 250 Å Al foil at $V = 34$ kV for various angles Θ

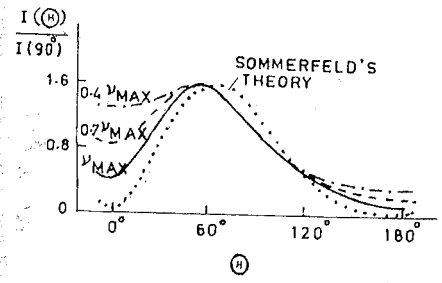

Fig. 1.19. Angular distribution (shape function) from the observed spectral distribution curves at various angles shown in Fig. 1.18. The theoretical curve (dotted) is according to (1.70)

with the results of *Honerjäger* [1.15]. These curves can also be drawn on a polar diagram, as shown in Fig. 1.20. Experiments at higher energies (45–170 kV) have been made by *Thordarson* [1.19] and *Sesemann* [1.12]. In their experiments, the transmission target formed the window in the X-ray tube and the intensity of continuous radiation transmitted through the target was easily observed, down to $\Theta = 0°$. Such a transmission target approaches a thin target in its effect.

Measurements on a thick target of ^4Be have been made by *Determann* [1.20] at a voltage $V = 140$ kV. His results (Fig. 1.21) show that even for such a light element as beryllium the distribution of intensity is nearly the same in all directions. In particular, the intensity at $\Theta = 0$ is not only not zero, as theoretically predicted by *Sommerfeld*, but even exceeds the intensity at 90° and is only a little less than the maximum intensity.

Note that the mean depth of X-ray production inside a solid target is of the order of 10^4 Å [1.21].

1.15 Shortcomings of Classical Theory

There is a strong resemblance between the theoretical curves of Fig. 1.14 and experimental curves of Fig. 1.20. However, there are significant differences that cannot be ignored, see Table 1.1.

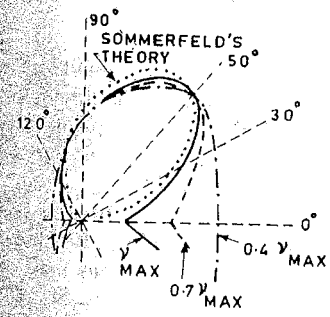

Fig. 1.20. Intensity as a function of direction in polar coordinates. The theoretical curve (dotted) is according to (1.70)

Table 1.1.

Classical theory	Experimental data	Remarks
1) Θ_{max} is $\sim 65°$ for $\frac{v}{c} \sim \frac{1}{3}$ (Fig. 1.14)	Θ_{max} is $\sim 55°$ for $\frac{v}{c} \sim \frac{1}{3}$ for thin targets (Fig. 1.20)	*Sommerfeld* assumed that the electrons are brought completely to rest in the target, whereas, in thin targets, the electrons are not greatly retarded while passing through them
2) Intensity is zero at $\Theta = 0°$ and $\Theta_4 = 180°$ (Fig. 1.14) for all frequencies	Intensity is not zero at $\Theta = 0°$, and $\Theta = 180°$ (Figs. 1.20, 21). For thin targets, the intensity at $\Theta = 0°$ is minimum for the cutoff frequency ν_{max} and increases for lower frequencies. For thick targets, intensity is almost as great at $\Theta = 0°$ as at $\Theta = 90°$	*Sommerfeld* assumed that the electrons are decelerated in the direction of motion. It appears that not all electrons do so and that some transverse motion takes place owing to collisions with the target atoms. Such transverse motions are least likely to occur in the first few atomic layers of the target from where the radiation near the ν_{max} is emitted. As electrons enter deeper in the target, they emit radiation of lower frequencies and also are more and more deflected
3) Polarization should be complete in the plane of the incident electron beam	Polarization is partial	All electrons are not decelerated in the direction of motion, as assumed by *Sommerfeld*
4) No sharp high-frequency limit is predicted	There is a sharp high-frequency limit, ν_{max}, determined by the voltage V on the X-ray tube	Quantum theory is needed to explain this cutoff frequency in a natural way. The maximum energy that an electron can give up is eV. When all of it is converted into a quantum of radiation energy, we get $eV = h\nu_{max}$, where h is Planck's constant

It is clear from Table 1.1 that the classical theory can give only qualitative agreement with experiment, in respect to low-frequency spectral distribution, spatial distribution and polarization. However, it utterly fails to explain the observed cutoff frequency ν_{max}. So, there is a conflict; to resolve it we must move out of the classical theory and use quantum ideas.

When an electron is deflected from its path or has its velocity changed, it emits radiation with amplitude proportional to its acceleration ($\dot{v}$). Because $m\dot{v} = Ze^2/r^2$, the acceleration of an electron produced by a nucleus eZ is proportional to e^2Z/m. The intensity is proportional to ($e \times$ amplitude)^2, that is,

e^6Z^2/m^2. Thus the total bremsstrahlung per atom varies as Z^2 and as $1/m^2$. It is a million times weaker for incident protons than for electrons. In individual deflection by a nucleus, the incident electron can radiate any amount of energy from zero up to its total kinetic energy $mv^2/2 = eV$, or $h\nu_{max} = eV$. These observed features have been used to develop a quantum theory of bremsstrahlung.

1.16 Kramers' Semiclassical Theory

A semiclassical quantum theory of the continuous spectrum was developed by *Kramers* [1.22] and by *Wentzel* [1.23]. *Kramers* first considered a classical theory of bremsstrahlung in nonrelativistic Coulomb collisions, then, using the Bohr correspondence principle, he introduced quantum theory into the calculation.

At low electron energies ($v/c \sim 1/3$) Sommerfeld's equation (1.70) gives the approximate intensity of soft (low-energy) X-rays, if empirical values of $\dot{v}$ are substituted. Single collisions between particles of like e/m do not produce dipole radiation[3] (1.60). Quadrupole radiation is possible but is weak. Therefore, for very low energies, where electron-electron collisions predominate, the radiation is due to the collective effects of the atomic electrons in retarding the incident electron. At higher energies, and particularly for heavy targets, the radiation is due to the deflection (and so deceleration) of the incident electron in the Coulomb field of a nucleus. For such electron collisions with nuclei, dipole radiation is possible. The contribution mainly comes from single collisions. The loss of electron kinetic energy due to the radiation is so small that it does not affect the electron trajectory.

As a model for this single-collision process, *Kramers* considered the collision of an electron of charge e, mass m, and velocity v with a fixed nucleus of point charge Ze. Let d_0 be the impact parameter and $\pi - 2\phi_0$ the angle of scattering (Fig. 1.22). The electron will describe a hyperbolic orbit with the nucleus at one of the foci such that (see Appendix A)

$$\tan \phi_0 = \frac{md_0v^2}{Ze^2} \tag{1.82}$$

[3] Consider a system of two charged particles. Uniform motion of the system as a whole (motion of center of mass) does not lead to radiation. Therefore, consider only the relative motion of the particles. Let the center of mass be the origin. Then the dipole moment of the system $\boldsymbol{D} = e_1\boldsymbol{r}_1 + e_2\boldsymbol{r}_2$ has the form

$$\boldsymbol{D} = \frac{e_1m_2 - e_2m_1}{m_1 + m_2}\boldsymbol{r} = \mu\left(\frac{e_1}{m_1} - \frac{e_2}{m_2}\right)\boldsymbol{r},$$

where $\boldsymbol{r} = \boldsymbol{r}_1 - \boldsymbol{r}_2$ and $\mu = m_1m_2/(m_1 + m_2)$.

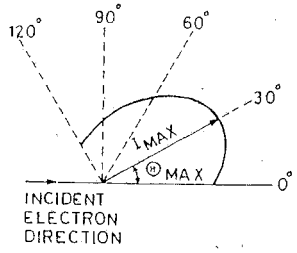

Fig. 1.21. Spatial distribution of $I_{tot}(\Theta)$ of continuous X-rays from a thick ^{4}Be target at $V = 140$ kV

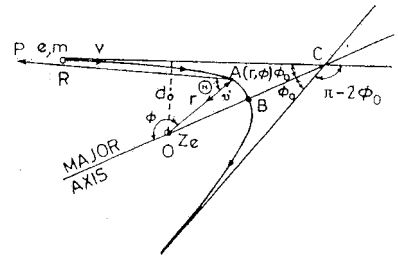

Fig. 1.22. The deflection of an electron along a parabolic path in the Coulomb field of the nucleus Ze. The impact parameter is d_0

The deflection of the electron in the Coulomb field of the nucleus will always imply an accelerated motion and hence a possibility of radiaton.

If ε is the eccentricity and r, ϕ the polar coordinates of any point A on the orbit, we have for an attractive potential

$$\frac{1}{r} = \frac{1-\varepsilon\cos\phi}{d_0\tan\phi_0} = \frac{1-\varepsilon\cos\phi}{d_0^2 v^2}\frac{Ze^2}{m}, \quad \varepsilon = \frac{1}{\cos\phi_0}, \tag{1.83}$$

where all the angles are measured from the major axis. Also

$$\dot{v} = \frac{dv(T)}{dT} = \frac{Ze^2}{mr^2}, \tag{1.84}$$

$$mr^2\dot{\phi} = d_0 mv = \text{constant (angular momentum is conserved)}, \tag{1.85}$$

$$dU = \frac{2e^2}{3c^3}\dot{v}^2\,dT \quad \text{[from (1.59)]}. \tag{1.86}$$

The total loss of energy is found by integrating (1.86) over the time. Using $r^2 d\phi = d_0 v dT$ one integrates over the directions of the outgoing electron,

$$\begin{aligned} U &= \int_{-\infty}^{+\infty}\frac{2e^2}{3c^3}\dot{v}^2\,dT = \frac{2Z^2e^6}{3c^3m^2}\int_{-\infty}^{+\infty}\frac{dT}{r^4} = \frac{2Z^2e^6}{3c^3m^2 d_0 v}\int_{\phi_0}^{2\pi-\phi_0}\frac{d\phi}{r^2} \\ &= \frac{2Z^4e^{10}}{3c^3m^4d_0^5v^5}\int_{\phi_0}^{2\pi-\phi_0}(1-\varepsilon\cos\phi)^2\,d\phi \\ &= \frac{2Z^4e^{10}}{3c^3m^4d_0^5v^5}[(2\pi-2\phi_0)(1+1/2\cos^2\phi_0)+3\tan\phi_0], \end{aligned} \tag{1.87}$$

where in the last step we have used $\varepsilon = 1/\cos\phi_0$.

If d_0 is large, ϕ_0 is large and the angle of scattering (deflection from the original direction) $\pi - 2\phi_0$ is small. For d_0 larger than the radius of the electron cloud of the atom, the deflection of the incident electron is negligible and hence

no radiation is emitted. We would therefore be interested in the case of small d_0 or *small* ϕ_0. For this case (1.87) reduces to

$$U \simeq \frac{2Z^4e^{10}}{3c^3m^4d_0^5v^5}[3\pi] = \frac{2\pi Z^4e^{10}}{c^3m^4d_0^5v^5}, \tag{1.88}$$

and

$$\varepsilon = \frac{1}{\cos\phi_0} \simeq 1 \quad \text{(orbit is a parabola)}. \tag{1.89}$$

The acceleration of the electron, $\dot{v}$, can be resolved into a component $\dot{v}_{\parallel} = -\dot{v}\cos\phi$ parallel to the axis of the parabola and a component $\dot{v}_{\perp} = -\dot{v}\sin\phi$ perpendicular to the axis.

To simplify further discussion we reduce the problem to a particular parabola for which

$$d_0 v = 1, \quad \frac{Ze^2}{m} = 1 \quad \text{and so} \quad U = \frac{2\pi e^2}{c^3}. \tag{1.90}$$

To obtain the spectral distribution, we recall, (1.60), that the energy of the electromagnetic radiation can be expressed in terms of the dipole moment of an electron harmonically oscillating about some point. To find the frequency distribution of the energy (1.86) radiated by an electron moving along a parabola, we resolve the component accelerations $\dot{v}_{\parallel}$ and $\dot{v}_{\perp}$ according to the frequencies of such oscillators, the aggregate of which (Fourier integral) gives the same effect as does the electron under study. Following *Kramers*, we define the Fourier transforms for motion along the *reduced parabola* (1.90) in terms of the *reduced frequency* γ as

$$\dot{v}_{\parallel}(t) = \int_0^{\infty}\psi(\gamma)\cos\gamma t\,d\gamma, \quad \dot{v}_{\perp}(t) = \int_0^{\infty}\Phi(\gamma)\sin\gamma t\,d\gamma, \tag{1.91}$$

and the inverse

$$\psi(\gamma) = \frac{1}{\pi}\int_{-\infty}^{+\infty}\dot{v}_{\parallel}(\tau)\cos\gamma\tau\,d\tau, \quad \Phi(\gamma) = \frac{1}{\pi}\int_{-\infty}^{+\infty}\dot{v}_{\perp}(\tau)\sin\gamma\tau\,d\tau. \tag{1.92}$$

It does not matter what variable is used in (1.92) on the right-hand side, as it is ultimately integrated out.

The total energy emitted is

$$U = \int_0^{\infty}U(\gamma)\,d\gamma = \int_{-\infty}^{+\infty}\frac{2e^2}{3c^3}\dot{v}^2\,dT = \frac{2e^2}{3c^3}\int_{-\infty}^{+\infty}(\dot{v}_{\parallel}^2+\dot{v}_{\perp}^2)\,dT = \frac{2\pi e^2}{c^3}, \tag{1.93}$$

where in the last step we have used (1.90). Using Parseval's formula

$$\int_{-\infty}^{+\infty}(\dot{v}_{\parallel}^2+\dot{v}_{\perp}^2)\,dT = 3\pi = \pi\int_0^{\infty}[\psi^2(\gamma)+\Phi^2(\gamma)]\,d\gamma. \tag{1.94}$$

Introduce the function

$$P(\gamma) \equiv \frac{1}{3}[\psi^2(\gamma) + \Phi^2(\gamma)] = \frac{c^3}{2\pi e^2} U(\gamma) = \frac{U(\gamma)}{U}, \quad \int_0^\infty P(\gamma)\, d\gamma = 1. \tag{1.95}$$

Then

$$U = \frac{2\pi e^2}{c^3} \int_0^\infty P(\gamma)\, d\gamma = \frac{2\pi e^2}{c^3}. \tag{1.96}$$

According to (1.95), the function $P(\gamma)$ determines the distribution of energy with reduced frequency for the reduced parabola. $P(\gamma)\, d\gamma$ gives the relative amount of radiation energy for which the reduced frequency lies between γ and $\gamma + d\gamma$. *Kramers* has estimated $P(\gamma)$ and found[4]

$$\int \frac{P(\gamma)}{\gamma} d\gamma = \text{const} = \frac{4}{\pi\sqrt{3}}. \tag{1.97}$$

We can translate our results from the reduced parabola to the actual parabola. From (1.83), the distance $0B$ of the perihelion B of the parabola from the focus 0 (Fig. 1.22), for the case ϕ_0 small, is

$$0B = \left[\frac{m}{Ze^2} \frac{d_0^2 v^2}{1 - \varepsilon \cos\phi} \right]_{\varepsilon = 1,\, \phi = 180^\circ} = \frac{m d_0^2 v^2}{2Ze^2}.$$

The angular velocity of the electron at the perihelion, from (1.85), is

$$\dot{\phi}_B = \frac{d_0 v}{(0B)^2} = \frac{4Z^2 e^4}{m^2 d_0^3 v^3} \quad \text{(actual)}$$

$$= 4 \quad \text{(reduced)}. \tag{1.98}$$

Therefore, if $\omega = 2\pi\nu$ is the frequency for the actual parabola,

$$\frac{2\pi\nu}{\gamma} = \frac{4Z^2 e^4}{m^2 d_0^3 v^3} \frac{1}{4},$$

$$\gamma = 2\pi\nu \frac{m^2 d_0^3 v^3}{Z^2 e^4}. \tag{1.99}$$

We can replace the reduced distribution function $P(\gamma)$ by the actual distribution function, such that $P(\gamma)\, d\gamma = P(\nu)\, d\nu$. Using (1.99),

[4] For the reduced orbit, in terms of an auxiliary variable z, $t = \frac{1}{2}(\frac{1}{3}z^3 + z)$, $\gamma = \frac{1}{2}(1 + z^2)$, $\cos\phi = (z^2 - 1)/(z^2 + 1)$, $\sin\phi = 2z/(1 + z^2)$, $\dot{v}_\perp = -\gamma^{-2} \sin\phi = 8z(1 + z^2)^{-3}$, and $\dot{v}_\parallel = -\gamma^{-2}\cos\phi = 4(1 - z^2)(1 + z^2)^{-3}$. Integration of (1.92) in the z variable gives $\Psi(\gamma) = \gamma i^{5/3} 3^{-1/2} H^1_{2/3}(i\gamma/3)$ and $\Phi(\gamma) = \gamma i^{4/3} 3^{-1/2} H^1_{1/3}(i\gamma/3)$, where $H^1_p(x)$ is the Hankel function of the first kind and order p. The Ψ and Φ are real for real γ. They can be plotted using expansions for H^1_p. Result (1.97) is general and holds for functions like H^1_p [1.24].

$$P(\nu) = P(\gamma)\frac{d\gamma}{d\nu} = \frac{2\pi m^2 d_0^3 v^3}{Z^2 e^4} P(\gamma). \tag{1.100}$$

As a result of each collision of the electron with the target atom, the electron radiates energy $U(\gamma)\, d\gamma$ between γ and $\gamma + d\gamma$. Using (1.95),

$$U(\gamma)\, d\gamma = UP(\gamma)\, d\gamma = UP(\nu)\, d\nu = U(\nu)\, d\nu = UP(\gamma)\frac{d\gamma}{d\nu} d\nu. \tag{1.101}$$

For a large number N of collisions, with the same impact parameter d_0, the energy of radiation between ν and $\nu + d\nu$ is given by

$$NU(\nu)\, d\nu = 2\pi N \frac{m^2 d_0^3 v^3}{Z^2 e^4} UP\left(2\pi\nu \frac{m^2 d_0^3 v^3}{Z^2 e^4}\right) d\nu, \tag{1.102}$$

where U is given by (1.88).

Kramers applied the *correspondence principle* to introduce the quantum ideas. As a result of the collision of an electron with a target atom, a photon of frequency ν and energy $h\nu$ is emitted. Let $q(\nu)\, d\nu$ be the *quantum probability* of a collision in which a photon of energy $h\nu$ with frequency between ν and $\nu + d\nu$ is emitted. For a large number N of collisions, the total energy emitted between ν and $\nu + d\nu$ is $NU(\nu)\, d\nu = Nq(\nu) h\nu\, d\nu$. Using the correspondence principle, we equate this with (1.102):

$$Nq(\nu) h\nu\, d\nu = NUP(\gamma)\frac{d\nu}{d\nu} d\nu \tag{1.103}$$

$$= 2\pi N \frac{m^2 d_0^3 v^3}{Z^2 e^4} UP\left(2\pi\nu \frac{m^2 d_0^3 v^3}{Z^2 e^4}\right) d\nu$$

$$= N \frac{4\pi^2 Z^2 e^6}{c^3 m^2 d_0^2 v^2} P\left(2\pi\nu \frac{m^2 d_0^3 v^3}{Z^2 e^4}\right) d\nu \text{ for } \nu < \nu_{\max},$$

$$= 0 \quad \text{for } \nu > \nu_{\max}, \tag{1.104}$$

where $\nu_{\max}$ is determined by the condition that the entire energy of the incident electron is emitted as a photon

$$eV = \tfrac{1}{2} m v^2 = h\nu_{\max}. \tag{1.105}$$

We can calculate the energy distribution in the continuous spectrum from a *thin* target. Let the thin target contain A atoms per cm^2 of atomic number Z. It is bombarded by a beam of electrons of velocity v in which n electrons in 1 s pass across a cross-section of 1 cm^2. Take $N = nA$. The spectral density $I(\nu)$ of the continuous spectrum between ν and $\nu + d\nu$ is then obtained by integrating (1.103) over all directions of the impact parameter d_0 and over all the values of this parameter, $0 < d_0 < \infty$, for the thin target surface. Thus

$$I(\nu)d\nu = N d\nu \int_0^\infty q(\nu) h\nu \, 2\pi d_0 \, dd_0$$

$$= N d\nu \frac{8\pi^2 Z^2 e^6}{c^3 m^2 v^2} \int P\left(2\pi\nu \frac{m^2 d_0^3 v^3}{Z^2 e^4}\right) \frac{dd_0}{d_0}. \tag{1.106}$$

From (1.99),

$$\frac{dd_0}{d_0} = \frac{Z^2 e^4}{2\pi m^2 v^3} \frac{d\gamma}{\nu 3 d_0^3} = \frac{1}{3} \frac{d\gamma}{\gamma}. \tag{1.107}$$

Therefore, for thin targets, the Kramers formula is

$$I(\nu)d\nu = N d\nu \frac{8\pi^3 Z^2 e^6}{3c^3 m^2 v^2} \int_0^\infty \frac{P(\gamma)}{\gamma} d\gamma = N \frac{32\pi^2 Z^2 e^6}{3\sqrt{3} c^3 m^2 v^2} d\nu$$

$$= \beta \frac{Z^2}{v^2} d\nu = \beta' \frac{Z^2}{V} d\nu \quad \text{for } \nu < \nu_{\max},$$

$$= 0 \qquad \text{for } \nu > \nu_{\max}, \tag{1.108}$$

where we have used (1.97) and

$$\beta = N \frac{32\pi^2 e^6}{3\sqrt{3} c^3 m^2}, \quad \beta' = N \frac{16\pi^2 e^5}{3\sqrt{3} c^3 m}. \tag{1.109}$$

$I(\nu)$ is the intensity integrated over all directions. It represents $h\nu$ times the cross-section for energy radiated between ν and $\nu + d\nu$ from a thin target. These predictions have been improved by *Landau* and *Lifshitz* [1.25]. Their general result in terms of $|H_{i\gamma}^1(i\gamma)| H_{i\gamma}^{1\prime}(i\gamma)$ reduces to (1.108) for the high-frequency limit. It is seen that $I(\nu)$ does not depend upon the frequency ν (Fig. 1.23a). This is in agreement with the experiments of *Nicholas* (1.13) (Fig.1.16). For a given Z and V, write (1.108) as

$$I(\nu) = \text{const.} \quad \text{for } \nu < \nu_{\max}$$

$$= 0 \qquad \text{for } \nu > \nu_{\max}. \tag{1.110}$$

For X-rays $\nu = c/\lambda$, where λ is the wavelength. We can go from $I(\nu)$ vs ν (Fig. 1.23a) curve to $I(\lambda)$ vs λ (Fig. 1.23b) curve by using the prescription

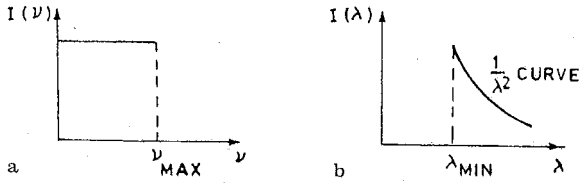

Fig. 1.23. **a** $I(\nu)$ vs ν plot, and **b** $I(\lambda)$ vs λ plot, for a thin target

$I(\nu)d\nu = I(\lambda)d\lambda$, which is necessary if the area under both curves is to be proportional to the energy in the spectrum. Since $-d\nu/d\lambda = c/\lambda^2$,

$$I(\lambda) = \frac{c}{\lambda^2} I(\nu) = \frac{b}{\lambda^2}, \quad \lambda > \lambda_{\min},$$

$$= 0, \quad \lambda < \lambda_{\min}, \tag{1.111}$$

where b is a constant and $\lambda_{\min}$ is the shortest wavelength emitted. This is plotted in Fig. 1.23b. *Duane* and *Hunt* [1.26] experimentally discovered the *short-wavelength limit*, also called the *Duane–Hunt limit*, and used it to determine the value of h/e,

$$\frac{h}{e} = \frac{V}{\nu_{\max}} = \frac{V\lambda_{\min}}{c} \quad \textit{(Duane–Hunt limit)}. \tag{1.112}$$

It is found that the following relationships hold:

$$\lambda_{\min} \nu_{\max} = c, \quad \lambda_{\min}[\text{Å}] = \frac{hc}{eV} = \frac{12398.1}{V[\text{volts}]}.$$

Accurate measurements of h/e have been made by *Ohlin* [1.27], *Bearden* et al. [1.28], and *Felt* et al. [1.29]. Use is made of the fact that the graph between $\nu_{\max}$ and V is a straight line.

The dependence of $I(\nu)$ on the tube voltage V, $I(\nu) \propto 1/V$, predicted by *Kramers* (1.108) has been experimentally verified by *Harworth* and *Kirkpatrick* [1.16]. They used a 199 Å nickel foil and varied the voltage from 8 to 180 kV. *Amrehn* and *Kulenkampff* [1.30] used a thin Ni target at 90° to the electron beam at $V = 25, 34, 40$ kV. For constant V, the intensity was independent of ν with a sharp cutoff. For constant ν, $I \propto 1/V$ of (1.108) was also confirmed. A minimum voltage is necessary to emit the radiation of a given frequency ν,

$$V_{\min} = \frac{h\nu}{e}. \tag{1.113}$$

For voltages $V > V_{\min}$ the $I(\nu)$ vs V curve is shown in Fig. 1.24 for a given ν. It is called an *isochromat*.

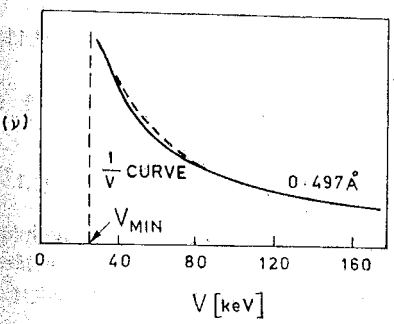

Fig. 1.24. Isochromat for a thin Ni target. Solid line is theoretical and dashed line is experimetal

Let us now calculate the spectral distribution for a *thick target* as is usually found in an X-ray tube. *Kramers* takes into account the decrease of velocity of the electrons with depth x in the target by applying the Thomson–Whiddington law [1.31] $dE/dx = -\text{const.}/E$ or

$$\frac{dv^4}{dx} = -bZ. \tag{1.114}$$

Bohr's theoretical value [1.32] of the constant is (see Appendix B)

$$b = \frac{16\pi e^4 L}{m^2} l, \tag{1.115}$$

where L is the number of atoms in 1 cm^3 of target and $l \simeq 6$.

To obtain the total radiation $I_{\text{tot}}(\nu)$ of frequency ν, integrate $I(\nu)$ over the depth x in the limits 0 to some x_ν, to which the velocity v_ν given by

$$\tfrac{1}{2}mv_\nu^2 = h\nu$$

corresponds. For $x > x_\nu$ the velocity will decrease and the kinetic energy of the electron will no longer be sufficient to emit a photon of frequency ν. Thus, for a thick target,

$$I_{\text{tot}}(\nu) = \int_0^{x_\nu} I(\nu)dx = \int_{v_0}^{v_\nu} I(\nu)\frac{dx}{dv}dv, \tag{1.116}$$

where v_0 is the initial velocity of electrons, $I(\nu)$ is given by (1.108), and $dx/dv = -4v^3/bZ$ by (1.114). Replace the number of atoms A per 1 cm^2 of thin target surface by the number of atoms L in 1 cm^3 of the thick target. Then

$$I_{\text{tot}}(\nu) = -\frac{4}{bZ}\int_{v_0}^{v_\nu} I(\nu)v^3 dv = -\frac{4}{Z}\frac{m^2}{16\pi e^4 Ll}nL\frac{32\pi^2 Z^2 e^6}{3\sqrt{3}c^3 m^2}\int_{v_0}^{v_\nu} vdv$$

$$= n\alpha_l Z(v_0^2 - v_\nu^2), \quad \alpha_l = \frac{4\pi e^2}{3\sqrt{3}lc^3}. \tag{1.117}$$

Thus, layers that cause equal electron-energy loss give equal intensities per unit frequency interval. At the Duane–Hunt limit, $mv_0^2/2 = h\nu_{\max}$, so that

$$I_{\text{tot}}(\nu) = n\alpha_l' Z(\nu_{\max} - \nu), \quad \alpha_l' = \frac{8\pi e^2 h}{3\sqrt{3}lc^3 m} = 495 \times 10^{-50} \tag{1.118}$$

This is in good agreement with the most complete empirical work of *Kulenkampff* [1.33] who found the following formula:

$$I_{\text{tot}}(\nu) = CZ[(\nu_{\max} - \nu) + aZ] \simeq CZ(\nu_{\max} - \nu), \tag{1.119}$$

where C and a are constants, and the aZ term is much smaller in magnitude, $aZ \ll \nu_{\max} - \nu$. It is of the same form as Kramers' result (1.118). If $I_{\text{tot}}(\nu)$, incident electron energy $h\nu_{\max}$, and emitted photon energy $h\nu$ are expressed in keV, and the radiated energy interval is taken as 1 keV instead of unit frequency, then $C/h = 2.2 \times 10^{-6}$.

From (1.118), the total intensity I of a continuous spectrum at voltage V is

$$I = n\alpha' Z\int_0^{\nu_{\max}} (\nu_{\max} - \nu)d\nu = n\alpha' Z\frac{1}{2}\nu_{\max}^2 = n\alpha' Z\left(\frac{eV}{h}\right)^2$$

$$= \left(\frac{2n}{3\sqrt{3}l}\right)\left(\frac{2\pi e^2}{hc}\right)\left(\frac{1}{mc^2}\right)Z(eV)^2 = kZT^2. \tag{1.120}$$

If I and the kinetic energy of the electron T are in MeV, the constant $k \simeq 1.1 \times 10^{-3}$ (MeV)$^{-1}$. This is in agreement with I given by the area under the experimental curve for the energy distribution of the continuous spectrum (Fig. 1.25a). If $I_{\text{tot}}(\nu)$ is plotted against ν (Fig. 1.25b), a straight line results, down to a frequency $\nu = \nu_{\max}/2$, in agreement with the empirical formula (1.119). The slope is independent of the voltage. The constant C varies by 10% at higher voltages (30–50 kV for W target).

Such curves were first obtained by *Ulrey* [1.34]. In later work (Fig. 1.25) several corrections were made to determine the actual distribution of the continuous X-ray spectrum as emitted in the target itself. These corrected curves can then be compared with the theory. The main corrections are: backscattering

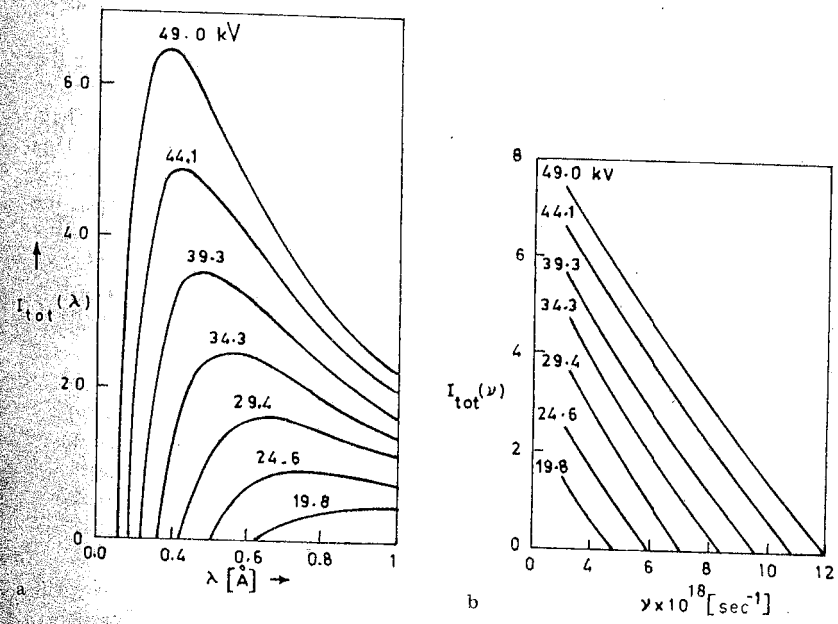

Fig. 1.25. **a** The spectral intensity $I_{\text{tot}}(\lambda)$ for a thick tungsten target versus λ, at various voltages V [1.35]. **b** $I_{\text{tot}}(\nu)$ vs ν plot

from the target; incomplete absorption in the detector; absorption in detector window, the atmosphere, the X-ray tube wall, and the target itself; reflectivity of the crystal analyzer; and removal of effects of order higher than the first. An empirical expression for $I_{tot}(\lambda)$ can be obtained from (1.119), by use of (1.111),

$$I_{tot}(\lambda) = \frac{c}{\lambda^2} I_{tot}(\nu) = \frac{CcZ}{\lambda^2}\left(c\frac{\lambda - \lambda_{min}}{\lambda\lambda_{min}} + aZ\right) \simeq \frac{Cc^2 Z}{\lambda^3 \lambda_{min}}(\lambda - \lambda_{min}), \quad (1.121)$$

which represents the experimental data (Fig. 1.25a) fairly well. Figure 1.25a shows that the wavelength of maximum intensity (hump), λ_m, depends on V, and that, approximately,

$$\lambda_m = \frac{3}{2}\lambda_{min}. \quad (1.122)$$

To calculate λ_m, we use $dI_{tot}(\lambda)/d\lambda = 0$ to get from (1.121)

$$\lambda_m = \frac{3}{2}\lambda_{min}\frac{1}{(1 + (a/c)Z\lambda_{min}} \simeq \frac{3}{2}\lambda_{min}. \quad (1.123)$$

The value of λ_{min} (or ν_{max}) corresponds to the maximum energy that an electron can emit in a single collision. In fact, it is more likely that the incident electrons give up less energy in individual collisions, and in a thick target undergo several collisions before coming to rest. This explains the occurrence of other X-ray photons of lower energies which give rise to the rest of the continuous spectrum (Fig. 1.25). The hump at $\lambda_m = 1.5\lambda_{min}$ merely reflects the statistically most probable energy loss. The nature of the curve changes to Fig. 1.23b when the target is so thin that multiple collisions are not likely. Then, in most of the collisions, either total energy is radiated or none at all. This explains the intensity maximum at λ_{min} (Fig. 1.23b). *Webster* [1.36] suggested that because the electrons quickly lose velocity as they enter the target, the radiation of maximum frequency can be emitted only from the surface layer of a thick target. A spectrum from such a target can then be thought of as a superposition of a succession of thin-target curves, Fig. 1.23b, modified by self-absorption in the target of incident electrons and of emitted X-ray photons. Webster's analysis is shown in Fig. 1.26.

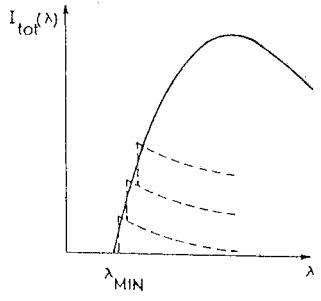

Fig. 1.26. Webster's analysis of a thick-target spectrum into a succession of thin-target spectra

Another quantitative test for Kramers' theory is provided by calculation of the *efficiency* of production of X-rays from thick targets:

$$\eta = \frac{\text{X-ray energy}}{\text{cathode-ray energy}} = \frac{I}{neV} = \frac{4\pi e^3}{3\sqrt{3}lc^3 mh} ZV = 9.2 \times 10^{-10} ZV, \quad (1.124)$$

where V is in volts. Determination of η has been made by *Rump* [1.37], *Dyson* [1.38], and *Green* [1.39]. The average empirical equation for the various data is $\eta = 11 \times 10^{-10} ZV$. Thus Kramers' theory is in good agreement with experiments. There is some evidence of departure from strict proportionality to Z [1.40].

For a tungsten ($Z = 74$) target operated at 50 kV, the efficiency is about 0.4%. The remainder of the energy appears as heat, which makes the cooling of targets necessary.

The process responsible for conversion of the incident electron energy into heat energy is the large impact parameter, small scattering angle, and multiple elastic scattering of electrons by atoms. An electron that traverses a thick target undergoes a large number of such small-angle (*glancing*) deflections and generally emerges at a small angle that is the cumulative statistical superposition of a large number of deflections. In most of these glancing deflections, radiation is not emitted; they lead to elastic processes that involve momentum transfers to recoiling target atoms. Only rarely is the electron deflected through a large angle; because these events are rare, such an electron makes only one such collision that leads to the emission of an X-ray photon. We can divide the angular range into two regions—one of relatively large scattering angles ($\theta = 2\pi\phi_0$, where ϕ_0 is shown in Fig. 1.22), which contains only the single scatterings that emit photons, and one region of very small scattering angles, which contains the heat-producing multiple elastic scatterings.

Quantum considerations show that the classical result, that radiation is emitted in *every* collision in which an electron is deflected, is incorrect. In quantum theory, there is a small but finite probability that a photon will be emitted each time the electron suffers a deflection. However, this probability is so small that usually no photon is emitted. In the few collisions that lead to photon emission, a relatively large amount of energy is radiated. Thus, the quantum theory replaces the multitude of small classical energy losses by a much smaller number of large energy losses; the averages are nearly equal in the two theories.

Kramers has not estimated the polarization of X-rays. However, a qualitative discussion based on his parabolic orbits is possible. Consider Fig. 1.9 with $\Theta = \pi/2$ as measured from the direction of initial velocity $\boldsymbol{v}$. At the point of observation P, the vector $\boldsymbol{E}$ is perpendicular to $\boldsymbol{R}$ and lies in a plane that contains $\boldsymbol{R}$ and $\dot{\boldsymbol{v}}$. If the impact parameter d_0 is small, the electron will approach the nucleus at 0 very closely (Fig. 1.27). The angle of scattering, that is, the angle between the direction of the initial velocity $\boldsymbol{v}$ and the direction of the final

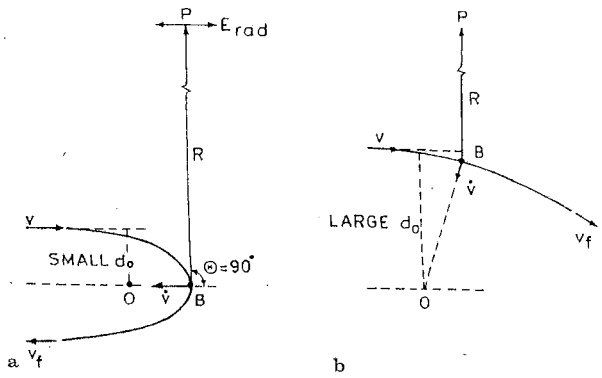

Fig. 1.27a. Orbit for small d_0 and large angle of scattering ($\pi - 2\phi_0 \simeq \pi$), and **b** for large d_0 and small angle of scattering ($\pi - 2\phi_0 = 0$)

velocity v_f, in this case is close to π. This is the case of *strong deflection*. The acceleration $\dot{v}$ is almost parallel to the axis of v and perpendicular to R. Therefore, the vector E of the radiation field attains its maximum value according to (1.57), $E_{rad} = (e/c^2 R)\dot{v}\sin\Theta$. Also, the electron radiates the maximum frequency ν_{max} at the instant when it passes the parihelion B (point of shortest distance from 0) of its orbit, in this case.

On the other hand, in the case of large d_0 (Fig. 1.27b) the deflection of the electron is small (weak deflection), the distance $0B$ is large, $\dot{v}$ is almost perpendicular to v and parallel to R making $E_{rad} \to 0$ due to (1.57), and the electron emits radiation of lower frequency (longer wavelength). Thus, at $v \simeq v_{max}$, the vector E is of great magnitude and parallel to v; at $v \simeq 0$ the vector E is small in magnitude and perpendicular to v. In both cases, the radiation is completely polarized. At $0 < v < v_{max}$ the polarization is only partial and changes sign at some point, in agreement with observations (Sect. 1.10).

1.17 Quantum Mechanical Considerations

Instead of using the correspondence principle on an ad hoc basis, full quantum mechanical calculations can be used. Early work on these lines is due to *Sommerfeld* [1.41]. This work was refined by workers such as *Weinstock* [1.42] and *Kirkpatrick* and *Wiedmann* [1.43]. They expressed the theory in such a way that its results can be compared directly with experiment.

Nonrelativistic theory of electron-nucleus bremsstrahlung based on Sommerfeld's approach has been described by *Berestetskii* et al. [1.44]. They also give the quasi-classical relativistic theory of bremsstrahlung. Full relativistic field-theory treatment is given in *Heitler* [1.45] and other recent books on the subject.

1.17.1 Born Approximation

We first present here a simple nonrelativistic perturbation calculation based on the Born approximation applicable when $Ze^2/\hbar v \ll 1$. We consider the dipole radiation during collision of two particles having different e/m values.

The dipole moment of two particles that have charges e_1, e_2 and masses m_1, m_2 in their center-of-mass system is (see p. 27)

$$\boldsymbol{D} = \mu\alpha_e \boldsymbol{r}, \quad \alpha_e = \frac{e_1}{m_1} = \frac{e_2}{m_2}, \tag{1.125}$$

where μ is the reduced mass, and $\boldsymbol{r} = \boldsymbol{r}_1 - \boldsymbol{r}_2$. The matrix element is

$$\boldsymbol{D}_{p'p} = \int \Psi^*_{p'} \boldsymbol{D}_{\text{operator}} \Psi_p \, d\tau = -\frac{1}{\omega^2}\int \Psi^*_{p'} \ddot{\boldsymbol{D}}_{\text{operator}} \Psi_p \, d\tau, \tag{1.126}$$

because in quantum mechanics $(v_x)_{p'p} \equiv (\dot{x})_{p'p} = \left[-\frac{\mathrm{i}}{\hbar}(E_i - E_f)\right] x_{p'p} = -\mathrm{i}\omega x_{p'p}$ and similarly $(\ddot{x})_{p'p} = -\omega^2 x_{p'p}$. Here $\omega = (E_i - E_f)/\hbar = (p^2 - p'^2)/2\mu$, with $p = \mu v$, $p' = \mu v'$ as the momenta of relative motion and $\hbar = h/2\pi$.

Because a force can be expressed as the negative gradient of the potential, we can write, in natural units ($\hbar = c = 1$),

$$\ddot{\boldsymbol{D}} = \mu\alpha\ddot{\boldsymbol{r}} = -\alpha_e \boldsymbol{V}\frac{e_1 e_2}{r}. \tag{1.127}$$

In the Born approximation $\psi_p = \exp(\mathrm{i}\boldsymbol{p}\cdot\boldsymbol{r})$, $\psi_{p'} = \exp(\mathrm{i}\boldsymbol{p}'\cdot\boldsymbol{r})$ and with $\boldsymbol{q} = \boldsymbol{p}' - \boldsymbol{p}$

$$\begin{aligned}\left(\boldsymbol{V}\frac{1}{r}\right)_{p'p} &= \int_0^\infty \int_0^\pi \mathrm{e}^{-\mathrm{i}\boldsymbol{q}\cdot\boldsymbol{r}}\left(\frac{\partial}{\partial r}\frac{1}{r}\right)\hat{\boldsymbol{n}}_r r^2 \, dr \sin\theta \, d\theta \, 2\pi \\ &= -2\pi\hat{\boldsymbol{n}}_r \int_0^\infty \int_{-1}^{+1} \mathrm{e}^{-\mathrm{i}qrx} dx \, dr = -4\pi\frac{\hat{\boldsymbol{n}}}{q}\int_0^\infty \frac{\sin(qr)}{r} dr \\ &= -4\pi\frac{\boldsymbol{q}}{q^2},\end{aligned}$$

$$\boldsymbol{D}_{p'p} = -\frac{1}{\omega^2}\ddot{\boldsymbol{D}}_{p'p} = +\frac{\alpha_e e_1 e_2}{\omega^2}\left(\boldsymbol{V}\frac{1}{r}\right)_{p'p} = -\frac{4\pi\alpha_e e_1 e_2}{\omega^2}\frac{\boldsymbol{q}}{q^2}. \tag{1.128}$$

The probability of dipole radiation is (for example, see [1.46])

$$dw = \frac{\omega^3}{2\pi}|\boldsymbol{e}\cdot\boldsymbol{D}_{p'p}|^2 \, \mathrm{d}\Omega_k = \frac{16\pi^2\alpha_e^2 e_1^2 e_2^2}{2\pi\omega q^4}(\boldsymbol{e}\cdot\boldsymbol{q})(\boldsymbol{e}^*\cdot\boldsymbol{q})\, d\Omega_k, \tag{1.129}$$

where $\boldsymbol{e}$ is the unit polarization vector. Normalizing the wave functions to one particle per unit volume ($V = 1$), the differential cross-section is

$$d\sigma_{kp'} = \frac{V\, d^3p'}{v\,(2\pi)^3} dw = \frac{e_1^2 e_2^2}{\pi^2}\alpha_e^2 \frac{v'}{v}\frac{\mu^2}{q^4}(\boldsymbol{e}\cdot\boldsymbol{q})(\boldsymbol{e}^*\cdot\boldsymbol{q})\frac{d\omega}{\omega} d\Omega_{p'} \, d\Omega_k, \tag{1.130}$$

for the emission of a photon $\boldsymbol{k}$ into the solid angle $d\Omega_k$ with the scattering of the

electron into the range of states $d^3p' = p'^2 dp' d\Omega_{p'}$, where $(p^2/2\mu) + (p'^2/2\mu) = \omega$ gives $dp' = \mu d\omega/p'$ or $d^3p' = \mu p' d\omega\, d\Omega_{p'}$.

To sum over polarizations, note that the two unit polarization vectors together with $\boldsymbol{k}/k$ form a mutually orthogonal system, so

$$\sum_{\text{pol}} (\boldsymbol{e}\cdot\boldsymbol{q})^2 + \frac{1}{k^2}(\boldsymbol{k}\cdot\boldsymbol{q})^2 = q^2,.$$

which gives

$$\sum_{\text{pol}} (\boldsymbol{e}\cdot\boldsymbol{q})^2 = q^2 \sin^2\Theta, \tag{1.131}$$

where Θ is the angle between $\boldsymbol{k}$ and $\boldsymbol{q}$, which lies in the scattering plane. Integrating over the directions of photons,

$$\int_0^\pi \sin^2\Theta\, d\Omega_k = 2\pi \int_0^\pi \sin^3\Theta\, d\Theta = 2\pi\frac{4}{3},$$

$$d\sigma_{\omega\theta} = \frac{8}{3\pi} e_1^2 e_2^2 \alpha_e^2 \frac{v'}{v}\frac{d\omega}{\omega}\mu^2 \frac{2\pi\sin\theta\, d\theta}{p'^2 + p^2 - 2pp'\cos\theta}, \tag{1.132}$$

where θ is the scattering angle. Integrating[5] over θ, we finally get

$$d\sigma_\omega = \frac{16}{3c^3} e_1^2 e_2^2 \alpha^2 \frac{\mu^2}{p^2}\log\left(\frac{p+p'}{p-p'}\right)\frac{d\omega}{\omega}. \tag{1.133}$$

For radiation in the field of a fixed center of Coulomb force (nucleus) this is equivalent to the bremsstrahlung cross-section in which v and v' are the initial and final velocities of the electron, $e_1 = -e$, $e_2 = Ze$, $m_1 = \mu$ and $m_2 = \infty$. With this interpretation, $T = p^2/2\mu$ is the kinetic energy of the primary electron and $T - \omega = p'^2/2\mu$ is the kinetic energy of the scattered electron. Then

$$d\sigma_\omega = \text{const}\cdot Z^2 \frac{d\omega}{\omega}\frac{1}{T}\log\frac{[T^{1/2} + (T-\omega)^{1/2}]^2}{\omega}. \tag{1.134}$$

Because intensity = energy × probability, $I(\omega)d\omega = \hbar\omega d\sigma_\omega$, we get the familiar result that intensity per unit frequency interval is independent of frequency (Fig. 1.23a). Further, at the Duane–Hunt limit, $v' = 0$, or $T = \hbar\omega_{\max}$, so $d\sigma_\omega$ vanishes. Thus we get the $\omega_{\max}$ cutoff in the intensity in a natural way and not in an ad hoc manner as in Kramers' semiclassical theory.

1.17.2 Sommerfeld's Result

Sommerfeld [1.41] has calculated the dipole matrix element by using Coulomb wave functions, instead of plane waves (1.141), for the incident and scattered

[5] $\int_{-1}^{+1} \frac{dx}{a-bx} = \frac{1}{-b}[\log(a-bx)]_{-1}^{+1} = \frac{1}{b}\log\frac{a+b}{a-b}$.

electrons. An electron of energy E, moving in the field of a nucleus of charge Ze, radiates a photon $\hbar\omega$ and is scattered with the energy $E' = E - \hbar\omega$. The optical transition probability is (Sect. 2.4)

$$A_{E\to E'} = \frac{4\omega^3 e^2}{3\hbar c^3}|r_{EE'}|^2, \tag{1.135}$$

$$r_{EE'} = \int \psi_{E'} r \psi_E\, dr. \tag{1.136}$$

The asymptotic Coulomb wave functions are of the form [1.47, 48]

$$\psi_E \sim \exp\{i[\boldsymbol{k}_e\cdot\boldsymbol{r} + n\ln(k_e r - \boldsymbol{k}_e\cdot\boldsymbol{r})]\} + \frac{f_E(\theta)}{r} \times \exp[i(k_e r - n\ln 2k_e r)],$$

$$\psi_{E'} \sim \exp\{-i[\boldsymbol{k}_e\cdot\boldsymbol{r} - n'\ln(k'_e r + \boldsymbol{k}'_e\cdot\boldsymbol{r})]\} + \frac{f_{E'}(\pi-\theta')}{r} \times \exp[i(k'_e r - n'\ln 2k'_e r)],$$

$$n = Ze^2 m/\hbar^2 k_e = Ze^2/\hbar v, \qquad n' = Ze^2 m/\hbar^2 k'_e = Ze^2/\hbar v'; \tag{1.137}$$

$\boldsymbol{k}_e$, $\boldsymbol{k}'_e$ are the wave vectors of initial and final electron motions,

$$\cos\theta' = \cos\theta\cos\theta_e + \sin\theta\sin\theta_e\cos(\phi - \phi_e) \tag{1.138}$$

where the electron is scattered into the solid angle $d\Omega_e$ about the direction (θ_e, ϕ_e). The $\psi_{E,E'}$ are correct wave functions when pure Coulomb scattering is considered neglecting screening. This is true for radiation by the electron mainly moving inside the K-shell (near $v_{\max}$).

For bremsstrahlung we need the differential cross-section in terms of the angle distribution of the emitted photons

$$d\sigma_\nu(\boldsymbol{e};\theta_e,\phi_e;\Theta,\Phi)\, d\Omega_e\, d\Omega_\nu\, d\nu, \tag{1.139}$$

where a photon of frequency between ν and $\nu + d\nu$, and polarization $\boldsymbol{e}$, is emitted in the direction (Θ, Φ) within the solid angle $d\Omega_\nu$. Then

$$d\sigma_\nu = B\frac{v'}{v}v^3|\boldsymbol{e}\cdot\boldsymbol{r}_{EE'}|^2, \tag{1.140}$$

where $B = 16\pi^3 e^2 m^2/(h^3 c^3)$. We write

$$\boldsymbol{r}_{EE'} = \boldsymbol{i}_x x_{EE'} + \boldsymbol{i}_y y_{EE'} + \boldsymbol{i}_z z_{EE'}, \tag{1.141}$$

and take $\boldsymbol{i}_x$ along the motion of the incident electron ($\boldsymbol{k}_e$). If $\boldsymbol{i}_y$ is perpendicular to the plane of scattering,

$$\sum_{\text{pol}} d\sigma_\nu = 2B\frac{v'}{v}v^3[|x_{EE'}|^2\sin^2\Theta + |z_{EE'}|^2(1+\cos^2\Theta)],$$

where the sum is over the photon polarizations and $|y_{EE'}|^2 = |z_{EE'}|^2$ because the

direction of incident electrons is an axis of complete symmetry when electron spin is neglected.

For continuous radiation the differential cross-section required is $\int \sum_{\text{pol}} d\sigma_\nu \, d\Omega_e$. It gives the intensity equation

$$I(\nu, \Theta) = I_x \sin^2\Theta + I_z(1 + \cos^2\Theta), \tag{1.142}$$

$$I_x = 2B \int |x_{EE'}|^2 \, d\Omega_e. \tag{1.143}$$

The evaluation of the Sommerfeld integrals (1.143) over all directions of emergence of the electrons is difficult and no closed form exists. *Weinstock* [1.8, 42] and *Sommerfeld* and *Maue* [1.49] have evaluated the integral by series expansion. The final form of the bremsstrahlung cross-section in the frequency range $d\nu$ is [1.44, 49]

$$d\sigma_\nu = \frac{64\pi^2}{3} Z^2 \alpha r_e^2 \frac{m^2c^2}{\hbar^2(k_e - k_e')^2} \frac{1}{(e^{2\pi n} - 1)(1 - e^{-2\pi n'})} \times \left(-\frac{d}{d\eta} |F(\eta)|^2 \right) \frac{d\nu}{\nu} \tag{1.144}$$

$$F(\eta) = {}_2F_1(in', in, 1, \eta), \quad \eta = -\frac{4k_e k_e'}{(k_e - k_e')^2} = -\frac{4nn'}{(n - n')^2}$$

where $\alpha = e^2/\hbar c = 1/137$, $r_e = e^2/mc^2$, and ${}_2F_1$ is the hypergeometric function.

For $n \gg 1$ and $h\nu \ll \hbar^2 k_e^2/2m$, (1.144) reduces to the classical result. For large velocities ($n \ll 1, n' \ll 1$),

$$F'(\eta) \approx \left(\frac{nn'}{\eta}\right) \log(1 - \eta),$$

$$d\sigma_\nu = \frac{16}{3} Z^2 \alpha r_e^2 \frac{c^2}{v^2} \log\left(\frac{v + v'}{v - v'}\right) \frac{d\nu}{\nu},$$

$$n = Ze^2/\hbar v \ll 1, \qquad n' = Ze^2/\hbar v' \ll 1, \tag{1.146}$$

which is the Born approximation result (1.133) for $m_2 = \infty$ and $e_2 = Ze$.

If a fast electron ($n \ll 1$) radiates a large fraction of its energy ($v' \ll v$), then

$$-\eta \approx \frac{4k_e'}{k_e} = \frac{4n}{n'} \ll 1,$$

$$F(\eta) \approx F(in', 0, 1, \eta) = 1,$$

$$F'(\eta) \approx -nn' F(1 + in', 1, 2, \eta) \approx -nn',$$

$$d\sigma_\nu = \frac{64\pi}{3} Z^3 \alpha^2 r_e^2 \left(\frac{c}{v}\right)^3 \frac{1}{1 - \exp(-2\pi n')} \frac{d\nu}{\nu}, \tag{1.147}$$

$$Ze^2/\hbar v \ll 1, \quad Ze^2/\hbar v' \gtrsim 1.$$

When $v \to v_{max}$ where $h\nu_{max} = \frac{1}{2}mv^2$, we have $v' \to 0$, $n' \to \infty$, and (1.147) gives

$$d\sigma_\nu = \frac{128\pi}{3} Z^3 \alpha^2 r_e^2 \left(\frac{c}{v}\right)^3 \frac{h\,d\nu}{mv^2}. \tag{1.148}$$

This is a finite limit because for $\nu > \nu_{max}$ highly excited Coulomb bound states are possible, ν_{max} remains the limit of continuous X-rays. *Kirkpatrick* and *Wiedmann* [1.43] and *Rao-Sahib* and *Wittry* [1.50] have developed empirical relations to approximate the Sommerfeld formula for thin targets, using *Bethe*'s retardation law [1.51]. If screening is allowed, *Sauter* [1.52] finds, using plane waves in the Born approximation for $\psi_{E,E'}$, that Z dependence changes for small ν values.

Recently *Pratt* and co-workers [1.53–56] have performed accurate numerical calculations for the atomic field bremsstrahlung. They consider a single electron transition in a relativistic, screened, self-consistent (Hartree–Fock–Slater) potential, with wave functions obtained in partial-wave series by numerically integrating the radial Dirac equation. This gives very good agreement with the recent data of *Hippler* et al. [1.57] as shown in Fig. 1.28. The difference between *Pratt*'s calculations and the Sommerfeld–Maue formula (1.144) for high Z is due to the screening of atomic electrons, as relativistic effects at such low incident electron energy are small. Very slow electrons can make several turns around the field before escaping. This affects the angular distribution of the radiation [1.56]. The angular distribution of the radiation has also been studied in detail both theoretically [1.58] and experimentally [1.59]. For review articles see *Koch* and *Motz* [1.60] and *Hippler* [1.61].

The high energy limit has been obtained by *Bethe* and *Maximon* [1.62]. *Elwert* and *Haug* [1.63] have obtained interpolating forms. *Pratt* [1.64] has reviewed these results and discussed the role of the *Elwert* factor [1.65]

$$f_E = \left(\frac{n'}{n}\right) \frac{(1 - e^{-2\pi n})}{(1 - e^{-2\pi n'})}.$$

1.17.3 Polarization

From (1.142), with $I_y = I_z$, the intensity and polarization of radiation emitted in the direction Θ are given by

$$I(\nu, \Theta) = I_x \sin^2\Theta + I_y + I_z \cos^2\Theta, \tag{1.149}$$

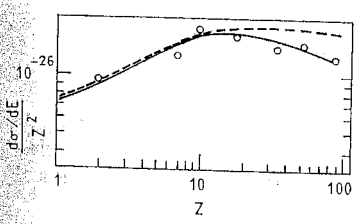

Fig. 1.28. Scaled cross-section $Z^{-2} d\sigma_\nu/d(h\nu)$ in cm²/keV vs Z for $T = 10$ keV, $h\nu = 9$ keV. The experimental points for gaseous targets are from [1.57, 61], the dashed curve from (1.144), and the solid line from the calculations in [1.56] as presented in [1.57]

$$P_{\mathrm{pol}}(\Theta) = \frac{I_{\parallel} - I_{\perp}}{I_{\parallel} + I_{\perp}} = \frac{(I_x \sin^2\Theta + I_z \cos^2\Theta) - I_y}{(I_x \sin^2\Theta + I_z \cos^2\Theta) + I_y}$$

$$= \frac{I_x \sin^2\Theta - I_y \sin^2\Theta}{I_x \sin^2\Theta + I_y(\cos^2\Theta + 1)}. \tag{1.150}$$

In Fig. 1.29, the origin of radiation is 0 and the point of observation A. The two vectors at A correspond to the two components of X-rays with mutually perpendicular directions of polarization. The one polarized with electric vector parallel to the y axis is of intensity I_y. The one polarized in the perpendicular direction to this contains, in general, incoherent resolved contributions from both I_x and I_z and is of intensity $I_x \sin^2\Theta + I_z \cos^2\Theta$. For $\Theta = 90°$, $P_{\mathrm{pol}}(90°) = (I_x - I_y)/(I_x + I_y)$. As

$$R_\Theta = \frac{I_y}{I_x \sin^2\Theta + I_z \cos^2\Theta}$$

$$= \frac{1 - P_{\mathrm{pol}}(\Theta)}{1 + P_{\mathrm{pol}}(\Theta)}, \tag{1.151}$$

$R_{90} = I_y/I_x$ is a measure of departure from complete polarization ($P_{\mathrm{pol}} = 1$). The departure is due to the transverse accelerations of incident electrons being non-zero. For detailed calculations see [1.66, 67] and the review [1.68].

From (1.149)

$$I(v, 0) = 2I_y, \quad I(v, 90°) = I_x + I_y. \tag{1.152}$$

Theoretical values of the intensity as functions of $v/v_{\max}$ (for $V = 20$ kV, $Z = 65$) and of V/Z^2 (for $v/v_{\max} = 1$) are shown in Fig. 1.30a, b, as calculated from the Sommerfeld theory by *Kirkpatrick* and *Wiedmann* [1.43].

Integration of (1.149) gives the total energy emitted over all directions,

$$I(v) = \int_0^{\pi} I(v, \Theta) 2\pi \sin\Theta \, d\Theta = \tfrac{8}{3}(I_x + 2I_y). \tag{1.153}$$

In view of Fig. 1.30b, this is approximately proportional to Z^2/V for a given v (Kramers result for a thin target). Exact calculations [1.43] show that $I(v)$ decreases with increasing v as compared to (1.110). This agrees with the measurements of *Motz* and *Placious* [1.69].

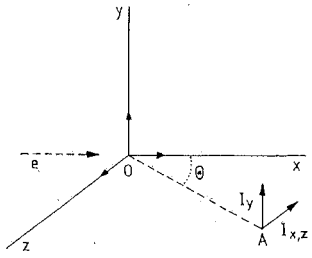

Fig. 1.29. Polarization components I_y and $I_{x,z} = I_x \sin^2\theta + I_z \cos^2\theta$ of X-rays, emitted at 0 by electrons incident from the left along the x axis and observed at A

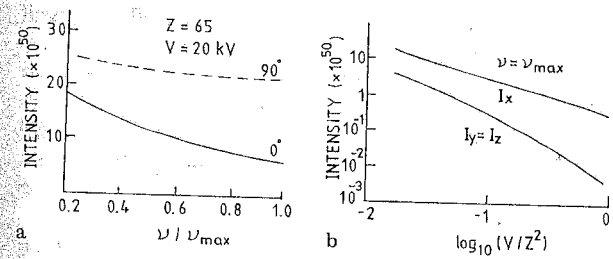

Fig. 1.30a, b. Continuous intensity calculated [1.43] from the Sommerfeld theory **a** as a function of $v/v_{\max}$ for $V = 20$ kV, $Z = 65$, and **b** as a function of V/Z^2 with V/Z^2 with V in esu. The unit of intensity is ergs/(unit frequency interval atoms incident electrons per cm^2)

From Fig. 1.30b we can obtain $P_{\mathrm{pol}}(90°) = (I_x - I_y)/(I_x + I_y)$. This predicted polarization (Fig. 1.31) based on the Sommerfeld theory agrees with the measured values [1.70–72]. *Gluckstern* and *Hull* [1.73] have calculated $P(\Theta)$ using the Born approximation. It agrees with the observations at high energy and low Z [1.74].

The polarization is maximum for $\Theta = 90°$. For relativistic energies ($\beta \sim 4/5$), the I_x, I_y include the factor $(1 - \beta\cos\Theta)^{-4}$, [1.75], then the maximum occurs for $\Theta < 90°$. In addition, the effect of electron spin shows up. The relativistic expression for bremsstrahlung contains a spin-independent part (due to change of orbital current) and a spin-dependent part (spin-flip, a change of spin current). The former gives plane polarized X-rays and latter circularly polarized X-rays. Their interference usually produces elliptic polarization [1.76, 77].

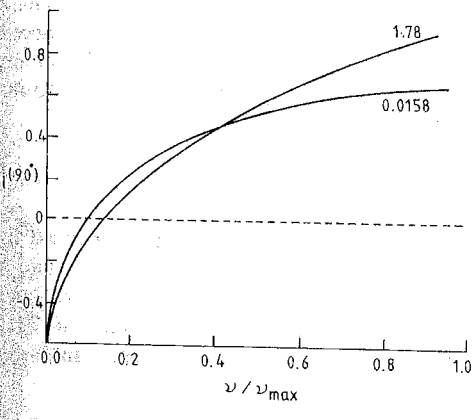

Fig. 1.31. Calculated $P_{\mathrm{pol}}(\Theta = 90°)$ as a function of $v/v_{\max}$ for $V/Z^2 = 1.78$, 0.0158, [1.43]

The incident electron beam was so far unpolarized. Additional effects arise if this is not so [1.78–80]. Longitudinally polarized fast β-rays from an $^{90}Y + {}^{90}Sr$ source are found to produce circularly polarized continuous X-rays when passed through magnetized iron [1.81]. *Güthner* has detected asymmetry of X-rays produced by transversely polarized β-rays [1.82]. Recent papers have discussed methods of generating polarized X-rays [1.83, 84], besides synchrotron radiation.

1.17.4 Screening

Little is known analytically about bremsstrahlung from a screened potential. Using the Thomas–Fermi atomic model, one obtains the constant value [1.85]

$$d\sigma_\omega = \frac{16}{3}\frac{Z^2 e^2}{c}\left(\frac{e^2}{mc^2}\right)^2 \ln\left(\frac{233m}{MZ^{1/3}}\right) d\omega,$$

where M is the mass of the atom. In the relativistic Born approximation, (1.139) is multiplied by the square of a form factor

$$F(q) = 1 - Z^{-1}\int \rho(r) e^{iq\cdot r}\, dr, \quad \int \rho(r)\, dr = Z,$$

where ρ is the charge density of atomic electrons and q the momentum transfer. In general, screening suppresses and flattens the bremsstrahlung spectrum. It is significant for high Z values.

1.18 Bremsstrahlung in Other Processes

In a collision of a heavy ion with a heavy atom, several bremsstrahlung processes are possible. The collision between the projectile and target nuclei produces *nucleus–nucleus bremsstrahlung* (NNB). In a (small impact parameter) heavy-ion–atom collision the projectile–target-nucleus electric dipole is accelerated, giving radiation. The dipole radiation of frequency ω into the solid angle $d\Omega_\omega$ varies as the difference between the projectile and target charge-to-mass ratio,

$$\frac{d^2\sigma_{\text{dip}}}{d\omega\, d\Omega_\omega} \sim \left(\frac{Z_P}{M_P} - \frac{Z_T}{M_T}\right)^2. \tag{1.154}$$

Compared to electrons, the deceleration of incident protons is reduced by a factor $(M_e/M_p) \sim 10^{-3}$. So in proton excitation the electric field and the radiation intensity are less by factors of 10^{-3} and 10^{-6}, respectively. For the $Z = 1$ target in proton excitation the dipole moment vanishes, so higher approximations (quadrupole moment) are needed. The quadrupole intensity is smaller by a factor α^2 but varies as the sum [1.86, 87]

$$\frac{d^2\sigma_{\text{quad}}}{d\omega\, d\Omega_\omega} \sim \left(\frac{Z_P}{M_P^2} + \frac{Z_T}{M_T^2}\right). \tag{1.155}$$

In an ion–atom collision with $Z_P/M_P \approx Z_T/M_T \approx 1/2$, the dipole intensity is considerably reduced due to the minus sign in (1.154). So the quadrupole term should be retained. Dipole NNB has been evaluated by *Adler* et al. [1.88]. *Reinhardt* et al. [1.86] have calculated dipole NNB (E1), quadrupole (E2) and their interference terms. The sum of these contributions agrees well with measurements of *Trautvetter* et al. [1.89] on NNB in 13 MeV $^{18}O + {}^{58}Ni$ collisions.

A projectile (velocity v_P) colliding with a target atom sees a free or loosely bound target electron coming towards it with velocity v_P or energy $T_P = 1/2 m_e v_P^2$. The electron is scattered by the Coulomb field of the projectile nucleus and emits the familiar electron–nucleus bremsstrahlung called *primary bremsstrahlung* (PB) or quasi-free electron bremsstrahlung (QFEB) (Fig. 1.32a). It is appreciable when the projective velocity is large compared to the orbital electron velocity to be scattered (Fig. 1.33). The knocked-out target atom electron radiates as if it has energy $m_e v_P^2/2$ in this secondary process. The high energy limit of the bremsstrahlung spectrum is $T_P(m_e/M_P) = (T_P/1837)$ MeV with T_P in MeV for a head-on collision. For protons of 1 MeV this is about 0.5 keV. The PB has been calculated by *Chu* et al. [1.90].

Classically, a projectile of velocity v_P can have binary collisions with loosely bound target electrons, producing ionized electrons. Their velocity can reach a value $2v_P$ [1.91]. They can collide with other target nuclei in solid targets and thereby emit bremsstrahlung with high energy limit $T_{max} \approx 2m_e v_P^2$. This is called

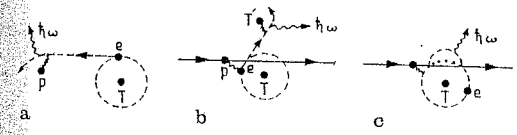

Fig. 1.32. **a** PB or QFEB; **b** SEB; **c** AB

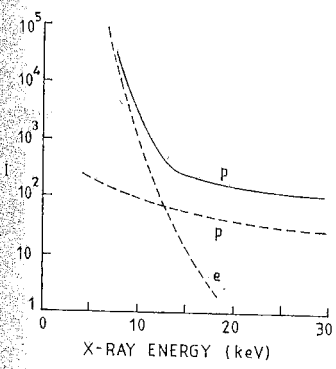

Fig. 1.33. Calculated (dashed) and observed (solid) radiation intensity for an electron (e) and 3 MeV proton (p). The observed rise below about 12 keV is due to the SEB process. I is in counts/energy interval (arbitrary) units

secondary-electron bremsstrahlung (SEB) (Fig. 1.32b). This process has been calculated by *Folkmann* et al. [1.92] and *Ishii* et al. [1.93].

In binary collisions between bound projectile and target electrons, bremsstrahlung is not directly produced. However, the dynamic polarization of the atomic clouds by an incoming particle can induce a dipole. This produces atomic bremsstrahlung (AB) (Fig. 1.32c) [1.94, 95]. The target atom electron is excited to a continuum state by the Coulomb interaction with the projectile and emits radiation while returning to its original state.

Particle-induced X-ray emission analysis (PIXEA) has been reviewed by *Walter* and *Willis* [1.96]. The particle can be p, α, ^{16}O, or some other ion. The molecular orbital X-rays are discussed in detail by *Anholt* [1.97].

The e–e bremstrahlung has been experimentally separated from the e–nucleus one by *Nakel* [1.98, 99]. The results agree with the calculations based on [1.63] (Fig. 1.34). For high Z, they disagree with the Bethe–Heitler theory [1.75].

Both PIXEA and *plasma excitation* have shown great promise, *Birks* and *Gilfrich* [1.100]. A plasma is a highly ionised gas with equal numbers of free (+) and (−) charges. Among other ways, a plasma is formed by a high-power laser beam falling on a target, or formed in a pulsed discharge tube with magnetic confinement. The X-rays are produced mainly by electron–ion collisions. The e–e collisions contribute appreciably for $k_B T > 10$ keV, where k_B is Boltzmann's

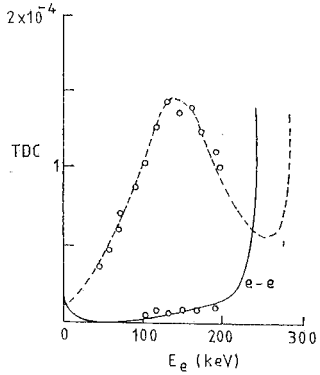

Fig. 1.34. Triply differentiated cross-section (TDC) $(Z^{-1})\, d^3\sigma/d\Omega_e\, d\Omega_\omega\, dE_e$ in b sr^{-1} keV^{-1} for e-nucleus (dashed) and e–e (solid) bremsstrahlung according to Elwert–Haug calculations including screening [1.63] as a function of outgoing electron energy E_e. The experimental points are from [1.99] for an incident electron energy of 300 keV, electron scattering angle $\theta_e = 20°$, photon ($\hbar\omega$) angle $\theta_\omega = -35°$ and thin copper target

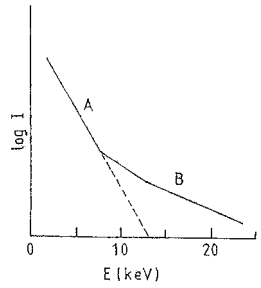

Fig. 1.35. Bremsstrahlung spectrum from a hot plasma

constant (8.64×10^{-5} eV/K) and T is the temperature in Kelvin. The 10 kV electrons of an X-ray tube correspond to 10^8 K, for thermal distribution. The thermal emission of hot plasma ($\sim 10^6$ K) is in the X-ray region (Fig. 1.34). The high-energy limit, where the extrapolated thermal line A meets the abcissa, indicates the plasma temperature. The non-thermal part B is due to superheated electrons. The decelerated charges are mainly responsible for bremsstrahlung, although other processes are present [1.101]. The electron can also interact with the plasma as a whole [1.102]. The area under the I–E curve (Fig. 1.35) is a measure of the number N of charged particles participating in the photon emission,

$$\int_0^\infty I(E)\, dE = N^2 T^{1/2}.$$

Thus Fig. 1.35 yields T and also N for the hot plasma. In laser-produced plasmas the X-rays are usually detected on films because of their short lifetime (~ 1 ns).

2. Characteristic X-Rays

In an atom, a centrally charged nucleus is surrounded by Z electrons. The electrons most tightly bound to the nucleus are called K-shell electrons, the next group the L-shell electrons, and so on. This is the picture of Bohr's atom which was given around 1913.

2.1 Line Emission

When fast cathode-ray electrons strike a target in the X-ray tube, mainly two things happen. 1) The incident electron is deflected in the collision process with the target atom, giving rise to the continuous radiation, as seen in Chap. 1, 2) The incident electron, if it has sufficient energy, may knock out one of the inner bound electrons in the target atom. If such a *hole* (or *vacancy*) is created (say) in the inner-most (K) shell, then according to the Bohr theory, an electron of the L or M shell can fall into the K shell, and a quantum of radiation is emitted. In this case the lines $K\alpha$, $K\beta$, . . . will appear in the emission spectrum (Fig. 2.1). A similar result follows in the case when an electron is knocked out from the L shell of the target atom. The X-ray K series looks like the Lyman series of the optical emission spectra of hydrogen, the L series like the Balmer series, etc.

Both of the processes 1) and 2) can compete with each other simultaneously. In some collisions, the incident electrons are deflected, and in others the inner electron from the target atom is knocked out. Experiments confirm this, because the line emission, *characteristic of the target atom*, appears as superimposed on the continuous emission (Fig. 2.2).

Figure 2.3 shows the spectrum for ^{42}Mo and ^{74}W at 35 kV. This voltage is not enough to excite the K lines of ^{74}W, and L lines would be off the diagram, at longer wavelengths.

Webster [2.1] increased the voltage on a rhodium (^{45}Rh) target X-ray tube and observed the intensity of the $K\alpha$ line at 0.613 Å. His experimental plot is shown in Fig. 2.4. It is an *isochromat*. The curve shows that the intensity increases gradually as the voltage increases, until at 23.2 kV the slope increases suddenly. This can be understood in the following way. Below 23.2 kV the X-ray intensity recorded at 0.613 Å is entirely due to the background continuous radiation, which increases slowly with voltage (see Fig. 1.25a). This radiation is

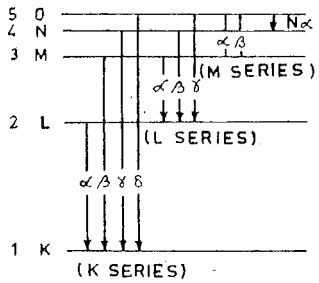

Fig. 2.1. The scheme of shells in an atom. The electronic transitions correspond to the X-ray emission lines in the quantum theory of Bohr

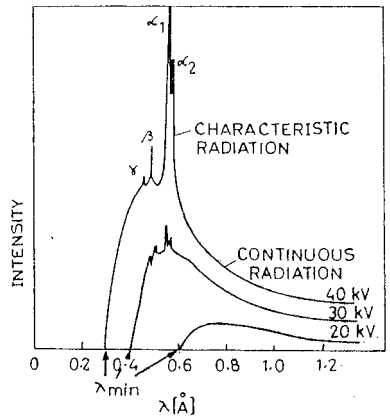

Fig. 2.2. X-ray spectrum of ^{47}Ag target at various tube voltages

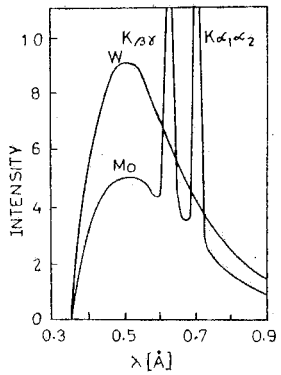

Fig. 2.3. X-ray spectrum from ^{42}Mo and ^{74}W at 35 kV

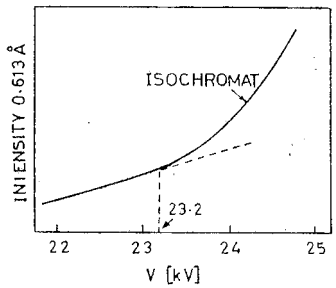

Fig. 2.4. Isochromat of rhodium $K\alpha$ line

not characteristic of ^{45}Rh, because a similar intensity would be observed for any target of comparable Z. At 23.2 kV, the incident electrons have just enough energy to eject the K-shell electrons from ^{45}Rh atoms. As soon as holes in the K-shell are produced, transitions from other shells occur. In particular, electrons from the L-shell undergo transitions to the K level (the hole in the K-shell is transferred to the L-shell), and give rise to the ^{45}Rh $K\alpha$ line of energy

$$E(K\alpha) = E_K - E_L = h\nu_{(K\alpha)} = hc/\lambda_{(K\alpha)}. \tag{2.1}$$

Here $E_K, E_L, \ldots$ are the energies required to remove a $K, L, \ldots$ electron, respectively. As the tube voltage is further increased, more K electrons are ejected, yielding a more intense $K\alpha$ line.

Before any of the K-characteristic X-rays are emitted, a K electron first must be ejected from the atom under study. The $K\alpha$ line emission will transfer this *hole* (initially in the K-shell) to the L-shell. We can now obtain in $L\alpha$ line when this hole in the L-shell is transferred to the M-shell (Fig. 2.1). Thus, the entire line-emission spectrum is produced because of an initial hole in the K-shell.

2.2 Moseley Law

According to the quantum theory of Bohr the frequency of a spectral line is given by

$$\nu = R_\infty c\left(\frac{M}{M+m}\right)Z^2\left(\frac{1}{n_f^2} - \frac{1}{n_i^2}\right), \tag{2.2}$$

where m is the electron mass, M is the nucleus mass, $R_\infty = 2\pi^2 me^4/ch^3 = 109737.31\,\mathrm{cm}^{-1}$ is the *Rydberg constant* for an atom of infinite mass, and n_i and n_f are the principal quantum numbers of the initial and final states of the atom involved in the transition, respectively.

The result (2.2) holds good for an atom that consists of a nucleus with one external electron. In a complex atom the nuclear charge will not be exactly Ze but modified by the presence of other external electrons in the atom. Because of this screening of the nuclear charge, the effective charge is usually written as $Z_{\mathrm{eff}} = Z - \sigma$, where σ is the *screening constant*. When this correction is included, the factor $M/(M+m)$ can be ignored, being a very small correction due to the motion of the nucleus about the center of mass of the system.

The $K\alpha$ line involves the transition of an electron from the initial L-shell (or state) $n_i = 2$ to the final K state $n_f = 1$ (Fig. 2.1)

$$\nu_K = R_\infty c(Z-\sigma_K)^2\left(\frac{1}{1^2} - \frac{1}{2^2}\right) = R_\infty c\frac{3}{4}(Z-\sigma_K)^2, \tag{2.3}$$

$$\left(\frac{\tilde{\nu}}{R_\infty}\right)_K^{1/2} = \left(\frac{\nu}{cR_\infty}\right)^{1/2} = 0.866(Z-\sigma_K) = a_K(Z-\sigma_K). \tag{2.4}$$

where $\tilde{\nu} = \nu/c = 1/\lambda$ is the *wave number*. For the $L\alpha$ line, due to a transition from M state to L state, $n_i = 3$ and $n_f = 2$,

$$\nu_L = R_\infty c\frac{5}{36}(Z-\sigma_L)^2.$$

Moseley [2.2] plotted $(\tilde{\nu}/R_\infty)^{1/2}$ of the measured $K\alpha$ line against Z. He obtained a straight line (Fig. 2.5) that could be expressed as

$$\left(\frac{\tilde{\nu}}{R}\right)_{K\alpha}^{1/2} = 0.874(Z - 1.13)\ (\textit{Moseley law}). \tag{2.5}$$

Precision measurements have shown that $(\tilde{\nu}/R_\infty)^{1/2}$ is not exactly a linear function of Z for the resolved $K\alpha_1$ and $K\alpha_2$ lines.

Moseley plots can be drawn for all lines in K, L, M, ... series. For the $L\alpha_1$ lines of elements with atomic number $Z > 62$ the values of constants in (2.6) are $a = 0.376$ and $\sigma = 7.90$. Knowing the $\tilde{\nu}/R_\infty$ value from (2.6) for a photon, we can calculate the wavelength by

$$\lambda(\text{Å}) = \frac{911.27}{\tilde{\nu}/R_\infty}. \tag{2.6}$$

In measurements using crystal spectrographs, the λ is usually given in the "eks" unit, XU, or in the "kiloeks" unit, kXU. The kXU was first introduced by *Wilson* [2.3]. *Bearden* [2.4] gives

$$1\ \text{kXU} = 1000\ \text{XU} = (1.002076 \pm 0.000005)\ \text{Å}. \tag{2.7}$$

The various conversion factors can be found from the following example [2.4]:

Line	[Å]	[keV]	$(\tilde{\nu}/R_\infty)$	[XU]	$(\tilde{\nu}/R_\infty)$ [cm/XU]
^{42}Mo $K\alpha_1$	0.709300	17.47934	1284.74	707.831	1287.40.

2.3 Classical Oscillator Model

To explain the discrete lines of a spectrum, the classical theory provides the atom with a set of electron oscillators, each of which corresponds to a definite line. In this model, the electron in an atom undergoes harmonic vibrations around the nucleus to which it is bound. The electron is decelerated as it moves away from the nucleus and accelerated when it moves toward it. We, therefore, expect it to emit radiation energy. When a line is strong, it is provided with a number of identical oscillators (the so-called *oscillator strength*).

For the one-dimensional harmonic oscillator (Fig. 2.6) the equation of motion is

$$x = x_0 \cos(\omega t) = x_0 \cos(2\pi\nu t), \tag{2.8}$$

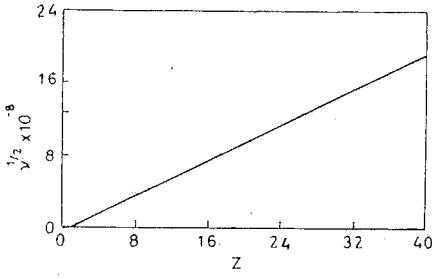

Fig. 2.5. Moseley plot for the $K\alpha$ line

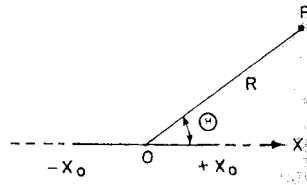

Fig. 2.6. The classical oscillator or dipole. P is the point of observation of the radiation from such a dipole

where x_0 is the amplitude, and ω the angular frequency. The acceleration at any point x is

$$a = \frac{d^2x}{dt^2} = -4\pi^2\nu^2 x.$$

From (1.58) the radiation intensity at the point P is

$$I(\Theta, x) = \frac{4\pi^3 e^2}{c^3} \frac{\sin^2\Theta}{R^2} \nu^4 x^2. \tag{2.9}$$

Suppose there are N atoms per 1 cm^3 with Z electrons per atom. The Z electrons can be divided into groups specified by the index j, with f_j electrons that have the same frequency ν. The number f_j is called the *oscillator strength* of the jth oscillator, and it satisfies the obvious sum rule

$$\sum_j f_j = Z. \tag{2.10}$$

Since $N_\nu = Nf_j$ is the number of oscillators per 1 cm^3 with frequency ν and amplitude x_0, the rate at which the energy is lost is obtained by integrating over a spherical surface and multiplying by N_ν,

$$-\frac{dU}{dt} = P = N_\nu \int_0^\pi I(\Theta, x)\, 2\pi R \sin\Theta\, R\, d\Theta = N_\nu \frac{32\pi^4 e^2}{3c^3} \nu^4 x^2. \tag{2.11}$$

The electron makes many oscillations per second. The average value $\langle x^2 \rangle$ of x^2 for the period $T = 1/\nu$ is

$$\langle x^2 \rangle = \frac{\oint x^2\, dt}{\oint dt} = \frac{\oint x_0^2 \cos^2 2\pi\nu t\, dt}{T} = \frac{1}{T} x_0^2 \int_0^T \cos^2 2\pi\nu t\, dt = \frac{1}{T} x_0^2 \frac{1}{2\nu}$$

$$= \frac{1}{2} x_0^2.$$

The power averaged over the period T, or intensity I, is

$$I \equiv \left\langle -\frac{dU}{dt} \right\rangle = \langle P \rangle = N_\nu \frac{32\pi^4 e^2}{3c^3} \nu^4 \langle x^2 \rangle = N_\nu \frac{16\pi^4 e^2}{3c^3} \nu^4 x_0^2. \tag{2.12}$$

In general, the oscillations of the dipole occur along some direction $r(x, y, z)$ with an amplitude $r_0(x_0, y_0, z_0)$. Then

$$\langle P \rangle = N_\nu \frac{32\pi^4 e^2}{3c^3} \nu^4 (\langle x^2 \rangle + \langle y^2 \rangle + \langle z^2 \rangle) = N_\nu \frac{16\pi^4 e^2}{3c^3} \nu^4 r_0^2, \tag{2.13}$$

where

$$r_0^2 = x_0^2 + y_0^2 + z_0^2 = 2(\langle x^2 \rangle + \langle y^2 \rangle + \langle z^2 \rangle). \tag{2.14}$$

2.4 Quantum Theory

We can invoke the correspondence principle to introduce the quantum ideas. Such an approach lacks rigor, but leads to the same result as would be given by a correct quantum mechanical derivation of the transition probability.

To convert the classical expression (2.13) into the corresponding expression in the quantum theory, we take the following three steps:

Step 1: We replace the classical frequency ν by the quantum frequency ν_{fi} of photons that are radiated during the transitions of the atom from the initial state i of energy E_i to the final state f of energy E_f

$$\nu \to \nu_{fi} = (E_i - E_f)/h, \quad (i \to f). \tag{2.15}$$

Step 2: We replace the amplitude x_0 of the oscillations of the dipole by the *matrix element* x_{fi}

$$x_0 \to x_{fi} = (f|x|i) = \int \psi_f x \psi_i \, d\tau, \quad d\tau = dx\, dy\, dz, \tag{2.16}$$

where ψ_i and ψ_f are the normalized initial- and final-state wave functions, respectively. Similarly, $y_{fi} = (f|y|i)$ and $z_{fi} = (f|z|i)$.

Step 3: We replace [2.5] the time average of the coordinate of the oscillator $\langle x^2 \rangle$ by the square of the matrix element of the same quantity for the transition $i \to f$,

$$\langle x^2 \rangle \to 2|x_{fi}|^2. \tag{2.17}$$

The factor 2 occurs on the right-hand side to give us the final result in agreement with the quantum mechanical result. The difference occurs because we have taken $\cos \omega t$ rather than the full exponential form to describe the oscillator.

Equation (2.17) gives the well-known connection between the classical quantities and the quantum mechanical quantities according to the *correspondence principle*. From (2.14, 17),

$$r_0^2 \to 4(|x_{fi}|^2 + |y_{fi}|^2 + |z_{fi}|^2) \equiv 4r^2(i,f). \tag{2.18}$$

For the emission process, the initial state consists of an atom excited (one electron missing) in an inner shell without the presence of quanta. In the final state, an X-ray quantum is emitted and the hole in the inner level is filled (*spontaneous emission*).

Let w_{fi} be the transition probability per unit time of an atom going from the state i to the state f. The correspondence principle allows us to write, from (2.13, 18), the total energy radiated per unit time, or the intensity of the line, in spontaneous emission as

$$I(i,f) = \langle P \rangle_{fi} = N_v h\nu_{fi} w_{fi} = N_v \frac{64\pi^4 e^2}{3c^3} \nu_{fi}^4 r^2(i,f). \tag{2.19}$$

We have interpreted the power as the product of the spontaneous rate of transition from i to f and the emitted photon energy $h\nu_{fi}$. Equation (2.19) gives

$$w_{fi} = \frac{64\pi^4 e^2}{3c^3 h} \nu_{fi}^3 r^2(i,f). \tag{2.20}$$

This is just the quantum mechanical result for spontaneous emission (see, for example, [2.6]).

If E is the energy of the atom, the Bohr radius a_0, or the dimension of the atom, is roughly $a_0 \sim e^2/E$. Putting $r_0 \sim a_0$,

$$w_{fi} \sim \frac{e^2}{\hbar c^3} \omega^3 a_0^2 \sim \frac{1}{137} \left(\frac{\omega e^2}{c\hbar\omega} \right)^2 \omega \sim \frac{\omega}{137^3}, \tag{2.21}$$

which is $\sim 10^8\ s^{-1}$ for the optical region and $\sim 10^{11}\ s^{-1}$ for X-rays.

In (2.19, 20), we should include two more factors. Before any X-ray emission line appears, the atom must be *ionized in an inner shell*. This ionized state is the initial excited state. In an X-ray tube, this occurs when the incident cathode electrons collide with the target atoms and ionize them. Therefore, we must introduce a function F_i that determines the *ionization probability* of an inner bound level i of the atom. The second factor is *statistical weight* g_i of the state i, which gives the number of different possible orientations of the underlying configuration that gives rise to the state under consideration.

For the emission of X-ray photons, therefore,

$$I(i,f) \sim \nu_{fi}^4 F_i g_i r^2(i,f). \tag{2.22}$$

Here F_i is the ionization probability for effectively one electron per 1 cm^3.

Inner-shell ionization will also occur when a target is bombarded by protons or heavier ions. The topic of X-ray production by heavy charged particles has been reviewed by *Merzbacher* and *Lewis* [2.7], *Ogurtsov* [2.8] and *Wille* and *Hippler* [2.9].

2.5 Ionization Function

We are interested in the relative intensity of a given (say K) line that arises in a particular transition $i \to f$ in a thin target, when the energy E of the incident electrons is varied. In such a case, we can treat all the quantities in (2.22) as constants except F_i, and write

$$I(i,f) \sim F_i \quad (\textit{thin target}) \tag{2.23}$$

2.5.1 Classical Theory

A satisfactory theory of ionization function is not available. *Davis* [2.10] made an *ad hoc* assumption that the relative excess of energy of the incident electrons over the binding energy E_i is a measure of the ionization probability. He took

$$F_i = (V_x - V_i)/V_x, \tag{2.24}$$

where eV_x is the energy of the incident electron at a depth x below the target surface, and eV_i is the ionization energy of the level i. The number of atoms that are excited to the ith level (hole created in the ith level) in 1 cm^2 of the layer dx per second is

$$dN_i = nNF_i \frac{dx}{\sin\psi} = nN \frac{V_x - V_i}{V_x} \frac{dx}{\sin\psi}, \tag{2.25}$$

where n is the number of incident electrons that cross a unit-area layer between x and $x+dx$ below the target surface, N is the number of collisions with target atoms per unit path length of the incident electrons, and ψ is the angle of incidence of the electrons from the target face (Fig. 2.7). The path length in the layer dx is $dx/\sin\psi$.

For a thick target, we can use the Thomson-Whiddington law (1.114) to get a relation between n and V_x, if we express the velocity v_x at depth x in terms of V_x and replace dx by $dx/\sin\psi$

$$\frac{1}{2}mv_x^2 = eV_x, \quad \frac{dv_x^4}{dx} = -bZ,$$

$$dV_x^2 = 2V_x dV_x = -a\frac{dx}{\sin\psi}; \quad a = \frac{4e^2bZ}{m^2}. \tag{2.26}$$

Substituting dx from (2.26) in (2.25) and integrating from the tube voltage V to V_i (corresponding to 0 to x, after which there is not enough energy left for ionization to be possible),

$$N_i = -\frac{2nN}{a}\int_V^{V_i}(V_x - V_i)\,dV_x = \frac{2nN}{a}[V(V/2-1) - V_i(V_i/2-1)]$$
$$\simeq \frac{nN}{a}(V^2 - V_i^2). \tag{2.27}$$

The total intensity $I_{tot}(i, f)$ can now be written as

$$I_{tot}(i,f) = \frac{16\pi^4 e^2}{3c^3} v_{fi}^4 N_i g_i r^2(i,f) = \text{const.}\,(V^2 - V_i^2), \tag{2.28}$$

in the simplified classical calculation of F_i presented here. This formula is found to be reliable up to $V = 3V_i$ for the intensity measurements of K lines made by

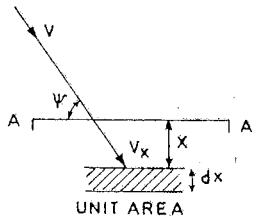

Fig. 2.7. A target layer at a depth x

Hill and *Terrey* [2.11]. For $V > 3V_i$ the depth of penetration of electrons into the target increases and the neglected factor of the absorption of X-rays within the target begins to predominate. Consequently, a lower intensity is observed than predicted by (2.28) (Fig. 2.8).

A classical theory of near-threshold ionization by electrons was first given by *Wannier* [2.12]. He related the ionization cross-section σ^i to the available phase space for two escaping electrons (one incident electron after scattering, and the other knocked-out atomic electron). For the uncorrelated motion of the two electrons, the available phase space, and so σ^i, increases linearly with excess energy, $\sigma^i = A(E - E_n)$, where E is the incident energy and E_n is the binding energy of the nth state. For the correlated motion the available phase space is reduced, and $\sigma^i = B(E - E_n)^{1.127}$ for single ionization.

2.5.2 Quantum Theory

In quantum mechanics the Born approximation is commonly used to find the excitation and ionization cross-sections. It is proportional to the absolute square of the matrix element of the Coulomb potential acting between the incident electron and the atomic electron,

$$\Psi_{final}(\boldsymbol{R}, \boldsymbol{r}) \frac{e^2}{|\boldsymbol{R}-\boldsymbol{r}|} \Psi_{initial}(\boldsymbol{R}, \boldsymbol{r})\, d\boldsymbol{r}\, d\boldsymbol{R}. \tag{2.29}$$

Here $\boldsymbol{R}$ is the position vector of the incident electron and $\boldsymbol{r}$ that of atomic electron, relative to the nucleus. In the plane wave Born approximation the wave functions Ψ are approximated by the product form

$$\Psi(\boldsymbol{R}, \boldsymbol{r}) = e^{i\boldsymbol{k}\cdot\boldsymbol{R}}\phi_0(\boldsymbol{r}),$$

where the projectile is the plane wave and $\phi_0(\boldsymbol{r})$ is the unperturbed ground state wave function of the atom.

We may deal with the inelastic scattering in the same way as the elastic scattering, in which case the differential cross-section in the center-of-mass system is given by the Born approximation formula

$$d\sigma_{n0}(\Omega) = \frac{4\pi^2 m^2 e^4}{h^4}\left(\frac{k_n}{k_0}\right)\left|\int \phi_n^*(\boldsymbol{r})\frac{e^{i\boldsymbol{K}\cdot\boldsymbol{R}}}{|\boldsymbol{R}-\boldsymbol{r}|}\phi_0(\boldsymbol{r})\,d\boldsymbol{r}\,d\boldsymbol{R}\right|^2 d\Omega, \tag{2.30}$$

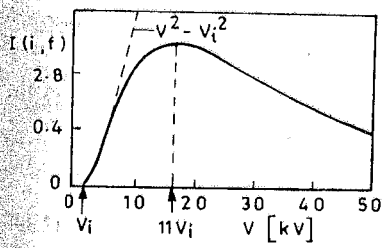

Fig. 2.8. The observed intensity $I(i, t)$ of the $K\alpha_{1,2}$ line of aluminium versus the voltage V in kV

where $\hbar\boldsymbol{k}_0$ and $\hbar\boldsymbol{k}_n$ are momenta of relative motion for the projectile before and after the collision, and $\hbar\boldsymbol{K} = \hbar(\boldsymbol{k}_0 - \boldsymbol{k}_n)$ is the momentum transfer of magnitude $\hbar K$ given by $K^2 = k_0^2 + k_n^2 - 2k_0 k_n \cos\theta$. The projectile is scattered into the solid angle $d\Omega = \sin\theta\, d\theta\, d\phi$. Integration on the coordinates of the incident electron using the formula

$$\int e^{i\boldsymbol{K}\boldsymbol{n}\cdot\boldsymbol{r}}(1/|\boldsymbol{R}-\boldsymbol{r}|)\, d\boldsymbol{R} = (4\pi/K^2)e^{i\boldsymbol{K}\boldsymbol{n}\cdot\boldsymbol{r}}$$

gives [2.13]

$$d\sigma_{n0}(\Omega) = \frac{4\pi^2 m^2 e^4}{\hbar^4}\left(\frac{k_n}{k_0}\right)\left|\frac{4\pi}{K^2}\int \phi_n^*(\boldsymbol{r})\, e^{i\boldsymbol{K}\cdot\boldsymbol{r}}\phi_0(\boldsymbol{r})\, d\boldsymbol{r}\right|^2 d\Omega. \tag{2.31}$$

The cross-section for the excitation of the nth state, when $d\sigma_{n0}$ is independent of ϕ, is

$$\sigma_{n0} = \int_0^\pi d\sigma_{n0}(\theta)\, 2\pi \sin\theta\, d\theta$$

$$= \frac{2\pi}{k_0 k_n}\int_{K_{\min}}^{K_{\max}} d\sigma_{n0}(K)\, K\, dK, \tag{2.32}$$

$$K_{\min} = k_0 - k_n, \quad K_{\max} = k_0 + k_n. \tag{2.33}$$

Using $(\hbar^2/2m)(k_0^2 - k_n^2) = E_n - E_0$ and $k_0 + k_n \simeq 2k_0$, for the small momentum transfer case

$$K_{\min} = k_0 - k_n \simeq (k_0^2 - k_n^2)/2k_0$$

$$= (m/\hbar^2 k_0)(E_n - E_0). \tag{2.34}$$

The $d\sigma_{n0}$ decreases rapidly as K increases, because

$$d\sigma_{n0} = \frac{4m}{\hbar^4}\left(\frac{k_n}{k_0}\right)\frac{e^4}{K^4}|\varepsilon_{n0}(K)|^2, \tag{2.35}$$

$$\varepsilon_{n0}(K) = \int \phi_n^*\, e^{iKz}\, \phi_0\, d\boldsymbol{r}. \tag{2.36}$$

The $\varepsilon_{n0}(K)$ is very small if $\exp(iKz)$ oscillates many times within the range of ϕ_0 and ϕ_n, that is, if

$$K^2 \gg Z^2/a_0^2 \tag{2.37}$$

where a_0/Z is the radius of the ground state orbit. As $Z^2e^2/2a_0$ is the ionization energy V_i of the normal atom, $d\sigma_{n0}$ is small when

$$K^2 \gg (2m/\hbar^2)V_i \equiv K_0^2. \tag{2.38}$$

To evaluate ε_{n0} approximately, write

$$\varepsilon_{n0}(K) = 1 + iKz + \cdots$$

$$\simeq iK\int \phi_n^* z\phi_0\, d\boldsymbol{r} \equiv iKz_{n0} \tag{2.39}$$

as $\int \phi_n^*\phi_0\, d\boldsymbol{r} = 0$. Thus

$$d\sigma_{n0} = \frac{4m^2}{\hbar^4}\left(\frac{k_n}{k_0}\right)\frac{e^4}{K^2}|z_{n0}|^2, \quad K < K_0. \tag{2.40}$$

For larger values of K, $d\sigma_{n0}(K)$ is negligible. Therefore, from (2.32, 40),

$$\sigma_{n0} \simeq \frac{8\pi m^2 e^4}{k_0^2\hbar^4}|z_{n0}|^2\int_{K_{\min}}^{K_0}\frac{dK}{K}$$

$$\simeq \frac{4\pi m^2 e^4}{k_0^2\hbar^4}|z_{n0}|^2 \ln\frac{2mv_0^2}{E_n - E_0}, \tag{2.41}$$

where (2.34, 38) give the limits and $\hbar k_0 = mv_0$. Thus σ_{n0} for *excitation* falls off as $v_0^{-2}\ln v_0$ at high velocities v_0 of impact.

The cross-section σ_{k0} for *ionization* can now be found. Let the wave number k_e of the ejected electron lie in dk_e at k_e. Then the energy lies between $\hbar^2 k_e^2/2m$ and $\hbar^2(k_e^2 + 2k_e dk_e)/2m$. Using the above method, the corresponding cross-section $\sigma_{k0}dk_e$ is found to be

$$\sigma_{k0}\, dk_e = \frac{4\pi m^2 e^4}{k_0^2\hbar^4}|z_{k_e 0}|^2 \ln\left(\frac{2mv_0^2}{E_{k_e} - E_0}\right)dk_e. \tag{2.42}$$

The total cross section for ionization σ^i [2.14, 15] is

$$\sigma^i = \int_0^{K_{\max}}\sigma_{k0}\, dk_e \simeq \frac{2\pi e^4}{mv_0^2}\frac{A}{|E_0|}\ln\left(\frac{2mv_0^2}{C}\right), \tag{2.43}$$

where

$$A = \int |z_{k_e 0}|^2\, dk_e$$

and $C(\sim E_0)$ is a certain mean of $E_{k_e} - E_0$. This result due to Bethe is the starting point for most treatments of σ^i. Use of the Born approximation is valid when the incident electron velocity is larger than the orbital velocity of atomic electrons for X-ray production. For more details see [2.16].

One can express (2.43) for the (n, l)th shell as

$$\sigma^i_{(n,l)} = \frac{2\pi e^4 Z_{nl}}{mv_0^2|E_{nl}|}\, b_{nl} \ln\frac{2mv_0^2}{B_{nl}}, \tag{2.44}$$

where Z_{nl} is the number of electrons in the (n, l) shell, $b_{nl} = 0.35$ for the K shell, and $B_{nl} = 1.65\, E_{nl}$. The two constants of Bethe's result, b_{nl} and B_{nl}, are fixed by comparison of calculations of *Burhop* [2.17] with experiments. The sum of (2.44) over all shells leads to the Bethe energy-loss formula for electrons in matter.

For the K shell ($Z_K = 2$) using excitation ratio $U \equiv E/E_K$, where E is the kinetic energy of incident electrons,

$$\sigma^i_{(K)} = \frac{2\pi e^4}{EE_K}\, b_K\,(\ln 4E - \ln B_K)$$

$$= (2\pi e^4/UE_K^2)b_K(\ln 4UE_K - \ln B_K). \tag{2.45}$$

Thus $\sigma^i_{(K)} E_K^2$ is the same function of U for *all* elements [2.18]. *Worthington* and *Tomlin* [2.19] suggested

$$B_K = (1.65 + 2.35 e^{(1-U)}) E_K, \tag{2.46}$$

It gives a value 1.65 E_K for large E_K (U small) and $4E_K$ for $E \gtrsim E_K$. For $b_K = 0.7$, $B_K = 4E_K$ (in eV), and e in esu,

$$\sigma^i_{(K)} E_K^2 = 2\pi e^4 \frac{\ln U}{U} (0.7 \times 9 \times 10^4)$$
$$= 9.12 \times 10^{-14} (\ln U)/U. \tag{2.47}$$

The Bethe formula agrees with experiment at large energies $U \geq 20$ (Fig. 2.9). Near the maximum (near $E/E_K \approx 4$, or roughly twice the bound electron velocity) it overestimates the data by about 30%. This is due to the neglect of electron exchange in the calculation. The exchange amplitude g is related to the direct amplitude f by $g/f = (K/k_0)^2$, which is small for large incident velocities. This improves the situation [2.20]. For fast electrons relativistic calculations have been made by *Perlman* [2.21], *Scofield* [2.22], and *Eschwey* and *Manakos* [2.23].

2.5.3 Heavy Projectiles

The probability of ionization by incident *heavy projectiles* (protons and ions) is similar to the case of incident electrons, for similar velocities. So $E_p = (1/2) M v_p^2$ for protons is of several MeV. The maximum energy transferred from a proton to an orbital electron is $4(m/M)E_p$. This is equal to the case of electron bombardment if $E_p = (M/4m)E_e$. The Bethe formula is independent of projectile mass [2.16], and so equal for electron or proton impact. However, the maximum in the cross-section for the proton case now occurs at an incident velocity roughly equal to the orbiting velocity of the bound electron. The Born approximation result shows a scaling behaviour of the type [2.7]

$$\sigma^i_{(K)} \Theta_K Z^4_{\text{eff}} / Z_p^2 = f(\eta_K / \Theta_K^2), \tag{2.48}$$

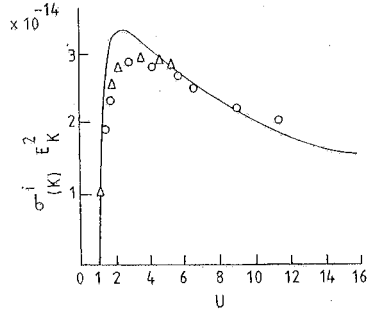

Fig. 2.9. Scaled total ionization cross-section $\sigma^i_{(K)} E_K^2$ vs relative kinetic energy U, for K-shell ionization by electron impact. The curve is from (2.47) and experimental points are for nickel (○) and silver (△). $\sigma^i_{(K)}$ is in cm² and E_K in eV

where Z_p is the projectile charge, Z_{eff} is the effective target nuclear charge ($Z_K = Z - 0.3$, $Z_L = Z - 4.15$ for K and L shells, respectively), $\eta_K = E/(Z^2_{\text{eff}}\, Ry)$, $\Theta_K = E_K/(Z^2_{\text{eff}}\, Ry)$, and Ry is the Rydberg energy. For recent data see [2.24–26]. The plane wave Born approximation theory is compared with experiments in Fig. 2.10, for proton impact. Due to the large mass-to-charge ratio of protons compared to electrons, ionization is possible in proton impact at low velocities ($v_1 \ll v_2$). Then the bound-electron wave function has enough time to adjust to the interaction. The resulting polarization of the electron cloud gives increased binding. Also, Coulomb deflection is significant for small v_1 processes. When corrections are made for increased binding and Coulomb deflection, the theory agrees with the experiment in Fig. 2.10 at low velocities (small η_K/Θ_K^2) also [2.26].

2.5.4 Intensity

The $\sigma^i_{(K)}$ is usually found by absolute measurements of the K X-ray intensity from electron (or other projectile) impact of solid targets. The loss of energy per centimetre path, $-dE/dx$, of an incident electron undergoing collisions that eject target atom electrons from any shell (K, L, M, ...) is given by

$$-\frac{dE}{dx} = n_a \frac{2\pi}{k_0 k_n} \sum_n \int_{K_{\min}}^{K_{\max}} (E_n - E_0)\, d\sigma_{0n}(K)\, K\, dK, \tag{2.49}$$

where n_a is the number of atoms per cm³, and the sum is over all the shells. The sum is not done immediately as $K_{\min}$ is a function of n. *Bethe* [2.13] has done it for hydrogen-like wave functions, but the results are not accurate. A useful form is [2.27, 28]

$$-\frac{dE}{dx} = \frac{2\pi e^4 n_a Z}{E} \ln \frac{2E}{I}, \tag{2.50}$$

where I is a mean excitation energy. One can write $n_a = N_A \rho / A$, where N_A is the Avogadro number, ρ the density and A the atomic weight. It differs from (2.44)

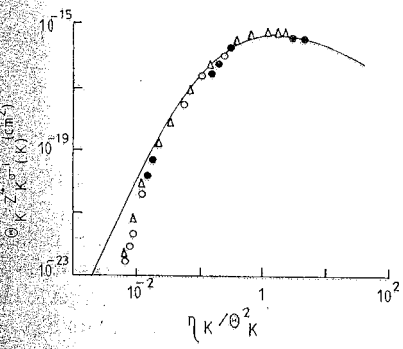

Fig. 2.10. Composite graph of the scaled cross-section $\Theta_K Z_K^4 \sigma^i_{(K)}$ for K-shell ionization by proton impact vs scaled incident energy η_K/Θ_K^2, for atomic targets $13 \geq Z_2 \geq 30$. A few experimental points are shown: ○ Fe [2.23], △ Ni [2.24] and • Cu [2.25]. The curve is the plane wave Born approximation calculation

as now b and B are averaged over all shells (electrons from all shells are involved). The slowly varying term $\ln(2E/I)$ can be neglected. Then integration gives the v^4 law of Whiddington,

$$\rho x \propto Z(E_0^2 - E^2) \propto (v_0^4 - v_x^4), \tag{2.51}$$

where E_0 and E are the initial and final energies of the electrons and ρx the mass thickness of the matter. It is supported by data [2.29, 30]. It gives $\rho(dx/dE) = -2kE$. Then the *number of K ionizations per electron is*

$$\begin{aligned} F_K &= \int_0^{x_K} \sigma^i_{(K)}\, n_a\, dx = \int_{E_0}^{E_K} (\sigma^i_{(K)})\, n_a \frac{dx}{dE}\, dE \\ &= \int_{E_K}^{E_0} \left(\frac{2\pi e^4}{EE_K} b_K \ln \frac{4E}{B_K}\right) \frac{2kEn_a}{\rho}\, dE \\ &= \frac{2n_a k}{\rho} 2\pi e^4 b \int_1^{U_0} \ln\left(\frac{4U}{a}\right) dU \\ &= (2n_a k/\rho)(2\pi e^4 b)[U_0 \ln(4U_0/a) - (U_0 - 1) - \ln(4/a)] \\ &= (2n_a k/\rho)(2\pi e^4 b)[U_0 \ln U_0 - (U_0 - 1)], \end{aligned} \tag{2.52}$$

where $a = B_K/E_K$. *Green* and *Cosslett* [2.31] use it to write the number of K photons generated by direct process per incident electron as

$$n_K = \tilde{\omega}_K F_K, \tag{2.53}$$

where $\tilde{\omega}_K$ is the probability that an atom ionized in the K shell will emit a K photon (the K fluorescence yield). To compare it with the observed absolute intensity of K radiation, several corrections are needed. For example, some of the photons are absorbed in the target material and some photons may belong to the continuous spectrum with energies greater than the K excitation energy. The uncertainty in the value of $\tilde{\omega}_K$ used makes theoretical predictions differ among themselves. Various corrections and experimental methods have been described by *Massey* and *Burhop* [Ref. 2.15, p. 160].

In early work *Webster* et al. [2.32] found that the intensity from a thick silver target when corrected for the absorption in the target varies as

$$I \propto (V - V_K)^{1.65}. \tag{2.54}$$

More recently *Campbell* [2.33] found a similar variation. Graphically,

$$U \ln U - (U-1) = 0.365(U-1)^{1.67}, \quad 1.5 < U < 15. \tag{2.55}$$

Campbell has also examined the theories of *Worthington* and *Tomlin* [2.19] and of *Archard* [2.34].

For $i(= K, L, \ldots)$ X-rays in thick targets, *Production efficiency* is defined either as the total number of i photons produced in the target per incident electron, or as the ratio of the total K X-ray energy produced in the target to the energy of an incident electron. The K X-ray *yield* Y_K (or *intensity* I_K) for a given

target in a given direction is defined as the number of K X-rays emitted per steradian per incident electron and does not include the K X-ray absorbed in the target. For a given emission angle,

$$Y_i = N_i/(\varepsilon_i n d\Omega), \quad i = K, L, \text{ etc.}, \tag{2.56}$$

where N_i is the number of i X-rays recorded by the detector, ε_i is the detector efficiency for measuring the i X-rays from a given element, n is the number of electrons incident on the target, and $d\Omega$ is the solid angle subtended by the detector aperture.

Agarwal and *Sparrow* [2.35] have recently measured the absolute intensities of ^{6}C K_α, ^{13}Al K, ^{26}Fe L and ^{29}Cu L lines produced by electron impact on thick targets. Their experimental arrangement is shown in Fig. 2.11 and Al K results in Fig. 2.12. The N_i is determined by recording the pulses from the detector in a multichannel analyser. In detection, first a certain fraction f^i_t of the incident i X-rays is *transmitted* through the detector window, then a certain fraction f^i_a of the transmitted i X-rays is *absorbed* in the detector and finally a certain fraction f^i_p of the absorbed i X-rays *produces pulses* that contribute to the observed peaks. Thus the detector efficiency is given by $\varepsilon_i = f^i_t f^i_a f^i_p$. The f^i_t is experimentally determined. The f^i_a is estimated by the quantity $[1 - \exp(-\mu_i x)]$ where x is the

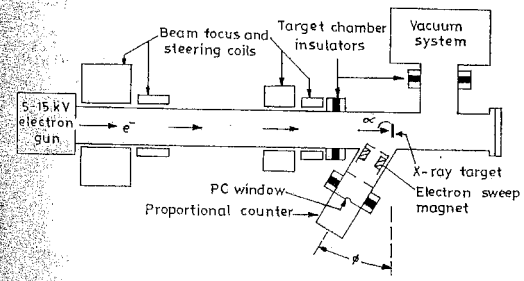

Fig. 2.11. The electron accelerator for the characteristic X-ray production [2.35]

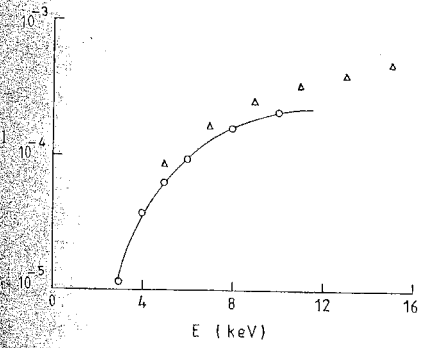

Fig. 2.12. Aluminium K intensity for $\alpha = 90°$, $\phi = 30°$. The curve connects the experimental points of *Dolby* [2.36], while triangles represent values of *Agarwal* and *Sparrow* [2.35]. I is in $\text{sr}^{-1}\,\text{electron}^{-1}$

thickness (in g/cm^2) and μ_i is the mass absorption coefficient of the detector material at the specified energy of the i X-ray. The fraction $f_p^i \simeq 1$.

For 2.28 MeV protons on thin targets the K X-ray yield I_K^p (X-ray per proton) data are given in [2.37, 38]. The cross-section is about three times that for the electron case. *Kahn* and *Potter* [2.39] used 0.1–0.5 MeV protons on thick targets. For recent proton and ion impact results see [2.40, 41]. The theoretical ionization cross-section is converted to the X-ray production cross-section by using single-hole fluorescence yields.

2.5.5 Molecular–Orbital X-Rays

Briggs [2.42] gave a quasi-static theory of molecular–orbital (MO) X-ray emission. There is a relation between the internuclear distance R and the transition energy $\Delta E_{if}(R)$. Several transitions $i \to f$ can occur for any R. For K (or 1 $s\sigma$) MO X-rays, the strongest transition is $2p\pi \to 1s\sigma$. The theory assumes that X-rays of energy E_x are emitted only at $R = R_g$ where $E_x = \Delta E_{if}(R_g)$. Then the emission probability $\Delta P_{if}(E_x)$ is

$$\Delta P_{if} = (2\Delta R/v_R)\,\lambda_{if}(R_g),$$
$$v_R = v\left(1 - \frac{V(R)}{E_c} - \frac{b^2}{R^2}\right)^{1/2}, \tag{2.57}$$

where λ_{if} is the radiative transition rate; v_R, the radial component of the ion velocity v; b, the impact parameter; V, the internuclear potential; and E_c, the centre-of-mass kinetic energy. The factor 2 in (2.57) occurs because $R = R_g$ at two points on the ion trajectory. The X-ray emission cross-section is found by integrating over the impact parameter,

$$\Delta\sigma_{ij}(E_x) = \int_0^{R_g} 2\pi b\,db\,\Delta P_{if}(E_x)$$
$$= 2\pi R_g^2(\Delta R_g/v)[-E_c^{-1}V(R_g)]^{1/2}\lambda_{if}(R_g) \tag{2.58}$$

when a vacancy is initially present in the MO. This equation is the starting point for various theories of MO X-rays as reviewed by *Anholt* [2.43]. *Schmidt-Böcking* et al. [2.44] find that K MO X-ray cross-sections in 32-MeV S + Ar collisions depend strongly on the projectile charge state. This is a vast, complicated topic involving many-electron processes.

2.6 Ratio of Characteristics to Continuous Radiation

From (1.119), for the continuous spectrum,

$$n_\nu = CZ(\nu_0 - \nu)/h\nu, \tag{2.59}$$

so the probability N_C for producing a bremsstrahlung photon with $h\nu > E_K$ is

$$N_C = \int_{\nu_K}^{\nu_0} n_\nu\,d\nu = \frac{CZ}{h}[\nu_0 \ln \nu - \nu]_{\nu_K}^{\nu_0}$$
$$= (CZ/h^2)E_K[U_0 \ln U_0 - (U_0 - 1)]. \tag{2.60}$$

Then (2.52) and (2.60) give

$$\frac{F_K}{N_C} = \frac{\text{probability of producing a } K \text{ ionization by } e \text{ impact}}{\text{prob. of producing a bremsstrahlung photon with } h\nu > E_K}$$
$$= \frac{4\pi h^2 e^4 b N_A k}{CZAE_K} \cdot \frac{[U_0 \ln(4U_0/a) - (U_0 - 1)\ln(4/a)]}{[U_0 \ln U_0 - (U_0 - 1)]}$$
$$\underset{a=4}{=} 4\pi h^2 e^4 b N_A k/(CZAE_K). \tag{2.61}$$

Experimentally *Tothill* [2.45] finds that for copper the ratio is low for the accelerating voltage V_0 near the excitation potential V_K. It rapidly rises until $V_0 \sim 3V_K$, then shows a broad maximum and becomes nearly independent of $U_0(F_K/N_C \sim 0.7$ for Cu) as suggested by the $a = B_K/E_K = 4$ result in (2.61). This gives information on B_K in (2.45). With $A \sim 2Z$ and $E_K \propto (Z-1)^2$, the ratio F_K/N_C is $\propto Z^{-4}$. Experimentally it varies as $\sim Z^{-3}$.

2.7 X-Ray Terms

The stationary states of the hydrogen-like atom are defined by the well-known wave functions

$$\psi_{nlm} = R_{nl}(r)\cdot Y_l(\theta)\cdot Z_m(\phi) = N_{nlm}e^{-\rho/2}\rho^l L_{n+l}^{2l+1}(\rho)\cdot p_l^m(\cos\theta)\cdot e^{im\phi},$$
$$(n = 1, 2, 3, \ldots;\ 0 \leqq l < n;\ -l \leqq m \leqq l;\ l, m \text{ both integers}), \tag{2.62}$$

where N_{nlm} is the normalization factor, and $\rho = Zr/a_0$ with a_0 as the radius of first Bohr orbit. The energy of a state or level depends only on n,

$$E_n = -R_\infty hc\frac{Z^2}{n^2}, \quad n = 1, 2, 3, \ldots K. \tag{2.63}$$

If we include spin, (2.59) suggests that the electrons in an atom can be described by *four* quantum numbers. The *principal quantum number* n (= 1, 2, 3, . . .) specifies the shell

n	: 1	2	3	4	5	6	7
Shell:	K	L	M	N	O	P	Q

and determines the energy. The *azimuthal* quantum number $l(=0, 1, 2, \ldots n-1)$ determines the orbital angular momentum

l	: 0	1	2	3	4	5	6
Symbol:	s	p	d	f	g	h	i

Each shell is subdivided into subshells according to the values of l

Shell	n:	1		2			3			4
Subshell	l:	0	0		1	0	1	2	0	
Designation	:	1s	2s		2p	3s	3p	3d	4s	⋯

The *magnetic* quantum number $m(=0, \pm 1, \pm 2, \ldots, \pm l)$ specifies the orientation of the electron's orbital[1] in a magnetic field. The *spin* quantum number $m_s\ (= \pm 1/2)$ describes the orientation of the spin.

A specification of n and l for all the electrons bound to a nucleus is called the *electronic configuration* of the atom (or ion). The assignment of the electrons to electronic quantum states is determined by 1) the thermodynamic considerations that require the lowest energy states to be filled up first, and 2) the exclusion principle of Pauli, according to which *no two electrons in an atom can have the same four quantum numbers.* Any subshell can contain up to $2(2l+1)$ electrons, because m can range from the value l down through zero to $-l$, making $2l+1$ different values; m_s can be either $1/2$ or $-1/2$. Thus, several states ψ_{nlmm_s} have the same energy E_n (degeneracy). The normal configuration of electrons in an atom is expressed as $1s^2\ 2s^2\ 2p^6\ 3s^2\ 3p^6\ 3d^{10}\ 4s^2 \ldots$. The total number of electrons in a shell (given n) is

$$\sum_{l=0}^{n-1} 2(2l+1) = 2n^2 \quad (\textit{total degeneracy}) \ . \tag{2.64}$$

For discussing atomic spectra, it is necessary to take into account the *spin-orbit* interactions. For this, it is convenient to define two different quantum numbers: the *total angular momentum* quantum number $j = l \pm m_s$, and the quantum number m_j that can have all integrally spaced values from $+j$ to $-j$. Each subshell with $l \geqq 1$ can now be further subdivided. For example, the $2p$ $(n=2, l=1)$ subshell can be subdivided into $2p_{1/2}$ $(n=2, l=1, j=1/2)$ and $2p_{3/2}$ $(n=2, l=1, j=3/2)$. Thus, the L $(n=2)$ shell has in all three subshells $2s_{1/2}$ $(n=2, l=0, j=1/2)$, $2p_{1/2}$ and $2p_{3/2}$. These are called the *spectroscopic terms*. When the spin-orbit interaction is included, we can think of each subshell, as defined by a given nl, being split into two nlj subshells, each composed of all electrons that have the same values of n, l, and j. *Each closed subshell contains* $2j+1$ *electrons*, one for each value of m_j. The distribution of quantum numbers among the lowest energy states is shown in Table 2.1. The magnetic quantum number m is unimportant in determining the energy. The electron distribution among the various energy states of free atom is given in Appendix D. A useful complete set of four quantum numbers is $nljm_j$.

The electrons in any completely filled shell or subshell contribute *zero* resultant angular momentum, both orbital and spin, to the angular momentum of the whole atom.

[1] The wave function for a single electron can be plotted and is called an orbital. Often m is written as m_l.

Table 2.1. Allowed combinations of quantum numbers

Shell	K	L			M				
n	1	2			3				
l	0	0	1		0	1		2	
j	$\frac{1}{2}$	$\frac{1}{2}$	$\frac{1}{2}$	$\frac{3}{2}$	$\frac{1}{2}$	$\frac{1}{2}$	$\frac{3}{2}$	$\frac{3}{2}$	$\frac{5}{2}$
m_j	$\pm\frac{1}{2}$	$\pm\frac{1}{2}$	$\pm\frac{1}{2}$	$\pm\frac{1}{2}\pm\frac{3}{2}$	$\pm\frac{1}{2}$	$\pm\frac{1}{2}$	$\pm\frac{1}{2}\pm\frac{3}{2}$	$\pm\frac{1}{2}\pm\frac{3}{2}$	$\pm\frac{1}{2}\pm\frac{3}{2}\pm\frac{5}{2}$
Number of	2	2	2	4	2	2	4	4	6
electrons	2	8			18				

Electrons that have the same n and l values are called *equivalent electrons.* The vacancy principle of *Pauli* [2.46] states that *from a configuration of z electrons that have the same nl values, the same spectroscopic terms will arise as in a configuration of the same nl electrons that lack z electrons to complete the closed shell.*

The X-ray characteristic spectra originate from the lack of one electron (a *hole*) in an inner closed shell. By the Pauli vacancy principle, the set of *X-ray terms* that arise from this circumstance will correspond to the set of terms of a hydrogen-like atom. The single hole behaves just like an "anti-electron" (not positron) with spin 1/2 outside the core in a hydrogen-like atom. Therefore, we can base our discussion of X-ray characteristic spectra on the theory of the spectra of hydrogen-like atoms. Within this approximation, we can assign the quantum numbers $nljm_j$ to the single hole.

The binding energy of the inner or core electrons in the atom is large. If such an electron is ejected, the *excited* atom becomes mechanically unstable with respect to ionization. This is accompanied by the readjustment of the electron cloud, and the formation of a stable ion. However, as the interaction between the electrons themselves in the atom is relatively weak, the probability of such an occurrence is comparatively small. Consequently, the life-time τ of the excited state is long. This makes the *width* $\Delta E \sim \hbar/\tau$ of the level so small that it is reasonable to regard the energies of an atom with a hole as discrete energy levels of quasi-stationary states of a hydrogen-like atom. These levels are called *X-ray terms* because the transitions between these levels give rise to X-ray line emission. It is important to realize that X-*ray states are hole states.*

2.8 Energies of Atomic X-Ray Levels and Energy-Level Diagrams

The discussion of the X-ray emission spectra can be based on the theory of the optical spectra of hydrogen-like atoms. The nonrelativistic Schrödinger equation gives

$$H_0 = \frac{p^2}{2m} - \frac{Ze^2}{r}, \quad H_0\psi_{nlm} = E_n\psi_{nlm}, \tag{2.65}$$

$$E_n = -R_\infty hc\frac{Z^2}{n^2} = -\frac{m\alpha^2c^2}{2}\frac{Z^2}{n^2}, \tag{2.66}$$

where $\alpha = e^2/\hbar c$ is the *fine-structure constant* and ψ_{nlm} is of the form (2.59). In this nonrelativistic theory, the wave function involves the quantum numbers n, l, m, but the energy depends only on n.

The relativistic expression for the energy of a free electron is

$$E_{\text{rel}} = (c^2p^2 + m^2c^4)^{1/2} = mc^2\left(1 + \frac{p^2}{m^2c^2}\right)^{1/2}$$
$$= mc^2\left(1 + \frac{p^2}{2m^2c^2} - \frac{p^4}{8m^4c^4} + \dots\right). \tag{2.67}$$

It involves the rest-mass energy mc^2. To a first approximation, the Hamiltonian for the electron in a Coulomb field can be written as

$$H = mc^2\left(1 + \frac{p^2}{m^2c^2}\right)^{1/2} - mc^2 - \frac{Ze^2}{r} = \left(\frac{p^2}{2m} - \frac{Ze^2}{r}\right) - \frac{p^4}{8m^3c^2}$$
$$= H_0 + H'. \tag{2.68}$$

where the perturbation term is

$$H' = -\frac{p^4}{8m^3c^2} = -\frac{1}{2mc^2}\left(\frac{p^2}{2m}\right)^2 = -\frac{1}{2mc^2}\left(H_0 + \frac{Ze^2}{r}\right)^2. \tag{2.69}$$

The resulting *relativistic correction* of the energy E_n is given by

$$E'_{\text{rel}} = \int \psi^*_{nlm} H' \psi_{nlm}\, d\tau$$
$$= -\frac{1}{2mc^2}\left(E_n^2 + 2Ze^2E_n\int R_{nl}^2\frac{1}{r}r^2\,dr + Z^2e^4\int R_{nl}^2\frac{1}{r^2}r^2\,dr\right). \tag{2.70}$$

Evaluating the integrals,

$$E'_{\text{rel}} = -E_n(\alpha Z)^2\frac{1}{n}\left(\frac{3}{4n} - \frac{1}{l+1/2}\right), \tag{2.71}$$

$$E_{nl} = E_n + E'_{\text{rel}} = E_n\left[1 - (\alpha Z)^2\frac{1}{n}\left(\frac{3}{4n} - \frac{1}{l+1/2}\right)\right]. \tag{2.72}$$

The energy now depends on both n and l. This *removes the degeneracy between states of the same n and different l.*

Now consider the effect of the electron *spin*. A Dirac electron has a magnetic moment $\boldsymbol{\mu}_s = (e\hbar/2mc)\boldsymbol{s}$, where $\boldsymbol{s}$ is the spin vector. When it moves in the central electric field, it sees the effective magnetic field $\boldsymbol{H} = (1/c)\boldsymbol{v}\times\boldsymbol{E}$. The resulting interaction term is

$$H'_{\text{spin-orbit}} = -\boldsymbol{\mu}_s\cdot\boldsymbol{H} = \frac{e\hbar}{2mc^2}\boldsymbol{s}\cdot(\boldsymbol{E}\times\boldsymbol{v}) = \frac{e\hbar}{2mc^2}\boldsymbol{s}\cdot\left(-\frac{\partial V}{\partial r}\hat{\boldsymbol{r}}_0\times\boldsymbol{v}\right), \tag{2.73}$$

where $\hat{\boldsymbol{r}}_0$ is a radial unit vector. Using $\hat{\boldsymbol{r}}_0 = \boldsymbol{r}/r$ and $V = Ze^2/r$, we get the *spin–orbit interaction* energy,

$$H'_{\text{spin-orbit}} = -\frac{e\hbar}{2m^2c^2}\frac{1}{r}\frac{\partial V}{\partial r}\boldsymbol{s}\cdot(\boldsymbol{r}\times\boldsymbol{p}) = \frac{Ze^2\hbar^2}{2m^2c^2}\frac{1}{r^3}\boldsymbol{l}\cdot\boldsymbol{s} = \zeta(r)\boldsymbol{l}\cdot\boldsymbol{s}, \tag{2.74}$$

where $\boldsymbol{l} = \boldsymbol{r}\times\boldsymbol{p}$ and $\boldsymbol{s}$ are in units of $\hbar$, and $\zeta(r) = Ze^2\hbar^2/2m^2c^2r^3$. The total unperturbed wave function is

$$\psi_{nlmm_s} = \psi_{nlm}\psi_{\text{spin}} = |nlm_l\rangle|m_s\rangle = |nlm_lm_s\rangle. \tag{2.75}$$

The correction due to $H'_{\text{spin-orbit}}$ is given by

$$(nlm_lm_s|H'_{\text{spin-orbit}}|nlm_lm_s) = (nl|\zeta(r)|nl)(lm|\boldsymbol{l}|lm)\cdot(m_s|\boldsymbol{s}|m_s), \tag{2.76}$$

because $\zeta(r)$ operates on the radial part $|nl) = R_{nl}(r)$, $\boldsymbol{l}$ on angular part $|lm) = Y_l(\theta)Z_m(\phi)$ and $\boldsymbol{s}$ on the spin part $|m_s) =$ Pauli spinor. Here

$$(nl|\zeta(r)|nl) = \frac{Ze^2\hbar^2}{2m^2c^2}\int_0^\infty\frac{1}{r^3}R_{nl}^2r^2\,dr = \frac{e^2\hbar^2Z}{2m^2c^2}\left(\frac{Z}{a_0}\right)^3\frac{1}{n^3l(l+1)(l+1/2)}$$
$$= R_\infty ch\alpha^2Z^4/[n^3l(l+1)(l+1/2)]. \tag{2.77}$$

The other matrix elements in (2.76) can be written immediately if we use the vector model to calculate the scalar product $\boldsymbol{l}\cdot\boldsymbol{s}$ (Fig. 2.13). Because of the magnetic coupling of $\boldsymbol{l}$ and $\boldsymbol{s}$, the total quantum number $\boldsymbol{j} = \boldsymbol{l}+\boldsymbol{s}$ is now a constant of motion. The states can be designated by jm_j in place of $m_l\,m_s$, where $j^2 = j(j+1)$ and $j_z = m_j\hbar$. The operator equation is

$$\boldsymbol{j}^2 = (\boldsymbol{l}+\boldsymbol{s})^2 = \boldsymbol{l}^2 + \boldsymbol{s}^2 + 2\boldsymbol{l}\cdot\boldsymbol{s}. \tag{2.78}$$

Because l, j and s are all good quantum numbers, $\boldsymbol{l}\cdot\boldsymbol{s}$ also has diagonal elements given by

$$(lj|\boldsymbol{l}\cdot\boldsymbol{s}|lj) = \tfrac{1}{2}[j(j+1) - l(l+1) - s(s+1)], \tag{2.79}$$

Fig. 2.13. Owing to the spin-orbit interaction, $\boldsymbol{l}$ and $\boldsymbol{s}$ process around $\boldsymbol{j} = \boldsymbol{l}+\boldsymbol{s}$, which remains fixed in the absence of external torques

where $s(s+1) = 3/4$. When $l > 0$, the value of j can be either $l+(1/2)$ or $l-(1/2)$. Thus, the spin–orbit interaction gives the correction to the energy

$$E'_{\text{spin-orbit}} = (nl|\zeta(r)|nl) \begin{cases} \frac{1}{2}l & \text{if } j = l+\frac{1}{2}, \\ -\frac{1}{2}(l+1) & \text{if } j = l-\frac{1}{2}. \end{cases} \tag{2.80}$$

We find that *the spin–orbit interaction removes the $m_l m_s$ degeneracy within each configuration* (same nl). Consequently, for the same n, l, the states of different j have different energies. [We are still left with a $(2j+1)$-fold degeneracy due to m_j which can take all integrally spaced values from $-j$ to $+j$. This can be removed by applying an external magnetic field.] *The state of lower j lies lowest*, as required by the Hund rule. The doublet separation $\zeta_{nl}(r)[l+(1/2)]$ is of magnetic origin and smaller than electronic energies by a factor of order α^2.

The fully corrected energy in the first approximation [we neglect higher terms in (2.64)] is

$$\begin{aligned} E_{nlj} &= E_n + E'_{\text{rel}} + E'_{\text{spin-orbit}} \\ &= -R_\infty hc\left[\frac{Z^2}{n^2} + \frac{\alpha^2 Z^4}{n^3}\left(\frac{1}{l+1/2} - \frac{3}{4n}\right) - \frac{\alpha^2 Z^4}{n^3}\frac{(lj|\boldsymbol{l}\cdot\boldsymbol{s}|lj)}{l(l+1)(l+1/2)}\right] \\ &= -R_\infty hc\left[\frac{Z^2}{n^2} + \frac{\alpha^2 Z^4}{n^4}\left(\frac{n}{j+1/2} - \frac{3}{4}\right)\right]. \end{aligned} \tag{2.81}$$

which holds for both $j = l+(1/2)$ and $j = l-(1/2)$. The relativistic Dirac theory provides the correct basis for this result. The spin–orbit interaction gives a correction of the same order of magnitude as the relativity correction. The net result is that the two levels that have the same j value but different values of l now have the same energy (are degenerate) (Fig. 2.14) in the hydrogen atom. The same situation persists even if the exact relativistic correction is included when the Dirac equation is solved. In the hydrogen atom, this degeneracy is removed by the radiation correction (Lamb shift). In hydrogen-like terms and in X-ray

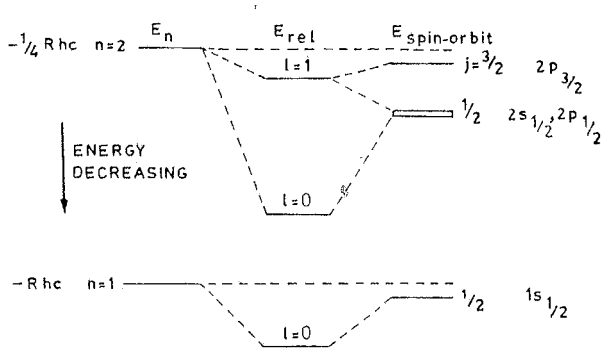

Fig. 2.14. The effect of various corrections on the energy level diagram of the hydrogen atom for *optical* levels with $n = 1, 2$

terms ($Z > 4$) this degeneracy is removed by the dominating effect of *screening* that depends on the l value and produces a large separation.

The (one or) two *levels* in which each configuration is split are together said to constitute a *doublet term*. The *terms* are designated as ^2S (doublet S), ^2P, ^2D . . . according to the l value. The separate levels are designated by adding the value of j as a subscript, thus $^2S_{1/2}$; $^2P_{1/2}$, $^2P_{3/2}$; $^2D_{3/2}$, $^2D_{5/2}$; etc. The quantum number n or the configuration label nl is sometimes prefixed to these symbols, and to specify an individual state the m_j value given as a superscript; thus $2\,^2P^{3/2}_{3/2}$ or $2p\,^2P^{-1/2}_{3/2}$.

In view of the Pauli vacancy principle, the X-ray levels are analogous to the levels of hydrogen-like atoms. Therefore, the energies of X-ray states (one inner electron missing) can at once be written from (2.81) provided that the following three modifications are made:

1) The electrons bound in an atom have negative energies, (2.81). For inner hole states, *the energy is taken to be positive.*

2) In the principal energy term, $E_n(\propto Z^2/n^2)$, the Z is replaced by an effective Z, $Z_{\text{eff}} = Z - \sigma_1(n, l)$, where σ_1 is called the *total screening constant.* The reason is that the actual nuclear charge seen by an inner shell electron is not Z but is screened by the other electrons that come in between. It is also affected by the other electrons in the external region. This screening will change as we go from one shell to another. Because *all* of the electrons of the atom affect this screening, σ_1 depends on n, l and Z. It separates the terms with same n but different l, like $L_I(2s_{1/2})$ and $L_{II}(2p_{1/2})$. They form the *screening doublets* (L_I–L_{II}, M_I–M_{II}, . . .).

3) In the second term of (2.81), the Z is replaced by $Z_{\text{eff}} = Z - \sigma_2(n, l)$, where σ_2 is called the *internal screening constant.* This second term contains the interaction of the magnetic moments l and s of a given electron with itself and with the magnetic moments of other electrons of the atom. However, the total magnetic moment of a closed shell is zero. Therefore, only the electrons of the excited shell (one electron missing) matter. Because the distribution of electrons in any such given shell remains the same for all elements, σ_2 does not depend on Z. In general, it depends on n, l.

With these modifications in (2.81), the energy of *atomic X-ray levels* is

$$E_{nlj} = +R_\infty hc\left\{\frac{[Z-\sigma_1(n,l)]^2}{n^2} + \frac{\alpha^2[Z-\sigma_2(n,l,j)]^4}{n^4}\left(\frac{n}{j+1/2} - \frac{3}{4}\right)\right\}. \tag{2.82}$$

Because of the presence of $\sigma_1(n, l)$ and $\sigma_2(n, l, j)$, the terms $2s_{1/2}(L_I)$ and $2p_{1/2}(L_{II})$, which were degenerate in (2.81), will have separate energies. The $(2j+1)$-fold degeneracy with respect to m_j remains in (2.82) and determines the *statistical weight* of the level.

A qualitative representation of the X-ray atomic energy levels is shown in Fig. 2.15. In X-rays it is customary *to choose the neutral atom in its ground state as the zero for energy measurements.* Then all other excited (hole) states have

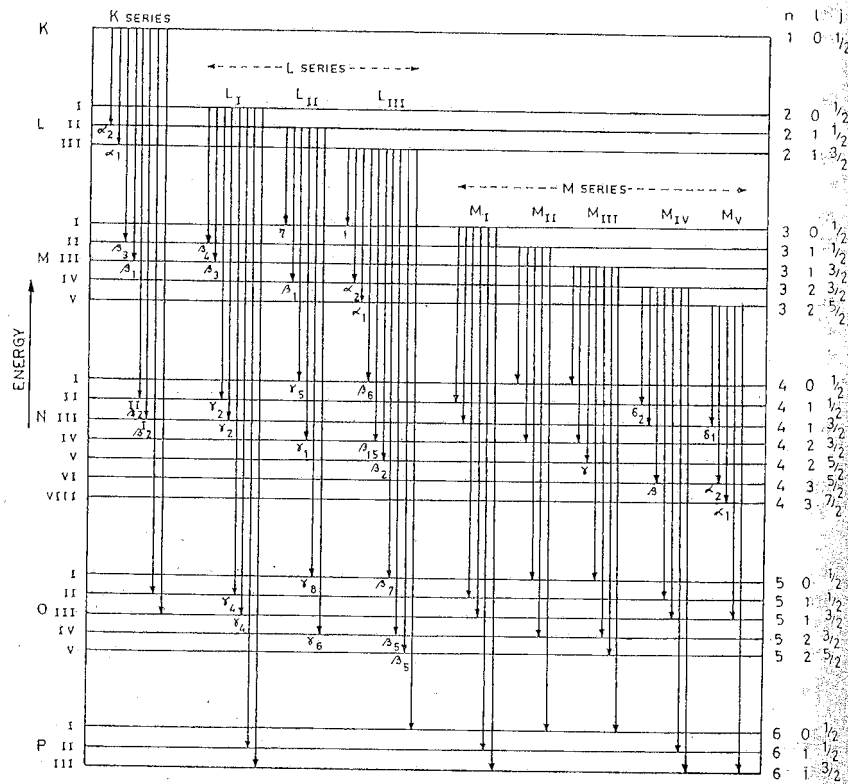

Fig. 2.15. Qualitative X-ray atomic energy level diagram. Some of the allowed electric-dipole hole transitions are shown by arrows. Selection rules are $\Delta l = \pm 1$, $\Delta j = 0$ or ± 1 (the j-transition $0 \rightarrow 0$ is forbidden)

positive energy. Although one-electron symbols are retained, each level denotes the energy of the entire system when one electron is missing from the particular electronic shell.

The photon energies of emitted X-ray lines can be shown as *hole transitions* from a higher level to a lower level on this energy level diagram with the *selection rules*

$$\left.\begin{aligned} &\Delta n \neq 0, \\ &\Delta l = \pm 1 \\ &\Delta j = 0, \pm 1 \end{aligned}\right\} \text{electric-dipole selection rules.} \tag{2.83}$$

The observed characteristic X-ray emission lines that obey these selection rules are called *diagram lines*. This nomenclature emphasizes that the condition

$h\nu_{fi} = E_i - E_f$, where E_i and E_f are given on the energy level diagram, gives the frequencies of all the observed emission lines. In general, lines that arise from one-electron (or one-hole) jumps between singly ionized states, with the inactive electrons retaining their original quantum numbers, as if frozen, are known as *diagram lines*; all others are *satellites* (see Chap. 4). The notation $K \rightarrow L_{III}$ indicates the transition of the hole. The conventional X-ray nomenclature of the type $K\alpha_1$ is adequate for the diagram lines.

Most of the features of X-ray spectra can be explained by a one-electron (or one-hole) jump model, using hydrogen-like wave functions. However, an adequate description of X-ray processes should, in general, take into account the manner in which the relatively inactive electrons are affected by the change of potential brought about either by the creation of the initial hole or by its decay. For this we need the many-electron wave functions of the initial and final states. The most accurate common representation of such wave functions is given by the Slater determinant of orthonormal spin orbitals

$$\Psi = (N!)^{-1} \det[\psi_{1s\alpha}(1), \psi_{1s\beta}(2), \psi_{2s\alpha}(3), \ldots, \psi_{\eta\lambda\beta}(N)]. \tag{2.84}$$

Minimizing the total energy of the product yields the Hartree–Fock equations, which can be solved to give ψ's that are good approximations to the spatial wave functions. To calculate state energies, *Bagus* [2.47] has used wave functions of the Slater type. Calculations of this kind for hole states are accurate (± 1 eV in 3000) but not available for many elements. In such cases, *Koopmans'* [2.48] theorem is often used, in which the one-electron orbital energy obtained from Hartree–Fock equations is used as the level energy. It implies that the inactive electron orbitals are identical in the initial and final states. It has been shown that inner-shell ionization energies calculated from Koopmans' theorem are related to a weighted-average energy for singly and multiply excited states that are created by a sudden ionization process [2.49]. The theoretical situation for the hole states and transition energies is not yet settled. *Huang* et al. [2.50] have made extensive calculations for these. *Deslattes* and co-workers [2.51–53] have used their results for critical comparison over a wide range of Z. The difference between the experimental and theoretical values for $K\alpha_1$ transitions is found to vary as $E^{1/2}$ (or as Z). Use of a multi-configuration interaction may remove this discrepancy.

2.9 Electric-Dipole Selection Rules

The transition probability per unit time for the spontaneous emission is given by (2.20)

$$w_{fi} = \frac{64\pi^4}{3c^3h} \nu_{fi}^3 |(f|\boldsymbol{D}(r)|i)|^2, \tag{2.85}$$

where $\boldsymbol{D} = e\boldsymbol{r}$ is the *electric-dipole moment*. The transitions between the initial

states $\psi_{n,l,m}$ and final states $\psi_{n',l',m'}$ will be possible if

$$\int \psi^*_{n',l',m'} |\boldsymbol{D}(r)| \psi_{nlm}\, d\tau \neq 0 \quad \textit{(dipole integral)}. \tag{2.86}$$

The components of $\boldsymbol{D}$ along x, y, z axes are

$$D_x = D(r)\sin\theta\cos\phi, \quad D_y = D(r)\sin\theta\sin\phi, \quad D_z = D(r)\cos\theta. \tag{2.87}$$

As $D(r) = er$ is a function of r alone, the dipole integral (2.86) is a product of three factors:

$$\int_0^\infty R^*_{n'l'}(r)|D(r)|R_{nl}(r) r^2\, dr,$$

$$\int_0^\pi Y^*_{l'm'}(\theta) \begin{vmatrix} \sin\theta \\ \sin\theta \\ \cos\theta \end{vmatrix} Y_{lm}(\theta)\sin\theta\, d\theta, \quad \int_0^{2\pi} Z^*_{m'}(\phi) \begin{vmatrix} \cos\phi \\ \sin\phi \\ 1 \end{vmatrix} Z_m(\phi)\, d\phi. \tag{2.88}$$

Consider the integral for D_z,

$$\int_0^\pi p^{m'}_{l'} |\cos\theta| P^m_l \sin\theta\, d\theta \int_0^{2\pi} e^{i(m-m')\phi}\, d\phi. \tag{2.89}$$

The ϕ integral is zero for $m \neq m'$. Therefore, we must have $m = m'$. For the θ integral, we use the recursion formula

$$|\cos\theta| p^m_l = \frac{l-m+1}{2l+1} p^m_{l+1} + \frac{l+m}{2l+1} P^m_{l-1}, \tag{2.90}$$

and the orthonormality of associated Legendre polynomials. Because $m = m'$, for (2.86) to be nonzero.

$$m = m', \quad l \pm 1 = l', \quad \text{(for } D_z\text{)}. \tag{2.91}$$

Consider D_y and D_z in the combinations

$$D(x+iy) = D(r)\sin\theta\, e^{i\phi}, \quad D(x-iy) = D(r)\sin\theta\, e^{-i\phi}. \tag{2.92}$$

For $D(x+iy)$, the integrals are

$$\int_0^\pi P^{m'}_{l'} |\sin\theta| P^m_l \sin\theta\, d\theta \int_0^{2\pi} e^{i(m-m'+1)}\, d\phi. \tag{2.93}$$

The ϕ integral is not zero only if $m+1 = m'$. Using the recursion formula

$$(1-\cos^2\theta)^{1/2} P^m_l = |\sin\theta| P^m_l = \frac{1}{2l+1}(P^{m+1}_{l+1} - P^{m+1}_{l-1}), \tag{2.94}$$

(2.86) is not zero only when $m+1 = m'$, $l \pm 1 = l'$, for $D(x+iy)$. Similarly, for $D(x-iy)$, we get $m-1 = m'$, $l \pm 1 = l'$.

The *electric-dipole-moment selection rules* can therefore be expressed as

$$\Delta l = \pm 1; \quad \Delta m = 0, \pm 1. \tag{2.95}$$

The observed emission lines shown in Fig. 2.15 obey these selection rules. It

remains to consider the radial part in (2.85), in the light of (2.95), for intensity calculations.

The total transition probability for a line of frequency ν is found by summing (2.85) over all states i and f that have the same energy difference,

$$w(\nu) \propto \sum_i \sum_f \nu^3 \left| \int_0^\infty R_{n'l'} R_{nl}\, r^3\, dr \right|^2 \delta(E_i - E_f - h\nu). \tag{2.96}$$

The energy dependence of states on m and spin s is negligible. The sum over s merely doubles every state. The sum over m gives

$$\sum |n', l|r|n, l-1)|^2 = [l/(2l-1)] \left| \int_0^\infty R_{n'l} R_{nl-1}\, r^3\, dr \right|^2,$$

$$\sum |(n', l|r|n, l+1)|^2 = [(l+1)/(2l+3)] \left| \int_0^\infty R_{n'l} R_{nl+1}\, r^3\, dr \right|^2. \tag{2.97}$$

2.10 Relative Intensities of Emission Lines in a Multiplet

The relative intensities of spectral lines can be defined either by means of their peak intensities or by the area below their intensity distribution curves.

A *multiplet of the* X-ray spectrum is *a group of lines whose initial states arise from a single configuration* nl, *and whose final states likewise arise from another single configuration* n′l′. A simple example is provided when the initial state or the final state is already a single level. Thus, $K\alpha_1\alpha_2$, $L\beta_3\beta_4$, Ll_η, being simple doublets, are multiplets (Fig. 2.16). Another example is the $L\beta_1\alpha_1\alpha_2$ triplet.

The intensity of the emission line is given by $I(if) \sim \nu^4_{fi} F_i g_i r^2(i,f)$, (2.22). The factors ν^4_{if} and F_i can be taken to be identical for the lines of any multiplet that

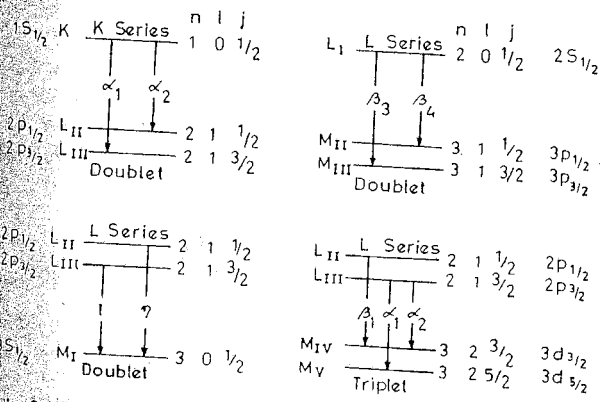

Fig. 2.16. Examples of multiplets

are close to each other. Thus, effectively the relative intensity of the lines of a multiplet depends on two factors,

$$I(i,f) \sim g_i r^2(i,f). \tag{2.98}$$

It is difficult to evaluate $r^2(i,f)$ from (2.97). To calculate the relative intensities of the lines of any one multiplet, the sum rule, discovered empirically by *Burger* et al. [2.54, 55], is used. It states that *if the separation of the splitting of either the initial or final levels of a multiplet is imagined to be reduced to zero, then the sum of the quantities* $g_i r^2(i,f)$ *for the lines whose frequencies would as a result appear to be the same is proportional to the statistical weights of the unreduced levels.* This sum rule can be obtained from the quantum mechanical considerations (see, for example, [2.56]).

We have seen (Sect. 2.8) that the statistical weight g of a term characterized by the quantum number j is $2j+1$. Let us apply the *Burger–Dorgelo–Ornstein* rule to the $K\alpha_1\alpha_2$ doublet (Fig. 2.16). Here one level is already common and so the reducing process is not necessary. We have

$$\frac{I(K\alpha_1)}{I(K\alpha_2)} = \frac{g_K r^2(\alpha_1)}{g_K r^2(\alpha_2)} = \frac{g_{L_{III}}}{g_{L_{II}}} = \frac{2\times\frac{3}{2}+1}{2\times\frac{1}{2}+1} = \frac{2}{1}. \tag{2.99}$$

This is in good agreement with experiments [2.57] over a wide range of atomic numbers:

Element	: ^{26}Fe	^{29}Cu	^{40}Zr	^{47}Ag
$I(K\alpha_2)/I(K\alpha_1)$:	0.500	0.497	0.502	0.499.

The $K\beta_1$, $K\beta_3$, if resolved, are also associated with j values 3/2 and 1/2, respectively. They will also be in the ratio 2/1 [2.58].

Let us now apply the above rule twice to the triplet $L\beta_1\alpha_1\alpha_2$ (Fig. 2.16). Imagine the separation of M_{IV} and M_V to be zero. Then the rule gives

$$\frac{I(L\alpha_1)+I(L\alpha_2)}{I(L\beta_1)} = \frac{g_{L_{III}} r^2(\alpha_1) + g_{L_{III}} r^2(\alpha_2)}{g_{L_{II}} r^2(\beta_1)} = \frac{g_{L_{III}}}{g_{L_{II}}} = \frac{2}{1}. \tag{2.100}$$

Now imagine the separation of L_{II} and L_{III} to be zero. Then

$$\frac{I(L\alpha_2)+I(L\beta_1)}{I(L\alpha_1)} = \frac{g_{L_{III}} r^2(\alpha_2) + g_{L_{II}} r^2(\beta_1)}{g_{L_{III}} r^2(\alpha_1)} = \frac{g_{M_{IV}}}{g_{M_V}} = \frac{2\times\frac{3}{2}+1}{2\times\frac{5}{2}+1} = \frac{2}{3}. \tag{2.101}$$

From (2.100, 101),

$$I(L\alpha_1)+I(L\alpha_2) = 2I(L\beta_1), \quad I(L\alpha_2)+I(L\beta_1) = \tfrac{2}{3}I(L\alpha_1),$$
$$I(L\alpha_1):I(L\alpha_2):I(L\beta_1) = 9:1:5 = 100:11:56, \tag{2.102}$$

again in close agreement with experiments [2.59]:

Element	: ^{42}Mo	^{47}Ag	^{74}W	^{78}Pt
$L\alpha_1:\alpha_2:\beta_1$	: 100:13:62	100:12:59	100:11.5:52	100:11.4:51.

Similar calculations yield the following theoretical values:

$$K \text{ series } : \alpha_1:\alpha_2 = \beta_1:\beta_2 = 2:1,$$
$$L \text{ series } : \gamma_3:\gamma_2 = \beta_3:\beta_4 = l:\eta = \beta_6:\gamma_5 = 2:1,$$
$$\alpha_1:\alpha_2:\beta_1 = \beta_2:\beta_{15}:\gamma_1 = 9:1:5,$$
$$\beta_5:\beta_6 = 2:1,$$
$$M \text{ series } : \alpha_1:\alpha_2:\beta_1 = 20:1:14. \tag{2.103}$$

These values are in fair agreement with the experimental values, so long as we use the quantities $g_i r^2(i,f)$ to calculate the intensity ratios. However, if we use the full expression $v_{fi}^4 F_i g_i r^2(i,f)$, (2.22), the agreement is spoiled. For example, if the v_{fi}^4 correction is included, the value of $L\beta_1$ would be decreased by a factor 0.57 in ^{74}W and 0.39 in ^{92}U, which completely upsets the agreement.

Again, $F(L_{II})$ and $F(L_{III})$ need not be equal even for high voltages on the X-ray tube. A rough classical estimate would give $F_i = E_i^{-1}$, where E_i is the energy transferred to the atom in the impact when it is put in the excited state i. If this factor is included, the intensity of $L\beta_1$ should be increased by the ratio $E(L_{II})/E(L_{III})$, that is, 1.13 for ^{74}W and 1.22 for ^{92}U.

Thus, with both of the factors $v_{fi}^4 F_i$ included, the total factor to be applied to the $L\beta_1$ line is 0.64 in ^{74}W and 0.48 in ^{92}U. This will change the theoretical $g_i r^2(i,f)$ ratios $L\alpha_1:\alpha_2:\beta_1 = 100:15:56$ to $v_{fi}^4 F_i g_i r^2(i,f)$ ratios 100:11:23.5. The new ratios are not in agreement with the experimental ratios 100:11.5:52 for ^{74}W and 100:11:49.5 for ^{92}U. This clearly shows that the theoretical discussion of the problem is inadequate. The relative intensities for several lines in the K and L series have been computed by *Massey* and *Burhop* [2.60].

Realistic calculations for relative line intensities have been made in the active-electron approximation, including the effects of retardation, by use of wave functions obtained by self-consistent relativistic Hartree-Fock methods with a Slater approximation to the exchange term [2.58, 61]. Relative intensities, corrected for self-absorption effects and for instrumental response, have also been measured [2.62, 63].

The intensity ratio $I(K\beta)/I(K\alpha)$ of the sum of the $\beta_1\beta_3$ doublet to the sum of the $\alpha_1\alpha_2$ doublet is not a constant number. It is a gross ratio involving several transitions when a K hole is filled from the M, N, . . . shells to that from the L shell. Theoretical values of *Scofield* [2.58] agree with the experiments (Fig. 2.17). The hole may be created by photoionization, electron or proton bombardment, or by nuclear electron capture [2.64].

2.11 Screening and Spin Doublets

Equation (2.81) is strictly valid only for the optical levels of the hydrogen atom ($Z = 1$). For hydrogen-like atoms ($Z > 1$) with one (valence) electron outside the core of $Z-1$ electrons, this equation will hold strictly only if the valence electron remains always outside the core and sees a shielded or screened effective nuclear

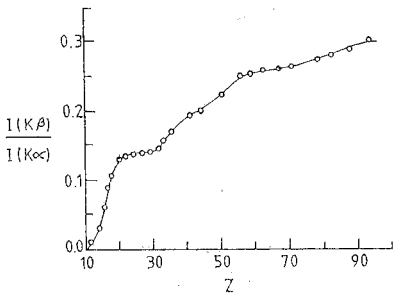

Fig. 2.17. The ratio $I(K\beta)/I(K\alpha)$ as a function of Z, as calculated by *Scofield* [2.58]. For the experimental points see references in [2.58]

charge eZ_{eff}, which is exactly $eZ_{\text{eff}} = e[Z-(Z-1)] = e$, as in the case of the hydrogen atom. However, $Z_{\text{eff}} > 1$ for hydrogen-like atoms because quantum mechanically there is a certain small but finite probability that the valence electron will be within the charge cloud of the core electrons (Fig. 2.18). During this time, the valence electron is closer to the nucleus and so is not screened by all of the $Z-1$ core electrons but only by a part of them, giving $Z_{\text{eff}} > 1$. In fact, as the distance r of the valence electron from the nucleus approaches zero, the valence electron begins to see the full charge $eZ_{\text{eff}} = eZ$. As it moves away from the nucleus, this is decreased, till it finally reduces to just e outside the core. We can, therefore, write $Z_{\text{eff}}(r) = Z - \sigma_1(r)$, with $\sigma_1(r) \to 0$ and $r \to 0$, $\sigma_1(r) \to Z-1$ as $r \to$ "radius of the atom". Thus $\sigma_1(r)$ is a measure of the incompleteness of screening. For the configuration nl we can write simply $Z_{\text{eff}} = Z - \sigma_1(n, l)$, because the radial probability density has a strong maximum at the appropriate value of r. Clearly $\sigma_1(n, l) < Z-1$ and $Z_{\text{eff}} > 1$, which makes the electron more strongly attracted to the nucleus than for hydrogen (Fig. 2.19). Because $\sigma_1(r)$ increases with r, we expect $\sigma_1(n, l)$ to increase with increase of n and l.

The X-ray terms (of positive energy) arise from the hole states in a manner analogous to the hydrogen-like states. We can replace the Bohr term $-R_\infty hc\,Z^2/n^2$ by $+R_\infty hc[Z-\sigma_1(n, l)]^2/n^2$, where the *total screening constant* $\sigma_1(n, l)$

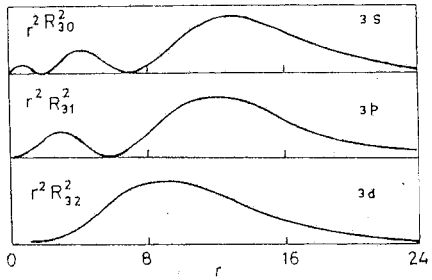

Fig. 2.18. Radial probability density for $n = 3$, $l = 0, 1, 2$, states of the hydrogen-like atoms, r is in units of a_0

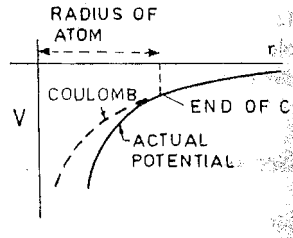

Fig. 2.19. The screening effect on the potential

separates out the X-ray levels with the same n and different l, such as L_I and $L_{II,\,III}$. Because the L_I state requires the removal of the more strongly bound $2s_{1/2}$ electron and L_{II} the removal of the comparatively less strongly bound $2p_{1/2}$ electron, the L_I level will have higher positive energy than the L_{II} level, and an X-ray screening doublet will be formed. The ordering of levels is obviously reversed when we go from optical spectra to X-ray spectra.

If we ignore the corrections that involve α^2 in (2.82),

$$E_{nlj} = +R_\infty hc\frac{Z_{\text{eff}}^2}{n^2} = +R_\infty hc\frac{[Z-\sigma_1(n,l)]^2}{n^2}, \tag{2.104}$$

or, using the relation

$$\frac{\tilde{\nu}}{R_\infty} = \left|\frac{E_{nlj}}{R_\infty hc}\right|, \tag{2.105}$$

$$\left(\frac{\tilde{\nu}}{R_\infty}\right)^{1/2}_{nlj} = \frac{Z-\sigma_1(n,\,l)}{n}. \tag{2.106}$$

For a given $n(=1, 2, 3, \ldots)$, we can express (2.106) as

$$\left(\frac{\tilde{\nu}}{R_\infty}\right)^{1/2} = aZ + b; \quad a = 1/n, \quad b = -\sigma_1/n. \tag{2.107}$$

This is called *Moseley's law for X-ray atomic levels.* A plot of experimental data against Z is nearly a straight line over significant intervals of Z (Fig. 2.20). It is

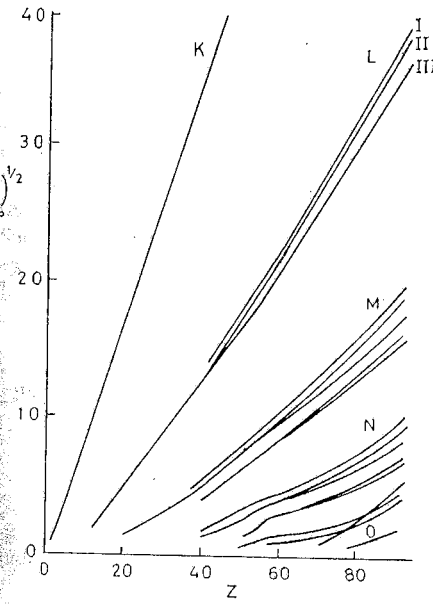

Fig. 2.20. Moseley diagram for the X-ray levels $K, L, M, \ldots$ where $\tilde{\nu}$ is wave number and $(\tilde{\nu}/R_\infty)^{1/2} = (E/13.6)^{1/2}$, E being in electron volts

called the Bohr–Coster diagram [2.65]. Sharp breaks in some of the straight lines are associated with changes of the filling of corresponding levels with electrons. For example, filling of the $N_{VI,\,VII}$ $(4f)$ level in the N-shell begins after $Z=57$, giving breaks in the lines for the M, N and O levels at $Z=57$.

Hertz [2.66] noted that on a Moseley plot (Fig. 2.20) the L_I and L_{II} are separated and run parallel, preserving a $\Delta(\tilde{\nu}/R_\infty)^{1/2}$ separation independent of Z. This is consistent with (2.106), because for $n=2$ the L_I, L_{II} separation is

$$\Delta\left(\frac{\tilde{\nu}}{R_\infty}\right)^{1/2}=\left(\frac{\tilde{\nu}}{R_\infty}\right)^{1/2}_{20j}-\left(\frac{\tilde{\nu}}{R_\infty}\right)^{1/2}_{21j}=\frac{Z-\sigma_1(L_I)}{2}-\frac{Z-\sigma_I(L_{II})}{2}$$

$$=\frac{\sigma_1(L_{II})-\sigma_1(L_I)}{2}=\frac{\Delta\sigma_1}{n}. \tag{2.108}$$

The finding of *Hertz* [2.66] that *the difference between the square roots of the energies of two screening-doublet levels is a constant essentially independent of* Z is called the *screening-doublet law* (or the *irregular-doublet law*). It is approximately true for screening doublets like L_IL_{II}, M_IM_{II}, $M_{III}M_{IV}$, etc. Because σ_1 takes into account the effect of the entire electron cloud, it depends on Z, and it is difficult to calculate it accurately[2]. Moseley plots provide a rough method for experimental determination of it. It is found that σ_1 increases with Z, as we expect. It increases with increasing Z, n and l.

Two levels with same n, l but different directions of spin, that is, with different values of j are called *spin doublets* ($L_{II}-L_{III}$, $M_{II}-M_{III}$ . . .). *Hertz* also noted that when the Moseley diagram for the X-ray atomic levels is drawn (Fig. 2.20), *the energy difference between two spin-relativity doublets is proportional to the fourth power of* $Z-\sigma_2$, where $\sigma_2(n,\,l)$ is the *internal screening constant* appropriate to the spin–orbit interaction. This is called the *spin-relativity doublet law* (or the *regular-doublet law*). Because only electrons inside the shell in question influence σ_2, following *Bohr* and *Coster* [2.65], we expect σ_2 to be independent of Z. But σ_2 increases for subshells farther from the nucleus. We can determine σ_2 from experiments. The σ_2 is smaller than σ_1 for a given $(n,\,l)$. The reason is that, for the spin–orbit interaction, it is the net electric intensity experienced by the electron that is significant, not the energy. A symmetric closed shell of electrons, external to the electron in question, takes no part in reducing the effective nuclear charge, insofar as the electric intensity is concerned, but it does insofar as energy is concerned.

---

[2] If a nucleus of charge $+Ze$ is surrounded by a spherical electron cloud of density $\rho(r)$, then the potential at a distance r_0 from the nucleus is

$$V(r_0)=\frac{Ze}{r_0}-\frac{1}{r_0}\int_0^{r_0}\rho(r)4\pi r^2dr-\int_{r_0}^{\infty}\rho(r)4\pi r dr=\frac{Ze}{r_0}-\frac{q_{r<r_0}}{r_0}-\frac{q_{r>r_0}}{r_{\text{ext}}},$$

where r_{ext} is the average radius for the charge distribution for $r>r_0$. The inside screening effect (second term) does not depend on the details of the charge distribution. The external screening effect (third term) depends on it; $\sim 1/r_{\text{ext}}$.

From (2.82) we get two separate terms.

For $j=l+(1/2)$,

$$E_{n,l,l+1/2}=+R_\infty hc\frac{[Z-\sigma_1(n,\,l)]^2}{n^2}+R_\infty hc\,\alpha^2\frac{[Z-\sigma_2(n,\,l)]^4}{n^4}\left(\frac{n}{l+1}-\frac{3}{4}\right). \tag{2.109}$$

For $j=l-(1/2)$,

$$E_{n,l,l-1/2}=+R_\infty hc\frac{[Z-\sigma_1(n,\,l)]^2}{n^2}+R_\infty hc\,\alpha^2\frac{[Z-\sigma_2(n,\,l)]^4}{n^4}\left(\frac{n}{l}-\frac{3}{4}\right). \tag{2.110}$$

These equations give the *spin-doublet formula*,

$$\Delta E=R_\infty hc\,\alpha^2\frac{[Z-\sigma_2(n,\,l)]^4}{n^3\,l(l+1)},\quad(|\Delta j|=1\text{ but same }nl) \tag{2.111}$$

for the separation of spin-doublets like $L_{II}L_{III}$, $M_{II}M_{III}$, $M_{IV}M_V$, $N_{II}N_{III}$, $N_{IV}N_V$ and $N_{VI}N_{VII}$. Unlike (2.108), here the separation depends strongly on Z, as observed by *Hertz*.

Two *lines* are called a *spin-doublet* when: 1) they have a common initial level and the final levels are a spin-doublet, or 2) they have a common final level and the initial levels are a spin-doublet. Spin doublets of K and L series are given below:

K-series	Lines	Levels (initial, final)
	$\alpha_1\alpha_2$	$(K,\,L_{III}L_{II})$
	$\beta_1\beta_3$	$(K,\,M_{III}M_{II})$
L-series	Lines	Levels (initial, final)
	ln	$(L_{III}L_{II},\,M_I)$
	$\alpha_2\beta_1$	$(L_{III}L_{II},\,M_{IV})$
	$\beta_6\gamma_5$	$(L_{III}L_{II},\,N_I)$
	$\beta_{15}\gamma_1$	$(L_{III}L_{II},\,N_{IV})$
	$\gamma_8\beta_7$	$(L_{III}L_{II},\,O_I)$
	$\beta_5\gamma_6$	$(L_{III}L_{II},\,O_{IV})$
	$\beta_4\beta_3$	$(L_I,\,M_{II}M_{III})$
	$\alpha_1\alpha_2$	$(L_{III},\,M_{IV}M_V)$
	$\gamma_2\gamma_3$	$(L_I,\,N_{II}N_{III})$
	$\beta_{15}\beta_2$	$(L_{III},\,N_{IV}N_V)$

The lines of spin-doublets are recognized by their having the same frequency difference all through the spectrum of one and the same element (given Z). Examples are the lines $K\alpha_1$ and $K\alpha_2$, the $L\beta_1$ and $L\alpha_2$, the $L\eta$ and Ll, and the $L\gamma_5$ and $L\beta_6$, all characterized by having the L_{II} and L_{III} levels either as initial or final levels. The lines of screening doublets arise due to transitions to and from the pair of levels $L_I L_{II}$, $M_I M_{II}$, $M_{III} M_{IV}$, $N_I N_{II}$, etc. There are no electric-dipole lines that form screening doublets by having L_I and L_{II} levels as initial or as final levels. However, one dipole line and one multipole line can form such a doublet, for example, $L\beta_3(L_I \to M_{III})$ and $L\beta_{10}(L_I \to M_{IV})$.

It is useful to calculate the wavelength difference $\Delta\lambda$ between the lines of a spin-doublet. Because $\nu = 1/\lambda$ and $h\Delta\nu = \Delta E$,

$$|\Delta\lambda| = \frac{\Delta\tilde{\nu}}{\tilde{\nu}^2} = \frac{R_\infty}{\tilde{\nu}^2}\Delta\left(\frac{\tilde{\nu}}{R_\infty}\right) = \frac{R_\infty\alpha^2}{n^3 l(l+1)}\frac{(Z-\sigma_2)^4}{\tilde{\nu}^2}. \tag{2.112}$$

From the Moseley law for lines, (2.4),

$$(\tilde{\nu}/R_\infty)^2 = A^4(Z-\sigma)^4 \quad \text{(for lines)}. \tag{2.113}$$

In general, $\sigma \neq \sigma_2$. However, for large Z we can take $\sigma \simeq \sigma_2$. Using this,

$$|\Delta\lambda| \simeq \frac{\alpha^2}{A^4 R_\infty n^3 l(l+1)}, \quad \textit{(spin doublets)}. \tag{2.114}$$

This approximate formula tells us that $\Delta\lambda$ for the lines of a spin-doublet will not depend on Z, in contrast to $\Delta\tilde{\nu}$ given by (2.111). It is supported by the data. Let us consider the spin doublet $K\alpha_1$, $K\alpha_2$ that arises from the transitions $K \to L_{III}$, $K \to L_{II}$, respectively. The measured values of $\Delta\lambda$ in XU remain between 4 and 5, whereas $\Delta(\tilde{\nu}/R_\infty)$ varies from about 100 to 25035 for Z values that range from 26(Fe) to 92(U).

The rule (2.111) for a spin doublet, that $\Delta\tilde{\nu}$ is the same for a given Z, and the rule (2.114), that $\Delta\lambda$ for a spin doublet is nearly constant for any Z, have together been very useful in systematizing X-ray spectra. There are some interesting exceptions to the constant $\Delta\lambda$ rule, which are connected with incomplete electronic shells (see, for example, [2.67]).

In Fig. 2.21 we show how the simple X-ray levels of the Bohr atom are split up through the relativity and spin effects, when screening is included (2.82). When the screening effects are not included, the levels with the same n, j values but different l values coincide (Fig. 2.14).

Experimental values of σ_1 and σ_2 can be obtained in the following way. The spin-doublet formula (2.111) can be used to determine approximately the internal screening constant σ_2,

$$\Delta\left(\frac{\tilde{\nu}}{R_\infty}\right) = \frac{\Delta E}{R_\infty hc} = \frac{E_i - E_f}{R_\infty hc} = \alpha^2\frac{[Z-\sigma_2(n,l)]^4}{n^3 l(l+1)}. \tag{2.115}$$

For $n=2$, $l=1$, this will correspond to the separation of spin-doublet levels $L_{II}L_{III}$. If we determine $\Delta(\tilde{\nu}/R_\infty)$ from the distance between the observed $K\alpha_1$

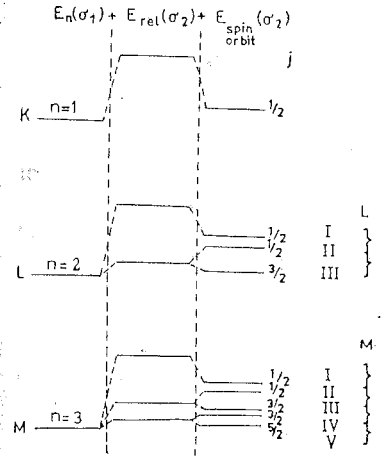

Fig. 2.21. Diagram showing the splitting of simple X-ray atomic levels as relativity and spin-orbit effects, together with screening effects, are introduced, (2.82)

and $K\alpha_2$ lines in Rydbergs, a value for σ_2 is obtained,

$$\Delta\left(\frac{\tilde{\nu}}{R_\infty}\right)_{expt} = \alpha^2\frac{[Z-\sigma_2(n=2,\,l=1)]^4}{2^4} \quad (\text{for } L_{II}L_{III}). \tag{2.116}$$

For a better approximation, we should improve (2.82) by including more terms in the relativistic correction (2.67). This gives the Bohr–Sommerfeld expression for orbital energies, with $x = n/(j+\frac{1}{2})$,

$$E_{nlj} = R_\infty hc\left[\frac{(Z-\sigma_1)^2}{n^2} + \frac{\alpha^2(Z-\sigma_2)^4}{n^4}\left(X-\frac{3}{4}\right) + \frac{\alpha^4(Z-\sigma_2)^6}{n^6}\left(\frac{1}{4}X^3+\frac{3}{4}X^2-\frac{3}{2}X+\frac{5}{8}\right) + \frac{\alpha^6(Z-\sigma_2)^8}{n^8}\left(\frac{1}{8}X^5+\frac{3}{8}X^4+\frac{1}{8}X^3-\frac{15}{8}X^2+\frac{15}{8}X-\frac{35}{64}\right)+\cdots\right]. \tag{2.117}$$

This equation, like (2.82), holds for $j = l + 1/2$ and $j = l - 1/2$. Using it, we get in place of (2.116), for the $L_{II}L_{III}$ doublet,

$$\Delta\left(\frac{\tilde{\nu}}{R_\infty}\right)_{expt} = \frac{\alpha^2(Z-\sigma_2)^4}{2^4}\left[1+\frac{5}{2}\frac{\alpha^2}{2^2}(Z-\sigma_2)^2+\frac{53}{8}\frac{\alpha^4}{2^4}(Z-\sigma_2)^4+\cdots\right]. \tag{2.118}$$

Sommerfeld [2.68] has shown that this can be solved for $Z-\sigma_2$ in an approximate manner to give the result

$$[Z-\sigma_2(n=2,\ l=1)]^2=\left[\frac{4}{\alpha}\sqrt{\Delta\left(\frac{\tilde{\nu}}{R_\infty}\right)_{\text{expt}}}-5\Delta\left(\frac{\tilde{\nu}}{R_\infty}\right)_{\text{expt}}\right]\times\left[1+\frac{19}{32}\alpha^2\,\Delta\left(\frac{\tilde{\nu}}{R_\infty}\right)_{\text{expt}}\right]. \tag{2.119}$$

Values of σ_2 for the $L_{II}L_{III}$ doublet, obtained by putting $K\alpha_1$, $K\alpha_2$ data for $\Delta(\tilde{\nu}/R_\infty)_{\text{expt}}$ in (2.119), are given in Table 2.2. Thus, both $\Delta\lambda$ and σ_2 remain nearly constant as predicted. Values of σ_2 for other spin-doublet levels can be found in a similar way. The average values of $\sigma_2(n, l)$ are given in Table 2.3. The value of $\sigma_2(n, l)$ increases with the increase in n and l, because the amount of screening from the nucleus also increases.

The above method cannot be used to find $\sigma_2(n, l=0)$ for *single* levels like $K, L_I, M_I, \ldots$ ($l=0$ and only a single value of $j=1/2$). We therefore first determine σ_1.

The formula (2.106) is much too rough for determining the X-ray total screening constant $\sigma_1(n, l)$. A better approximation is obtained by using (2.82, 105), for the level characterized by n, j, σ_1, σ_2,

$$\frac{\tilde{\nu}}{R_\infty}=\frac{(Z-\sigma_1)^2}{n^2}\left[1+\frac{\alpha^2(Z-\sigma_2)^4}{n^2(Z-\sigma_1)^2}\left(\frac{n}{j+1/2}-\frac{3}{4}\right)\right]. \tag{2.120}$$

Table 2.2. The internal screening constant σ_2 for the $L_{II}L_{III}$ doublet

Element	$\Delta\lambda(K\alpha_2-K\alpha_1)$ [XU]	$\Delta(\tilde{\nu}/R_\infty)$ (experiment)	$Z-\sigma_2$	σ_2
42 Mo	4.27	7.73	38.53	3.47
47 Ag	4.39	12.74	43.49	3.51
50 Sn	4.45	16.74	46.50	3.50
66 Dy	4.72	58.41	62.51	3.49
74 W	4.83	98.84	70.52	3.48
82 Pb	4.88	158.49	78.56	3.44

Table 2.3. Values of σ_2 for the X-ray spin-doublet levels

Level	n	l	σ_2
$L_{II,III}$	2	1	3.5
$M_{II,III}$	3	1	8.5
$M_{IV}M_V$	3	2	13.0
$N_{II,III}$	4	1	17.0
$N_{IV,V}$	4	2	24
$N_{VI,VII}$	4	3	34

Using $(1+x)^{1/2}\simeq 1+\frac{1}{2}x$,

$$\left(\frac{\tilde{\nu}}{R_\infty}\right)^{1/2}=\frac{Z-\sigma_1}{n}+\frac{\alpha^2}{2n^3}\frac{(Z-\sigma_2)^4}{Z-\sigma_1}\left(\frac{n}{j+1/2}-\frac{3}{4}\right). \tag{2.121}$$

Similarly, for the second level of a screening doublet (like $2s_{1/2}$, $2p_{1/2}$ or L_I, L_{II}) characterized by $n, j, \sigma_1', \sigma_2'$,

$$\left(\frac{\tilde{\nu}'}{R_\infty}\right)^{1/2}=\frac{Z-\sigma_1'}{n}+\frac{\alpha^2}{2n^3}\frac{(Z-\sigma_2')^4}{Z-\sigma_1'}\left(\frac{n}{j+1/2}-\frac{3}{4}\right). \tag{2.122}$$

For a screening doublet, n and j are the same but l differs by 1. From (2.121, 122),

$$\Delta\left(\frac{\tilde{\nu}}{R_\infty}\right)^{1/2}=\left(\frac{\tilde{\nu}}{R_\infty}\right)^{1/2}-\left(\frac{\tilde{\nu}'}{R_\infty}\right)^{1/2}=\frac{\sigma_1'-\sigma_1}{n}+\frac{\alpha^3}{2n^3}\left(\frac{n}{j+1/2}-\frac{3}{4}\right)\left(\frac{(Z-\sigma_2)^4}{Z-\sigma_1}-\frac{(Z-\sigma_2')^4}{Z-\sigma_1'}\right). \tag{2.123}$$

Here $\sigma_1=\sigma_1(n=2,\ l=0)$ and $\sigma_1'=\sigma_1(n=2,\ l=1)$, for example, for the screening doublet L_I, L_{II}. We again get (2.108) when the second term is ignored.

We already know σ_2 for the L_{II} level (Table 2.3). Using this σ_2 and the experimental values of $(\tilde{\nu}/R_\infty)^{1/2}$, we can calculate the total screening constant σ_1 for the L_{II} levels of various elements from (2.122). These values of σ_1 (L_{II}) are plotted against Z, see Fig. 2.22. Although σ_2 is independent of Z, σ_1 increases slowly with Z with changes in slope associated with the filling of shells. However, $\Delta\sigma_1$ should remain independent of Z(2.108). This fact can be exploited to find σ_2 for the level L_I, by using a method of trial and error. Experimental values of $(\tilde{\nu}/R_\infty)^{1/2}$ are selected for the L_I level, and various numerical values of σ_2(not known for L_I) are substituted by hand in (2.121). This gives a set of curves for the σ_1 versus Z plot. It contains one curve for each value of σ_2 used. From this set, the curve that runs parallel to the $\sigma_1(L_{II})$ curve for the L_{II} level drawn earlier (Fig. 2.22) is selected. This gives us $\sigma_1(L_I)$ for the L_I level (Fig. 2.22) and also the corresponding σ_2 for the L_I level. The values of σ_2 found by trial in this way are given in Table 2.4. The value for the K level has been added for the sake of completeness.

The foregoing interpretations cannot be true in a precise sense because, quantum mechanically, no sharp distinction between internal and external shells is meaningful. Therefore, there is not much to be gained by attempting to choose σ_1 and σ_2 in such a way as to represent the data best. The Bohr–Sommerfeld result (2.82) is in accord with the main facts; that is all that can be expected. For recent calculations see [2.69–71].

In the exact Dirac relativistic theory of the hydrogen atom, the relativistic and spin–orbit effects are not treated separately as they are implied in the theory. Therefore, we can use a single screening constant σ_{nlj}, which allows us to replace Z by $Z-\sigma_{nlj}$. The Dirac theory gives the term-value equation, which

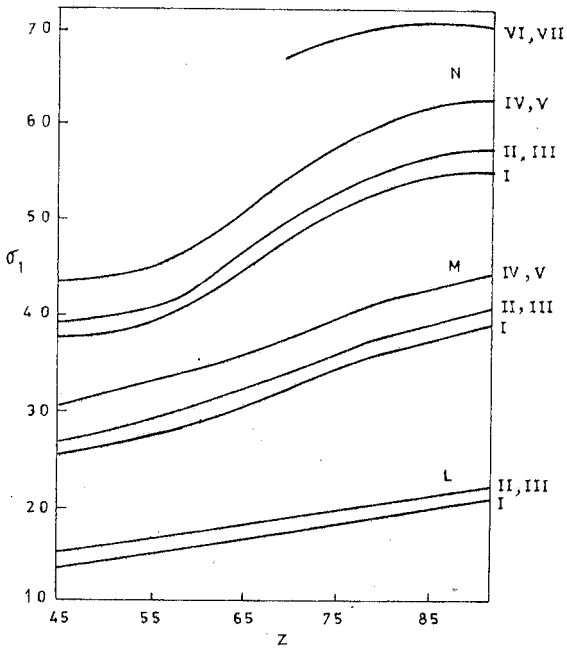

Fig. 2.22. The screening constant $\sigma_1(n, l; Z)$ as a function of Z

Table 2.4. $\sigma_2(n, l)$ for individual levels

Level	σ_2
K	0
L_I	2.0
M_I	6.8
N_I	14

includes both the relativistic effect and the spin–orbit effect, as

$$E_{nlj} = mc^2(1+(\alpha Z_{nj})^2\{n-j-\tfrac{1}{2}+[(j+\tfrac{1}{2})^2-(\alpha Z_{nj})^2]^{1/2}\}^{-2})^{-1/2}, \quad (2.124)$$

where Z_{nj} is the effective atomic number, $Z_{nj} = Z - \sigma_{nlj}$. It can be expressed as Z minus a sum over occupied orbitals of the product of electron numbers and orbital screening constants, so that the matrix equation is

$$Z_{nj} = Z - S_{nj}N_{nj} + S_{nj}. \quad (2.125)$$

Here N_{nj} is the orbital occupation matrix and S_{nj} is the screening matrix. *Veigele* et al. [2.72] have written a screening parameter program based on the Dirac theory.

So far, we have considered the energy of X-ray atomic levels (hole states) as analogous to the optical levels of hydrogen-like atoms, on the basis of Pauli's vacancy principle and Koopmans' theorem [2.69, 70]. The same results follow by taking into account all of the electrons in the closed shell with a given configuration [2.73, 74]. The result (2.111) is found to be independent of the type of coupling (*LS* applicable for low Z; *jj* for high Z due to strong spin-orbit interaction) present in the atom.

2.12 Quantum Theory of Spontaneous Emission of X-Ray Lines and Multipoles

In an X-ray tube, the target atom is excited by bombardment with cathode electrons. As a result, an atom emits an X-ray photon without electromagnetic radiation being present initially to induce the radiative process. Such a process is called *spontaneous emission*. Einstein calculated the transition probability for spontaneous emission on semiclassical consideration, using the results of induced processes. For a full quantum mechanical treatment, we have to consider the quantization of the pure radiation field.

The interaction between the atom and the radiation field, treated as one dynamical system, can bring about radiative transitions even if *in the initial state no light quanta exist*. When the entire system (atom + radiation field) is treated as a single entity, the Hamiltonian is independent of time, and a transition between atomic levels is to be thought of as a redistribution of the energy between the two parts of the coupled system.

The interaction term can be found by considering the Hamiltonian

$$H = \left[\frac{1}{2m}\left(\boldsymbol{p} - \frac{e}{c}\boldsymbol{A}\right)^2 + e\phi\right] + H_{\text{radiation}}. \quad (2.126)$$

where $\boldsymbol{A}$ and ϕ are the vector and scalar potentials of the radiation field. The interaction term is

$$H' = -\frac{e}{mc}\boldsymbol{p}\cdot\boldsymbol{A} = \frac{ie\hbar}{mc}\nabla\cdot\boldsymbol{A}. \quad (2.127)$$

We can quantize the radiation field by enclosing it in a certain volume V with $\boldsymbol{A}$ periodic on the walls. The radiation field can then be regarded as an infinite set of harmonic oscillators, one for each value of the propagation vector $\boldsymbol{k}_l$ and a particular direction of polarization $\boldsymbol{e}_l$. Therefore $\boldsymbol{A}$ may be expressed as [2.6]

$$\boldsymbol{A} = \left(\frac{4\pi c^2}{V}\right)^{1/2}\sum_l \boldsymbol{e}_l\left(q_l\, e^{i\boldsymbol{k}_l\cdot\boldsymbol{r}} + q_l^{\dagger}\, e^{-i\boldsymbol{k}_l\cdot\boldsymbol{r}}\right), \quad (2.128)$$

where the q's have the nonvanishing matrix elements

$$q_{n-1,n} = \left(\frac{n\hbar}{2\omega}\right)^{1/2} e^{-i\omega t}, \quad q^{\dagger}_{n+1,n} = \left[\frac{(n+1)\hbar}{2\omega}\right]^{1/2} e^{i\omega t}. \tag{2.129}$$

Here $q^{\dagger}_{n+1,n}$ means that initially we have n photons and finally $n+1$ photons. In our case $n=0$ and $q^{\dagger}_{1,0}$ is the *only* nonvanishing matrix element for the emission of one photon. So, the matrix element for the spontaneous emission is

$$H'_{f,i;i,0} = -\frac{e}{mc}\left(\frac{2\pi c^2\hbar}{V\omega}\right)^{1/2} \int \psi_f^* \, e^{-i\boldsymbol{k}\cdot\boldsymbol{r}} (\boldsymbol{e}\cdot\boldsymbol{p}) \psi_i \, d\tau \,. \tag{2.130}$$

Expand $\exp(-i\boldsymbol{k}\cdot\boldsymbol{r})$ in (2.130) as

$$e^{-i\boldsymbol{k}\cdot\boldsymbol{r}} = 1 - i\boldsymbol{k}\cdot\boldsymbol{r} + \frac{1}{2!}(i\boldsymbol{k}\cdot\boldsymbol{r})^2 - \cdots \,. \tag{2.131}$$

The term $(\boldsymbol{k}\cdot\boldsymbol{r})^n$ is said to give the electric-2^{n+1}-pole and the magnetic-2^n-pole transitions. Retaining only the first term, $\exp(-i\boldsymbol{k}\cdot\boldsymbol{r}) \to 1$, we get the *electric-dipole transition.*

2.12.1 Spontaneous Electric-Dipole Transition

The replacement $\exp(-i\boldsymbol{k}\cdot\boldsymbol{r}) \to 1$ is equivalent to replacing the atom by an electric dipole,

$$\frac{1}{m}(\boldsymbol{p})_{fi} = \frac{d}{dt}(\boldsymbol{r})_{fi} = \frac{1}{i\hbar}\Big[\boldsymbol{r}, H_0\Big]_{fi} = \frac{1}{i\hbar}(E_i - E_f)(\boldsymbol{r})_{fi} = i\omega_{fi}(r)_{fi} \,. \tag{2.132}$$

In this approximation, (2.130) becomes

$$H'_{f1;i0} = -i\left(\frac{2\pi\hbar}{V\omega}\right)^{1/2} \omega_{fi} \, e\cdot(e\boldsymbol{r})_{fi} \,. \tag{2.133}$$

This is the *electric-dipole matrix element for the spontaneous-emission process.* The transition probability per unit time is given by

$$w_{fi} = \frac{2\pi}{\hbar}|H'_{f1;i0}|^2 \, \rho(E) = \frac{4\pi^2}{V\omega}\omega_{fi}^2 |\boldsymbol{e}\cdot(e\boldsymbol{r})_{fi}|^2 \, \rho(E), \tag{2.134}$$

where $\rho(E)$ is the density of final continuum states of the emitted photon. Phase-space considerations give (for photons $E = \hbar\omega = pc$),

$$\rho(E) = \frac{d}{dE}\left(\frac{p^2 dp d\Omega}{h^3/V}\right) = \frac{d}{d\hbar\omega}\left(\frac{V\omega^2 d\omega}{8\pi^3 c^3} d\Omega\right) = \frac{V\omega^2}{8\pi^3\hbar c^3} d\Omega \,. \tag{2.135}$$

Putting $\omega_{fi} = \omega$,

$$w_{fi} = \frac{\omega_{fi}^3}{2\pi\hbar c^3} \int |\boldsymbol{e}\cdot(e\boldsymbol{r})_{fi}|^2 \, d\Omega \,. \tag{2.136}$$

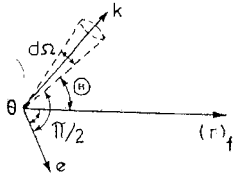

Fig. 2.23. Angles for the integration between $\boldsymbol{k}$ and $(\boldsymbol{r})_{fi}$

Let $\boldsymbol{e}$, $\boldsymbol{k}$ and $\boldsymbol{r}_{fi}$ be in the plane of the paper, for convenience, with $\theta = (\boldsymbol{e}, \boldsymbol{r}_{fi})$ and $\Theta = (\boldsymbol{k}, \boldsymbol{r}_{fi})$ (Fig. 2.23). Because $(\boldsymbol{e}, \boldsymbol{k}) = \pi/2$, we can write $(\boldsymbol{e}\cdot\boldsymbol{r}_{fi}) = r_{fi}\cos\theta = r_{fi}\sin\Theta$, and

$$w_{fi} = \int_0^{\pi}\int_0^{2\pi} \frac{\omega_{fi}^3}{2\pi\hbar c^3}|(e\boldsymbol{r})_{fi}|^2 \sin^2\Theta \, d\Theta \, d\Phi = \frac{4}{3}\frac{e^2\omega_{fi}^3}{\hbar c^3}|r_{fi}|^2, \tag{2.137}$$

in exact agreement with the semiclassical result for the spontaneous-emission rate, (2.20), derived earlier. The intensity will be proportional to the energy emitted per second, $\hbar\omega_{fi}$.

2.12.2 Spontaneous Higher-Multipole Transitions

Let us consider the next term, $-i\boldsymbol{k}\cdot\boldsymbol{r}$, in the expansion (2.131). Its contribution to the matrix element is

$$h_{fi} = C\frac{ie}{mc}\int \psi_f^*(\boldsymbol{k}\cdot\boldsymbol{r})(\boldsymbol{e}\cdot\boldsymbol{p})\psi_i \, d\tau = h_{fi}^M + h_{fi}^Q \,, \tag{2.138}$$

where $C = (2\pi c^2\hbar/V\omega)^{1/2}$ and

$$h_{fi}^M = C\frac{ie}{2mc}\int \psi_f^*[(\boldsymbol{e}\cdot\boldsymbol{p})(\boldsymbol{k}\cdot\boldsymbol{r}) - (\boldsymbol{e}\cdot\boldsymbol{r})(\boldsymbol{k}\cdot\boldsymbol{p})]\psi_i \, d\tau \,, \tag{2.139}$$

$$h_{fi}^Q = C\frac{ie}{2mc}\int \psi_f^*[(\boldsymbol{e}\cdot\boldsymbol{p})(\boldsymbol{k}\cdot\boldsymbol{r}) + (\boldsymbol{e}\cdot\boldsymbol{r})(\boldsymbol{k}\cdot\boldsymbol{p})]\psi_i \, d\tau \,. \tag{2.140}$$

Using the identity $(\boldsymbol{a}\times\boldsymbol{b})\cdot(\boldsymbol{c}\times\boldsymbol{d}) = (\boldsymbol{a}\cdot\boldsymbol{c})(\boldsymbol{b}\cdot\boldsymbol{d}) - (\boldsymbol{a}\cdot\boldsymbol{d})(\boldsymbol{b}\cdot\boldsymbol{c})$, we obtain

$$h_{fi}^M = C\frac{ie}{2mc}\int \psi_f^*(\boldsymbol{e}\times\boldsymbol{k})\cdot(\boldsymbol{p}\times\boldsymbol{r})\psi_i \, d\tau = C\frac{ie}{2mc}\int \psi_f^*(\boldsymbol{k}\times\boldsymbol{e})\cdot\boldsymbol{L}\,\psi_i \, d\tau \,, \tag{2.141}$$

where $\boldsymbol{L} = \boldsymbol{r}\times\boldsymbol{p}$ is the orbital angular momentum. Consider an electron that moves with speed v in a circle of radius r. It creates a current $ev/2\pi r$ in a loop of area πr^2 and has orbital angular momentum $l = mvr$. Therefore, the equivalent dipole magnetic moment is

$$\mu = \frac{ev}{2\pi r}\frac{\pi r^2}{c} = \frac{e}{2mc}l \quad \text{or} \quad \boldsymbol{\mu} = \frac{e}{2mc}\boldsymbol{L}. \tag{2.142}$$

These considerations suggest

$$h_{fi}^{M} = iC(\boldsymbol{k}\times\boldsymbol{e})\int \psi_f \boldsymbol{\mu}\psi_i\, d\tau\,, \tag{2.143}$$

for a *magnetic-dipole transition.*

The matrix element h_{fi}^{Q} can be simplified by using $\boldsymbol{p} = m\dot{\boldsymbol{r}}$ so that

$$\boldsymbol{pr}+\boldsymbol{rp} = \frac{im}{\hbar}\left([H,\boldsymbol{r}]\boldsymbol{r}+\boldsymbol{r}[H,\boldsymbol{r}]\right) = \frac{im}{\hbar}[H,\boldsymbol{rr}]\,, \tag{2.144}$$

$$h_{fi}^{Q} = C\frac{e}{2\hbar c}(E_f - E_i)\int \psi_f^*(\boldsymbol{e}\cdot\boldsymbol{r})(\boldsymbol{k}\cdot\boldsymbol{r})\psi_i\, d\tau$$

$$= C\frac{\omega}{2c}|\boldsymbol{k}|(er^2)_{fi}\cos(\boldsymbol{e},\boldsymbol{r})\cos(\boldsymbol{k},\boldsymbol{r})\,, \tag{2.145}$$

where $\boldsymbol{e},\boldsymbol{r}$ means the angle between $\boldsymbol{e}$ and $\boldsymbol{r}$. As h_{fi}^{Q} involves r^2, it gives rise to the *electric-quadrupole transition.*

The electric-dipole transitions give most intense lines because

$$\frac{\text{magnetic-dipole moment}}{\text{electric-dipole moment}} \sim \frac{(e/mc)\,mvr}{er} = \frac{v}{c} \ll 1\,, \tag{2.146}$$

$$\frac{\text{electric-quadrupole moment}}{\text{electric-dipole moment}} \sim \frac{er^2\omega/c}{er} \sim \frac{r}{\lambda}\,. \tag{2.147}$$

For valence electrons, r is of the order of 1 Å. Therefore, in optical spectra ($\lambda \sim 5000$ Å) $r/\lambda \ll 1$; consequently the intensities of electric-quadrupole lines are low. Even for soft X-rays ($\lambda \sim 100$ Å), $(r/\lambda)^2 \sim 10^{-4}$, which indicates low transition probability. For hard X-rays ($\lambda \sim 1$ Å), inner-core electrons are involved, with $r \sim 0.1$ Å. At these distances our approximation is not very good, but we still find $(r/\lambda)^2 \lesssim 10^{-2}$. Therefore, higher-order multipole transitions are *weak*, but they exist.

2.13 Parity Selection Rules and Forbidden Lines

The wave function $\psi(x, y, z)$ is said to have *even* (+) or *odd* (−) *parity*, which depends on the sign in the equation

$$\psi(x, y, z) = \begin{cases} +\psi(-x, -y, -z) & \text{even parity}, \\ -\psi(-x, -y, -z) & \text{odd parity}, \end{cases} \tag{2.148}$$

under reflection through the origin of coordinates ($x\to -x$, $y\to -y$, $z\to -z$). In our matrix elements, we have integrals of the form

$$I = \int_{-a}^{+a} F(x)dx, \quad F(x) = \psi^*(x)O_{op}(x)\psi(x), \tag{2.149}$$

$$I = \begin{cases} \text{not zero} & \text{if } F(x) = +F(-x), \\ \text{zero} & \text{if } F(x) = -F(-x), \end{cases} \tag{2.150}$$

although $F(x)$ has not been explicitly specified.

In the matrix elements, the overall parity

$$F(x) = \psi^*(x)O_{op}(x)\psi(x)$$

$$= (\pm 1)\psi^*(-x)\cdot(\pm 1)O_{op}(-x)\cdot(\pm 1)\psi(-x) = \pm F(-x), \tag{2.151}$$

where O_{op} is any of the operators like er for electric dipole, $\boldsymbol{\mu}$ for magnetic dipole, and (er^2) for electric quadrupole. In all, we have the following eight distinct possibilities:

ψ_f^*	O_{op}	ψ_i	F
+	+	+	+
+	+	−	−
−	+	+	−
−	+	−	+
+	−	+	−
+	−	−	+
−	−	+	+
−	−	−	−

For polar coordinates, the reflection through the origin ($\boldsymbol{r}\to -\boldsymbol{r}$) implies

$$r\to r, \quad \theta\to\pi-\theta, \quad \phi\to\phi+\pi, \tag{2.152}$$

as limits of θ are from 0 to π. For $\psi(r,\theta,\phi) = R_{nl}(r)Y(\theta)Z(\phi)$ reflection means

$$R_{nl}(r)\to R(r),$$

$$Y_{l|m|}(\theta)\to Y_{l|m|}(\pi-\theta) = P_l^{|m|}(-\cos\theta),$$

$$Z_{|m|}(\phi)\to Z_{|m|}(\phi+\pi) = e^{i|m|(\phi+\pi)},$$

$$\psi(r,\theta,\phi)\to\psi(r,\pi-\theta,\phi+\pi). \tag{2.153}$$

In our case, $Z_{|m|}(\phi+\pi) = (-1)^{|m|}e^{i|m|\phi} = (-1)^{|m|}Z_{|m|}(\phi)$. Therefore, $Z_{|m|}(\phi)$ has the parity of $|m|$. For $Y_{l|m|}(\theta)$,

$$Y_{l|m|}(\pi-\theta) = P_l^{|m|}(-\cos\theta) = (-1)^{l-|m|}P_l^{|m|}(\cos\theta) = (-1)^{l-|m|}Y_{l|m|}(\theta).$$

The explanation is that $P_l^m(x)$ is equal to an even part $(1-x^2)^{|m|/2}$ times a polynomial in x that has the parity of $l-|m|$ for $x\to -x$. Thus, for the whole function $\psi(r,\theta,\phi)\to(-1)^{|m|}(-1)^{l-|m|}\psi(r,\theta,\phi) = (-1)^l\psi(r,\theta,\phi)$. In other words, *all states with even l are even, and all those with odd l are odd.*

We now get the following table of parities and matrix elements I for the electric-dipole transition:

ψ_f	r	ψ_i	F	$I_{(er)}$	Remark
+	−	+	−	zero	forbidden
+	−	−	+	nonzero	allowed
−	−	+	+	nonzero	allowed
−	−	−	−	zero	forbidden

Because, for even $l=0, 2, 4, \ldots, \psi$ has even parity and for odd $l=1, 3, 5, \ldots, \psi$ has odd parity, we are led to the familiar selection rule

$$\Delta\pi, \text{ yes}; \quad \Delta l(\text{yes}) = \pm 1 \quad (\textit{electric dipole}),$$
$$(\Delta j = 0 \text{ or } \pm 1, \text{ the } j\text{-transition } 0 \to 0 \text{ forbidden}), \tag{2.154}$$

where $\Delta\pi$ means change in parity. It follows that *all spectral lines due to electric-dipole radiation arise from transitions between states of opposite parity*. This is called the *Laporte rule*.

Orbital angular momentum $\boldsymbol{L}=\boldsymbol{r}\times\boldsymbol{p}$ is a *pseudovector*, because it does not change its sign under parity transformation, as do other *polar* or ordinary vectors (r or p); $\boldsymbol{r}\times\boldsymbol{p}\to(-\boldsymbol{r})\times(-\boldsymbol{p})=\boldsymbol{r}\times\boldsymbol{p}$. Therefore, unlike $\boldsymbol{r}$, the dipole magnetic moment is a pseudovector; it gives the following table:

ψ_f	μ	ψ	F	$I_{(\mu)}$
+	+	+	+	nonzero
+	+	−	−	zero
−	+	+	−	zero
−	+	−	+	nonzero

In this case, we get nonvanishing matrix components only between states of the *same parity*, which is just the opposite of the Laporte rule for electric-dipole radiation. The selection rules are

$$\Delta\pi, \quad \text{no}; \quad \Delta l = 0 \quad (\textit{magnetic dipole}),$$
$$(\Delta j = 0 \text{ or } \pm 1, \text{ the } j\text{-transition } 0 \to 0 \text{ is forbidden}). \tag{2.155}$$

Because r^2 is a scalar, $r^2 \to r^2$ under parity transformation, for *electric-quadrupole radiation* we get the same table as for the magnetic-dipole case. The selection rules are

$$\Delta\pi, \text{ no}; \quad \Delta l = 0 \text{ or } \pm 2 \quad (\textit{electric quadrupole}),$$
$$(\Delta j = 0, \pm 1 \text{ or } \pm 2, \text{ the } j\text{-transitions } 0 \to 0, \tfrac{1}{2} \to \tfrac{1}{2} \text{ and}$$
$$0 \not\rightleftarrows 1 \text{ are forbidden}) \tag{2.156}$$

Diagram lines that are not allowed by the electric-dipole selection rules (2.154) are called *forbidden lines*. Weak forbidden lines are observed, which obey selection rules like (2.155) or (2.156), for higher poles. In Fig. 2.24, we show transitions for some of the important (forbidden) quadrupole lines that have been observed in spite of their small intensities. The forbidden lines are *diagram lines* in the sense that their transitions can be shown on the energy-level diagram similar to that used for the electric-dipole allowed lines (Fig. 2.15).

The forbidden lines $K\beta_5$ ($K \to M_{IV,V}$ unresolved) and $K\beta_4$ ($K \to N_{IV,V}$ unresolved) have been observed by *Duane* [2.75], *Ross* [2.76], *Carlsson* [2.77] and more recently, for example, by *Leiro* [2.78]. *Ross* has estimated that the intensity of the forbidden line $K\beta_5$ in ^{42}Mo and ^{42}Rh is of the order of 1/1000 of that of the allowed $K\alpha_1$ ($K \to L_{III}$) line. However, in ^{46}Pd it is nearer 1/250. Resolved

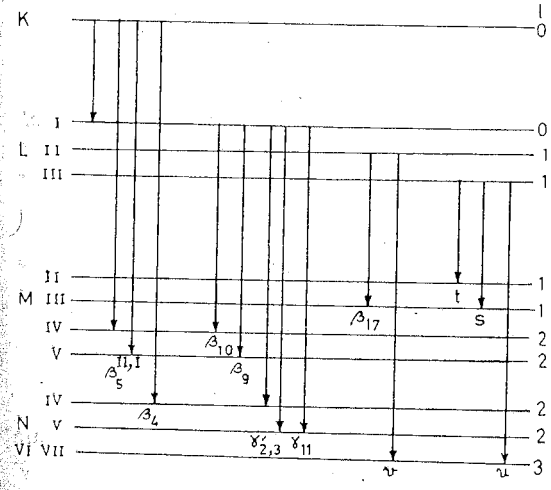

Fig. 2.24. Energy-level diagram showing the observed forbidden lines. Energy levels are not to scale

lines $K\beta_5^{II}(K \to M_{IV}$; 625.78 XU); $K\beta_5^{I}(K \to M_V$; 625.62 XU); $K\beta_4^{II}(K \to N_{IV}$; 618.95 XU) and $K\beta_4^{I}(K \to N_V$; 618.73 XU) *have been reported for* ^{42}Mo by *Hulubei* [2.79]. For other such measurements see the wavelength tables of *Cauchois* and *Sénémaud* [2.80], *Sandström* [2.67] and *Bearden* [2.4]. The $K \to L_I$ line has been observed by *Beckman* [2.81]. It is a magnetic-dipole line with an intensity of 0.02 compared to the $K\alpha_1$ line.

In the L series, the most intense observed forbidden lines are $L\beta_{10}$ ($L_I \to M_{IV}$) and $L\beta_9$ ($L_I \to M_V$). *Allison* and *Armstrong* [2.82] found that the intensity ratio of these lines to the allowed line $L\alpha_1$ ($L_{III} \to M_V$) is about 1/300 at 30.7 kV in ^{74}W. In Table 2.5, we give a list of some of the important observed forbidden lines in the K series and the L series.

Table 2.5. Observed forbidden lines

Transition	Symbol	Parity ($i-f$)	Transition	Symbol	Parity ($i-f$)
$K \to L_I$	—	even–even	$L_{II} \to M_{III}$	$L\beta_{17}$	odd–odd
$K \to M_{IV,V}$	$K\beta_5^{II,I}$	even–even	$L_{II} \to N_{VI,VII}$	Lv	odd–odd
$K \to N_{IV,V}$	$K\beta_4^{II,I}$	even–even	$L_{III} \to M_{II}$	Lt	odd–odd
$L_I \to M_{IV}$	$L\beta_{10}$	even–even	$L_{III} \to M_{III}$	Ls	odd–odd
$L_I \to M_V$	$L\beta_9$	even–even	$L_{III} \to N_{VI,VII}$	Lu	odd–odd
$L_I \to N_{IV,V}$	$L\gamma'_{2,3}$	even–even			
$L_I \to N_V$	$L\gamma_{11}$	even–even			

It may happen that a forbidden line coincides with an allowed line. An unexpected increase of the ratio $K\beta_2/K\beta_1$ led *Meyer* [2.83] to show that for elements with $Z<32$, the quadrupole line $K\beta_5$ overlaps the β_2 line.

Relative intensities of lines arising from magnetic-dipole and electric-quadrupole transitions have been carefully measured recently by *Smither et al.* [2.62], and *Rao et al.* [2.63]. The angular correlation of X-ray emission has been studied by *Catz* [2.84] from the point of view of admixed magnetic-quadrupole with electric-dipole radiation. The mixing ratios are now measurable from angular correlation experiments [2.85].

For recent calculations see [2.86, 87]. *Marrus and Schmieder* [2.88] have given a simple formula for the $ns \rightarrow 1s$ transitions.

2.14 Absorption Discontinuities

In an X-ray tube continuous X-rays are also produced. When these X-rays are passed through an absorbing material, changes occur in the distribution of intensity with wavelength (or frequency). These changes are gradual, owing to the scattering of X-rays within the material but become abrupt when the incident photon has just enough energy $h\nu$ to remove one of the inner electrons in the absorbing atom to *outside* the atom or at least outside the system of complete shells. At this energy, heavy absorption occurs and a sudden change of the intensity transmitted through the materials is observed. This is the so-called *absorption discontinuity* or the *absorption edge* (Fig. 2.25). On the high-frequency side of this edge, the continuous spectrum is considerably weakened. The edge corresponds to the minimum energy of a photon absorbed by a given level. The absorption edge is thus a characteristic feature of the absorbing element.

We cannot have an absorption line in normal atoms corresponding to a transition of the electron from the K-level to, say, L_{III} level (or of the hole from the L_{III} level to K level) because in normal atoms, the L_{III}, or the other inner levels, are full (no vacancy to which the electron can go) according to the Pauli exclusion principle. The shift of emphasis from electron to hole is useful in this sense in discussing X-ray absorption spectra. We can say that, in normal atoms, the holes are on the outside, so the X-ray absorption spectrum is produced by the transition of one of these outer holes to an inside shell. The absorption spectrum is, as a result, directly affected by the external structure of the atoms and the way in which it is influenced by the physical and chemical state in the absorbing material. It is therefore necessary to state carefully what we mean by the outside of the atom in discussing the absorption spectra.

In early days, it was proposed by *Barkla* [2.89], on the basis of his absorption studies, that in an X-ray absorption process the atom is completely ionized, that is, an inner electron is removed from a given inner shell to "infinity". This explains that there is one edge for each spectral series or subseries (one K; three L: L_I, L_{II}, L_{III}; five M edges ; etc.). However, it is an oversimplification of the problem as can be seen from the following argument. If

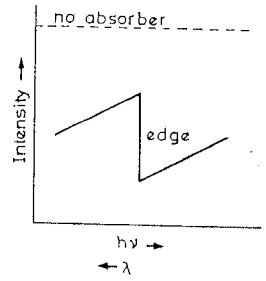

Fig. 2.25. Effect of the absorber on the distribution of transmitted intensity in a continuous spectrum

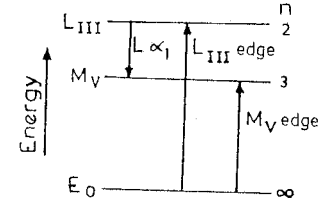

Fig. 2.26. Origin of L_{III} edge, M_V edge and $L\alpha_1$ line, with the outside of the atom defined as $n = \infty$

a frozen orbital model is adapted (Koopmans' theorem approximation), the energies of the states can be associated with the active electron or hole. According to this view, Fig. 2.26 shows the hole transitions for the L_{III} edge, M_V edge, and the $L\alpha_1$ emission line. It gives relationships of the type

$$\begin{aligned} h\nu_{L\alpha_1} &= L_{III} - M_V, \\ h\nu_{L_{III}\,\mathrm{edge}} &= L_{III} - E_0, \\ h\nu_{M_V\,\mathrm{edge}} &= M_V - E_0. \end{aligned} \tag{2.157}$$

Here L_{III} and M_V designate the energies of corresponding levels and E_0 of the *zero level*, that is, the energy of an electron removed to rest at an infinite distance from the atom. From (2.157),

$$h\nu_{L\alpha_1} = h\nu_{L_{III}\,\mathrm{edge}} - h\nu_{M_V\,\mathrm{edge}}. \tag{2.158}$$

This is *not* in agreement with experiment.

Later on, *Siegbahn* [2.90] proposed the following explanation. In the absorption process, the atom is not ionized, but instead is excited by the transition of an inner shell electron to an unfilled external level. These transitions also *obey the electric-dipole selection* rule, $\Delta l = \pm 1$, that has been established for the emission lines. The absorption edge is determined by a transition to the first such allowed unfilled level.

In ^{42}Mo, the level $N_{IV,V}$ is partially filled, and the $N_{VI,VII}$ level is completely unoccupied. All of the shells within $N_{IV,V}$ are fully occupied. The transitions allowed by the selection rules for the L_{III} edge, the M_V edge, and the $L\alpha_1$ line in this theory are now drawn as shown in Fig. 2.27 (compare with Fig. 2.26) and described by the relations

$$\begin{aligned} h\nu_{L\alpha_1} &= L_{III} - M_V, \\ h\nu_{L_{III}\,\mathrm{edge}} &= L_{III} - N_{IV,V}, \\ h\nu_{M_V\,\mathrm{edge}} &= M_V - N_{VI,VII}, \end{aligned} \tag{2.159}$$

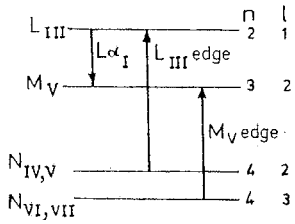

Fig. 2.27. Origin of L_{III} edge, M_V edge, and $L\alpha_1$ line in the Siegbahn model

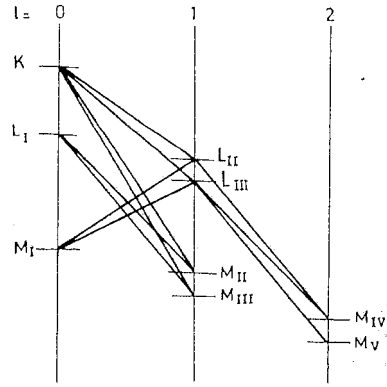

Fig. 2.28. The Siegbahn–Grotrian energy-level diagram for an atom

It is clear from (2.159) that the equality (2.158) is not valid. In fact,

$$h\nu_{L\alpha_1} > h\nu_{L_{III}\,\text{edge}} - h\nu_{M_V\,\text{edge}}, \tag{2.160}$$

in agreement with experiments.

Idei [2.91] pointed out that it is possible to calculate the energy-level system of an atom from the $h\nu$ (or $\tilde{\nu}/R$) values of one of its absorption limits (say, L_{III} edge) and its emission lines. In early work [2.90], the L_{III} level was chosen as the fundamental level, because it could be measured with high precision. Ascribing to the L_{III} edge an energy identical with that of the L_{III} level, the relative energies of all of the other levels can be deduced by following the transitions for the emission lines back and forth (Appendix C). Several combinations are possible, which increases the reliability of the result. It is easy to identify these lines with specific transitions by using the Siegbahn–Grotrian diagram shown in Fig. 2.28. It is obtained from Figs. 2.15, 21 by separating the levels according to their l quantum numbers.

If Siegbahn's idea is correct, the X-ray absorption spectrum of a free atom ought to show a series of absorption lines, corresponding to higher empty optical levels, following the edge. This structure has been found for the inert gases. The absorbing material is in solid form in the usual experiments. In the solid state, the optical (outer) levels will be distorted and broadened to form a *band* due to the hybridization of neighboring-atom valence orbitals. Some structure still remains, according to *Kossel* [2.92], although the conditions are complicated. It is called the *Kossel structure* close to the main absorption edge on the high-energy side, and has been observed experimentally.

An emission line will *not* appear if there are normally no electron in the initial level for the transition of the electron. Accordingly, elements with low atomic number Z are poor in lines and spectral series, compared to those with high Z.

Let us now see what emission lines can possibly appear for each atom as Z changes and what is the closest external (optical) level to which the inner-shell electrons can be excited in the absorption process. In Appendix D the distribution of electrons in the various levels of the free atoms is given. We should compare this with the energy level and transition diagram (Fig. 2.15).

We make this comparison with the K series as an example (Fig. 2.29) to see how the X-ray spectra vary with increase of Z in free atoms and in solids. The first electron appears at the $L_{II,III}$ level with boron (^{5}B). Therefore, the $K\alpha_{1,2}$ line can first appear in a free boron atom. However, in solids it is observed even for ^{3}Li and ^{4}Be. In fact, all lines of the K series appear sooner than the first electron appears at the corresponding level of the free atom, see Table 2.6. This indicates that, as a result of chemical bonding in a solid, the external electrons of the atom are excited to the next optical level, from where these electrons can complete the transition to the hole left in the K level. Such lines are called semioptical for the elements ^{17}Cl, ^{18}Ar, ^{19}K and ^{20}Ca.

In Table 2.6 we also show the elements in which the levels $L_{II,III}$, $M_{II,III}$, ... are first filled up. So long as the level $N_{II,III}$ is partially filled, the line $K\beta_2$ occurs during the transition $K \rightarrow N_{II,III}$, whereas the K edge is due to the same transition but in the opposite direction, $N_{II,III} \rightarrow K$. With increasing Z, when the level $N_{II,III}$ is filled, the absorption process removes the K electron to the next level $O_{II,III}$ allowed by the selection rule, whereas the $K\beta_2$ line is still due to the transition $K \rightarrow N_{II,III}$. As a result, the K edge energy now exceeds the photon energy of the $K\beta_2$ line. *Sandström* [2.93] studied the change of the difference of these two energies by plotting the difference between their $\tilde{\nu}/R_\infty$ values against Z (Fig. 2.30). As expected, this difference is nearly zero up to $Z = 35$; then it begins to increase sharply.

Thus, in solids, the external (valence) electrons are redistributed. The intensity of an observed line depends on the number of electrons in the outer level

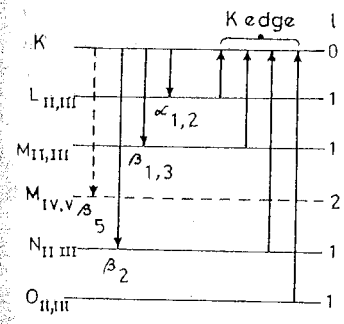

Fig. 2.29. Possible lines of K series and the K absorption edges of different elements. $K\beta_5$ is a quadrupole line. Other transitions obey the dipole rule $\Delta l = \pm 1$

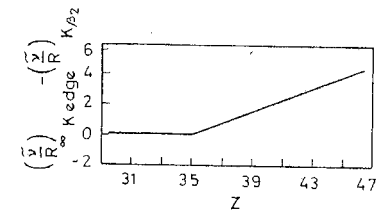

Fig. 2.30. $\Delta\tilde{\nu}/R_\infty$ for the K edge and $K\beta_2$ line showing the effect of the electron configuration

Table 2.6. Appearance of the first line of the K series with an increase in Z

Level	K line	First appearance		Element for which the level is first filled in free atom
		Free atoms	Solids	
$L_{II,III}$	$\alpha_{1,2}$	5 B	3 Li	10 Ne
$M_{II,III}$	$\beta_{1,3}$	13 Al	11 Na	18 Ar
$M_{IV,V}$	β_5	21 Sc	17 Cl	29 Cu
$N_{II,III}$	β_2	31 Ga	30 Zn	36 Kr
$O_{II,III}$	—	49 In	—	54 Xe

that can participate in the transition and also on the probability of the transition. Both of these factors change with the increase of the atomic number Z, when chemical bonding is present. Therefore, the variation of the relative intensities of the lines with Z is a topic of interest. This variation has been studied theoretically [2.60] and experimentally by several workers [2.83, 94–101].

In Fig. 2.31 we show a plot of the relative intensity of the $K\beta_2$ line with respect to the line $K\beta_1$ of unchanging intensity, versus Z. We also show by a dotted curve the number of electrons $N(4p)$ present in the level $4p(N_{II,III})$ as a function of Z. Clearly, the line $K\beta_2$ appears first at ^{30}Zn but attains a constant relative intensity only near ^{50}Sn. The initial rise up to ^{36}Kr can be attributed mainly to the gradual filling up to the $N_{II,III}$ level. We have seen that, even in solids, this level is filled up at ^{36}Kr. Therefore, beyond ^{36}Kr the increase of intensity is because of a change of the probability of the transition $K \rightarrow N_{II,III}$.

In Fig. 2.32, we show the change of the relative intensity of the quadrupole line $K\beta_5$ with Z. For $Z > 30$ the level $M_{IV,V}$ is an internal level; therefore the $K\beta_5$ has the usual low intensity of a quadrupole line. With decrease of Z the level $M_{IV,V}$ becomes external, that is, a level of valence electrons. In metals, it ceases to be a sharp atomic level and becomes a broad band that overlaps the neighbouring levels. The electrons of the overlapping levels are indistinguishable; they acquire common properties, and the quadrupole line become a

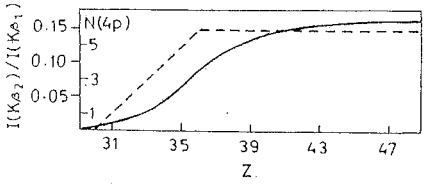

Fig. 2.31. Solid curve: the relative intensity of the $K\beta_2$ line. Dashed curve: the number of electrons $N(4p)$ at the level $4p$ $(N_{II,III})$ of free atoms

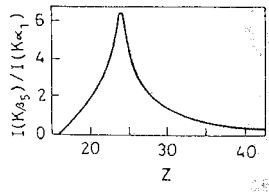

Fig. 2.32. Relative intensity of the line $K\beta_5$ versus Z

dipole line. This, of course, brings about a sharp increase of intensity. With a further decrease of Z, the level $M_{IV,V}$ becomes unoccupied, resulting in the decrease of intensity of the line $K\beta_5$ to zero at ^{16}S.

It is now evident that an inner-shell hole can be created either during collision of bombarding cathode electrons with the target atoms in an X-ray tube, or during absorption of X-ray photons of sufficient energy by the atoms of the absorbing material. In the former case, we get both continuous and characteristic spontaneous emission of X-rays; in the latter case, the induced-absorption process is followed by induced emission of characteristic lines alone (fluorescence radiation). No line in a series can have λ shorter than that of the series absorption edge. For example, some $L_{I,II}$ lines may have shorter λ than the L_{III} edge, but no L_{III} line is of shorter λ than the L_{III} edge. This has a bearing on induced emission. Thus Ba K lines can excite Ba L lines, but not the Ba K lines.

The spectrum with $0.5\,\text{Å} \lesssim \lambda \lesssim 2\,\text{Å}$ is called the *hard* X-ray region (can penetrate air or matter), and with $2\,\text{Å} \lesssim \lambda \lesssim 1000\,\text{Å}$ the *soft* X-ray region.

2.15 Comparison of Optical and X-Ray Spectra

Following are some of the essential features in which the optical spectra differ from the X-ray spectra:

1) Optical spectra states are truly stationary states of a neutral atom.	1) X-ray spectra states are quasi-stationary states of an inner-shell ionized atom.
2) The valence electron in the outermost part of the atom is excited to a higher unoccupied stationary state; the electron emits radiation when it goes back to the ground state, remaining inside the atom throught.	2) First, one inner hole is created to excite the atom. Then, an electron from an occupied state of higher quantum number fills this hole, to emit an X-ray line. We thus have a transfer of hole (or electron) between inner levels which are occupied in the normal atom.
3) The optical terms depend on both the initial and final states of the outer electron. Therefore, optical spectra change their characteristics as we go from one element to another and form compounds because of the changes of energies of the outer electron groups. The frequencies of lines, and also their ex-	3) The inner electron groups are similarly arranged for all except the very light elements. Therefore, the only spectral differences to be expected are those that result from the different stability of these inner-shell electrons for different values of the effective nuclear charge, as we go from one element to another

citation potentials, increase periodically with Z.

and form compounds. The frequencies of the lines, and also thier excitation potentials, increase steadily, not periodically, with increasing Z (Moseley law).

4) Generally, incomplete shells (less than half full) participate.

4) Complete shells participate, from which one electron is missing.

5) The optical terms may or may not be hydrogen-like.

5) In the frozen orbital approximation, the X-ray terms are given by the Dirac electron theory of hydrogen-like states applicable to a hole in the inner shell.

6) Optical atomic absorption spectra usually show line absorption due to the transition of the valence electron from the ground state to a higher vacant state. Both the initial and final states are stationary states and so have sharply defined energy values.

6) X-ray spectra usually show absorption edges due to the removal of an inner electron to an empty state above the Fermi level, because all of the other states below the Fermi level are full, by the Pauli exclusion principle.

2.16 Nomenclature of X-Ray Lines

The literature contains several systems of labelling energy levels and emission lines. The Bohr and Coster notation, Table 2.7, is widely accepted for energy levels. We have also used this notation.

For X-ray lines, the designations given by *Siegbahn* [2.90] (Fig. 2.15) are commonly used. Because there is no agreed system of names, except for the most prominent lines, it becomes necessary to state the transition in terms of the

Table 2.7. Various notations for the energy levels

Sommerfeld	K	L_{11}	L_{21}	L_{22}	M_{11}	M_{21}	M_{22}	M_{32}	M_{33}
Early papers	K	L_3	L_2	L_1	M_5	M_4	M_3	M_2	M_1
Mott and others	K	L_1	L_2	L_3	M_1	M_2	M_3	M_4	M_5
Some journals	K	L_1	L_2	L_3	M_1	M_2	M_3	M_4	M_5
Bohr and *Coster*	K	L_I	L_{II}	L_{III}	M_I	M_{II}	M_{III}	M_{IV}	M_V
Optical symbols	$1^2S_{1/2}$	$2^2S_{1/2}$	$2^2P_{1/2}$	$2^2P_{3/2}$	$3^2S_{1/2}$	$3^2P_{1/2}$	$3^2P_{3/2}$	$3^2D_{3/2}$	$3^2D_{5/2}$

initial and final levels involved. The general basis of Siegbahn's nomenclature is as follows. First the series is given the name K, L, M, . . . that corresponds to $n = 1, 2, 3, \ldots$ for the initial X-ray state (hole state). Then, the strongest unresolved line in the series is named α, the next strongest β, and so on. Under high resolution the α line is in general a doublet: the more-intense component is called α_1 and the weaker α_2. In the L series the β_1 line is next strongest. There are many weaker lines in the same wave-length region; these are named $\beta_2, \beta_3, \ldots, \beta_{15}$. A similar system is followed for the γ lines. The relative positions of the less-prominent lines vary from element to element. A nomenclature that seems logical for one element may appear arbitrary for an element of much different Z. In many cases, the lines took names in the order of their discovery, and often the names given by the discoverers have persisted.

In 1952 *Agarwal* [2.102] suggested that a systematic approach would be to name each line K, L, M, . . . corresponding to $n = 1, 2, 3, \ldots$ for the initial state, and $\alpha, \beta, \gamma, \ldots$ corresponding to $\Delta n = 1, 2, 3, \ldots$ for the difference of n from the initial to the final state. Superscripts (subscripts) 1, 2, 3 might be used for the initial (final) energy levels involved in the transition [2.103]. Thus, the $K\alpha_1$ $(K \rightarrow L_{III})$ line might be written as $K\alpha_3^1$, $K\alpha_2$ $(K \rightarrow L_{II})$ as $K\alpha_2^1$, $K\beta_1 (K \rightarrow M_{III})$ as $K\beta_3^1$, $L\alpha_1 (L_{III} \rightarrow M_V)$ as $L\alpha_5^3$, $L\beta_1 (L_{II} \rightarrow M_{IV})$ as $L\alpha_4^2$, $L\eta (L_{II} \rightarrow M_I)$ as $L\alpha_1^2$, $L\gamma_1$ $(L_{II} \rightarrow N_{IV})$ as $L\beta_4^2$, $L\gamma_8 (L_{II} \rightarrow O_I)$ as $L\gamma_1^2$, and so on. Obviously, an α line would be softer (of lower frequency) than a β line, and $L\alpha_2^1$ would be softer than $L\alpha_3^1$, etc. For electric-dipole (allowed) lines, the difference between the superscript and the subscript can be only 1 or 2, with following combinations forbidden:

Superscript	2	3	4	5 . . .
Subscript	3	2	5	4

These are the superscripts and subscripts that, along with the combinations differing by 0, 3, 4, . . . , etc., occur for the forbidden lines. Thus, $L\beta_{10}$ $(L_I \rightarrow M_{IV})$ is $L\alpha_4^1$, $L\beta_{17} (L_{II} \rightarrow M_{III})$ is $L\alpha_3^2$, Ls $(L_{III} \rightarrow M_{III})$ is $L\alpha_3^3$, etc.

This systematic nomenclature, if accepted, would introduce some order into the tables and diagrams of the emission lines in X-ray spectra. We give here the identifications of characteristic lines according to *Bearden* [2.104] and in this nomenclature (in parentheses):

K series	L series	
$KL_{II}\alpha_2(\alpha_2^1)$	$L_I M_{II}\beta_4(\alpha_2^1)$	$L_I O_{II,III}\gamma_4(\gamma_{2,3}^1)$
$KL_{III}\alpha_1(\alpha_3^1)$	$L_I M_{III}\beta_3(\alpha_3^1)$	$L_{II} M_I\eta(\alpha_1^2)$
$KM_{II}\beta_3(\beta_2^1)$	$L_I M_{IV}\beta_{10}(\alpha_4^1)$	$L_{II} M_{III}\beta_{17}(\alpha_3^2)$
$KM_{III}\beta_1(\beta_3^1)$	$L_I M_V\beta_9(\alpha_5^1)$	$L_{II} M_{IV}\beta_1(\alpha_4^2)$
$KN_{II,III}\beta_2(\gamma_{2,3}^1)$	$L_I N_{II}\gamma_2(\beta_2^1)$	$L_{II} N_I\gamma_5(\beta_1^2)$
$KN_{IV,V}\beta_4(\gamma_{4,5}^1)$	$L_I N_{III}\gamma_3(\beta_3^1)$	$L_{II} N_{IV}\gamma_1(\beta_4^2)$
		$L_{II} N_{VI}\nu(\beta_6^2)$

$L_{II}O_I\gamma_8(\gamma_1^2)$
$L_{II}O_{IV}\gamma_6(\gamma_4^2)$
$L_{III}M_Il(\alpha_1^3)$
$L_{III}M_{II}t(\alpha_2^3)$
$L_{III}M_{III}s(\alpha_3^3)$
$L_{III}M_{IV}\alpha_2(\alpha_4^3)$
$L_{III}M_V\alpha_1(\alpha_5^3)$

$L_{III}N_I\beta_6(\beta_1^3)$
$L_{III}N_{IV}\beta_{15}(\beta_4^3)$
$L_{III}N_V\beta_2(\beta_5^3)$
$L_{III}N_{VI,VII}u(\beta_{6,7}^3)$
$L_{III}O_I\beta_7(\gamma_1^3)$
$L_{III}O_{IV,V}\beta_5(\gamma_{4,5}^3)$

M series

$M_{III}N_V\gamma(\alpha_5^3)$
$M_{IV}N_{II}\zeta_2(\alpha_2^4)$
$M_{IV}N_{VI}\beta(\alpha_6^4)$
$M_VN_{III}\zeta_1(\alpha_3^5)$
$M_VN_{VI}\alpha_2(\alpha_6^5)$
$M_VN_{VII}\alpha_1(\alpha_7^5)$

3. Interaction of X-Rays with Matter

In optics, the term *dispersion* means the separation of electromagnetic waves into their component wavelengths. The first treatment in the X-ray region was given by Compton. He adapted the theory developed earlier for the optical region by *Lorentz* [3.1]. He assumed that the electrons in atoms can act like oscillators. Thus in the classical dispersion theory the atoms scatter X-rays as if they contain electric dipole oscillators of certain definite natural frequencies, which represent the atomic absorption frequencies.

3.1 Free, Damped Oscillator

Let a classical oscillator consist of an electron that oscillates along the x axis, about a central point, under a restoring force $F(x)$. Then $F(x) = m\ddot{x} = -m\omega_0^2 x$, where m is the electron mass and $\omega_0 = 2\pi\nu_0$ is the initial angular frequency of the oscillations. The general solution is

$$x = x_0 e^{i\omega_0 t}. \tag{3.1}$$

In (2.8), we used only the real part of this solution.

An oscillating electron is accelerated. Therefore, it emits radiation at a rate given by Larmor's formula (1.59),

$$-\frac{dU}{dt} = \frac{2e^2}{3c^3}\ddot{x}^2. \tag{3.2}$$

Because of this loss of energy of radiation, the amplitude of oscillations will gradually decrease, as if the electron were being retarded by a frictional force ϕ. We can find the fictitious force ϕ by equating the work done by it in unit time to the negative of the energy radiated in that time,

$$\phi\dot{x} = -\frac{2e^2}{3c^3}\ddot{x}^2.$$

Thus ϕ is equivalent to the radiation damping.

In this equation, $\dot{x}$ and $\ddot{x}$ are basically uncorrelated; consequently, there is no solution for ϕ that would hold for all times. We seek a solution that represents

an average over a long time interval t_1 to t_2,

$$\int_{t_1}^{t_2} \phi\dot{x}\,dt = -\frac{2e^2}{3c^3}\int_{t_1}^{t_2} \ddot{x}^2\,dt = -\frac{2e^2}{3c^3}\left((\dot{x}\ddot{x})_{t_1}^{t_2} - \int_{t_1}^{t_2} \dot{x}\dddot{x}\,dt\right).$$

The motion being periodic and choosing $\ddot{x} = 0$ at $t = t_1$ and $t = t_2$,

$$\int_{t_1}^{t_2}\left(\phi - \frac{2e^2}{3c^3}\dddot{x}\right)\dot{x}\,dt = 0.$$

This suggests that we can identify the damping force as

$$\phi = \frac{2e^2}{3c^3}\dddot{x}. \tag{3.3}$$

It is called *radiation damping* or the *Lorentz frictional force.*

The motion of the electron under the combined effect of the restoring force $F(x)$ and the Lorentz frictional force $\phi(\ddot{x})$ is given by Newton's law, $m\ddot{x} = F(x) + \phi(\ddot{x})$. Thus, for the free, damped, oscillations of an electron,

$$\ddot{x} - \alpha\dddot{x} + \omega_0^2 x = 0, \quad \alpha = 2e^2/3mc^3 = 6.2 \times 10^{-24}\,\text{s}. \tag{3.4}$$

This is the *Abraham–Lorentz equation* of motion. It includes, in some approximate and time-average way, the reactive effects of the emission of radiation.

3.2 Form and Width of Lines

As α is a small quantity in (3.4), we can make the approximation $\dddot{x} = -\omega_0^2\dot{x}$. Then (3.4) becomes

$$\ddot{x} + \gamma\dot{x} + \omega_0^2 x = 0, \quad \gamma = \alpha\omega_0^2 = \frac{2e^2\omega_0^2}{3mc^3} = \frac{8\pi^2 e^2}{3mc\lambda_0^2}. \tag{3.5}$$

For $\lambda_0 = 1\,\text{Å}$, $\omega_0 = 1.8 \times 10^{19}\,\text{s}^{-1}$ and $\gamma/\omega_0 = \alpha\omega_0 = 1.14 \times 10^{-4}$, that is, $\gamma/\omega_0 \ll 1$ for the X-ray region. For *small* γ, the solution of (3.5) is

$$x = (x_0 e^{-\gamma t/2})e^{i\omega_0 t} = x_0 e^{(i\omega_0 - \gamma/2)t}, \tag{3.6}$$

as can be verified by direct substitution. It has the desired form because the amplitude $x_0\exp(-\gamma t/2)$ is gradually (exponentially) damped as time passes.

For an accelerated charge, the field is given by (1.57).

$$E = \frac{e}{c^2 R}\ddot{x}\sin\Theta, \tag{3.7}$$

at the point P (Fig. 2.6). From (3.6), for small γ,

$$\ddot{x} = (i\omega_0 - \gamma/2)^2 x_0 e^{(i\omega_0 - \gamma/2)t} \simeq -\omega_0^2 x_0 e^{(i\omega_0 - \gamma/2)t}. \tag{3.8}$$

The electromagnetic field at the point P, at the time of observation t, is determined by the state of the oscillator R/c seconds earlier. So at the instant

$t - R/c$,

$$E = \frac{e}{c^2 R}\sin\Theta\left[-\omega_0^2 e^{(i\omega_0 - \gamma/2)(t - R/c)}\right] = E_0 e^{-\gamma t/2} e^{i\omega_0(t - R/c)}, \tag{3.9}$$

where

$$E_0 = -\frac{e}{c^2 R}\sin\Theta\,\omega_0^2 x_0 e^{\gamma R/2c}, \tag{3.10}$$

is a constant for a fixed point P.

The radiation emitted by the oscillator is not monochromatic, because of the radiation damping. The *linewidth* can be obtained by making a Fourier analysis of the field,

$$E(t) = \int_0^\infty E_\omega e^{i\omega t}\,d\omega = E_0 e^{-\gamma t/2} e^{i\omega_0(t - R/c)}. \tag{3.11}$$

If we assume $E(t) = 0$ for $-\infty < t < 0$, then

$$\begin{aligned} E_\omega &= \frac{1}{\pi}\int_{-\infty}^{+\infty}(E(t)e^{-i\omega t}\,dt = \frac{1}{\pi}\int_0^\infty (E(t)e^{-i\omega t}\,dt \\ &= \frac{E_0}{\pi}e^{-i\omega_0 R/c}\int_0^\infty e^{-[i(\omega - \omega_0) + \gamma/2]t}\,dt \\ &= \frac{E_0}{\pi}e^{-i\omega_0 R/c}\frac{1}{i(\omega - \omega_0) + \gamma/2} \end{aligned} \tag{3.12}$$

and

$$|E_\omega| = \frac{E_0}{\pi}\left[\frac{1}{(\omega - \omega_0)^2 + \gamma^2/4}\right]^{1/2}. \tag{3.13}$$

Thus

$$E(t) = \frac{E_0}{\pi}e^{-i\omega_0 R/c}\int_0^\infty \frac{e^{i\omega t}}{i(\omega - \omega_0) + \gamma/2}\,d\omega. \tag{3.14}$$

This shows that the field of a classical oscillator can be represented in the form of a continuous set of simple harmonic oscillators of the type (3.12).

The spectral intensity (a real quantity) is given by

$$I_\omega = \frac{c}{4\pi}|E_\omega|^2 = \frac{c}{4\pi^3}\frac{E_0^2}{(\omega - \omega_0)^2 + \gamma^2/4}. \tag{3.15}$$

This expression has a maximum at $\omega = \omega_0$,

$$(I_\omega)_{\max} = I_{\omega_0} = \frac{cE_0^2}{\pi^3\gamma^2}, \quad I_\omega = \frac{I_{\omega_0}}{\left(\dfrac{\omega - \omega_0}{\gamma/2}\right)^2 + 1}. \tag{3.16}$$

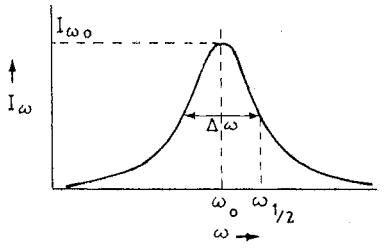

Fig. 3.1. The dispersed shape of a spectral line at ω_0

This distribution of intensity as a function of frequency is called the *dispersion formula*; it determines the shape of the spectral line (Fig. 3.1). It is in agreement with experiments in which symmetrical lines are observed [3.2].

The value of frequency at half intensity, $\omega_{1/2}$, is determined by

$$I_{\omega_{1/2}} = \frac{I_{\omega_0}}{\left(\frac{\omega_{1/2}-\omega_0}{\gamma/2}\right)^2 + 1} = \tfrac{1}{2} I_{\omega_0}. \tag{3.17}$$

This gives

$$|\omega_{1/2} - \omega_0| = \tfrac{1}{2}\gamma. \tag{3.18}$$

Therefore, the *full width at half maximum* (FWHM) is

$$\Delta\omega = \gamma = \frac{8\pi^2 e^2}{3mc\lambda_0^2}, \tag{3.19}$$

$$\Delta\lambda = \frac{\lambda_0^2}{2\pi c}|\Delta\omega| = \frac{4\pi e^2}{3mc^2} = \frac{4\pi}{3} r_e = 0.118\,\text{XU}. \tag{3.20}$$

The factor $r_e = e^2/mc^2 = 2.818 \times 10^{-13}$ cm is the classical electron radius (calculated from $e^2/r = mc^2$). Obviously, $\Delta\lambda$ is a universal constant, independent of the frequency of the oscillator and of the wavelength λ_0 corresponding to the intensity maximum of the line. This conclusion is not supported by experiments, because radiation damping is not the only source of the width of a spectral line. The full width of the $K\alpha_1$ line at half intensity varies from 1.50 XU for ^{20}Ca ($\lambda_0 = 3351$ XU) to 0.16 XU for ^{74}W ($\lambda_0 = 208.6$ XU). For Mo $K\alpha_1$, *Gokhale* [3.3] gives $\Delta\lambda = 0.26$ mÅ. *Thomsen* [3.2] finds FWHM to be 0.255×10^{-3} Å (or 6.28 eV) for Mo$K\alpha_1$ and 0.226×10^{-3} Å (or 8.97 eV) for Ag$K\alpha_1$.

If I_0 is the intensity at $t = 0$, then from (3.9),

$$I(t) = \frac{c}{4\pi}|E(t)|^2 = I_0 e^{-\gamma t}. \tag{3.21}$$

We define the effective *lifetime* τ of the oscillator as the time at which the intensity is decreased by the factor $1/e$. Thus,

$$I(\tau) = I_0 e^{-\gamma\tau} = I_0 \exp(-1), \tag{3.22}$$

$$\gamma\tau = 1, \quad \gamma = \Delta\omega = \frac{1}{\tau}, \quad \Delta\nu = \frac{\Delta\omega}{2\pi} = \frac{1}{2\pi\tau}. \tag{3.23}$$

If τ is short, the oscillations are rapidly damped, the motion is no longer simple harmonic, and the width is large. This is in qualitative agreement with observations.

The relation $\Delta\omega\tau = 1$ is equivalent to the relation

$$\Delta E \Delta t \sim \hbar, \tag{3.24}$$

where $\Delta E = \hbar\Delta\omega$. Equation (3.24) is the quantum mechanical relation between the lifetime and the energy width of a state.

3.3 Forced, Damped Oscillator

We assume that the velocity of the electron is non-relativistic. Therefore, the effect of the magnetic vector in the external incoming radiation can be neglected.

The equation of motion of a bound electron that belongs to the q shell and is in an external (polarized) plane wave field, is

$$\ddot{x} + \gamma\dot{x} + \omega_q^2 x = -\frac{e}{m} E_0 e^{i\omega(t-y/c)}. \tag{3.25}$$

Here ω_q is a natural frequency of the electron and q refers to K, L, M, etc. The electromagnetic wave

$$E(y, t) = E_0 e^{i\omega(t-y/c)}$$

propagates along the y axis and is polarized in the xy plane. The negative sign means that the force exerted on the electron of charge $-e$ is $-eE$. The electric vector of this wave is parallel to the x axis. At $y = 0$, $t = 0$, the field strength is E_0; at $y = 0$, $t = t$, it is $E_0 \exp(i\omega t)$; at $y = y$, $t = t$, E is equal to a value that the electric field had y/c second earlier, at the point $y = 0$.

We seek a solution of (3.25) in the form of oscillations with the frequency and phase of the inducing field,

$$x = x_0 e^{i\omega(t-y/c)}. \tag{3.26}$$

Substitution of this in (3.25) gives for a forced, damped, oscillator

$$x(t) = -\frac{e}{m} E_0 \frac{1}{(\omega_q^2 - \omega^2) + i\gamma_\omega} e^{i\omega(t-y/c)}, \quad \gamma_\omega = \alpha\omega^2, \tag{3.27}$$

where $\gamma_\omega = (2e^2/3mc^3)\omega^2$ is the radiation damping term. The axis of the dipole oscillator of moment $D(t) = -ex(t)$ is parallel to the direction of the incident electric vector. The oscillating dipole is the source of radiation of the same frequency. From (1.60), the electric vector at time t in the equatorial plane of the dipole is ω^2/rc^2 times the dipole moment D at the time $t - r/c$. Therefore, the

amplitude A of the scattered wave at unit distance in the equatorial plane is

$$A = \frac{e^2}{mc^2}\frac{\omega^2 E_0}{\omega_q^2 - \omega^2 + i\gamma\omega}. \tag{3.28}$$

The *scattering factor f of the dipole* is defined by

$$f = \frac{\text{amplitude scattered by oscillator}}{\text{amplitude scattered by free electron}}. \tag{3.29}$$

The scattering by a free electron is given by (3.28) with $\omega_q = 0$ and $\gamma = 0$, because in the absence of restoring force the natural frequency is also zero. Thus, for the free electron $A' = -(e^2/mc^2)E_0$ at unit distance in the equatorial plane. The negative sign implies that the wave scattered by the free electron in the forward direction (scattering angle zero) has a phase *opposite* to that of the primary wave. Then

$$f = \frac{\omega^2}{\omega^2 - \omega_q^2 - i\gamma\omega}. \tag{3.30}$$

With this definition when $f > 0$ the scattered wave is *opposed* in phase to the primary wave. If $\omega \gg \omega_q$, then $f \to 1$ as γ is small. If $\omega \ll \omega_q$, then $f < 0$ and the dipole scatters a wave in phase with the primary wave. However, when ω is nearly equal to ω_q, γ cannot be neglected and f becomes *complex*,

$$f = f' + if''$$

$$f' = \frac{\omega^2(\omega^2 - \omega_q^2)}{(\omega^2 - \omega_q^2)^2 + \gamma^2\omega^2}, \quad f'' = \frac{\gamma\omega^3}{(\omega^2 - \omega_q^2)^2 + \gamma^2\omega^2}. \tag{3.31}$$

3.4 Complex Dielectric Constant

Because x represents the displacement of the electron under the action of the electric field, it is connected with the *polarization* of the medium (Fig. 3.2). If n_q is the number of q-type electrons per unit volume, the volumetric polarization of the medium is given by $P_q = -n_q e x$. The dielectric permeability of a medium ε_q is

$$\varepsilon_q = 1 + 4\pi\frac{P_q}{E}$$

$$= 1 + \frac{4\pi n_q e^2}{m[\omega_q^2 - \omega^2 + i\gamma_\omega\omega]}. \tag{3.32}$$

Separating the real and imaginary parts, the complex dielectric constant is

$$\varepsilon_q = 1 - 2\delta_q - i2\beta_q, \tag{3.33}$$

$$\delta_q = -\frac{2\pi n_q e^2 m(\omega_q^2 - \omega^2)}{m^2(\omega_q^2 - \omega^2)^2 + 4e^4\omega^6/9c^6} = \frac{2\pi n_q e^2}{m\omega^2} f', \tag{3.34}$$

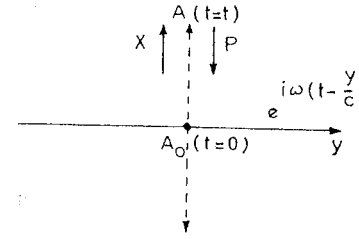

Fig. 3.2. The electromagnetic wave moves along the y axis with the electric vector parallel to the x axis. It displaces the electron initially ($t = 0$) at A_0 to A by an amount x

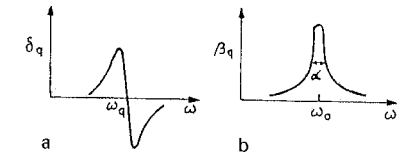

Fig. 3.3a, b. The dependence of **a** δ_q on ω, and of **b** β_q on ω

$$\beta_q = \frac{4\pi n_q e^4 \omega^3}{3c^3[m^2(\omega_q^2 - \omega^2)^2 + 4e^4\omega^6/9c^6]} = \frac{2\pi n_q e^2}{m\omega^2} f''. \tag{3.35}$$

In Fig. 3.3 we have plotted δ_q and β_q, as a function of the frequency ω of the incident radiation. We find δ_q is zero at $\omega = \omega_q$, and β_q has a maximum at this frequency (resonance absorption). Also, δ_q is strongly frequency dependent near this frequency and undergoes a change in sign. This is the phenomenon of *anomalous dispersion*.

In addition to the primary electromagnetic wave, we have the electromagnetic wave radiated by q-type electrons that are under forced oscillations. The resultant wave is propagated through the medium with a phase velocity v given by the well-known relation $v = c/\varepsilon^{1/2}$. Because of ε, it is a complex quantity.

It is useful to define the so-called complex-wave slowness, S_q, by

$$S_q = v_q^{-1} = \frac{1}{c}\varepsilon^{1/2} = \frac{1}{c}(1 - 2\delta_q - i2\beta_q)^{1/2}$$

$$\simeq \frac{1}{c}(1 - \delta_q - i\beta_q) \equiv S_r - iS_i, \tag{3.36}$$

where δ_q and β_q are small quantities ($\sim 10^{-6}$). For the wave in the medium,

$$E_q(y, t) = E_{0,q}e^{i\omega(t - y/v_q)} = (E_{0,q}e^{-\omega S_i y})e^{i\omega(t - S_r y)}. \tag{3.37}$$

Thus, the amplitude is exponentially damped as y in the medium increases. If $|E_q(y)|$ is the amplitude at a depth y in the medium,

$$|E_q(y)| = E_{0,q}e^{-\omega S_i y}, \tag{3.38}$$

the complex nature of the dielectric constant, and hence of the phase velocity, leads to attenuation (or absorption) of the wave. The intensity is

$$I_q(y) = I_{0,q}e^{-(2\omega S_i)y} = I_{0,q}e^{-(\tau_q)y}, \tag{3.39}$$

where

$$(\tau_q) = 2\omega S_i = 2\omega v_{i,q}^{-1} = \frac{2\omega}{c}\beta_q = \frac{4\pi}{\lambda}\beta_q \tag{3.40}$$

is the *partial linear absorption coefficient* for the q-type electrons.

We have shown that the real part of the complex dielectric constant is related to the phase velocity of waves in the medium, and the imaginary part, β_q, with the absorption. This is a general result. The amount of energy abstracted from the incident wave is converted to energy of the bound-electron system.

3.5 Refractive Index

The *refractive index* is defined as the ratio of the phase velocities in vacuum and in the medium, c/v_q. Because v_q is complex, we get a complex refractive index, μ_c. The *partial refractive index* for the q-type electrons is

$$\mu_{c,q} = \mu_q - i\mu_{i,q} = \varepsilon_q^{1/2} = cv_q^{-1} = 1 - \delta_q - i\beta_q, \tag{3.41}$$

where we have used (3.36), and $\mu_q = 1 - \delta_q$ is the real part of $\mu_{c,q}$. The *unit decrement* δ_q gives the departure of μ_q from 1.

For X-ray frequencies, from (3.34),

$$\delta_q = \frac{2\pi n_q e^2 m(\omega^2 - \omega_q^2)}{m^2(\omega^2 - \omega_q^2)^2 + 4e^4\omega^6/9c^6} \simeq \frac{2\pi n_q e^2}{m}\frac{1}{\omega^2 - \omega_q^2}, \tag{3.42}$$

where we have neglected the small radiation damping term $(4e^4/9c^6)\omega^6$. This is easily justified. For quartz (SiO_2) the largest value of ω_q is obtained for the K electrons of silicon (^{14}Si),

$$\omega_{(Si)K} = 2\pi c/\lambda_{(Si)K} = 2.8 \times 10^{18}\,s^{-1},$$

where $\lambda_{(Si)K} = 6.73$ Å. For incident X-rays of wavelength 1 Å,

$$\omega = 2\pi c/\lambda = 18.9 \times 10^{18}\,s^{-1} > \omega_{(Si)K},$$

$$(\omega^2 - \omega_{(Si)K}^2)^2 = 1.2 \times 10^{77},$$

$$(4e^4/9c^6)\omega^6 m^{-2} = \alpha^2\omega^6 = 1.8 \times 10^{69} \ll (\omega^2 - \omega_{(Si)K}^2)^2.$$

Thus, the approximation is good for all the electrons of ^{14}Si.

If the medium contains electrons of various natural frequencies ω_q,

$$\mu_c = \mu - i\mu_i = \sum_q \mu_{c,q} = 1 - \sum_q(\delta_q + i\beta_q) = 1 - \delta - i\beta, \tag{3.43}$$

where $\delta = \sum_q \delta_q$, $\beta = \sum_q \beta_q$. Now δ gives the unit decrement of the refractive index μ.

For the X-ray frequencies ($\omega \gg \omega_q$),

$$\delta = \sum_q \delta_q = \frac{2\pi e^2}{m}\sum_q \frac{n_q}{\omega^2 - \omega_q^2} \simeq \frac{2\pi e^2}{m\omega^2}\sum_q n_q = \frac{e^2 n\lambda^2}{2\pi mc^2}, \tag{3.44}$$

where n is the total number of electrons per unit volume of medium. For X-rays being dispersed by crystals like quartz, calcite, etc., in a spectrograph, the unit decrement δ is a small positive quantity, and

$$\mu = 1 - \delta \lesssim 1 \quad \text{(X-rays)}. \tag{3.45}$$

(For optical frequencies, in a glass prism, $\omega < \omega_q$, so that $\mu > 1$). It follows that *for X-rays the medium of a quartz crystal is less dense than a vacuum.*

If $N_A = 6.0225 \times 10^{23}$ is Avogadro's number, A the atomic weight, Z the atomic number and ρ the density, then (3.44) gives with $n = ZN_A\rho/A$

$$\frac{\delta}{\lambda^2} = \frac{e^2 N_A}{2\pi mc^2}\frac{Z\rho}{A} = 2.7 \times 10^{10}\frac{Z\rho}{A} = \text{const.}, \quad (\lambda \ll \lambda_K). \tag{3.46}$$

For ^{13}Al ($A = 27$, $\rho = 2.7$), $\delta = 1.74 \times 10^{-6}$ for the Mo $K\alpha$ (0.708 Å) radiation. The experimental value is 1.68×10^{-6}. Therefore, the Lorentz theory is satisfactory for $\lambda \ll \lambda_K$).

Larsson [3.4] has compared his experiments on calcite ($CaCO_3$) with (3.42),

$$\delta = \frac{2\pi e^2}{m}\sum_q \frac{n_q}{\omega^2 - \omega_q^2} = \frac{e^2}{2\pi mc^2}\lambda^2 \sum_q \frac{n_q\lambda_q^2}{\lambda_q^2 - \lambda^2}. \tag{3.47}$$

For a compound, $n_q = (n_A\rho/M)z_q$, where z_q is the number of electrons of the q-type and M is the molecular weight. If λ_K is the K-edge wavelength of Ca, we can separate out the term for the z_K electrons in the K level of Ca and write

$$\frac{\delta}{\lambda^2} = \frac{e^2 N_A}{2\pi mc^2}\frac{\rho}{M}\left(\frac{z_K\lambda_K^2}{\lambda_K^2 - \lambda^2} + \sum_{q \neq K}\frac{z_q\lambda_q^2}{\lambda_q^2 - \lambda^2}\right).$$

Near the absorption edge, $\lambda \approx \lambda_K$, it is the first term in the parentheses that will cause departure from the value given by (3.46) for the case $\lambda \ll \lambda_K$. Therefore, for the remaining electrons $\lambda < \lambda_q$, and

$$\sum_{q \neq K}\frac{z_q\lambda_q^2}{\lambda_q^2 - \lambda^2} = \frac{1}{1 - (\lambda/\lambda_q)^2}\sum_{q \neq K} z_q \simeq \sum_{q \neq K} z_q = Z_M - z_K,$$

$$\frac{\delta}{\lambda^2} = \frac{e^2 N_A}{2\pi mc^2}\frac{\rho}{M}\left[\frac{z_K\lambda_K^2}{\lambda_K^2 - \lambda^2} + (Z_M - z_K)\right]$$

$$= 2.68 \times 10^{-6}\frac{\rho}{M}\left[\frac{2\lambda_K^2}{\lambda_K^2 - \lambda^2} + (Z_M - 2)\right]. \tag{3.48}$$

For $CaCO_3$, $\rho = 2.71$ gcm^{-3}, $M = 100.07$, $Z_M = 50$, $z_K = 2$, $\lambda_K = 3.06$ Å, so that

$$\frac{\delta}{\lambda^2} = 0.0732 \times 10^{-6}\left(\frac{18.78}{9.390 - \lambda^2} + 48\right).$$

Experimental points for known emission lines between 1.5 Å and 3.7 Å, show that the Lorentz theory gives correct results for $\lambda \ll \lambda_K$. Near the absorption edge, $\lambda \approx \lambda_K$, the agreement breaks down. The reason is that we have neglected

the damping factor, which becomes important in this region. Also, the Lorentz theory does not include the effect of absorption near the edge. For $\lambda \gg \lambda_K$ the effects of other absorption edges appear and spoil the agreement with this simple theory. Near the absorption edge δ/λ^2 is not constant and anomalous dispersion occurs (δ/λ^2 varies with λ).

3.6 Correction of the Bragg Equation

Bragg [3.5] suggested that in the diffraction of X-rays by the atoms of a crystal lattice there occurs, *as it were*, specular (mirror-like) reflection of the X-rays from the internal atomic planes. Each plane reflects only a very small fraction of the radiation, as with a very lightly silvered mirror, such that the angle of incidence is equal to the angle of reflection.

Consider a set of parallel lattice planes spaced equal distances d apart (Fig. 3.4). The radiation of wavelength λ is incident at a glancing angle θ. The path difference for rays reflected from the adjacent planes is $2d\sin\theta$. It is the extra distance travelled *inside* the crystal. The radiation reflected from successive planes will arrive at $PP'P''$ in phase, to give constructive interference (strong reflection), whenever the path difference is an integral multiple of wavelength, $n\lambda$ ($n = 0, 1, 2, 3, \ldots$). Thus the condition for constructive reflection of the incident radiation is simply

$$2d\sin\theta = n\lambda \quad (n = \text{order of reflection}). \tag{3.49}$$

This is the *Bragg law*, and θ is the *Bragg angle*. Bragg reflection can occur only for $\lambda \leqq 2d$. For the visible light $\lambda \gg 2d$.

We should correct (3.49) for the effect of refraction of X-rays when they enter the crystal ($\mu \lesssim 1$) (Fig. 3.5). This will alter the required path difference. Inside the crystal the wavelength λ becomes λ' and the corresponding Bragg angle is θ'. The refractive index can be defined, as in optics, by

$$\mu = 1 - \delta = \lambda/\lambda' = \cos\theta/\cos\theta'. \tag{3.50}$$

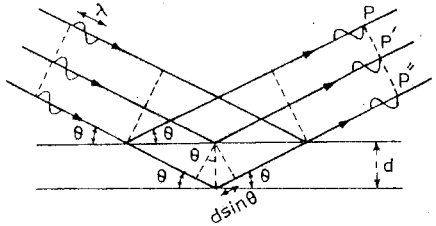

Fig. 3.4. Derivation of the Bragg equation

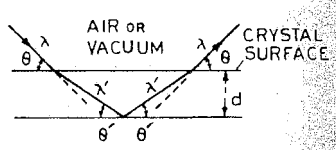

Fig. 3.5. Construction for the modified Bragg law. Rays bend away from the normal because $\mu < 1$

Within the crystal the Bragg law is

$$n\lambda' = 2d\sin\theta'. \tag{3.51}$$

From (3.50, 51),

$$\mu = \frac{\lambda}{\lambda'} = \frac{\lambda}{2(d/n)\sin\theta'} = \frac{n\lambda}{2d\left(1 - \dfrac{\cos^2\theta}{\mu^2}\right)^{1/2}}. \tag{3.52}$$

Rearrangement gives

$$n\lambda = 2d\sin\theta\left(1 + \frac{\mu^2 - 1}{\sin^2\theta}\right)^{1/2}. \tag{3.53}$$

Because μ is nearly one, we can write $\mu^2 - 1 = (\mu+1)(\mu-1) \simeq 2(-\delta)$ and

$$n\lambda \simeq 2d\sin\theta\left(1 - \frac{2\delta}{\sin^2\theta}\right)^{1/2} = 2d\sin\theta\left(1 - \frac{\delta}{\sin^2\theta} + \ldots\right)$$

$$\simeq 2d\sin\theta\left(1 - \frac{\delta}{\sin^2\theta}\right), \tag{3.54}$$

to the first power in the small quantity δ. This is the *modified Bragg law*. It is sufficient if absorption inside the crystal is negligible [3.6].

We can write (3.54) in terms of a fictitious angle θ_B as

$$n\lambda = 2d\sin\theta_B, \quad \mathrm{Sin}\,\theta_B = \sin\theta\left(1 - \frac{\delta}{\sin^2\theta}\right) = \sin\theta - \frac{\delta}{\sin\theta}. \tag{3.55}$$

Then $\sin\theta - \sin\theta_B = \Delta(\sin\theta) = \cos\theta(\Delta\theta)$, and

$$\Delta\theta = \theta - \theta_B = \frac{\sin\theta - \sin\theta_B}{\cos\theta} = \frac{\delta}{\sin\theta\cos\theta} = \frac{2\delta}{\sin 2\theta} > 0,$$

$$\Delta\theta \approx \delta/\theta \sim 10^{-6}/\theta \quad (\text{for small } \theta). \tag{3.56}$$

Thus, a significant deviation from the Bragg law occurs only for small θ.

No modification of the Bragg equation is needed if the symmetrical reflection occurs from the planes that are perpendicular to the surface of a thin crystal

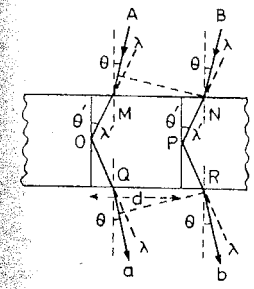

Fig. 3.6. Symmetrical reflection from planes perpendicular to the crystal surface (Laue case)

(like mica or quartz sheet). The path difference between two parallel rays A and B arises entirely from the distances travelled *outside* the crystal, and is equal to $2MN\sin\theta = 2d\sin\theta$ as shown in Fig. 3.6. Therefore, the condition for constructive interference is $n\lambda = 2d\sin\theta$. This is just the usual Bragg equation. It is a symmetrical reflection in the Laue geometry.

3.7 Measurement of Refractive Index

3.7.1 The Method of Critical Angle of Reflection

The real refractive index is given by (3.50) where the angles θ and θ' are shown in Fig. 3.7a. For X-rays, $0 < \delta \ll 1$; therefore,

$$\Delta\theta = \theta - \theta' > 0,$$

$$\cos\theta' = (1-\delta)^{-1}\cos\theta \simeq (1+\delta)\cos\theta,$$

$$\cos\theta - \cos\theta' \equiv \Delta(\cos\theta) \equiv -\sin\theta\,\Delta\theta = -\delta\cos\theta,$$

$$\Delta\theta = \delta\cot\theta. \tag{3.57}$$

Obviously, the angle of deviation $\Delta\theta = 0$ for $\theta = \pi/2$. As θ decreases, $\Delta\theta$ increases and is maximum at $\theta' = 0$ (Fig. 3.7b). The angle θ for this value of θ' is the minimum (*critical*) angle, θ_c, at which the X-ray beam can enter a medium through a surface of separation. From (3.50),

$$\mu = 1 - \delta = \cos\theta_c = 1 - \frac{1}{2!}\theta_c^2 + \frac{1}{4!}\theta_c^4 - \ldots, \tag{3.58}$$

and for small values of θ_c,

$$\theta_c = (2\delta)^{1/2}. \tag{3.59}$$

For a given substance, δ/λ^2 is nearly constant. Therefore, we have $\theta_c \propto \lambda$. From the known values of δ we can compute θ_c, see Table 3.1, or we can reverse the procedure.

For glancing angles $\theta < (2\delta)^{1/2}$, none of the rays are transmitted; that is, *all* of the rays incident at $\theta < \theta_c$ are reflected at the surface (*total reflection*) (Fig. 3.7c).

Compton [3.7] and *Smith* [3.8] have used (3.59) to measure δ. It is difficult to measure accurately the small angle θ_{min}.

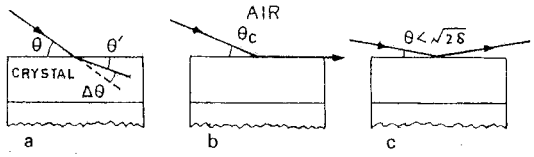

Fig. 3.7. **a** $\theta > (2\delta)^{\frac{1}{2}}$; **b** $\theta_c = (2\delta)^{\frac{1}{2}}$; **c** $\theta < (2\delta)^{1/2}$

Table 3.1. Some values of the critical angle θ_c

Substance	λ[Å]	$\delta \times 10^6$	θ_c
Glass	0.7078	1.64	6′10″
Calcite	1.537	8.80	14′25″
Quartz	10.0	356	91′40″

3.7.2 The Method of Symmetrical Reflection

For a given emission line of wavelength λ, measured in two different *orders of reflection* n_1 and n_2, we have from the modified Bragg law (3.54)

$$\frac{\lambda}{2d} = \frac{1}{n_1}\left(\sin\theta_1 - \frac{\delta}{\sin\theta_1}\right) = \frac{1}{n_2}\left(\sin\theta_2 - \frac{\delta}{\sin\theta_2}\right),$$

or

$$\delta = \frac{n_1^{-1}\sin\theta_1 - n_2^{-1}\sin\theta_2}{(n_1\sin\theta_1)^{-1} - (n_2\sin\theta_2)^{-1}}. \tag{3.60}$$

Stenström [3.9] measured δ from this equation by measuring θ at various n. It is not a very accurate method, because the deviations from the Bragg angle are very small in symmetrical reflections.

3.7.3 The Method of Unsymmetrical Reflection

The deviation is enhanced in the unsymmetrical reflection. For most glasses $\delta \approx 2\times10^{-6}$, so that $\theta_{min} = (\Delta\theta)_{max} = 2\times10^{-3}$ rad $\approx 7'$. At $\theta = 0.1$ rad $= 5.73°$ we get $\Delta\theta = \delta\cot\theta = 2\times10^{-5}$ rad $\approx 4''$. Thus, a decrease from $5.73°$ to $7'$ enhances the angle of deviation by a factor of 100. At $\theta = 45°$, we have $\Delta\theta = \delta = 2\times10^{-6}$ rad $\approx 0.4''$.

Let a portion of the crystal be ground to form a surface that makes an angle α with the reflecting atomic planes (Fig. 3.8). The ray S is reflected in a

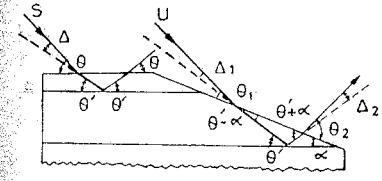

Fig. 3.8. Symmetrical, S, and unsymmetrical, U, reflections from a crystal wedge

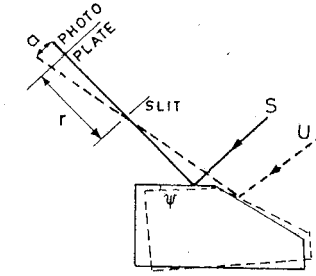

Fig. 3.9. Determination of δ by the method of rotation of the crystal wedge

symmetrical way and the ray U in the unsymmetrical way. The glancing angle for U is much smaller, and so the deviation caused by refraction is much larger than for S.

The crystal is mounted in a spectrometer and the spectral lines are recorded for the two cases S and U. From (3.50) and Fig. 3.8,

$$\mu = 1-\delta = \frac{\cos\theta}{\cos\theta'} = \frac{\cos\theta_1}{\cos(\theta'-\alpha)} = \frac{\cos\theta_2}{\cos(\theta'+\alpha)}, \tag{3.61}$$

$$\theta = \theta' + \Delta, \quad \theta_1 = \theta' - \alpha + \Delta_1, \quad \theta_2 = \theta' + \alpha + \Delta_2. \tag{3.62}$$

Because Δ and Δ_2 are small,

$$1-\delta = \frac{\cos\theta'\cos\Delta - \sin\theta'\sin\Delta}{\cos\theta'} \simeq 1 - \tan\theta'\sin\Delta,$$

$$\sin\Delta = \delta\cot\theta' \approx \delta\cot\theta. \tag{3.63}$$

Similarly,

$$\sin\Delta_2 \simeq \delta\cot(\theta'+\alpha) \approx \delta\cot(\theta+\alpha). \tag{3.64}$$

Δ_1 is also a small quantity but greater than Δ and Δ_2. Therefore, in a slightly better approximation,

$$1-\delta = \frac{\cos(\theta'-\alpha+\Delta_1)}{\cos(\theta'-\alpha)} = \cos\Delta_1 - \tan(\theta'-\alpha)\sin\Delta_1$$

$$= \left(1 - \frac{1}{2!}\Delta_1^2 + \cdots\right) - \tan(\theta'-\alpha)\sin\Delta_1,$$

$$\delta \simeq \tfrac{1}{2}\Delta_1^2 + \tan(\theta-\alpha)\sin\Delta_1. \tag{3.65}$$

From (3.62)

$$\Delta_1 = \theta_1 + \theta_2 - 2\theta + 2\Delta - \Delta_2. \tag{3.66}$$

We can measure θ, θ_1 and θ_2. From (3.66), we obtain $\Delta_1 \approx \theta_1 + \theta_2 - 2\theta$. This is put in (3.65) to give an approximate value for δ. We can now determine Δ and Δ_2 from (3.63, 64), and then a better value for Δ_1 from (3.66). Thus, δ can be found from (3.65) by successive approximations.

Another way of making the measurements is shown in Fig. 3.9. The crystal wedge is placed on the cross table of a spectrometer and a particular line is recorded through the symmetrical reflection, S. The crystal is now rotated by a small angle ψ and the same line is recorded through an unsymmetrical reflection, U. The angular distance between the two lines is a/r (Fig. 3.9). Because of the refraction effect, this angle will be less than ψ,

$$\psi - \frac{a}{r} = \varepsilon > 0.$$

From Fig. 3.8,

$$\varepsilon = \Delta_1 - \Delta = \Delta_1 - (\theta - \theta'). \tag{3.67}$$

From (3.61, 67),

$$1-\delta = \frac{\cos(\theta'-\alpha+\Delta_1)}{\cos(\theta'-\alpha)} = \frac{\cos(\theta+\varepsilon-\alpha)}{\cos(\theta'-\alpha)} = \frac{\cos\theta}{\cos\theta'}. \tag{3.68}$$

These relations give

$$\tan\theta' = \frac{\cos(\theta+\varepsilon-\alpha)}{\sin\alpha\cos\theta} - \cot\alpha, \quad \delta = 1 - \frac{\cos(\theta+\varepsilon-\alpha)}{\cos(\theta'-\alpha)}. \tag{3.69}$$

We can measure θ, α, and ε. Thus δ can be calculated from (3.69).

The methods based on unsymmetrical reflections have been used to find δ by *Hatley* and *Davis* [3.10, 11], and *Davis* and *Nardoff* [3.12, 13]. In these experiments, α was chosen close to θ' so that θ_1 is small and the deviation Δ_1 is large.

3.7.4 The Method of Refraction in a Prism

A narrow X-ray beam falls on the prism at a point A close to its edge (Fig. 3.10). This reduces the absorption of X-rays in the crystal. The reflected ray is AB and the refracted ray is AC. With the prism removed, the direct ray is recorded at D. The three rays recorded at B, C and D provide enough data for the determination of δ.

For large deviation Δ^θ, the angle θ is chosen to be small and close to the critical angle. Then the refracted ray emerges from the prism base at almost a right angle and its deviation at this point can be neglected. With $\theta = \theta' + \Delta^\theta$,

$$\delta = 1 - \frac{\cos\theta}{\cos\theta'} = \frac{\cos(\theta-\Delta\theta)-\cos\theta}{\cos\theta'} = \frac{2\sin(\theta-\Delta\theta/2)\sin\Delta\theta/2}{\cos\theta'}$$
$$\simeq (\theta - \Delta\theta/2)\Delta\theta.$$

From the experiment, we can measure $2\theta = BD/AD$ and $\Delta\theta = DC/AD$.

This method has been used by *Larsson* et al. [3.14]. *Davis* and *Slack* [3.15, 16] placed the prism between two calcite crystals in the parallel position of a double-crystal spectrometer.

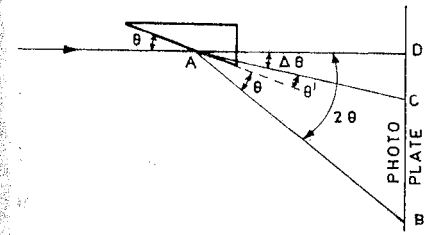

Fig. 3.10. Refraction in a prism

3.8 Absorption of X-Rays and Dispersion Theory

We can calculate the amount of energy abstracted from the incident X-rays and converted to energy of the bound electrons in an atom, which form a system of oscillators.

3.8.1 Absorption by an Undamped Oscillator

In the first approximation, we neglect the damping factor. Under the influence of the electric field of the incident X-rays, the electron in an atom is accelerated from rest to

$$\ddot{x} = -\frac{e}{m}E, \quad E = E_0 \sin\frac{2\pi}{T}t,$$

where T is the time period. If we average over one-half the period,

$$\langle \ddot{x} \rangle = -\frac{e}{m}\langle E \rangle. \tag{3.70}$$

Assume the acceleration to be uniform. Then the path s travelled by the electron in time $T/2$ is

$$s = \frac{1}{2}\langle \ddot{x} \rangle \left(\frac{1}{2}T\right)^2 = -\frac{1}{8}\frac{e}{m}\frac{\langle E \rangle}{\nu^2} = -\frac{1}{8}\frac{e\langle E \rangle}{mc^2}\lambda^2. \tag{3.71}$$

In the second half of the period, the electron is brought back to rest. The total path travelled in the whole period is

$$x_T = 2s = -\frac{1}{4}\frac{e\lambda^2}{mc^2}\langle E \rangle. \tag{3.72}$$

The restoring force is

$$F(x) = -m\omega_q^2 x, \quad \omega_q = 2\pi\nu_q = 2\pi c/\lambda_q, \tag{3.73}$$

where ω_q is the natural frequency of the free oscillations of the absorbing electron of the q-type. The energy absorbed is given by the work done over the path x_T,

$$W_T = -\int_0^{x_T} F(x)dx = \tfrac{1}{2}m\omega_q^2 x_T^2 = \frac{e^2\lambda^4}{32mc^4}\omega_q^2\langle E \rangle^2. \tag{3.74}$$

Therefore, the rate of energy absorption is

$$\dot{W} = \frac{1}{T}W_T = \frac{c}{\lambda}W_T = \frac{\pi^2 e^2 \lambda^3}{8mc\lambda_q^2}\langle E \rangle^2. \tag{3.75}$$

The intensity I represents the energy of radiation that crosses unit area, held normal to the beam, in 1 s, and is $I = \frac{c}{4\pi}\langle E^2 \rangle$. We define the absorption

coefficient τ_e as the ratio of the energy $\dot{W}$ absorbed (abstracted) per unit time to the intensity I,

$$\tau_e = \frac{\dot{W}}{I} = \frac{\pi^3 e^2 \lambda^3}{2mc^2\lambda_q^2}\frac{\langle E \rangle^2}{\langle E^2 \rangle}. \tag{3.76}$$

Because $E(t) = E_0 \sin(2\pi t/T)$,

$$\langle E \rangle = \frac{1}{T/4}\int_0^{T/4} E(t)dt = \frac{2}{\pi}E_0, \quad \langle E^2 \rangle = \frac{1}{T/4}\int_0^{T/4} [E(t)]^2 dt = \frac{1}{2}E_0^2,$$

$$\langle E \rangle^2/\langle E^2 \rangle = 8/\pi^2 \simeq 0.81. \tag{3.77}$$

Therefore for one electron of the q-type,

$$\tau_e = \frac{4\pi e^2}{mc^2\lambda_q^2}\lambda^3. \tag{3.78}$$

If there are z_q electrons at the q level, the partial atomic absorption coefficient τ_q is given by

$$\tau_q = z_q\tau_e = 4\pi r_e \lambda^3 z_q/\lambda_q^2, \tag{3.79}$$

where $r_e = e^2/mc^2$. The *atomic absorption coefficient* is

$$\tau_a = \sum_q \tau_q \equiv 4\pi r_e \lambda^3 \sum_{q=1}^{z} z_q/\lambda_q^2. \tag{3.80}$$

For the K level, $z_K = 2$, $E_K = R_\infty hcZ^2$, $\lambda_K = \lambda_{K\,\text{edge}} = c/\nu_K = hc/E_K = 1/R_\infty Z^2$. Therefore, from (3.79)

$$\tau_K = 8\pi r_e R_\infty^2 Z^4 \lambda^3 = 8.6 \times 10^{-26} Z^4 \lambda^3 (\lambda \text{ in Å}). \tag{3.81}$$

There is some loss of radiation from the incident beam because of the scattering. We can define the *atomic attenuation coefficient* μ_a as

$$\mu_a = \tau_a + \sigma_a, \tag{3.82}$$

where τ_a is the *true* atomic absorption coefficient and σ_a the *atomic scattering coefficient*, $\sigma_a \ll \tau_a$.

In Fig. 3.11, we show the observed variation of μ_a for ^{78}Pt as a function of λ of incident X-rays. The discontinuities are called *absorption edges* and occur at wavelengths that are characteristic of the absorbing element. They are related to the energies required to knock K, L, M, etc., electrons out of the atom. For this reason, the true atomic absorption coefficient τ_a is called the *photoelectric atomic absorbption coefficient*. The gradual rise of the absorption curve is proportional to λ^3. A plot of μ_a as a function of λ^3 gives straight-line sections. The emission lines of each series of a given Z occur at the longer wavelength side of the corresponding edge. The absorption is relatively low on this side, so an element is relatively transparent to its own spectral lines.

For other elements, similar curves are obtained, with edges at different characteristic wavelengths. A plot of μ_a against Z^4 gives a linear relationship.

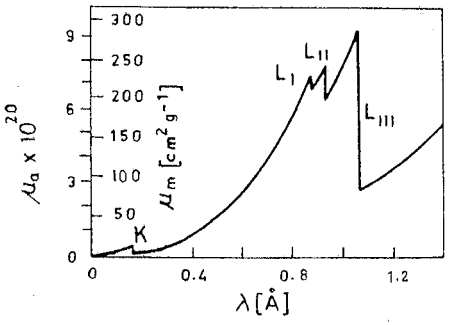

Fig. 3.11. Variation of μ_a with λ for platinum

This suggests that we can write the observed dependence as

$$\mu_a = \tau_a + \sigma_a = \begin{cases} c_a\lambda^3 Z^4 + \sigma_a \text{ for } \lambda < \lambda_K \\ c'_a\lambda^3 Z^4 + \sigma_a \text{ for } \lambda > \lambda_K \end{cases}, \tag{3.83}$$

where $c_a = 2.25 \times 10^{-2}$ cm and $c'_a = 0.32 \times 10^{-2}$ cm for λ in cm. For $\lambda < \lambda_K$,

$$\tau_a = \tau_K + \tau_L + \tau_M + \cdots = c_a\lambda^3 Z^4, \tag{3.84}$$

where

$$\tau_K = (c_a - c'_a)Z^4\lambda^3 = 1.92 \times 10^{-2} Z^4\lambda^3, \tag{3.85}$$

$$\tau_L + \tau_M + \cdots = c'_a\lambda^3 Z^4. \tag{3.86}$$

The theoretical numerical factor in (3.81) is too large by a factor of about four. The reason is that we have neglected the radiation damping effect.

3.8.2 Absorption by a Damped Oscillator

When the radiation damping is included, we have to follow the Lorentz treatment (Sect. 3.3). From (3.35, 40),

$$(\tau_q) = \frac{2\omega}{c}\beta_q = \frac{4\pi n_q e^2}{mc}\frac{\gamma_\omega \omega^2}{(\omega_q^2 - \omega^2)^2 + \gamma_\omega^2\omega^2} = \frac{4\pi n_q e^2}{mc\omega} f''(\omega), \tag{3.87}$$

For ω close to ω_q, write $\omega_q^2 - \omega^2 \simeq 2\omega_q(\omega_q - \omega)$ and replace ω by ω_q elsewhere to get

$$(\tau_q) \simeq \frac{6\pi n_q c^2}{\omega_q^2}\frac{1}{1 + [(\omega_q - \omega)^2/\gamma/2]^2}. \tag{3.88}$$

In view of (3.5), we have replaced γ_ω by γ in this region of ω.

Comparison of (3.88) with (3.17) shows that the improved classical theory leads to a line absorption, and not to a simple λ^3 dependence as given by (3.79) or by the experimental result (3.85). In X-rays, we observe an absorption edge at ω_q and *not* an absorption line.

This discrepancy between the Lorentz theory and experiments requires a radical modification of the theory. It can be done only in a highly artificial and formal manner, as shown below.

The natural frequency $\omega_q (q = K, L, M, \ldots)$ is related to the absorption edges (K, $L, M, \ldots$). The ejection of an electron from a $K, L, M, \ldots$ shell is accompanied by a transition to a higher energy state. As other inner shells are already full, the most likely transitions are to the *continuum* of states that have positive energies (Fig. 3.12). Each such transition corresponds to a possible value of ω_q ($\omega_q, \omega'_q, \omega''_q, \ldots, \omega_j \ldots, \infty$); therefore, we can associate it with a *virtual oscillator*. Obviously, the frequency range of these virtual oscillators should be from ω_q to ∞. This amounts to distributing the z_q electrons of the q-type (originally of frequency ω_q) over *all* frequencies ω_j in the range $\omega_q < \omega_j < \infty$.

Let us assign to each frequency ω_j a certain fraction $f_q(\omega_j)$ of the classical oscillators. It represents the *oscillator strength* (Sect. 2.3). To frequencies ω_j of the continuous spectrum corresponds, more appropriately, a spectral density of oscillator strength, $df_q/d\omega_j$. It satisfies the condition

$$z_q = \int_{\omega_q}^{\infty} f_q(\omega_j)d\omega_j, \quad f_q(\omega_j) = \frac{df_q}{d\omega_j}. \tag{3.89}$$

Here $(df_q/d\omega_j)d\omega_j$ is the number of virtual oscillators with frequencies between ω_j and $\omega_j + d\omega_j$.

Let n_q be the number of q-type electrons in 1 cm^3. Because z_q is the number of q-type electrons in one atom, the number of atoms in 1 cm^3 is n_q/z_q. The *partial atomic absorption coefficient* τ_q is defined in terms of the partial linear absorption coefficient (τ_q), (3.87), as

$$\tau_q = \frac{(\tau_q)}{n_q/z_q} = \frac{6\pi c^2}{\omega^2}\frac{z_q}{1 + (\omega_q - \omega)^2(\omega_q + \omega)^2/\gamma_\omega^2\omega^2}. \tag{3.90}$$

Using (3.89) for z_q, replacing ω_q by ω_j for the virtual oscillators and integrating

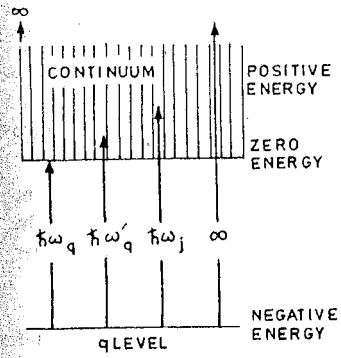

Fig. 3.12. Frequencies of virtual oscillators

from ω_q to ∞ for the spectral continuum gives

$$\tau_q = \frac{6\pi c^2}{\omega^2} \int_{\omega_q}^{\infty} \frac{f_q(\omega_j)d\omega_j}{1+(\omega_j-\omega)^2(\omega_j+\omega)^2/\gamma_\omega^2\omega^2}. \tag{3.91}$$

The expression under the integral has a sharp maximum at $\omega_j \approx \omega$. This means that only virtual oscillators of frequencies close to the frequency ω of the incident X-rays will absorb effectively. Therefore, we can replace ω_j by ω everywhere except in the difference $(\omega_j-\omega)$ term. Also we can neglect the variation of $f_q(\omega_j)$ over the narrow region in which effective contributions to the integral occur and simply use $f_q(\omega)$. Thus,

$$\begin{aligned}\tau_q(\omega) &= \frac{6\pi c^2}{\omega^2} f_q(\omega) \int_{\omega_q}^{\infty} \frac{d\omega_j}{1+[\omega_j-\omega)/\gamma_\omega/2]^2} \\ &= \frac{6\pi c^2}{\omega^2} f_q(\omega)\left[\frac{1}{2}\gamma_\omega\left(\tan^{-1}\frac{\omega_j-\omega}{\gamma_\omega/2}\right)_{\omega_q}^{\infty}\right] \\ &= \frac{3\pi c^2\gamma_\omega}{\omega^2} f_q(\omega)\left(\tan^{-1}\infty - \tan^{-1}\frac{\omega_q-\omega}{\gamma_\omega/2}\right).\end{aligned} \tag{3.92}$$

Because $\omega > \omega_q$ and $\gamma_\omega/2$ is very small, the term $(\omega_q-\omega)/(\gamma_\omega/2)$ will be a very large negative number for all ω not very close to ω_q. In this region,

$$\frac{\omega_q-\omega}{\gamma_\omega/2} \approx -\infty, \quad \tan^{-1}\frac{\omega_q-\omega}{\gamma_\omega/2} \approx -\frac{\pi}{2}.$$

Thus, for ω not close to ω_q, (3.92) becomes

$$\tau_q(\omega) = \frac{3\pi^2c^2\gamma_\omega}{\omega^2} f_q(\omega) = \frac{2\pi^2e^2}{mc} f_q(\omega) = 2\pi^2 cr_e f_q(\omega). \tag{3.93}$$

This shows that *the measurement of the photoelectric (true) absorption coefficients provides a direct knowledge of oscillator strengths.*

If we use (3.89) and remember that ω and ω_j are the same, for our purpose here, then from (3.93),

$$\frac{1}{2\pi^2 cr_e}\int_{\omega_q}^{\infty}\tau_q(\omega)d\omega = \int_{\omega_q}^{\infty} f_q(\omega)d\omega = z_q, \tag{3.94}$$

or the number of virtual oscillators z_q assigned to ν_q is

$$\frac{1}{\pi cr_e}\int_{\nu_q}^{\infty}\tau_q d\nu = z_q. \tag{3.95}$$

To check the *sum rule* (3.95), we can evaluate the left-hand side either by the graphical integration of the actual observed absorption curve, or we can use the empirical law,

$$\tau_q = c_q Z^4\lambda^3, \quad 0<\lambda<\lambda_q,$$

where c_q is given by experiments. Both methods give nearly the same result.

Table 3.2. Calculated values of z_K, with $c_K = 1.92\times10^{-2}$ cm from experiment

Element	λ_K [Å]	$Z^4\lambda_K^2$	z_K (calculated)
13 Al	7.9481	1.80×10^6	1.96
29 Cu	1.3806	1.35	1.46
42 Mo	0.6198	1.20	1.30
47 Ag	0.4859	1.15	1.25
50 Sr	0.4247	1.13	1.22
79 Au	0.1536	0.92	1.00

Therefore,

$$z_q = \frac{c_q Z^4}{\pi cr_e}\int_{\lambda_q}^{0}\lambda^3\left(-\frac{c}{\lambda^2}\right)d\lambda = \frac{c_q Z^4}{2\pi r_e}\lambda_q^2, \tag{3.96}$$

where λ is in cm. From the Moseley law, $\lambda_q^2 Z^4$ is nearly constant. Table 3.2 gives some values of z_K according to (3.96), with $c_K/2\pi r_e = 1.92\times10^{-2}/(2\pi\times2.82\times10^{-13}) \simeq 10^{10}$; $z_K \simeq Z^4[\lambda_K^2(in\ \text{Å})]\times10^{-6}$. For the K level, the left-hand side of the sum rule (3.95) is consistently much less than the right-hand side value, $z_K = 2$, which is known to be correct from the Pauli principle. Thus, the classical approach needs to be revised [3.17], especially regarding the number of oscillators per cm^3.

From $\tau_q = c_q Z^4\lambda^3$ and (3.96),

$$\tau_q = 2\pi r_e\frac{\lambda^3}{\lambda_q^2}z_q = 4\pi^2 cr_e\frac{\omega_q^2}{\omega^3}z_q. \tag{3.97}$$

Comparison with (3.37) shows that the inclusion of the effect of radiation damping has decreased the value of τ_q by a factor of two. Even now it is higher than the observed value. The reason is that, in the photoelectric absorption process, the atom gets excited, and the fluorescent radiation that results returns part of the absorbed energy to the electromagnetic field. We have not corrected for this, so far.

Equation (3.97) gives the general law of absorption, obtained in a semi-empirical manner, in that we have used the experimental λ^3 law. The atomic absorption coefficient is

$$\tau_a = 2\pi r_e\lambda^3\sum_q\frac{z_q}{\lambda_q^2} = 1.77\times10^{-12}\lambda^3\sum_q\frac{z_q}{\lambda_q^2}, \tag{3.98}$$

where λ is in cm. The experimental results [3.18] give

$$\tau_a = 1.71\times10^{-12}\lambda^3\sum_q\frac{z_q}{\lambda_q^2}. \tag{3.99}$$

From (3.93, 97), the oscillator-strength density is

$$f_q(\omega) = \frac{1}{2\pi^2 c r_e}\tau_q(\omega) = 2\frac{\omega_q^2}{\omega^3} z_q. \quad (\omega \simeq \omega_j) \tag{3.100}$$

$$f_q(\lambda) = -f_q(\omega)\frac{d\omega}{d\lambda} = \frac{2\pi c}{\lambda^2} f_q(\omega) = 2\frac{\lambda}{\lambda_q^2} z_q, \tag{3.101}$$

where $f_q(\lambda)$ is such that for the continuous absorption

$$\int_0^{\lambda_q} f_q(\lambda)\, d\lambda = z_q. \tag{3.102}$$

The connection (3.100) is the basis for the dispersion formulae given by *Kronig* [3.19], *Kallmann* and *Mark* [3.20], and *Bothe* [3.21]

3.9 Kramers–Kallmann–Mark Theory of Refractive Index

From (3.32, 41),

$$\mu_{c,q} = 1 + \frac{2\pi n_q e^2}{m}\frac{1}{\omega_q^2 - \omega^2 + i\gamma_\omega \omega} = 1 - \delta_q - i\beta_q. \tag{3.103}$$

The virtual oscillator distribution (3.100), that leads to the correct absorption law, can now be profitably introduced in the form

$$\frac{f_q(\omega_j)}{z_q} = \frac{2\omega_q^2}{\omega_j^3}, \quad \omega_q < \omega_j < \infty. \tag{3.104}$$

The subscript j distinguishes between the incident radiation frequency ω and the virtual-oscillator frequency ω_j.

Each electron of the q-type is to be replaced by a distribution of virtual oscillators, (3.104), with frequencies in the range ω_q to ∞ (Fig. 3.12). This means that the distribution per electron, $f_q(\omega_j)/z_q$, will now replace unity in the numerator of the second term in (3.103),

$$\mu_{c,q} = 1 + \frac{4\pi e^2 n_q \omega_q^2}{m}\int_{\omega_q}^{\infty} \frac{d\omega_j}{\omega_j^3(\omega_j^2 - \omega^2 + i\gamma_\omega \omega)}. \tag{3.105}$$

Integration[1] gives

$$\mu_{c,q} = 1 + \frac{4\pi e^2}{m} n_q \omega_q^2 \left[\frac{1}{2\omega(i\gamma_\omega - \omega)}\left(\frac{1}{\omega_q^2} + \frac{1}{\omega(i\gamma_\omega - \omega)}\ln\frac{\omega_q^2}{\omega_q^2 - \omega^2 + i\gamma_\omega\omega}\right)\right]. \tag{3.106}$$

[1] Use $\int \frac{dx}{x^3(a+bx^2)} = \int\left(\frac{1}{ax^3} - \frac{b}{ax(a+bx^2)}\right)dx = -\frac{1}{2ax^2} - \frac{b}{a}\left(\frac{1}{2a}\ln\frac{x^2}{a+bx^2}\right)$

Put $s = \omega/\omega_q$, $d = \gamma_\omega/\omega_q$, where d characterizes the damping. Then

$$\delta_q + i\beta_q = \frac{2\pi e^2}{m}\frac{n_q}{\omega_q^2}\frac{\ln(1 - s^2 + isd) + (s^2 - isd)}{(s^2 - isd)^2}. \tag{3.107}$$

To separate the real and imaginary parts, put, for the case $s < 1$,

$$\ln(1 - s^2 + isd) = a + ib,$$

$$1 - s^2 + isd = e^{a+ib} = e^a\cos b + ie^a \sin b,$$

$$1 - s^2 = e^a \cos b, \quad sd = e^a \sin b,$$

$$a = \frac{1}{2}\ln[(1 - s^2)^2 + s^2 d^2], \quad b = \tan^{-1}\frac{sd}{1 - s^2} = \tan^{-1} y,$$

$$(s^2 - isd)^2 = s^2(s^2 - d^2) - i2s^3 d.$$

Thus, for $s < 1$, or $\omega < \omega_q$,

$$\delta_q + i\beta_q = \frac{2\pi e^2}{m}\frac{n_q}{\omega_q^2}\frac{\{\frac{1}{2}\ln[(1 - s^2)^2 + s^2 d^2] + s^2\} - i(sd - \tan^{-1} y)}{s^2(s^2 - d^2) - i2s^3 d},$$

$$\delta_q = \frac{2\pi e^2}{m}\frac{n_q}{\omega_q^2}\frac{\frac{1}{2}(s^2 - d^2)\ln[(1 - s^2)^2 + s^2 d^2] - 2sd\tan^{-1} y + s^2(s^2 + d^2)}{s^2(s^2 + d^2)^2},$$

$$\beta_q = \frac{2\pi e^2}{m}\frac{n_q}{\omega_q^2}\frac{sd\ln[(1 - s^2)^2 + s^2 d^2] + (s^2 - d^2)\tan^{-1} y + sd(s^2 + d^2)}{s^2(s^2 + d^2)^2}. \tag{3.108}$$

Because of the complex nature of the logarithm, we get a different result for the case $s > 1$. Put

$$\ln[-(s^2 - 1 - isd)] = a + ib,$$

whence, with $e^{-i\pi} = -1$,

$$s^2 - 1 - isd = e^a e^{i(b-\pi)}$$

$$a = \tfrac{1}{2}\ln[(s^2 - 1)^2 + s^2 d^2], \quad b = \pi - \tan^{-1}(-y), \quad y = \frac{sd}{1 - s^2}.$$

Proceeding as before, for $s > 1$, or $\omega > \omega_q$,

$$\delta_q = \frac{2\pi e^2}{m}\frac{n_q}{\omega_q^2} \times \frac{\frac{1}{2}(s^2 - d^2)\ln[(s^2 - 1)^2 + s^2 d^2] + 2sd\tan^{-1}(-y) + s^2(s^2 + d^2) - 2\pi sd}{s^2(s^2 + d^2)^2}$$

$$\beta_q = \frac{2\pi e^2}{m}\frac{n_q}{\omega_q^2} \times \frac{sd\ln[(s^2 - 1)^2 + s^2 d^2] - (s^2 - d^2)\tan^{-1}(-y) + sd(s^2 + d^2) + \pi(s^2 - d^2)}{s^2(s^2 + d^2)^2}.$$

Because γ_ω is a small quantity, we can neglect d^2. Then

$$\delta_q \simeq \frac{2\pi e^2}{m}\frac{n_q}{\omega_q^2}\frac{1}{s^2}\cdot\begin{cases}1+s^{-2}\ln(1-s^2), & \text{for } s<1,\\ 1+s^{-2}\ln(s^2-1)-s^{-3}2\pi d, & \text{for } s>1.\end{cases} \tag{3.109}$$

In the limit $s \gg 1$, from (3.109), on using L'Hôpital's rule,

$$\delta_q \simeq \frac{2\pi e^2}{m}\frac{n_q}{\omega_q^2}\frac{1}{s^2} = \frac{2\pi e^2}{m}\frac{n_q}{\omega^2}, \quad (\omega \gg \omega_q), \tag{3.110}$$

$$\delta = \sum_q \delta_q \simeq \frac{2\pi e^2}{m\omega^2}\sum_q n_q = \frac{e^2\lambda^2}{2\pi mc^2}n, \quad (\lambda \ll \lambda_q). \tag{3.111}$$

This agrees with the simple Lorentz-theory result (3.44), as expected. We are away from the absorption edge and so corrections that arise from the continuum absorption are not important.

Let us neglect damping, $d = 0$. Then, from (3.109),

$$\delta_q \simeq \frac{2\pi e^2}{m}\frac{n_q}{\omega^2}\begin{cases}1+(\omega_q^2/\omega^2)\ln[1-(\omega^2/\omega_q^2)], & \text{for } \omega<\omega_q,\\ 1+(\omega_q^2/\omega^2)\ln[(\omega^2/\omega_q^2)-1], & \text{for } \omega>\omega_q,\end{cases} \tag{3.112}$$

$$\frac{\delta}{\lambda^2} = \frac{\sum_q \delta_q}{\lambda^2} = \frac{e^2}{2\pi mc^2}\left(\sum_q n_q + \lambda^2\sum_q \frac{n_q}{\lambda_q^2}\ln\left|1-\frac{\lambda_q^2}{\lambda^2}\right|\right). \tag{3.113}$$

For a compound: $n_q = (N_A\rho/M)z_q$, $\sum_q z_q = Z_M$, $\sum_{q\neq K} z_q = Z_M - z_K$. When λ is close to λ_K, we have $\lambda \ll \lambda_{q\neq K}$ for all of the remaining levels. We can set $(\lambda^2/\lambda_q^2)\ln|1-(\lambda_q^2/\lambda^2)| = 0$ for them. Then for $z_K = 2$ and λ in Å,

$$\frac{\delta}{\lambda^2} = \frac{e^2 N_A\rho}{2\pi mMc^2}\left(Z_M + z_K\frac{\lambda^2}{\lambda_K^2}\ln\left|1-\frac{\lambda_K^2}{\lambda^2}\right|\right)$$

$$= 2.68\times 10^{-6}\frac{\rho}{M}\left(Z_M + 2\frac{\lambda^2}{\lambda_K^2}\ln\left|1-\frac{\lambda_K^2}{\lambda^2}\right|\right), \tag{3.114}$$

For calcite ($CaCO_3$), we finally get [3.22],

$$\frac{\delta}{\lambda^2} = 0.0732\times 10^{-6}\left(50 + \frac{2\lambda^2}{9.390}\ln\left|1-\frac{9.390}{\lambda^2}\right|\right). \tag{3.115}$$

This is different from the Lorentz-theory result (3.48). For $\lambda \gg \lambda_K$ and $\lambda \ll \lambda_K$ it has, however, the same limits as the Lorentz theory.

Figure 3.13, compares this theory [3.20] with the data of *Larsson* [3.4] on calcite. It is in closer agreement with the data than the simple Lorentz theory, especially for $\lambda \leqq \lambda_K$. For $\lambda \simeq \lambda_K$, we cannot expect good agreement because we have neglected the damping term; it becomes important in this region. At $\lambda \sim \lambda_K/2$, the present theory predicts a broad maximum, unlike the Lorentz theory. *Larsson* has found evidence for its existence in quartz. The theory of *Kramers, Kallmann* and *Mark* gives qualitatively the observed shape of the

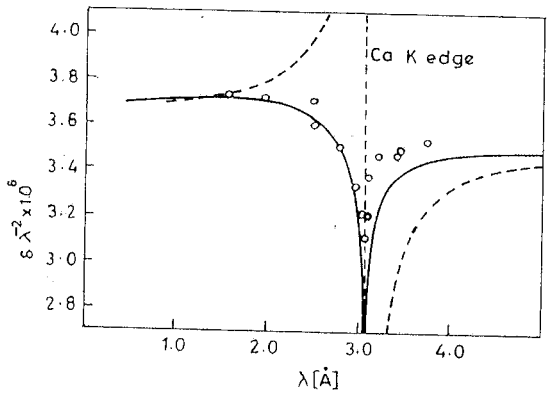

Fig. 3.13. Plot of δ/λ^2 versus λ[Å] for calciite. The solid curve is from the theory of Kramers, Kallmann and Mark (3.115). For comparison, the Lorentz-theory curve (dashed), is also given. The experimental points are from [3.4]

X-ray dispersion curve. For further improvement we have to consider the quantum theory of dispersion.

Föll and *Ulmer* [3.23] have used the modified Bragg law (3.54) and (3.113) for the absolute determination of $2d$ by measuring a bremsstrahlung isochromat.

3.10 Quantum Theory of Dispersion

3.10.1 Oscillator Strength

Suppose that $\rho(\omega_q)$ is the energy density of the incident radiation in the neighbourhood $\omega = \omega_q$. The definition of the atomic absorption coefficient implies that the energy absorbed per atom in unit time is

$$\left(\frac{dU}{dt}\right)_{\text{classical}} = c\tau_q(\omega)\rho(\omega_q) = \frac{2\pi^2 e^2}{m}f_q(\omega)\rho(\omega_q), \tag{3.116}$$

using (3.93) for $\tau_q(\omega)$. It represents the *induced* absorption of energy per second by the classical oscillators. This formula was first obtained by *Ladenburg* [3.17]. With $\nu_q = \omega_q/2\pi$, we obtain

$$\left(\frac{dU}{dt}\right)_{\text{classical}} = \frac{\pi e^2}{m}f_q(\nu)\rho(\nu_q), \quad f_q(\nu) = \frac{df_q}{d\nu}. \tag{3.117}$$

In the quantum theory, the energy absorbed per atom per second, in the electronic transition $i \to f$, can be expressed as

$$\left(\frac{dU}{dt}\right)_{\text{quantum}} = h\nu_{\text{fi}}b_{\text{i}\to\text{f}}\rho_{\text{fi}}, \tag{3.118}$$

where $\nu_{fi} = (E_f - E_i)/\hbar$, is the absorbed frequency ($E_f > E_i$), $b_{i\to f}$ is the transition probability for the *induced* absorption, and ρ_{fi} is the density of the incident radiation of frequency ν_{fi}. Once in the excited state f, a *spontaneous* emission of radiation of frequency ν_{fi} occurs because of the electronic transition $f \to i$.

If N_i atoms per cm^3 are in the initial quantized state i and N_f in the final state f, then, according to Einstein, at equilibrium,

$$N_i h\nu_i b_{i\to f}\rho_{fi} = N_f h\nu_{fi}(a_{f\to i} + b_{f\to i}\rho_{fi}). \tag{3.119}$$

Here $a_{f\to i}$ is the probability for a spontaneous-emission transition $f \to i$, and $b_{f\to i}$ is the probability of an induced-emission transition in the presence of the radiation. N_i and N_f are related by the Boltzmann factor

$$N_i = N_f e^{(E_f - E_i)/kT} = N_f e^{h\nu_{fi}/kT},$$

where k is the Boltzmann constant and T is the temperature [K]. From (3.119),

$$\rho_{fi} = \frac{a_{f\to i}}{b_{i\to f}e^{h\nu_{fi}/kT} - b_{f\to i}}.$$

Comparison with Planck's law for the blackbody-radiation density,

$$\rho_\nu = \frac{8\pi h\nu^3 d\nu}{c^3(e^{h\nu/kT} - 1)},$$

reveals that

$$b_{i\to f} = b_{f\to i}, \quad a_{f\to i} = \frac{8\pi h\nu_{fi}^3}{c^3} b_{f\to i}. \tag{3.120}$$

Therefore

$$\left(\frac{dU}{dt}\right)_{\text{quantum}} = \frac{c^3}{8\pi\nu_{fi}^2} a_{f\to i}\rho_{fi}. \tag{3.121}$$

By the correspondence principle, we can equate (3.117, 121) to get

$$f_q(\nu) = \frac{mc^3}{8\pi^2 e^2 \nu_{fi}^2} a_{f\to i} = \frac{mh\nu_{fi}}{\pi e^2} b_{i\to f} = f_{i\to f}. \tag{3.122}$$

Here we have identified ν_q with ν_{fi}, $\rho(\nu_q)$ with ρ_{fi}, and $f_{i\to f}$ is analogous to the classical-oscillator strength $f_q(\nu)$. By convention, the absorption oscillator strength is taken to be positive.

From (2.19), for a single oscillator,

$$\frac{dU}{dt} = \frac{64\pi^4 e^2}{3c^3}\nu_{fi}^4 r^2(i,f) = h\nu_{fi}a_{f\to i} = \frac{8\pi^2 e^2 h\nu_{fi}^3}{mc^3} f_{i\to f}, \tag{3.123}$$

using (3.122) in the last step. Thus, the oscillator strength is proportional to $r^2(i,f)$, that is, the transition probability. Specifically

$$f_{i\to f} = \frac{8\pi^2 m}{3h}\nu_{fi}(|x_{i\to f}|^2 + |y_{i\to f}|^2 + |z_{i\to f}|^2). \tag{3.124}$$

If the transitions involve the continuum,

$$\frac{df_{i\to f}}{dE} = \frac{8\pi^2 m}{3h}\nu_{fi}\frac{d}{dE}(|x_{i\to f}|^2 + |y_{i\to f}|^2 + |z_{i\to f}|^2), \tag{3.125}$$

where $df_{i\to f}/dE$ is the *oscillator-strength density* of the atom, in the energy interval dE at ν_{fi}, for the absorption transition from state i to state f.

Quantum theory defines the ν_{fi} and $f_{i\to f}$ in terms of the eigenvalues and eigenfunctions of the Schrödinger equation. Analytical solutions are possible when the one-electron approximation is made.

The ground-state wave function of the hydrogen atom is spherically symmetric. Therefore, the dipole-matrix elements are equal[2], $|x_{i\to f}|^2 = |y_{i\to f}|^2 = |z_{i\to f}|^2$, and (3.124) becomes

$$f_{i\to f} = \frac{2m}{\hbar^2}(E_f - E_i)|(f|x|i)|^2 = \frac{2m}{\hbar}\omega_{fi}|x_{fi}|^2. \tag{3.126}$$

Equation (3.123) determines intensity and so will have contributions from all of the final states. *Kuhn* [3.24] and *Thomas* [3.25] showed (see Appendix F) that, for a one-electron system,

$$\frac{2m}{\hbar^2}\sum_f (E_f - E_i)|(f|x|i)|^2 \equiv \sum_f f_{i\to f} = 1. \tag{3.127}$$

For an atom that contains Z electrons, we can generalize this *sum rule* to

$$\sum_f f_{i\to f} = Z. \tag{3.128}$$

When both discrete and continuous absorption are present,

$$\sum_f^{\text{discrete}} f_{i\to f} + \int_{\substack{\text{ionization}\\ \text{threshold}}}^{\infty} (df_{i\to f}/dE)dE = Z. \tag{3.129}$$

Broad spectral data are now used to investigate these sum rules [3.26–29].

Because $b_{i\to f} = b_{f\to i}$, and $\nu_{fi} = -\nu_{if}$, we have $f_{f\to i} = -f_{i\to f}$, that is, the emission oscillator strength is negative.

Sugiura [3.30] has calculated the oscillator strength for the normal state of hydrogen as the initial state, and checked (3.129) (Table 3.3). For the (optical) Lyman series we need $|\int \psi_{n10} \times \psi_{100}|^2$. This requires evaluation of the radial integral $\int_0^\infty r^2\, dr\, R_{n10}(r)\, r\, R_{100}(r)$, where the radial wave functions are known for the hydrogen atom. The result is (for example, [3.26])

$$|(n10)| \times |100|^2 = \frac{1}{3}\frac{2^8 n^7 (n-1)^{2n-5}}{(n+1)^{2n+5}} a_0^2, \quad \text{(Lyman series)}.$$

---

[2] $|(f|x|i)|^2 = (i|x|f)(f|x|i) = (i|x^2|i) = \int |\psi_i|^2 x^2 dx$, because $|f><f| = \int |\psi_f|^2 dx = 1$.

Table 3.3. Oscillator strengths in the Lyman series

n	Term	$f_{1\to n}$
2	Lyman α	0.4162
3	Lyman β	0.0791
4	—	0.0290
5	—	0.0139
6	—	0.0078
7	—	0.0048
8	—	0.0032
9	—	0.0022
$\sum_{10}^{\infty}$	10th Lyman line to series limit	0.0079
$\int_{\text{threshold}}^{\infty} df$	continuous spectrum	0.5641
		0.437
$\sum+\int$	line + continuous	Sum 1.0011

An estimate for $n = 2$ gives

$$f_{1\to 2} = \frac{2mc^2}{(\hbar c)^2}(E_2 - E_1)\frac{1}{3}\frac{2^{15}}{3^9}a_0^2$$

$$= \frac{2 \times 0.51\,\text{MeV}}{(197.3 \times 10^{-5})^2\,[\text{MeV}]^2\,[\text{Å}]^2}(10.18[\text{eV}])\frac{1}{3}\frac{2^{15}}{3^9}(0.53)^2[\text{Å}]^2 = 0.4162.$$

The strengths $f_{1\to n}$ of discrete transitions can be shown as a histogram, that is, as a set of rectangular blocks whose respective areas are equal to the $f_{1\to n}$ and whose bases correspond to the energies E_n. Figure 3.14 shows the positions and oscillator strengths of the discrete spectrum of hydrogen, together with the adjoining positive-energy continuum, in a manner applicable to the Lyman series of other atoms. If we plot each energy level E_n ($E_2 = 3.4$ eV, $E_3 = 1.51$ eV, . . .) against the principal quantum number n of the corresponding line in the Lyman series and draw a smooth curve through these points then the base of the histogram block that represents the oscillator strength $f_{1\to n}$ should equal the slope of the curve, dE_n/dn, at n. The top of the histogram equals $f_{1\to n}(dn/dE_n)$, to give the area as $f_{1\to n}$. These tops form a staircase that constitutes an extrapolation of the positive-energy continuous spectrum. Because $(df/dE)_K$ is proportional to $\tau_K(E)$, such a plot represents the absorption spectrum.

Calculation of the continuous-spectrum contribution (Table 3.3) is rather involved, because it requires the construction of the correct positive-energy function in the Coulomb field. *Sugiura* [3.30] showed that, for a single electron

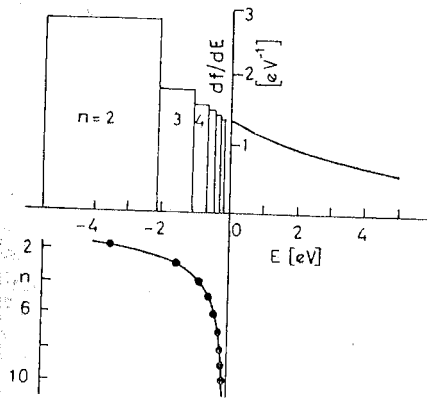

Fig. 3.14. Oscillator-strength distribution in the bound states and part of the continuum of the hydrogen atom [3.29]

bound in a Coulomb field in its ground state, the oscillator strength density $df/d\omega$, for frequency ω in the K oscillator continuum, is given by

$$d(|x_{i\to f}|^2 + |y_{i\to f}|^2 + |z_{i\to f}|^2) = 2^7 a_0^2 s^{-5} g(s) dE, \tag{3.130}$$

$$\left(\frac{df}{d\omega}\right)_K d\omega = \frac{2^7}{3}\frac{g(s)}{s^4}\omega_K^{-1}, \tag{3.131}$$

where we have used (3.125), $s = \omega/\omega_K$, ω_K being the K absorption frequency, and

$$g(s) = \exp\left(-\frac{4}{(s-1)^{1/2}}\tan^{-1}(s-1)^{1/2}\right)(1 - e^{-2\pi/(s-1)^{1/2}})^{-1}. \tag{3.132}$$

By graphical integration over the K continuum, from $s = 1$ to $s = \infty$, he found a value 0.437 for the oscillator strength (Table 3.3).

The case of atoms with more than one electron has been discussed by *Kronig* and *Kramers* [3.31]. We have seen that a hydrogen-like (one-hole) model is reasonable for the X-ray spectra. For the X-ray K absorption, the K electrons cannot go to L, M, . . . levels, because they are full. Therefore, for the X-ray case, the oscillator strength for a K electron is more nearly that for the continuous absorption in the hydrogen Lyman series, $f(\text{cont})_K = 0.437$. This is considerably less than unity. For $N_i = 2$, the theoretical total oscillator strength for the K level in the one-electron approximation is then nearly 0.88.

The experimental value of $f(\text{cont})_K$ can be estimated with the help of the empirical formula for the atomic absorption coefficient,

$$\tau_K(\omega) = C_K\omega^{-n} = (\omega_K/\omega)^n\tau_K(\omega_K), \quad \text{for } \omega > \omega_K,$$
$$\tau_K(\omega) = 0, \quad \text{for } \omega < \omega_K, \tag{3.133}$$

$$\int \frac{df_K}{d\omega}d\omega = f(\text{cont})_K = \frac{mcC_K}{2\pi^2e^2}\int_{\omega_K}^{\infty}\frac{d\omega}{\omega^n} = \frac{mc}{2\pi^2e^2}\frac{\omega_K}{n-1}\tau_K(\omega_K), \tag{3.134}$$

where we have used (3.93). From the knowledge of n and $\tau_K(\omega_K)$ from the experiments, we can estimate $f(\text{cont})_K$. It is consistently higher than the theoretical value 0.88 obtained above. This shows that the approximation of an atom with one electron (hole) is not satisfactory. The effect of screening must be included. *Wolf* [3.32] has made calculations for the L-shell electrons.

3.10.2 Hönl Theory

Hönl [3.33] has modified Sugiura's quantum-mechanical calculation to include the effect of screening. According to *Hönl*, we can write (3.131, 132), with sufficient accuracy within the limits $\omega_K < \omega_j < 4\omega_K$, as

$$g(s) \simeq 3^{-1}\exp(-4)(4s-1), \tag{3.135}$$

$$\left(\frac{df}{d\omega_j}\right)_K \simeq \frac{2^7}{9}\exp(-4)\frac{\omega_K^2}{\omega_j^4}(4\omega_j-\omega_K), \tag{3.136}$$

$$f(\text{cont})_K = \int_{\omega_K}^{\infty}\left(\frac{df}{d\omega_j}\right)_K d\omega_j = \frac{2^7}{9}\exp(-4)\omega_K^2\left(\frac{2}{\omega_K^2}-\frac{1}{3\omega_K^2}\right) = 0.434.$$

The screening constants are taken to be equal, $\sigma_1 = \sigma_2 = 0.3$. For $n = 1, j = 1/2$, (2.82) gives E_K,

$$W_K = E_K - \varepsilon = R_\infty hc[(Z-\sigma)^2 + (\alpha^2/4)(Z-\sigma)^4] - \varepsilon. \tag{3.137}$$

The small correction ε takes care of the effect of the external electrons on the K level. We can write, $\hbar\Omega_K = W_K = E_K(1-\Delta_K) = \hbar\omega_K(1-\Delta_K)$, where

$$\begin{aligned}\Delta_K &= \varepsilon/E_K = 1 - W_K/E_K = 1 - \hbar\Omega_K/E_K \\ &= 1 - \frac{1/\lambda_K}{R_\infty[(Z-\sigma)^2 + (\alpha^2/4)(Z-\sigma)^4]} \\ &= 1 - \frac{911/\lambda_K}{(Z-0.3)^2 + 1.33\times 10^{-5}(Z-0.3)^4}, \quad (\lambda_K \text{ in Å}).\end{aligned} \tag{3.138}$$

Because $\omega_K = \Omega_K/(1-\Delta_K)$, for any atom with $z_K = 2$,

$$f_K(\omega_j) = \left(\frac{df}{d\omega_j}\right)_K = \frac{2^7}{9}\exp(-4)z_K\frac{\Omega_K^2}{(1-\Delta_K)^2\omega_j^4}\left(4\omega_j - \frac{\Omega_K}{1-\Delta_K}\right), \tag{3.139}$$

$$f(\text{cont})_K = \int_{\Omega_K}^{\infty}\left(\frac{df}{d\omega_j}\right)_K d\omega_j = \frac{2^8}{9}\exp(-4)\left[\frac{2}{(1-\Delta_K)^2} - \frac{1}{3(1-\Delta_K)^3}\right]. \tag{3.140}$$

Values calculated from this formula by *Hönl* are given in Table 3.4. They are in good agreement with the estimated experimental values.

Wheeler and *Bearden* [3.34] have evaluated $f(\text{cont})_K$ in a simple way. Let p be an occupied level of an atom, other than K. Then, by the sum rule, for the K electrons,

$$f(\text{cont})_K = 2\left(1 - \sum_p^{\text{discrete}} f_{K\to p}\right), \tag{3.141}$$

where $f_{K\to p}$ is the oscillator strength of the virtual oscillator associated with the transition $K\to p$. The sum we require now extends over the relatively few occupied quantized states, instead of the continuum of the Hönl method. We can estimate $f_{K\to p}$ from (3.126), by the use of Hartree wave functions. The calculated values are very close to those given by Hönl's method. In recent years, more realistic wave functions, and atomic wave functions tabulated by *Herman* and *Skillman* [3.35], have been used (for details and references see [3.29]). *Lassettre* and *Francis* [3.36] have defined a *generalized oscillator strength*. It depends on both the momentum transferred to the oscillator and the energy involved.

Hönl developed a quantum dispersion theory by the use of (3.139) for $f_q(\omega_j)$. From (3.104, 105), replacing each q electron by a distribution of virtual oscillators,

$$\mu_{c,q} = 1 + \frac{2\pi e^2 n_q}{m z_q}\int_{\omega_q}^{\infty} f(\omega_j)\frac{1}{\omega_j^2 - \omega^2 + i\gamma_\omega\omega}d\omega_j = 1 - \delta_q - i\beta_q, \tag{3.142}$$

$$\begin{aligned}\delta_q &= -\frac{2\pi e^2 n}{m}\int_{\omega_q}^{\infty} f(\omega_j)\frac{(\omega_j^2-\omega^2)d\omega_j}{(\omega_j^2-\omega^2)^2 + \gamma_\omega^2\omega^2} \\ &\simeq -\frac{2\pi e^2 n}{m}\int_{\omega_q}^{\infty} f(\omega_j)\frac{1}{\omega_j^2-\omega^2}d\omega_j,\end{aligned} \tag{3.143}$$

where, in (3.143), $n = n_q/z_q$ is the number of atoms per unit volume of the medium that contains the q electrons in question, and γ_ω^2 is a small term.

Table 3.4. Oscillator strengths according to Hönl's theory

Element	λ_K [Å]	$1-\Delta_K$	$f(\text{cont})_K$	
			Theoretical	Experimental
13 Al	7.94	0.710	1.53	1.40
29 Cu	1.38	0.795	1.31	1.35
42 Mo	0.618	0.818	1.24	1.25
50 Sn	0.424	0.844	1.18	1.15
74 W	0.178	0.857	1.15	—
79 Au	0.153	0.890	1.07	1.02

From (3.139, 143), with $z_K = 2$,

$$\delta_K = -\frac{2\pi e^2 n}{m}\frac{2^8\exp(-4)\Omega_K^2}{9(1-\Delta_K)^2}\left(4\int_{\Omega_K}^{\infty}\frac{d\omega_j}{\omega_j^3(\omega_j^2-\omega^2)} - \frac{\Omega_K}{1-\Delta_K}\int_{\Omega_K}^{\infty}\frac{d\omega_j}{\omega_j^4(\omega_j^2-\omega^2)}\right)$$

$$= \frac{e^2 n}{2\pi m(c/\lambda)^2}\frac{2^8\exp(-4)}{9}\left[\frac{2}{(1-\Delta_K)^2}\left(\frac{1}{s^2}\ln|s^2-1|+1\right)\right.$$

$$\left. -\frac{1}{(1-\Delta_K)^3}\left(\frac{1}{2s^3}\ln\left|\frac{s-1}{s+1}\right| s^2+\frac{1}{2}+\frac{1}{3}\right)\right], \tag{3.144}$$

where $s = \omega/\omega_K = \lambda_K/\lambda$, and we have used $x^{-m}(a+bx^n)^{-p-1} = (1/a)x^{-m}(a+bx^n)^{-p} - (b/a)x^{-m+n}(a+bx^n)^{-p-1}$ to simplify the second integration.

As $s\to\infty$, or $\lambda\to 0$, the expression has the limit

$$\left(\frac{\delta_K}{\lambda^2}\right)_{\lambda\to 0} = \frac{e^2 n}{2\pi mc^2}\frac{2^8\exp(-4)}{9}\left[\frac{2}{(1-\Delta_K)^2} - \frac{1}{3}\frac{1}{(1-\Delta_K)^3}\right]. \tag{3.145}$$

Comparison with (3.140) gives

$$\left(\frac{\delta_K}{\lambda^2}\right)_{\lambda\to 0} = \frac{e^2 n}{2\pi mc^2} f(\text{cont})_K. \tag{3.146}$$

When $s\to 0$, or $\lambda\to\infty$, the application of the L'Hôpital rule to (3.144) gives

$$(\delta_K/\lambda^2)_{\lambda\to\infty} = 0. \tag{3.147}$$

Thus, for $\lambda \gg \lambda_K$, the dispersion of K electrons is cut out.

For calcite ($CaCO_3$), from (3.138, 140),

$$1-\Delta_K = 0.760, \quad f(\text{cont})_K = 1.41. \tag{3.148}$$

When $\lambda \simeq \lambda_K$, we have $\lambda \ll \lambda_q$ for $q \neq K$ (rest of the levels). Thus, for all the remaining levels $s \gg 1$, and for $\lambda \simeq \lambda_K$

$$\frac{\delta}{\lambda^2} = \frac{\sum_q \delta_q}{\lambda^2} = \frac{\delta_K}{\lambda^2} + \frac{1}{\lambda^2}\sum_{q\neq K}\delta_q = \frac{\delta_K}{\lambda^2} + \frac{e^2 N_A\rho}{2\pi mMc^2}\sum_{q\neq K} f_q; \tag{3.149}$$

$$\left(\frac{\delta}{\lambda^2}\right)_{\lambda\to 0} = \frac{e^2 N_A\rho}{2\pi mMc^2}\sum_q f_q = \frac{e^2 N_A\rho}{2\pi mMc^2} Z_M, \tag{3.150}$$

where the sum is over all the atoms of the molecule, and $\sum_q f_q = Z_M$, even though $f_K < z_K$. The reason for this last statement is that when a K electron is ejected in an absorption process, an electron from a higher level can fill the vacancy and absorb at the K level. Thus, a transfer of part of the oscillator strength of other levels to the K level occurs. The total oscillator strength will then be equal to Z for the whole atom, and Z_M for the molecule.

For $\lambda \gg \lambda_K$, the dispersion of the K electrons is cut out, (3.147), and

$$\left(\frac{\delta}{\lambda^2}\right)_{\lambda\to\infty} = \frac{e^2 N_A\rho}{2\pi mMc^2}(Z_M - f_K). \tag{3.151}$$

For $\lambda \simeq \lambda_K$, we can use (3.149) with $\sum_{q\neq K} f_q = Z_M - f_K$, and (3.144) for δ_K/λ^2 together with (3.145, 150), to get

$$F \equiv \frac{2\pi mMc^2}{e^2 N_A\rho}\frac{\delta}{\lambda^2} - Z_M = \frac{2^8\exp(-4)}{9}\left[\frac{2}{(1-\Delta_K)^2}\left(\frac{1}{s^2}\ln|s^2-1|\right)\right.$$

$$\left. -\frac{1}{(1-\Delta_K)^3}\left(\frac{1}{2s^3}\ln\left|\frac{s-1}{s+1}\right| + \frac{1}{s^2}\right)\right]$$

$$= 1.82\frac{1}{s^2}\ln|s^2-1| - 0.60\frac{1}{s^3}\ln\left|\frac{s-1}{s+1}\right| - 1.20\frac{1}{s^2}. \tag{3.152}$$

Figure 3.15 shows that this result of *Hönl* agrees well with data on both sides of the K edge.

Parratt and *Hempstead* [3.37] have calculated the dispersion of copper for the wide range $0.1 < \lambda < 100$ Å (Fig. 3.16). It shows that near the absorption edges, the dispersion is essentially determined by the contribution of oscillator strengths of only one electron shell corresponding to the edge in question. Thus, Fig. 3.16 reveals that normal dispersion exists only in the region $\lambda \ll \lambda_K$. Anomalous dispersion prevails the rest of the spectrum.

3.10.3 Variation of X-Ray Atomic Scattering Factor in the Region of Anomalous Dispersion

Hönl [3.33] and *Parratt* and *Hempstead* [3.37] approximate the energy dependence of the final-state oscillator density by a power series in their theories. They obtain analytical expressions and universal curves for the anomalous dispersion of the real part of f. *Cromer* and *Liberman* [3.38] use relativistic wave functions to evaluate the photoelectric absorption coefficient, related to the imaginary part of f.

The dispersion theory is tested by the measurement of (1) refractive indices of materials, and (2) the atomic scattering factor for λ close to an absorption edge.

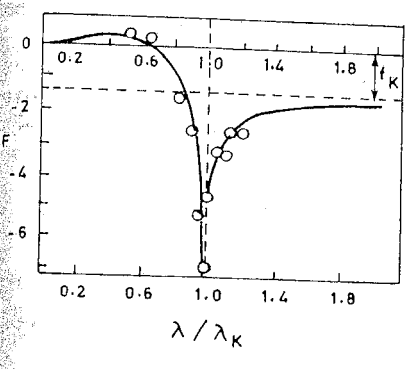

Fig. 3.15. Comparison of Hönl's dispersion theory with the data on calcite

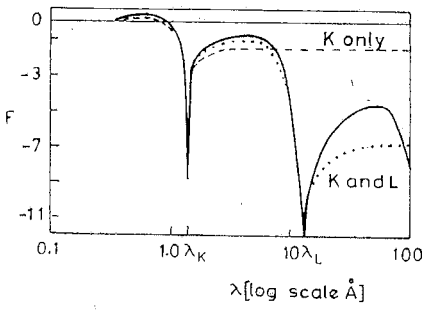

Fig. 3.16. Theoretical plot of the dispersion of copper against λ[Å] on a log scale. The result of taking only the K electrons into account is shown by the dashed curve; the result of considering both the K and L electrons is shown by the dotted curve

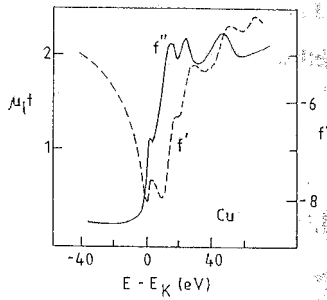

Fig. 3.17. Graph of absorption $\mu_i t$ (or f'') (solid curve) and of the anomalous dispersion correction (dashed curve) near the K edge of copper [3.44]. The latter is the Krammers–Kronig transform of the former

With the help of (3.34, 35), the atomic scattering factor, at scattering angle zero, is expressed as

$$f = \frac{m\omega^2}{2\pi e^2}\left|\sum_q z_q(\delta_q + i\beta_q)\right|$$
$$= \frac{2\pi mc^2}{e^2\lambda^2}\left|z_K(\delta_K + i\beta_K) + (Z_M - z_K)\frac{e^2\lambda^2}{2\pi mc^2}\right|, \tag{3.153}$$

where δ_q and β_q are given by the Kramers–Kallmann–Mark theory or the Hönl theory. The K electrons produce an anomalous effect. For calculations

$$f = \frac{2\pi Mc^2}{e^2\lambda^2}\left[\left(z_K\delta_K + (Z_M - z_K)\frac{e^2\lambda^2}{2\pi mc^2}\right)^2 + z_K^2\beta_K^2\right]^{1/2} \tag{3.154}$$

It agrees with the measurements on ^{26}Fe by *Glocker* and *Schäfer* [3.39] near the K absorption edge.

Experimentally f in the X-ray region is found by (i) measuring absolute integrated intensities of Bragg reflections [3.40]; (ii) determining the refractive index from total reflection [3.41, 42]; (iii) observing X-ray interference [3.43, 44]; and (iv) applying the dispersion relation to absorption spectra [3.45].

The refractive index $\mu_c = \mu - i\mu_i$ in (3.43) is given by

$$\mu = 1 - \delta = 1 - \frac{\lambda^2 e^2}{2\pi mc^2} nf'$$
$$= 1 - \frac{\lambda^2 e^2}{2\pi mc^2} n(Z + \Delta f'), \tag{3.155}$$

$$\mu_i = \beta = \frac{\lambda}{4\pi}\tau_\omega = \frac{2\pi ne^2}{m\omega^2} f'', \tag{3.156}$$

where β is related to f'' (3.87) and τ_ω is a (linear) absorption coefficient for waves of frequency ω. If λ is much shorter than wavelength of any absorption edge of the atom, then δ/λ^2 is constant and f can be taken as equal to Z. As λ approaches an absorption edge, f begins to depend on ω, and a dispersion correction $\Delta f'$ is needed. From the variation of δ/λ^2 we can find $\Delta f'$. Thus the measurement of μ gives a check on the dispersion theory. Experiments based on angular deviations give effectively $1-\delta$, and so determine $\Delta f'$. The critical angle methods are complicated by absorption.

The interference method was first used by *Bonse* and *Meterlik* [3.44a]. The intensity I_0 produced by the interference of two beams having amplitudes A_1 and A_2 and phase difference ϕ is

$$I_0 = A_1^2 + A_2^2 + 2A_1A_2\cos\phi. \tag{3.157}$$

Here A_1, A_2 are fixed while ϕ may vary. When a sample of thickness t is placed in the (say) A_2 beam, the intensity becomes

$$I_s = A_1^2 + A_2^2 e^{-\mu_l t} + 2A_1A_2 e^{-1/2\mu_l t}\cos\left(\frac{2\pi t}{\lambda}\delta + \phi\right), \tag{3.158}$$

where μ_l is the conventional linear attenuation coefficient (Sect. 3.12). The interference fringes, with and without the sample, can be analysed to provide estimates of δ and β, and hence f' and τ_q. In particular, [3.43, 44],

$$f'(E) = \frac{2\pi\phi(E)}{n\lambda r_e t} - Z, \tag{3.159}$$

where $\phi(E)$ is the phase shift of two oscillatory curves gained by rotating a phase shifter plate, one measured with the sample in the A_2 beam and one without it. The results for copper are shown in Fig. 3.17. The two distinct minima in f' correspond to inflection points in the absorption curve. In general, $f'(E)$ appears to behave like the negative derivative of $f''(E)$ [3.45, 46].

Dreier et al. [3.45] have used the fact that the imaginary part f'' (3.35, 40),

$$f''(\omega) = (\omega/4\pi r_e cn)(\tau_q), \tag{3.160}$$

is related to the real part $f'(\omega)$ of the atomic scattering factor f by the *dispersion relation* (Kramers–Kronig integral)

$$f'(\omega_0) = \frac{2}{\pi}P\int_0^\infty \frac{f''(\omega)}{\omega_0^2 - \omega^2}d\omega, \tag{3.161}$$

where P dernotes the principal value [3.47]. The imaginary part, $f''(\omega)$, is known from absorption measurements. Their results agree with those of the interferometer method.

3.11 Quantum Theory of Line Shape and Photoabsorption Curve Shape

Let w_{fi} be the transition probability per unit time of the transition $i \to f$. The total probability per unit that the atom will leave the state i in some way and make a transition to some other state f is

$$P_i = \sum_f w_{fi}. \tag{3.162}$$

When P_i is large, the time for which the atom exists in the excited state i is small. We define the *effective lifetime* of the atomic state i as

$$\tau_i = 1/P_i \tag{3.163}$$

The associated indeterminacy of the energy of the level is

$$\Delta E_i \propto 1/\tau_i = P_i. \tag{3.164}$$

This indeterminancy has a statistical meaning: The range of energy values ΔE_i at E_i will result when one atom is excited numerous times to the level i, or when many atoms are simultaneously excited to the level i.

Figure 2.15 shows that the closer the i shell is to the nucleus of the atom, the greater are the number of possible transitions $i \to f$, and so the larger is the value of P_i. We expect $\Delta E_K > \Delta E_L > \Delta E_M$, etc. The outer optical level f can, therefore, be taken to be sharp. For this reason, it is sometimes called the *resonance level*, and the linewidth and shape are completely determined by the width and shape of the internal level i for the transition $i \to f$ (Fig. 3.18).

The integral intensity of the symmetrical line, I_i, from (3.16) is

$$I_i = 2\int_{\omega_0}^{\infty} I_\omega \, d\omega = 2I_{\omega_0} \int_{\omega_0}^{\infty} \frac{d\omega}{1+\left(\frac{\omega-\omega_0}{\gamma/2}\right)^2}$$

$$= 2I_{\omega_0} \frac{1}{2}\gamma \int_0^{\infty} \frac{dx}{1+x^2} = \frac{1}{2}\pi\gamma I_{\omega_0}. \tag{3.165}$$

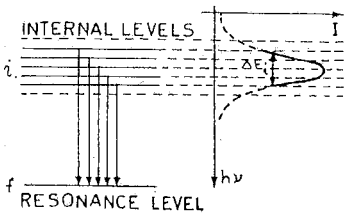

Fig. 3.18. Schematic diagram for the shape of a level

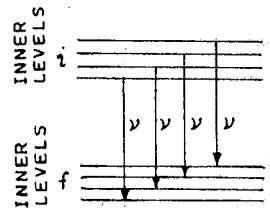

Fig. 3.19. Schematic diagram for the shape of a spectral line

Replacing I_{ω_0} by $(2/\pi\gamma)I_i$ in (3.16), we obtain the dispersion formula

$$I_\omega d\omega = \frac{2}{\pi\gamma} \frac{I_i}{1+\left(\frac{\omega-\omega_0}{\gamma/2}\right)^2} d\omega, \quad \textit{(Lorentz line shape)}. \tag{3.166}$$

By the correspondence principle, the probability $w(\omega)\,d\omega$ in the quantum theory that the emitted photon of energy $\hbar\omega$ has frequency in the range ω and $\omega + d\omega$ is given by the ratio $I_\omega\, d\omega / I_i$. Thus,

$$w(E)\,dE = w(\omega)\,d\omega = \frac{1}{\hbar} w(\omega)\,dE = \frac{\gamma_i}{2\pi\hbar\left[(\gamma_i/2)^2 + \frac{1}{\hbar^2}(E-E_i)^2\right]} \mathrm{d}E, \tag{3.167}$$

where γ_i, according to (3.23, 163), is related to P_i,

$$\gamma_i = 1/\tau_i = P_i = \sum_f p_{fi}. \tag{3.168}$$

By (3.19), $\gamma_i = \Delta\omega = (\Delta E)/\hbar$ characterizes the width of the level i, where ΔE is the FWHM value of $w(E)$.

In the X-ray emission process $i \to f$, both the i and f levels (hole states) are inner levels. Therefore, the width of the line will depend on the sum of the widths of both the initial and final states.

If the energy of the level i is between E and $E + dE$ and of the level f between E' and $E' + dE'$ after the transition, then the energy $\hbar\omega$ of the emitted photon will lie within the limits of $\hbar\omega = E - E' - dE'$ to $\hbar(\omega + d\omega) = E - E' + dE$. This means $\hbar d\omega = dE + dE'$. The line whose frequency lies between ω and $\omega + d\omega$ will arise when various transitions between the i and f levels occur (Fig. 3.19). The probability for such a complex process can be expressed as

$$w(E)w(E')\,dE dE' =$$

$$\frac{\gamma_i\gamma_f}{(2\pi\hbar)^2} \frac{dE dE'}{\left[\left(\frac{1}{2}\gamma_i\right)^2 + \frac{1}{\hbar^2}(E-E_i)^2\right]\left[\left(\frac{1}{2}\gamma_f\right)^2 + \frac{1}{\hbar^2}(E'-E_f)^2\right]}.$$

We can put $E' = E - \hbar\omega$ and integrate over all possible energies of the level i, that is, over E. As before, this gives the ratio $I_\omega\, d\omega / I_i$,

$$\frac{I_\omega d\omega}{I_i} = \int_{-\infty}^{+\infty} w(E)w(E-\hbar\omega)\,dE\,dE'$$

$$= \frac{b_i b_f}{\pi^2} da_0 \int_{-\infty}^{+\infty} \frac{da}{\left(a^2+b_i^2\right)\left[(a-a_0)^2+b_f^2\right]}$$

$$= \frac{b_i b_f}{\pi^2} da_0 \int_{-\infty}^{+\infty} \frac{da}{(a+ib_i)(a-ib_i)(a-a_0+ib_f)(a-a_0-ib_f)},$$

with

$$a = (E-E_i)/\hbar, \quad b_i = \gamma_i/2,$$

$$a_0 = [\hbar\omega-(E_i-E_f)]/\hbar, \quad b_f = \gamma_f/2,$$

$$\hbar\omega_{fi} = E_i-E_f, \quad da_0 = d(\omega-\omega_{fi}) = d\omega = (dE')/\hbar.$$

Integrating along the real axis with poles at $a = ib_i$ and $a=a_0+ib_f$ gives

$$\frac{I_\omega d\omega}{I_i} = \frac{b_i b_f}{\pi^2} da_0 2\pi i \left\{\left[\frac{1}{(a+ib_i)(a-a_0+ib_f)(a-a_0-ib_f)}\right]_{a=ib_i} + \left[\frac{1}{(a+ib_i)(a-ib_i)(a-a_0+ib_f)}\right]_{a=a_0+ib_f}\right\}$$

$$= \frac{b_i+b_f}{\pi}\frac{da_0}{(b_i+b_f)^2+a_0^2} = \frac{\gamma_i+\gamma_f}{2\pi}\frac{d\omega}{(\gamma_f/2+\gamma_f/2)^2+(\omega-\omega_{fi})^2}.$$

Writing the total linewidth as $\gamma_{if}=\gamma_i+\gamma_f=\hbar^{-1}[{}^i\Delta E)_i+(\Delta E)_f]$,

$$I_\omega d\omega = \frac{(2\pi)^{-1}\gamma_{if} I_i}{(\gamma_{if}/2)^2+(\omega-\omega_{fi})^2}\, d\omega. \tag{3.169}$$

This has the same form as the classical dispersion formula (3.166). These results were first obtained by *Weisskopf* and *Wigner* [3.48].

We can now discuss the quantum theory of the shape of the *absorption discontinuity* when the electron is removed from an inner level i to the continuous-energy region, f, of an atom (photoelectric absorption). The dispersed shape of the inner level is given by (3.167)

$$w(E_i)\,dE_i = \frac{\Gamma_i/2\pi}{(\Gamma_i/2)^2+(E_i-E_{i_0})^2}\, dE_i, \tag{3.170}$$

where E_{i_0} is the energy of the distribution maximum, and Γ_i is defined by

$$\gamma_i = (\Delta E)_i/\hbar = \Gamma_i/\hbar. \tag{3.171}$$

Let E_{f_0} denote the beginning of the continuous region of positive energies. This region can be regarded as a closely spaced set of resonance levels f. The threshold energy of the absorbed (incident) photon is $E=E_i+E_{f_0}$. If the photon has more energy than this, the electron will make a transition from the inner level E_i to one of the resonance levels E_f of the continuous set that extends beyond E_{f_0} (Fig. 3.20a). Then $E = \hbar\omega = E_i+E_f$.

The partial absorption coefficient $\tau_f(E)$ of the f resonance level, when the initial state has the distribution (3.170), is given by (Fig. 3.20b)

$$\tau_f(E) = Cw(E_i) = Cw(E-E_f) = C\frac{\Gamma_i/2\pi}{(\Gamma_i/2)^2+(E-E_{i_0 f})^2}, \tag{3.172}$$

where C is a constant and $E_{i_0 f} = E_{i_0}+E_f$. Each resonance level f will give an absorption line of the shape (3.172), Fig. 3.20b, with the same width Γ_i and

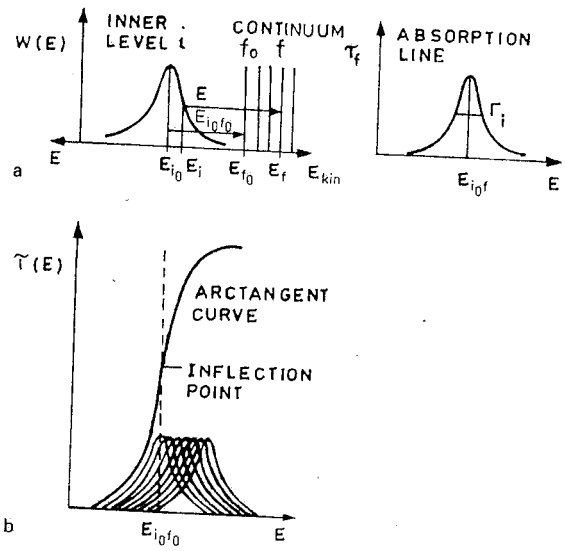

Fig. 3.20. (Topleft, **a**) Absorption of a photon of energy E by a resonance level f. (Top right, **b**) τ_f for the single resonance level f. (Bottom, **c**) Total absorption coefficient $\tau(E)$ for the entire continuum above E_{f_0}

constant C. The maxima of these lines will correspond to the energies $E_{i_0 f}$, that have the range $E_{i_0 f_0} \leqq E_{i_0 f} \leqq \infty$, where $E_{i_0 f_0} = E_{i_0}+E_{f_0}$. The set of these lines is shown in Fig. 3.20c.

The total absorption coefficient $\tau(E)$ is obtained by integrating (3.172) over all possible values of $E_{i_0 f}$,

$$\tau(E) = \frac{C\Gamma_i}{2\pi}\int_{E_{i_0 f_0}}^{\infty}\frac{dE_{i_0 f}}{(\Gamma_i/2)^2+(E-E_{i_0 f})^2} = -\frac{C}{\pi}\left(\tan^{-1}\frac{E-E_{i_0 f}}{\Gamma_i/2}\right)_{E_{i_0 f}=E_{i_0 f_0}}^{\infty}$$

$$= C\left(\frac{1}{\pi}\tan^{-1}\frac{E-E_{i_0 f_0}}{\Gamma_i/2}+\frac{1}{2}\right). \tag{3.173}$$

Here C is determined by the condition $\tau(\infty) \equiv \tau_\infty = C$ at $E = \infty$. This is drawn as the *arctangent curve* in Fig. 3.20c, and gives the shape of the absorption discontinuity.

When the photon energy E is equal to $E_{i_0 f_0}$ (Fig. 3.20a), we get $\tau(E_{i_0 f_0}) = \tau_\infty/2$. This point of the arctangent curve is the *inflection point* (Fig. 3.20c) and is identified with the energy position of the absorption edge (or the Fermi level). For the points $E_{1/4}$ and $E_{3/4}$ we have $\tau(E)$ equal to $\tau_\infty/4$ and $3\tau_\infty/4$, respectively. They are given by

$$E_{1/4} = E_{i_0 f_0}-\tfrac{1}{2}\Gamma_i, \quad E_{3/4} = E_{i_0 f_0}+\tfrac{1}{2}\Gamma_i,$$

so that

$$E_{3/4}-E_{1/4}=\Gamma_i. \tag{3.174}$$

This determines the width at half maximum of the initial state. Such an analysis was first given by *Richtmyer* et al. [3.49]. It was developed by them for the transitions of an inner-level electron to a continuous energy band of a metal. However, their approximation works better for atoms than for solids. In fact, for metals, if the correct Fermi distribution is assumed, $\tau(E)$ is given by

$$\tau(v)=A'\left(\tan^{-1}\frac{B}{(2v_e)^{1/2}-A}+\tan^{-1}\frac{B}{(2v_e)^{1/2}+A}\right)+\frac{1}{2}B'\ln\frac{v_F+D+A(2v_i)^{1/2}}{v_e+D-A(2v_e)^{1/2}}, \tag{3.175}$$

where hv_e is the difference between the Fermi energy and the mean energy of electrons in the metal,

$$A=(D+v_e+v-v_{iof_0})^{1/2},\quad B=(D-v_e+v-v_0)^{1/2},$$

$$D=[(v_e+v-v_{iof_0})^2+(\Gamma_i/2)^2]^{1/2},\quad A'=C'A,\quad B'=C'B,$$

and $C'=$constant. Level widths obtained from this exact result do not differ appreciably from those given by (3.173).

3.12 Absorption Coefficients

When an X-ray beam passes through an absorber, it is attenuated. The degree of attenuation depends on scattering and various absorption processes. Without going into the details of these processes, *Lambert's law* states that *equal paths in the same absorbing medium attenuate equal fractions of the radiation.* Suppose, for the path length dx, that the intensity I is reduced by an amount dI. Then, $dI/I \propto dx$, or

$$dI/I=-\mu_l dx,\quad I=I_0e^{-\mu_l x}, \tag{3.176}$$

where μ_l is the *linear attenuation coefficient*. The negative sign indicates that I decreases as x increases. $I=I_0$ at $x=0$. All of the quantities except μ_l can be measured. Such measurements show that μ_l depends on the state (gas, liquid or solid) of the material. Therefore, it is useful to define the *mass attenuation coefficient* μ_m, that does not depend on the particular phase of the material.

Consider an X-ray beam of intensity I with a unit cross-section. If ρ is the density of the material, a mass $dm=\rho dx$ will be crossed along the path length dx. In this layer,

$$dI/I=-\mu_m dm=-\mu_m\rho dx,\quad I=I_0e^{-\mu_m m}=I_0e^{-\mu_m\rho x}, \tag{3.177}$$

where $m=\rho x$ is the mass per unit area, or *plane density*, in g cm^{-2}. In the form (3.177), it is called the *Bouguer–Lambert–Beer exponential attenuation law*

[3.50]. The mass attenuation coefficient $\mu_m=\mu_l/\rho$ [cm^2/g] is the property of a substance. At a given λ, it is different for every substance. For a given substance, it is different for every λ. Tables are given by *Bertin* [3.51], *Henke* et al. [3.52], *Hubbell* et al. [3.53] and others. Many compilations show its need and also reveal the dissatisfaction felt by the various compilers.

Let us now find the attenuation per atom of the material. The number of atoms in dm is given by

$$dn=\frac{dm}{\text{mass of each atom}}=\frac{dm}{A/N_A}=\frac{\rho dx}{A/N_A},$$

where A is the atomic weight and N_A Avogadro's number. Thus

$$dI/I=-\mu_a dn=-(\rho N_A/A)\mu_a dx,\quad I=I_0e^{-\mu_a n}, \tag{3.178}$$

where μ_a is the *atomic attenuation coefficient*. Because dn is the number of atoms per cm^2 of a layer of material, μ_a is in cm^2. Both μ_m and $\mu_a=(\mu_l/\rho)(A/N_A)=\mu_l/n$ (cm^2/atom) are quoted for the elements.

The dimension of μ_a suggests that it can be interpreted as the atomic cross-section σ_a of the interaction. If one photon per second is incident on unit area and there is one atom per unit area of material, the probability of absorbing or scattering this photon per second will be equal to μ_a.

The *molecular attenuation coefficient* μ_{mol} gives absorption per mole per unit area (or per gramme atom per unit area)

$$\mu_{mol}=\mu_m A\,[\text{cm}^2/\text{mol}]. \tag{3.179}$$

For a compound or an alloy

$$\mu_m(\text{compound})=\sum_i \mu_{mi}W_i,\quad i=A,B,C,\ldots \tag{3.180}$$

where μ_{mi} and W_i are individual mass attenuation coefficients and weight fractions. For instance, for Cu K radiation, $\mu_m(KBr)=\mu_{mK}W_K+\mu_{m\,Br}W_{Br}=(150\times0.328)+(92\times0.672)=111.4$ cm^2/g.

The number of electrons per unit area is $dn_e=Zdn$. Therefore,

$$dI/I=-(\mu_a/Z)dn_e,\quad I=I_0e^{-\mu_e n_e}, \tag{3.181}$$

where μ_e is called the *electronic attenuation coefficient*. It has the dimension of cm^2 and is equal to μ_a/Z (Table 3.5).

When X-rays pass through matter, the intensity is decreased (attenuated) because the photons are either absorbed or scattered by the atoms of the material. Photoelectric or *true* absorption (designated τ) occurs when an inner electron of the atom is completely removed from its shell. The scattering takes place mainly because of the collision of X-ray photons with the loosely bound outer electrons of the atom. Assuming these two processes to be independent, we can express μ_a as the sum of atomic coefficients of photoabsorption τ_a and of scattering σ_a,

$$\mu_a=\tau_a+\sigma_a. \tag{3.182}$$

Table 3.5. Various attenuation coefficients

Coefficient	Dimension
Atomic μ_a	$(\text{length})^2$
Electronic $\mu_e = \mu_a/Z$	$(\text{length})^2$
Mass $\mu_m = \mu_a N_A/A$	$(\text{length})^2\ (\text{mass})^{-1}$
Linear $\mu_l = \rho\mu_a N_A/A$	$(\text{length})^{-1}$

Scofield [3.54] has prepared a theoretical photoelectric absorption cross-section data set for photon energies 1 keV to 1.5 MeV for all Z. It agrees with the semiempirical data [3.52]. For a recent review see [3.55].

Similarly,

$$\mu_l = \tau + \sigma, \quad \mu_m = \tau_m + \sigma_m, \quad \mu_e = \tau_e + \sigma_e,$$

where

$$\tau_e = \frac{\tau_a}{Z} = \frac{A}{N_A Z}\tau_m = \frac{A}{N_A Z_\rho}\tau.$$

The electronic absorption coefficient of photoabsorption, τ_e, represents an average value for all of the electrons (including the innermost K electrons) of the atom.

Although σ_m remains constant, τ_m (like τ_a) increases rapidly with λ and Z. Usually, $\tau_m \gg \sigma_m$; for example, absorption exceeds scattering by a factor of 350 even for ^{24}Cr at $\lambda \sim 1$ Å. For long wavelengths and heavier elements, $\mu_a \simeq \tau_a$ and $\mu_m \simeq \tau_m$.

For the separate q levels of the atom,

$$\tau_a = \sum_q \tau_q = \tau_K + (\tau_{L_I} + \tau_{L_{II}} + \tau_{L_{III}}) + \cdots, \quad \lambda < \lambda_K, \tag{3.183}$$

$$\tau_a = \tau_{L_I} + \tau_{L_{II}} + \tau_{L_{III}} + \tau_{M_I} + \cdots, \quad \lambda_K < \lambda < \lambda_L. \tag{3.184}$$

The variation of τ_a with λ and Z is given by

$$\tau_a \simeq CZ^4\lambda^3, \tag{3.185}$$

where the constant C decreases suddenly at each absorption edge. It is obvious from (3.185) that short-wavelength X-rays are highly penetrating; they are therefore called *hard*, whereas long-wavelength X-rays are easily absorbed and are said to be *soft*.

Another useful formula for the linear absorption coefficient away from any characteristic edges is the *Victoreen formula*, $\mu_l = C\lambda^3 - D\lambda^4$ [3.56].

At constant λ, τ_a increases with Z. If X-rays of a given λ can excite the K levels of the light elements up to a certain value of Z, at which λ becomes greater than λ_K for this element, C decreases suddenly at this Z value. Consequently, a

discontinuity occurs on a τ_a versus Z plot (Fig. 3.21). An increase of τ_a with Z again occurs until a new discontinuity is found at another Z value, where the L_I level ceases to absorb, and so on.

A useful quantity is the mass absorption coefficient of the target for its own characteristic radiation ($\nu = \nu_K$, say). In this region the absorption is mainly photoelectric. The data of *Cooke* and *Stewardson* [3.57] show that for constant incident energy

$$\tau_{mK} \propto Z^{9/2}(A_N/A)E^{-3}$$
$$\propto Z^{9/2}(A_N/A)(Z-1)^{-6} \propto Z^{-5/2}, \tag{3.186}$$

where $\nu \propto (Z-1)^2$ by the Moseley law for the $K\alpha$ radiation.

A parameter of interest is $\tau_{mK}\rho x \propto Z^{-5/2}$, where x is the depth of penetration of electrons in the target material (Fig. 3.22, curve A). For a constant value of E/E_K, $\tau_{mK}\rho x$ varies as $Z^{-5/2}E^{1.7} \simeq Z^{0.9}$ (Fig. 3.22, curve B).

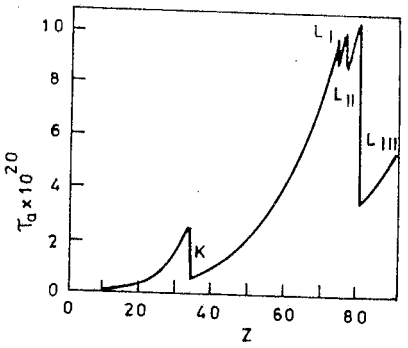

Fig. 3.21. Plot of τ_a as a function of Z for $\lambda = 1$ Å

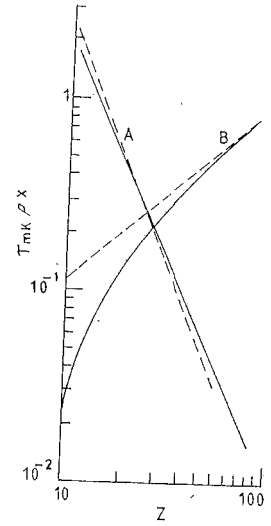

Fig. 3.22. $\gamma_{mK}\rho x$ versus Z for incident electron energy (A) $E =$ 40 keV electrons (dashed curve for $Z^{-5/2}$ variation), and (B) $E/E_K = 4$ (dashed curve for $Z^{0.9}$ variation). The electron penetration depth is x and E_K depends on Z. The full curves use ranges given by *Nelms* [3.58] and measured values of τ_m

3.12.1 Quantum Theory of Photoabsorption

The oscillator strength f_q and photoabsorption coefficient τ_q are directly related (3.93). Therefore, from the quantum theoretical result (3.131) of Sugiura, in the hydrogen-like approximation,

$$\tau_K = \frac{2^8\pi e^2}{3mc}\frac{\nu_K^3}{\nu^4}\frac{e^{-4\eta_K \tan^{-1}(1/\eta_K)}}{1-e^{-2\pi\eta_K}}, \tag{3.187}$$

where

$$\eta_K = \left(\frac{\nu_K}{\nu-\nu_K}\right)^{1/2}; \quad \nu_K = R_\infty c Z^2.$$

This result was first derived by *Stobbe* [3.59] and recently discussed by *Wagenfeld* [3.60]. It has the limiting cases:

1) $\nu \simeq \nu_K (\eta_K \gg 1)$:

$$1-e^{-2\pi\eta_K} \simeq 1, \quad \tan^{-1}\eta_K^{-1} \simeq \eta_K^{-1},$$

$$\tau_K \simeq \frac{2^8\pi e^2 R_\infty^3 \exp(-4)}{3mc^2} Z^6\lambda^4 = 1820 Z^6\lambda^4, \quad (\lambda \text{ in cm}). \tag{3.188}$$

2) $\nu \gg \nu_K \quad (\eta_K \ll 1)$:

$$1-e^{-2\pi\eta_K} \simeq 2\pi\eta_K \simeq 2\pi(\nu_K/\nu)^{1/2}, \quad \exp(-4\eta_K \tan^{-1}\eta_K^{-1}) \simeq 1,$$

$$\tau_K \simeq \frac{2^7 e^2 R_\infty^{5/2}}{3mc^2} Z^5\lambda^{7/2} = 478 Z^5\lambda^{7/2}. \tag{3.189}$$

For the L_I and $L_{II,\,III}$ states, *Stobbe* obtained

$$\tau_{L_I} = \frac{2^{11}\pi e^2}{2mc}\frac{\nu_L^3}{\nu^4}\left(1+3\frac{\nu_L}{\nu}\right)\frac{\exp(-8\eta_L \tan^{-1}|1/\eta_L))}{1-e^{-4\pi\eta_L}}, \tag{3.190}$$

$$\tau_{L_{II}} + \tau_{L_{III}} = \frac{2^{12}\pi e^2}{3mc}\frac{\nu_L^4}{\nu^5}\left(3+8\frac{\nu_L}{\nu}\right)\frac{\exp(-8\eta_L \tan^{-1}(1/\eta_L))}{1-e^{-4\pi\eta_L}}, \tag{3.191}$$

where $\eta_L = \left(\frac{\nu_L}{\nu-\nu_L}\right)^{1/2}; \quad \nu_L = R_\infty c Z^2 \frac{1}{2^2} = \frac{c}{\lambda_L}.$

The corresponding limiting expressions are,

1) $\nu \simeq \nu_L \quad (\eta_L \gg 1)$:

$$\tau_{L_I} \simeq \frac{2^5\pi e^2 R_\infty^3 \exp(-8)}{3mc^2} Z^6\lambda^4\left(1+3\frac{\lambda}{\lambda_L}\right)$$

$$= 4.17 Z^6\lambda^4(1+8.25\times 10^4 Z^2\lambda), \tag{3.192}$$

$$\tau_{L_{II}} + \tau_{L_{III}} \simeq \frac{2^4 e^2 R_\infty^4 \exp(-8)}{3mc^2} Z^8\lambda^5\left(3+8\frac{\lambda}{\lambda_L}\right)$$

$$\simeq 2.29\times 10^5 Z^8\lambda^5(3+2.20\times 10^5 Z^2\lambda). \tag{3.193}$$

2) $\nu \gg \nu_L \quad (\eta_L \ll 1)$:

$$\tau_{L_I} \simeq \frac{2^4 e^2 R_\infty^{5/2}}{3mc^2} Z^5\lambda^{7/2} = 5.98 Z^5\lambda^{7/2}, \tag{3.194}$$

$$\tau_{L_{II}} + \tau_{L_{III}} \simeq \frac{2^3 e^2 R^{7/2}}{mc^2} Z^{7/2}\lambda^{9/2} = 9.84\times 10^5 Z^7\lambda^{9/2}. \tag{3.195}$$

From these relations,

$$\tau_{L_I}/(\tau_{L_{II}} + \tau_{L_{III}}) = \begin{cases} 2/11 & \text{for } \nu \simeq \nu_L \\ (1/6)(\nu/\nu_L) & \text{for } \nu \gg \nu_L, \end{cases} \tag{3.196}$$

$$\tau_K \simeq 8\tau_{L_I} \simeq \frac{4}{3}\frac{\lambda_L}{\lambda}(\tau_{L_{II}} + \tau_{L_{III}}) \gg \tau_{L_{II}} + \tau_{L_{III}}. \tag{3.197}$$

Thus, mainly $L_{II,\,III}$ levels absorb at $\nu \simeq \nu_L$, L_I at $\nu \gg \nu_L$, and K levels at $\nu \gg \nu_K$. Measurements of the relative number of photoelectrons ejected from an atom by X-rays fully support these results.

To find the numerical values of the absorption coefficients from Stobb's equations, we should be able to calculate the frequencies ν_K and ν_L for the K and L absorption edges. For this, we can use the semiempirical method of *Slater* [3.61] (see Appendix G) to estimate the screening constants σ_q. Then

$$\nu_q = \frac{(Z-\sigma_q)R_\infty c}{n_q^2}. \tag{3.198}$$

Stobbe simplified the calculation by using $Z_{\text{eff}} = (Z-0.3)$ for the K level, and $(Z-2\times 0.85-7\times 0.35) = (Z-4.15)$ for the L level, as suggested by *Slater*, For more details, see [3.62].

3.12.2 Various Attenuation Processes

Equation (3.182) can be written in greater detail, by taking into account the various attenuation processes, as

$$\sigma_{\text{tot}} = \mu_a = \tau_a + \sigma_{\text{coh}} + \sigma_{\text{incoh}} + \kappa, \tag{3.199}$$

where σ_{tot} is the total cross-section per atom in barns/atom (1 barn = 10^{-22} cm^2), τ_a is the atomic photoelectric cross-section, σ_{coh} the coherent (Rayleigh) scattering cross-section, σ_{incoh} the incoherent (Compton) scattering cross-section, and κ the electron-positron pair-production cross-section. The mass attenuation coefficient is related to σ_{tot} by

$$\mu_l/\rho = \mu_m = \sigma_{\text{tot}} N_A/A. \tag{3.200}$$

To get an idea, the contributions to μ_l[cm^{-1}] for silicon at photon energy 8.048 KeV (Cu Kα_1) are 14.3.3 (Photoelectric), 1.861 (coherent) and 0.222 (Compton).

As discussed by *Berger* [3.63], *Allison* [3.64] and *Hubbell* [3.65], it is useful to define the *mass energy absorption coefficient* μ_{en}/ρ. It is related to, and yet distinct from, the mass attenuation coefficient μ_l/ρ. The latter is a measure of the average number of interactions between incident photons and matter that occur in a given mass-per-unit-area thickness of the material traversed. On the other hand, μ_{en}/ρ is a measure of the average fractional amount of incident photon energy transferred to kinetic energy of charged particles as a result of these interactions. Analogous to (3.200),

$$\mu_{en}/\rho = \sigma_{en} N_A/A, \quad \sigma_{en} = \tau_a f_\tau + \sigma_{incoh} f_{incoh} + \kappa f_\kappa. \tag{3.201}$$

Here the fractions f_τ, f_{incoh} and f_κ weight the corresponding cross-sections.

The agreement between experiment and theory is not good near the absorption edge. Small oscillations in the absorption coefficient (Fig. 3.17, curve f'') occur here. A double-logarithmic plot (Fig. 5.7), used to test (3.199), suppresses them. We can say that (3.199) does not give a universal prescription for finding σ_{tot} for matter in the condensed state. It is good only as far it goes.

3.13 Absorption-Jump Ratios

Figure 3.11 shows that we obtain two values of τ_m on either side of the q absorption edge at λ_q. Let us denote the mass absorption coefficient just on the short-wavelength side of λ_q by $\tau_m(\lambda_q)$ and that just on the long-wavelength side of λ_q by $\tau'_m(\lambda_q)$, $\tau_m(\lambda_q) > \tau'_m(\lambda_q)$. The ratio

$$r_q = \tau_m(\lambda_q)/\tau'_m(\lambda_q) = \tau_a(\lambda_q)/\tau'_a(\lambda_q) > 1, \tag{3.202}$$

is called the *absorption-jump ratio* of the q level.

Several empirical relations have been suggested for r_K:

1) *Jönsson* [3.66]:

$$r_K = \lambda_{L_I}/\lambda_K. \tag{3.203}$$

2) *Rindfleisch* [3.67]:

$$r_K = aZ^b, \quad \log_{10} a = 1.805283, \quad b = -0.6207. \tag{3.204}$$

3) *Laubert* [3.68]:

$$r_K = a\lambda_K^b, \quad \log_{10} a = 0.857652, \quad b = 0.0843. \tag{3.205}$$

4) *Tellez-Plasencia* [3.69]:

$$r_K = (a + bZ)^{-1}, \quad a = 0.051167, \quad b = 0.0024882. \tag{3.206}$$

The absorption curves can be fitted with the formulae [3.70],

$$\begin{aligned} \tau_a &= CZ^p\lambda^n, && \text{for } \lambda < \lambda_K, \\ \tau'_a &= C'Z^{p'}\lambda^n, && \text{for } \lambda_K < \lambda < \lambda_L, \end{aligned} \tag{3.207}$$

where, $C = 2.64 \times 10^{-26}$, $p = 3.94$, $C' = 8.52 \times 10^{-28}$, $p' = 4.30$, and $n = 3$. *Agarwal* [3.71] has shown that (3.202, 207) lead to the empirical formula (3.204).

From (3.183, 184), we get $\tau_a = \tau_K + \tau'_a$. Therefore,

$$(r_K - 1)/r_K = \tau_K/\tau_a. \tag{3.208}$$

In the region $\lambda \lesssim \lambda_K$, the photoelectric absorption is mainly because of the K-shell electrons. Therefore, $(r_K - 1)/r_K$ gives the fraction of the total number of ejected photoelectrons that come from the K shell.

In a similar way, we can find the jump ratios for the absorption edges L_I, L_{II}, L_{III}, M_I, etc. Values of r and $(r-1)/r$ for the K and L_{III} edges are given by *Bertin* [3.51].

A universal absorption curve ($\log\tau_m$ versus $\log\lambda$) was drawn by *Jönsson* [3.66]. He used τ_m for $\lambda < \lambda_K$, and $\tau_m r_K = \tau_m(\lambda L_I/\lambda_K)$ for $\lambda_K < \lambda < \lambda_{L_I}$. It can be extended on the same principle for longer wavelengths. A similar curve has been drawn by *Böklen* and *Geiling* [3.72].

3.14 Total Reflection

Let us assume that the material does not absorb X-rays, $\beta = 0$. Then $\mu = 1 - \delta$ is real and the usual laws of reflection can be applied. We have seen, (3 .59), that X-rays are totally reflected from a plane surface at glancing angles less than a certain *critical* angle θ_c, given by $\theta_c = (2\delta)^{1/2}$. For $\delta = 3 \times 10^{-6}$, we get $\theta_c = 2.4 \times 10^{-3}$ radians $\simeq 8'$.

Compton [3.7] found that, for the W L line, $\lambda = 1.279$ Å, $\theta_c = 10'$ for a sheet of plane glass and $\theta_c = 22.5'$ for a sheet of silver. These results agree with (3.59) when theoretical values of δ are used.

Prins [3.73] pointed out that the sharpness of the limit of total reflection depends on the absorption in the material. The effect is well known in optics. Let us assume the Fresnel laws of reflection to be applicable for X-rays as well. If the electric vector $E_\perp$ in the incident radiation is perpendicular to the plane of incidence, and $E'_\perp$ is the electric vector in the reflected radiation (Fig. 3.23), Fresnel's formula gives

$$E'_\perp = \frac{\sin\theta - \mu\sin\theta'}{\sin\theta + \mu\sin\theta'} E_\perp. \tag{3.209}$$

Here θ and θ' are the glancing angles of incidence and refraction, respectively. Use of $\cos\theta = \mu\cos\theta'$ and $\mu^2 = 1 - 2\delta - i2\beta$ gives

$$\frac{E'_\perp}{E_\perp} = \frac{\sin\theta - (\mu^2 - \cos^2\theta)^{1/2}}{\sin\theta + (\mu^2 - \cos^2\theta)^{1/2}}, \tag{3.210}$$

$$\frac{I'_\perp}{I_\perp} \simeq \left|\frac{\theta - (\theta^2 - 2\delta - i2\beta)^{1/2}}{\theta + (\theta^2 - 2\delta - i2\beta)^{1/2}}\right|^2 = \frac{(\theta - a)^2 + b^2}{(\theta + a)^2 + b^2}, \tag{3.211}$$

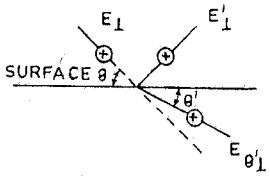

Fig. 3.23. Reflection and refraction of polarized X-rays

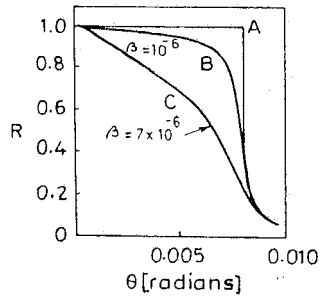

Fig. 3.24. Reflection coefficient R of iron for X-rays as a function of θ, with $\delta = 30 \times 10^{-6}$. A, negligible absorption. B, weak absorption ($\lambda \gtrsim \lambda_K$). C, strong absorption ($\lambda \lesssim \lambda_K$)

where $I'_\perp/I_\perp = R$ is the ratio of the incident and reflected intensities and

$$(\theta^2 - 2\delta - i2\beta)^{1/2} = a + ib, \quad a^2 - b^2 = \theta^2 - 2\delta, \quad ab = -\beta,$$

$$a^2 = \tfrac{1}{2}\{[(\theta^2 - 2\delta)^2 + 4\beta^2]^{1/2} + (\theta^2 - 2\delta)\},$$

$$b^2 = \tfrac{1}{2}\{[(\theta^2 - 2\delta)^2 + 4\beta^2]^{1/2} - (\theta^2 - 2\delta)\}.$$

If the electric vector of the incident X-rays lies in the plane of reflection, we get a result of slightly different form than (3.211). However, it gives the same numerical values, within the limits of experimental error [3.74].

The reflection curves given by (3.211) for zero, small and large absorption are shown in Fig. 3.24. Only the curve for $\beta = 0$ (zero absorption) shows a sharp limit of total reflection. Experimental work of *Prins* on an iron mirror clearly showed the difference of sharpness of total reflection for wavelengths on the two sides of the Fe K edge. This gaves definite evidence for the existence of anomalous dispersion.

Kiessig [3.75] measured reflection curves, for nickel mirrors deposited by evaporation on glass, with the help of an ionization spectrometer. For thin films, he detected maxima and minima as θ was altered. They were produced because of the *interference* between the X-rays reflected from the outer surface and those reflected from the nickel-glass surface inside the film. The value of δ is greater for nickel than for glass, and so the latter is a normal reflection from an optically denser medium. Because θ is small, the path difference between the rays reflected from the upper and lower surfaces is small enough to give interference even in the X-ray region. From the spacing of maxima and minima, the thickness of the nickel film can be determined. For the measurement of refractive index by X-ray interferometry, see [3.62].

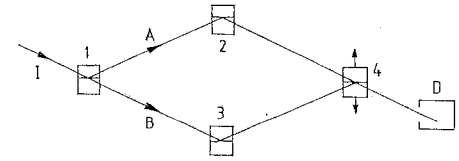

Fig. 3.25. X-ray interferometer: I: X-ray beam; 1: beam-splitter crystal; 2, 3: mirror crystals; 4: analyzer crystal; D: detector

3.15 X-Ray Interferometry

Bonse and *Hart* [3.76] used four almost perfect crystals, aligned with planes parallel to one another (Fig. 3.25). The crystals behave as if they are part of the same perfect crystal. The path lengths of the splitbeams A and B are kept equal for constructive interference; D is displaced normal to the reflective planes. At some point the path of the ray B is changed by $\lambda/2$ while the interfering ray A remains unaffected. This gives destructive interference. For displacement by exactly one lattice spacing, again constructive interference occurs. The displacement is measured by optical interferometer with simultaneous recording of the fringes. It directly gives the grating constant in absolute units. As λ is not involved in this calculation, a wide band of wavelengths is effective. A review by *Hart* and *Bonse* [3.77] gives the principles and applications of X-ray interferometry. *Deslattes* [3.78] has precisely measured the silicon lattice constant by X-ray interference. In the near future it may not be necessary to use a separate unit, like XU, for X-ray wavelengths.

X-ray interference can be used to study the bonding geometry of surface absorbates by using dynamical diffraction in both the *Bragg* [3.79, 80] and *Laue* [3.81] geometries. An X-ray standing-wave field is formed in the single-crystal surface by the interference of two coherently coupled plane waves.

4. Secondary Spectra and Satellites

In an atom, ionization can be caused not only by electron impact, but also by energetic photons. In the photoionization process, the incident photon is absorbed and a single electron is ejected. It is a one-step process, $A + h\nu \rightarrow A^+ + e^-$. It plays an important role in the absorption of X-rays in matter. During the last 20 years, X-ray photoelectron spectroscopy (XPS) has become a powerful tool to probe the interactions within atoms, molecules and solids, starting with the work of *Siegbahn* et al. [4.1].

Any other process occurring simultaneously with photoionization would be a two-step process. We shall briefly discuss all these processes in this chapter.

4.1 Photoelectric Effect

In XPS, more commonly known as ESCA (electron spectroscopy for chemical analysis), one usually measured photoelectron line intensities and angular distributions. We deal here with the simple case of atoms. The theory of photoionization cross-section and angular distribution for the absorption by a K electron will give some insight into the process.

An incident quantum $h\nu_0$ of X-rays can remove a K electron, for example, out of an atom and thus cause the emission of K characteristic radiation, provided that $h\nu_0 \geqq E_K$, where E_K is the binding energy of the K electron. The incident photon is absorbed in the process. The ejected electron is called a *photoelectron* and the emitted characteristic radiation is called *fluorescent* (or *secondary*) radiation. Such a photoabsorption process is responsible for the *true* absorption of X-rays. This phenomenon is the X-ray counterpart of the photoelectric effect in the ultraviolet region; there, photoelectrons are ejected from the outer shells of a metal atom. Einstein showed that a proper energy-conservation equation can be written from the viewpoint of the quantum theory.

$$h\nu_0 = \tfrac{1}{2}mv^2 + E_q, \tag{4.1}$$

where $mv^2/2$ is the kinetic energy of the ejected electron and E_q is binding energy of the electron in the q shell.

4.2 Quantum Theory of the Photoelectric Effect

4.2.1 Born Approximation

Fot a K-shell electron

$$E_q = E_K = \frac{mZ^2e^4}{2\hbar^2} = \frac{1}{2}Z^2\left(\frac{e^2}{\hbar c}\right)^2 mc^2 = \frac{1}{2}Z^2\frac{mc^2}{137^2}. \tag{4.2}$$

For most of the elements $Z \ll 137$, and $E_q \ll h\nu_0 \ll mc^2$. Therefore, from (4.1), $h\nu_0 - E_q = mv^2/2$, we have $mv^2/2 \gg (1/2)Z^2mc^2/137^2$, or

$$\frac{Z}{137}\frac{c}{v} \ll 1. \tag{4.3}$$

This is the criterion for the validity of the Born approximation.

From (2.130), the matrix element for the absorption of a photon is

$$H' = -\frac{e}{m}\left(\frac{\hbar}{V\nu_0}\right)^{1/2}\int \psi_f^*(\boldsymbol{p}_{op}\cdot\boldsymbol{e}_0)e^{i\boldsymbol{k}_0\cdot\boldsymbol{r}}\psi_i d\tau, \tag{4.4}$$

where $\boldsymbol{p}_{op}$ is the momentum operator of the electron, and $\boldsymbol{k}_0$, $\boldsymbol{e}_0$ are the propagation and unit polarization vectors of the incident photon, For the K-shell electron

$$\psi_i = \left(\frac{a^3}{\pi}\right)^{1/2}e^{-ar}, \quad a = Z/a_0, \quad a_0 = \hbar^2/me^2. \tag{4.5}$$

Because of the large volume V of the cube taken, $V \gg a$, we have simply normalized ψ_i over the whole space.

In the Born approximation, ψ_f is a plane wave normalized to the cube,

$$\psi_f = V^{-1/2}e^{i\boldsymbol{p}\cdot\boldsymbol{r}/\hbar}, \tag{4.6}$$

where $\boldsymbol{p}$ is the momentum of the ejected (free) electron. Because $\boldsymbol{P}_{op}$ is Hermitian, and ψ_f is an eigenstate of momentum,

$$\langle f|\boldsymbol{p}_{op}\cdot\boldsymbol{e}_0 e^{i\boldsymbol{k}_0\cdot\boldsymbol{r}}|i\rangle = \boldsymbol{p}\cdot\boldsymbol{e}_0\langle f|e^{i\boldsymbol{k}_0\cdot\boldsymbol{r}}|i\rangle,$$

$$H' = -\frac{e}{mV}\left(\frac{a^3\hbar}{\pi v_0}\right)^{1/2}\boldsymbol{p}\cdot\boldsymbol{e}_0\int_V e^{i(\boldsymbol{k}_0-\boldsymbol{p}/\hbar)\cdot\boldsymbol{r}}e^{-ar}d^3\boldsymbol{r}, \tag{4.7}$$

where $\boldsymbol{p}$ is number.

The factor e^{-ar} allows the integration over V to be extended over all space. Consider the integral

$$\begin{aligned}\int d^3\boldsymbol{r}e^{i\boldsymbol{\lambda}\cdot\boldsymbol{r}}\frac{e^{-ar}}{r} &= \int_0^{2\pi}d\phi\int_0^{\pi}\sin\theta\,d\theta\int_0^{\infty}r^2dr e^{i\lambda r\cos\theta}\frac{e^{-ar}}{r}\\ &= 2\pi\int_0^{\infty}rdre^{-ar}\int_{-1}^{+1}d(\cos\theta)e^{i\lambda r\cos\theta}\\ &= \frac{2\pi}{i\lambda}\int_0^{\infty}dre^{-ar}(e^{i\lambda r}-e^{-i\lambda r})\\ &= \frac{2\pi}{i\lambda}\left(\frac{1}{a-i\lambda}-\frac{1}{a+i\lambda}\right) = \frac{4\pi}{a^2+\lambda^2}.\end{aligned} \tag{4.8}$$

Differentiation of this integral with respect to a gives

$$\int d^3\boldsymbol{r}e^{i\boldsymbol{\lambda}\cdot\boldsymbol{r}}e^{-ar} = \frac{8\pi a}{(a^2+\lambda^2)^2}. \tag{4.9}$$

From (4.7, 9),

$$H' = -\frac{e}{mV}\left(\frac{a^3\hbar}{\pi v_0}\right)^{1/2}(\boldsymbol{p}\cdot\boldsymbol{e}_0)\frac{8\pi a}{(a^2+\lambda^2)^2}, \tag{4.10}$$

where $\lambda = \boldsymbol{k}_0 - \boldsymbol{p}/\hbar$.

The differential cross-section is given by

$$d\sigma = \frac{w}{v/V} = \frac{V}{v}\frac{2\pi}{\hbar}\rho_f|H'|^2\,d\Omega, \tag{4.11}$$

where ρ_f is the density of the final states and the incident flux is v/V. For the photon $v = c$. For the photoelectron in the final state, $\varepsilon^2 = c^2p^2 + m^2c^4$, $\varepsilon d\varepsilon = c^2pdp$. From phase-space considerations, the number of states with momenta between p and $p+dp$ is $\rho_p\,dpd\Omega = p^2\,dpd\Omega/(h^3/V)$. Therefore, the number of states for the photoelectron that has energy between ε and $\varepsilon+d\varepsilon$ is $\rho_\varepsilon d\varepsilon d\Omega = (p\varepsilon/h^3c^2)d\varepsilon d\Omega$ and, with total final energy $\varepsilon \simeq mc^2$,

$$\begin{aligned}d\sigma &= \frac{V}{c}\frac{2\pi}{\hbar}\frac{mpV}{h^3}\frac{64\pi e^2\hbar a^5(\boldsymbol{p}\cdot\boldsymbol{e}_0)^2}{m^2V^2v_0(a^2+\lambda^2)^4}d\Omega\\ &= 32Z^5a_0^2\frac{pc}{h\nu_0}\left(\frac{\boldsymbol{p}\cdot\boldsymbol{e}_0}{mc}\right)^2\frac{1}{(Z^2+a_0^2\lambda^2)^4}d\Omega.\end{aligned} \tag{4.12}$$

For $h\nu_0 \gg E_B$, we can write (4.1) as $h\nu_0 \simeq p^2/2m$. Therefore,

$$\begin{aligned}&\frac{pc}{h\nu_0}\left(\frac{\boldsymbol{p}\cdot\boldsymbol{e}_0}{mc}\right)^2 \simeq \frac{2p}{mc}(\hat{\boldsymbol{p}}\cdot\boldsymbol{e}_0)^2,\\ &\lambda^2 = \hbar^{-2}(\hbar\boldsymbol{k}_0-\boldsymbol{p})^2 = \hbar^{-2}[(h\nu_0/c)^2 - 2(h\nu_0/c)p\hat{\boldsymbol{k}}_0\cdot\hat{\boldsymbol{p}} + p^2]\\ &\quad \simeq \hbar^{-2}[p^2 - (p^3/mc)\hat{\boldsymbol{k}}_0\cdot\hat{\boldsymbol{p}} \simeq (p/\hbar)^2[1-(v/c)\hat{\boldsymbol{k}}_0\cdot\hat{\boldsymbol{p}}],\end{aligned} \tag{4.13}$$

where we have used $k_0 = 2\pi\nu_0/c$, $\hat{\boldsymbol{p}} = \boldsymbol{p}/p$, $\hat{\boldsymbol{k}}_0 = \boldsymbol{k}_0/k_0$, and $h\nu_0/c \simeq p^2/2mc \ll p$ for the nonrelativistic electron ($p \ll mc$). Thus, with kinetic energy $E = p^2/2m$,

$$\frac{d\sigma}{d\Omega} = \frac{64Z^5a_0^2\alpha^8(2E/mc^2)^{1/2}(\hat{\boldsymbol{p}}\cdot\boldsymbol{e}_0)^2}{\left[(\alpha Z)^2 + \frac{2E}{mc^2}\left(1-\frac{v}{c}\hat{\boldsymbol{k}}_0\cdot\hat{\boldsymbol{p}}\right)\right]^4}. \tag{4.14}$$

Let $\hat{\boldsymbol{k}}_0$ be along the z axis, and the two photon-polarization directions $\boldsymbol{e}_0^{(1)}$, $\boldsymbol{e}_0^{(2)}$ be along the x and y directions, respectively. Let $\boldsymbol{p}$ make an angle θ with the z axis, so that

$$\begin{aligned}&\hat{\boldsymbol{p}} = (\sin\theta\cos\phi, \sin\theta\sin\phi, \cos\theta),\\ &(\hat{\boldsymbol{p}}\cdot\boldsymbol{e}_0^{(1)})^2 = \sin^2\theta\cos^2\phi, \quad (\hat{\boldsymbol{p}}\cdot\boldsymbol{e}_0^{(2)})^2 = \sin^2\theta\sin^2\phi.\end{aligned} \tag{4.15}$$

For unpolarized photons, we average over the two polarization directions,

$$\langle(\hat{p}\cdot\boldsymbol{e}_0)^2\rangle_{\mathrm{av}} = \tfrac{1}{2}(\sin^2\theta\cos^2\phi + \sin^2\theta\sin^2\phi) = \tfrac{1}{2}\sin^2\theta. \tag{4.16}$$

with $\hat{k}_0\cdot\hat{p} = \cos\theta$, finally

$$\frac{d\sigma}{d\Omega} \simeq f(\alpha, a_0/Z)F(\theta), \quad f(\alpha, a_0/Z) = 2^{3/2}Z^5\alpha^8 a_0^2\left(\frac{E}{mc^2}\right)^{-7/2},$$

$$F(\theta) = \frac{\sin^2\theta}{\left(1-\frac{v}{c}\cos\theta\right)^4} \simeq \sin^2\theta\left(1+4\frac{v}{c}\cos\theta\right), \tag{4.17}$$

where for light elements $h\nu_0 \gg E_B$, or equivalently $(\alpha Z)^2(mc^2/2E) \ll 1$.

Because $h\nu_0 \simeq E$, and the integrated cross-section is related to the mass absorption coefficient $\tau_m = N_A\sigma/A$, we find that $\tau_m \propto v_0^{-7/2}Z^5$, or $\tau_m = \mathrm{const}\,\lambda_0^{3.5}Z^5$, in agreement with (3.189).

The angular distribution is given by $F(\theta)$. It is a $\sin^2\theta$ distribution for $v/c \ll 1$. No photoelectrons are emitted in the forward direction $\theta = 0$ and the maximum emission occurs at $\theta = \pi/2$ (Fig. 4.1a). A simple reason for this is that the ejected electron accepts the unit of angular momentum transferred in the absorption process (dipole selection rule). In the ionization of an s electron to a p photoelectron, the axis of the p-wave function is defined by the electric vector of the radiation. If this is taken as the z axis, the angular part of the electron wave function is the same as that of an atomic p_z electron, Y_{10}, and the probability is proportional to $Y_{10}^2 = (3\pi/4)\cos^2(90-\theta) = (3\pi/4)\sin^2\theta$. For large values of v/c (hard X-ray region) the retardation term $(v/c)\cos\theta$ in the denominator gives a strong tilt in the forward direction because of the fourth power.

The above results break down for very low or very high energies. At low energies (near the absorption edge), $h\nu_0 \sim E_q$, the ψ_f cannot be taken as a plane

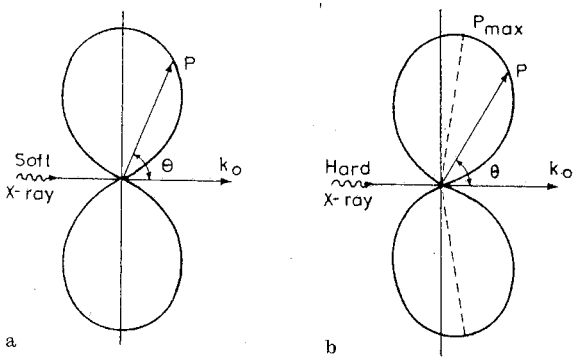

Fig. 4.1a, b. Angular distribution of the photoelectrons for **a** soft X-rays, and **b** hard X-rays

wave. The Coulomb wave function for positive energy must be used. *Stobbe* [4.2] obtained the result (3.187) in this way. The cross-section is diminished near the K edge ($\eta_K \to \infty$) by a factor $2\pi\exp(-4) = 0.12$. For the relativistic case, $v \sim c$, the calculations have been done by *Sauter* [4.3]. The cross-section here falls as v_0^{-1}.

For L-shell electrons, results have been obtained by *Schur* [4.4]. For a calculation for atoms, see the work of *Cooper* and *Zare* [4.5].

For the core electrons (those not in the valence shells) the XPS line intensities can be assumed to be independent of the molecular binding or slid-state effects [4.6]. So for a simple quantitative analysis of a solid sample it is enough to know the atomic photoionization cross-sections $\sigma_{z,nl}$ measured by, say, *Scofield* [4.7]. *Carter* et al. [4.6] give the formula

$$\frac{I_{Z,nl}}{I_{C,1s}} = \frac{\sigma_{Z,nl}}{\sigma_{C,1s}}\left(\frac{h\nu - E_q(Z,nl)}{h\nu - 285}\right)^{1/2},$$

where the C_{1s} peak is the chosen intensity standard. The square-root term arises [4.8] because the electron mean free path is proportional to $(\mathrm{K.E.})^{1/2}$, where K.E. is the kinetic energy.

An early calculation by *Yang* [4.9] gives the angular distribution for the process $A + r \to A^+ + e^-$ as

$$F(\theta) = a + b\cos^2\theta,$$

where θ is measured from the electric vector of the X-rays. It is recast as

$$d\sigma/d\Omega = (\sigma/4\pi)[1+\beta P_2(\cos\theta)],$$

$$P_2(\cos\theta) = \tfrac{3}{2}\cos^2\theta - \tfrac{1}{2}, \quad -1 \le \beta \le 2, \tag{4.18}$$

where the *asymmetry parameter* β characterizes the angular distribution. The range of β ensures that the cross-section is non-negative [4.10]. The $\cos^2\theta$ distribution results for $\beta = 2$. At the "magic" angle $\theta = \cos^{-1}\sqrt{1/3} = 54.74°$ the $P_2(\cos\theta)$ vanishes. Then the photocurrent is proportional to σ, independent of both the polarization of the X-rays and the photoelectron angular distribution. For more details see [4.11].

4.2.2 Shake-up Structure

Strictly speaking, photoionization is a transition between two states characterized by N-electron wave functions [4.12]. The one-electron approximation has, therefore, only a limited validity. In this approximation the primary states are the ones roughly described by Koopmans' theorem, in the sense that the electron density in the ionic state resembles the original system with a hole in the concerned orbital. The most-probable continuum wave function is the one that results when the photoelectron accepts the unit of angular momentum transferred in the absorption process [4.13]. In such a simple description, the relaxation of the passive electrons' orbitals toward the hole in the final state, to

minimize the total energy of the system, has been ignored. This relaxation, even without explicitly involving configuration interaction (spin–orbit and spin–spin), constitutes a many-body effect and has important consequences for both the energy and intensity of the primary states.

The perturbation of the Coulomb potential felt by the outer electrons, when a core-level electron is ejected, causes their collapse towards the positive hole, creating the relaxation energy E_q^R and allowing the possibility of excitation of the valence electrons. The *shake-up* and *shake-off* processes are manifestations of this relaxation phenomenon.

The relaxation of the valence electrons reduces the energy of the final state by E_q^R, Thus $E_q' = E_q - E_q^R$, where E_q is the orbital energy when an electron is removed from the q orbital, all other energy levels remaining undisturbed (Koopmans' theorem frozen-orbital value). Experimentally, high energy peaks on the high-binding-energy side of the core level X-ray photoelectron spectroscopy (XPS) peaks have been observed in compounds of the transition elements and in rare gases. They may be regarded as the excitation of a valence electron to an unoccupied level (shake-up) simultaneously with the core-electron ejection. The separation of the shake-up satellites in XPS from the main core-level (primary) peak corresponds to the valence-level excitation energies concerned. The shake-up structure (Fig. 4.2) observed in XPS is of much current theoretical [4.14, 15] and experimental [4.16, 17] interest.

The shake-off process can also occur when the second electron is ejected rather than excited (a double-ionization process). The partition of the kinetic energy between the two ejected electrons shows up as steps followed by a continuum, instead of the peaks found for the shake-up. Because there is always a finite value of E_q^R, it follows that there must always be shake-up and shake-off structures, even if their intensities are low. The selection rules for the shake-up transitions are $\Delta L = 0, \pm 2$. The many-electron and final-state effects in photoemission in solids have received considerable attention in recent years [4.18].

Recently a *resonance effect* has been found in photoelectron spectra. There is emission enhancement observed in outer core levels at the onset of excitations from deeper core levels. It can be understood in terms of Fano resonance [4.19, 20], that is, one discrete state interacting with a continuum. On oxidation of Yb ($4f^{14}$) one $4f$ electron is lost to a bonding orbital leaving the ground state configuration $4f^{13}$ in Yb_2O_3. This situation is close to the Fano model. Near

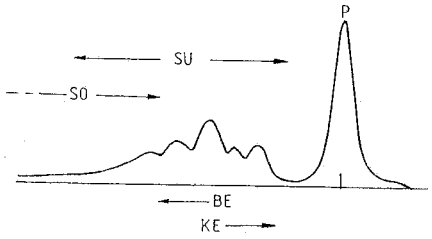

Fig. 4.2. Photoelectron spectrum (schematic) showing shake-up (SU) and shake off (SO) satellites. The peak P is due to the single hole ionization

the 4d absorption edge (~180 eV) *Johansson* et al. [4.21] found a pronounced enhancement in the peak at 12 eV binding energy. It is ascribed to the intereference between an autoionization process $4d^{10}4f^{13} \rightarrow 4d^9 4f^{14}$ (absorption) $\rightarrow 4d^{10}4f^{12} + e$ (autoionization), and the direct photoemission from the valence band $4d^{10}4f^{13} \rightarrow 4d^{10}4f^{12} + e$. Interference occurs (Fano resonance) because the initial and final states are the same [4.22].

The theory of photoemission involves a description of (i) the equilibrium and excited electronic structure of a material, (ii) its interaction with ion array, and (iii) the incident X-rays. No complete theory has yet been developed. Sophisticated Hartree–Fock based models exist [4.23] which include both many-electron and relativistic effects.

Although they depend on material and frequency, the penetration depths of X-rays in solids are always more than 100 Å. In XPS (5–1500 eV), the escape (or penetration) depths are less than 40 Å. Thus ESCA gives information about *surface* properties.

4.3 Experimental Systems

In XPS the sample (gas, liquid or solid) is bombarded by monochromatic soft X-rays. *Henke* [4.24] designed a low-Z anode X-ray tube (Fig. 4.3) for this. The spectrum of elements like Mg and Al is dominated by the intense $K\alpha$ line (Mg 1253.4 eV, Al 1486.6 eV). A beryllium window (10–30 μm thick) is reasonably transparent to them. In the ultra-soft X-ray region (100–200 eV) *Krause*

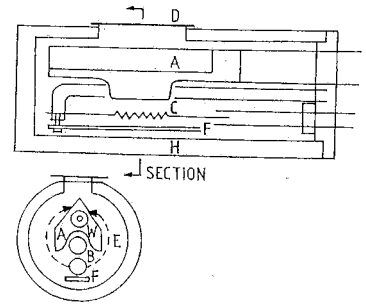

Fig. 4.3. Demountable Henke X-ray tube. A: anode, C: cathode, F: focusing strip, D: thin window, H: tube housing, W: water cooling for the anode, E: electron path. Except for the anode, the entire tube is grounded

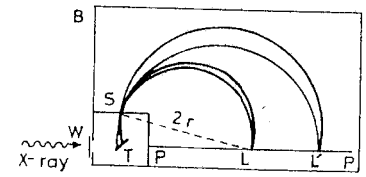

Fig. 4.4. Robinson's magnetic spectrograph, B: evacuated box, W: window, T: target of the sample material, S: slit, and PP: photographic plate. The known magnetic field H is applied perpendicular to the plane of the diagram. E_{kin} can be calculated from He $v/c = mv^2r$, as r is measured

[4.25] suggested the use of the Mζ transition ($4p_{3/2} \rightarrow 3d_{5/2}$) in the elements Y to Mo (for example, Y 132.3 eV, Zr 151.4 eV) with a thin polymeric window.

Hovland [4.26] deposited a thin layer ($\sim 10^3$ Å) of the specimen material on a thin Al foil (~ 6 μm). A sharp scanning electron beam falling on the other side of the foil produced Al X-rays in a small area. They excite photoelectrons from the corresponding spot on the specimen.

For the study of valence states (sensitive to chemical binding), low energy photons from a rare-gas discharge tube [He(*I*) (21.2 eV) or He(*II*) (40.8 eV)] are used. Then it is called ultraviolet photoelectron spectroscopy (UPS).

In recent years, monochromatized synchrotron radiation has become a superior single source for both XPS and UPS [4.27]. It has reduced the distinction between them. Both are commonly called ESCA to emphasize that binding energies are unique to each atom. This radiation is intense, collimated and polarized. The polarized photons can give information on the symmetry of the electronic states being probed.

The ESCA has its origin in the early work of *Robinson* and *Rawlinson* [4.28]. In their magnetic spectrograph (Fig. 4.4) the photoelectrons of *equal velocity* were focused by a known (transverse) magnetic field on a photographic plate. The high-energy cutoffs of the broad recorded bands were related to E_q. *Siegbahn* [4.1] received the 1981 Nobel Prize for developing a high-resolution photoelectron spectrometer using a magnetic analyzer. The photographic recording is replaced by a multichannel detector (usually an electron multiplier with gain of the order of 10^6 in the pulse counting mode). The resolution ultimately depends on the monochromaticity of the X-rays. The limiting factor is the inherent linewidth of the $K\alpha$ line of the anode (Mg or Al, say).

A modern ESCA instrument employs an electrostatic analyzer rather than a magnetic one. Common are hemispherical [4.29, 30] and cylindrical mirror analyzers (CMAS) [4.31–33]. The electrons are dispersed according to their kinetic energy along a radial or axial coordinate after being reflected by a potential-V applied to the outer cylinder of a CMA. A typical CMA is shown in Fig. 4.5. The collection efficiency depends on the electron energy [4.34]. For a lower resolution [higher $\Delta E_{\text{kin}}/E_{\text{kin}} = 21$ (sin $\theta \Delta\theta)^3$] higher efficiency is achieved. The efficiency η of a dispersive analyzer [4.35] is given by

$$\eta \propto (AB\Omega)\,\delta E_{\text{kin}}, \tag{4.19}$$

where A is the source area, B the intensity of the electron source, Ω the solid angle over which the electrons are accepted into the energy analyzer, and δE_{kin} is the range of electron energies analyzed at one time by (say) the multichannel

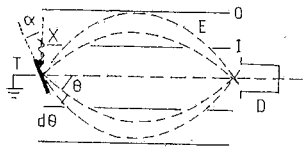

Fig. 4.5. Cylindrical mirror electron energy analyzer (CMA). *T*: target, *X*: X-rays, *E*: electron path, *D*: electron multiplier, *I* and *O*: coaxial cylinders of the analyzer

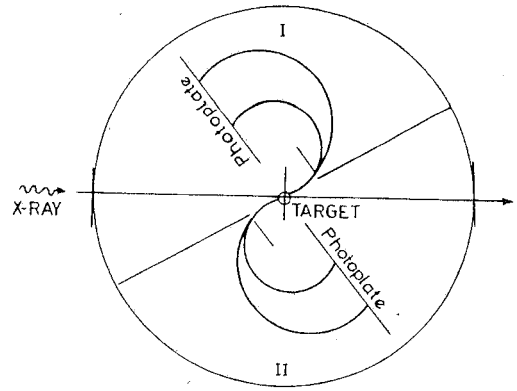

Fig. 4.6. Watson's magnetic spectrograph

detector. The δE_{kin} is about 10% of E_{kin}, while the resolution ΔE_{kin} is about 0.01% of E_{kin}, for a detector of $\lesssim 1000$ channels.

The XPS instruments for measuring E are readily modified for angle resolved studies [4.36] to give $E(\theta)$. *Watson* [4.37] used the method of magnetic analysis from solid samples placed at the centre of a twin-quadrant-shaped magnetic spectrograph (Fig. 4.6). The two spectrographs (*I* and *II*) are rotated about an axis to change θ. The measurements confirm the result (4.17). In the case of CMA a simple device is to place a mask with an aperture in it, at the front end of the instrument [4.38]. A rotation of the mask varies the angle of collection. For more details see [4.39].

For metallic samples the Fermi level in the sample is the reference level. Then (Fig. 4.7)

$$\begin{aligned} h\nu_0 &= E_q^{\text{vac}} + E_{\text{kin}}^{\text{vac}}, \quad E_q^{\text{vac}} = E^{\text{vac}} - E_q \\ h\nu_0 &= E_q^{\text{F}} + E_{\text{kin}}^{\text{F}} + \phi_{\text{sp}}, \end{aligned} \tag{4.20}$$

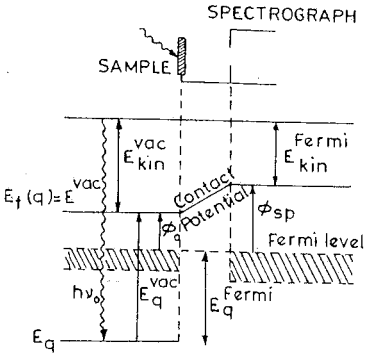

Fig. 4.7. Energy-level diagram of a metallic sample in electrical contact with the spectrograph

where E_q^{vac} is the q electron binding energy referred to the vacuum level of the sample, E_q the total energy of the initial state, $E^{vac} = E_f(q)$ the total energy of the final state with a hole in the q subshell, E_{kin}^F the kinetic energy measured in the spectrograph, and ϕ_{sp} the spectrograph work function. The work function ϕ_0 of the sample does not enter (4.20). Clearly, $E_q^{vac} - E_q^F = \phi_0$ and $E_{kin}^{vac} - E_{kin}^F = \phi_{sp} - \phi_0$. It is enough to measure ϕ_{sp} once. *Nordling* [4.40] used (4.20) to determine the binding energies of K and L electrons in elements like Cu, Zn and Ga. If the sample is not a metal, ϕ_0 is replaced by $\phi_0 + \phi_c$, where ϕ_c accounts for the charge built up on the sample.

With modern refined ESCA techniques compilations of inner-level energies have been made [4.39].

In X-ray absorption-edge spectroscopy the photon energy is varied keeping electron energy fixed (say, K level electron). The details of the spectra display the density of states for the unoccupied levels. In the XPS the energy distribution of the emitted electrons is measured keeping photon energy fixed. It gives the binding energy of the (occupied) core levels. To study the unoccupied states one can also measure *inverse photo-emission*. The sample is bombarded by an electron beam of variable energy and well-defined direction. The energy of the emitted photons is analyzed [4.41].

4.4 Auger Effect and its Relation to ESCA and X-Ray Spectra

Auger [4.42] used a Wilson chamber to study the photoeffect and observed a group of *slow* monoenergetic electrons whose energies could not be explained by the energy-conservation equation $E_{kin} = h\nu_0 - h\nu_q$. These electrons are called *Auger electrons*. Auger found that:

1) The photoelectron and the accompanying Auger electron appear at the same point (or atom).

2) The direction of ejection of the Auger electron is random and independent of the direction taken by the photoelectrons.

3) If the energy $h\nu_0$ of the incident X-rays is increased, the range of the photoelectrons increases, but that of the Auger electrons remains constant; that is, the energy of the Auger electrons does not depend on $h\nu_0$.

4) The range of the Auger electrons increases with the atomic number Z of the sample atom.

5) Not all photoelectrons are accompanied by Auger electrons.

In Auger's experiments on argon, the ejection of the photoelectron left the argon atom with a hole in the K shell. The atom can return to the ground state by various processes. We consider here two dominant processes. The first of these is the usual *radiative process* (Fig. 4.8a) in which an electron from one of the upper levels (say, L level) fills the vacancy and a characteristic emission line ($K\alpha$) is emitted, $h\nu_{K\alpha} = E_K - E_L$. The second process involves a *radiationless transition* in which, instead of the emission of the Ar $K\alpha$ line in the electronic

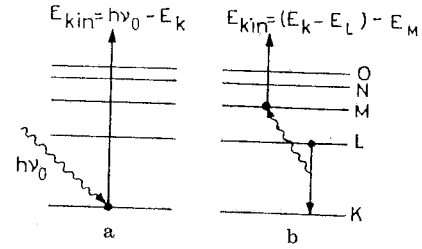

Fig. 4.8. a Photoelectron process, and **b** Auger process ($K \rightarrow LM$)

transition from the L shell to the K shell, the energy $E_K - E_L$ is taken up to eject a second L (or M) electron, resulting in the atom being doubly ionized, $K \rightarrow LM$ (Fig. 4.7b). Thus, in an Auger transition, an electron is emitted, rather than a photon, when an excited atom goes to a lower energy state.

The notation $K \rightarrow LM$ (also written as KLM) means that the initial vacancy is in the K level, and the final vacancies are in the L and M levels; the radiationless transition is $K \rightarrow L$, and the Auger electron is ejected from the M level.

The Auger process has three important consequences in X-ray spectra:

1) The Auger process competes with the radiation process in the de-excitation of an atom. Therefore, according to the theory of Weisskopf and Wigner (Sect. 3.11) it *influences the width of X-ray emission lines.*

2) The Auger process transfers a vacancy in one shell to another, and so *influences the intensity of X-ray emission lines.*

3) The Auger process leads to a state of double ionization in an atom, and so it *provides one cause for the appearance of the satellite lines in X-ray spectra* that arise from transitions in atoms doubly ionized in inner shells.

The Auger effect has been reviewed by *Burhop* and *Asaad* [4.43], *Bambynek* et al. [4.44], *Chattarji* [4.45], *McGuire* and *Holloway* [4.46], and *Fuggle* [4.47].

Typical spectra for oxygen in X-ray spectroscopy, XPS and AES (Auger electron spectroscopy) are compared in Fig. 4.9. The OK X-ray spectrum from the target Li_2CO_3 shows two K peaks as the bonding of oxygen to carbon and lithium is different (they are not α_1 and α_2). The XPS shows a sharp 1s line of

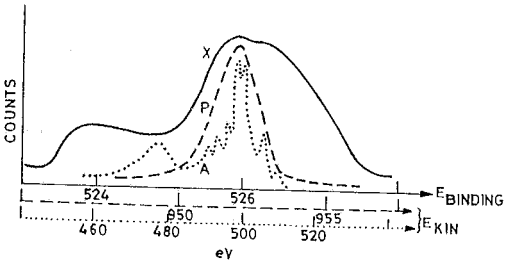

Fig. 4.9. Typical oxygen spectra in X-ray spectroscopy (X, solid) XPS (dashed) and AES (A, dotted)

oxygen in acetone CH_3COCH_3 using AlK radiation. The AES of C_3O_2 gives about eleven maxima of which the $\Delta l = 1$ selection rule accounts for six Auger lines KL_iL_j, $i \leq j = 1, 2, 3$.

4.4.1 Auger Effect and Widths of X-Ray Emission Lines and Absorption Edges

The probability that an atom in the state i has an energy between E and $E + dE$ is given by (3.167)

$$W_i(E)dE = \frac{\Gamma_i/2\pi}{(E_i - E)^2 + (\Gamma_i/2)^2} dE, \tag{4.21}$$

where E_i is the most-probable energy of the state, and Γ_i is the width of the state. If in a transition $i \to f$ a photon of approximate frequency $\nu_{fi} = (E_i - E_f)/h$ is emitted, then by (3.169),

$$I_{if}(\nu) = \frac{(2\pi)^{-2}(\Gamma_i + \Gamma_f)\nu}{(\nu_{fi} - \nu)^2 + [(2h)^{-1}(\Gamma_i + \Gamma_f)]^2}. \tag{4.22}$$

Here $I_{if}(\nu)$ is the energy radiated per transition in the frequency range ν and $\nu + d\nu$, and $\Gamma_i + \Gamma_f$ is the sum of the widths of the initial and the final states.

Let p_i^R and p_i^A be the probabilities of an atom leaving the initial excited state i by radiative and Auger transitions, respectively. The mean life-time τ of the state i is given by

$$\tau_i = 1/(p_i^R + p_i^A). \tag{4.23}$$

The uncertainty principle gives for the width Γ_i of the initial state

$$\Gamma_i = \hbar/\tau_i = \hbar(p_i^R + p_i^A) = \Gamma_i^R + \Gamma_i^A, \tag{4.24}$$

where $\Gamma_i^R = \hbar p_i^R$ is the *radiation width* and $\Gamma_i^A = \hbar p_i^A$ is the *Auger width*. Thus, the total width of the initial hole state is made up of two partial widths. The absorption can be similarly treated.

4.4.2 Auger Effect and the Intensities of X-Ray Emission Lines

Let n_i be the number of atoms per unit time ionized in an inner shell i. At equilibrium, this will equal the rate at which atoms leave the state i by all possible transitions, radiative or Auger, to states of equal or lower energy. Let $p_{i\to f}^R$ be the transition rate for a radiative transition $i \to f$, and $\Gamma_{i\to f}^R = \hbar p_{i\to f}^R$ the corresponding width.

The total number $n_{i\to f}$ of radiation quanta that correspond to the transition $i \to f$ emitted per unit time is

$$n_{i\to f} = n_i \Gamma_{i\to f}^R/(\Gamma_i^R + \Gamma_i^A). \tag{4.25}$$

Thus the Auger transition probability affects the absolute intensity of the X-ray line. For the transition $a \to b$,

$$n_{a\to b} = n_a \Gamma_{a\to b}^R/(\Gamma_a^R + \Gamma_a^A). \tag{4.26}$$

The relative intensity of the two lines,

$$\frac{I_{i\to f}}{I_{a\to b}} = \frac{\nu_{fi} n_i \Gamma_{i\to f}^R(\Gamma_a^R + \Gamma_a^A)}{\nu_{ba} n_a \Gamma_{a\to b}^R(\Gamma_i^R + \Gamma_i^A)}, \tag{4.27}$$

is also influenced by the Auger process.

If the initial state is the same, the relative intensity

$$\frac{I_{i\to f}}{I_{i\to b}} = \frac{\nu_{fi}\Gamma_{i\to f}^R}{\nu_{bi}\Gamma_{i\to b}^R}, \tag{4.28}$$

is independent of the Auger transitions from the initial state. The effect on the satellite lines will be discussed in Sect. 4.8.

4.5 Basic Theory of the Auger Effect

There are two ways of looking at an Auger process:

1) It is a process of *radiationless reorganization* of an atom ionized in an inner shell because of a *direct interaction of two electrons.*

2) A quantum of X-rays is first produced, then absorbed by an outer electron of the atom in which it originates, and finally the outer electron is ejected from the atom (*internal conversion*).

In the nonrelativistic limit, both points of view lead to the same result [4.48].

4.5.1 The Non-relativistic Theory Based on Direct Interaction of Two Electrons

Let $\psi_i(\boldsymbol{r}_1)$ and $\chi_i(\boldsymbol{r}_2)$ be the initial single-electron wave functions of the two electrons concerned, in an atom with a hole in an inner level. Let $\psi_f(\boldsymbol{r}_1)$ be the final wave function of one of the electrons in this level and $\chi_E(\boldsymbol{r}_2)$ the final wave function of the other electron in a continuum states of positive energy. The Coulomb interaction $e^2/|\boldsymbol{r}_1 - \boldsymbol{r}_2|$ is the perturbation that causes this transition. The number of radiationless transitions that occur in time dt is given by the first-order perturbation theory as

$$b_n dt = \frac{2\pi}{\hbar}\left|\int\int \psi_f^*(\boldsymbol{r}_1)\chi_E^*(\boldsymbol{r}_2)\frac{e^2}{|\boldsymbol{r}_1 - \boldsymbol{r}_2|}\psi_i(\boldsymbol{r}_1)\chi_i(\boldsymbol{r}_2)d^3\boldsymbol{r}_1 d^3\boldsymbol{r}_2\right|^2 dt. \tag{4.29}$$

We shall now see qualitatively under what conditions $b_n dt$ is large. Consider the well-known Auger process $L_I \to L_{III}M_{IV,V}$, where the radiationless transi-

tion $\psi_i \to \psi_f$ corresponds to $L_I \to L_{III}$. The wave functions are

$$
\begin{aligned}
L_I: &\quad \psi_i(\boldsymbol{r}_1) = u_{2s}(r_1)/r_1, \\
L_{III}: &\quad \psi_f(\boldsymbol{r}_1) = u_{2p}(r_1)P_1(\cos\theta_1)/r_1, \\
M_{IV,V}: &\quad \chi_i(\boldsymbol{r}_2) = u_{3d}(r_2)P_2(\cos\theta_2)/r_2, \\
E > 0: &\quad \chi_E(\boldsymbol{r}_2) = \sum_l (2l+1) f_l(kr) P_l(\cos\theta)/kr_2.
\end{aligned} \tag{4.30}
$$

Here $u_{nl}(r)/r$ is the radial part of the wave function, and for the continuum, $f_l(kr) \sim \sin(kr - l\pi/2 + \delta_l)$, δ_l being the phase shift caused by the perturbing potential. The angle θ is between $\boldsymbol{r}_2$ and the propagation vector $\boldsymbol{k}$ of the Auger electron that has the energy $E = \hbar^2 k^2/2m$. We consider only the simple case of the magnetic quantum number $m = 0$. The expansion of $1/r$ is

$$
\begin{aligned}
&1/|\boldsymbol{r}_1 - \boldsymbol{r}_2| = \sum_{n=0}^{\infty} a_n(r_1, r_2) P_n(\cos\Theta) \\
&a_n = \begin{cases} r_1^n / r_2^{n+1} & \text{for } r_1 < r_2 \\ r_2^n / r_1^{n+1} & \text{for } r_2 > r_1 \end{cases}, \\
&\Theta = \text{angle between } \boldsymbol{r}_1 \text{ and } \boldsymbol{r}_2.
\end{aligned} \tag{4.31}
$$

From (4.29–31), we get the transition rate into unit solid angle in the direction of $\boldsymbol{k}$. If $\boldsymbol{k}$ makes an angle α with the polar axis, and β is the azimuthal angle, we can integrate over all angles of ejection to find the total rate for the Auger transition. The expansion

$$
\begin{aligned}
P_l(\cos\theta) = P_l(\cos\theta_2)P_l(\cos\alpha) + 2 \sum_{m=1}^{l} \frac{(l-m)!}{(l+m)!} P_l^m(\cos\theta_2) P_l^m(\cos\alpha) \\
\cos m(\phi_2 - \beta),
\end{aligned}
$$

and a similar expansion for $P_n(\cos\Theta)$, show that the angular integrations are

$$
\iint P_n(\cos\Theta) P_1(\cos\Theta_1) \sin\theta_1 \, d\theta_1 \, d\phi_1, \tag{4.32}
$$

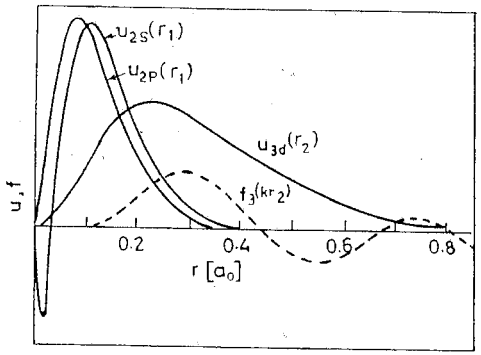

Fig. 4.10. Radial functions for the Auger-transition probability for the process $L_I \to L_{III} M_{IV,V}$

which vanishes unless $n = 1$, and

$$
\iint P_1(\cos\theta_2) P_2(\cos\theta_2) P_1(\cos\theta) \sin\theta_2 \, d\theta_2 \, d\phi_2, \tag{4.33}
$$

which vanishes unless $l = 1$ or 3. Therefore, the radial integrals are of the type

$$
\iint a_n(r_1, r_2) u_{2s}(r_1) u_{2p}(r_1) u_{3d}(r_2) f_l(kr_2) \, dr_1 \, dr_2, \tag{4.34}
$$

with $l = 1$ or 3 and $n = 1$.

In Fig. 4.10 we show the forms of the Hartree-type functions u_{nl} for $Z \sim 50$. The functions $u_{2s}(r_1)$ and $u_{2p}(r_1)$ overlap considerably to make the integral over r_1 large. The figure also shows a typical form of $f_{l=3}(kr_2)$. The asymptotic form is given by [4.49]

$$
\begin{aligned}
f_l = &\frac{(2\pi)^{1/2}}{[E + 2V - l(l+1)/r^2]^{1/4}} \\
&\times \cos\left\{ \int_R^r [E + 2V(\rho) - l(l+1)/\rho^2]^{1/2} \, d\rho \right\},
\end{aligned} \tag{4.35}
$$

where V is the effective Coulomb potential and R is the lower limit chosen so as to obtain coincidence of zero points with the numerically integrated function. If f_l has a zero in the region of r_2 where $u_{3d}(r_2)$ is large, the Auger transition rate will be small. For small k (low velocity of the ejected Auger electron) only the $l = 1$ partial wave will contribute significantly and the Auger transition probability will increase with k. As k increases, the first zero of $f_l(kr_2)$ occurs for smaller values of r_2 and eventually falls in the region where $u_{3d}(r_2)$ is large. Therefore, the major contribution to (4.34) comes from $l = 3$. For larger values of k, a great deal of cancellation occurs in the r_2 integration for all l, and the Auger transition probability decreases again. The kinetic energy $\hbar^2 k^2/2m$ of the ejected Auger electron will vary considerably with Z. Therefore, the Auger transition probability depends strongly on Z. Inclusion of the exchange integral does not alter these conclusions.

Coster and *Kronig* [4.50] were the first to employ such arguments to clear up many puzzling anomalies in L series. Detailed calculations have been carried out for Au by *Massey* and *Burhop* [4.51]. They considered transitions of the type $X_i \to X_f Y$, where X_i and X_f pertain to the same shell (say, L) but different subshells (say, L_I and L_{III}). Such transitions in Auger processes are said to give rise to radiationless processes of the *Coster–Kronig type*. If two of the final state holes are located in the same main shell as the initial hole, we get *super Coster-Kronig processes*.

4.5.2 Possible Auger Transitions of the Coster–Kronig Type ($X_i \to X_f Y$)

Let E_{X_i}, E_{X_f} be the ionization energies of the two inner sublevels and E_Y the energy of the outer level from which the Auger electron is ejected in the Coster–Kronig-type process $X_i \to X_f Y$. The kinetic energy of the Auger electron

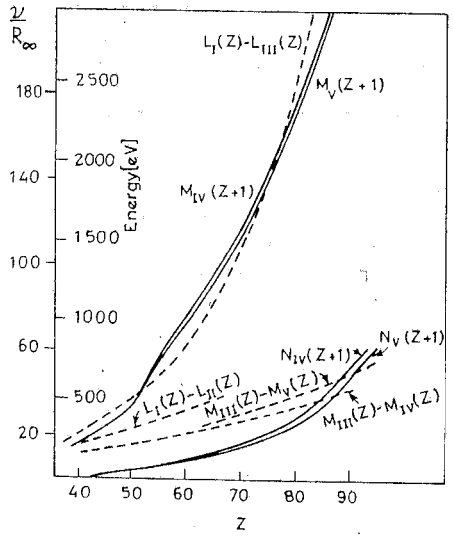

Fig. 4.11. Variation with Z of the ionization energies of the M_{IV}, M_V, N_{IV}, N_V levels (solid curves) and differences in ionization energies L_I–L_{II}, L_I–L_{III}, M_{III}–M_{IV}, M_{III}–M_V (dashed curves) to find for what ranges of Z the Coster–Kronig transitions can occur

is $E_{\text{kin}} = E_{X_i} - E_{X_f} - E_Y$. The process will occur only if $E_{\text{kin}} > 0$, or

$$E_{X_i} - E_{X_f} > E_Y. \tag{4.36}$$

In Fig. 4.11, we show the variation of $E_{X_i} - E_{X_f}$ and E_Y with Z for a number of levels that participate in the process. Clearly, the transition $L_I \rightarrow L_{III} M_{IV,V}$ is energetically possible for $Z < 50$ and again for $Z > 73$. Similarly, the transition $M_{III} \rightarrow M_{IV} N_{IV,V}$ can occur for $Z < 84$. In Table 4.1 we give a list of the possible Coster–Kronig transitions, according to *Cooper* [4.52]. In the curves of Fig. 4.11 and the figures of Table 4.1, the energies of the inner levels correspond to the atomic number Z, whereas those for the outer level correspond to the atomic number $Z+1$. Because of the change of the screening when one inner electron is missing, the outer electron sees a field of charge $Z+1$, in the first approximation. Thus, for the transition $L_I \rightarrow L_{III} M_{IV}$, to a good approximation, $E_{\text{kin}} = L_I(Z) - L_{III}(Z) - M_{IV}(Z+1)$, where the level symbol denotes the energy of the corresponding level. For the transition to occur, we must have $[L_I(Z) - L_{III}(Z)] > M_{IV}(Z+1)$. *Cauchois* [4.53] has constructed an energy-level diagram for the doubly ionized atoms from the data on the satellite lines. Table 4.2 shows $\Delta E(L_{III})$, the difference in the L_{III} ionization energy for an atom already ionized in the $M_{IV,V}$ shell and a normal atom. In our notation

$$\begin{aligned} \Delta E(L_{III}) &= (L_{III} M_{IV,V} - M_{IV,V}) - L_{III} \\ &= [L_{III}(Z) + M_{IV,V}(Z+1) - M_{IV,V}(Z)] - L_{III}(Z) \\ &= M_{IV,V}(Z+1) - M_{IV,V}(Z). \end{aligned} \tag{4.37}$$

This equation is approximately satisfied (Table 4.2).

Table 4.1. Possible Auger transitions of the Coster-Kronig type $(X_i X_f Y)$

Process	Z	Process	Z	Process	Z	Process	Z
$L_I L_{II} N_I$	<70	$M_I M_{II} M_{IV}$	<34	$M_{III} M_V N_V$	<91	$N_I N_V N_V$	<87
N_{II}	<75	M_V	<34	N_{IV}	<89	$N_{II} N_{III} o_{III}$	>66
N_{III}	<81	$M_{III} N_V$	<87	N_{III}	<77		<55
N_{IV}	<92	N_1	<50	N_{II}	<70	o_{II}	<86
$L_{III} M_I$	<31	M_V	<34	N_I	<57		>66
M_{II}	<36	M_{IV}	<34	M_V	<37		<55
M_{III}	<37	$M_{IV} M_V$	<44	$M_{IV} M_V O_{III}$	<85	N_{VII}	<80
M_{IV}	>73	M_{IV}	<43	O_{II}	<82	N_{VI}	<80
	<50					$N_{IV} N_V$	<60
M_V	>77	$M_V M_V$	<45	$N_I N_{II} O_{III}$	<88	N_{IV}	<60
	<50	$M_{II} M_{III} N_{IV}$	>65	O_{II}	<85	$N_V N_V$	<62
			<48				
$L_{II} L_{III} M_{IV}$	<30	N_V	>65			$N_{III} N_{IV} O_I$	<87
			<48				
M_V	<30	$M_{IV} N_I$	<88	O_I	<79	N_{III}	<86
	>90	M_V	<35	N_{VII}	<80	N_{VI}	<85
$M_I M_{II} N_{VII}$	<91	M_{IV}	<35				
N_{VI}	<91	$M_{III} M_{IV} N_V$	<85	N_{VI}	<80	N_V	<57
N_V	<72	N_{IV}	<84	N_V	<53	N_{IV}	<56
N_{IV}	<71	N_{III}	<71	N_{IV}	<53	$N_V O_I$	<89
N_{III}	<53	N_{II}	<65	$N_I N_{III} N_{VI}$	<92	N_{VIII}	<87
						N_{VI}	<86
N_{II}	<53	N_I	<55	N_V	<53	N_V	<57
N_I	<47	M_V	<36	N_{VI}	<53	$N_{IV} N_V O_{IV,V}$	<81
		M_{IV}	<36	$N_{IV} N_V$	<84	$N_V N_{VI} N_{VII}$	<91
				N_{IV}	<80	N_{VI}	<91
						$N_{VII} N_{VII}$	<91

Table 4.2. Difference of X-ray energy levels in eV between atoms doubly ionized and singly ionized in an inner shell [4.53]

Element	$\Delta E(L_{III})$	$\Delta E(M_V)$	$\Delta E(N_V)$	$\Delta E(O_V)$	$E_{M_{IV}}(Z+1) - E_{M_{IV}}(Z)$	$E_{M_V}(Z+1) - E_{M_V}(Z)$
78 Pt	89	52	19	0	94	89
79 Au	92	53	19	0.4	94	89
81 Tl	98	55	21	1.1	108	95
82 Pb	101	57	23	2.0	99	92
83 Bi	104	60	27	2.5	—	—
88 Ra	116	65	28	4.0	—	—
90 Th	125	70	36	6.3	122	109

We have mentioned earlier that at the ionization of the inner shells by electrons or photons there is a finite probability for an outer-shell electron to be simultaneously excited to a bound state (shake-up) or to a continuum state (shake-off). In Auger-electron spectra these multiply excited initial states give rise to satellite peaks. Other satellite peaks occur because of the excitations in the final state.

The shake-off in the M shell at the ionization of the K shell in Ar gives a satellite on the low-energy side of the normal KLL Auger line. The energy of the normal Auger transition can be written as $E = K - LL$. For the case of shake-off in the M shell, we have $E^M = KM - LLM$. The shift is $\Delta = E - E^M = K - KM - (LL - LLM)$, where $KM - K = BE$ of the M electron in the ion with a K hole = ionization potential (I) of KII. Similarly, $LLM - LL$ = ionization potential of CaIII. Thus, $\Delta = I(\mathrm{Ca}III) - I(KII) = 51.21 - 31.81 \simeq 19.4$ eV, which is in approximate agreement with the observed value 17.0 eV [4.54].

4.5.3 Auger Transitions and Widths of Levels

When the probability of Auger transition from the L_I excited state is large, the lifetime of this state is reduced consequently its width is increased. *Richtmyer* et al. [4.55] found this to be so in their study of L_I, L_{II} and L_{III} absorption edges in ^{79}Au. A fit of the arctangent curve, (3.173), to the observed shape of the edge yields the width of the initial state responsible for the absorption. The data on the widths of L levels are also available from precise measurements of the emission line widths. In Fig. 4.12a, we show the variation of the observed widths of the lines of the L series with Z [4.56, 57].

We need more information on the widths of the final states to be able to correctly assess L-level widths from these data. However, the large increase of the widths of the group of L_I lines (γ_3, γ_2, β_3, β_4) for $Z > 70$ is obvious (Fig. 4.12a). The lines β_1, γ_1, β_2 originate from an initial L_{II} or L_{III} state.

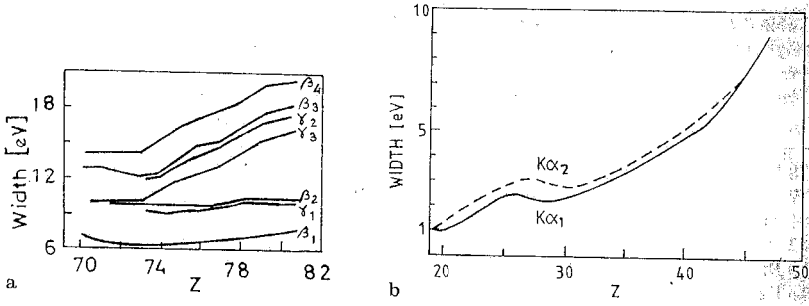

4.12a, b. Variation of the widths of the **a** L lines, and **b** K lines with Z

This marked increase with Z of the widths of L_I lines is associated with an increase of width of the L_I level for just these elements ($Z > 73$), because of the possibility of the Auger transition. In the absence of a selective Auger effect of this kind, the dependence of width on Z is determined [4.58] by the radiative transition probabilities,[1] that are proportional to Z^4. The Auger width of the K level does not depend on Z [4.59]. Therefore, a general increase of the total widths with Z can be expressed as

$$\Gamma = A + RZ^4, \tag{4.38}$$

where $A = \mathrm{const}(Z)$ gives the Auger contribution, and RZ^4 the radiative contribution. The K linewidths (Fig. 4.12b) observed by *Brogren* [4.60] confirm (4.38).

The observed level widths in gold are [4.58]:

Level	K	L_I	L_{II}	L_{III}	M_I	M_{II}
Width [eV]	54	8.7	3.7	4.4	15.5	10.7
Lifetime [10^{-18}s]	12.2	80	178	150	42.6	61.7

4.5.4 Auger Transitions and Relative Intensities of L-Series Lines

We have seen, (4.25), that the intensities of lines are influenced by the presence of the Auger process. The Auger width in (4.27) is increased for atoms in the L_1 state, as just discussed. Therefore, the intensity of lines that have L_I as the initial state is reduced, relative to the intensity of lines that have L_{II} and L_{III} as initial states. The physical reason is that because of the radiationless transitions, the holes in L_I are transferred to L_{II} or L_{III}. These levels consequently gain in holes at the expense of L_I, and so give relatively stronger emission lines when the radiative transitions finally occur.

In Fig. 4.13, we show the variation with Z of the observed intensities [4.56, 57, 61] of the lines $L\beta_3$ ($L_I \rightarrow M_{III}$) and $L\beta_4$ ($L_I \rightarrow M_{II}$) relative to $L\beta_1$ ($L_{II} \rightarrow M_{IV}$). The variation can be understood on the basis of the Coster–Kronig theory.

Figure 4.11 shows that, for the transition $L_I \rightarrow L_{III}M_{IV,V}$, the kinetic energy of the Auger electron increases from zero for Z slightly above 50 to about 100 eV for $Z = 41$, and increases rapidly for smaller Z. On the basis of the non-relativistic theory given earlier, *Coster* and *Kronig* estimated that the Auger transition for this transition reaches a maximum for an ejected-electron energy of about 100 eV. A maximum for such a small value of E_{kin} implies that *each of*

---

[1] The radiative dipole transition rate is given by $p^{\mathrm{R}}_{i\rightarrow f} = (64\pi^4\nu^3 e^2/3hc^3)|\int \psi_f^* \boldsymbol{r} \psi_i d\tau|^2$, for $h\nu = E_i - E_f$. In the hydrogenic model, say, for the $L_{III} \rightarrow K$ transition, $\psi_i = (1/8\pi^{1/2})\,(Z/a_0)^{5/2}\gamma\,\mathrm{e}^{-Zr/2a_0}\sin\theta\,\mathrm{e}^{\pm i\phi}$, $\psi_f = \pi^{-1/2}\langle Z/a_0\rangle^{3/2}\mathrm{e}^{-Zr/a_0}$, and use of $\int_0^\infty \mathrm{e}^{-ar} r^n dr = n!/a^{n+1}$ gives $p^{\mathrm{R}} \propto Z^4$.

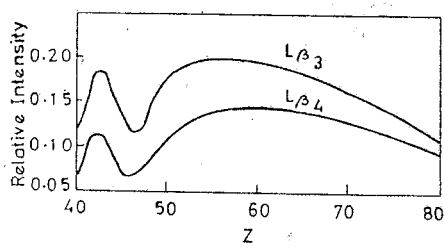

Fig. 4.13. Intensities of the lines $L\beta_3$ and $L\beta_4$, relative to that of $L\beta_1$, as a function of Z

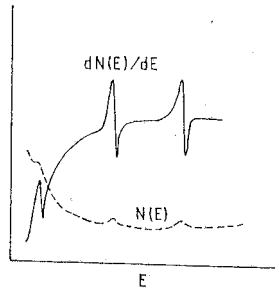

Fig. 4.14. A typical $N(E)$ and $dN(E)/dE$ plot for the Auger spectrum.

the possible Auger transitions will occur with appreciable probability for Z values near the cutoff for the transition concerned. With the help of Table 4.1, this rule explains the variation shown in Fig. 4.13.

For $Z = 40$, the Auger-transition probability for $L_I \rightarrow L_{II} M_{IV,V}$ is maximum by the above rule, and the relative intensities of $L\beta_3$ and $L\beta_4$ lines that originate in L_I show a decrease. For $Z = 42$ this Coster–Kronig transition is no longer possible (Fig. 4.11); consequently the relative intensities increase. As Z increases further, the transition $L_I \rightarrow L_{III} M_{IV,V}$ becomes possible, with a large probability at $Z = 45$ or 46. Therefore, the curves of Fig. 4.13 show a minimum around this Z value. This transition ceases to occur at $Z = 52$; therefore, the curves rise again. The final fall of the curves is because of the Coster–Kronig transition $L_I \rightarrow L_{III} M_{IV,V}$ that begins to occur at $Z > 73$.

Measurements [4.56] show that the intensities of $L\beta_2$, $L\beta_4$ relative to $L\beta_1$ and of $L\gamma_2$ ($L_I \rightarrow N_{II}$), $L\gamma_3$ ($L_I \rightarrow N_{III}$) relative to $L\gamma_1$ ($L_{II} \rightarrow N_{IV}$) decrease with increasing Z for $Z > 73$. On the other hand, the intensity of $L\beta_2$ ($L_{III} \rightarrow N_{VI}$) relative to $L\beta_1$ ($L_{II} \rightarrow M_{IV}$) remains constant for $Z > 73$, as would be expected on the basis of the foregoing arguments.

It is clear that the Auger process is very complex and is not yet fully understood. Even for free atoms, the calculations are difficult. *McGuire* [4.62] has made calculations for heavy atoms where *jj* coupling is applicable. For self-consistent-field calculations see [4.63].

4.6 Detection of Auger Electrons

Auger-electron spectroscopy (AES) has become an important tool in the study of atoms, molecules and solids. Therefore, several techniques have been developed for their detection and analysis.

In Robinson's magnetic-spectrograph analysis, the lines of Auger electrons could be easily separated from those of the photoelectrons by using the fact that

the kinetic energy of the former, unlike that of the latter, is independent of the incident-photon energy. Also, the relative intensities of photoelectrons for given incident radiation do not remain constant for large changes of Z, whereas the Auger-electron intensities remain approximately constant.

The Wilson cloud-chamber method was used by *Auger* [4.42] to photograph the Auger tracks in gases and vapours. As the frequency of the narrow beam of incident X-rays is increased, the length of the tracks of the photoelectrons increases, but that of the Auger electrons remains constant. The length of the Auger-electron tracks increases with the atomic number Z of the gas. The typical approximate values of the Auger-electron energy in the transition $K \rightarrow LL$ for different gases are given in Table 4.3. For elements of low Z, the Auger tracks are very short. For 25 keV X-rays, ^{36}Kr ($E_K \simeq 14$ keV) gives photoelectrons and Auger electrons of almost the same range. An instrument (like CMA) can be used for both XPS and AES, when the sample is a solid.

The energy distribution $N(E)$ of the secondary electrons from the top layers of a solid can be measured as a function of energy E. It shows weak, broad peaks just below the corresponding transition energies of the emitting atoms. They are superposed on photoelectron spectra when excited by X-rays. *Harris* [4.64] found that the Auger signal/background ratio is enhanced by taking the derivative of the signal. Thus $dN(E)/dE$ is recorded rather than the $N(E)$ spectra. In it each Auger peak appears as a double peak (Fig. 4.14).

Auger electrons have small and characteristic energies (mean free path ~ 10 Å). They are useful in the study of solid surfaces [4.46]. In general, three different levels are involved in an Auger process. The initial vacancy of a core level E_1 is filled by an electron from a higher level E_2, and the energy $E_2 - E_1$ set free by this transition is transferred to another electron in the valence band E_3, which comes out with a characteristic kinetic energy E_{kin} given by (see Fig. 4.15)

$$E_2 - E_1 = E_F - E_3 + E_{\text{kin}} + \phi_{\text{sp}}. \tag{4.39}$$

Note that the experiment does not distinguish between the transitions (*I*) $E_1 \rightarrow E_2 E_3$ and (*II*) $E_1 \rightarrow E_3 E_2$, because the initial and final electron configurations do not differ.

The E_{kin} for the Auger electrons is a characteristic quantity of the element and so its determination can identify the presence of certain elements in the

Table 4.3. Auger-electron energies for the Auger transition *KLL* for different gases

Element	$E_K - 2E_L$ [keV]
18 Ar	3.14
36 Kr	10.7
54 Xe	24.15
80 Hg	55.4

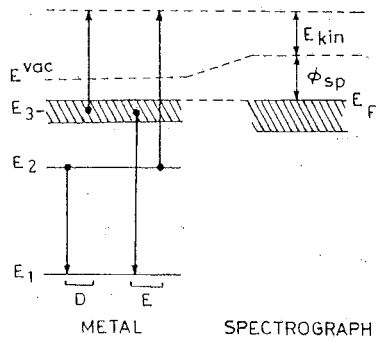

Fig. 4.15. Auger electrons come out of the surface with the same E_{kin} in the direct (D) and exchange (E) Auger processes I and II

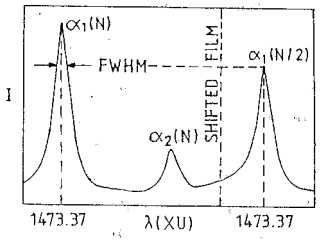

Fig. 4.16. Microphotometer record of the full-intensity (number of counts N) tungsten $L\alpha_1$, α_2 and the half-intensity (number of counts $N/2$) tungsten $L\alpha_1$ ($L_{III}M_V$) line, recorded on the same film.(After [4.70])

sample surface (ESCA). To detect these electrons, use can be made of the retarding-field analyzer (RFA), which collects all electrons with sufficient energy to surmount a variable retarding electric field in the detector. Dispersive types of magnetic or electrostatic analyzers can also be used.

Recently *McGilp* et al. [4.65] measured the $N_{VI,VII}O_{IV,V}O_{IV,V}$ Auger spectra of Tl, Pb and Bi using Mg $K\alpha$ X-ray excitation. The observed spectra are in good agreement with calculations if the initial and final states are treated in jj and $jj-LS$ (intermediate) coupling, respectively. A broad background feature with a maximum at ~ 90 eV is attributed to the presence of NNO Coster–Kronig and NNN super Coster–Kronig transitions that give rise to Auger electrons of kinetic energies between 20 eV and 120 eV. A super Coster–Kronig transition arises if the available energy is enough, not only to excite, but to eject an electron from the same shell. Evidence for $N_{II}N_{III}N_{IV,V}$ super Coster–Kronig processes in $4p$ photoelectron spectra of metallic Nb, Mo, Ru and Rb has been found by *Nyholm* and *Martensson* [4.66]. The available kinetic energy is shared by the super Coster–Kronig electron and the photoelectron, and so the latter shows a continuum instead of a sharp line in the spectrum.

4.7 X-Ray Line Width

The observed FWHM of an X-ray emission line depends on (i) life-time broadening, (ii) hyperfine interactions, (iii) multiplet splitting, (iv) solid-state and chemical effects, and (v) apparatus broadening. Of these, (ii) is extremely

small and has been measured only relatively recently [4.67]; (iii) is negligible for the deeper levels in heavy atoms; (iv) is unimportant for lines arising from transitions involving inner levels; and (v) depends on the experimental arrangement used (and can be estimated and corrected for). Thus for suitably chosen lines, the width arises from (i) and is equal to sum of the widths of the levels involved. The width of a level Γ is a direct consequence of the uncertainty relation $\Gamma\tau \sim \hbar$, where τ is the lifetime of the level; τ is equal to the reciprocal of the total transition rate (4.23) of filling the hole characterising the level. As in (4.24), the width of a level is given by

$$\Gamma = \Gamma^{R} + \Gamma^{A} + \Gamma^{C}, \tag{4.40}$$

where Γ^{C} is the Coster–Kronig width.

Self-consistent-field calculations of transition rates, both radiative [4.68] and nonradiative [4.69] are now available. The linewidth measurements provide a valuable check on the correctness of these calculations [4.44].

Gokhale [4.70] used a double exposure method to accurately measure FWHM of the $K\alpha_1$ and $K\alpha_2$ lines of elements Rb (37) to Sn (50). The line of interest is photographed on the single-coated X-ray film (height about 2 cm). The height of the line being much larger (about 8 cm), its upper portion is simultaneously detected by a scintillation counter. The film holder is then displaced parallel to itself by a small distance. The same film is again exposed, at the same ratings of the X-ray tube, until the number of counts is exactly half that of the first exposure. This gives two neighbouring impressions of the same line, one with half the intensity of the other, and both on the same background (Fig. 4.16). The width of the full-intensity line is now measured on the microphotometer record at the level of the maximum of the half intensity line. The exposures are so chosen that the density of blackening for both the exposures lies in the linear part of the response curve of the film.

The correction for the instrumental broadening effect comes mainly from crystal diffraction. For this the spectra are analyzed in terms of a function $I(z)$ that contains the Lorentzian natural shape of the line $f(x)$ and the Gaussian instrumental response $g(x)$ of the apparatus. *Amorim* et al. [4.71] take the observable function to be the convolution integral of $f(x)$ and $g(x)$,

$$I(z) = \int g(x) f(z-x)\,dx, \tag{4.41}$$

where

$$f(x) = \frac{h}{(x_0 - x)^2 + (\Gamma/2)^2},$$

$$g(x) = H \exp(-x^2/2\sigma^2). \tag{4.42}$$

Here h is the Lorentzian amplitude, x_0 the centroid of the peak, Γ the FWHM of $f(x)$, H the height of $g(x)$ and σ the width of $g(x)$. The integral is performed numerically.

Measured values of *Gokhale* et al. [4.70] are nearer to the theoretical values [4.69] than those measured by the double-crystal spectrometer [4.72].

4.8 Satellites

Close to prominent allowed diagram lines weak lines often occur in X-ray emission spectra. Because of their closeness to a strong parent line, they are called *satellites*. They are also called *nondiagram lines* because they cannot be understood as simple transitions on the usual X-ray energy-level diagram of a singly ionized atom (Fig. 2.15). The reason is that the X-ray satellite lines arise from transitions in atoms multiply ionized in inner shells. For example, $K\alpha_3$, $K\alpha_4$, the satellite lines of the parent line $K\alpha_{1,2}(K\rightarrow L)$, are produced by the transitions $KL\rightarrow LL$, $KK\rightarrow KL$, in doubly ionized atoms. The satellite lines usually occur on the high-energy side of the diagram lines. They were first observed by *Siegbahn* and *Stenström* [4.73]. Atoms doubly ionized in inner shells may be produced 1) directly by the cathode-electron impact, or 2) by an Auger transition after a single ionization.

The lifetime of an X-ray state is very short, $\sim 10^{-16}$ s. Also, the density of electrons in the cathode beam is small compared to that of target atoms. Therefore, it is almost impossible for the same atom to be struck twice in succession, resulting in two electrons being knocked out. In fact, to produce the satellites on the high-energy side of a $K\alpha$ line, the cathode electrons in an X-ray tube had to be given a minimum energy E_K+E_L, by increasing the voltage, that was sufficient to knock out a K and an L electron simultaneously, by a single impact. This led *Wentzel* [4.74] to postulate the existence of *an initial state of double ionization of the atom for the production of satellites.*

Druyvesteyn [4.75] used this postulate to assign double-ionization states for the observed satellites and to calculate their frequencies. In the Druyvesteyn–Wentzel theory, a satellite is produced when a *single* transition of the type $AY\rightarrow YB$ occurs among the doubly ionized states. The satellite is situated on the high-energy side of the parent line $A\rightarrow B$. The additional hole Y acts as a spectator.

The frequency $\nu K\alpha_{3,4}$ of the satellite $K\alpha_{3,4}(KL\rightarrow LL)$ that belongs to the parent line $K\alpha_{1,2}(K\rightarrow L)$ of an element of atomic number Z is given by

$$(h\nu_{K\alpha_{3,4}})_Z=(KL)_Z-(LL)_Z. \tag{4.43}$$

For the parent line

$$(h\nu_{K\alpha_{1,2}})_Z=K_Z-L_Z. \tag{4.44}$$

In the first approximation,

$$(KL)_Z=K_Z+L_{Z+1}, \tag{4.45}$$

$$(LL)_Z=L_Z+L_{Z'+1}, \tag{4.46}$$

where $Z'+1$ denotes that the nuclear charge is somewhat less screened, because it is an L, not a K, electron that is absent; $L_{Z+1}>L_{Z'+1}$. It follows that

$$(h\nu_{K\alpha_{3,4}})_Z=(h\nu_{K\alpha_{1,2}})_Z+\Delta, \tag{4.47}$$

where $\Delta=(L_{Z+1}-L_{Z'+1})>0$ is a small *positive* quantity. Thus, the removal of the $L_{III}(2p)$ electron increases the distance and hence the energy difference between $L(2p)$ and $K(1s)$ levels, with the resulting production of the $K\alpha_3(KL_{III}\rightarrow L_{III}L_{III})$, $K\alpha_4(KL_{III}\rightarrow L_{III}l_{II})$ satellites (Fig. 4.17). Note that KL_{II} would be the same as KL_{III}. With improved experiments and quantum mechanical calculations, five $K\alpha$ satellites have been identified [4.76–78]. The spectroscopic notations now generally accepted are shown in Fig. 4.17b. The notation is valid for the light elements ($Z<16$), where LS coupling is applicable.

The configuration $(1s^{-1}2s^{-1})$ gives rise to two even terms, $^1S_0$ and $^3S_1$. The J values that arise from $2p^{-1}$ (or $2p^5$) are the same as for a single p electron. Four terms with $J=0, 1, 1, 2$ arise. In the LS coupling, the terms of the $(1s\,2p^5)$ and $(2s\,2p^5)$ configurations can be classified as a singlet $^1P_1$ and a triplet

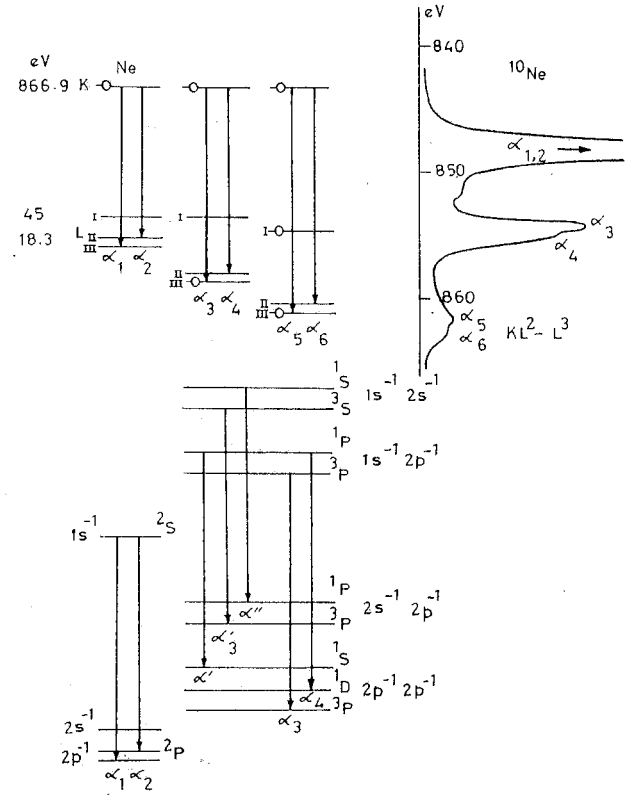

Fig. 4.17. Transitions for the $K\alpha$ satellites: (top, **a**) X-ray notation, and (below, **b**) spectroscopic notation

$^3P_{0,1,2}$, the singlet-triplet difference being large compared to the small spread of the triplet (shown as one level in Fig. 4.17b). The number of terms that arise from $2p^4$ (or $2p^{-1}2p^{-1}$) is limited by Pauli's principle, because we have equivalent holes, and only $^1D_2$, $^1S_0$, $^3P_{0,1,2}$ occur in the LS coupling. In the LS coupling, we get the following five $KL \rightarrow LL$ multiplets:

Initial configuration	Transition	Multiplet	Satellite
$KL_{II,III}$	$(1s^{-1}2p^{-1})^1P \rightarrow (2p^{-1}2p^{-1})^1S$	$^1P-{}^1S$	α'
KL_I	$(1s^{-1}2s^{-1})^3S \rightarrow (2s^{-1}2p^{-1})^3P$	$^3S-{}^3P$	α'_3
KL_I	$(1s^{-1}2s^{-1})^1S \rightarrow (2s^{-1}2p^{-1})^1P$	$^1S-{}^1P$	α''
$KL_{II,III}$	$(1s^{-1}2p^{-1})^3P \rightarrow (2p^{-1}2p^{-1})^3P$	$^3P-{}^3P$	α_3
$KL_{II,III}$	$(1s^{-1}2p^{-1})^1P \rightarrow (2p^{-1}2p^{-1})^1D$	$^1P-{}^1D$	α_4

The splitting of ^1S and ^1D states can be found from α' and α_4 that have the same initial state.

For $10 \leqq Z \leqq 40$, a more detailed study given by *Demekhin* and *Sachenko* [4.79] is suitable where both LS and jj (and intermediate js) couplings are considered. A two-hole state has more levels than those given by the $(Z+1)$-approximation. Also, for $10 < Z < 40$ the intermediate coupling is more appropriate. In this coupling, the energies of the KL states are expressed as [4.80]

$$
\begin{aligned}
E(KL_I;\ ^1S_0) &= E(K)+E(L_I)+F^0(1s,2s)+G^0(1s,2s),\\
E(KL_I;\ ^3S_0) &= E(K)+E(L_I)+F^0(1s,2s)-G^0(1s,2s),\\
E(KL_{II};\ ^1P_1) &= E(K)+E(L_{II})+F^0(1s,2p)-\tfrac{3}{4}\zeta+\{[\tfrac{1}{3}G^1(1s,2p)-\tfrac{1}{4}\zeta]^2\\
&\quad +\tfrac{1}{2}\zeta^2\}^{1/2},\\
E(KL_{II};\ ^3P_0) &= E(K)+E(L_{II})+F^0(1s,2p)-\tfrac{1}{3}G^1(1s,2p),\\
E(KL_{III};\ ^3P_1) &= E(K)+E(L_{II})+F^0(1s,2p)-\tfrac{3}{4}\zeta-\{[\tfrac{1}{3}G^1(1s,2p)-\tfrac{1}{4}\zeta]^2\\
&\quad +\tfrac{1}{2}\zeta^2\}^{1/2},\\
E(KL_{III};\ ^3P_2) &= E(K)+E(L_{II})+F^0(1s,2p)-\tfrac{1}{3}G^1(1s,2p)-\tfrac{3}{2}\zeta. \qquad (4.48)
\end{aligned}
$$

Here $E(K)$ is the ionization energy for creating a hole in the $1s_{1/2}$ state of the atom, F^i and G^i are slater integrals giving interaction energies between the indicated electron pairs, and ζ is the spin–orbit interaction energy for $2p$ subshells given by [4.80]

$$\zeta = \tfrac{2}{3}[E(L_{II})-E(L_{III})].$$

Relations (4.48) and similar ones for two-hole $2p$ states have been used [4.78, 79] for calculating $KL \rightarrow LL$ transition energies. The $K\alpha''\alpha_3\alpha_4 (KL \rightarrow LL)$ and $K\alpha_5\alpha_6$ (triple hole $KLL \rightarrow LLL$) satellites have been observed recently in ^{10}Ne, under both primary excitation [4.81] and secondary excitation.

In early days, it was believed that satellites are not found in the fluorescent radiation. They have now been observed when the energy of the incident photon is sufficient to remove two electrons from an atom. In secondary excitation, α satellites have been studied by *Babu* et al. [4.82], and Åberg et al. [4.77]. *Sawada* et al. [4.83] observed the $K\alpha_{3,4}$ satellites when the incident-photon energy was enough to remove a K electron of atom Z and an L electron of atom $Z+1$. They found (Table 4.4), for example, that a Ni $K\alpha_1$ incident photon is able to excite only the $K\alpha_{1,2}$ lines of Fe, but a Cu $K\alpha_1$ photon is able to excite the $K\alpha_{3,4}$ satellites as well. *Deslattes* [4.84] and *Carlson* and *Krause* [4.85] have shown that the probability of double ionization is appreciable, provided that the energy of the incident photon is great enough. This has led to a theory of X-ray satellites based on the sudden approximation calculation [4.86].

The transitions for the $K\beta$ satellites are now also understood [4.87, 88]. For example, the satellite $K\beta'''$ of the parent line $K\beta_{1,3}(K \rightarrow M_{II,III})$ is assigned the transition $KL_{III} \rightarrow L_{III}M_{II,III}$. The relevant equations are

$$
\begin{aligned}
(h\nu_{K\beta_{1,3}})_Z &= K_Z-(M_{II,III})_Z, \quad \text{(parent line)}.\\
(h\nu_{K\beta'''})_Z &= (KL_{III})_Z-(L_{III}M_{II,III})_Z, \quad \text{(satellite)}. \qquad (4.49)
\end{aligned}
$$

We can write

$$
\begin{aligned}
(h\nu_{K\beta'''})_Z &= [K_Z+(L_{III})_{Z+1}]-[(L_{III})_Z+(M_{II,III})_{Z+1}]\\
&= (K-L_{III})_Z+(L_{III}-M_{II,III})_{Z+1}\\
&= (K-M_{II,III})_Z+[(L_{III}-M_{II,III})_{Z+1}-(L_{III}-M_{II,III})_Z]\\
&= (h\nu_{K\beta_{1,3}})_Z+\Delta, \qquad (4.50)
\end{aligned}
$$

$$\Delta = (L_{III}-M_{II,III})_{Z+1}-(L_{III}-M_{II,III})_Z = \Delta_{Z+1}-\Delta_Z. \qquad (4.51)$$

Although $L_{III} \rightarrow M_{II,III}$ is a forbidden transition ($\Delta l = 0$), both Δ_Z and Δ_{Z+1} can be computed in terms of the known energy levels of atoms of atomic number Z and $Z+1$. It clearly shows that the satellite photon energy cannot be determined by a transition on the energy-level diagram of the atom Z alone. By Moseley's law, $\Delta_{Z+1} > \Delta_Z$, $\Delta > 0$, and the satellite is displaced by Δ towards the high-energy side of the parent line. The Wentzel–Druyvesteyn theory shows a close approximation with the data for the K-series satellites.

Table 4.4. Double-ionization energies and incident-photon energies for $Z = 24$, 25 and 26

Element	$^{24}Cr_{[eV]}$	$^{25}Mn_{[eV]}$	$^{26}Fe_{[eV]}$	Lines excited
K_Z	5973	6526	7094	
L_{Z+1}	654	720	796	
K_Z+L_{Z+1}	6627	7246	7890	
Incident-photon energies used	Fe $K\alpha_1$: 6386 Co $K\alpha_1$: 6912	Co $K\alpha_1$: 6912 Ni $K\alpha_1$: 7458	Ni $K\alpha_1$: 7458 Cu $K\alpha_1$: 8028	$K\alpha_{1,2}$ lines only $K\alpha_{1,2}$ and $K\alpha_{3,4}$

We can use Moseley's law for the forbidden (diagram) line $L_{III} \rightarrow M_{II,III}$ to write

$$\Delta_{Z+1} = \tilde{\nu}_{Z+1}/R_\infty = a^2[(Z+1)-\sigma]^2,$$
$$\Delta_Z = \tilde{\nu}_Z/R_\infty = a^2(Z-\sigma)^2,$$
$$\Delta = (\Delta\tilde{\nu})/R_\infty = 2a^2[Z-(\sigma-\tfrac{1}{2})]. \qquad (4.52)$$

Thus, $\Delta \propto Z$. It is difficult to verify this relation because the satellites appear as diffuse and faint lines at the foot of the parent line and the same satellite rarely occurs for a wide range of Z values. In fact, some workers have shown that a $((\Delta\tilde{\nu})/R_\infty)^{1/2}$ versus Z plot (semi-Moseley plot) for the satellites gives straight lines over a limited range of elements and helps to identify single types of satellites for various elements. The identification can be based on both energy [4.76] and intensity [4.77] considerations. The observed relative intensity of $K\alpha$ satellites decreases with increasing Z (Fig. 4.18a). It reflects the variation with Z of the relative probability of a double KL ionization to that of a single K ionization [4.68].

High-energy satellites have also been observed in the L and M spectra. *Coster* and *Kronig* [4.50] were the first to consider the Auger process as responsible for double ionization of the atom and consequent emission of L series satellites. According to this view, the appearance and intensity of the L-satellite lines should directly reflect the probability of the associated Auger transition. There is ample evidence for this. Figure 4.18 shows the variation with Z of the ratio of satellite to parent intensities for the satellites of $L\alpha_1 (L_{III} \rightarrow M_V)$

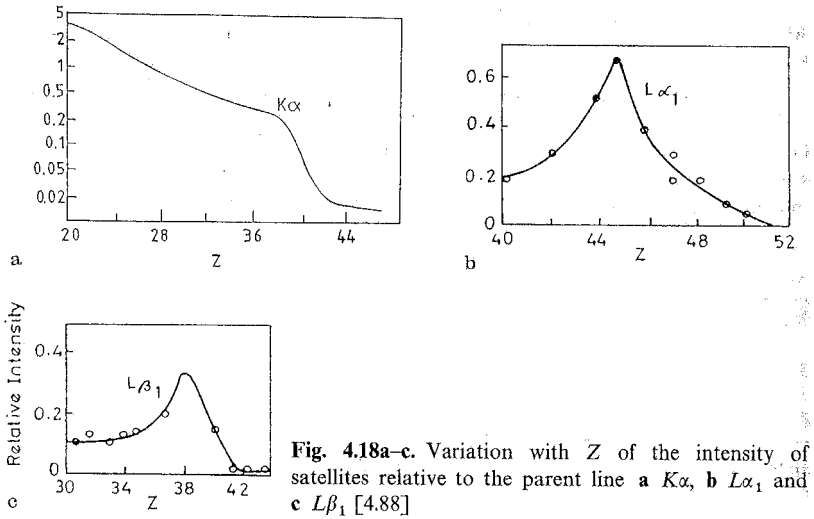

Fig. 4.18a–c. Variation with Z of the intensity of satellites relative to the parent line **a** $K\alpha$, **b** $L\alpha_1$ and **c** $L\beta_1$ [4.88]

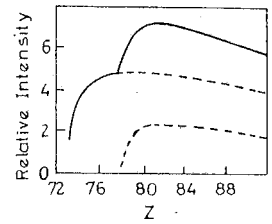

Fig. 4.19. Variation with Z (> 72) of the intensity of satellites in percent of $L\alpha_1$. Solid curve: total relative intensity; dotted curve: breakup in the groups $L_{III}M_V$ and $L_{III}M_{IV}$

and $L\beta_1 (L_{II} \rightarrow M_{IV})$. We have seen that the Coster–Kronig transition probability for $L_I \rightarrow L_{II}M_{IV,V}$ is about a maximum for $Z=40$ and zero for $Z=42$ (compare with Fig. 4.18c). The Coster–Kronig transition $L_I \rightarrow L_{III}M_{IV,V}$ has maximum probability at $Z=45$ or 46 and zero at $Z=52$ (compare with Fig. 4.18b). This process again becomes possible for $Z>73$, when $L_I \rightarrow L_{III}$ energy is enough to ionize the M_V sublevel. For $Z>77$, this energy can also ionize the M_{IV} sublevel. The relative intensities of $L\alpha_1$ satellites show sharp rises at $Z>73$ and $Z>77$ (Fig. 4.19).

Thus, the Coster–Kronig [4.50] theory gives satisfactory correlations for the L-series satellites. This success led *Parratt* [4.89] to classify the observed Ag L satellites, *Richtmyer* and *Ramberg* [4.90] to compute correctly the satellites of $L\alpha_{1,2}$ and $L\beta_2$ in ^{79}Au, *Pincherle* [4.91] to propose a general classification of the L satellites for $37<Z<56$, and *Cauchois* [4.92] to establish systematics for the L satellites in heavy elements. *Krause* et al. [4.93] studied in detail the Zr L satellites.

In the M series, the Coster–Kronig process is responsible for the high-energy satellite $(M_V N_{IV,V} \rightarrow N_{IV,V} N_{VII})$ of the $M\alpha_1 (M_V \rightarrow N_{VII})$ line. The relative intensity of this line increases from ^{78}Pt to ^{82}Pb and decreases sharply for ^{90}Th and ^{92}U. The reason is that the radiationless transition $M_{III} \rightarrow M_V$ cannot create a hole in the M_V level and simultaneously in the N_{IV} level (Auger electron emitted) for $Z>89$ and N_V level for $Z>91$ (see Table 4.1).

Wavelengths of the satellie lines have been compiled [4.94].

4.8.1 Low-Energy Satellites

X-ray K and L satellites have also been observed on the low-energy side of the parent lines. In the $K\beta$ series, *Beuthe* [4.95] observed such a satellite in many elements from ^{23}V to ^{32}Ge and named it $K\eta$. He found it to be a broad line with a sharp edge on the high-energy side. *Ford* [4.96] detected $K\eta$ in ^{19}K to ^{24}Cr and *Valasek* [4.97] in ^{17}Cl. *Blokhin* [4.98] explained it by the forbidden transition $K \rightarrow M_I$ and simultaneous ejection of an $M_{II,III}$ electron to the Fermi level, for the elements ^{23}V to ^{29}Cu. *Sawada* et al. [4.99] resolved $K\eta$ into two components from ^{24}Cr to ^{30}Zn and named the longer-wavelength one Kl. They explained

them on the basis of two-electron jumps in a doubly ionized atom,

$$K\eta = KL_{II} - L_I M_I = K_Z + (L_{II})_{Z+1} - (L_I)_Z - (M_I)_{Z+1},$$

$$Kl = KL_{III} - L_I M_I = K_Z + (L_{III})_{Z+1} - (L_I)_Z - (M_I)_{Z+1}.$$

The $K\beta'$ satellite of ^{24}Cr is explained [4.98] by the transition $K \rightarrow M_{II,III}$ (parent line $K\beta_1$), with simultaneous ejection of an electron from the $M_{IV,V}$ level of the atom into the conduction band of the solid target. The short-wavelength end of $K\beta'$ corresponds to the Fermi energy and the line shape mirrors the density of states of the conduction band.

Hulubei [4.100] observed a low-energy satellite of $K\alpha$ and *Hulubei* et al. [4.101] of $K\beta_1$. *Aberg* and *Utriainen* [4.102, 103] detected a very complex structure on the low-energy side of $K\alpha$ and $K\beta$.

The best explanation seems to lie in terms of the simultaneous excitation of an outer-shell electron and emission of an X-ray photon. This is called the *radiative Auger effect*. Because an electron in the outer (say, M) shell absorbs a part of the radiation energy, the energy of the satellite is decreased relative to that of the parent line.

A radiative Auger transition is a double-electron transition, where an outer-shell electron $n_f l_f$ makes a transition to an inner-shell hole $n_i l_i$ and where another outer-shell electron $n_{f'} l_{f'}$ is simultaneuosly excited into a bound or continuous state εl. (If ε is a bound or optical state, the transition is often called a semi-Auger transition.) These transitions correspond to a discrete and continuous distribution of photon energies $h\nu$ such that

$$h\nu = E_i - E_{ff'} - \varepsilon. \tag{4.53}$$

Here E_i is the $n_i l_i$ ionization energy of the neutral system, and $E_{ff'}$ the energy required for the simultaneous ionization of the two electrons $n_f l_f$ and $n_{f'} l_{f'}$ from the neutral system. The range $0 \leqq \varepsilon \leqq (E_i - E_{ff'})$ gives a distribution of photon energies (broad diffuse satellite). Note that $(E_i - E_{ff'})$ is just the energy of the Auger electron in the radiationless transition $i \rightarrow ff'$

Radiative Auger processes have been interpreted recently by *Åberg* [4.104] in terms of shake-off and interaction between single- and double-hole configurations in the final state. *Rooke* [4.105] suggested that the energy of the principal line is attenuated by simultaneous plasmon excitation. A molecular orbital interpretation has been given by *Urch* [4.106].

To conclude this section, we can say that there exist many processes (including crossover transitions in compounds) that contribute to the satellite structure. We have discussed some of them here. Recently *Briand* et al. [4.107] observed $KK \rightarrow KL$ X-rays using radioactive samples with solid-state detectors. Initial double ionization occurs in the state (K^{-2}) for $Z \geqslant 31$. They called these new weak satellites *hypersatellites*. *Briand* et al. [4.108] were the first to observe K hypersatellite lines $(K\alpha^h)$ in Cu, Ni and Fe under electron bombardment, using crystal spectrometry. Heavy-ion collision can also give rise to K hypersatellites [4.109, 110]. The $K\alpha^h - K\alpha$ energy differences have been carefully measured [4.111, 112]. Hyper-satellites also occur in L spectra [4.113, 114].

Briand et al. [4.108] have calculated in a simple way the energy of the $K\alpha$ hypersatellite $(K^{-2} \rightarrow K^{-1} L^{-1})$ by using the effective screening parameter of *Bergström* and *Hill* [4.115].

$$\Delta Z = [B_{K^2}(Z) - B_K(Z)]/[B_K(Z+1) - B_K(Z)]. \tag{4.54}$$

Here B_K is the binding energy of a K electron for a neutral atom and B_{K^2} is the energy needed to remove a K electron in an atom already ionized in the K shell. Thus ΔZ represents the change of screening between the first and second K ionization. Besides the total energy of the K^{-2} state, we also need the energy value of the $K^{-1} L^{-1}_{II,III}$ state. *Desclaux* et al. [4.111] find that in this case $\Delta Z = 1 \pm 0.01$. Thus the energy needed to remove an $L_{II,III}$ electron, after K shell ionization, is equal to the single-electron binding energy of the atom $Z+1$.

The ΔZ of a K^{-2} state is estimated on the basis of the total energy of helium-like ions obtained in first-order perturbation theory

$$B = 2Z^2 B_H - \tfrac{5}{4} Z B_H, \tag{4.55}$$

where $Z^2 B_H$ is the binding energy of hydrogen-like ions. Then

$$\Delta Z = 5Z/(8Z-1), \tag{4.56}$$

which approaches a constant value 0.625 for high Z values. Using this ΔZ for K^{-2}, and $\Delta Z = 1$ for the $K^{-1} L^{-1}_{II,III}$ state, the energy shift of $K\alpha^h$, with respect to $K\alpha$, should vary linearly with Z for high Z.

Multihole states created by shake-off and Coster–Kronig processes give X-ray satellites that may or may not be distinguishable from the parent diagram lines. According to the analysis of Zr L satellites by *Krause* et al. [4.93], the satellites caused by an LM Coster–Kronig state appear on the high-energy side of the parent line, and those caused by an LN shake-off state fall within the parent line. Thus, only a fraction of the satellites is observable and a diagram line may be contaminated by hidden satellites.

The subject of satellites is not simple and we are far from any satisfactory understanding of this complex problem. Some useful review articles are by *Hirsh* [4.88], *Edwards* [4.116] and *Åberg* [4.117].

4.9 Fluorescence

Each absorption edge is accompanied by X-ray emission lines, also called a fluorescence spectrum. Fluorescence competes with the Auger-electron emission as a de-excitation process, following the creation of an inner-shell hole. The former dominates in the heavier atoms and the latter for $Z < 15$, Table 4.5. The fluorescent radiation is in the X-ray region and consists only of the characteristic line spectra.

Suppose X-rays incident on unit volume of an element eject q-type $(q = K, L, M, \ldots)$ photoelectrons from n_q atoms per second. In the steady state, $n_q = n_{q,A} + n_{q,R}$ will return to the un-ionized or normal configuration, where $n_{q,A}$

is the number of atoms that emit Auger electrons (radiationless transition) and $n_{q,R}$ is the number of atoms that emit fluorescent radiation (radiative transition). Of these $n_{q,R}$ atoms, a number $n^1_{q,R}$ will emit the line $q\alpha_1$ as a step in the process, $n^2_{q,R}$ will emit the line $q\alpha_2$, etc. Thus

$$n_{q,R} = n^1_{q,R} + n^2_{q,R} + \cdots = \sum_i n^i_{q,R}. \tag{4.57}$$

The sum is over all lines of the q series.

We define the *fluorescence yield* $\tilde{w}_q$ by

$$\tilde{w}_q = \frac{\sum_i n^i_{q,R}}{n_q} = \frac{n_{q,R}}{n_{q,A} + n_{q,R}}. \tag{4.58}$$

Thus, for a sample of many atoms, if in a given time 100 vacancies occur, and 40, 20, 6, and 1 photons are emitted corresponding to $K\alpha_1$, $K\alpha_2$, $K\beta_1$, and $K\beta_2$ respectively, then $\tilde{w}_q = 0.67$. Also, $n_{K,A}/n_K = 1 - \tilde{w}_K = 0.33$, or 33 vacancies are filled in this particular case via the Auger process due to the Auger effect $\tilde{w}_q < 1$. In terms of the corresponding transition probabilities (P) and widths (Γ),

$$\tilde{w}_q = \frac{P_{q,R}}{P_{q,A} + P_{q,R}} = \frac{\Gamma^R_q}{\Gamma^A_q + \Gamma^R_q}. \tag{4.59}$$

Great care is needed in the proper definitions of the quantities that are measured [4.44].

The dominant contribution to $P_{q,R}$ comes from the electronic-dipole transitions

$$P_{q,R}\, dt = \frac{64\pi^4 \nu^3}{3hc^3} |M|^2\, dt, \quad M = e\int \psi_f^* r \psi_i\, d\tau. \tag{4.60}$$

Theoretical calculations of $\tilde{w}_K$ have been made by *Burhop* [4.118] and *Pincherle* [4.119] using a nonrelativistic theory, and by *Massey* and *Burhop* [4.120] using a relativistic theory.

Integration of (4.29) gives complicated expressions for the Auger transition rate, but it shows that the rate is independent of the atomic number. On the other hand, as in (4.38), the integration of (4.60) gives for the radiative transition rate a Z^4 dependence[1]. Therefore, we can approximate (4.59) as

$$\tilde{w}_K = \frac{bZ^4}{a + bZ^4} = \frac{1}{1 + a_K Z^{-4}}, \tag{4.61}$$

[1] This can also be seen by regarding the radiating atom as a damped harmonic oscillator. From (3.2) $\langle -dU/dt \rangle = (2e^2/3c^3)\langle \ddot{x}^2 \rangle = (2e^2/3c^3)(\ddot{x}_0^2/2)$, where $\ddot{x}_0$ is the peak acceleration. For weak damping $\ddot{x} = 2\pi\nu\dot{x}_0$. With $U = m\dot{x}_0^2/2$, we have relaxation time = (energy stored)/(mean energy loss per s) $= U/\langle -dU/dt \rangle = 3mc^3/(8\pi^2 e^2 \nu^2)$. By Moseley's law, $\nu \propto Z^2$, relaxation time $\propto 1/Z^4$, or the transition probability $\propto Z^4$.

Table 4.5. Probability (P) of the Auger-electron emission relative to the X-ray emission, as a function of Z

Z:	10	15	20	25	30	40	45	50	55	65	70
P:	0.99	0.95	0.86	0.71	0.55	0.31	0.22	0.16	0.11	0.09	0.07

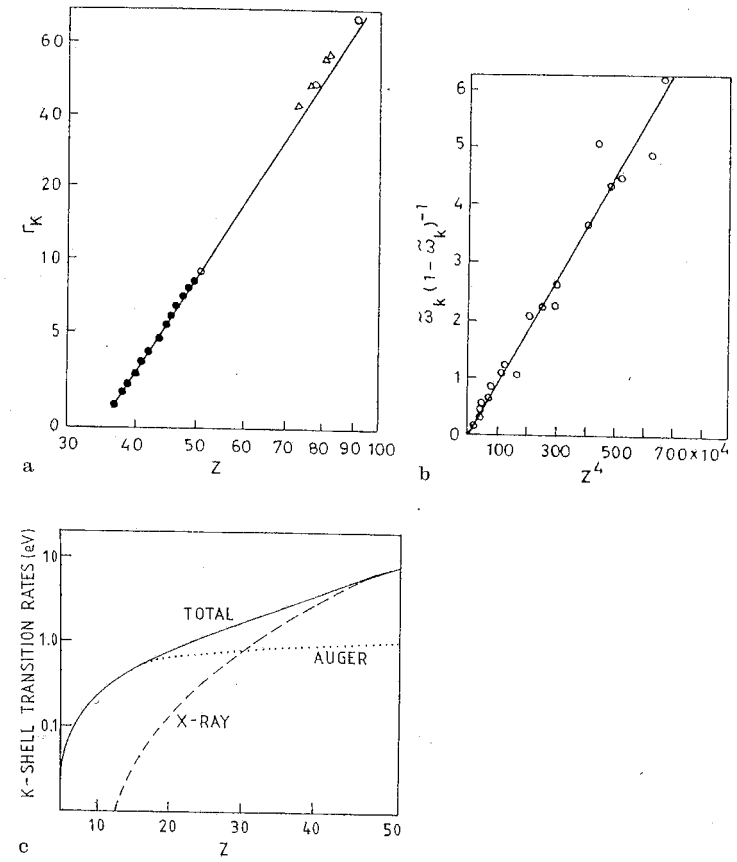

Fig. 4.20. **a** K-level width as a function of Z. The straight line represents $\Gamma_K = 1.73 \times Z^{3.93} \times 10^{-6}$ eV. The measurements are by *Massey* [4.51] ○; *Gokhale* [4.70] ●; *Laskar* [4.122] △. **b** Plot of $\tilde{w}_K/(1 - \tilde{w}_K)$ versus Z^4. The points represent averaged values of various measurements. **c** K-shell X-ray and Auger transition rates as functions of Z. The X-ray rates represent calculations of *Walters* and *Bhalla* [4.63] and vary as Z^4 for $Z > 40$. Auger rates represent calculations of *McGuire* [4.62]. The total level width is due to *Kostroun* et al. [4.123]

where $a_K = a/b$ is adjustable constant. *Leisi* et al. [4.121] used $K\alpha$ line-width information with measurements of L_{II} and L_{III} level widths to show that for $Z > 40$, K-level widths can be represented by the relation

$$\Gamma_K = 1.73 \times Z^{3.93} \times 10^{-6}\,\text{eV}. \tag{4.62}$$

It is compared with experiments [4.51, 70, 122] in Fig. 4.20a. In Fig. 4.20b, we show a plot of $\tilde{w}_K/(1-\tilde{w}_K)$ versus Z^4 along with the experimental points. A straight line given by (4.61) with $a_K = 1.12 \times 10^6$ provides a good fit. The theoretical value is close to this [4.123]. For $Z > 10$ Auger rates vary relatively little with Z (Fig. 4.20c).

A relation similar to (4.61) is found to be applicable for the L-shell fluorescence, although the agreement with the experiments is not so good as in the K-shell case. K-shell radiative transition probabilities have been calculated by *Scofield* [4.68] to give K_β/K_α X-ray intensity ratio in agreement with experiments.

A more accurate relation is

$$[\tilde{w}_q/(1-\tilde{w}_q)]^{1/4} = A_q + B_q Z + C_q Z^3,$$

where *Colby* [4.124] suggests $A_K = -0.03795$, $B_K = 0.03426$, $C_K = -0.1163 \times 10^{-5}$ using recent data [4.125] on $\tilde{w}_K$.

4.10 Measurement of Fluorescence Yield

Auger [4.42], *Bower* [4.126], and *Martin* and *Eggleston* [4.127] used (4.58) to determine $\tilde{w}_q$ in gases filled in a cloud chamber. To find $n_q = n_{q,A} + n_{q,R}$ it is necessary only to detect *all* of the photoelectron tracks whose range corresponds to the ejection of electrons from the q level of atoms in the gas. This range is determined by $h\nu - E_q$, where $h\nu$ is the incident X-ray photon energy. To determine $n_{q,R} = n_q - n_{q,A}$, we need only locate all of Auger electron tracks ($n_{q,A}$) that are emitted from the *same* atoms. For example, the Auger electrons will have energies $E_K - 2E_L$ and $E_L - 2E_M$ when the K-shell vacancy is filled by Auger transitions.

It is a statistical method. If in all, n tracks are observed, and m of these are recognized as Auger tracks, then the fluorescence yield is $(n-m)/n$. The probably error of m/n is 0.6475 $[m(n-m)/n^3]^{1/2}$.

In ^{36}Kr, Auger found 223 tracks of K photoelectrons. Of these, 109 were accompanied by an Auger electron. Therefore $\tilde{w}_K = (223-109)/223 = 0.51$. Example values are given in Table 4.6.

For solid specimens, the power can be directly measured in the incident X-ray beam and in the fluorescent radiation from the atoms. The rate of inner-shell ionization is related to the absorption coefficient. For this, we must know the spectral composition of the primary beam.

To ensure a definite composition of the incident beam, three methods are available: 1) crystalline diffraction, 2) suitable filters [4.128] and 3) pure

Table 4.6. Average values of fluorescence yield [4.124]

Element	$\tilde{w}_K$	$\tilde{w}_L$	$\tilde{w}_M$
18 Ar	0.097	—	—
26 Fe	0.324	0.003	—
36 Kr	0.629	0.019	—
42 Mo	0.749	0.039	0.001
54 Xe	0.876	0.110	0.003
80 Hg	0.952	0.366	0.028

characteristic fluorescent radiation from a metal plate exposed to primary X-rays.

A typical experimental arrangement used by *Compton* [4.129] and *Stephenson* [4.130] is shown in Fig. 4.21a. X-rays fall on a metal plate R_1 and its characteristic K-series fluorescent radiation is used as the incident beam for the specimen R_2 under study. The ionization chamber A measures the ionization current I produced by the fluorescent radiation from R_2, and B measures the current I_0 produced by the direct beam with R_2 removed.

The intensity of incident X-rays at a depth X in R_2 is

$$I_x = I_0 e^{-\mu x/\sin\phi}, \tag{4.63}$$

where $\mu = \sigma + \tau$ is the total linear attenuation coefficient, and ϕ is the glancing angle of incidence of X-rays from R_1 on R_2, Fig. 4.21b. The decrease of the initial-beam intensity when it passes through a layer dx at x is

$$dI_x = -\frac{\tau+\sigma}{\sin\phi} I_0 e^{-\mu x/\sin\phi}\, dx. \tag{4.64}$$

If I_0 is the energy of X-rays per cm^2 falling on R_2, then the radiation incident on a surface s of R_2 is $I_0 s \sin\phi$. Therefore, the part of this energy that undergoes photoelectric absorption in dx at x is

$$dE = \tau s I_0 e^{-\mu x/\sin\phi}\, dx. \tag{4.65}$$

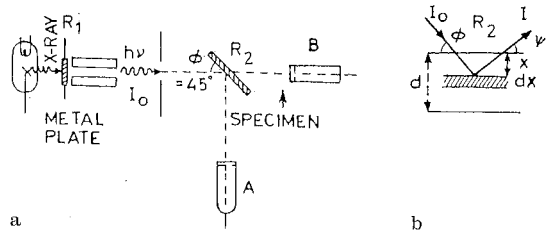

Fig. 4.21. a Compton's arrangement for the measurement of fluorescence yield, and **b** path of X-rays in the excitation of fluorescence in solids

This is the energy absorbed by all of the q levels of the atoms in R_2 in the layer dx. Writing

$$dE=\sum_q dE_q, \quad \tau=\sum_q \tau_q, \tag{4.66}$$

and using (3.208), we have from (4.65),

$$dE_q=\frac{r_q-1}{r_q}\tau s I_0 \, e^{-\mu x/\sin\phi}\, dx. \tag{4.67}$$

Here r_q is the absorption-jump ratio at the q edge, and $\tau_q/\tau=(r_q-1)/r_q$ gives the fraction of the total number of photoelectrons that come from the q level when X-rays are absorbed.

If $n_q s dx$ atoms in the volume sdx of R_2 are excited in the q level,

$$dE_q=h\nu n_q s dx=h\nu(n_{q,R}/\tilde{w}_q)s dx, \tag{4.68}$$

using (4.58) and $n_{q,R}=\sum_i n^i_{q,R}$. *If* p_i is the probability that an atom excited to the q level will emit a line i of the q series, then $n^i_{q,R}=p_i n_{q,R}$ and from (4.67, 68),

$$n^i_{q,R}\, s dx=p_i\frac{\tilde{w}_q r_q-1}{h\nu \quad r_q}\tau s I_0 \, e^{-\mu x/\sin\phi}\, dx. \tag{4.69}$$

It follows that the energy of the secondary X-rays with a frequency ν_i of the line i emitted in *all* directions from the volume sdx is

$$(dE_q)_i=h\nu_i n^i_{q,R}\, s dx=\frac{\nu_i}{\nu}\frac{r_q-1}{r_q}\tau\tilde{w}_q p_i s I_0 \, e^{-\mu x/\sin\phi}\, dx. \tag{4.70}$$

This energy leaves R_2 at an angle ψ (Fig. 4.21b) and undergoes absorption along the path $x/\sin\psi$. The intensity dI_i of the line i of the secondary spectra at a distance R from the volume sdx is

$$dI_i=\frac{(dE_q)_i}{4\pi R^2}e^{-\mu_i x/\sin\psi}$$

$$=\frac{\nu_i}{\nu}\frac{I_0}{4\pi R^2}\tilde{w}_q\frac{r_q-1}{r_q}\tau p_i s\, e^{-(\mu/\sin\phi+\mu_i/\sin\psi)x}\, dx, \tag{4.71}$$

where μ_i is the total linear attenuation coefficient of the line i in R_2. Integration over x from 0 to d gives

$$I_i=\frac{I_0}{4\pi R^2}\tilde{w}_q\frac{r_q-1}{r_q}s\sin\phi\frac{\tau}{\mu}p_i\frac{\nu_i/\nu}{1+\dfrac{\mu_i\sin\phi}{\mu\sin\psi}}\times[1-e^{-(\mu/\sin\phi+\mu i/\sin\psi)d}]. \tag{4.72}$$

The usual choice is $\phi=\psi=45°$.

The total intensity of the q-series spectra at a distance R from R_2 is

$$I_q=\sum_i I_i. \tag{4.73}$$

The probability p_i can be found from the relative intensities of the lines of the q-series from R_2,

$$p_i=I'_i/\sum_i I'_i. \tag{4.74}$$

The measurement of I_q/I_0 allows us to determine $\tilde{w}_q$ from (4.72–74).

The results of $\tilde{w}_K$ and $\tilde{w}_L$ measurements as a function of Z are shown in Fig. 4.22. For a given Z, the difference $\tilde{w}_K-\tilde{w}_L$ is large, 0.5 to 1.0, but for a given λ this difference is small, 0.15 to 0.2. A plot of $\tilde{\omega}_K/(1-\tilde{\omega}_K)$ versus Z^4 gives approximately a straight line (Fig. 4.20). There is an increasing demand for accurate fluorescence-yield data [4.131], as it provides useful information for quantitative X-ray spectroscopy.

When continuous radiation is used to excite λ_i, all the wavelengths between λ_{min} and λ_{edge} corresponding to λ_i are considered I_i depends in (4.72) on both μ (absorption of primary wavelengths by the specimen) and μ_i (attenuation of the secondary excited λ_i). The excitation efficiency depends on the overlap area of the continuum $J(\lambda)$ and absorption curve of the element (Fig. 4.23). The short-wave-length region in $J(\lambda)$ may excite λ_i at such a depth that it cannot emerge

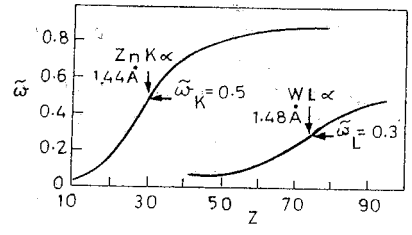

Fig. 4.22. Fluorescence yield as a function of Z is of form (4.61)

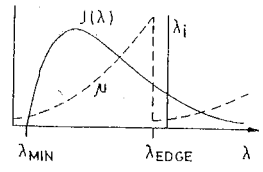

Fig. 4.23. Effective region of secondary radiation excitation. $J(\lambda)$ represents the X-ray tube spectrum

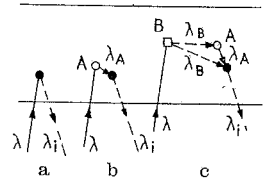

Fig. 4.24. a Excitation of λ_i by primary (tube) λ; **b** λ first excites λ_A from a matrix element A, then λ_A excites λ_i ($\lambda_A<\lambda_i$); **c** λ first excites λ_B from a matrix element B, then λ_B excites λ_A from A, which finally excites λ_i ($\lambda_B<\lambda_A<\lambda_i$). Also, enhancemet by λ_B on λ_i can occur

from the specimen. The most efficient exciting wavelengths in $J(\lambda)$ lie close to the absorption edge of the excited element on the short-wavelength side of the edge.

The secondary fluorescence and tertiary fluorescence (Fig. 4.24) processes give rise to enhancement.

4.11 Autoionization and Internal Conversions

A secondary process that resembles Auger ionization is *autoionization*. It can occur when a sample is exposed to photons or electrons of suitable energies. In the initial state, an inner electron is promoted to an outer (optical) level. If the excitation energy exceeds the ionization energy of any of the other electrons present, the excited atom will eject an electron and reorganize to an ion (Fig. 4.25). The ejected electron is called *autoionization electron*. In the Auger process, the initial step requires the ejection of an inner-shell electron, rather than a promotion to a higher level, and the final state is a doubly ionized ion, rather than a singly ionized ion.

The incident photon $h\nu$ that is absorbed in the process must have an energy equal to the difference of energy between the ground-state atom A and the excited atom A^* (Fig. 4.25) if $h\nu$ is varied, autoionization levels will show up as resonance peaks superimposed on the expected steps for the various ionization potentials (Fig. 4.26) Autoionization will be detected in the usual photoelectron spectroscopy only if $h\nu$ happens to coincide with an autoionization level. Autoionization affects photoelectron spectra of molecules [4.132].

The possibility of the *internal conversion* process was discussed in Sect. 4.5. The β-ray spectra from a nucleus consist of electrons that have a continuous range of energy from zero up to a definite upper limit. Sometimes superimposed on this continuous distribution there occur several sharp lines. These lines

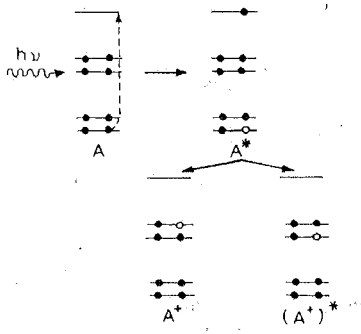

Fig. 4.25. Autoionization process possible in an atom A; following an initial excitation process $A \rightarrow A^*$; ●: electron, ○: hole

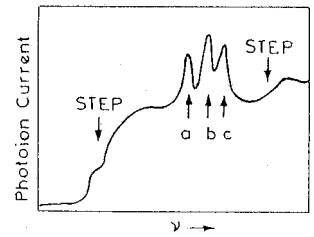

Fig. 4.26. The resonance autoionization structure: *a*, *b*, *c*, indicate autoionization levels

correspond to electrons that are homogeneous in energy, and arise from the internal conversion of the γ-radiation that accompanies the β-decay, by the electrons of the atom of the origin of γ-radiation. It is anlogous to the Auger process [4.133].

4.12 Muonic X-Rays

When a negatively charged particle (like μ^-, π^-, K^-) replaces an electron in an atom, a *mesonic atom* is formed. In this atom, the energy level of the mesons are analogous to those of electrons in a normal atom and characterized by the same quantum numbers n, l. When the half-spin μ^- replaces the electron, it is called *muonic atom*. Muonic atoms have the same quantum number j, as normal atoms. Except for the mass ($m_\mu \simeq 207\, m_e$), the μ^- behaves like an electron. The simplest system is *muonic hydrogen* (p^+, μ^-).

The energy levels $E(n, l)$ of a mesonic atom are related to $E_0(n, l)$ of an ordinary atom by

$$E(n, l) = (M^*/m^*) E_0(n, l), \tag{4.75}$$

where $M^*(m^*)$ is the reduced mass of the meson (electron). The mean distance $\bar{r}_M$ of the meson from the nucleus in the ground state is smaller than the Bohr radius a_0 in the same ratio,

$$a_0/\bar{r}_0 = Z(M^*/m^*). \tag{4.76}$$

For muonic silver this gives $\bar{r}_0 \simeq 5 \times 10^{-13}$ cm which is approximately equal to the radius of the silver nucleus. Therefore, the muon spends a considerable part of its time in the interior of the nucleus.

When μ^- are brought to rest in a target, muonic atoms of the target element are formed, usually by the replacement of one of the valence electrons by the μ^-. This forms a highly excited state. The de-excitation occurs in about 10^{-13} s, first by means of radiationless Auger processes in which the μ^- falls successively to states of lower excitation, the excess energy being used to eject electrons from the atom. When the principal quantum number n reduces to less than about 5 in heavier atoms, the radiative transitions become more probable than Auger transitions, and *muonic* X-rays are emitted. The single muon in the muonic atom continues to make de-excitation transitions until it reaches the K shell, because the Pauli principle does not inhibit it.

The $K\alpha_{1,2}$ lines in the muonic X-rays were resolved by *Fitch* and *Rainwater* [4.134]. *Kessler* et al. [4.135] observed the muonic X-ray Lyman ($np \rightarrow 1s$) and Balmer ($nd \rightarrow 2p$) series of ^{22}Ti. The energies of the first four lines in the H Lyman series in eV are 10.15, 12.04, 12.69, 13.00. The electron is so far away from the nucleus in hydrogen that the latter behaves as a point charge. If we calculate the Lyman series of muonic Ti on this picture, they would be exactly $Z^2(m_\mu^*/m_e^*) \simeq 10^5$ times the energies for hydrogen: 1015,, 1204, 1269, 1300 (in

keV, X-ray region). The observed values are 935, 1124, 1190, 1221 keV, all with energies about 80 keV less than expected on the assumption of a point nucleus. The muonic Ti Balmer-series lines are found almost at the expected positions of 188, 254, 284, 301 keV. This shows that the $1s$ level is strongly affected by the nuclear size, whereas the $2p$ level (with larger value of $\bar{r}$) is little affected. Muonic transition energies are given by *Wu* and *Willets* [4.136] for $\mu K\alpha_1$ and $\mu K\alpha_2$ X-rays.

Nuclear-size effects become significant with increase of Z, because the nuclear radius increases, whereas the mean radius of the $1s$ orbit, $\bar{r}_0$, decreases.

Treating the meson as a heavy electron, for a point nucleus the energy is given by (2.81) in the Dirac theory with m_e replaced by m_μ. The change in the Coulomb interaction energy due to the finite nucler volume is in the first-order perturbation theory,

$$\Delta E^{\text{Coul}} = \int_0^\infty d^3\gamma |\psi|^2 [V(r) - (Ze^2/r)], \tag{4.77}$$

where $V(r)$ and Ze^2/r are the potentials due to the finite and point nucleus, respectively, and the radial wave function at small γ is

$$\psi = C(Z, n, l)\gamma^{l+1}, \quad C^2 = \{2Z\mu/[(l+1)a_{0\mu} m_\mu]\}^{2l+3} [1/(2l+2)!]. \tag{4.78}$$

Assuming a charge distribution $\rho(r)$ such that

$$\int_0^\infty \rho(r) 4\pi r^2 dr = Ze,$$

then

$$\Delta E^{\text{Coul}} = \frac{C^2(Z, n, l)}{(2l+2)(2l+3)} \int_0^\infty \rho(\gamma)\gamma^{2(l+1)} r^2 dr. \tag{4.79}$$

This result is poor for high Z and $l = 0, 1$. A more exact result is due to *Fitch* and *Rainwater* [4.134], and *Ford* and *Hill* [4.137]. The measurements of muonic X-ray spectra in various elements suggest a nuclear-charge distribution of the form

$$\rho(r) = \rho_0 (1 + e^{(r-R)/z})^{-1}, \tag{4.80}$$

where z determines the thickness of the nuclear surface, and R is practically the radius at which the electric charge density has become one-half its value at the center. A useful review article is by *Burhop* [4.138]. In contrast with μ^-, π^- have a strong interaction with nucleons. Therefore, π-mesonic atoms are not useful for studying nuclear radii.

K-mesic X-rays were reported for the first time by *Burleson* et al. [4.139]. They were further studied by *Wiegand* and *Mack* [4.140].

5. Scattering of X-Rays

An X-ray beam that passes through an absorber is attenuated. The degree of attenuation depends upon both photoabsorption and scattering processes. Scattering occurs when an X-ray photon interacts with one of the electrons of the absorbing element. If this collision is elastic (no energy is lost in the collision process), the scattering is said to be *coherent* (Rayleigh scattering). Because no change of energy is involved, the coherently scattered radiation remains *unmodified* (same wavelength as the incident beam), and there is a definite relationship between the phase of the scattered beam and that of the incident beam. X-ray diffraction is a special case of coherent scattering. In X-ray spectroscopy, this diffraction process provides a method for the wavelength separation.

It can also happen that in the collision process a small fraction of the energy of an incident X-ray photon is transferred to a loosely bound electron of the target atom. Then the scattering is said to be *incoherent* (Compton scattering). The incoherently scattered radiation is *modified* (slightly longer wavelength than that of the incident beam) and has no fixed relation to the phase of the incident beam. It cannot produce interference effects and so unavoidably contributes to the uniform background of diffraction patterns.

In Fig. 5.1 we show the more important of the processes responsible for the attenuation of the primary beam that passes through an absorber.

5.1 Classical Theory of Thomson and Rayleigh (Coherent) Scattering

The coherent scattering of radiation by a free electron was first discussed by J. J. Thomson in terms of classical electrodynamics. Let an unpolarized X-ray beam propagate along the y axis and encounter an electron at 0 (Fig. 5.2). Let $E = E_0 \exp(i\omega t)$ be the electric field of the incident wave at the point 0 at time t. If the electron has a velocity small compared to c, it would receive an acceleration $\boldsymbol{a}$, such that $\boldsymbol{a} = e\boldsymbol{E}/m$. This accelerated electron, in turn becomes a source of radiation of the same frequency ω. This kind of interaction gives the scattered

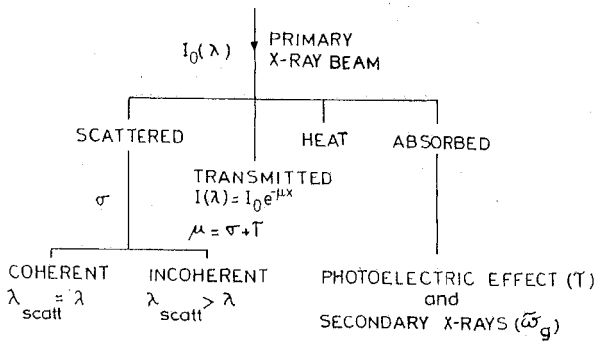

Fig. 5.1. Attenuation processes

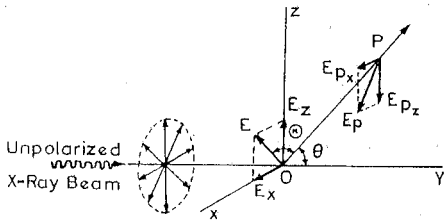

Fig. 5.2. Coherent scattering of X-rays by a single electron at 0

wave at a point P, at the same time t, of the form (1.63)

$$E_p = -E\frac{e^2}{mc^2R}\sin\Theta, \quad E = E_0 e^{i\omega\left(t-\frac{R}{c}\right)}, \tag{5.1}$$

where R is the distance OP and Θ the angle between the scattering direction and the direction of acceleration of the electron. The negative sign simply means that the wave scattered by the free electron in the forward direction has a phase opposite to that of the primary wave[1].

For convenience, let the point of observation P lie in the yz plane. We consider the components of E along the x and z axes. From (5.1), in the scattered beam at P (Fig. 5.2),

$$E_{Px} = \frac{e^2 E_x}{mc^2 R}, \quad E_{Pz} = \frac{e^2 E_z}{mc^2 R}\cos\theta. \tag{5.2}$$

[1] For an oscillator $E(t) = (\omega^2/cR)ex(t) = (\omega^2 e^2 E_0/mc^2 R)\ (\omega_0^2 - \omega^2 + i\gamma\omega)^{-1}\ \exp(i\omega t)$, (Sect. 3.3). For a free electron $\gamma = 0$, $\omega_0 = 0$, and so $E(t)/E_{free}(t) = (-\omega^2)\ (\omega_0^2 - \omega^2 + i\gamma\omega)^{-1}$. The minus sign means that the wave scattered by the free electron has an opposite phase to that of the incident wave.

The energy per unit volume that flows past the point P is proportional to $E_P^2 = E_{Px}^2 + E_{Pz}^2$. For an unpolarized primary beam, on the average, $\langle E_x\rangle^2 = \langle E_z\rangle^2 = \langle E\rangle^2/2$. Therefore,

$$\langle E_P\rangle^2 = \frac{e^4\langle E\rangle^2}{m^2c^4R^2}\left(\frac{1+\cos^2\theta}{2}\right), \tag{5.3}$$

and the intensity ($I = c|E|^2/4\pi$) of coherent scattering by one electron is obtained by multiplying both sides of (5.3) by $c/4\pi$,

$$I_e = I_0\frac{e^4}{m^2c^4R^2}\left(\frac{1+\cos^2\theta}{2}\right) = I_0\frac{r_e^2}{R^2}\left(\frac{1+\cos^2\theta}{2}\right). \tag{5.4}$$

This is the *Thomson equation*. The quantity in parentheses is called the *polarization factor*. Plane polarization occurs for $\theta = 90°$, $E_{Pz} = 0$. As $I_e \propto 1/m^2$, the contribution of the nucleus is negligible.

Compton and *Hagenow* [5.1] studied polarization of X-rays scattered by two thin foils P_1 and P_2 (Fig. 5.3). The primary beam from an X-ray tube with its axis parallel to x is polarized so that its electric vector E is parallel to x. Consequently the electrons in P_1 are accelerated only along x_1x_1' and a scattered beam is observed in the z direction but not parallel to x. Because the polarization of the primary beam is not complete, a much larger intensity is merely observed along z than along x, as found by Barkla (Sect. 1.13). The X-ray beam scattered along z can have E parallel to x only and so can accelerate the electrons in P_2 only along x_2x_2'. Thus, the observed intensity of the twice-scattered beam changes from a maximum along y to a minimum along x_2x_2'. *Compton* and *Hagenow* found this to be so. It shows that the electromagnetic-wave treatment of Thompson is correct and that in coherent scattering by electrons the X-rays get polarized. The nucleus of an atom cannot participate in this kind of scattering because it cannot be accelerated by E because of its large mass.

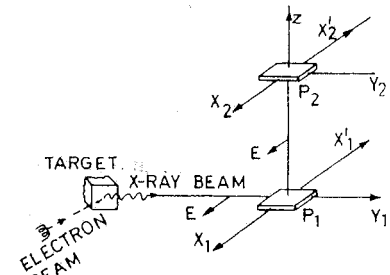

Fig. 5.3. Polarization of X-rays by scattering

The classical differential cross-section per electron for Thomson scattering is given by

$$\left(\frac{d\sigma_e}{d\Omega}\right)_{\text{Thom}} = \frac{\text{Energy radiated per unit time and unit solid angle}}{\text{Incident-energy flux in energy per unit area and unit time}}$$

$$= \frac{I_e R^2}{I_0} = r_e^2\left(\frac{1+\cos^2\theta}{2}\right) \tag{5.5}$$

The total power scattered is obtained by integration over the surface of a sphere of radius R,

$$P_e = \int_0^\pi I_e 2\pi R^2 \sin\theta\, d\theta = I_0 \pi r_e^2 \int_0^\pi (1+\cos^2\theta)\sin\theta\, d\theta = I_0 \frac{8\pi}{3} r_e^2. \tag{5.6}$$

The *classical scattering cross-section per electron* is

$$\sigma_e = \int_0^\pi \left(\frac{d\sigma_e}{d\Omega}\right)_{\text{Thom}} 2\pi \sin\theta\, d\theta = \frac{P_e}{I_0} = 6.66\times 10^{-25}\ \text{cm}^2. \tag{5.7}$$

We now consider the cooperative effect of all of the electrons in an atom (Rayleigh scattering). The electrons are all forced into vibration at the frequency of the incident X-rays. If this frequency is much greater than the natural frequencies of the atomic electrons, the scattered radiation from all of the electrons will be in antiphase with the incident radiation [5.2]. The scattering is coherent and so the amplitudes are added before squaring to give the intensity. The cross-section per electron is now non-additive, so we speak of an atomic scattering cross-section σ_R such that

$$\sigma_R = \frac{8\pi}{3} r_e^2 f^2(\theta),$$

where $f(\theta)$ is the atomic scattering factor. It is defined with respect to σ_e for a free electron. Although σ_R is small compared with other processes, the effect is the basis of X-ray diffraction.

If the material contains n electrons per unit mass that scatter X-rays independently of each other according to (5.4), we can define the *mass scattering coefficient* as

$$\sigma_m = n\sigma_e = (N_A Z/A)\sigma_e \quad [\text{cm}^2\,\text{g}^{-1}]. \tag{5.8}$$

Setting $Z/A \simeq 0.5$, we get $\sigma_m \simeq 0.20$. Thus, σ_m is a universal constant and does not depend on the scattering material.

It may be noted that electrons do not scatter X-rays independently of each other, and Thomson's theory does not include the quantum effects. For light elements, however, (5.7) is in good agreement with experiments.

5.2 Incoherent (Compton) Scattering

Consider a photon with initial momentum $\boldsymbol{p}$ ($p = h\nu/c$) and energy $h\nu$, incident upon a stationary electron of rest mass m. After the collision, the photon has momentum $\boldsymbol{p}'$($p' = h\nu'/c$), and the electron recoils at an angle ϕ with momentum $\boldsymbol{p}$, see Fig. 5.4. The paths of the incident and the scattered photon define the *scattering plane* and θ is the *scattering angle*. The momentum normal to this plane is zero. Therefore, the path of the recoil electron must lie in the scattering plane.

Conservation of momentum and energy gives

$$h\nu/c = (h\nu'/c)\cos\theta + P\cos\phi, \tag{5.9}$$

$$0 = (h\nu'/c)\sin\theta - P\sin\phi, \tag{5.10}$$

$$h\nu + mc^2 = h\nu' + (p^2c^2 + m^2c^4)^{1/2}. \tag{5.11}$$

These can be combined to give

$$mc^2(\nu - \nu') = h\nu\nu'(1-\cos\theta) \tag{5.12}$$

or equivalently, the equation for the *Compton effect* [5.3] is

$$\lambda' - \lambda = (h/mc)(1-\cos\theta) = 0.0243\,(1-\cos\theta)\,\text{Å}. \tag{5.13}$$

The term h/mc is the *Compton wavelength* of the electron. Note that $\lambda' > \lambda$. The increase of the wavelength of the incoherently scattered line ($h\nu'$) depends only on the scattering angle θ. This is confirmed by experiments (Fig. 5.5a).

The *modified line* (λ') is observed to be broader than the primary or *unmodified line* (λ). The reason is that the electrons in the target atom are not initially at rest, as assumed.

The unmodified line (no change of wavelength) is also observed along with the modified line. The reason is that for a part of the time the electron behaves essentially as a *free* particle at rest, as assumed above, and for a part of the time it behaves as *bound* to the rest of the atom. In the latter case, the collision is between the incident photon and the whole atom of mass $M \gg m$. Then h/mc is to be replaced by h/Mc in (5.13). Because $h/Mc \simeq 0$, we get $\lambda' = \lambda$. The observed fact that the unmodified line is hardly detected for low Z atoms and becomes stronger for high Z atoms (Fig. 5.5b) confirms this.

The Compton shift of wavelength, $\lambda' - \lambda$, for a given θ, is independent of the energy $h\nu$ of the incident photon. On the other hand, the associated shift of

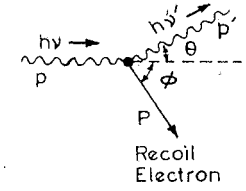

Fig. 5.4. Compton scattering

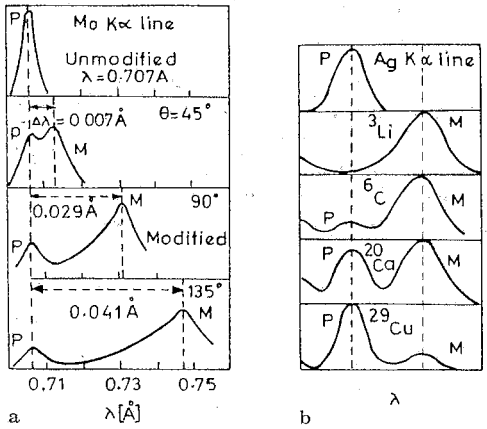

Fig. 5.5a, b. Compton scattering **a** of Mo $K\alpha$ line by graphite at various angles, and **b** of Ag $K\alpha$ line by different atoms at 120°

energy, $h\nu - h\nu'$, determined by (5.12), increases as $h\nu$ increases. This follows from the reciprocal relationship between frequency and wavelength.

From (5.9–11),

$$E_{\text{kin}} = h\nu - h\nu' = h\nu \frac{2\alpha\cos^2\phi}{(1+\alpha)^2 - \alpha^2\cos^2\phi} = h\nu \frac{\alpha(1-\cos\theta)}{1+\alpha(1-\cos\theta)} \tag{5.14}$$

$$\cos\phi = (1+\alpha)\frac{1-\cos\theta}{\sin\theta} = (1+\alpha)\tan\theta/2, \tag{5.15}$$

where $\alpha = h\nu/mc^2$. For $\alpha \ll 1$ ($h\nu \ll mc^2$, X-ray region) the recoil electron comes out with energy less than $h\nu$ by a factor of approximately $2\alpha\cos^2\phi$. Thus, the Compton recoil electrons possess much less energy than the photoelectrons and are confined to angles less than 90°. The maximum energy of the recoil electron is when $\phi = 0$,

$$E_{\text{kin, max}} = \frac{h\nu}{1+(2\alpha)^{-1}} = h\alpha[1-(2\alpha)^{-1}+(2\alpha)^{-2}- \ldots]. \tag{5.16}$$

The recoil electrons have been observed by *Wilson* [5.4] in a cloud chamber. *Bless* [5.5] used a magnetic spectrograph to verify (5.16, 17). The angles θ and ϕ were measured by *Hofstadter* and *McIntyre* [5.6].

Klein and *Nishina* [5.7] applied Dirac's relativistic theory of the electron to the Compton-scattering problem. They obtained a general expression for the differential cross-section for initially unbound and stationary electrons. A perturbation calculation in quantum electrodynamics gives (see, for example [5.8]) the unpolarized cross-section as

$$d\sigma_e = \frac{1}{2}r_e^2\left(\frac{\nu'}{\nu}\right)^2\left(\frac{\nu}{\nu'}+\frac{\nu'}{\nu}-\sin^2\theta\right)d\Omega\left[\frac{\text{cm}^2}{\text{electron}}\right], \tag{5.17}$$

where the scattered photon $h\nu'$ goes into the solid angle $d\Omega = 2\pi\sin\theta\, d\theta$. Substituting $\nu/\nu' = 1+\alpha(1-\cos\theta)$ from (5.12),

$$d\sigma_e = r_e^2\left(\frac{1}{1+\alpha(1-\cos\theta)}\right)^2\left(\frac{1+\cos^2\theta}{2}\right)\left(1+\frac{\alpha^2(1-\cos\theta)^2}{(1+\cos^2\theta)[1+\alpha(1-\cos\theta)]}\right)d\Omega \tag{5.18}$$

In the forward direction $\theta = 0$, it approaches the classical value (5.5) $(d\sigma_e/d\Omega)_{\theta=0} = r_e^2 = 79.41\times10^{-27}\,\text{cm}^2/(\text{electron}\times\text{steradian})$. The Klein–Nishina formula (5.18) is plotted in Fig. 5.6, and is in excellent agreement with experiments. It reduces to (5.5) for $\lambda = \infty$. *Singhal* and *Burns* [5.9] have recently verified both (5.12) and the angular dependence of (5.18), using simple equipment. They used a 1−mCi ^{137}Cs source ($h\nu = 662$ keV), cylindrical Al scatterer, 2×2 inch NaI detector, with associated electronics, and a multichannel analyzer (100 channels). The angular range covered was 30° to 120°. The integration of (5.18) over $d\Omega$ gives the total cross-section

$$\sigma_e = 2\pi r_e^2\left[\frac{1+\alpha}{\alpha^2}\left(\frac{2(1+\alpha)}{1+2\alpha}-\frac{\log(1+2\alpha)}{\alpha}\right)+\frac{\log(1+2\alpha)}{2\alpha}-\frac{1+3\alpha}{(1+2\alpha)^2}\right]\left[\frac{\text{cm}^2}{\text{electron}}\right], \tag{5.19}$$

$$\sigma_e = \frac{8\pi}{3}r_e^2(1-2\alpha) \simeq \frac{8\pi}{3}r_e^2, \quad (\alpha \ll 1), \tag{5.20}$$

$$\sigma_e = \pi r_e^2\frac{1}{\alpha}\left(\log 2\alpha + \frac{1}{2}\right), \quad (\alpha \ll 1). \tag{5.21}$$

Thus, the Compton cross-section drops off at high energies. At energies above a few MeV, the dominant absorption process is pair production (photon → electron + positron).

In a thin absorber of thickness dx, having N_a atoms per cm^3, there are N_aZ electrons per cm^3 and N_aZdx electrons per cm^2. Suppose a beam of n photons, each of energy $h\nu$, passes through the absorber. The number dn of these photons

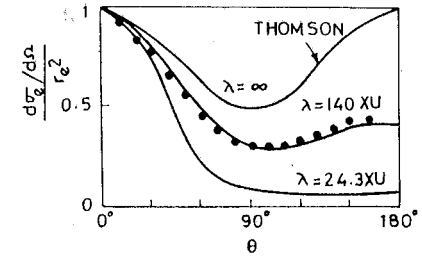

Fig. 5.6. $(d\sigma_e/d\Omega)/r_e^2$ versus θ plot. The experimetal points are for carbon at λ = 140 XU

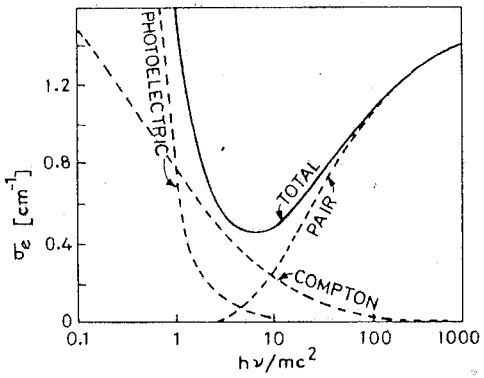

Fig. 5.7. Total linear attenuation coefficient for lead as a function of $h\nu/mc^2$

that experience Compton collisions and are thereby removed from the beam is

$$-\frac{dn}{n}=(N_a Z dx)\sigma_e. \tag{5.22}$$

We define the Compton total linear attenuation coefficient as

$$\sigma_1=N_a Z\sigma_e \text{cm}^{-1}=N_A\rho(Z/A)\sigma_e \text{cm}^{-1}, \tag{5.23}$$

where the number N_a is given by

$$N_a\left[\frac{\text{atoms}}{\text{cm}^3}\right]=N_A\left[\frac{\text{atoms}}{\text{mole}}\right]\frac{\rho[\text{g/cm}^3]}{A[\text{g/mole}]}. \tag{5.24}$$

Figure 5.7 shows the total linear attenuation coefficient for ^{82}Pb as a function of $h\nu/mc^2$.

The polarization is the same for unmodified and modified X-rays. A detailed review on the Compton effect is given by *Evans* [5.10].

5.3 X-Ray Raman and Plasmon Scattering

Scattered radiation, whose frequency is changed corresponding to transitions between the bound states of the target atom, was discovered in the visible region by *Raman* [5.11]. The process is known as *Raman scattering*. The frequency ν'_R of the modified line of Raman type is given by [5.12]

$$h\nu'_R=h\nu-\delta E, \tag{5.25}$$

where ν is the frequency of the incident radiation and δE is the energy difference required for the transition of the atom from the ground state to an optical (excited) state.

The existence of Raman lines in the X-ray region was predicted by *Dumond* [5.13] and later by *Sommerfeld* [5.14]. They have now been unambiguously observed in light elements by *Das Gupta* [5.15] and others [5.16–18].

The incident radiation excites a core electron from an atom in a solid to one of the vacant levels above the Fermi energy. The scattered radiation suffers a corresponding loss in its energy. A band spectrum, called the *Raman band*, is produced. The transition probability, in the dipole approximation, is the same as that of K-absorption. Thus the shape of the observed Raman band reflects the K-absorption spectrum with an edge and a peak on its low-energy end.

The energy loss of the incident radiation in Raman scattering in light elements is less than several hundred eV (55 eV for Li, 112 eV for Be). In Compton scattering it is several hundred eV. Hence, the Raman bands overlaps the tail of the Compton peak. While the Compton peak, shifts with the scattering angle θ and shows a dispersion relation $\omega=\hbar(2m)q^2$, where $\hbar q$ is the momentum transfer to the electron, the Raman peak is independent of θ and shows $\omega=$const.

Das Gupta [5.15] used a bent mica ($d=2.554$ Å) Cauchois spectrograph as analyzer, K X-rays of ^{29}Cu and ^{42}Mo as incident radiation, and carbon as scattering material. His main result for the Cu $K\alpha_{1,2}$ radiation scattered at $\sim 90°$ is shown in Fig. 5.8. The observed shift of the Raman line relative to the primary (Rayleigh) wavelength is 57.1 XU. This corresponds to an energy shift of 282 eV, which is close to the excitation energy of the K electrons of carbon (284 eV).

A resonant enhancement in the Raman scattering, when the incident X-ray energy is near an atomic absorption edge, has also been observed [5.19, 20]. A second-order perturbation theory of the *resonant X-ray Raman effect* has been given by *Bannett* and *Freund* [5.21].

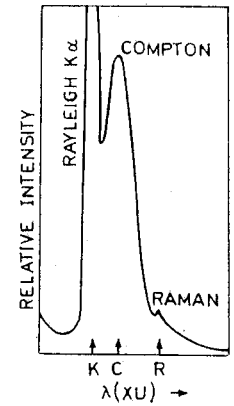

Fig. 5.8. Spectroscopic analysis of Cu $K\alpha_{1,2}$ radiation scattered at 90° by polystyrene (carbon): K (Rayleigh Cu $K\alpha_{1,2}$ 1540 XU); C (Compton peak at 90°); R (Raman line 1597.1 XU)

Besides the one-electron excitation of Compton and Raman scattering, electrons can also be collectively excited in plasmon scattering. The *plasmon* peak was predicted by *Pines* [5.22] and has been observed recently [5.23–25]. The frequency ν_P of the modified line of *plasmon scattering* is given by

$$h\nu'_P = h\nu - E_P, \tag{5.26}$$

where E_P is the plasmon-excitation energy of the scattering material.

Consider the conduction-band electrons that form an electron gas. In the absence of collisions, the equation of motion of a free electron in an electric field is $md^2x \times dt^2 = -eE$. If x and E have the time dependence $\exp(-i\omega t)$, then $x = eE/m\omega^2$. The dipole moment p of the electron is $p = -ex = -e^2E/m\omega^2$, and the polarization is $P = -nex = -(ne^2/m\omega^2)E$, where n is the electron concetration. The dielectric function at frequency ω is $\varepsilon = 1 + 4\pi P(\omega)/E(\omega)$, or

$$\varepsilon(\omega) = 1 - \frac{4\pi ne^2}{m\omega^2} = 1 - \frac{\omega_p^2}{\omega^2}, \tag{5.27}$$

where $\omega_p = 4\pi ne^2/m$ is called the *plasma frequency*. A *plasmon* is a quantized plasma oscillation. It can be excited by a photoelectron escaping from the material (extrinsic plasmon) or an X-ray photon passing through a thin metallic film (intrinsic plasmon). The charge of the electron, or the electric field of the radiation, couples with the electrostatic field fluctuations of the plasma oscillations. In general, $E_p = \hbar\omega_p = \hbar 4\pi ne^2/m_{\text{eff}}$, where m_{eff} is the effective mass of the electron. In Fig. 5.9 we show a microphotometer record of the spectrogram of the Cu $K\beta_1$ line scattered by beryllium at scattering angle 10°. The plasmon has

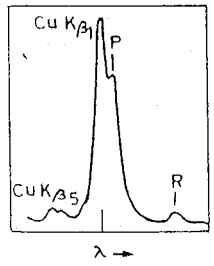

Fig. 5.9. The Rayleigh line (Cu $K\beta_1$, $\lambda = 1.39222$ Å), plasmon scattering line P ($\lambda = 1.39528$ Å), and the Raman scattering line R ($\lambda = 1.41087$ Å) from beryllium for the scattering angle 10°. Displacement of P is 19.6 eV and of R, 117.8 eV

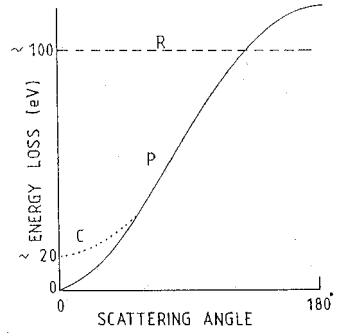

Fig. 5.10. General forms of the dispersion relations for the Raman (R), Compton (C) and Plasmon (P) scatterings. The scattering angle corresponds to the momentum transfer, and the energy loss to $\hbar\omega$

a finite lifetime ($\sim 10^{-16}$s), the spectrum has a narrow width. The dispersion relation is (Fig. 5.10)

$$\omega(q) = \omega_p[1 + (3/10)(v_F/\omega_p)^2 q^2], \tag{5.28}$$

where v_F is the Fermi velocity. For small q, the energy loss of the incident X-rays due to the plasmon excitation is $\hbar\omega_p$. For solids $\hbar\omega_p$ is about 10–20 eV, and so the plasmon line overlaps with the Compton peak (Fig. 5.9). The intrinsic plasmon line is observed only at small scattering angles.

Besides the volume or bulk plasmons (5.27) in a free electron gas, one can also have surface plasmons [5.26]. They can couple to photons [5.27]. *Harsh* and *Agarwal* [5.28] have used the hydrodynamical model [5.29] to study the surface plasmon dispersion relation for the plane-bounded electron gas. Their results agree with the measurements of *Kunz* [5.30] and *Arakawa* et al. [5.31].

Ley et al. [5.32] have detected several peaks due to plasmon losses in X-ray photoelectron spectra (Fig. 5.11). *Mahan* [5.33] and *Feibelman* and *Eastman* [5.34] have given a three-step model related to the specific observed features: (1) Optical excitation gives the primary peak at the maximum kinetic energy allowed,

$$E_{\text{kin}} = h\nu - E_q. \tag{5.29}$$

(2) *Transport to the Surface* of the photoelectron produces the bulk plasmon loss spectrum,

$$E_{\text{kin}} = h\nu - E_q - n\hbar\omega_p, \quad n = 1, 2, \ldots. \tag{5.30}$$

(3) *Escape into the vacuum* yields surface plasmon peaks with characteristic energy loss [5.22, 28, 35] of $\hbar\omega_s = \hbar\omega_p/\sqrt{2}$,

$$E_{\text{kin}} = h\nu - E_B - n\hbar\omega_p - \hbar\omega_s. \tag{5.31}$$

All of these features are known in *electron energy-loss spctroscopy* [5.36] where the electron source is outside the sample.

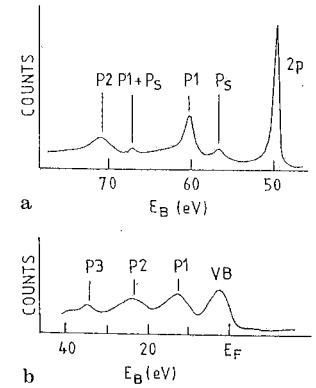

Fig. 5.11a, b. Photoelectron spectra of Mg metal using Al $K\alpha$ X-rays: **a** $2p$ region and **b** valence band region. Peaks $2p$ and VB are single-electron excitation primary peaks; $P1$, $P2$, ... are bulk plasmon peaks ($n = 1, 2, \ldots$) as photoelectrons move through the metal: P_s, $P1 + P_s$ are surface plasmon peaks

X-ray double plasmon satellites at an energy distance $2\hbar\omega_p$ on the high or low energy side of the main line have been observed [5.37, 38]. *Harsh* and *Agarwal* [5.39] have calculated the relative intensities of such satellites for Na and Cu, and compared them with experiments [5.37]. *Agarwal* and *Harsh* [5.40] have discussed the effect of collective elctron oscillations at the surface of metal compounds in X-ray absorption spectra. They have also discussed [5.40] the effect of double plasmon oscillations on the K and L absorption edges and accounted for the various unexplained chemical shifts of edges.

6. Chemical Shifts in Emission Spectra

The study of chemical bonding by X-ray and photoelectron spectroscopy has been a major area of research over the past three decades. The information obtained by these two methods is complementary. Besides this we shall also discuss here the correlation of factors like effective nuclear charge and bond length with X-ray energies and spectral shapes.

6.1 Solid-State Effects and Bonding

6.1.1 Metallic Bond

Each atom has a set of discrete energy levels. Consider an assembly of N such free atoms. The quantum-state distribution for this system is just that of an atom duplicated N times. As atoms are brought together to form a crystal, the wave functions of the outer electrons in the neighbouring atoms begin to *overlap*. That is, the outer electrons, originally bound to one nucleus, begin to feel the potentials of the neighbouring nuclei. This introduces a perturbation. The general effect of a perturbation is to remove the degeneracy (to separate out the levels that had the same unperturbed energies). Therefore, N-fold degenerate outer levels get separated and form a *bond* of energy levels. The degree of the removal of degeneracy depends on the strength and nature of the perturbation, and on the symmetry of the system. The perturbation felt by the core electrons is weak. Therefore, the inner levels remain sharp (localized orbitals).

Each atomic level can accommodate two electrons by the Pauli exclusion principle. Therefore, the band of certain energy width would consist of $2N$ levels. If each atom happens to have only one valence electron, then only the lower half of the levels in the energy band (called the *valence band*) would be occupied and the upper half would remain empty, at absolute-zero temperature.

The energy E_F of the highest occupied level is called the *Fermi energy*. The energy states in the bands are very closely spaced ($\sim 10^{-22}$ eV). Therefore, the distribution of the energy levels in the entire band can be conveniently described by the *density of states* $N(E)$, $N(E)dE$ being the number of electronic states per unit volume with energies between E and $E+dE$. A band is a state of high delocalization.

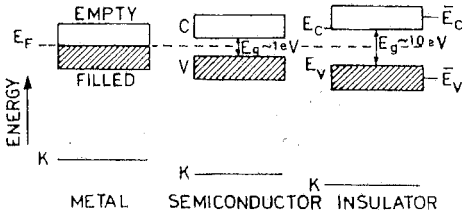

Fig. 6.1. Simplified energy-level diagram for a metal, a semiconductor, and an insulator. In the semiconductor, or insulator the shaded (blank) area of average energy $\bar{E}_v$ ($\bar{E}_c$) indicates the occupied (unoccupied) valence V (conduction C) band of edge E_v (E_c). K is an inner level. E_g is the forbidden gap. E_F is the Fermi energy

In a metal (Fig. 6.1) the states above E_F in the valence band are empty and easily accessible. Therefore, metals (like copper, silver, gold, etc.) are good conductors of electricity. If a compound is formed (for example, an oxide of copper) or in some elements (like silicon and germanium) the unoccupied band (*conduction band*) gets separated from the occupied band (*valence band*)[1] and a forbidden region of energy, called the *energy gap* (or *band gap*), E_g, appears between them (Fig. 6.1). When $E_g \sim 1$ to 2 eV, light quantum, or even thermal energy at room temperature can easily excite a few electrons across the gap from the highest point in the valence band (*valence-band edge*, E_v) to the lowest point in the conduction band (*conduction-band edge*, $E_c = E_g + E_v$). This makes conduction possible on a limited scale and the material is a *semiconductor*.

When $E_g \sim 5$ to 10 eV, conduction is not possible at room temperature and the material is an *insulator*.

We have also *semimetals*, like arsenic, antimony, and bismuth. In a semimetal, the conduction-band is only slightly lower in energy than the valance-band edge.

The function

$$f(E, T) = \frac{1}{\exp[E - E_F)/kT] + 1}, \quad (k = \text{Boltzmann constant}), \tag{6.1}$$

is called the *Fermi function*. It gives the fraction of states with energy E that are filled at the temperature T (Fig. 6.2). All states with $E < E_F$ are filled at $T = 0$, and there is at least one state with energy $E = E_F$ occupied at $T = 0$. For most semiconductors, the Fermi level is at the *middle* of the energy gap.

It is usual, in solid-state physics, to take $E_F = 0$. Then the conduction-band states have positive energies and the valence-band and inner bound states have negative energies. The energy-level diagram is aligned with E_F above the core

[1] The meaning of 'valence band' is more restricted in this context compared to that in a metal.

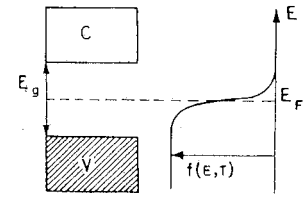

Fig. 6.2. Location of the Fermi level

levels. Therefore, for solids it is usual to draw the inner K level at the bottom, rather than at the top, of the energy level diagram.

Some workers have regarded the crystal as a giant molecule (for example, see [6.1]) and used chemical-bonding language to discuss the X-ray spectra. We shall now briefly define the technical words used in such discussions.

6.1.2 Ionic and Covalent Bonds

Kossel suggested in 1916 that elements placed just before (after) a noble gas in the periodic table can attain a noble-gas structure by gaining (losing) electrons and forming negatively (positively) charged ions. Thus ^{17}Cl, with a structure KL $3s^2\,3p^5 = 2.8.7$ can become a chloride ion Cl^- with a structure [Ar] = 2.8.8 by gaining an electron, and ^{11}Na, KL $3s = 2.8.1$, can form a sodium ion Na^+, [Ne] = 2.8, by losing and electron. Both Na^+ and Cl^- have stable structures and form Na^+Cl^- under an *ionic bond*. When many ions are held together by such electrostatic forces, we get an *ionic crystal*.

Two chlorine atoms cannot form an ionic bond to give Cl_2 because neither can transfer an electron to the other. To explain the formation of such molecules, Lewis suggested in 1916 that atoms can attain a noble-gas structure, not only by complete transference of electrons, as in ionic bonding, but also by sharing electrons. The shared pair of localized electrons constitute a *covalent bond*. The covalent bond is directed in space.

The force that binds a metal atom to a number of electrons within its sphere of influence is called a *metallic bond*. The valence electrons in a metallic bond are spread over the crystal, more or less uniformly. Therefore, metallic bonds are nondirectional and weaker than covalent bonds. Most actual bonds are intermediate in type (mixture of ionic and covalent, or of covalent and metallic forces).

The sharing of electrons in strong bonds among atoms essentially determines the electronic structure of interest in the X-ray spectroscopy. The valence-electron localization increases in going from the metallic through covalent to ionic bonding (Fig. 6.3). In ionic compounds, the electrons are localized on one of the atoms, in covalent compounds between the atoms, and in metals throughout the lattice.

The dipole-matrix element for the X-ray K emission (and absorption) process involves the wave functions of the outer bonding states and the inner 1s

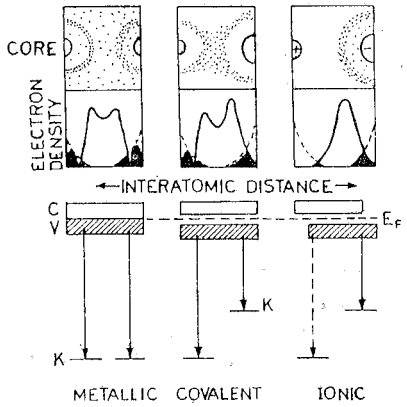

Fig. 6.3. Valence-electron distribution for metallic, covalent and ionic bondings (dots: valence electrons). Qualitative electron-density distributions for third-row cations (Al, Si, etc.) and second-row anions (C, N, O, etc.) are indicated (solid curve: $2p + 3p$; dashed curve: $1s$ electron density). The fully shaded regions show where the valence and $1s$ electron densities overlap. The K spectra shown below arise from these regions. In ionic solids, the valence electron that undergoes transition for the cation K spectra belongs to the anion (crossover transition, dashed line) (After Nagel, D.J.: Eighteenth ACAXA, Denver 1969)

state. Therefore, the K spectra arise from those regions where the valence and $1s$ electron densities overlap (Fig. 6.3).

We shall use both the band and bond theories to discuss X-ray spectra. For metallic and ionic solids reliable band calculations have become available in recent years.

6.1.3 Hybridized Orbitals

When two atoms are brought together, their atomic orbitals overlap. In a simple approximation, the *hybridized orbital* Φ is a linear combination (super-position) of two atomic orbitals ψ_{nl},

$$\Phi_{ll'} = \psi_{nl} \pm \psi_{nl'}. \tag{6.2}$$

The associated probability density contains the interference effects given by $\pm(\psi^*_{nl}\psi_{nl'} + \psi^*_{nl'}\psi_{nl})$. The valence orbitals are usually the s and p ones, with occasionally a small admixture of d states. Thus, a hybridized orbital mixes the s and p, and possibly d, atomic orbitals. This leads to the formation of *bonding* and *antibonding* states (Fig. 6.4) with an energy separation (gap) $E_{g,\,bond}$. We have [6.3, 4]

$$E_{g,\,bond} = \bar{E}_c - \bar{E}_v > E_g, \tag{6.3}$$

where $E_g = E_c - E_v$, and $\bar{E}_c$ ($\bar{E}_v$) is the *average* conduction- (valence-) band

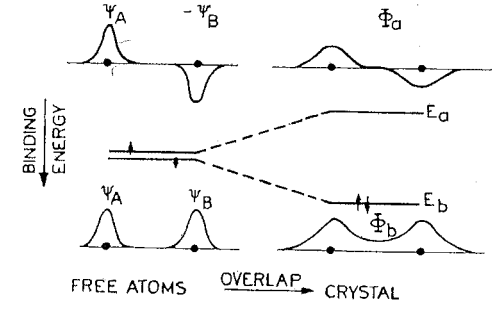

Fig. 6.4. Formation of bonding and antibonding states in the LCAO approximation. E_b (E_a) is the bonding (antibonding) energy level

energy. For example, in Si and ZnO, E_g is 1.1 and 3.6 eV, compared to $E_{g,\,bond} = 4.8$ and 12 eV, respectively.

To see the origin of $E_{g,\,bond}$, consider the simplest case of a diatomic molecule AB. The molecular orbital Φ in the region of each atom resembles the atomic orbitals ψ_A and ψ_B. We can write, in the approximation of the linear combination of atomic orbitals (LCAO),

$$\Phi = C_A\psi_A + C_B\psi_B, \tag{6.4}$$

where constants C_A and C_B are chosen to give lowest energy to the molecular orbital. Because Φ^2 is a measure of electron density at any point, it gets contributions from ψ_A^2 and ψ_B^2 in the ratio of $C_A^2 : C_B^2$.

For a homonuclear diatomic molecule ($A = B$), $C_A^2 = C_B^2$, or $C_A = \pm C_B$. Thus

$$\Phi_a = \psi_A - \psi_B, \quad (\textit{antibonding}), \tag{6.5}$$

$$\Phi_b = \psi_A + \psi_B, \quad (\textit{bonding}). \tag{6.6}$$

The energies of these molecular orbitals are

$$\begin{aligned} E_a &= (\int \Phi_a^* H \Phi_a d\tau)/\int \Phi_a^* \Phi_a d\tau \\ &= [\int(\psi_A - \psi_B)H(\psi_A - \psi_B)d\tau]\int/\int(\psi_A - \psi_B)^2 d\tau \\ &= \tfrac{1}{2}(H_{AA} + H_{BB} - 2H_{AB}) = \tfrac{1}{2}(E_A + E_B - 2E_{AB}), \end{aligned} \tag{6.7}$$

where H is the Hamiltonian and we have taken $\int \psi_A\psi_B d\tau = \delta_{AB}$ for the denominator. Similarly,

$$E_b = \tfrac{1}{2}(E_A + E_B + 2E_{AB}). \tag{6.8}$$

Because E_A, E_B and E_{AB} are all negative quantities, Φ_b is more stable than the $1s$ orbital of the atom A (*or* B), whereas Φ_a is less stable (Fig. 6.4). Clearly, $E_{g,\,bond} = 2E_{AB}$ in this case.

In addition to classifying orbitals as bonding and antibonding, it is useful to classify them in terms of their symmetry about the internuclear axis. In Fig. 6.5, we illustrate the formation of molecular orbitals out of $2s$ and $2p_z$ atomic orbitals of two atoms A and B.

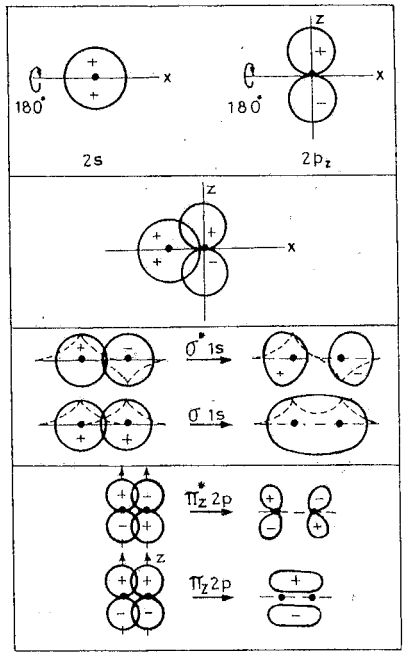

Fig. 6.5. Formation of molecular orbitals in simple cases. First row: atomic orbitals (2*s* is symmetric about *x* axis, and $2p_z$ is unsymmetrical about *x* axis because of θ, ϕ dependence, $r\cos\theta$): Second row: nearly zero overlap and so molecular orbital is not formed. Third row: σ^* 1*s* (antibonding) and $\sigma 1s$ (bonding) molecular orbitals from two 1*s* atomic orbitals, with symmetry about the nuclear axis. Fourth row: $\pi_z^* 2p$ and $\pi_z 2p$ bonds that are unsymmetrical about the nuclear axis. The dashed curves represent the wave functions and the solid curves the boundary surface of an orbital

In order of increasing energy the molecular orbitals are: $1s\sigma < 1s\sigma^* < 2s\sigma < 2s\sigma^* < 2p\sigma < 2p_z\pi = 2p_y\pi < 2p_z\pi^* = 2p_y\pi^* \ldots$ etc. The asterisk indicates an antibonding level. The subscripts g (gerade = even) and u (ungerade = odd) indicate behavior under the operation of a twofold rotation. For example, an *s* orbital is rotated into itself, whereas a p_z orbital is turned into minus itself (the phases of its lobes change sign).

The overlapping orbitals can be combined to form molecular orbitals if they have similar energy and similar symmetry. The strength of such a covalent bond depends on the extent of overlap achieved. This is known as the *principle of maximum overlap*. For example, in a polar diagram (Fig. 6.6) the *p* orbitals are concentrated in a particular direction and their lobes are longer than the radius of the corresponding spherical *s* orbital. Therefore, they can overlap with other *s* or *p* orbitals more effectively than two *s* orbitals can overlap (Figs. 6.5, 6); *s*–*p* σ

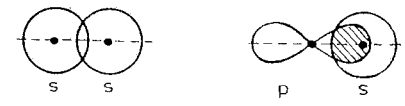

Fig. 6.6. Overlap between two *s* orbitals, and one *p* and one *s* orbital

bonds are stronger than *s*–*s* bond, and *p*–*p* σ bonds are stronger still. The relative bond strengths are of the order s–$s : p$–$p = 1 : 1.732 : 3$.

Sometimes certain symbols of group theory are also used. Lowercase symbols (a_{1g}, a_{2u}, e_g, etc.) are used to indicate one-electron wave functions (orbitals). Uppercase symbols (A_{1g}, E_g, T_{1u}, etc.) are used to describe electronic energy levels. The symbols *A* (or *a*) and *B* (or *b*), with any suffixes, indicate single degeneracy, *E* (or *e*) indicates double degeneracy, and *T* (or *t*) indicates triple degeneracy. The symbol t_{2g}^3 indicates that these orbitals are occupied by three electrons. Other subscripts (for example, 1, 2, or primes) serve only to distinguish general symmetry properties. Thus, t_{1g} and t_{2g} represent two sets of triply degenerate orbitals, all centrosymmetric (g).

6.1.4 Coordination

In covalent structures, the directed orbitals are oriented towards the nearest-neighbour atoms, so that the energy of occupied bonding orbitals is decreased. Semiconductors usually have structures such that each atom is *tetrahedrally coordinated*, corresponding to the sp^3 orbitals directed towards the corner of a tetrahedron. A number of binary compounds $A^N B^{8-N}$ with 8 valence electrons per atom pair occur in this coordination. If $\bar{N}$ is the average number of electrons per atom, then for such structures the *coordination number* is $8 - \bar{N}$.

Besides the tetrahedral sp^3 ($\bar{N} = 4$) structures, we also have layer structures of hexagonal symmetry with sp^2 bonds lying in the *xy* plane (like graphite).

An exception to the rule that the sp^3 bonding requires $\bar{N} = 4$, is provided by *fluorite structures* with formula RX_2. They contain eight electrons per formula unit ($A_2^{II}B^{IV}$: Mg_2Si), or sixteen ($A^{II}B_2^{VII}$: CdF_2 or $BaCl_2$; $A^{IV}B_2^{VI}$: GeO_2). Mg_2Si is covalent, CdF_2 is ionic, and GeO_2 has some covalent and some ionic properties.

The rule that *s* and *p* orbitals hybridize to form directed bonds is usually valid so long as $E_{g,\,\text{bond}} > E_{np} - E_{ns}$ where $E_{np} - E_{ns}$ is the energy difference between the *np* and *ns* valence electrons of the free atom. If $E_{np} - E_{ns}$ is large the energy gap between the bonding $(sp^3)^+$ states and antibonding $(sp^3)^-$ states is weakened or even destroyed, and the crystal becomes metallic (for example, Pb with large *n*).

The column *VI* (except oxygen) are called *chalcogenides*. The crystals of S, Se and Te are semiconductors with a structure of spiral chains parallel to the *z* axis.

A combination of one *s*-, three *p*- and two *d*-atomic orbitals leads to six hybrid orbitals that are directed *octahedrally* (away from the origin in the $\pm x$, $\pm y$ and $\pm z$ directions). We can have d^2sp^3 or sp^3d^2 octahedral hybridization. An example is provided by sulphur hexafluoride. The ground-state arrangement of electrons in the sulphur atom is

	1s	2s	$2p_x$	$2p_y$	$2p_z$	3s	$3p_x$	$3p_y$	$3p_z$	3d
S	:↑↓	↓↑	↓↑	↓↑	↓↑	↓↑	↓↑	↓	↓	
S**	:↓↑	↓↑	↓↑	↓↑	↓↑	↓	↓	↓	↓	↓↓

Before sulphur can form octahedral bonds by sp^3d^2 hybridization, a double *promotion* is necessary to give the excited states S**. The overlap with $2p$ orbitals of fluorine will then yield the octahedral SF_6 molecule.

In PCl_5, we have sp^3d-hybrid orbitals directed towards the corners of a *trigonal* bi-pyramid.

The *spinels* are a group of complex oxides with general formula $M^{2+}M_2^{3+}O_4$, where M may be Mn, Fe or Co, or a number of other transition metals. The oxides Fe_3O_4 and Mn_3O_4 are spinels, with formulae $Fe^{2+}Fe_2^{3+}O_4$ and $Mn^{2+}Mn_2^{3+}O_4$. In the crystal structure of a spinel, one-third of the metallic ions are surrounded, tetrahedrally, by four O^{2-} ions, and two-thirds are surrounded, octahedrally, by six O^{2-} ions, In a *normal* spinel (Mn_3O_4), all of the M^{3+} ions occur at octahedral sites, and all of the M^{2+} ions at tetrahedral sites. In the *inverted* spinel (Fe_3O_4), half of the M^{3+} ions occur at tetrahedral sites and the other M^{3+} and M^{2+} ions occupy octahedral sites.

6.1.5 Ionic Character of Covalent Bonds

If A and B are unlike atoms, the pair of shared electrons may not be shared equally in a covalent bond. For example, if B has stronger attraction for electrons than A, the shared pair will be attracted towards B and away from A. Such displacement of electrons in a covalent bond gives the bond some ionic character. The actual bond then can be represented as a *resonance* hybrid between the covalent and ionic forms,

$$A-B \leftrightarrow A^+B^-.$$

The *ionicity of a bond* is defined as the fraction f_i of ionic or hetero-polar character in the bond compared to the fraction f_c of covalent or homo-polar character, such that

$$f_i+f_c=1. \tag{6.9}$$

a) *Coulson's Definition of Ionicity.* The valence wave function can be written as (6.4), or simply as

$$\Phi_{\text{valence}}=\psi_{sp^3}(A)+\lambda\psi_{sp^3}(B), \tag{6.10}$$

for the orbitals in tetrahedrally coordinated A^NB^{8-N} semiconductors, considered here for simplicity. The trial wave function (6.10) is put in the wave equation and the best value of λ is obtained by minimizing the energy. Because $\psi(A)$ and $\psi(B)$ are assumed to be orthogonal, following *Coulson* et al. [6.5], we

can define ionicity as

$$f_i=\frac{P(A)-P(B)}{P(A)+P(B)}=\frac{1-\lambda^2}{1+\lambda^2}, \tag{6.11}$$

where $P(A)$ is the probability of finding a valence electron on A.

b) *Pauling's Definition of Ionicity.* The tendency of an atom to attract electrons to itself when forming molecule is called the *electronegativity* of the atom. Generally, small atoms attract electrons more than large ones. Also, atoms with nearly filled shells tend to be more electronegative than those with sparsely occupied ones. Two atoms with similar electronegativities form covalent bonds. A large difference in electronegativity yields an ionic bond. Rather than have two extreme forms, *Pauling* [6.6] related the ionic character of a bond to the difference in electronegativity.

In a bond A–B, let a number $x_A(x_B)$ denote the electronegativity of the atom $A(B)$. If $x_A<x_B$, then B has greater power to attract an electron than A. One can think that on bonding a certain number of electrons, proportional to $|x_A-x_B|$, are transferred from A to B, until the electronegativities of the two atoms are equalized. This may give partially charged atoms in the molecule. $|x_A-x_B|$ is a measure of ionicity. Clearly, the Coulomb interaction, between the ionic charge left behind and the valence charge transferred, is proportional to $|x_A-x_B|^2$.

As $|x_A-x_B|$ increases, $f_i\to 1$, $0\leqq f_i\leqq 1$. Also, the ionicity of an A–B bond should be the same as that of a B–A bond, $f_i(A,B)=f_i(B,A)$. These consideration led *Pauling* [6.6] to define the ionicity of a single bond as

$$f_i=1-e^{-0.25(x_A-x_B)^2}. \tag{6.12}$$

In molecules, the coordination number of an atom is less than or equal to its valence N. On the other hand, in crystals the coordination number usually exceeds N. In A^NB^{8-N} crystals it is usually 4 or 6. To accommodate this fact, *Pauling* introduced the concept of *resonating bonds*. The N valence bonds per atom are pictured as shared with all of the 4 (or 6) nearest neighbours of each atom. This implies that the degree of covalency $f_c=1-f_i$ is also shared and we must replace the single-bond ionicity f_i by a resonating-bond ionicity f_i^{res},

$$1-f_i^{\text{res}}=(N/n)(1-f_i)=(N/n)\,e^{-0.25(x_A-x_B)^2}, \tag{6.13}$$

where n is the number of nearest neighbours. This definition is applicable to *crystals*. Pauling's values of x_A are given in Appendix H.

c) *Effective-Charge Approach.* An electron in a bond is assumed to be attracted by one of the two nuclei with a Coulomb force $Z_{\text{eff}}e^2/r^2$, where eZ_{eff} is the effective nuclear charge felt by the electron at a mean distance r from the nucleus. Slater's method can be used to estimate Z_{eff}. *Pauling's* value of x_A can be represented in [6.7–10] by a formula of the form

$$x_A=aZ_{\text{eff}}/r^p+b. \tag{6.14}$$

Allred and *Rochow* [6.7] use $a=0.359$, $p=2$, $b=0.744$. Values of partial charges in polyatomic ions (like NH_4^+, OH^-, CO_3^{2-} etc.) have been given by *Sanders* [6.11]. His two principles are: 1) When two or more atoms, initially different in electronegativity, combine chemically, they become adjusted to an equal intermediate electronegativity in the compound. 2) The electronegativity of all of the atoms in a compound is the geometric mean of the electronegativities of all of the atoms before combination. *Sanders* further assumes that a group of atoms that make up a positive or negative ion can be treated as a single atom that has an electronegativity that corresponds to their geometric mean. Different workers assign different values to x_A. It is the relative values that matter. *Pauling's* values are commonly used.

d) *Phillips' Definition of Ionicity.* For a crystal $A^N B^{8-N}$, the potential can be written as

$$V(\text{crystal})=\sum_{\alpha} V_A(\boldsymbol{r}-\boldsymbol{r}_\alpha)+\sum_{\beta} V_B(\boldsymbol{r}-\boldsymbol{r}_\beta), \tag{6.15}$$

where r_α, r_β label the lattice sites of the sublattices of the A, B atoms, respectively, and V_A, V_B are the screened Coulomb potentials seen by valence electrons of atoms A, B. For each cell, we can separate V (crystal) into the parts that are even and odd with respect to the interchange of A and B. *Phillips* [6.3, 4] associates these parts with covalent and ionic potentials,

$$V_{\text{covalent}}=V_A+V_B, \quad V_{\text{ionic}}=V_A-V_B. \tag{6.16}$$

We expect f_c and f_i to be related to certain average values of (6.16), calculated with respect to suitable wave functions of the crystal.

In crystallography, it is found useful to express the *bond length* r_{AB} between nearest neighbours, in a given state of valence hybridization, as the sum of *covalent radii* r_A and r_B,

$$r_{AB}=r_A+r_B. \tag{6.17}$$

The tetrahedral covalent radii in angstroms have been given by *Pauling*: C(0.77), O(0.66), F(0.64), Cu(1.35), S(1.04) Cl(0.99), Pb(1.46), etc.

The effective potential is taken to be of the form $V=(Ze^2/r)\exp(-k_s r_{AB}/2)$, where Ze^2/r is the Coulomb part and $\exp(-k_s r_{AB}/2)$ is the Thomas–Fermi exponential screening factor [6.12]. The screening wave number k_s is equal to $(\pi a_0)^{-1}\, 4k_F$, where k_F is the Fermi momentum of a free electron gas of density equal to that of valence electrons, and a_0 is the Bohr radius.

Phillips [6.3] expresses the energy gap between the bonding and antibonding states as

$$E_{g,\,\text{bond}}=E_h+iC, \quad E_{g,\,\text{bond}}^2=E_h^2+C^2, \tag{6.18}$$

where C represents the ionic (charge transfer) and E_h the covalent contribution to $E_{g,\,\text{bond}}$. The complex energy gap (6.18) means that in the (E_h, C) plane we can define a phase angle ϕ by $\tan\phi=C/E_h$. The requirements $f_i(A,B)=f_i(B,A)$, $0\leqq f_i\leqq 1$ and $f_i+f_c=1$, suggest the definitions

$$f_i=\sin^2\phi=C^2/E_{g,\,\text{bond}}^2; \quad f_c=\cos^2\phi=E_h^2/E_{g,\,\text{bond}}^2. \tag{6.19}$$

f_i defined by (6.19) is called the *spectroscopic ionicity.*

Phillips uses the one-electron approximation of *Penn* [6.13] for diamond-like semiconductors to determine E_h and C.

We expect C to depend on V_A-V_B. *Van Vechten* [6.8] finds

$$C(A,B)=b(z_A e^2/r_A-z_B e^2/r_B)\exp(-k_s r_{AB}/2), \tag{6.20}$$

where $b\simeq 1.5$. *Penn* [6.13] finds $E_h\propto r_{AB}^{-2.48}$. Phillips has calculated C, E_h and f_i for many compounds (Table 6.1) [6.14].

It is useful to compare (6.20) to *Pauling's* electronegativity difference $\Delta_{AB}^-=x_A-x_B$. It turns out that approximately (Table 6.1),

$$C(A,B)=a_c\Delta_{AB}^-(\text{eV})+b_c, \tag{6.21}$$

where $a_c=5.75$ and $b_c=0$. By the same reasoning, E_h depends on V_A+V_B, so that approximately (Table 6.1),

$$E_h(A,B)=a_h\Delta_{AB}^+(\text{eV})+b_h, \tag{6.22}$$

Table 6.1. Average energy gaps in some $A^N B^{8-N}$ compounds [6.3] $\Delta_{AB}^{\pm}=|x_A\pm x_B|$ are calculated on the Pauling scale. The forbidden energy gap is given for comparison

Crystal	$\Delta_{AB}^-(\Delta_{AB}^+)$	$C(E_h)$ [eV]	$E_{g,\,\text{bond}}$ [eV]	f_i	E_g [eV]
Si	0 (3.6)	0 (4.77)	4.77	0	1.14
BP	0.1(4.1)	0.68(7.44)	7.47	0.006	—
SiC	0.7(4.3)	3.85(8.27)	9.12	0.177	3
AlSb	0.4(3.4)	2.07(3.53)	4.14	0.250	1.52
BN	1.0(5.0)	7.71(13.1)	15.2	0.256	—
GaSb	0.3(3.5)	2.10(3.55)	4.12	0.261	0.78
AlAs	0.5(3.5)	2.67(4.38)	5.14	0.274	2.16
BeS	1.0(4.0)	3.99(6.31)	7.47	0.286	—
GaAs	0.4(3.6)	2.90(4.32)	5.20	0.310	1.43
InSb	0.2(3.6)	2.10(3.08)	3.73	0.312	0.18
GaP	0.5(3.7)	3.30(4.73)	5.75	0.327	2.26
InAs	0.3(3.7)	2.74(3.67)	4.58	0.357	0.35
InP	0.4(3.8)	3.34(3.93)	5.16	0.421	1.35
GaN	1.4(4.6)	7.64(7.64)	10.8	0.500	—
ZnTe	0.5(3.7)	4.48(3.59)	5.74	0.609	2.26
ZnO	1.9(5.1)	9.30(7.33)	11.8	0.616	3.2
ZnS	0.9(4.1)	6.20(4.82)	7.85	0.623	3.6
CdS	0.8(4.2)	5.90(3.97)	7.11	0.685	2.42
CdTe	0.4(3.8)	4.90(3.08)	5.79	0.717	1.45

where $\Delta^{+}_{AB} = x_A + x_B$, and $a_h = 4.2$, $b_h = -11$. In this approximation,

$$f_i = [1 + (E_h/C)^2]^{-1} \simeq [1 + (4.2\Delta^{+}_{AB} - 11)^2/(5.75\Delta^{-}_{AB})^2]^{-1}. \quad (6.23)$$

Levine [6.15] has extended *Phillips'* theory to more complex crystals (like Al_2O_3, $LiGaO_2$, and $NaClO_3$) where each bond is characterized by a polarizability, an ionicity, an everage symmetric and antisymmetric potential, and an average number of electrons per bond (instead of the average number of elctrons of *Phillips'* theory). The last point arises because the number of bonding electrons may differ in each type of bond (μ). *Levine* writes for individual bonds,

$$\begin{aligned}
&(E^{\mu}_{g,\,bond})^2 = (E^{\mu}_h)^2 + (C^{\mu})^2,\\
&f^{\mu}_i = (C^{\mu}/E^{\mu}_{g,\,bond})^2, \quad f^{\mu}_c = (E^{\mu}_h/E^{\mu}_{g,\,bond})^2,\\
&E^{\mu}_h = 39.74\,(r^{\mu}_{AB})^{-2.48}\,\text{eV},\\
&C^{\mu} = b^{\mu}\exp(-k^{\mu}_s r^{\mu}_0)\left(\frac{z^{\mu}_A e^2}{r^{\mu}_A} - \frac{z^{\mu}_B e^2}{r^{\mu}_B}\right)\text{eV},
\end{aligned} \quad (6.24)$$

where z^{μ}_A is the number of valence electrons of μ-type on A, k^{μ}_s depends on the number of valence electrons of the bond μ in unit volume, and $b_{\mu} = 0.089 \times$ (average coordination number)^2.

e) *Concept of Effective Charge.* Effective charge is that charge on an atom which is sufficient to explain the properties of a compound when the atom is bound to it. Three main different approaches have been used to define the effective charge: 1) thermochemical theory of *Pauling* [6.6], 2) valence-bond molecular-orbital theory of *Coulson* [6.5], and 3) the dielectric theory of *Szigeti* [6.16]. The formation of the chemical bond results in a rearrangement of the outer electrons of the participating atoms. In particular, the more-electronegative atom (anion B) receives electrons from the less-electronegative atom (cation A) (Fig. 6.7). Therefore, the charge redistribution on bonding can be equated to alteration of the charge on an ion, in the first approximation. The effective nuclear charge is related to the electronegativity, (6.14). Following *Pauling* [6.6], and *Mooser* and *Pearson* [6.17], it has been suggested [6.18–20] that the effective charge q on a cation in a molecule can be expressed as

$$q = \sum_{\mu} f_{i,\mu} = \sum_{\mu} \{1 - \exp[-0.25(x_A - x_B)^2]\}_{\mu}, \quad (6.25)$$

where $f_{i,\mu}$ is the partial ionicity of the bond μ, as given by (6.12). The sum is over the bonds that connect the cation A with the different neighbours B.

In estimating q, methods with different degrees of sophistication and rigor can be used [6.21]. However, simple calculations of the Pauling type are in reasonable agreement with the sophisticated calculations based on self-consistent-field programs. We shall, therefore, consider only the simple free-ion models.

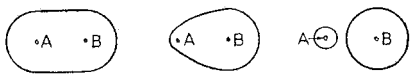

Fig. 6.7a–c. Shape of orbital representing different bondings: **a** covalent ($A-B$), **b** covalent with ionic character ($A-B \leftrightarrow A^+ + B^-$), and **c** ($A^+ + B^-$)

Suchet [6.22] has expressed the effective charge as

$$q(\text{cation}) = n[1 - 0.01185(Z/r' + Z'/r)] = -(n/n')\,q(\text{anion}), \quad (6.26)$$

where $Z(Z')$ and $r(r')$ are the total number of electrons and the ionic radii (following *Pauling*) of the atoms present at the cation (anion) site, and $n(n')$ gives the number of electrons transferred from the cation (anion).

Syrkin and *Dyatkina* [6.23] and *Coulson* et al. [6.5] have given a concept of effective charge by considering localized molecular–orbital bonds in the $A^N B^{8-N}$ compounds.

Szigeti [6.16] calculated the macroscopic polarization by taking into account the effect of only near neighbours and defined effective charge in terms of dynamic charges based on the infrared spectra.

If the interatomic distance R between the atoms in a molecule AB is increased by x, then the static charge $q(0)$ supported by A in the initial situation becomes

$$q(x) = q(0) + x(dq/dx). \quad (6.27)$$

The dipole moment P can be written as the sum of the relative shifts of two atoms with charges $\pm q(0)$ and the transfer of the charge dq/dx over R,

$$P = xq(0) + xR(dq/dx). \quad (6.28)$$

If e is the "dynamic charge" defined as $P = ex$,

$$e = q(0) + R(dq/dx). \quad (6.29)$$

Batsanov and *Ovsyannikova* [6.24] have expressed the coordination effective charge q as

$$q = N - nf_c, \quad (6.30)$$

Where N is the valency, n is the coordination number, and f_c the covalency.

6.2 Chemical Shifts of Emission Lines

Lindh and *Lundquist* [6.25] were the first to observe the effect of chemical combination on X-ray line spectra. *Ray* [6.26], *Backlin* [6.27], and *Deodhar* [6.28] showed that the wavelength of S $K\alpha_{1,2}$ lines depends on the particular sulphate in which the sulphur is found.

Valence electrons penetrate the ion core slightly ($\sim 10\%$ or less of their probability distribution) (Fig. 2.16). When they happen to be inside the core, their charge repels the charge of the core electrons. In other words, the effect of the valence charge in the core region is to *screen* partially the core electron–nucleus attraction. This reduces the binding energies of the core levels.

In the bond formation, some valence charge is removed (or transferred) from the atom. Consequently, the screening is reduced, the cation-core electrons (like K, L) are attracted more strongly to the nucleus, and their binding energies become more negative (larger in magnitude). This change of the binding energies would be more if the number of valence electrons that participate in the bond (oxidation number) were greater. Detailed calculations based on approximate many-electron functions [6.29, 30] have shown that both of the core levels, K and $L_{II,III}$, that participate in the $K\alpha_{1,2}$ transitions, are shifted in the same direction (towards higher binding energy), as expected on the basis of the changes of the screening of core electrons.

Thus all inner (core) levels of an atom are shifted by a few eV when the valence electron configuration changes on bonding. The binding energy increases (decreases) if electrons are lost (gained). The shifts are the same for all levels, to a first approximation. However, small differences are always present. They result in X-ray line shifts that are smaller by nearly one order of magnitude.

Photoelectron studies [6.31] have directly confirmed this predicted increase of the binding energies of the inner electrons of sulphur with oxidation (Fig. 6.8). They found that: 1) The K, L binding energies increase with oxidation number. 2) All of the three levels K, L_I, $L_{II,III}$ show an energy shift of about 1 eV per degree of oxidation. 3) The shifts are somewhat large for the K level than for the L levels. These observations are supported by the X-ray-emission chemical-shift data. It would be wrong to assume that (ion) core-level shifts can be ignored while discussing X-ray emission and absorption spectra.

Faessler and *Goehring* [6.32] have observed the shifts of the sulphur $K\alpha$ doublet in a large number of different compounds. They find that the effective charge of the atom determines the chemical shifts of the lines with respect to their positions in element: S^{2-} (−0.14 eV), S^{2+} (+0.31 eV), S^{4+} (+0.95 eV), S^{6+} (+1.19 eV). The maximum shift is 1.33 eV, or about 3 XU (between S^{6+} and S^{2-}).

It must be noted that, by photoelectron spectroscopy, the *total* shifts of each individual level (K, L_I, $L_{II,III}$, etc.) are measured separately, whereas in the X-ray spectra the small *differences* of shifts of the two core levels involved in the transition are measured. Because the shifts of the K and L levels are about the same, and in the same direction, much smaller shifts (~1 eV) of the $K\alpha_{1,2}$ emission lines are obtained in the lighter elements (like ^{14}Si, ^{15}P, ^{16}S) and the theoretical interpretation is more difficult. The shifts become even smaller (~0.1 eV) as the atomic number increases. For example, the Cu $K\alpha_1$ line shifts by only 0.11 eV [6.33] in going from Cu (metal) to CuO.

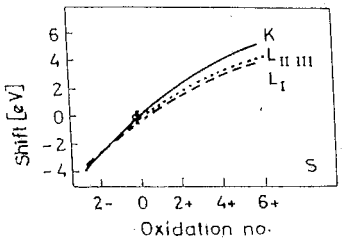

Fig. 6.8. Chemical shifts of the K, L_I, $L_{II,III}$ levels of S for different oxidation numbers, by photoelectron spectroscopy

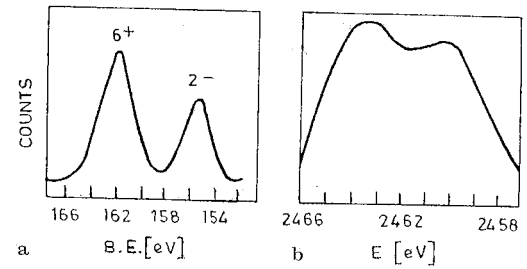

Fig. 6.9a,b. Sulphur spectrum from sodium thiosulphate by **a** photoelectron (2p level, Mg $K\alpha$ line as source), and **b** X-ray (S $K\beta$ line) spectroscopy

Sodium thiosulphate, $Na_2S_2O_3$, has the following structure:

$$2Na^+ \left[\begin{array}{c} O \\ | \\ O\text{–}S\text{–}S \\ | \\ O \end{array} \right]^{2-} , \qquad (6.31)$$

with two sulphur atoms in *different* chemical positions with oxidation numbers 6+ (central atom) and 2− (ligand atom). In the ground state, the electronic structure of S is $[KL]\ 3s^2 3p^4$. In the thiosulphate ion, the s and p orbitals hybridize in the central sulphur atom to give six s^2p^4 hybrid orbitals and a resulting sixfold covalent bond. On the other hand, the ligand sulphur atom is bounded by receiving two hybrid orbital electrons from the central sulphur into its two half-filled 3p orbitals. Therefore, the outer orbital-electron density is different for the two sulphur atoms with a resulting difference of the binding energies of core electrons. Direct evidence has come for this from photoelectron spectroscopy [6.18] where two (2p level) lines are obtained (Fig. 6.9a), one from the central S^{6+} atom and the other at lower energy (by about 6 eV) from the ligand S^{2-} atom. Similarly, two (K level) lines have been observed[2] by *Fahlman* et al. [6.31].

[2] Electron binding energies determined by the photoelectron-spectroscopic method have the Fermi level (E_F) as a reference level. One can argue that the level shifts are observed because the Fermi level is shifted to different positions in the forbidden energy gap E_g between the valence-band edge and the conduction-band edge. This explanation is not acceptable because different energies of an electron line are found from sulphur atoms in different chemical positions in the same substance.

In the X-ray emission spectra also, two doublets ($K\alpha_{1,2}$) are observed [6.34] corresponding to the two kinds of sulphur atoms: $K\alpha_1$ (5358.49 XU), $K\alpha_2$ (5361.35 XU) from S^{6+} central atom, and $K\alpha_1$ (5361.35 XU), $K\alpha_2$ (5363.95 XU) from S^{2-} ligand atom. (Because S^{6+} $K\alpha_2$ and $S^{-2}K\alpha_1$ overlap, only three lines are observed.) Further confirmation comes from the S $K\beta$ ($3p \rightarrow 1s$) line (Fig. 6.9b) where two peaks are observed.

The energy difference dE per angular increment $d\theta$ of a Bragg spectrometer is determined by

$$\lambda[\text{Å}] = (2d/n)\sin\theta = 12398.1/E[\text{eV}], \quad dE/d\theta = -(12398.1/\lambda)\cot\theta,$$
$$|dE| = (4.32/\lambda)\cot\theta\,[\text{eV}], \tag{6.32}$$

for $d\theta = 0.02°$ (usual angular precision). This gives about 5 eV for $\lambda = 1$ Å and 0.5 eV for $\lambda = 10$ Å. Thus, the dispersion is not enough for the measurements of X-ray chemical shifts at shorter wavelengths that occur in heavier elements. For chemical shifts of the order of 0.1 eV to 1 eV, high-precision spectrometry becomes necessary [6.35].

Gokhale et al. [6.36] have carefully measured the chemical shift of the $K\alpha_1$ line of tin (^{50}Sn) in its oxides [$E(\text{SnO}) - E(\text{Sn}) = 0.09$ eV, $E(\text{SnO}_2) - E(\text{Sn}) = 0.173$ eV]. The chemical shifts of $K\alpha$ and $K\beta$ lines in heavy elements ($Z > 36$) have been observed by *Petrovich* et al. [6.37] and theoretically analyzed by *Coulthard* [6.38]. *Koster* and *Mendel* [6.39] have extensively studied the X-ray $K\beta$ emission spectra ($K\beta'''$, β_5, β'', β_1, β') of 3*d*-transition metals and compounds. The energies involved in electron transitions in these compounds can be used to construct a composite energy diagram, if use is made of the photoelectron data for which the Fermi energy provides the reference level (Fig. 6.10). In such a diagram, the levels belong to the constituent atoms or ions and represent the energy states of the compound.

The transitions for the X-ray emission are possible not only between levels of the same species but *crossover* transitions are also possible. The binding energy of 1*s* electron of Ca in CaO is 4038 eV [6.40]. The energy of oxygen $K\alpha$ is 525 eV

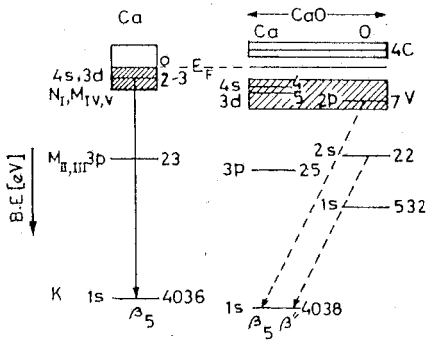

Fig. 6.10. Energy levels in eV of Ca and CaO. The crossover transitions are shown by dashed lines. E_F is Fermi level at zero energy, C is the empty conduction band, and V is the full valence band

[6.41]. The energy of $K\beta_5$ is found to be 4031 eV. The $K\beta_5$ of a pure metal results from the 3*d*, $4s \rightarrow 1s$ transition. In a compound all valence electrons are used in bond formation and so the $K\beta_5$ line arises between the level mainly characterized by 2*p*(O) and 1*s*(Ca). If this is a crossover transition, the oxygen $L_{II,III}$ would be at 7 eV, and the K binding energy in CaO would be $525 + 7 = 532$ eV. This is in good agreement with the value 532 eV, as measured in MgO and Al_2O_3 [6.40, 42]. The residual charge on the oxygen is nearly equal for these three compounds (in electron units: -1.8 for MgO, -1.6 for Al_2O_3, -1.8 for CaO). The line $K\beta''$ at -15 eV with respect to $K\beta_5$ is explained by the crossover transition $2s(\text{O}) \rightarrow 1s(\text{Ca})$; the L_I level of oxygen then is situated at 22 eV. From photoelectron spectroscopy, this value is 23.7 eV [6.42]. The position of the Ca K-absorption edge at 4041 eV in CaO [6.43] places the conduction band centered at 4 eV above E_B. Two satellite peaks at 527 and 528 eV are found in the oxygen spectrum [6.41]. These can be explained by the valence-band transitions $3d(\text{Ca}) \rightarrow 1s(\text{O})$ and $4s(\text{Ca}) \rightarrow 1s(\text{O})$.

We expect larger shifts for the $K\beta_5$ emission because the transition involves the valence band and an inner level. The shift of the valence band is large because of the appearance of the forbidden energy gap. *Koster* and *Mendel* [6.39] observed a marked chemical shift only for the $K\beta_5$ band. In Ca, the $K\beta_5$ appears as a broad line, with shape dependent only on the bonding of the calcium atoms. In CaO, the band-like nature of this line arises because of the formation of a molecular orbital of Ca and O. *Fischer* [6.44] has drawn similar conclusions about the $K\beta$ emission bands of Al and Al_2O_3. The X-ray emission spectra support the conclusions drawn on the basis of photoelectron spectroscopy.

6.2.1 Level Shift

The shift of energy of a photoelectron or an X-ray line on bonding is determined by self-atom and neighbour-atom effects. Besides the exact but difficult calculations based on the Hartree–Fock–Slater theory, one can correlate the line shifts in photoelectron and X-ray spectroscopy with parameters such as ionicity, effective charge, valence and coordination number. We shall first discuss the self-atom (free-ion) effects.

The energy of a core level (nl) is essentially given by

$$E_{nl} = (13.6/n^2)(Z - \sigma_{nl})^2, \tag{6.33}$$

where σ_{nl} is the screening constant. The derivative of this equation with respect to σ_{nl} gives in the free-ion model

$$|\Delta E_{nl}| = (27.2/n^2)(Z - \sigma_{nl})\Delta\sigma_{nl}. \tag{6.34}$$

The $\Delta\sigma_{nl}$ can be estimated from the assumed charge transfer and the known screening constants [6.45–47].

The core electron energy depends on the attractive potential of the nuclei and the repulsive core Coulomb interaction with all the other electrons. A

change in the bonding of an atom involves a redistribution of its valence charges and a different potential due to the nuclear and electronic charges on all the other atoms in the compound. This picture relates the binding energy difference ΔE_i^c of a core level c for an atom i in two different compounds A and B, and the valence charges q^A and q^B, respectively [6.48].

$$\Delta E_i^c(A,B)=K_c(q_i^A-q_i^B)+(V_i^A-V_i^B). \tag{6.35}$$

The first term gives the difference in the electron–electron interaction between the core orbital c and the valence charges q^A and q^B. A simple classical electrostatic model in which the atomic orbitals are concentric spherical shells [6.31] gives a screening potential inside such a shell as

$$K_c q_i = q_i/\bar{r}_{v,i}, \tag{6.36}$$

where $\bar{r}_{v,i}$ is the mean radius of the valence-electron orbital of atom i. It is a self-atom effect. For $\bar{r}_{v,i}=1$ Å, the coupling constant K_c (two-electron integral between core and valence electrons) is about 14 eV per unit charge. The second term in (6.35) can be represented by a Madelung potential. In the point charge approximation

$$V_i=-\sum_{i\neq j} q_j/R_{ij}. \tag{6.37}$$

It is a sum over potentials due to ionic charges q_j centred at positions R_{ij} relative to the atom i. They decrease the shifts to about a few eV or less. It is a neighbour-atom effect. If there is no charge transfer in the reference system B, (6.35) reduces to the formula of *Siegbahn* et al. [6.18, 49]

$$\Delta E_i^c=K_c(q_i^A/r)-\sum_j (q_j/R_{ij})+l, \tag{6.38}$$

where l is an adjustable constant. The charges q_i can be derived by (6.30) with f_i given by *Pauling* or *Phillips* and *Van Vechten*. Results (6.35, 38) give observed shifts in many small molecules [6.48, 50, 51]. and in solids [6.52] Being a rigorous ground state model, it fails to consider the *relaxation energy* E_R [6.53, 54] due to the flow of electrons towards the hole suddenly created in the photo-emission process. This screening (final state effect) lowers the energy of the hole state and so of the measured binding energy. A term $\Delta E_R=E_R^A-E_R^B$ should be added to (6.35). In fact, the binding energy of neutral atom even in a metal can differ from that of a free atom by up to 10 eV due to E_R [6.55, 56].

There is a close relation between chemical shifts and alloy heat of formation. Recently *Martensson* and *Johansson* [6.57] have used the relation

$$\Delta E^c=E(A,B)+E(A+1,A)-E(A+1,B), \tag{6.39}$$

where $E(A,B)$ is the energy of solution of a metallic atom A in the matix B, and $A+1$ is the $(Z+1)$ element relative to A. These energies reduce approximately to solution energies of binary alloys.

Using Coulomb (C) and exchange (A) integrals, the quantum mechanical calculation of *Nefedov* [6.58] gives

$$\Delta E_{1s}=C(1s,ns)-\tfrac{1}{2}A(1s,ns). \tag{6.40}$$

Potential change due to the difference in electron distribution $\Delta\rho$ on bonding *is*

$$\Delta V(r)=\frac{1}{r}\int_0^r \Delta\rho(r)dr+\int_r^\infty \frac{\Delta\rho(r)}{r}dr. \tag{6.41}$$

Shubaev [6.59] evaluates

$$\Delta E_{1s}=\int_0^\infty R_{1s}^2(r)\,\Delta V(r)dr \tag{6.42}$$

where $R_{1s}(r)$ is the radial wave function.

6.2.2 X-Ray Line Shift

The shift of an X-ray line $E=E_j-E_i$ can be expressed as

$$\begin{aligned}\Delta E_v&=E_v^s-E_v^r=(E_j^s-E_i^s)-(E_j^r-E_i^r)\\&=(E_j^s-E_j^r)-(E_i^s-E_i^r)=\Delta E_j-\Delta E_i.\end{aligned} \tag{6.43}$$

In the free-ion model (6.35),

$$\Delta E_v=\Delta E_j-\Delta E_i=(K_j-K_i)\Delta q=K_{ij}\Delta q. \tag{6.44}$$

K_i has been calculated empirically, semi-empirically and quantum mechanically.

Neglecting exchange interactions, *Nefedov* [6.60] estimates Coulomb interaction using Slater functions, to get

$$\Delta E_{K\alpha}=a\,E_{K\alpha}\sum_i^q \sqrt{I_i} \tag{6.45}$$

Here i labels the outer electrons, q of which are missing, I is the ionization energy and a is an empirical parameter. *Clementi* [6.61] relates $\Delta E_{K\alpha}$ for third-row elements to the degree of ionization, using a self-consistent free-ion model. *Shubaev* [6.62] writes $\Delta E_v=b\Delta q$, where b ranges from 0.33 for Mg to 1.32 for S in eV/charge unit. Line shifts for the 3rd transition elements depend on the participation of 4*s* and 3*d* electrons in the bonding, so *Leonhardt* and *Meisel* [6.63] write

$$\Delta E_{K\alpha}=b_{4s}\Delta q_{4s}+b_{3d}\Delta q_{3d}. \tag{6.46}$$

Sumbaev [6.64] has calculated empirical values for K_{12} in (6.46) and suggested

$$\Delta E_v=(f_i^s-f_i^r)\sum_l N_l C_l. \tag{6.47}$$

where f_i is Pauling ionicity, N_l is valence decomposed according to the angular momentum of the contributing orbital, and C_l is in eV per 1-subshell electron.

He finds straight line plots

$$\Delta E_{K\alpha_1}/f_i = xC_{sp} - (N-x)C_{4d}, \tag{6.48}$$

where N depends on Z, $f_i^r = 0$ for the pure reference element, and x is the number of sp electrons. For the *IV*, *V*, *VI* rows, $C_{sp} \simeq 80$ meV, $C_d = -115$ meV. Thus s, p electrons in the bonding (Cu – Se, Ag – Te) give positive shifts, whereas d (and f) electrons give negative shifts.

Tilgner et al. [6.65] have used chemical shifts of $K\alpha$ and $K\beta$ doublets of Ga and As to calculate effective atomic charges in the free-ion model.

Karalnik [6.66] obtained the line shift as

$$\frac{E_v^s - E_v^r}{\sigma^s - \sigma^r} = \frac{\Delta E_v}{\Delta\sigma} = \frac{E_v(Z) - E_v(Z+1)}{1}, \tag{6.49}$$

where $\Delta\sigma$ determines the change in outer-valence-electron screening for 1 unit change of nuclear charge.

The K_{ij} values in (6.44) can be calculated quantum mechanically in various ways. In terms of the screening constants

$$K_{ij} = \sigma_{ik} - \sigma_{jk}, \tag{6.50}$$

where

$$\sigma_{i(nl)} = \int_0^{r_i(\max)} R_{(nl)}^2(r)\, ds. \tag{6.51}$$

The partial charge can be calculated with hydrogen-like functions. They can be obtained through self-consistent calculations involving atoms and ions.

Leonhardt and *Meisel* [6.63] have compared various methods of calculations and concluded;

(1) Different quantum-mechanical procedures give results $\Delta E_v = f(q)$ in good agreement (Fig. 6.11).

(2) The dependence on q is not linear. It is described by $\Delta E_v = aq^b$. For the third period elements, $a = 0.2$ and $b = 1.6$.

(3) Using Koopman's theorem, in terms of orbital energies,

$$\Delta E_K = (E_{2p} - E_{1s})_{\text{ion}} - (E_{2p} - E_{1s})_{\text{atom}}. \tag{6.52}$$

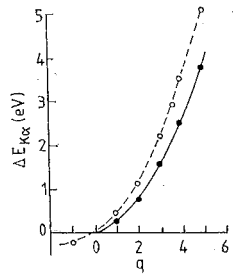

Fig. 6.11. Chemical shifts ΔE_{K_α} as a function of the charges q on free sulphur ions calculated by different methods using (6.44, 52). • *Leonhardt* and *Meisel* [6.63], ○ *Coulson* and *Zauli* [6.67]

If level energies are calculated in the equivalent-core method based on the $Z \rightarrow Z+1$ approximation, the agreement with the observed shifts is good.

The considerations for the X-ray line shifts also hold for the chemical shifts of satellites. *Demekhin* and *Sachenko* [6.68] used the ionic model to show that the K satellites of third-row elements shift more than the parent $K\alpha_{1,2}$ lines when M-shell electrons go in bonding. A dramatic change also occurs in the intensity ratio of $K\alpha_4$ and $K\alpha_3$ satellites [6.69–71] on compound formation. *Benka* and *Uda* [6.72] have given a molecular-orbital model for the chemical effects on the relative intensities of K X-ray fluorescence satellites in covalent compounds.

6.3 Appearance Potential Spectroscopy

Park et al. [6.73, 74] have developed the soft X-ray appearance potential spectroscopy (APS) for finding the binding energies of core electrons of atoms in a solid surface. It is based on energy-dispersive X-ray spectrometry. It uses the fact that the plot of total electron-excited X-ray emission intensity against the X-ray tube-potential shows discontinuities at the *appearance potentials* (excitation potentials for X-rays of distinct energy) of characteristic X-rays.

The vacuum chamber ($\sim 10^{-9}$ torr) houses the filament, specimen target, and detector (Fig. 6.12). When the target potential V is swept, discontinuities

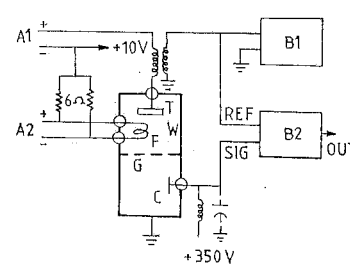

Fig. 6.12. X-ray appearance potential spectrometer. *F*: filament; *T*: specimen target; *C*: detector (collects photo-electrons from the chamber walls); *G*: grid; *W*: baked vacuum chamber; *A1*: 0–1 kV ramp power supply for *T*; *A2*: power supply for *F*; *B1*: 6 kHz oscillator (0.4 V rms); *B2*: phase-lock amplifier

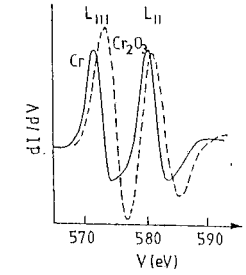

Fig. 6.13. A typical X-ray appearance potential spectrum showing the Cr L_{III} excitation discontinuity in pure and oxidized nickel (after [6.75]). To convert the accelerating potential V to the binding energy, the work function $e\phi$ for the filament (4.5 eV for tungsten) is added, as V is the potential difference between the target and the filament Fermi levels ($E_F = 0$ for the excitation processes inside the target)

appear in the detected radiation intensity I. These are accentuated with respect to the background by electronic differentiation. To get dI/dV, a modulating potential (say, 0.4 V rms) from an oscillator of frequency ~ 6 kHz, is superposed on the target potential. The intensity fluctuations are recorded synchronously with a phase-lock amplifier tuned to the modulating frequency. The resulting dI/dV (Fig. 6.13) is plotted on a recorder or displayed on an oscilloscope.

The 2-keV electrons penetrate only 10–20 atom layers in T, so soft X-ray APS investigates surfaces for core-electron binding energies and their chemical shifts.

To understand qualitatively the observed spectrum of Cr in Fig. 6.13, consider the oversimplified band model (Fig. 6.14a) for the $3d$ transition metals with the Fermi level E_F lying in the midst of a narrow $3d$ band which is superimposed on a broad free-electron-like $4s$ band [6.75]. To simplify the convolution, we represent the conduction band density distribution by a series of rectangular functions (Fig. 6.14a). A series of ramp portions then give the convolution (Fig. 6.14b). This shape approximates the X-ray excitation curve (isochromat) of a transition metal. It is obtained by setting the analyzer to accept a given X-ray line and varying the sample potential across the threshold for the excitation of that line. As in Auger spectra (Fig. 4.14), in the total X-ray emission

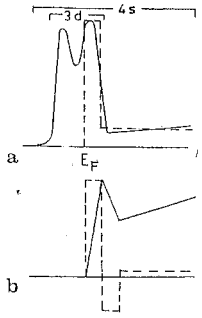

Fig. 6.14. a Approximate shape (solid line) of the density of states in the $3d$ transition metals, and the rectangular functions $N(E)$ (dashed) used to approximate it. **b** The self-convolution of the $N(E)$ function (solid), $\int_0^E N(E-W)N(W)dW$, which approximates an X-ray excitation curve (isochromat), and the differential excitation curve (dashed) $\frac{d}{dE}\int_0^E N(E-W)N(W)dW$

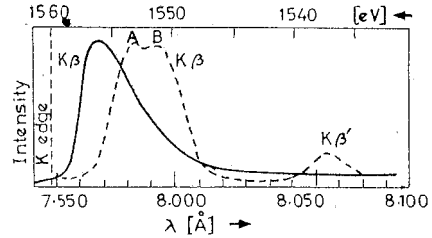

Fig. 6.15. The Al $K\beta$-band emission spectra of Al metal (solid curve) and sixfold coordinated corundum (α-Al_2O_3, dashed curve). The $K\beta'$ is a satellite

plot the excitation curves of all levels of surface atoms are superposed on a smooth background. For enhancement, the data are taken as the derivative of the total X-ray emission with respect to the accelerating voltage. For the rectangular representation considered here, the result is shown in Fig. 6.14b. Thus the observed spectrum should show a peak, a small undershoot, and a step for each of the core levels. The Cr $L_{II,III}$ APS (Fig. 6.13) reveals these features. The L_{III} threshold shifts from 573.5 to 574.1 eV and the width increases by 0.8 eV (loss of d band electrons) on oxidation (Fig. 6.13).

6.4 Resonance X-Ray Emission Spectroscopy

X-ray resonance lines were first observed in solids by *Bonnelle* and *Karnatak* [6.76] in the soft X-ray M spectra of rare earth Gd and Gd_2O_3. They correspond to the radiative de-excitation of the initially excited $3d^9 4f^{q+1}$ states. In this process the initial state is a highly excited neutral. A core-shell electron is lifted to an unoccupied bound level situated above the Fermi level in a metal, or above the bottom of the conduction band in a semiconductor. Resonance radiation is due to the direct radiative decay back to the ground state neutral. It is a reverse absorption. The intense resonance line is always found to correspond to the most intense absorption line arising from transitions to discrete states.

Resonance lines have also been detected by *LaVilla* [6.77] in the $K\alpha$ emission spectra of molecular gases. *Siegbahn*'s group has also observed this effect [6.78]. It usually occurs in the spectrum excited by direct electron bombardment. Then the target moleculr electron can absorb any fraction of the energy from the incident electron. On the other hand, in photon excitation the target electrons can absorb only the whole quantum of energy of the incident photon. Unless the incident photon spectrum has an emission line in coincidence with a strong absorption peak, the probability is small for the occurrence of the initial excited state. Synchrotron radiation will be useful for such experiments in the future.

As unoccupied levels near the Fermi level participate in this effect, it provides an insight into the localization of excited states and their dependence on chemical properties.

6.5 Width and Fine Structure of Emission Lines

The shift of $K\alpha$ lines on bonding is a second-order effect that results from the change of screening of the inner $1s$ and $2p$ electrons when a change occurs in the valence-electron shell. The direct effect of the chemical bond is to perturb the valence-electron states. Therefore, the line of shortest wavelength in each series is always strongly affected by the chemical state of the emitting atom. In this case, there is not only a wavelength shift but also a change of the width and shape of the line.

The kinetic energy E of an electron in the valence band of a metal of *width* $E_F - E_0$ is $E_{kin} = E - E_0$, where E_0 is the energy of the lowest state of the valence band and $E_0 < E < E_F$. The smallest cell in the phase space, as given by the uncertainty principle, is

$$\Delta p_x \Delta p_y \Delta p_z \Delta x \Delta y \Delta z = (\Delta p)^3 \Delta V = h^3. \tag{6.53}$$

By the Pauli principle, it can contain two electrons. If $\Delta V = GV_a$, where G is a large whole number and V_a is the atomic volume, (6.53) becomes

$$(\Delta k)^3 = (GV_a)^{-1}, \tag{6.54}$$

where $p = hk$, $\Delta p = h\Delta k$. Thus, each pair of electrons occupies a cell of volume $(GV_a)^{-1}$ in the wave-vector space (k_x, k_y, k_z). We can write $V_a = V_e/n$, where V_e is the volume of the unit cell and n the number of atoms in the cell.

If there are N valence electrons per atom, or GN electrons per volume GV_a, that behave as almost-free electrons in the valence band, then the corresponding states occupy a volume

$$\tfrac{1}{2} GN(\Delta k)^3 = N/(2V_a), \tag{6.55}$$

in k space. At absolute-zero temperature, these electrons will occupy a sphere in k space such that

$$N/(2V_a) = (4/3)\pi k_F^3, \tag{6.56}$$

where k_F is the radius of the *Fermi surface*. The maximum kinetic energy is given by $E_F - E_0 = (hk_F)^2/2m$, so that (6.56) gives

$$N = (8\pi/3)(2m)^{3/2}(V_a/h^3)(E_F - E_0)^{3/2}. \tag{6.57}$$

If the observed emission-band width is ΔE,

$$\Delta E = (E_F - E_0) + (\Delta E)_i, \tag{6.58}$$

where $(\Delta E)_i$ is the width of the inner level involved. From (6.57, 58),

$$N/V_a = 4.53 \times 10^{-3}[\Delta E - (\Delta E)_i]^{3/2}, \tag{6.59}$$

where V_a is in Å^3 and energy in eV.

In brass, with Cu 70% + Zn 30% by atoms, each Zn atom gives two valence electrons to one from each Cu atom. The unit cell of brass is *fcc* with $a = 3.67$ Å and $n = 4$. Therefore, for the $K\beta_{2,5}$ lines of Cu and Zn that arise from a transition between the composite valence band of the brass to the K levels of Cu and Zn [6.79],

$$N = (30 \times 2 + 70 \times 1)/100 = 1.3, \quad V_a = a^3/4 = 12.4\,\text{Å}^3$$

$$\Delta E - (\Delta E)_K = 8\,\text{eV}. \tag{6.60}$$

From the absorption spectrum, we get $(\Delta E)_K$ as 1.3 ± 0.5 eV for Cu and 1.5 ± 0.5 eV for Zn [6.80]. Therefore, the width of the calculated emission band is 9.3 eV for Cu and 9.5 eV for Zn. The observed width of Cu $K\beta_{2,5}$ is 8.8 eV and of

Zn $K\beta_2$ is 9.0 eV. The agreement is within experimental error. The observed width increases with the increase of N as the Zn content of the alloy is increased, in agreement with (6.59). The theory works because α brass behaves as a metal. The widths of bands in Cu and Zn are found to be nearly the same. This shows that the valence band is common to both of the components of the alloy.

The measured and calculated values [6.81–84] of emission-band widths associated with the outer electrons are given in Table 6.2. For metals and metallic alloys, the two are close to each other, but for the non-metals (B, C, Si, P and S) the two differ considerably. This shows that the theory of free electrons is not applicable to non-metals.

It has been found that in many cases (like Ti, Mn, Cu) the observed lines are *asymmetrical*. The excess width on the low-energy side can arise from transitions between excitation states of the valence-electron configuration type [6.85], from unidentified satellites, and from Compton scattering.

Dodd and *Glen* [6.86] have studied the K-emission spectra of Mg, Al, a nd Si in elements and in oxides. Figure 6.15 shows how both the shape and wavelength of the Al $K\beta$-emission band [6.44, 86] change on oxidation. The observed change from line to band shape on oxidation is common for such light elements. The electronic configuration for the ^{13}Al atom is $[KL]3s^2 3p^1$.

Consider the usual band model for the weak, broad $K\beta_{1,3}$ line ($3p \rightarrow 1s$, $M \rightarrow K$) in metal. The approximate atomic-orbital ionization energies [in eV] are: Al $3s(10.6)$ $3p(6.0)$ O $2s(28.4)$ $2p(13.6)$. The band-like nature of the line in Al_2O_3 arises because of the formation of the common energy band of the molecular orbital of Al $3s3p$ and O $2p$. The cross-over transitions (Fig. 6.16a) for the band $K\beta$ and the satellite $K\beta'$ give the energy difference between them as equal to Al $3p(6.0)$ minus O $2s(28.4)$, that is, ~ 22 eV. The observed value is ~ 16 eV, which is of the same order. Thus, the band picture can account for the high-energy shift of the $K\alpha$ line (discussed earlier), the low-energy shift the $K\beta$ line, together with a change of the shape from line to band, and the appearance of the low-energy satellite $K\beta'$.

Dodd and *Glen* [6.86], *Urch* [6.87] and *Grunes* [6.88] found an interpretation based on the molecular-orbital picture more rewarding. In particular,

Table 6.2. Observed and calculated values of bandwidths

Band	ΔE [eV] Obs. (Calc.)	Band	ΔE [eV] Obs. (Calc.)
Li K	4.2 (4.7)	Na L_{III}	3.7 (3.2)
Be K	14.7 (14.3)	Mg L_{III}	7.2 (7.2)
B K	31 (25.2)	Si L_{III}	18.2 (1.27)
C K	33 (21.9)	P L_{III}	43 (11.5)
Mg K	7.4 (7.2)	S L_{III}	49 (14.3)
Al K	12.7 (11.7)	Cu L_{III}	6.8 (7.1)
Si K	18 (12.7)	Cu M_{III}	7.5 (7.1)

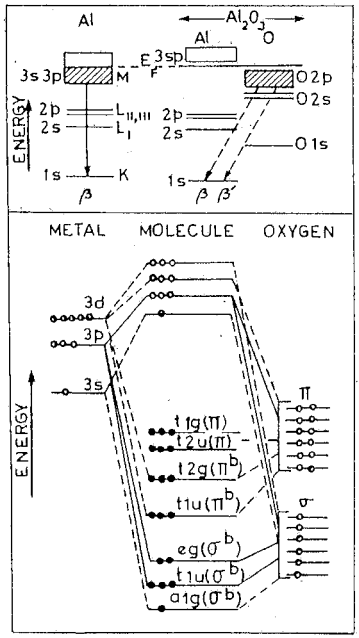

Fig. 6.16. (**a**, top) The $K\beta$ emission transitions in Al and α-Al_2O_3 in the band picture. (**b**, bottom) The molecular-orbital energy-level diagram for octahedrally (sixfold) coordinated α-Al_2O_3. Solid dot is occupied ($\uparrow\downarrow$)

Urch has shown that the observed relative intensities of low-energy satellites are in better agreement with this approach.

Following the work of *Ballhausen* and *Gray* [6.89] on transition-metal complexes, the molecular-orbital energy-level diagram can be drawn for octahedrally coordinated oxides of Mg, Al and Si (Fig. 6.16b). The relative energy levels are approximate. The $3p(\pi)$ bonding orbitals, with group t_{1u} symmetry, are occupied and lie at a higher energy than the $3p(\sigma)$ bonding orbitals also with t_{1u} symmetry. Assuming that the $3p \rightarrow 1s$ transition can occur for both $3p$ bonding orbitals (π or σ), *Dodd* and *Glen* suggest that the higher-energy peak A in the α-Al_2O_3 $K\beta$ band arises from a $3p(\pi^b) \rightarrow 1s$ transition, and the lower-energy peak b from a $3p(\sigma^b) \rightarrow 1s$ transition, Figs. 6.15, 16b.

6.6 Anisotropic X-Ray Emission Lines

The K-emission band of graphite has been measured by many workers. The various results show some differences in their intensity distributions. The reason for this is now known. Being a highly anisotropic crystal, graphite emits an X-ray spectrum that consists of two sub-bands (π and σ) of different polarizations. The intensity ratio of these two sub-bands depends on the orientation

of the graphite crystal relative to the propagation direction of the emitted radiation. This anisotropic emission of characteristic X-rays is to be found in all non-cubic molecules and solids. It can be used to separate and identify orbitals of different symmetry and to determine their energy spacings [6.90, 91].

The differently polarized components are experimentally separated by the anisotropic emission feature of a radiating dipole. A dipole emits no intensity along its axis, therefore its radiation is suppressed in the spectrum if the axis points in the direction of the spectrometer entrance. Measurements made with different dipoles in the sample so oriented, in turn, produce an equal number of spectral traces. Each such track lacks just one polarization component. This is the basis of *polarized X-ray emission spectroscopy* (PXES). The analysis is simple for layer crystals and for crystals containing molecules with the same orientation in space.

In the experimental set up for PXES (Fig. 6.17) the single crystal emission sample is suitably oriented relative to a crystal analyzer or grating. The radiation components with the polarization $\boldsymbol{e}_p$ parallel to the diffraction plane (p-component) and with $\boldsymbol{e}_s$ perpendicular to this plane (s-component) are reflected with different intensities, depending on the polarization ratio R of the analyzer. For an ideal crystal R is $|\cos 2\theta|$, so at a Bragg angle $\theta = 45°$ and near it, the pure s-component of the radiation is reflected while the p-component is suppressed. In general, the measured intensity of frequency ω is

$$I(\boldsymbol{e}_s, \boldsymbol{e}_p) = I(\boldsymbol{e}_s) + RI(\boldsymbol{e}_p). \tag{6.61}$$

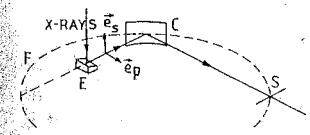

Fig. 6.17. PXES using a Johann-type spectrometer. F: focussing circle; C: analyzing crystal; S: slit to the detector; E: emission sample; $\vec{e}_s$, $\vec{e}_p$: polarization vectors

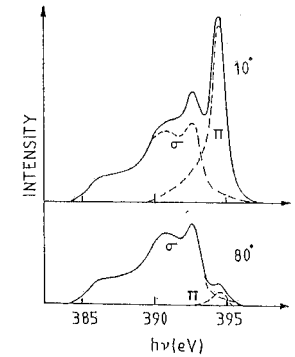

Fig. 6.18. The nitrogen K emission bands for BN samples at take-off angles 10° and 80°, together with the separation in the σ- and π-bands (after the work of *Wiech* and *Faessler* [6.93])

Here $I(e_s, e_p)$ is expressed in terms of intensity $I(e)$ of the emitting sample with given orientation ($e = e_s$ and $e = e_p$, respectively). In the dipole approximation

$$I(e) = I_x \sin^2\theta\cos^2\phi + I_y \sin^2\theta\sin^2\phi + I_z\cos^2\theta. \tag{6.62}$$

Thus (6.61) gives a set of linear combinations of I_x, I_y and I_z weighted according to the sample orientation. From measurements for different orientations I_x, I_y, I_z can be calculated [6.92].

For trigonal, tetragonal, or hexagonal crystals, with the z-axis parallel to the axis of 3-, 4-, or 6-fold symmetry,

$$I_x = I_y = I_\sigma + I_z = I_\pi, \tag{6.63}$$

where π and σ refer to the bond type in the sample. From (6.62, 63)

$$I(e) = I_\sigma \sin^2\theta + I_\pi\cos^2\theta. \tag{6.64}$$

Then (6.61) is resolved in terms of I_σ and I_π. One observes a superposition of σ- and π-radiation. The observed anisotropy changes with the change in take-off angle. Wiech's group has confirmed this by detailed studies of the polarized K spectra of hexagonal boron nitride [6.93]. As BN has a layered structure, similar to graphite, the effect is easy to detect and analyze. Anisotropic emission is found for both B and N.

Within the hexagonal layer planes in BN exist a set of trigonal σ-bonds. The bonds between the layers are effected by the π-orbitals. For $\sigma \rightarrow 1s$ transitions the radiation is polarized parallel to the layer planes. For $\pi \rightarrow 1s$ the radiation is polarized perpendicular to this plane (maximum intensity parallel to the layers). The angular dependence of intensity can be used to separate σ- and π-contributions in the spectra (Fig. 6.18). These σ- and π-bands are closely related to the local partial density of states around the sites of the N atoms.

Recently *Tegeler* et al. [6.94] have measured and separated the σ- and π-bands of the CO_3^{2-} anion in calcite ($CaCO_3$) by recording the C K and O K anisotropic emission spectra. This gives the sequence and binding energies of the valence orbits.

Thus PXES is now a powerful tool for obtaining information on molecular orbital energies, symmetries, populations and locations.

6.7 Nuclear Finite-Size Effects

There is an overlap between the atomic electron wave functions with the nucleus. This overlap (nuclear finite-size effect) results in a decrease of the electron binding energy as compared to the point nucleus case. The effect is significant for the atomic s-electrons. It is largest for the $1s$ electrons. Thus K X-rays can yield information on nuclear structure.

In two difference isotopes of the same element, the number Z of protons of the nucleus is the same, but the number A-Z of neutrons is different. This makes the spatial distributions of the nuclear charges different in the two nuclei. The

resulting difference in the overlap slightly alters the transition energy involved in the X-ray emission. The isotope shift can therefore be used to explore the mechanism by which the nuclear charge distribution is affected as neutrons are added to the nucleus.

The observed isotope shift of X-rays can have two causes: a Coulomb shift and a mass shift. For two heavy isotopes, the Coulomb shift in K X-ray energies dominates, as the reduced mass varies very little from one isotope to another. *Seltzer* [6.95] uses a rapidly converging sum of even charge moments to write

$$\Delta E^{\mathrm{Coul}} = C_1\Delta\langle r^2\rangle + C_2\langle r^4\rangle + C_3\Delta\langle r^6\rangle + \cdots, \tag{6.65}$$

where $\Delta\langle r^{2n}\rangle = \int \Delta\rho r^{2n}\,dv / \int \rho\,dv$, and ρ is the nuclear charge density. *Barrett* [6.96] assumes a potential $V(r) = Ce^{-\alpha r}r^k$, giving

$$\Delta E^{\mathrm{Coul}} = B\Delta\langle e^{-\alpha r}r^k\rangle, \tag{6.66}$$

where $\alpha(Z)$ and $k(Z)$ are parameters.

The K X-ray isotope shift was first reported for $^{235-238}$U by *Brockmeier* et al [6.97]. Other results are due to *Sumbaev* and *Mezentsev* [6.98], *Chesler* and *Boehm* [6.99], and *Lee* et al. [6.100]. For $^{92-100}$Mo, E^{Coul} is only 35 meV; it increases to 1800 meV for the isotope pair $^{235-238}$U. Comparison of Hg isotope shifts [6.100] with muonic X-ray data show that they give consistent results for the nuclear radius.

7. Absorption Spectra

This first X-ray absorption spectrum was recorded by M. de Broglie in 1913. He used a rotating crystal as analyzer and film as detector. He found two sharp discontinuities on the film. They were independent of the X-ray tube settings. They turned out to be the self-absorption spectra of Br and Ag contained in the photographic emulsion. The subject has grown rapidly after this discovery.

7.1 Absorption Edge

Lambert's law (3.177) is

$$I = I_0 e^{-\tau_m m}, \tag{7.1}$$

where $m = \rho x$ is the mass-per-unit area of the absorbing film. Defining I and τ_m as the intensity and the mass absorption coefficient on the low-energy side of the absorption edge, and I' and τ_m' the values on the high-energy side, *Sandström* [7.1] suggested that the optimum thickness (m_{op}) of the absorber for the maximum contrast ($I - I'$ maximum) is obtained by setting $d(I - I')/dm = 0$. This gives

$$m_{op} = \frac{\ln \tau_m' - \ln \tau_m}{\tau_m' - \tau_m} = 2.30 \frac{\log \tau_m' - \log \tau_m}{\tau_m' - \tau_m}, \quad [\text{in g cm}^{-2}]. \tag{7.2}$$

Values of $\tau_m = (N_A/A)\tau_a$ and τ_m' can be found from (3.185), or similar formulae.

For the photography of absorption fine structure on the high-energy side of the edge, a suitable practical formula is obtained if we maximize the small change of intensity $\delta I' = \delta[I_0 \exp(-\tau_m' m)] = -m I_0 \exp(-\tau_m' m)\delta\tau_m'$ on the high-energy side of the edge. Equating the derivative of $\delta I'$ with respect to m to zero [7.2],

$$I_0 \delta\tau_m'(\tau_m' m_{op} - 1)e^{-\tau_m' op} = 0, \quad m_{op} = \rho x_{op} = 1/\tau_m', \tag{7.3}$$

where τ_m' is the average mass absorption coefficient in the fine-structure region. *Krishnan* and *Nigam* [7.3] showed that the smaller thickness given by (7.3) gives more-pronounced fine structure in Ni foils.

When the effects on absorption introduced by a counter used as a detector are included, *Parratt* et al. [7.4] suggested that the thickness should be such that

$I/I_0 \simeq 0.10$, which leads to

$$m_{op} = -\ln(0.10)/\tau'_m. \tag{7.4}$$

These results are applicable if the readings of the detector (such as an ionization chamber or a counter) are proportional to intensity I. In the photographic method, the microphotometer reading is a measure of optical density (blackening) and is not proportional to I. Therefore, we should find a relation between the optical density D and the exposure time t.

Optical density is defined in terms of the film's ability to transmit visible light,

$$D = \log_{10}(J_0/J), \tag{7.5}$$

where $J_0(J)$ is the light incident upon (transmitted through) the X-ray film under study. The deflection l on a microphotometer record is proportional to J. Therefore,

$$D = \log_{10}(l_0/l), \tag{7.6}$$

where $l_0(l)$ is the deflection from the unexposed (exposed) portion of the X-ray film. The deflections are measured from the line of no transmission taken as the zero line; $l_0 > l$.

The quantity D is proportional to the total number of X-ray quanta that fall on unit area of the film (containing a given amount of silver per unit area) provided that D is less than 0.7. Therefore, for $D < 0.7$,

$$D = \log_{10}(l_0/l) = bIt, \tag{7.7}$$

where b is a constant. If $D(D')$ is the optical density on the low- (high-) energy side of the edge ($D > D'$),

$$D = \log(l_0/l) = bIt, \quad D' = \log(l_0/l') = bI't,$$

$$\Delta l = l - l' = l_0(e^{-2.30bIt} - e^{-2.30bI't}). \tag{7.8}$$

The optimum value of t is given by

$$(dl/dt)_{t=t_{op}} = 2.30bl_0(Ie^{-2.30bIt_{op}} - I'e^{-2.30bI't_{op}}) = 0,$$

$$t_{op} = \frac{\log(I/I')}{b(I-I')}. \tag{7.9}$$

Using $I/I' = D/D'$, and $b(I-I') = (D-D')/t$,

$$t_{op} = \frac{\log(D/D')}{D-D'}t. \tag{7.10}$$

The right-hand side is estimated from an exposure for any reasonable time t.

For small variations $\delta D'$ of the optical density D' on the high-energy side of the absorption edge (fine-structure region), we write $D - D' = \delta D'$, and

$$t_{op} = \frac{\log(1+\delta D'/D')}{\delta D'}t = \frac{1}{\delta D'}[0.434\ln(1+\delta D'/D')]t \approx (0.434/D')t. \tag{7.11}$$

For $t = t_{op}$,

$$(D')_{op} = 0.434, \tag{7.12}$$

A simple rule is just to select *half-value thickness*, that is, the thickness that reduces the intensity on the high-energy side of the edge of about half its initial value. For $I/I_0 = 1/2$, $x_{1/2} = \ln 2/\mu_l = 0.693/\mu_l$, where μ_l is in cm^{-1}. For Cu, at $\lambda = 1.5$ Å, $x_{1/2} = 0.0016$ cm.

For absorption experiments in gases, knowledge of the gas pressure that would give the maximum intensity difference at the edge is needed. Jönson's formula,

$$\tau_m = (Z/A)(\tau_e)_K N_A(E_\alpha/E_K),$$

where E_α is the value of the energy level of the long-wavelength edge, gives τ_m between two absorption edges. Therefore, (7.2) gives [7.5]

$$\rho x = \frac{AE_K(\log E_K - \log E_{L_I})}{Z(\tau_e)_K N_A(E_K - E_{L_I})}, \tag{7.12}$$

where x is the path length and ρ is the density of the absorbing gas. This formula overestimates the pressure. Using (3.204), *Agarwal* [7.6] suggested

$$\rho x = \frac{AaZ^b\log(aZ^b)}{Z(\tau_e)_K N_A(aZ^b - 1)}, \quad [\mathrm{g\,cm^{-2}}], \tag{7.13}$$

where $a = 1.8053$ and $b = -0.6207$. For oxygen, this formula gives $\rho x = 0.8 \times 10^{-4}\,\mathrm{g\,cm^{-2}}$. The density and pressure (in mm) are related by $\rho = (A/22400)(p/760)$. For $x = 2$ cm, the pressure p comes out to be less than 3 mm Hg.

In Fig. 7.1a, we show the transitions responsible for the last emission line of a series and for the corresponding absorption edge and accompanying absorption

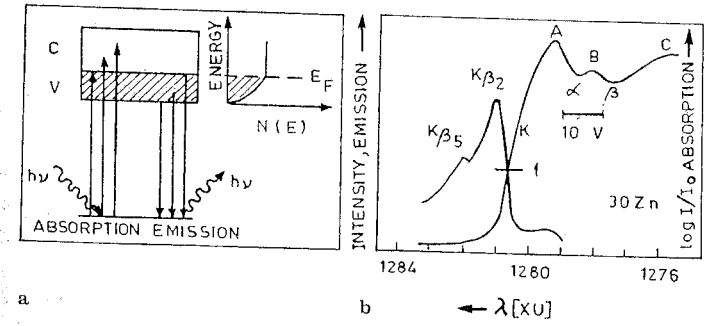

Fig. 7.1. a Transitions for the emission and absorption bands in metals. **b** The relation between the K emission and the K absorption bands in Zn. The absorption maxima (A, B, C, . . .) and minima (α, β, γ, . . .) occur on the high energy side of the absorption edge ($Zn\lambda_K = 1280.7$ XU). The inflection point is marked f

band or structure on the high-energy side, in a metal. The line has the structure of an emission band with a high-energy limit that corresponds to E_F and the main absorption edge also corresponds to E_F. Therefore, in a metal, the observed edge of the emission band coincides with that of the main absorption edge [7.7] (Fig. 7.1b). The shape of the line and of the absorption edge depends on the width of the inner level involved and the transition probabilities. Let us now try to indicate the senses in which various terms are used, sometimes vaguely, in discussing absorption spectra.

Absorption discontinuity is the general region of an X-ray absorption spectra where the transmitted intensity, or absorption coefficient, varies suddenly (almost discontinuously) with λ or ν.

Absorption edge refers to the portion of absorption discontinuity that extends from the maximum of transmitted intensity (minimum absorption coefficient) to the minimum of transmitted intensity (maximum absorption coefficient).

Absorption limit (or *threshold*) refers to the inflection point of the longest wavelength in any cure (absorption coefficient or microphotometer curve) that represents an absorption edge.

Main edge refers to the entire jump of the absorption edge, including any fine structure within the edge. The X-ray absorption main edge structure (XAMES) region extends about 10 eV on both sides of the absorption limit [7.8].

Near edge structure extends on the high energy side of the main edge, from ~ 10 eV to ~ 40 eV from the edge. In this X-ray absorption near edge structure (XANES) region the excited photoelectron has a wavelength greater than the interatomic distance d in the sample.

Extended fine structure is the undulation of the transmitted intensity (or absorption coefficient) found on the high-energy side of the main edge and extending from ~ 40 eV to ~ 100 eV from the edge. It is called the extended X-ray absorption fine structure (EXAFS) region.

White line is a sharp line-like absorption often observed in the initial absorption rise at the edge of a semiconductor, an insulator, or a semimetal. It is called a white line (WL) because of its appearance on the X-ray film. Its presence masks the true position of the absorption edge.

The X-ray absorption fine structure (XAFS) is the general name which includes XAMES, XANES, WL and EXAFS.

There are several prescriptions in use for locating the position of an edge. We give here the two methods that are usually followed.

1) The true absorption coefficient curve is easily drawn if the ionization chamber (or counter) is used, because then the intensity is directly proportional to the reading of the detector. The arctangent curve, (3.173), is fitted to the observed edge shape and the inflection point is located with sufficient accuracy. Even without this fit, the inflection point is sufficiently well defined on the absorption-coefficient curve. The wavelength of this point gives the absorption limit [7.9].

2) If the photographic method is used, the microphotometer curve itself is directly used for locating the absorption limit, because it is not easy to convert it into the absorption-coefficient curve, in view of the nonlinearity of the intensity versus blackening curve. This method does not involve statistical counting errors; moreover, it simultaneously records all wavelengths of interest. The inflection point is usually found near the middle of the absorption edge. When not clearly marked, the usual practice is to identify the middle of the absorption jump with the absorption limit.

Microphotometer curves are not true curves of relative transmitted intensity, mainly because the relation between incident intensity and film blackening varies with λ. In the absorption-limit measurements, we are concerned with a very small portion (a few XU) of the curve, so this photographic effect is negligible. The thickness of the absorber also has a minor effect on the location of the inflection point [7.4, 10]. In most cases, these effects are small compared to the experimental errors.

Matthews [7.11] compared the absorption-limit values determined from the absorption-coefficient curves with those obtained from microphotometer curves. The arctangent equation (3.173) and Lambert's law can be written as

$$\tau(\nu) = C\left\{\frac{1}{2} - \frac{1}{\pi}\tan^{-1}[a(\nu_0 - \nu)]\right\}, \quad I/I_0 \equiv I_r = e^{-\tau x}, \tag{7.14}$$

where C and $a^{-1} = \Gamma_i/2$ are constants, and ν_0 is the frequency of the absorption limit. These equations give

$$d\tau/d\nu = (Ca/\pi)[1 + a^2(\nu_0 - \nu)^2]^{-1}$$

$$d^2\tau/d\nu^2 = (2Ca^3/\pi)(\nu_p - \nu)[1 + a^2(\nu_0 - \nu)^2]^{-2},$$

$$dI_r/d\nu = -xe^{-\tau x}(d\tau/d\nu), \quad d^2I_r/d\nu^2 = x^2e^{-\tau x}(d\tau/d\nu)^2 - xe^{-\tau x}(d^2\tau/d\nu^2).$$

Consider the absorption limit of frequency ν_1 on a curve that represents the actual transmitted intensity, such that $\nu_0 - \nu_1 = \delta\nu$. At $\nu = \nu_1$, $d^2I_r/d\nu^2 = 0$, or

$$x(d\tau/d\nu)^2 = d^2\tau/d\nu^2,$$

$$x(Ca/\pi)^2[1 + a^2(\delta\nu)^2]^{-2} = (2Ca^3/\pi)(\delta\nu)[1 + a^2(\delta\nu)^2]^{-2},$$

whence

$$\delta\nu = Cx(2a\pi)^{-1}. \tag{7.15}$$

The asymptotic behaviour of (7.14) gives $C = \tau_h - \tau_l$, where $\tau_h(\tau_l)$ is the limiting value at the high (low) frequency side of the main edge. Also, $a^{-1} = \Gamma_i/2$,

where Γ_i is the width of the initial atomic level. Therefore, (7.15) becomes

$$\delta\nu = \nu_0 - \nu_1 = [x\Gamma_i(\nu)/4\pi](\tau_h - \tau_l) > 0,$$
$$\delta\lambda = \lambda_0 - \lambda_1 = -[x\Gamma_i(\lambda)/4\pi](\tau_h - \tau_l) < 0, \quad (7.16)$$

where $\Gamma_i(\nu) = \nu_{3/4} - \nu_{1/2}$, (3.174), and $\delta\nu/\Gamma_i(\nu) = -\delta\lambda/\Gamma_i(\lambda)$. The difference $\delta\nu = \nu_0 - \nu_1$ being positive, this analysis shows that the asborption limit obtained from an intensity curve would have lower frequency.

Beckman et al. [7.12] found that, for the K edge of gold, the inflection point of the intensity curve occurs at a wavelength 0.026 ± 0.010 XU longer than the inflection on the corresponding absorption-coefficient curve. They found $\tau_h = 16.2\ \text{mm}^{-1}$, $\tau_l = 5.49\ \text{mm}^{-1}$, and $\Gamma_i(\lambda) = 0.14$ XU as read directly from the curve. When these values are put in (7.16), we get $\delta\lambda \simeq -0.011$ XU, which agrees rather well with the observed value, within the experimental errors.

The difference $\delta\lambda$ given by (7.16) is opposite in direction to the shift of the absorption limit caused by the finite thickness of the absorber. Therefore, it is possible [7.11] that the absorption-limit values obtained from microphotometer curves may be nearer the true absorption limit than most of those obtained from absorption-coefficient curves.

7.2 Nature of the Absorption Spectrum and the White Line

Consider a typical example of the Cu K absorption spectrum (Fig. 7.2) collected in one experiment [7.13]. For ease of discussion it is divided into three regions: XAMES ($K1$, $K2$, A), XANES (B, C), and EXAFS (D, E, F, etc). They differ in the strength of electron scattering involved. For low photoelectron energies (XAMES and XANES regions) the cross-sections are high, resulting in strong modulations in the absorption coefficient $\mu_i(E)$. As energy increases (EXAFS regions) the modulations become weaker, indicating smaller cross-sections. The observed high intensity of EXAFS is due to the backscattering effect from atoms surrounding the absorbing atom, and so does not reflect the overall scattering strength.

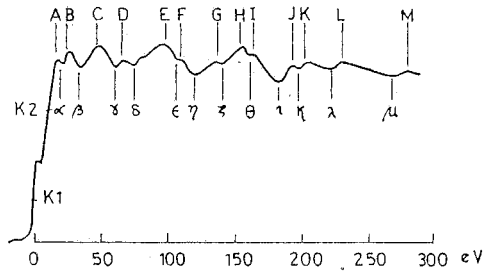

Fig. 7.2. Extended fine structure at the CuK edge [7.13]

The X-ray absorption spectrum, due to excitation of a core level $i = (n, l, j)$, is described in the dipole approximation by [7.14]

$$\mu_i(E) = (4\pi^2/\Omega)\alpha h\nu \sum_f \langle\psi_i|\hat{e}\cdot\boldsymbol{r}|\psi_f\rangle^2 \delta(h\nu - E_f + E_i), \quad (7.17)$$

where Ω is the unit cell volume, $\alpha = e^2/\hbar c$ and $\hat{e}$ is the polarization vector of the incident radiation. The important part is to evaluate the final states $|\psi_f\rangle$. Two approaches are possible: (i) scattering, and (ii) band structure formalism. The former is generally applicable where ψ_f, to begin with, is a solution for the excited atom potential. This ψ_f is improved to include the single backscattering from neighbouring atoms, the spatial variation of the scattered wavelets and, at low energies, multiple scattering effects. Unlike the scattering approach, the band structure formalism implies a periodic potential. The advantageous feature is that it includes multiple scattering to infinite order. Therefore, XAMES and low energy XANES can profitably be discussed in terms of hybridization and density of states. *Müller* [7.15] has reconciled these two viewpoints. In particular, the white line near the edge, a spectacular feature of X-ray absorption, can be understood in terms of band calculations.

7.2.1 White Line

The K absorption of argon (Fig. 7.3) has been carefully measured [7.16]. For free atoms in a gas, the final states in the hydrogenic approximation are the atomic states for resonance lines. These lines are broadened to about 0.58 eV, which is the finite width (Γ_i) of the inner K level in ^{18}Ar (the width of the $4p$ final level is negligible). *Parratt* [7.17] has called them the *bound-ejected-electron* excitation states. Thus, the spectrum should exhibit a few allowed absorption lines of a Rydberg series ($1s \rightarrow np$, $n > 3$) converging to the absorption limit ($1s \rightarrow \infty$) that are broadened by Auger-effect decay of the corresponding discrete lines. This broadening makes most of the lines of the series, except the first few

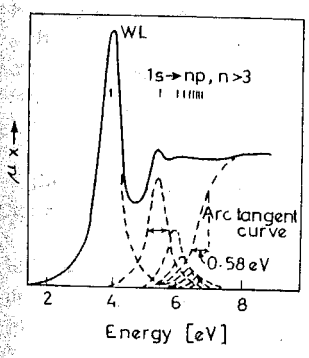

Fig. 7.3. The solid curve represents the K absorption spectrum (uncorrected) of gaseous ^{18}Ar. The resonance lines and the main absorption edge (arctangent curve) at the series limit are shown by dashed curves

(Fig. 7.3), merge smoothly into one another and into the adjoining continuum (positive energy states), which marks the series limit of the atomic levels. The actual photoabsorption limit, is therefore, not observed, because it is masked by the absorption lines. The first strong line appears as a *white line* (WL) on the photographic plate [7.18]. According to *Fonda* and *Newton* [7.19] the X-ray absorption begins at the energy corresponding to raising the atom to its first vacant excited state, and should not be identified with the onset of the photo-effect. The reason is that the sudden onset of the K-shell photo-cross-section is compensated by a nearly equal and opposite discontinuity in the elastic X-ray cross-section.

Parratt calculated the outer atomic states by assuming that the ^{18}Ar atom with a hole in the K level behaves approximately as a ^{19}K atom. The first allowed transition in argon is $1s \rightarrow 4p$, followed by transitions to the subsequent np states whose energy separation is the same as that of the optical levels in potassium. The p-level separations for potassium are $4p-5p = 1.44$ eV, $5p-6p = 0.53$ eV, $6p-7p = 0.25$ eV, etc. The arctangent curve with $\Gamma_i = 0.58$ eV is first drawn at the Rydberg series limit to merge with the observed continuous curve. The first two resolved peaks are then drawn as emission lines with the Lorentz shape and equal width (0.58 eV). Very little freedom is left, so the remaining lines are drawn at Rydberg positions with heights adjusted to give the observed curve when added to the arctangent curve (Fig. 7.3). The relative intensities of these lines are found to be 100:34:18:8.5, etc. The inflection point on the arctangent curve gives the true position of the photoabsorption edge. Similar attempts to analyze the K edge in argon and other inert gases have been made by *Watanabe* [7.20], *Bagus* [7.21], *Mitchell* [7.22], *Vainshtein* and *Narbutt* [7.23] and *Barinskii* and *Nadzhakov* [7.24].

In *solids* of heavier atoms, the width of the inner level increases and the dispersion on the high-energy side of the edge becomes poor. Consequently, in the L-absorption spectrum of atoms bound in compounds, the lines are not resolved; they are merged to give an asymmetrical WL structure. It has been possible to analyze, as in the case of argon, the L_{III}-absorption edges of transition atoms bound in compounds that exhibit strong WL structure [7.25]. *Agarwal* and *Agarwal* [7.26] have analyzed the WL structure observed by them at the Er L_{II} edge in Er_2O_3 and the Ho L_{III} edge in Ho_2O_3, by the method of *Parratt*. This method of analysis (superposition of an arctangent curve with a Lorentzian) has been used recently by *Croft* et al. [7.27] to study the Ce valence variation in intermetallic alloys on the basis of L_{III} absorption results. In rare earths the vestiges of the atom-like $2p_{3/2} \rightarrow 5d$ transition give a Lorentzian feature along with onset of the continuum absorption. Thus when a strong WL is present, the position of the main edge is not visible but is usually on the high-energy side of the WL. In this sense a WL is a pre-absorption, although in the literature it is often included in XANES.

According to *Cauchois* and *Mott* [7.28] a WL structure can arise in solids if there are unoccupied electronic states of the required symmetry with a high density of states at the absorption edge. The well-known cases are the $L_{II,III}$ edges ($2p \rightarrow nd$) of transition elements where there is a high density of empty d states. The ns final states are unimportant for WL as normally the s-symmetric portion of the density of states is small and spread out in energy. The same is true for np final states. The white line is observed in the $L_{II,III}$ edge of transition elements in the metallic state [7.29–32] but not for the L_I edge, as expected from this point of view. However, in most of these cases the WL is not very sharp, the arctan structure of the main edge is retained (not replaced by a sharp line shape, as in Ar), and only a pronounced maximum (usually marked A) immediately on the high-energy side of the edge is observed. The situation is further complicated by the self-absorption lines [7.33]. A similar pronounced maximum is also observed in the ^{33}As metal edge [7.28, 34] note that As is a semimetal.

Experiments indicate that WL in the $L_{II,III}$ edge is limited to metals where unoccupied d states occur at the Fermi energy. Exceptions are rare [7.35]. For example, Ti L_{III} absorption shows no WL [7.36] although it is a transition metal with a high density of unoccupied d states. Also, platinum shows a strong WL in L_{III} absorption but not in L_{II} [7.35]. *Mott* [7.37] first suggested that spin–orbit effects can cause a difference between the L_{II} and L_{III} edge. The only unoccupied d level in the Pt *atom* is $d_{5/2}$, which is probed by L_{III} absorption ($p_{3/2} \rightarrow d_{5/2}$) but not by L_{II} ($p_{1/2} \rightarrow d_{3/2}, s$). This means that vacancies in the d *band* retain the $d_{5/2}$ character [7.35].

Sham [7.38] finds that WL occurs in Pd $L_{II,III}$ absorption but not in Ag $L_{II,III}$. The reason is that Pd has a high density of unoccupied d states above E_F while Ag has none. The observed intensity ratio of the WL (L_{III}/L_{II}) is $\sim$2.6/1, a bit larger than the statistical value 2/1. It means there is more $d_{5/2}$ than $d_{3/2}$ character in the 4d vacant state. (This is not like Pt metal where the 5d vacant state is almost entirely $d_{5/2}$ in character [7.35]). Across the period, the main group elements have partially occupied 5s and 5p states. So the situation turns around and only L_I absorption in In and Sn shows a WL. It means that there is high density of p states just above E_F and these states are more localized than those of the noble metals. Compared to the 5p, the 5s states are nearly occupied and the 5d states are far away from E_F. *Lye* et al. [7.39] have measured white lines in $L_{II,III}$ absorption of lanthanide (Ln) and heavy transition metal (Yb, Re, Os, Ir) complexes. They are associated with $2p \rightarrow$ final d states. No WL is found for $2s \rightarrow$ final p state L_I absorption. The statistical predictions alone give an intensity ratio $4 \times 10 : 2 \times 6$ for $L_{III}:L_I$, and 5:3 for $L_{II}:L_I$. This WL study is useful for biological systems as Ln ions bind strongly to natural and artificial membranes.

A strong WL (Fig. 7.4a) is usually observed in the K-absorption spectra of transition-metal compounds [7.41–43], and $L_{II,III}$ absorption spectra of rare-earth compounds [7.26, 27, 40, 44–46]. Because of scattering effects, the WL gets broadened as the absorber becomes thick [7.4, 43, 47].

The normal electronic configuration of the rare earth (RE) ions in the trivalent state is [Xe] $4f^n$, with $n = 0, 1, \ldots, 14$ for La^{3+}, Ce^{3+}, $\ldots$, Lu^{3+}, respectively. The white lines in the $L_{II,III}$ absorption arise from the $2p \rightarrow 5d$ ($^2P_{3/2} \rightarrow {}^2D_{5/2}$) and $2p \rightarrow 5d$ ($^2P_{1/2} \rightarrow {}^2D_{3/2}$) transitions for L_{III} and L_{II}, respect-

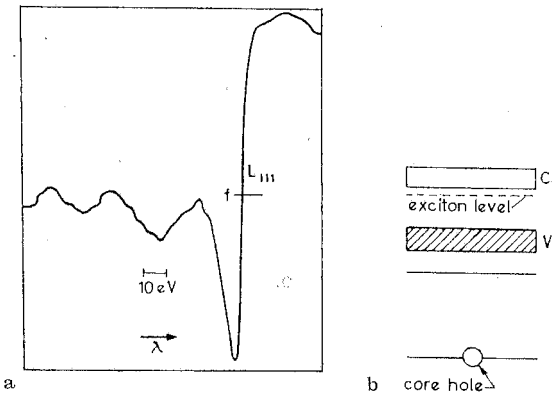

Fig. 7.4. **a** Microphotometer record of the WL in the Gd L_{III} edge. Spectrograph: 40 cm Cauchois curved crystal. Crystal: mica (100). Absorber thickness: Gd_2O_3 12 mg cm^{-2}. Target: Pt. Exposure: 4 h at 32 kV, 5 mA. Reference lines: Fe (3 min.), Ni (3 min.), Co (9 min.), [7.40]. **b** Formation of excition with a vacancy in the core

ively. As the *d* final states in all the RE^{3+} ions are empty, a strong WL occurs with uniform intensity across the 4*f* series [7.44, 45].

The *K*- and L_I-edge spectra probe the *p*-symmetric final states. Normally the *p*-symmetric final density of states is small and spread out in energy, so it is unlikely to produce a WL. However, if a sharp WL is observed in the *K* absorption of a semiconductor, it is possible that the screened hole in the inner-core level and the ejected electron form hydrogen-like bound states, called the *exciton states*, just below the conduction-band edge and within the forbidden energy gap (Fig. 7.4b). The initial transition being to this sharp exciton level of suitable symmetry [7.48], an absorption line is observed that merges with the main edge because the exciton levels converge to a series limit. These are not the usual exciton states, in which a hole in the valence band and a corresponding electron in the conduction band are attracted to each other to form a bound system with energy levels given by the Bohr formula; such an exciton is free to move through the crystal. The kind of exciton postulated here (Fig. 7.4b) cannot move through the crystal because the hole occurs in an inner-core level and the hole-electron separation is of the order of the atomic radius; the energy levels are similar to those of a free atom of atomic number $Z+1$ rather than hydrogen-like.

Seka and *Hanson* [7.42] prefer to give a molecular-orbital picture to explain the white-line structure observed in the transition-metal compounds. *Hedman* et al. [7.49] interpret the WL observed by them in Mo $L_{II,III}$ absorption as a $2p \rightarrow 4d$ transition, and the splitting of the WL for high oxidation states ($+VI$, $+V$) as ligand-field splitting.

Bhide and *Bhat* [7.50], *Singh* and *Agarwal* [7.51], *Agarwal* and *Johri* [7.52] and *Nigam* et al. [7.53] have investigated the *K*-absorption spectra of ions in *solutions*. In general, it is found that, compared to the spectra of gaseous molecules, the selective-absorption lines show smaller intensity, greater width and a high energy shift that is independent of the nature of the solvent shell around the ion. The greater width is because external levels of ions are split under the perturbation caused by the solvent molecules that form a shell around the ion. Much work remains to be done in the area of WL studies.

7.3 X-Ray Absorption Main Edge Structure

The theory of the shape and width of the main edge given by *Richtmyer*, *Barnes* and *Ramberg* is applicable to both *metals* and *semiconductors*, provided that the transitions of the inner electrons beyond the Fermi levels involve a wide band of allowed states. Only then is the assumption of the conduction band as a region of continuous distribution of available energy values, made in the theory, satisfied. The inflection point of the arctangent curve characterizes the position of the Fermi level, and its shape yields the width Γ_i of the inner level [7.7].

The *K*-absorption edge of ^{30}Zn provides a good example. The electronic structure of the Zn atom is $[KL]3s^2 3p^6 3d^{10} 4s^2$. Thus, the relatively narrow 3*d* band is full. In the solid state, some hybridization of 4*s*–4*p* bands makes the upper part of the 4*s* band free; except for the beginning, the entire 4*p* band is also freed. The allowed transition from 1*s* to the very wide 4*p* band gives the arctan form to the main edge [7.54] (Fig. 7.5).

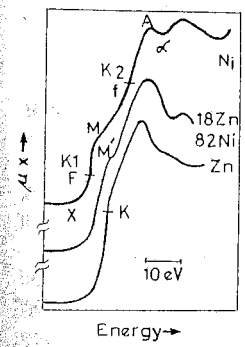

Fig. 7.5. The *K*-absorption edge of ^{30}Zn, ^{28}Ni in metals and of Zn in alloy (18Zn 82Ni)

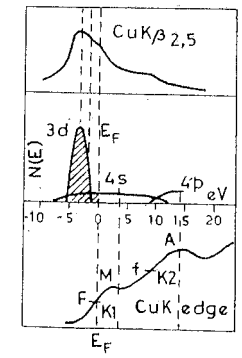

Fig. 7.6. (Top) Cu $K\beta_{2,5}$ emission, (middle) density-or-states curve, and (bottom) *K*-absorption spectrum of ^{29}Cu metal [7.56]

The interpretation of the main edge becomes complicated in the case of transition metals with incomplete d shells. For example, the electronic structure of the ^{28}Ni atom is $[KL]3s^2 3p^6 3d^8 4s^2$. In the metal, $4s$–$3d$ hybridization occurs. We have 60% atoms with $3d^9 4s^1$ and 40% with $3d^{10} 4s^0$ electronic structure. In fact, the next highest and normally unoccupied $4p$ orbitals overlap both of the $4s$ and $3d$ orbitals. We thus have s-p-d hybridization of the orbitals. It is convenient to describe this situation in terms of the density-of-states curve, $N(E)$, which gives the number of orbitals available at each admissible energy value E:

$$N(E) = N_{oc}(E) + N_{unoc}(E), \tag{7.18}$$

$$\tau(E) \propto P_{ab}(E) \cdot N_{unoc}(E), \quad \text{(absorption)}, \tag{7.19}$$

$$I(E) \propto P_{em}(E) \cdot N_{oc}(E), \quad \text{(emission)}, \tag{7.20}$$

where P is the transition probability, and $N_{oc}(N_{unoc})$ denotes the density of occupied (unoccupied) states.

Beeman and *Friedman* [7.7] assumed that $P_{ab}(E)$ in (7.19) is either constant or a very slowly varying function of energy E in the region studied. If this is true, the absorption spectrum should mirror the density-of-states curve of the metal or semiconductor.

The transition probability cannot be calculated exactly. The $1s \rightarrow ns$ and $1s \rightarrow nd$ transitions are Laporte forbidden. However, according to band calculations [7.55], the final states have sufficient admixtures of s, p and d orbitals to permit us to relax the selection rule and to allow transitions from the inner $1s$ level to the admixed high density of d states. *Yeh* and *Azaroff* [7.54] have studied XAMES in ^{30}Zn and ^{28}Ni K edges in metals and solid solutions of Zn in fcc Ni (Fig. 7.5).

The metallic ^{28}Ni K-absorption edge, XMA in Fig. 7.5, shows structure ($K1$, $K2$). The initial absorption rise XM (called $K1$) arises from transitions to the states of s-p-d admixed symmetry, and the second absorption rise MA (called $K2$) from transitions to the Laporate-allowed states of nearly pure $4p$ symmetry. The inflection point F on $K1$ locates the Fermi level E_F. Above E_F, the s-p-d admixed states first acquire pure s symmetry just around M and finally pure $4p$ symmetry around the inflection point f of $K2$. The kink at M arises because the transition probability suddenly decreases for the pure s character of states at M and this causes a decrease of the absorption. The structure $K2$ that ends in peak A is assigned $1s \rightarrow 4p$ transitions, and the region beyond A shows maxima of absorption, corresponding to the transitions $1s \rightarrow np$, $n = 5, 6, 7$, etc.

In the solid state, the solubility of Zn in Ni is less than 25 at.%, so that $3d$ holes of Ni atoms are not saturated completely. However, the area below the curve $K1$ of the Ni edge decreases monotonically as the Zn content increases. On the other hand, the simple Zn metal edge develops a kink M' (Fig. 7.5) as it donates s and d electrons to Ni and develops empty high-density d states. This kink becomes more peaked as the Zn content decreases because there can then be more s-d vacancies per atom.

It is instructive to compare the theoretical density-of-states curve for ^{29}Cu metal [7.56] with the observed Cu $K\beta_{2,5}$ emission and Cu K-absorption spectra (Fig. 7.6). According to *Burdick* [7.56] the filled (shaded) states have largely $3d$ symmetry, but there is an increasing admixture of $4s$ and $4p$ symmetry as E_F is approached. About 4 eV above E_F, the $4s$ symmetry becomes more predominant, whereas at higher energies it becomes purely $4p$.

Just *below* E_F, $N_{oc}(E)$ is not high, but relatively large emission is found because the states have strongly admixed p symmetry. At lower energies, $N_{oc}(E)$ increases but the admixture of p symmetry decreases, so that the emission curve does not continue to rise.

Just *above* E_F, $N_{unoc}(E)$ states of s-p-d hybridization exist, so that the absorption rises rapidly ($K1$). At about 4 eV above E_F, the states have predominantly s symmetry, so that the transition probability decreases and gives less absorption at M (Fig. 7.6 bottom). At slightly higher energies, the states assume pure $4p$ character, and the absorption rises rapidly again. The subsequent maxima arise from transitions between $1s \rightarrow np$, $n \geqq 5$, states.

Both ^{28}Ni and ^{29}Cu have identical crystal structures; they differ only in that Ni has one less electron. Therefore, they show nearly similar $K1$, $K2$ structures in the main absorption edge. Although the $P(E)$ term is not calculated in (7.19, 20), the positions of the observed structures in the spectra near E_F can be correlated with the corresponding regions of the calculated energy band [7.57, 58]. The observed XAMES in the Ni K-absorption shows a definitely diminished contrast in the high energy structure compared to theory. It is attributed to "hot electron" broadening, the name given to the lifetime broadening associated with the decay of the photo-ejected electron to E_F [7.57]. It obviously vanishes at E_F. Although no actual calculations exist, a general theory given by *Kane* [7.59] has been discussed by *Goodings* and *Harris* [7.60] and *Nagel* [7.61]. A linear augmented plane wave (APW) calculation by *Muller* et al. [7.62] of the $3d$ transition-metal K edges, including both initial and final state broadening effects, agrees with the observed features.

The K-absorption spectra of the $4d$ transition metals (^{37}Rb, ^{38}Sr, ^{39}Y, . . . , ^{47}Ag) have been recorded, for example, by *Agarwal* and *Singh* [7.63], *Bhide* and *Kaicker* [7.64], *Singh* and *Agarwal* [7.51], *Kostroun* et al. [7.65], and *Agarwal* and *Johri* [7.52, 66]. The Rb K edge in the metal (in vacuum) was first recorded by *Agarwal* and *Singh* [7.63]. The measurements of *Kostroun* et al. [7.65] and *Agarwal* and *Johri* [7.52, 66] clearly revealed the existence of structures $K1$ and $K2$ with the kink M between them, as in the case of the $3d$ transition metals. The kink M disappears for ^{47}Ag which has a filled d band [7.65].

Muller et al. [7.67] have used the linear APW method to calculate the XAMES of K absorption in $4d$ metals. They find good agreement with the experiments. In particular, the structure $K1$ ending in a peak M, $K2$ ending in a peak A, and the subsequent peak B, are identified with peaks in the density of final states having $4d$-, $5p$-, and $4f$-orbital structure. The two valleys (regions of decreased absorption) between these peaks correspond to valleys in the density of final states due to hybridization of $5p$ orbitals with the $4d$ and $4f$ orbitals.

The observed split structure ($K1$, $K2$) can also be looked upon as arising from the effect of edge singularity in the absorption spectra of core electrons in metals with an empty or incomplete shell, as discussed by *Kotani* and *Toyozawa* [7.68]. They treat the empty or incomplete shell as a nondegenerate localized state that interacts with the conduction band through a mixing interaction. In the initial state of the transition, the empty state of each atom is high enough above E_F for the mixing of the two states to be negligible. However, in the final state of the transition, the empty level of the excited atom is lowered because of the potential of a core hole left behind. When the lowered empty state remains close to, but above E_F, a singular absorption edge $K1$ appears at the Fermi energy, as expected, with an asymmetric antiresonance dip $K2$ around the lowered empty state. The theoretical shape of the absorption spectra, given by *Kotani* and *Toyozawa*, shows a striking resemblance to the Rb metal edge observed by *Agarwal* and *Johri* [7.52].

Recently *Agarwal* and *Balakrishnan* [7.69] have observed a kink F on the low-energy side in the XAMES of Dy L_{III} absorption (Fig. 7.7a). This kink is not found in the L_I edge. They have explained F by assuming that the sudden creation of a $2p$ core hole causes the empty localized $4f$ level E_f, initially above the top of the $5d$–$6s$ unoccupied band of width D, to be pulled down to the final level E_{fF} degenerate with the Fermi level E_F (Fig. 7.7b). The coupling of the core hole to the $4f$ level thus produces a resonance state of width Γ at the unoccupied band edge, centred at E_F. The resulting sudden enhancement in the density of states near E_F gives the kink F in L_{III} due to the transition $2p \rightarrow 4f$, assuming an overlap of the d and f wave functions [7.70, 71].

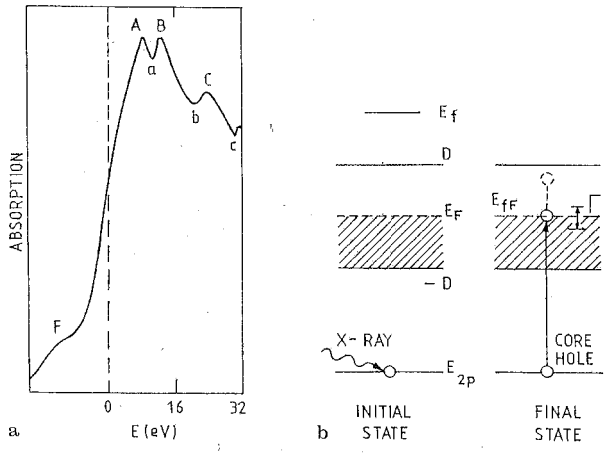

Fig. 7.7. a XAMES in Dy L_{III} absorption showing the kink F which is not found in the L_I edge. **b** The core hole in the level E_{2p} pulls the empty localized level E_f to the final level E_{fF} (width Γ) degenerate with the Fermi level E_F [7.69]

XAMES is sensitive to the chemical environment in solutions as well. *Moss* et al. [7.72] recommend an adjustable sample holder for X-ray absorption studies in liquids. *Huang* et al. [7.73] have used such a cell to record the XAMES in K absorption of potassium ions in various solutions and in frog blood cells. The hydration shells have the least regular and rigid structure and so give rise to a smeared spectrum. The blood cell spectrum differs from that of the aqueous solution indicating a more complex binding of K^+. The cell, therefore, be regarded as an aqueous solution [7.73].

7.4 Chemical Shifts of Absorption Edges

Even in early days of X-ray spectroscopy, *Bergengren* [7.74], and *Lindh* [7.75] showed that chemical combination affects X-ray emission and absorption spectra. Since then, considerable work has been reported on *chemical shifts* of X-ray absorption edges. These have been reviewed several times [7.57, 76–81].

As shown in Fig. 7.8, two main factors contribute to the observed high-energy shifts of X-ray absorption edges: 1) the tighter binding of the core level because of the change of the effective charge (or screening) of the nucleus caused by the participation of the valence electrons in the chemical-bond formation, and 2) the appearance of the energy gap E_g when we go from a metal to a compound (semiconductor or insulator).

Direct evidence for the first factor is provided by photoelectron spectroscopy. The second factor, E_g, is related to phenomena such as covalency, effective charge, coordination number, crystal structure, etc. In Phillips' approach, the *bond parameters* C, $E_{g,\,bond}$, f_i are important. Because the various

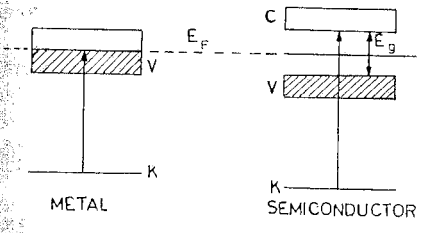

Fig. 7.8. Relative-energy diagram of a metal and the corresponding semiconductor

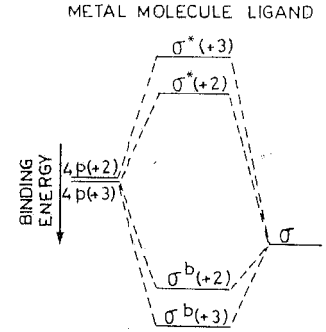

Fig. 7.9. Simplified molecular-orbital diagram for the changes of energy levels as a function of oxidation state [7.97]

factors contribute simultaneously, it is very difficult to give a satisfactory and general theory for the shift of the edges.

By combining the inner-level shift data from photoelectron spectroscopy and X-ray absorption shift data, some valuable information may be obtained on the changes that occur in the conduction band alone, when bonding occurs [7.13]. Ionic bonds, being stronger than covalent bonds, give larger shifts.

Because of the selection rules, the absorption transitions for the different edges probe different regions of the conduction band. A combination of such information can tell us about the nature of the redistribution of electrons in the conduction band when chemical bonds are formed. For emission spectra, *Wiech* [7.82] found that the sum of different valence-band spectra (that is, K and $L_{II,III}$ band spectra) approximates the total density of states $N_{oc}(E) = N_{oc,s}(E) + N_{oc,p}(E)$, where the suffixes s, p denote the symmetry involved. The same would hold for absorption spectra, where information about $N_{unoc}(E)$ would be obtained. For compounds few $N(E)$ calculations exist.

The shift of the X-ray absorption edge i ($i = K, L, M, \ldots$) of an element in a compound with respect to that of the pure element is written as

$$\Delta E_{ab} = E_i(\text{compound}) - E_i(\text{element}).$$

In general, the shift ΔE is positive (towards high energy) and ranges usually from ~ 1 eV to ~ 15 eV.

Agarwal and *Verma* [7.83] suggested an empirical rule for ΔE_{ab}: *In general, the chemical shift is towards the high-energy side of the metal edge; it increases progressively with increase of the valence of the cation, unless the shift is either suppressed by the covalent character of the bond or enhanced by the formation of a metal–metal bonding.*

The first part of the rule, namely the valence dependence of the shift, is well known [7.76, 84]. *Boehm* et al. [7.85] *Vainshtein* [7.86] and *Miller* [7.87] used this dependence to determine the valences of the absorbing ions in compounds. *Sapre* and *Mande* [7.88] tested this rule and found that the covalence suppresses the shift, not only for the cations but also for the anions. Moreover, anions show a negative (low-energy) shift. The metal–metal bond is known to be present in Cl–Hg–Hg–Cl (mercurous chloride). Other examples are the Pb–Pb bond in $Pb_2(CH_3)_6$ and Cu–Cu bond in $[Cu(Acetate)_2H_2O]_2$. Recently *Agarwal* and *Balakrishnan* [7.89] observed a large Dy L_{III} edge shift in $Dy_2(CH_3COO)_6$. They suggested that the six acetate groups bridge between the two rare earth atoms that are in a metal–metal bond. Unless other factors intervene, the metal–metal bond results in large shifts.

Ovsyannikova et al. [7.90], and *Dey* and *Agarwal* [7.43, 91] suggested the following empirical formulas, respectively:

$$\Delta E_{ab} = \text{const.}[N - (1 - f_i)n], \tag{7.21}$$

$$\Delta E_{ab} - \delta E = \text{const.}\, N^2 f_i, \tag{7.22}$$

where N is the valence, f_i is the Pauling ionicity for a crystal (6.13), n is the coordination number and δE is the promotion energy required to promote an

electron ($s \rightarrow p$), in the metal atom, to enable it to display the required oxidation number. ΔE_{ab} has been correlated [7.92, 93] with the ionicity of Phillips (6.19), Van Vechten (6.20), and Levine (6.24).

Comparison of (7.21) with (6.30) shows that $\Delta E_{ab} \propto$ effective charge q. Quite often, Suchet's method of evaluating q (6.26) has been employed to relate ΔE with q [7.81, 94]. The chemical shifts of the K edges in spinels, chalcogenides and intercalation compounds [7.93, 95] yield valuable information about the nature of bondings in such substances. For many compounds ΔE_{ab} has been collected [7.96] and correlated with q. However, all these attempts have little theoretical value. Also q values differ for the same ion in different calculations. More work needs to be done on this.

Glen and *Dodd* [7.97] and *Seka* and *Hanson* [7.42] applied molecular-orbital theory to explain the nature and shifts of the X-ray absorption edges in transition-metal octahedral and tetrahedral complexes. Glen and Dodd observed that the main peak A in the Mn K edge shifts towards the high-energy side in the manganese oxide spectra as the oxidation state increases: MnO (oxidation 2; peak A above edge 16.0 eV), Mn_3O_4 (2, 3; 20.3 eV), MnO_2 (4; 23.6 eV). This can be explained with the help of Fig. 7.9. The more-oxidized metal forms a stronger bond with the ligand (oxygen); therefore, there is a greater overlap of the metal and ligand orbitals. This gives more-stable occupied bonding orbitals. On the other hand, the empty antibonding orbitals, which are obtained by changing the signs of the ligand wave functions and the overlap integral, are less stable because of the stronger repulsive forces. The absorption transitions are to the unoccupied antibonding orbitals. Therefore, the spectral shifts are to higher energies. In this approach also, quantitative calculations are not available. Recent studies on chemical shifts [7.73, 98–100] cover a broad range of systems.

7.5 X-Ray Absorption Near Edge Structure

If a small region in Fig. 3.11, containing (say) the K edge and the smooth-looking absorption curve on the short wavelength side of the K edge, is enlarged, it reveals fluctuations or *fine structure* that extends about 1000 eV from the edge. This absorption spectrum is usually separated, for the purpose of calculation, into three groups: XAMES [7.6] in the region about $\pm$ 10 eV from the absorption threshold, XANES [7.101] in the region ~ 10 to ~ 40 eV beyond the threshold, and EXAFS (named at the International Conference on Physics of Non-crystalline Solids held at Delft in 1964) in the region ~ 40 to about 1000 eV. The old names are Kossel structure [7.102] for XANES and Kronig structure for EXAFS

During the last two decades there has been a spurt of activity in X-ray absorption work. This has led to a lot of progress and some confusion over the definitions involved in the discussions.

X-ray absorption is a one-electron excitation. The final state ψ_f in (7.17)

depends on the system involved, so it is useful to distinguish between the following cases [7.103].

(i) *Rydberg states.* In the K absorption of rare gases (Fig. 7.3) a series of bound Rydberg states appear below the continuum threshold energy E_0 given by the fitted arctangent curve. It gives rise to a WL structure that completely masks the absorption *edge* which is defined by the transition of a core electron to a continuum of final states. In this sense WL is a pre-absorption near the edge and so included in XANES.

(ii) *Bound resonance states.* In semiconductors the exciton states appear just below the conduction band edge because the core hole is not completely screened by the valence electrons. In transition metal compounds bound molecule-like states occur below E_0. Also, when vacant states occur in the highly localized d states near the Fermi level, the WL in the L absorption spectrum has a large atomic character. It can be described as an atom-like bound resonance. Such structures are also a part of XANES.

(iii) *XAMES.* In metals the core hole is well screened by the conduction electrons in the valence band. No bound states are present. Due to variations in the local and partial density of states near E_F, however, some structure (like $K1$ and $K2$ in Cu) can occur within $\pm$ 10 eV of E_0, that is, within the main edge itself. Being of entirely different character, it should be distinguished from XANES. We have called it XAMES.

(iv) *Multiple scattering resonances.* When the photoelectron kinetic energy is greater than $\sim$ 10 eV, the inelastic scattering with valence electrons at binding energies less than 10 eV is significant. Consequently the mean free path of the photoelectron falls to a few angstroms. The elastic scattering is mainly due to bound electrons at greater binding energy, which generally do not participate in the chemical bonding (that is, remain in an atom-like potential). Hence the structures above 10 eV, due to interference effects on the photoelectron wave function ψ_f, determined by the elastic scattering with neighbouring atoms, can be described by multiple scattering within a small atomic cluster (Fig. 7.10a). The resulting *multiple-scattering resonances* of the photoelectron in the continuum give rise to XANES in the range $\sim$ 10 to $\sim$ 40 eV. On increasing the energy of the photoelectron beyond $\sim$ 40 eV we enter the single scattering region of EXAFS (Fig. 7.10b).

In this section we discuss *XANES due to multiple scattering in the region* $\sim$ 10 to $\sim$40 eV. In order to clarify the notation the near edge structures of the type (i) and (ii) are called WL structures, and the term XANES is reserved for the Kossel structure in the 10–40 eV region. Thus, essentially the structures are of four basic types: WL, XAMES, XANES (Kossel) and EXAFS (Kronig).

In XANES the multiple scattering resonances in the energy range $\sim$ 10 to $\sim$ 40 eV depend on the relative atomic positions of neighbouring atoms in several shells. Therefore it is sensitive to the stereochemical coordination (geometry of the arrangement of neighbouring atoms).

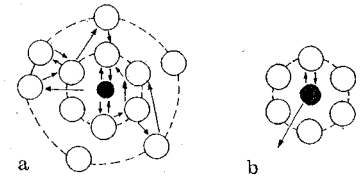

Fig. 7.10. a Multiple scattering processes responsible for XANES; **b** single scattering processes responsible for EXAFS. • absorbing atom, ○ shell atoms

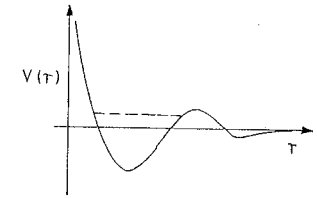

Fig. 7.11. The electronegative effective potential barrier, with a quasi-bound state

The energy range of XANES can be fixed as follows. The single scattering approximation is not valid if the photoelectron wavelength $\lambda = h/p = 2\pi/k$ is greater than the interatomic distance d. Hence in XANES the wavevector is such that $k < 2\pi/d$. As energy is $\hbar^2k^2/2m$ and $\hbar^2/2m = \hbar^2c^2/2mc^2 = [(1970\,\text{eV Å})^2/(1.02 \times 10^6\,\text{eV})] \simeq 4\,\text{eV Å}^2$, the energy range is given by $(\hbar^2k^2/2m) < (\hbar^2/2m)(4\pi^2/d^2)$,

$$E[\text{eV}] < (151/d^2) - V, \tag{7.23}$$

where V is the Fermi energy in metals. As E depends on d and V, the XANES energy range is different for the different substances. For Al ($d = 2.8$ Å, $V = 11.7$ eV) the energy range above E_0 is only 9 eV, so Al L_{III} absorption spectra can be explained by the single scattering theory of EXAFS up to very low energy. In small diatomic molecules, like hydrocarbons ($d \sim 1.2$ Å, $V \sim 10$ eV), the XANES range is 90 eV and so EXAFS is rarely observed. In most of the cases, the XANES energy range is 10–40 eV above E_0.

Nefedov [7.104] and *Dehmer* [7.105] were the first to assign XANES to "inner well resonances" induced by an electronegative potential barrier on the first-neighbour atoms. The concept of effective potential barrier is borrowed from atomic physics. It forms a kind of "edge" (Fig. 7.11) that traps the final state photoelectron wave function ψ_f. A quasi-bound state is formed that decays away with a lifetime determined by the tunneling probability through the barrier.

In atomic physics the repulsive centrifugal barrier, $V_{\text{centri}} \sim l(l+1)/r^2$, gives barriers both around the origin and at some distance away. In molecules the barrier can be created by

(a) a repulsive force due to the Pauli exclusion principle;
(b) centrifugal effects.

The ψ_f must be orthogonal to all occupied orbitals due to (a). In the spirit of pseudopotential theory, it is assumed [7.104, 105] that one may replace the orthogonality constraints by effective potential barriers in the neighbourhood of the electronegative atoms in the molecule.

The centrifugal effect (b) is more tangible. It provides a potential barier of height $\sim l(l+1)/R^2$, where R is the radius of the cluster beyond which the potential is negligible. This idea works, in general, for diatomic molecules. For extended media (crystals) the R cannot be defined [7.106].

One can follow various approaches for the multiple scattering: real space multiple scattering [7.107, 108], so-called $X\alpha$[1] multiple scattering [7.110, 111], or cross-section calculations, starting from the band structure, in k space [7.62]. All of them reach the same conclusion that XANES above ~ 10 eV is mainly given by the geometry of the arrangement of neighbour atoms. Thus XANES gives information on coordination geometry and bonding angle [7.108, 112] not given by EXAFS.

Natoli [7.106] has used multiple scattering theory to predict the relation

$$k_r \cdot R = \text{const.}, \tag{7.24}$$

between the bond length R and the photoelectron wave vector k_r at a resonance (absorption maximum). Such a relation is expected in the framework of the multiple scattering model. The resonant behaviour reduces to a kinetic energy effect, with constraints imposed by the boundary conditions (zeros of ψ_f at the singularities of the atomic potentials, corresponding to the free propagation of the photoelectron from one side to another). The relation (7.24) implies

$$(E_r - \bar{V})R^2 = \text{const.} = C_r, \quad \text{(XANES)}, \tag{7.25}$$

where the inner potential $\bar{V}$ can be taken as the multiple scattering muffin-tin potential in the interstitial region. The muffin-tin potential represents an isolated ion within a sphere of specified radius r_0 about each lattice point. It is flat in the interstitial regions. Formally, the muffin-tin potential is

$$\begin{aligned} V_{MT}(r) &= V(|r-R|) \quad \text{for } |r-R| < r_0, \quad \text{core region} \\ &= \bar{V} = \text{const.} \quad \text{for } |r-R| > r_0, \text{ interstitial region} \end{aligned} \tag{7.26}$$

where r_0 is less than half the nearest-neighbour distance. A plot of $(E_r - \bar{V})$ versus $1/R$ gives a straight line.

In (7.25), $\bar{V}$ is not experimentally known, *Natoli* [7.106] extended the use of a relation similar to (7.25) for bound or exciton resonances (WL), that is,

$$(E_{WL} - \bar{V})R^2 = C_{WL}, \quad \text{(WL)}. \tag{7.27}$$

Subtraction of (7.27) from (7.25) gives

$$(E_r - E_{WL})R^2 = C_r - C_{WL} = \text{const.} \tag{7.28}$$

Thus the energy separation between the WL and the first XANES peak (after the main edge) is a function of the bond length. Various oxides of Mn and V give

[1] In the $X\alpha$ potential the Hartree–Fock exchange term is replaced by its statistical average over all occupied spin orbitals, and is evaluated using the local electron charge density [7.109].

results that verify (7.28) [7.106]. The constant is found to be about 80 eV Å^2 for the measured values of $E_{WL}(3d)$ and $E_r(4p)$.

Polarised studies give pronounced XANES [7.113]. The intensity, shape and position of observed polarized XANES act as indications of the electronic and geometric environment of the metal centre.

A conventional X-ray tube can be used as a source of X-rays for XAMES and XANES work because it provides a reliable energy calibration with the help of reference emission lines. When intense synchrotron radiation is used, the energy calibration of monochromators is a continuing problem due to heating of the dispersive crystals by the absorbed X-ray power.

7.6 Extended X-Ray Absorption Fine Structure

7.6.1 History of EXAFS

EXAFS has an instructive history of 50 years (1920–1970). The salient events are given here.

1920–1930. The absorption fine structure was observed just above the K main edge [7.114–118]. *Kossel* [7.102] suggested that these near-edge structures are connected with the transition of an ejected K electron to discrete optical levels of an atom.

1930–1940. Experiments extended the range of observed fine structure to hundreds of eV beyond the main edge [7.119–121]. Its temperature dependence was also detected [7.122]. It was noted that metals with the same crystal structure had a similar-looking fine structure. This suggested that EXAFS is connected with the long-range order (lro) present in solids. *Kronig* [7.123] assumed that the photoelectron of momentum $p = \sqrt{2mE}$ is Bragg reflected as it traverses the lattice array according to the equation

$$2d\cos\phi = n\lambda_e, \quad \lambda_e = h/p = h/\sqrt{2mE}, \tag{7.29}$$

where λ_e is the de Broglie wavelength of the ejected electron, d is the lattice spacing and ϕ is the angle between the electron propagation direction and the normal to a reflecting lattice plane. Using $d = a/(h^2+k^2+l^2)^{1/2}$ for cubic systems, where a is the periodic spacing length and h, k and l are the Miller indices, integration over all possible propagation directions for unpolarized X-rays (for polycrystalline absorbers) gives *Kronig*'s formula

$$E = \frac{h^2}{8m}\frac{(\alpha^2+\beta^2+\gamma^2)}{a^2}, \tag{7.30}$$

where α, β and γ are integers. These energies are forbidden to the photoelectrons and so correspond to the absorption minima. As (7.30) implies a three-dimensional ordered crystal, *Azaroff* [7.124] classified it as a *longrange order* theory. It predicted several features of the EXAFS data: (i) similar structure for similar

lattices, (ii) r^{-2} dependence, (iii) r versus temperature dependence and (iv) increasing energy separation of absorption maxima with energy from the edge.

Hanawalt [7.125] also studied EXAFS in molecules for which the lro formula (7.30) failed. Presence of EXAFS in amorphous materials created problems for the lro theory. Realizing this, *Kronig* [7.126] also created a *short-range order* (sro) theory for molecular EXAFS. As his basic physical idea is correct, and relevant even today, we review it here.

In (7.19), fluctuations in $\tau(E)$ are related to rapid changes in $P_{ab}(E)$ and/or $N_{unoc}(E)$. In the lro theories lattice modulated plane waves (Bloch functions) are used to describe the ejected electrons, and so $\tau(e) \sim N_{unoc}(E)$. In sro theories $\tau(E) \sim P_{ab}(E)$, as photoelectron final states are those that follow scattering by neighbouring atoms.

Let $\tau_a(E)$ denote the absorption coefficient for the isolated atom A and $\tau_M(E)$ that for A in a molecule AB. According to Kronig, the change of the absorption by a diatomic molecule is determined by the ratio

$$\chi(E) = \frac{\tau_M(E)}{\tau_a(E)} = \frac{P_M(E)}{P_a(E)}, \tag{7.31}$$

where P_a and P_M are the corresponding probabilities of the transitions.

The ejected positive-energy electron can be represented by a plane wave, $\psi_k(x, y, z) = N e^{ikr}$, where N is the normalization constant and $k = (2mE)^{1/2}/\hbar$. If $\psi_i(x, y, z)$ is the bound-state wave function of the initial core state, the probability P is proportional to the square of the matrix element of the oscillator amplitude,

$$P \propto (|x_{i\to k}|^2 + |y_{i\to k}|^2 + |z_{i\to k}|^2),$$

$$x_{i\to k} = \iiint \psi_k^*(x, y, z) x \psi_i(x, y, z) dV, \quad dV = dx\,dy\,dz.$$

If we designate the matrix elements $x_{i\to k}, y_{i\to k}, z_{i\to k}$ for an isolated atom by x_a, y_a, z_a, and for a bound atom by x_M, y_M, z_M, then

$$\chi(E) = \frac{x_M^2 + y_M^2 + z_M^2}{x_a^2 + y_a^2 + z_a^2}. \tag{7.32}$$

The wave function for the inner state $\psi_i(x, y, z)$ is the same in both cases. Let the electron in a state k move along the x axis that passes through the atom A. The plane wave that represents the electron has the form $\psi_k(x) = N\exp(ikx)$. Then, for a single atom,

$$x_a = \iiint \psi_k^*(x) x \psi_i(x, y, z)\, dx\,dy\,dz, \quad y_a = z_a = 0. \tag{7.33}$$

The plane-wave front from A is elastically scattered by B if it reaches the point X on the x axis (Fig. 7.12). In elastic scattering, the magnitude of the wave vector, k, is conserved. The amplitude of the scattered spherical wave near the atom A can be expressed as $f(\theta)/R$ where R is the distance between the atoms, θ is the scattering angle, and $f(\theta)$ is the angle-distribution function. If $R \gg \lambda$, the

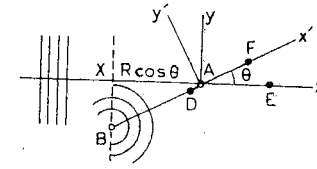

Fig. 7.12. Calculation for absorption by a diatomic molecule. $AB = R$, $AD = R(1 - \cos\theta)$, $DB = R\cos\theta$, $AE = x$, $AF = x$

spherical wave near A can be approximated by a plane wave $(f(\theta)/R)\exp(ikx')$, that propagates along the x' axis,

$$\psi_{sc}^B(x') = N(f(\theta)/R)\exp(ikx'). \tag{7.34}$$

Let us investigate the scattered wave at the point F on the interatomic axis x' (Fig. 7.12). We can find the time and path lengths traversed by the incident wave and the scattered wave from the instant when the former reached the atom A. In this time interval, the scattered wave traversed the distance $BD = XA = R\cos\theta$ along the x' axis. At some subsequent time t, when the incident wave is at the point E, with coordinate x, the scattered wave will be at the point F with coordinate x'. Clearly,

$$x = AE = DF = DA + x' = R(1 - \cos\theta) + x'. \tag{7.35}$$

It follows that at F

$$\psi_{sc}^B(x') = N\frac{f(\theta)}{R} e^{ik[R(1-\cos\theta)+x']} = q\psi_k(x'), \tag{7.36}$$

where q does not depend on x', and we can take $N = 1$,

$$q = \frac{f(\theta)}{R} e^{ikR\,1-(\cos\theta)}. \tag{7.37}$$

The two waves (incident + scattered from B) act simultaneously on the atom A. The total wave function $\Psi_{tot}(x, y, z)$ can be expressed as

$$\Psi_{tot}(x, y, z) = \psi_k(x) + \psi_{sc}^B(x') = \psi_k(x) + q\psi_k(x'). \tag{7.38}$$

The matrix element x_M then is

$$x_M = \iiint \Psi_{tot}^*(x, y, z) x \psi_i(x, y, z) dV$$

$$= x_a + q^* \iiint \psi_k^*(x') x \psi_i(x, y, z) dV, \tag{7.39}$$

where x_a is given by (7.33). If ψ_i has spherical symmetry, $\psi_i(x, y, z) = \psi_i(x', y', z')$, where the frame x', y', z' obtained by rotation through an angle θ around the z axis is related to x, y, z by

$$x = x'\cos\theta - y'\sin\theta, \quad y = x'\sin\theta + y'\cos\theta, \quad z = z',$$

$$dx\,dy\,dz = dV = dx'\,dy'\,dz' = dV'.$$

It follows that (7.39) can be written as

$$x_M = x_a + q^* \iiint \psi_k^*(x')(x'\cos\theta - y'\sin\theta)\psi_i(x', y', z')dV'$$
$$= x_a + q^*(x_a\cos\theta - y_a\sin\theta) = x_a(1 + q^*\cos\theta),$$

because $y_a = 0$. In the same way,

$$y_M = q^* x_a \sin\theta, \quad z_M = 0.$$

We can now evaluate (7.32),

$$|x_M|^2 = x_a^2|1 + q^*\cos\theta|^2 = x_a^2(1 + q^*\cos\theta)(1 + q\cos\theta)$$
$$= x_a^2[1 + (q + q^*)\cos\theta + |q|^2\cos^2\theta],$$
$$|y_M|^2 = x_a^2|q|^2\sin^2\theta,$$
$$\chi(E) = \frac{x_M^2 + y_M^2}{x_a^2} = 1 + (q + q^*)\cos\theta + |q|^2. \tag{7.40}$$

We can average this expression over $\cos\theta$, dropping the small $|q|^2$ term,

$$\langle\chi(E) - 1\rangle = \frac{\int_{-1}^{+1}[(q + q^*)\cos\theta]d(\cos\theta)}{\int_{-1}^{+1} d(\cos\theta)} = \tfrac{1}{2}\int_0^{\pi}[(q + q^*)\cos\theta]\sin\theta\, d\theta$$

$$= \frac{e^{ikR}}{2R}\int_{-1}^{+1} f(\theta)e^{-ikR\cos\theta}\cos\theta\, d(\cos\theta) + \text{c.c}$$
$$= \frac{e^{ikR}}{2R}\left[\frac{1}{ikR}e^{-ikR\cos\theta}f(\theta)\cos\theta\right]_{-1}^{+1} + \cdots + \text{c.c}$$
$$\simeq \frac{e^{2ikR}}{2ikR^2}(f(\pi) - f(-\pi)) + \text{c.c}$$
$$= \frac{|f(\pi)|}{kR^2}\sin(2kR + \delta), \tag{7.41}$$

where the last step uses $f(\pi) = |f(\pi)|e^{i\delta}$, δ being the phase shift on single backscattering.

We have to evaluate $f(\theta)$ by taking some potential form for the scattering by the atom B [7.127]. *Petersen* [7.127] introduced the idea of adding the phase shift in the photoelectron wave function caused by the potentials of the absorbing atom A in addition to the backscattering atom B. For a symmetrical multiatomic molecule [7.128]

$$\langle\chi(E) - 1\rangle = \sum_j \langle\chi_j - 1\rangle. \tag{7.42}$$

1940–1950. Kostarev [7.129] made the next advance in 1941. He realized that

EXAFS is caused only by the transition probabilities and so the Kronig–Petersen sro theory is also applicable to solids. He developed in 1949 a compact expression [7.129] which agreed with data. At the same time *Hayasi* [7.130] interpreted *Kronig*'s formula (7.30) as the case $\phi = 0$, that is, the case where the photoelectron is reflected back to the absorbing atom by lattice planes at right angles to the possible propagation directions. The increased overlap of the two wave functions results in a large transition probability. For cubic crystals, the energy values are still determined by (7.30), but now they correspond to absorption maxima instead of minima. It is difficult to locate the true zero exactly along the energy scale. A relative displacement can take us from the positions of Kronig's minima to Hayasi's maxima, so it is difficult to decide which interpretation is correct [7.43]. In fact, it took about 40 years to discover that both these lro theories are incorrect [7.131].

1950–1960. In 1957 *Shiraiwa* et al. [7.132] further developed *Kronig*'s sro theory. They first accounted for the lifetime of the excited photoelectron and core hole state through a mean free path. The q in (7.41) was estimated by taking the potential of each neighbouring atom to be a square well of radius a. They found

$$\chi(k) \propto -\sum_j\left(-\frac{2m}{\hbar^2}Va^3\right)\frac{N_j}{r_j^2}\sin 2kr_j\left(\frac{\cos 2ka}{(2ka)^2} - \frac{\sin 2ka}{(2ka)^3}\right)e^{-\mu r_j}, \tag{7.43}$$

where $\exp(-\mu r_j)$ accounts for the decrease in amplitude of the ejected electron due to the mean free path effect (scattering from neighbouring atoms), and the subscript denotes the jth shell, containing N_j atoms, at a distance r_j from the absorbing atom. It gives sine-like scattering from each shell with the EXAFS signal proportional to N_j and inversely proportional to r_j^2. As $a \ll r_j$ the square-bracket term is a modulating factor for $\sin 2kr_j$. It gave a fairly good agreement with the data on Cu, Ni and Fe.

1960–1970. In 1961 *Kozlenkov* [7.133] compared the various sro theories and found them more general and acceptable than the lro theories. He used the square-well potential for calculating $f(\theta)$ and so the scattering phase shifts δ_j from the neighbouring atoms. He essentially found

$$\chi(k) \propto -\sum_j \frac{N_j}{r_j^2}\sin[2kr_j + 2\delta_j(k)]. \tag{7.44}$$

Vishnoi and *Agarwal* [7.134] improved the approximation by performing an integration corresponding to a uniform distribution of all the atoms in a shell over a spherical surface of radius r_j. *Shmidt* [7.135] used the sro theory of *Kozlenkov* and included the damping of the amplitude of EXAFS due to averaging within a coordination sphere. It gave a Debye–Waller-type factor to account for the thermal disorders. This provided the last missing link for a modern theory. *Jope* [7.136] also discussed the temperature effect.

Around 1966 attempts were made to use EXAFS for obtaining quantitative information. *Levy* [7.137] calculated first coordination distance r_1 from the

energy separation ΔE between the first EXAFS maximum and the next minimum. Assuming $2kr_1$ as the argument of the sine scattering term in Kozlenkov's theory (7.44), he found

$$r_1[\text{Å}] = (151/\Delta E)^{1/2}, \quad \Delta E \text{ in eV}. \tag{7.45}$$

Lytle [7.138] employed a "particle in a box" theory to calculate r_1. It was generalized by *Agarwal* and *Johri* [7.139] to a "double-potential" model to account for chemical effects (or electronegativity).

In 1970 *Sayers* et al. [7.140] gave a qualitative theory for cubic crystals which considered thermal and static disorder effects, and damping due to the mean free path length.

By this time the various elements of the modern theory were known, but they were yet to be put together in a grand design. Even confusion whether the lro or sro theory is correct was still around. In 1970 *Perel* and *Deslattes* [7.141] observed: "Neither of the (EXAFS) theories discussed here (sro and lro) can account for even the gross characteristics of the absorption spectra . . .". The main reason for the confusion was the lack of detailed agreement between any theory and the experiments (often not reliable).

After 1970. The landscape suddenly changed in 1971 when *Sayers* et al. [7.142] pointed out, on the basis of the earlier formula [7.140], that a Fourier transform of the EXAFS data with respect to the photoelectron wave number will peak at distances corresponding to the nearest-neighbour coordination shell of atoms. This is theory-independent as the data themselves are transformed.

Quick and reliable EXAFS measurements became possible with the availability of synchrotron radiation sources of X-rays.

In 1974, *Stern* [7.143] showed that the periodic potential, kernal of the lro theories, is not the physical origin of EXAFS. The method of EXAFS now emerged as a quantitative tool for determining short-range parameters through the pioneering work of *Lytle* et al. [7.144, 145]. The theory has matured since then in the hands of *Kincaid* and *Eisenberger* [7.146], *Ashley* and *Doniach* [7.147], *Lee* and *Pendry* [7.148] and others. In 1977, *Lee* and *Beni* [7.149] gave ab initio evaluations of central atom and scattering phase shifts, leading to accurate determinations of coordination distances. *Teo* and *Lee* [7.150] used these calculations to tabulate phase shifts and back-scattering functions for $6 \le Z \le 82$.

Comprehensive reviews of EXAFS have been written by *Lee* et al. [7.151] and *Hayes* and *Boyce* [7.152].

7.6.2 Basic Theory of EXAFS

In the dipole approximation the photoabsorption cross-section is

$$\mu(\nu) = 4\pi^2 \alpha h\nu \sum_f |\langle \psi_i | \sum_{n=1}^{N} \hat{\boldsymbol{e}} \cdot \boldsymbol{r}_n | \psi_f \rangle|^2 \, \delta(E_i^T + h\nu - E_f^T),$$

where ψ_i and ψ_f are the initial- and final-state wave functions of the full N-electron Hamiltonian with total energies E_i^T and E_f^T, and r_n is the position of the nth electron. In Koopman's approximation ($E_i^T - E_f^T \simeq E_i - E_f$) it reduces to the one-electron expression (7.17).

In (7.17), $\mu(E) \propto \langle \psi_i | \hat{\boldsymbol{e}} \cdot \boldsymbol{r} | \psi_f \rangle^2$, for the K absorption, ψ_i is the $1s$ atomic wave function and ψ_f is the final photoelectron wave function including scattering from the near neighbours. In the sro theory EXAFS is due to the matrix element. The variations in the matrix elements are associated with those in ψ_f because ψ_i is fixed at a given core level ($1s$ level here). Essentially ψ_f is of Kronig's form (7.38), $\psi_f = \psi_k + [f(\theta)/r]\exp[ikr(1-\cos\theta)]$. Substitute this ψ_f in $\langle \psi_i | \hat{\boldsymbol{e}} \cdot \boldsymbol{r} | \psi_f \rangle^2$. Remembering that $\hat{\boldsymbol{e}} \cdot \boldsymbol{k}$ is related to $\hat{\boldsymbol{e}} \cdot \boldsymbol{r}$ (Sect. 1.17) and that the amplitude for the atomic photoelectric effect (4.7) involves $\hat{\boldsymbol{e}} \cdot \boldsymbol{k}$, we can write the emission rate as

$$P(\hat{\boldsymbol{k}}) = D|M|^2 |(\hat{\boldsymbol{e}} \cdot \hat{\boldsymbol{k}}) + \frac{f(\theta)}{r} e^{ikr(1-\cos\theta)} \hat{\boldsymbol{e}} \cdot \boldsymbol{r}|^2$$

Here D is a slowly varying factor that includes the density of states, M is the matrix element of the ejected (free) electron ψ_k with the K-shell electron radial wave function ψ_i [see (4.7)] and $\hat{\boldsymbol{k}} = \boldsymbol{k}/k$.

We follow a simple treatment given by *Lee* [7.153] and *Lee* et al. [7.151] to obtain the EXAFS $\chi(k)$. Suppose the single neighbour B is located at $\boldsymbol{r}_1$ relative to the absorbing atom A (Fig. 7.13). The probability of emitting a K-shell photoelectron in the direction $\hat{\boldsymbol{k}}$ is given by

$$P(\hat{\boldsymbol{k}}) = C \left| \hat{\boldsymbol{e}} \cdot \hat{\boldsymbol{k}} + \frac{f(\theta)}{r_1} e^{ikr_1(1-\cos\theta)} \hat{\boldsymbol{e}} \cdot \hat{\boldsymbol{r}}_1 \right|^2, \tag{7.46}$$

where $\hat{\boldsymbol{e}}$ is the polarization direction of the X-ray, θ is the angle between $\hat{\boldsymbol{k}}$ and $\hat{\boldsymbol{r}}_1$, and C is taken as a constant. Figure 7.13 shows that the two terms in (7.46) describe the interference of the direct beam with the beam that propagates first to $\boldsymbol{r}_1$ and is then scattered through an angle θ with scattering amplitude $f(\theta)$. The difference in the interference path length is $\boldsymbol{r}_1(1-\cos\theta)$ which gives the phase factor $kr_1(1-\cos\theta)$. To get the total absorption coefficient we integrate over all $\hat{\boldsymbol{k}}$.

The term of interest is the cross term

$$\int \frac{d\hat{\boldsymbol{k}}}{4\pi} \left(\hat{\boldsymbol{e}} \cdot \hat{\boldsymbol{k}} \frac{f(\theta)}{r_1} e^{ikr_1(1-\cos\theta)} \hat{\boldsymbol{e}} \cdot \hat{\boldsymbol{r}}_1 + \text{c.c} \right)$$
$$= 2\mathcal{R}e\{e^{ikr_1} \hat{\boldsymbol{e}} \cdot \hat{\boldsymbol{r}}_1 J/r_1\}, \tag{7.47}$$

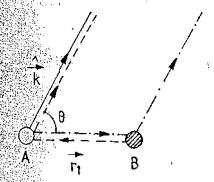

Fig. 7.13. Interference between the photoelectron beam (solid line) emitted by the absorbing atom A and (i) the beam (dash-dot line) scattered by the neighbour B at r_1 and (ii) the beam (dashed line) backscattered by B. Integration over θ gives the EXAFS. Process (ii) leads to the central atom phase shift

where

$$J = \int \frac{d\hat{\boldsymbol{k}}}{4\pi} \hat{\boldsymbol{e}} \cdot \hat{\boldsymbol{k}} \, \mathrm{e}^{-\mathrm{i}kr_1 \cos\theta} f(\theta). \tag{7.48}$$

We choose $\boldsymbol{r}_1$ to be the z-axis and use the identify

$$\hat{\boldsymbol{e}} \cdot \hat{\boldsymbol{k}} = \sum_m \frac{4\pi}{3} Y_{lm}^*(\hat{\boldsymbol{k}} \cdot \hat{\boldsymbol{r}}_1) \, Y_{lm}(\hat{\boldsymbol{e}} \cdot \hat{\boldsymbol{r}}_1), \tag{7.49}$$

where Y_{lm} are spherical harmonics. The azimuthal angle integration is simple and only the $m = 0$ term is left,

$$J = \hat{\boldsymbol{e}} \cdot \hat{\boldsymbol{r}} \tfrac{1}{2} \int \cos\theta \, \mathrm{e}^{-\mathrm{i}kr_1 \cos\theta} f(\theta) \, d(\cos\theta). \tag{7.50}$$

To integrate (7.50) we use the standard expansions

$$\mathrm{e}^{-\mathrm{i}kr_1 \cos\theta} = \sum_l (2l+1)(-\mathrm{i})^l j_l(kr_1) P_l(\cos\theta), \tag{7.51}$$

$$f(\theta) = \sum_l f_l P_l(\cos\theta), \tag{7.52}$$

where the partial scattering amplitude is

$$f_l = \frac{1}{2\mathrm{i}k}(2l+1)(\mathrm{e}^{2\mathrm{i}\delta_l} - 1). \tag{7.53}$$

Here δ_l is the phase shift due to the scattering by B. Then

$$J = \sum_l \hat{\boldsymbol{e}} \cdot \hat{\boldsymbol{r}}_1 \, \mathrm{i} \frac{\partial}{\partial(kr_1)} [(-\mathrm{i})^l j_l(kr_1)] f_l, \tag{7.54}$$

where the spherical Bessel function has the asymptotic form

$$j_l(kr_1) \to \frac{1}{kr_1} \sin(kr_1 - \tfrac{1}{2} l\pi). \tag{7.55}$$

From (7.54, 55)

$$J = \frac{\hat{\boldsymbol{e}} \cdot \hat{\boldsymbol{r}}_1}{kr_1} \frac{1}{2} \, \mathrm{i}[f(k,\pi)\mathrm{e}^{\mathrm{i}kr_1} + f(0)\mathrm{e}^{-\mathrm{i}kr_1}], \tag{7.56}$$

where $f(k,\pi)$ is the *backscattering* amplitude. In view of the optical theorem

$$\mathscr{I}m\{f(0)\} = \frac{k}{4\pi} \int |f(\theta)|^2 \, d(\cos\theta) \, d\phi, \tag{7.57}$$

the second term in (7.56), involving the forward-scattering amplitude, is exactly cancelled by the square of the second term in (7.46). Therefore, finally

$$\chi(k) = \frac{\Delta\mu}{\mu_0} = -3 \frac{(\hat{\boldsymbol{e}} \cdot \hat{\boldsymbol{r}}_1)^2}{kr_1^2} \mathscr{I}m\{f(k,\pi)\mathrm{e}^{2\mathrm{i}kr_1}\}, \tag{7.58}$$

where $\Delta\mu = \mu - \mu_0$ is the oscillatory part of the K-shell absorption coefficient for the material and μ_0 is the structureless (atom-like) background. This result is equivalent to the sro theory result (7.42) of *Kronig* [7.126] and *Shiraiwa* et al. [7.132].

The backscattering amplitude is given by

$$\begin{aligned} f(k,\pi) &= |f(k,\pi)|\mathrm{e}^{\mathrm{i}\delta(k)} \\ &= \frac{1}{2\mathrm{i}k} \sum_l (2l+1)(\mathrm{e}^{2\mathrm{i}\delta_l} - 1)(-1)^l. \end{aligned} \tag{7.59}$$

It remains to consider the central atom phase shift. Its significance was recognized by *Kostarev* [7.129], *Kozlenkov* [7.133] and *Sayers* et al. [7.142]. In our derivation (Fig. 7.13) the direct beam and the scattered beams are both outgoing waves. They are phase shifted by the same amount. The phase shift δ_1^A due to A is therefore cancelled in calculating the interference path length. To regain δ_1^A, we have to go to a higher-order scattering process. In this process (Fig. 7.13) the photoelectron goes from A to B, is backscattered by B, and is scattered again by A in the direction $\hat{\boldsymbol{k}}$. The probability amplitude for this is

$$A_2(\hat{\boldsymbol{k}}) = \hat{\boldsymbol{e}} \cdot \hat{\boldsymbol{r}}_1 \frac{\mathrm{e}^{2\mathrm{i}kr_1}}{r_1^2} f(k,\pi) f_A(k, 2\pi - \theta), \tag{7.60}$$

where f_A is the scattering amplitude by the central atom A. This term is to be added to the amplitude in (7.46) and then squared. The leading term contains a product of $\hat{\boldsymbol{e}} \cdot \hat{\boldsymbol{k}}$ and A_2. When this is integrated over all $\hat{\boldsymbol{k}}$ directions, it projects out only the $l = 1$ component of the scattering amplitude f_A. Use of (7.53) then gives the additional contribution P_2 to the probability,

$$P_2 = -\mathscr{I}m\left\{(\mathrm{e}^{2\mathrm{i}\delta_1^A} - 1) f(k,\pi) \frac{\mathrm{e}^{2\mathrm{i}kr_1}}{kr_1^2}\right\}. \tag{7.61}$$

When combined with (7.58), it yields exactly the central atom phase shift. Thus, for the single neighbour B,

$$\begin{aligned} \chi(k) &= -3 \frac{(\hat{\boldsymbol{e}} \cdot \hat{\boldsymbol{r}}_1)^2}{kr_1^2} \mathscr{I}m\{\mathrm{e}^{2\mathrm{i}kr_1 + 2\mathrm{i}\delta_1^A} f(k,\pi)\} \\ &= -3 \frac{(\hat{\boldsymbol{e}} \cdot \hat{\boldsymbol{r}}_1)^2}{kr_1^2} \mathscr{I}m\{\mathrm{e}^{2\mathrm{i}kr_1 + 2\mathrm{i}\delta_1^A + \delta(k)} |f(k,\pi)|\}. \end{aligned} \tag{7.62}$$

For unpolarized X-rays and N_j neighbours, the K edge EXAFS is given by

$$\chi(k) = -\sum_j \frac{N_j}{kr_j^2} |f_j(k,\pi)|^2 \sin[2kr_j + \delta_j(k) + 2\delta_1^A(k)], \tag{7.63}$$

where N_j neighbours are located at a radial distance r_j from the absorbing atoms and the sum is over all such shells. The photoelectron wave vector is defined by

$$k[\text{Å}^{-1}] = [(2m/\hbar^2)(\hbar\omega - E_0)]^{1/2} = 0.5123(\hbar\omega - E_0)^{1/2}, \tag{7.64}$$

where $\hbar\omega$ is the X-ray energy and E_0 is the threshold energy in eV. The scattering from each atom contributes a sinusoidal variation to the absorption.

We now consider the inelastic effects due to the lattice vibration and lifetime. The lattice vibration effect has been discussed by *Schmidt* [7.135] and *Beni* and *Platzman* [7.154]. The time scale of EXAFS is much shorter than that of atomic vibration, so EXAFS refers to an instantaneous picture of the atomic configuration. We should take an average over all such configurations. The instantaneous location of the atom is $\boldsymbol{r}_j = \boldsymbol{r}_j^0 + \boldsymbol{u}_j$, where $\boldsymbol{r}_j^0$ is the equilibrium position taken as zero for the central atom. The phase factor associated with the displacement $\boldsymbol{u}_j$ requires the evaluation of

$$\begin{aligned}\langle e^{i2k|r_j - r_0|}\rangle &\approx \langle e^{i2k\hat{r}_j^0\cdot(r_j - r_0)}\rangle \\ &= e^{i2kr_j^0}\langle e^{i2k\hat{r}_j^0\cdot(u_j - u_0)}\rangle \\ &= e^{i2kr_j^0}e^{-2k^2\sigma_j^2},\end{aligned} \tag{7.65}$$

where the last step follows for harmonic oscillators[2] and $\sigma_j^2 = [\langle \hat{\boldsymbol{r}}_j^0\cdot(\boldsymbol{u}_j - \boldsymbol{u}_0)\rangle]^2$. It introduces a Debye–Waller-like factor $\sigma(T)$ in the $\chi(k)$ due to thermal vibrations at temperature T. Its effect is to smear out the EXAFS oscillations. The Debye–Waller factor involved in EXAFS is different from that used in crystallography. In EXAFS it refers to the root-mean-square *relative* displacement *along the bond direction* and not the absolute root-mean-square displacement of individual atoms.

The electrons that have suffered inelastic losses will not be left with the proper wave vector to contribute to the interference process. In a rough way, it is accounted for by an exponential damping term $\exp[-2r_j/\lambda_j(k)]$ where $\lambda_j(k)$ is the mean-free path of the photoelectrons. The limited range of the photoelectrons in the energy region of interest (50–1000 eV), imposed by this term, makes sro description of EXAFS feasible, even in crystals.

With these two correction terms, the $\chi(E)$ for the K (or L_I) edge spectra is given by

$$\chi(k) = -\sum \frac{N_j}{kr_j^2}|f_j(k,\pi)|\sin[2kr_j + \phi_j(k)]e^{-2\sigma_j^2k^2}e^{-2r_j/\lambda_j(k)}, \tag{7.66}$$

where $\phi_j(k)$ is the total phase function given by

$$\phi_j(k) = \delta_j(k) + 2\delta_1^A(k). \tag{7.67}$$

This is the short-range *single electron single-scattering* EXAFS *formula*. Multiple scattering has been ignored. Equation (7.66) has also been derived [7.147, 148] using Green's functions and generalizations to muffin-tin scattering potentials.

[2] If ϕ_i are harmonic oscillator wave functions,

$$\begin{aligned}\langle\phi_i|iQ\cdot\delta\boldsymbol{u}|\phi_i\rangle &\approx \langle\phi_i|1 + iQ\cdot\delta\boldsymbol{u} - \tfrac{1}{2}(Q\cdot\delta\boldsymbol{u})^2|\phi_i\rangle \\ &= 1 - \tfrac{1}{2}Q^2\langle\phi_i|(\hat{Q}\cdot\delta\boldsymbol{u})^2|\phi_i\rangle \approx e^{-Q^2\langle(\hat{Q}\cdot\delta\boldsymbol{u})^2\rangle},\end{aligned}$$

as the average of the $Q\cdot\delta\boldsymbol{u}$ term vanishes.

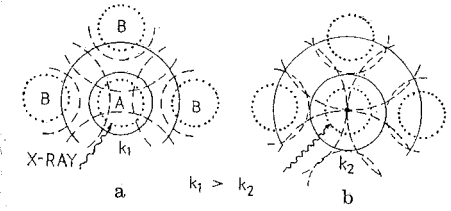

Fig. 7.14a, b. Outgoing photoelectron waves (nodes denoted by solid lines) from the central atom A propagate to neighbouring atoms B. The backscattered waves (nodes denoted by dashed lines) interfere **a** destructively, or **b** constructively, with the outgoing wave at the central atom depending on the energy of the photoelectron for a given r_j

The variation in ψ_f leads to oscillations in (7.66). The ψ_f variation has a simple physical meaning (Fig. 7.14). When an X-ray photon is absorbed, the photoelectron is ejected. It is represented by an outgoing spherical wave (Fig. 7.14). For an isolated atom it gives just a smooth absorption. The EXAFS oscillations occur when the backscattered waves from the surrounding atoms interface with the outgoing wave, This interference can either decrease or increase the photoelectron wave function in the region of the initial state (that is, near the origin). A decrease occurs if the interference is destructive (Fig. 7.14a) and an increase if constructive (Fig. 14b). The phase between the outgoing and incoming parts can be varied by changing the X-ray energy $\hbar\omega$ and thereby the photoelectron de Broglie wavelength. The change in the photoelectron wave function modifies the overlap with the core state (here $1s$ state) in the dipole matrix element and so the absorption.

In (7.67), the phase shift $\delta_j(k)$ is due to backscattering from the jth neighbouring atom. The term $2\delta_1^A(k)$ gives twice the central atom phase shift due to the presence of the potential of the absorbing atom. The $l = 1$ photoelectron wave (excited from the $l = 0$, $1s$ state) has to pass through this potential on going out and again on coming in after backscattering. The value of δ_1^A is different from δ_j as the central atom A is a photoexcited atom. The wave function at the origin is modulated according to total phase factor $\phi_j(k)$. This accounts for the sinusoidal term in (7.66).

For the $L_{II,III}$ edge EXAFS the $\chi(k)$ formula is complicated. However, the $p \to d$ transition is stronger than the $p \to s$ one by a factor of 50, so the $L_{II,III}$ EXAFS can be analyzed using a simple formula like (7.66), with $\delta_1^A(k)$ replaced by $\delta_2^A(k)$ and the overall minus sign removed [7.8, 151].

7.6.3 EXAFS Experiment and Form

In the 1930s X-ray absorption spectra were recorded in transmission through a thin absorber using a low-power X-ray tube as a source, a Bragg spectrometer as a wavelength analyzer and a film as a detector. Little work was done in the 1940s and 1950s. The work picked up in the 1960s. Use of synchrotron radiation as a powerful source of continuous X-rays brought rapid changes and improvements in measurement techniques (Fig. 7.15).

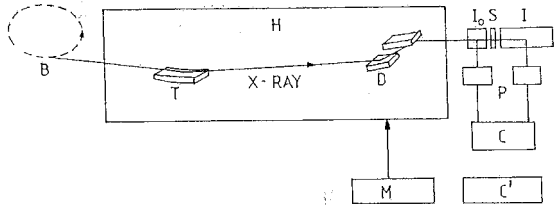

Fig. 7.15. Modern arrangement for measuring EXAFS using synchrotron radiation. *B*: storage ring e^- beam; *H*: helium atmosphere; *T*: Toroidal mirrors; *D*: double crystal monochromator; I_0, *I*: ionization chambers for measuring incident and transmitted intensities: *S*: sample; *P*: *I* to *V* preamp; *C*: two channel counter; *C'*: computer; *M*: stepping motor for changing the angle of *D* to vary beam energy on *S*

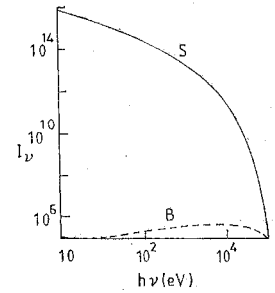

Fig. 7.16. The intensity I_ν (photons/s eV mrad) of bremsstrahlung (*B*) from a rotating anode X-ray tube and (*S*) synchrotron storage ring at Stanford

The EXAFS studies employ two sources for continuous X-ray: (1) the bremsstrahlung output from a laboratory X-ray tube (preferably with a rotating anode for high intensity), and (2) the (highly polarized) synchrotron radiation from electron storage rings or synchrotrons. These sources are compared in Fig. 7.16 for intensity. In spite of the greater brightness of synchrotron radiation, for concentrated samples the bremsstrahlung from an X-ray tube (flux $\sim 10^6$ to 10^8 photons/s in a 10 eV bandwidth) is a satisfactory source [7.8, 151] for EXAFS work when a curved crystal (focusing type) spectrograph is used as the analyzer.

The resolution needed for EXAFS is not very great. For $r < 5$ Å, the energy separation ΔE between adjacent maxima, roughly given by

$$2r\Delta k = \pi, \quad \Delta E[\text{eV}] \sim 7k\Delta k, \tag{7.68}$$

is 5 eV at $k = 2\text{Å}^{-1}$ and 25 eV at $k = 10\,\text{Å}^{-1}$. In a typical case ($r \sim 3$ Å), data with $k > 3\,\text{Å}^{-1}$ are analyzed, and $\Delta E \sim 15$ eV. The distortions in the data are avoided if the resolution is not poorer than ~ 5 eV. For curved crystals, the intensity and resolution criteria are discussed by *Berreman* [7.155].

As EXAFS is an interference effect, the phase of the oscillations depends on the distance r_j from the absorbing atom to the neighbouring atom *j* involved in

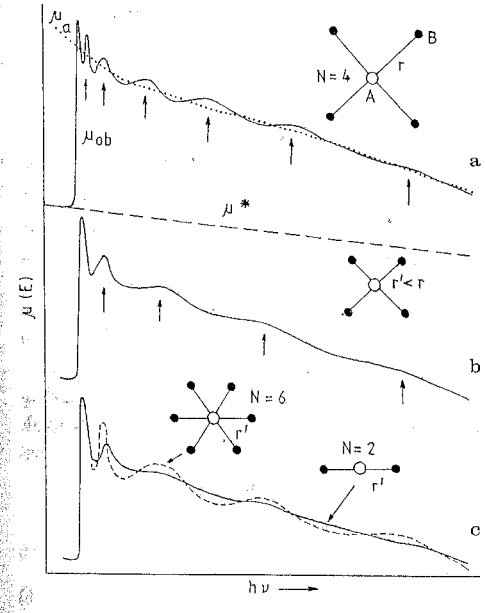

Fig. 7.17. Comparison of EXAFS for substances differing in r_j and N_j: **a** typical EXAFS showing μ_{ob}, μ_a and μ^* (see text); **b** typical EXAFS for the same number of nearest neighbours but smaller shell radius compared to case **a**; **c** effect of changing the number of nearest neighbours

the backscattering. Besides other factors, the amplitude of the EXAFS oscillations depends on the number of nearest neighbours N_j at a given distance r_j. In fact, mere comparison of two EXAFS spectra can reveal useful information (Fig. 7.17). The shorter bonds give larger spaced oscillations and the EXAFS amplitude increases with the number of neighbour atoms, in agreement with (7.66).

7.6.4 Data Analysis: Fourier Transform

Quantitative analysis requires the EXAFS signal per absorbing atom for a given core excitation. It means all background due to other absorption processes should be removed. Also, the EXAFS function should be normalized on a per-atom basis.

The observed pre-absorption background is extrapolated (from ~ 1000 eV below threshold) to energies above the edge using a suitable polynomial μ^* (Fig. 7.17a). The Victoreen formula [7.156] $ae^{-3} + bE^{-4}$ can be used for this. There is no analytic expression for the smooth, atom-like absorption μ_a about which the observed μ_{ob} oscillates. The investigator must judge the points that

represent μ_a (Fig. 7.17b). Then the EXAFS $\chi(E)$ is defined by [7.157]

$$\chi(E) = \frac{\mu_{ob} - \mu_a}{\mu_a - \mu^*} = \frac{\mu - \mu_0}{\mu_0}, \tag{7.69}$$

where $\mu = \mu_{ob} - \mu^*$ represents the K-shell absorption for the material alone, and $\mu_0 = \mu_a - \mu^*$. It is now converted to $\chi(k)$ by using (7.64). This normalization method divides out the λ^3 variation and subtracts the absorption due to other materials (and electrons in the same atom). It is essential for the quantitative analysis of structural parameters. If only interatomic distances are of interest, the Fourier transform of any straightened out EXAFS function is sufficient.

The Fourier transform of the data itself is obviously independent of any theory. The μ is proportional to the cross-section σ. It may appear from (7.69) that the Fourier transform of σ is involved, rather than the amplitude $f(\theta)$ as it should be. In the scattering theory the Fourier transform of the scattering amplitude gives information on the distance between scattering centres. A look at (7.58) shows that the oscillating part x depends only on the interference (cross) term (7.47), which has only the backscattering amplitude $f(\theta)$.

The Fourier transform is defined by

$$f(r) = \int F(k) e^{-2ikr}\, dk, \tag{7.70}$$

$$F(k) = \int f(r) e^{2ikr}\, dr. \tag{7.71}$$

$F(k)$ is the Fourier transform of $f(r)$. The quantities k and r have a mutually reciprocal nature. Consider the case where $f(r)$ is a Dirac δ-function located at a point other than the origin, say, $f(r) = \delta(r - r_1)$. This represents a δ-function at $r = r_1$. Its Fourier transform is

$$F(k) = \int_{-\infty}^{\infty} \delta(r - r_1) e^{2ikr}\, dr = e^{2ikr_1}. \tag{7.72}$$

They are plotted in Fig. 7.18. If (7.72) is put in (7.70), the result is the δ-function. The $\chi(k)$ in (7.62) or the first term in the sum (7.63) is the oscillatory-like $F(k)$ in (7.72). So when this $\chi(k)$ for $j = 1$ is Fourier transformed, the result would be a (sharp) peak at $r = r_1 - a_1$, where the shift a_1 arises because of the k-dependent phase shifts not included in the Fourier transform. Similar considerations apply to the other terms in the sum (7.66).

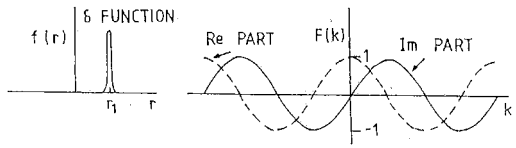

Fig. 7.18. The Dirac δ-function $\delta(r - r_1)$ and its Fourier transform $F(k) = \exp(2ikr_1)$

Sayers et al. [7.142] followed this line of argument, well known in X-ray scattering work. They boldly demonstrated that, in a theory-independent way, the Fourier transform of the observed EXAFS data with respect to the photoelectron wave vector k gives peaks at distances corresponding to the positions r_j of near neighbours.

The normalized $\chi(k)$ is Fourier transformed [7.142–145] over the measured finite k range k_{min} to k_{max}

$$R_n(r) = \frac{1}{(2\pi)^{1/2}} \int_{k_{min}}^{k_{max}} k^n \chi(k) e^{-2ikr}\, dk, \tag{7.73}$$

where k^n is a weight factor with the usual choice $n = 1$, 2 or 3. All EXAFS data show a decreasing amplitude with increasing k-values, either due to the scattering power of the neighbouring atoms, or due to disorder effects. The EXAFS function contains valuable information at high k values, so k^n is used to compensate for the damping. A k^3 factor roughly equalizes the EXAFS signal by neutralizing the $1/k$ term in the EXAFS equation (7.66) and the $1/k^2$ dependence of the backscattering amplitude factor at large k-values. The finite range of the transform introduces terminal ripples. If desired, they can be minimized by using simple window functions [7.158]. The lower limit is restricted to $k_{min} > 3$ Å because the region $0 < k < 3$ Å is the XANES region, where multiple scattering effects dominate.

The Fourier transform (7.73) is comlex, so a real part $R_n^r(r)$ and an imaginary part $R_n^i(r)$ are produced. The magnitude of the radial distribution function $|R_n(r)|$, $|R_n|^2 = (R_n^r)^2 + (R_n^i)^2$, gives a simple physical picture of the local structure. Peaks appear at $r = r_j - a_j$.

The transform (7.73) implies

$$R_n(r) \propto \frac{1}{(2\pi)^{1/2}} \int_{k_{min}}^{k_{max}} \frac{k^n}{kr_j^2} \sin[2kr_j + \phi_j(k)] e^{-2ikr}\, dk.$$

If $\phi(k)$ is linear in k, and effectively k_{min} and k_{max} are taken to be 0 and ∞, respectively, then the transform is reduced to δ-functions at $r = r_j - a_j$.

The shift in the peak by a_j can be understood as follows. It is the total phase shift function $\phi_j(k)$ which is measured in EXAFS. It can be approximated by a linear function of k [7.144],

$$\phi_j(k) \simeq \alpha_j - \beta_j k. \tag{7.74}$$

The total argument of the sine function becomes

$$\delta^t \equiv 2kr_j + \phi_j(k) \simeq 2k(r_j - \tfrac{1}{2}\beta_j) + \alpha_j, \tag{7.75}$$

so the Fourier transformation yields $|R_n(r)|$, which peaks at $r = r_j - (\alpha_j/2) = r_j - a_j$, $\alpha_j > 0$.

An example of $\chi(k)$ versus k and its Fourier transform is given in Fig. 7.19 for the L_{III} EXAFS of holmium [7.8] taking $E_0 = 0$.

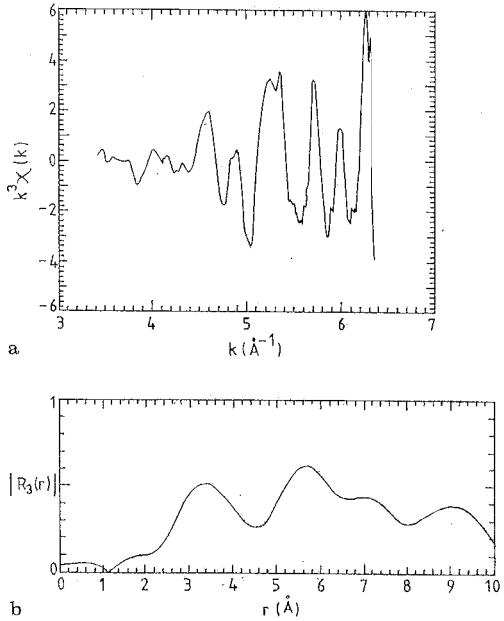

Fig. 7.19. **a** $k^3\chi(k)$ for holmium as a function of k with $E_o = 0$; **b** $|R_3(r)|$ [7.8]

7.6.5 Graphical Method for Bond Length

The EXAFS formula (7.66) is of the form

$$\chi(k)=\sum_j B_j(k)\sin[2kr_j+\phi_j(k)],$$

$$B_j(k)=(N_j/kr_j^2)F_j(k)\,e^{-2\sigma_j^2k^2},$$

$$F_j(k)=|f_j(k,\pi)|\,e^{-2r_j/\lambda}, \tag{7.76}$$

where $B_j(k)$ is the total scattering amplitude of the jth shell of a number N_j of atoms and the amplitude factor $F_j(k)$ accounts for the elastic electron backscattering amplitude $f(k,\pi)$ and inelastic effects due to λ.

Use (7.74) to define an n_j by [7.144]

$$2k(r_j-\tfrac{1}{2}\beta_j)+\alpha_j=(n_j+\tfrac{1}{2})\pi, \tag{7.77}$$

where $n_j=0,2,4,\ldots$ corresponds to $|\chi(k)|$ maxima and $n_j=1,3,5,\ldots$ to minima. Neglecting $E_0 k=(0.263E)^{1/2}$, where E is the energy of the peak in the EXAFS, a straight line plot of $n_{j=1}$ against $k\,[\text{Å}^{-1}]$ for the observed maxima and minima determines $r_1-\beta_1/2=r_1-a_1$ from the slope. Treating $\phi(k)$ as a parameter is convenient because phase shift calculations will require the exact knowledge of atomic potentials.

Once a_1 [and so δ^t in (7.75)] is evaluated for a standard (known r_1), the r_1 for the unknown compounds can be determined [7.144], using

$$r_b=r_a+(\delta_b^t-\delta_a^t)/2(k^2-0.263\Delta)^{1/2},$$

where Δ is a small change in the inner potential due to bonding. Plot r_b for various values of Δ (usually $-10\,\text{eV}<\Delta<10\,\text{eV}$). For the proper Δ, r_b becomes constant for all k. This gives r_b and Δ in a self-consistent way.

Agarwal and *Balakrishnan* [7.89] measured EXAFS in several rare-earth metals and compounds. They found two distinct lines, of different slopes, corresponding to $j=1$ and 2 in (7.77). For the structures in Tb, Dy and Ho, atoms occur at the first nearest neighbour distance of ~ 3.6 Å and the second nearest neighbour distance of ~ 5.6 Å. Each of these two sets of atoms produces its own main set of oscillations. The nearer set gives low-frequency (larger-spaced) oscillations that fall on the straight line with the smaller slops (Fig. 7.20).

Recently *Halaka* et al. [7.159] and *Mahto* and *Chetal* [7.160] have suggested

$$\phi_j(k)=(n_j+\tfrac{1}{2})''=2kr_j+c_{j0}+c_{j1}\,e^{-c_{j2}k}. \tag{7.78}$$

For copper $c_{10}=-12.5$, $c_{11}=3.0$ and $c_{12}=0.25$ with $r_1=2.56$ Å, and $\phi_1(k)$ value (in radians) changes from -11.325 for $k=3.75\,\text{Å}^{-1}$ to -11.98 for $k=7\,\text{Å}^{-1}$.

One can isolate the first peak in the radial distribution function (from $r_1-\Delta r$ to $r_1+\Delta r$) and back-transform it to k space. The resulting simple expression is

$$k^n\chi_1(k)=(2\pi)^{1/2}\int_{r_1-\Delta r}^{r_1+\Delta r}R_n(r)\,e^{2ikr}\,dr$$

$$=k^nB_1(k)\sin[2kr_1+2\phi_1(k)],$$

$$B_1(k)=(N_1/kr_1^2)\,F_1(k)\,e^{-2k^2\sigma_1^2}. \tag{7.79}$$

A curve-fitting to the data curve by varying the initial estimates of each quantity involved in this $\chi_1(k)$ can yield N_1, r_1, σ_1 and the type of near neighbours [through the atomic uniqueness of $F(k)$ and $\phi(k)$].

The Debye–Waller factor $\sigma^2(T)$ is given by $\sigma^2(T)=2\sigma_\infty^2(1-\gamma)$. The displacement correlation function γ ensures that only the out-of-phase thermal motion of atoms contributes to $B_1(k)$. The mean square displacement in the Debye

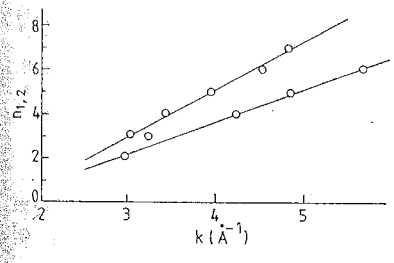

Fig. 7.20. Plot of (7.77) for the L_{III} EXAFS of dysprosium [7.89]

model for a monatomic cubic crystal is given by

$$\sigma_\infty^2=\frac{3\hbar^2}{k_B M\Theta_D}\left(\frac{\Phi_D(\Theta_D/T)}{\Theta_D/T}+\frac{1}{4}\right)$$

where k_B is the Boltzmann constant, M atomic mass, θ_D Debye temperature, $\Phi_D(\chi)$ Debye function an T absolute temperature.

Measurements at two different temperatures will give information on σ when $[B_1(T)/B_1(T')]$ is plotted against k^2. The back-transformed peak area gives B_1. The slope of the straight-line plot gives $\sigma_1^2(T)-\sigma_1^2(T')$. Comparison can be made with the harmonic oscillator model or the Einstein model of solids [7.145]. *Tranquada* and *Ingalls* [7.161] have recently determined the anharmonicity in CuBr by measuring $\chi(k)$ at 72, 210 and 295 K.

Information on the number of atoms N_j is contained in the amplitude term in (7.76, 79). We have seen that a_1(or $\beta_1/2$) can be obtained for a standard system and transferred to related unknown systems to predict r_1. This concept of *phase shift transferability* relies on the fact that the core electron potential remains the same and dominates the scattering process. For closely related systems, having the same backscattering neighbours and mean free path, (7.79) gives

$$\frac{B_a(k)}{B_b(k)}=\frac{N_a}{N_b}\left(\frac{r_b}{r_a}\right)^2 e^{-2\sigma_a^2k^2+2\sigma_b^2k^2}$$

$$\ln(B_a/B_b)=\ln[(N_a/N_b)(r_b/r_a)^2]+2(\sigma_b^2-\sigma_a^2)k^2. \tag{7.80}$$

A plot of $\ln(B_a/B_b)$ against k^2 gives a straight line. The intercept at $k=0$ gives the log of the ratio of N/r^2 for the two materials. The slope gives the difference in the Gaussian broadenings.

7.6.6 Curve Fitting Method

The curve fitting method [7.162, 163] avoids taking the Fourier transform and directly attempts to best fit the $k^n\chi(k)$ data in k space, using a phenomenological relation based on [7.70]. It requires a functional form as well as the starting values for the parameters of each fitted term. Again the phase shift and amplitude functions are found empirically by comparison to a standard model. *Shulman* et al. [7.162] use

$$\chi(k)=\left(\frac{\sum_{n=0}^{4}a_nk^n}{1+\sum_{n=0}^{2}b_n(k-c)^{n+2}}\right)\sum_j\sin\left(2kr_j+\sum_{n=0}^{2}\alpha_n\right) \tag{7.81}$$

to fit the data.

7.6.7 E_0 Problem

The phase shifts are unique only if the energy threshold E_0 is exactly known on the main edge. Unfortunately this is not possible due to XAMES. A change of

$\Delta E_0=E_0'-E_0$ in E_0 changes k and $\phi(k)$ to

$$k'=[k^2-0.263(\Delta E_0)]^{1/2}, \tag{7.82}$$

$$\phi'(k')=\phi(k)-2(k'-k)r$$

$$=\phi(k)-0.263r(\Delta E_0)/k, \tag{7.83}$$

where $0.263(\Delta E_0)\ll k^2$. Clearly $\phi'(k')-\phi(k)$ is not linear in k and decreases with increasing k. Only the $2kr$ term remains linear in the entire phase. The phase shifts are more sensitive to a shift in E_0 at small k than at large k. However, a change in r will effect $\phi(k)$ mainly at high k values by $2k(\Delta r)$. In fact, by adjusting E_0 one cannot produce an artificially good fit with the wrong distance r.

Work of *Lee* and *Beni* [7.149], *Stearns* [7.164] and *Agarwal* [7.8] shows that the E_0 problem needs to be emphasized, and has no simple solution.

7.6.8 Applications of EXAFS

a) *Amorphous materials.* The lack of extensive regular structure in amorphous substances limits the structural information from diffraction studies. For amorphous alloy systems (or glasses) with dilute impurities, this problem becomes severe.

EXAFS has the advantage of probing the near-neighbour environment of each component species separately by tuning the X-ray energy to the absorption edge of each of them. It then provides information on interatomic distance, coordination number and degree of disorder for the major as well as the minor atomic components [7.165, 166].

b) *Surface structure. Surface* EXAFS (SEXAFS) has been used to study the ordered layers on substrates. One exploits its atomic specificity and bond orientation sensitivity based on the polarization dependence of the photo-absorption cross-section [7.167]. *Roubin* et al. [7.168] have found strong anisotropy of the surface Debye–Waller factor in SEXAFS. They have studied temperature-dependent $\chi(k)$ for two different polarizations. The SEXAFS can also determine site geometry in a disordered system without depending on polarization [7.169].

c) *High pressure* EXAFS. EXAFS studies have many applications in mineralogy and geochemistry. The effect of high pressure is to change all the properties of a substance. An important change is a pressure-induced phase change. For example, at atmospheric pressure RbCl has the structure of NaBr. At 5.2 kbar it transforms to the cesium chloride structure and N changes from 6 to 8. The EXAFS derived bond compression can be used to determine the pressure [7.170, 171]. The $\chi(k)$ for a given shell is written in terms of the cumulants[3] $\sigma^{(n)}$ that

[3] $\langle e^{2ikr}\rangle=\exp\left\{\sum_{n=1}^{\infty}[(2ik)^n/n!]\,\sigma_n\right\}$, where σ_n are the cumulants in a statistical analysis.

characterize the various distribution functions,

$$\chi(k) = (N/kr^2)\,F(k)\,e^{-2r/\lambda}e^{A}\sin\Phi,$$

$$A = -2\sigma^2k^2 + \tfrac{2}{3}\sigma^{(4)}k^4 + \cdots,$$

$$\Phi = 2kr + \phi(k) - (4\sigma^2k/r)[(1+(r/\lambda))] - \tfrac{4}{3}\sigma^{(3)}k^3 + \cdots. \tag{7.84}$$

The parameters N, r and σ^2 change significantly when pressure is applied. As before, the term

$$\ln|\,N_a r_a^2/N_b r_b^2\,| - (2\Delta r/\lambda) - 2\Delta\sigma^2k^2 + \tfrac{2}{3}\Delta\sigma^{(4)}k^4 + \cdots \tag{7.85}$$

is given by $\ln|\,\chi_a/\chi_b\,|$. Also, the phase difference between the two runs gives

$$2k\{\Delta\bar{r} - (\Delta\sigma^2/r)[1+(\bar{r}/\lambda)] - \tfrac{4}{3}\Delta\sigma^{(3)}k^3 + \cdots\}. \tag{7.86}$$

The essential point is that there is slight coupling between fits to Δr and $\Delta\sigma^2$, versus pressure.

d) *Time-resolved* EXAFS. EXAFS has a high event rate. Using a beam of 10^{12} photons $s^{-1}\,eV^{-1}$ one can measure microsecond (or submicrosecond) resolved EXAFS spectra [7.172]. It can be used to study the kinetics of a biochemical process. One measures, at a given X-ray energy, a time sequence of EXAFS points following sample exposure. The process is repeated at different energies as desired. *Chance* et al. [7.173] have studied the 4K metastable state Mb* Co using about 10^5 signal photons per data point.

e) EXAFS *of high-T_c superconductors.* Recently, superconductivity has been discovered in layered perovskite structures with unprecedented high transition temperatures (T_c) [7.174]. The structure and local chemical environment is found to play an important role. In the new materials, e.g. $La_{1.8}Ba_{0.2}CuO_{4-x}$ and $YBa_2Cu_3O_{7-x}$, the Cu–O distance along the c-axis is the key factor. The EXAFS of these susbstances has been used to explore these features [7.175]. The X-ray absorption measurements are made near the K edges of Cu and Sr, and L edges of Ba and La, as a function of temperature (4–300 K).

The crystal structure is the tetragonal K_2NiF_4 structure. It consists of two-dimensional layers of copper-oxygen octahedra elongated along the c-axis separated by layers of La which share oxygen in a rock-salt-like structure. The EXAFS studies show that the planar Cu–O(1) bonds are strong, while the Cu–O(2) bonds along the c-axis are somewhat weaker. The doping of pure La_2CuO_4 with divalent Ba (or Sr) substitutes for the trivalent La. The Ba also dopes the Cu–O conduction band. The doping affects primarily the locations and distributions of the O(2) atoms. These findings are significant for an understanding of the phenomenon.

Detailed review articles are now available [7.176] on the principles and applications of EXAFS.

7.7 Isochromats

A spectrometer is set to reflect a certain definite wavelength λ_0 into the detector and the voltage is varied from a value below the threshold V_0 necessary to produce λ_0, $eV_0 = hv_0 = hc/\lambda_0$, to a value above V_0. For the voltage V_0, the wavelength λ_0 is the Duane–Hunt limit of bremsstrahlung. The curve of intensity as a function of the voltage in such an experiment is called an *isochromat*, because it represents the intensity variation at a *single* wavelength λ_0. The intensity suddenly rises at $V = V_0$. For $V > V_0$, *Du Mond* and *Bollman* [7.177] observed distinct structures within about 15 volts above the threshold V_0.

The spectrometer can also be set to record (say) the $K\alpha_1$ line of the target element. As the voltage on the X-ray tube is slowly raised from just below to just above the excitation voltage V_K for the $K\alpha_1$ line, the observed intensity of the $K\alpha_1$ line begins to rise and then shows fine structure, as shown in Fig. 7.21 [7.178, 179]. *Johansson* [7.180] found a similar fine structure near the Duane–Hunt limit of the continuous spectrum. *Spijkerman* and *Bearden* [7.181] used this method to determine the value of h/e as $(1.37949 \pm 30\text{ ppm}) \times 10^{-17}$ erg s/esu.

Nijboer [7.182], *Ulmer* [7.183] and *Böhm* and *Ulmer* [7.184] explained the fine structure near the initial rise in the isochromat by considering solid-state effects, such as the allowed and forbidden energy bands for electrons moving in solids, and the density of states. This is similar to the theory of EXAFS in X-ray absorption.

Bergwoll and *Tyagi* [7.185] studied the isochromats of several transition metals. They attributed the first maximum in the initial rise ("foot" structure) to transitions to the empty d states and suggested that the subsequent structures are the "echoes" of the first two maxima, a phenomenon that is consistent with plasmon theory. Other studies on transition metals also exist [7.186–188] *Speier* et al. [7.189] have studied the bremsstrahlung isochromat spectra in the XANES and EXAFS region (up to 400 eV above the Fermi level). The observed extended fine structure does not depend on the phase shift of the absorbing

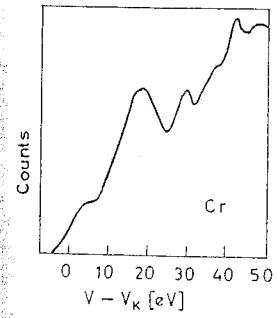

Fig. 7.21. A typical isochromat [7.178]

atom, as no core level excitation is involved. It is essentially a total density of states effect.

Experimental methods like de Haas–van Alphen effect, cyclotron resonance, magnetic-acoustic effect, and electronic specific heat give information only about the Fermi surfaces and electronic states in their vicinity. On the other hand, X-ray emission and absorption spectra can explore the entire band structure. We know that for inner-level widths $\Delta E_K > \Delta E_L > \Delta E_M$, etc. Also, energy measurements are more accurate in the long wavelength region, (6.32). These two considerations suggest that favourable conditions for the study of valence and conduction bands occur when shells near the valence band participate in the transitions. This takes us to *soft* X-ray emission and absorption spectroscopy.

8. Soft X-Ray Spectroscopy

Soft X-ray spectroscopy has developed into a major area of research for the study of solids [8.1–6]. We shall give here only a brief account of this topic.

Air shows high absorption in the wavelength region 2–2000 Å. It becomes necessary to evacuate the spectrograph for study of such radiation. Therefore, it is called the *vacuum ultraviolet region. Schumann* [8.7] built the first vacuum spectrograph, with a fluorite prism as analyzer. The region from 1000 Å to 2000 Å is known as the *Schumann region.* The extreme ultraviolet region extends from 2 Å to 1000 Å, and the part from 20 Å to 500 Å is usually called the *soft X-ray region.*

The levels of a valence electron in a solid form a continuum (valence band) that can be specified by a density function $N(E)dE$. The main aim of the soft X-ray spectroscopy (SXS) is to investigate this function experimentally.

The presence of the valence and conduction bands in solids drives us into the region of SXS to enable us to obtain the required information. The reason is that it would be impossible to try to disentangle the structure of the $N(E)$ curve from the radiation emitted or absorbed in the transitions between pairs of levels both of which are members of the continuum. On the other hand, if one of the participating levels is a discrete level, the structure of the continuum is rather directly reflected in the emitted (or absorbed) radiation. The discrete (sharp) levels correspond to electrons bound more or less completely to individual atoms. The actual width of the discrete level used sets a limit to the resolution with which the continuum structure of allowed symmetry can be probed ($\Delta E_K > \Delta E_L > \Delta E_M$ etc. for core levels).

The resolution of the spectrometer, $E/|dE| = [n\lambda/(4d^2 - n^2\lambda^2)^{1/2}](1/d\theta)$, increases with λ; (6.32) $dE \propto 1/\lambda$. For ^{8}O K emssion ($\sim$525 eV, $\sim$24 Å), dE/E is 2/525 or 0.4% because two maxima only 2 eV apart are easily separated by the spectrometer. The longer wavelength L emission spectrum from ^{16}S would give far more detail than the ^{16}S K spectrum. Thus, for both theoretical and technical reasons, this resolution is maximum for the soft X-ray region ($\sim$20 to $\sim$500 Å). In this region, the inner X-ray levels are often sharp to within 0.1 eV; this is enough for resolution of all the main features in the $N(E)$ curve. We are, therefore, led to SXS for the study of bands in solids. As Z increases, the soft X-ray wavelength region shifts from K spectra to L, M, N . . . spectra (Fig. 8.1).

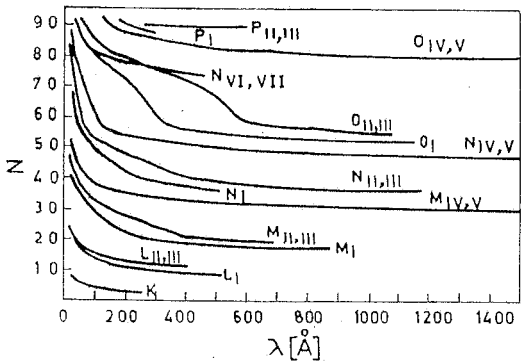

Fig. 8.1. Variation of the binding energy of atomic levels with Z

8.1 Conventional Sources

For *emission* work, a glass soft X-ray tube is preferred because it can be outgassed more thoroughly. Cleanliness of target, filament and other accessories is necessary. A general diagram of the X-ray tube used by *Skinner* is shown in Fig. 8.2. It was run at 3500 V and 250 mA. This voltage is more than enough to excite the soft X-ray wavelengths. For long exposures (many hours), the purity of the target material was ensured by use of a rotatable target; fresh layers of the material under study were periodically deposited on it. High vacuum was

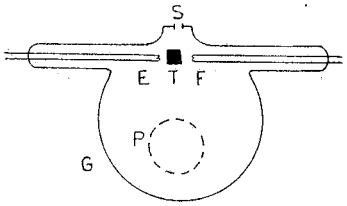

Fig. 8.2. Soft X-ray tube. *G*: glass bulb, *P*: pump tube, *E*: evaporating filament, *T*: rotatable target, *f*: X-ray filament, *S*: spectrograph slit

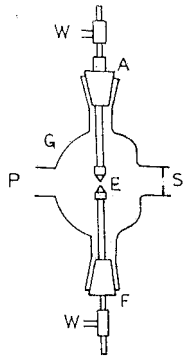

Fig. 8.3. Vacuum spark source. *A*: adjustable holder, *E*: electrodes, *S*: slit to spectrometer, *G*: glass bulb, *F*: fixed holder, *P*: pipe to pump, *W*: water end for cooling

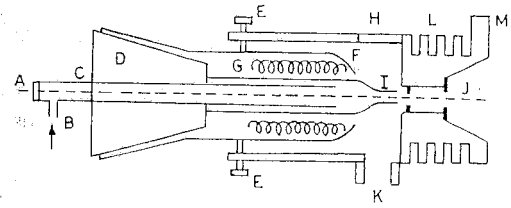

Fig. 8.4. Lyman discharge tube. *A*: glass window, *B*: gas inlet, *C*: brass cathode, *D*: pyrex taper joint, *E*: centering screws, *F*: glass tube, *G*: glass wool, *H*: glass window, *I*: quartz capillary, *J*: brass baffle plates, *K*: to pump, *L*: cooling fins, *M*: Al anode, below *E*: glass to metal seal

maintained and a slit was used in the place of a window, because soft X-rays are highly absorbable.

For *absorption* work, the continuous radiation emitted by the Skinner tube at $V<5$ kV is very weak and easily absorbed, even by the substrate of the absorbing material. Therefore, it becomes necessary to use line spectra emitted by highly ionized atoms. Such spectra are easily produced in condensed-spark discharges between metallic electrodes of Ag, Al, Cu, Fe and Mo (Fig. 8.3). They give fairly dense line spectra in the region of interest. Another useful source is a Lyman discharge tube (Fig. 8.4). In this source, a condensed spark is sent through a quartz capillary in which helium or argon is maintained at a pressure of about 1 mm Hg. The capillary is directed toward the slit of the spectrograph.

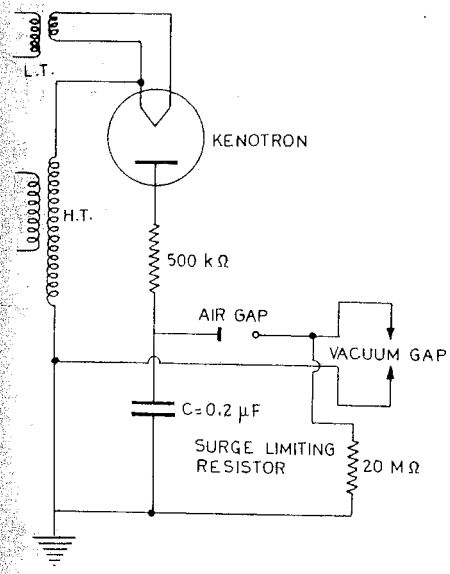

Fig. 8.5. Circuit diagram for condensed-spark source

It gives very strong lines in the soft X-ray region, for absorption work. The source also acts as a filter. If the gas pressure is ~ 1 mm Hg, it will absorb radiation of wavelengths shorter than its absorption edge (He: 505 Å, Ar: 786 Å). This reduces the problem of overlapping orders and simplifies the analysis at longer wavelengths. If the gas pressure is 0.2 mm Hg, the shorter wavelengths are not strongly absorbed.

The periodic spark is obtained by discharging a 0.2 μF condenser that is charged to about 30 kV by transformers and rectifiers (Fig. 8.5). Other laboratory line sources are also known. For example, radiofrequency oscillators can excite electrodeless ring discharges [8.8] and linear discharges [8.9] to produce soft X-rays. Use of a microwave source and cavity is also possible for this purpose [8.10–12].

8.2 The Synchrotron as a Source

Tomboulian and *Hartman* [8.13] showed that the magnetic bremsstrahlung (orbital radiation from a synchrotron) can be used as strong continuous radiation for soft X-ray absorption spectroscopy. In recent years, much literature has appeared on the extreme-ultraviolet spectroscopy of gases and solids by use of synchrotron radiation [8.6, 14–17].

Qualitative radiation patterns from electrons in a circular orbit are shown in Fig. 8.6. An electron moving through a perpendicular magnetic field has an acceleration toward the orbit centre. In a frame of reference moving with the electron, a Larmor radiation pattern is emitted (Sect. 1.9). This pattern resembles a torus centred on the electron with the plane of maximum intensity tangent to the electron orbit (Fig. 8.6a). For highly relativistic electrons, as viewed in the laboratory frame, the radiation is confined to a narrow cone tangent to the orbit (Fig. 8.6b). The radiation is highly polarized with the electric vector E in the plane of the orbit [8.18].

The frequency of the radiation changes along with the pattern. At $v \ll c$ it is equal to the rotation frequeny; at $v \sim c$ the radiant energy is distributed among many higher harmonics of the rotation frequency and the spectrum is essentially

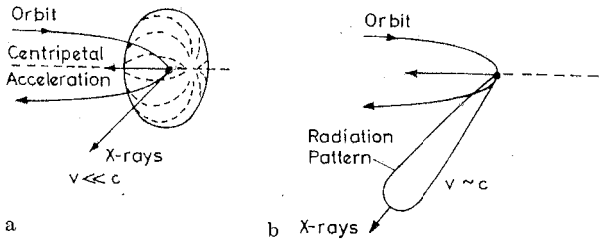

Fig. 8.6a, b. Radiation pattern from electrons in a circular orbit **a** at low energy, and **b** at high energy

a continuum. Several synchrotrons are in use for SXS. The German Electron Synchrotron (DESY) produces an intense continuous spectrum in the hard X-ray region (~ 1 Å), whereas Tantalus *I* (University of Wisconsin) radiates most copiously in the soft X-ray region (~ 100 Å),

8.2.1 Theory

Defining $c\boldsymbol{\beta}$ as the instantaneous velocity of the particle and $\kappa = 1 - \boldsymbol{n}\cdot\boldsymbol{\beta} = s/R$, see (1.44), $\boldsymbol{n} = \boldsymbol{R}/R$, we can write (1.53a) as [8.18]

$$\frac{1}{e}E(\boldsymbol{x},t) = \left(\frac{(\boldsymbol{n}-\boldsymbol{\beta})(1-\beta^2)}{\kappa^3 R^2}\right)_{\text{ret}} + \left(\frac{\boldsymbol{n}/c}{\kappa^3 R}\times[(\boldsymbol{n}-\boldsymbol{\beta})\times\dot{\boldsymbol{\beta}}]\right)_{\text{ret}}. \tag{8.1}$$

Larmor's formula (1.59) can be written as

$$P = \frac{2}{3}\frac{e^2}{m^2c^3}\left(\frac{d\boldsymbol{p}}{dt}\cdot\frac{d\boldsymbol{p}}{dt}\right), \tag{8.2}$$

where $\boldsymbol{p}$ is the momentum. The Lorentz invariant generalization is

$$P = \frac{2}{3}\frac{e^2}{m^2c^3}\left(\frac{dp_\mu}{d\tau}\frac{dp_\mu}{d\tau}\right), \tag{8.3}$$

where $d\tau = dt/\gamma$ is the proper time element and p_μ is the momentum-energy four-vector of the charged particle. The scalar product in (8.3) is

$$\frac{dp_\mu}{d\tau}\frac{dp_\mu}{d\tau} = \left(\frac{d\boldsymbol{p}}{d\tau}\right)^2 - \frac{1}{c^2}\left(\frac{dE}{d\tau}\right)^2 = \left(\frac{d\boldsymbol{p}}{d\tau}\right)^2 - \beta^2\left(\frac{dp}{d\tau}\right)^2. \tag{8.4}$$

Thus (8.3) reduces to (8.2) as $\beta \to 0$. Using $E = \gamma mc^2$ and $\boldsymbol{p} = \gamma m\boldsymbol{v}$, (8.3) gives the Liénard result in terms of $\boldsymbol{\beta}$ and $\dot{\boldsymbol{\beta}}$,

$$P = \frac{2}{3}\frac{e^2}{c}\gamma^6[(\dot{\boldsymbol{\beta}})^2 - (\boldsymbol{\beta}\times\dot{\boldsymbol{\beta}})^2]. \tag{8.5}$$

For $\boldsymbol{\beta}$ and $\dot{\boldsymbol{\beta}}$ parallel it gives (1.72),

The situation changes for circular accelerators like the synchrotron. Here $\dot{\boldsymbol{\beta}}$ is perpendicular to $\boldsymbol{\beta}$. The $\boldsymbol{p}$ changes rapidly in direction as the particle rotates, while the change in energy per revolution is small,

$$\left|\frac{d\boldsymbol{p}}{d\tau}\right| = \gamma\left|\frac{d\boldsymbol{p}}{dt}\right| = \gamma\omega|\boldsymbol{p}| \gg \frac{1}{c}\frac{dE}{d\tau}. \tag{8.6}$$

Then (8.3) is approximately

$$P = \frac{2}{3}\frac{e^2}{m^2c^3}\gamma^2\omega^2|\boldsymbol{p}|^2 = \frac{2}{3}\frac{e^2c}{\rho^2}(\beta\gamma)^4, \tag{8.7}$$

where $\omega = c\beta/\rho$ and ρ is the orbit radius. As $\gamma = E/mc^2$, this result due to Liénard

shows that, for $\beta \to 1$, $P \propto E^4$ and $P \propto 1/\rho^2$. The energy radiated per revolution is

$$\delta E = \frac{2\pi\rho}{c\beta} P = \frac{4\pi}{3}\frac{e^2}{\rho}\beta^3\left(\frac{E}{mc^2}\right)^4$$

$$\xrightarrow[\beta \simeq 1]{} 88.5\frac{(E[\mathrm{GeV}])^4}{\rho[\mathrm{meters}]}[\mathrm{keV}]. \tag{8.8}$$

In a low-energy synchrotron, $\rho \sim 1$ m, $E_{\max} \sim 0.3$ GeV, and so $\delta E_{\max} \sim 1$ keV per revolution. The power radiated is

$$P[\mathrm{watts}] = \frac{10^6}{2\pi}\frac{\delta E[\mathrm{MeV}]}{\rho[\mathrm{meters}]} J[\mathrm{amps}], \tag{8.9}$$

where J is the circulating beam current.

8.2.2 Angular Distribution

From (8.1), the radial component of Poynting's vector is found to be

$$(\boldsymbol{S}\cdot\boldsymbol{n})_{\mathrm{ret}} = \frac{e^2}{4\pi c}\left(\frac{1}{\kappa^6 R^2}|\boldsymbol{n}\times[(\boldsymbol{n}-\boldsymbol{\beta})\times\dot{\boldsymbol{\beta}}]|^2\right)_{\mathrm{ret}} \tag{8.10}$$

Here $\boldsymbol{S}\cdot\boldsymbol{n}$ is the energy per unit area per unit time, observed at the observation point at time t, due to radiation emitted by the charge at time $T = t - R(T)/c$. Thus the power radiated per unit solid angle in terms of the charge's own time is

$$\frac{dP(T)}{d\Omega} = R^2(\boldsymbol{S}\cdot\boldsymbol{n})\frac{dt}{dT} = \kappa R^2 \boldsymbol{S}\cdot\boldsymbol{n}$$

$$= \frac{e^2}{4\pi c}\frac{|\boldsymbol{n}\times[(\boldsymbol{n}-\boldsymbol{\beta})\times\dot{\boldsymbol{\beta}}]|^2}{(1-\boldsymbol{n}\cdot\boldsymbol{\beta})^5}. \tag{8.11}$$

If the acceleration is for a short time ($\boldsymbol{\beta}$, $\dot{\boldsymbol{\beta}}$, $\boldsymbol{n}$ and R change negligibly), then (8.11) is proportional to the angular distribution of the energy radiated.

If Θ is the angle of observation measured from the direction of $\boldsymbol{\beta}$, then for the linear motion ($\boldsymbol{\beta}$ and $\dot{\boldsymbol{\beta}}$ parallel),

$$\left(\frac{dP(T)}{d\Omega}\right)_{\mathrm{lin}} = \frac{e^2\dot{v}^2}{4\pi c^3}\frac{\sin^2\Theta}{(1-\beta\cos\Theta)^5}. \tag{8.12}$$

For a charge in instantaneously circular motion ($\boldsymbol{\beta}$ perpendicular to $\dot{\boldsymbol{\beta}}$),

$$\left(\frac{dP(T)}{d\Omega}\right)_{\mathrm{cir}} = \frac{e^2\dot{v}^2}{4\pi c^3}\frac{1}{(1-\beta\cos\Theta)^3}\left(1-\frac{\sin^2\Theta\cos^2\Phi}{\gamma^2(1-\beta\cos\Theta)^2}\right). \tag{8.13}$$

Here $\boldsymbol{\beta}$ is along the z-axis, $\dot{\boldsymbol{\beta}}$ is along the x-axis and the direction of observation $\boldsymbol{n}$ makes a polar angle Θ, Φ. The radiation is peaked in forward direction for $\beta \to 1$. There is a narrow cone (searchlight beam) along $\boldsymbol{\beta}$. Integrating (8.12, 13) over all

angles, the total power radiated is found to be

$$[P(T)]_{\mathrm{lin}} = \frac{2}{3}\frac{e^2}{c^3}\dot{v}^2\gamma^6, \tag{8.14}$$

$$[P(T)]_{\mathrm{cir}} = \frac{2}{3}\frac{e^2}{c^3}\dot{v}^2\gamma^4. \tag{8.15}$$

It is useful to compare them for the same magnitude of applied force. For circular motion, the rate of change of momentum (=applied force) is $\gamma m\dot{v}$, and

$$[P(T)]_{\mathrm{cir}} = \frac{2}{3}\frac{e^2}{m^2c^3}\gamma^2\left(\frac{d\boldsymbol{p}}{dt}\right)^2. \tag{8.16}$$

Comparison with (8.2) shows that for a given magnitude of applied force, $P_{\mathrm{cir}}/P_{\mathrm{lin}} = \gamma^2 \gg 1$. In a 200 MeV synchrotron, $\gamma_{\max} \sim 400$.

The radius ρ of the circular path is given by

$$\rho = v^2/\dot{v}_\perp \simeq c^2/\dot{v}_\perp, \tag{8.17}$$

where $\dot{v}_\perp$ is the perpendicular component of $\dot{v}$. The searchlight radiation will be visible to a fixed observer (detector) only for a short while when $\boldsymbol{\beta}$ is directed towards the observer during a revolution. The observer will receive one pulse per revolution. From (1.68), $\gamma\Theta_{\max} = 1/2$. Therefore the natural angular unit is γ^{-1}. The half-power points in a plot like Fig. 1.19 occur at $\gamma\Theta = 0.23$ and $\gamma\Theta = 0.91$. The angular half-width of the distribution at half maximum is given in all cases by

$$\delta = 1/\gamma = mc^2/E. \tag{8.18}$$

Thus the particle will emit radiation towards the observer only for a time interval $\Delta T \sim \rho/c\gamma$. The observer sees it for a time interval $\Delta t \sim \langle dt/dT\rangle \Delta T$, where $\langle dt/dT\rangle = \langle\kappa\rangle \sim \gamma^{-2}$. So, at the detector,

$$\Delta t \sim (\rho/c)\gamma^{-3}. \tag{8.19}$$

By the general arguments about Fourier integrals, a pulse of this duration will contain frequency components up to a critical frequency ω_c,

$$\omega_c \sim (1/\Delta t) \sim (c/\rho)\gamma^3 = \omega_0\gamma^3, \quad \gamma \gg 1, \tag{8.20}$$

where ω_0 is the angular frequency of rotation. Thus a relativistic circulating particle emits a broad spectrum of frequencies if $E \gg mc^2$, up to γ^3 times the fundamental frequency. A typical distribution is shown in Fig. 7.16. For a 200 MeV synchrotron, $\gamma_{\max} \sim 400$, $\omega_c \sim 6\times10^7\,\omega_0$, $\omega_0 \sim 3\times10^8\,\mathrm{s}^{-1}$, and so $\omega_c \sim 2\times10^6\,\mathrm{s}^{-1}$ (or $\lambda \sim 1000$ Å). The spectrum goes beyond the visible region, although ω_0 is in the 100 MHz range.

A detailed theory has been given by *Schwinger* [8.19]. Excellet accounts of the theory are found in [8.18, 20].

The radiation from most accelerators is spread over a region ranging from X-rays to the infrared. At present, synchrotrons are the only source of continuous radiation which can give useful itensity in the soft X-ray region.

The angular and spectral distribution of the energy radiated by a monoenergetic electron in circular motion is given by [8.18, 19]

$$\frac{dI(\omega)}{d\Omega}=\frac{e^2}{3\pi^2 c}\left(\frac{\omega\rho}{c}\right)\left(\frac{1}{\gamma^2}+\psi^2\right)^2\left(K_{2/3}^2(\xi)+\frac{\psi^2}{\gamma^{-2}+\psi^2}K_{1/3}^2(\xi)\right), \tag{8.21}$$

where ψ is the azimuthal angle of observation measured relative to the orbit plane, $\xi=(\omega\rho/3c)(\gamma^{-2}+\psi^2)^{3/2}$, and $K_{1/3,2/3}$ are modified Bessel functions of the second kind. The first term in the right-mask set of parentheses corresponds to radiation with electric vector parallel to the electron orbit, and the second to radiation with the electric vector perpendicular to the orbit plane. The second term goes to zero as $\psi\to 0$. For observation in the plane of the orbit, the radiation is completely plane polarized in the plane of motion. Integration over angles shows that radiation with parallel polarization has seven times as much energy as with perpendicular polarization.

The properties of the K_ν functions

$$K_\nu(x)\to\frac{\Gamma(\nu)}{2}\left(\frac{2}{x}\right)^\nu, \quad \text{for } x\ll 1,$$

$$K_\nu(x)\to\left(\frac{\pi}{2x}\right)^{1/2}\mathrm{e}^{-x}, \quad x\gg 1, \tag{8.22}$$

shows that the intensity is negligible for $\xi\gg 1$. For too large ω, ξ is large at all angles. The critical frequency ω_c, beyond which there is almost no radiation at any angle, is defined by $\xi=1$ for $\psi=0$, or

$$\omega_c=3\gamma^3 c/\rho=3(E/mc^2)^3 c/\rho \tag{8.23}$$

in agreement with the estimate (8.20). A critical harmonic frequency is usually defined as $\omega_c=n_c\omega_0$, $\omega_0=c/\rho$, with harmonic number

$$n_c=\omega_c/\omega_0=3(E/mc^2)^3. \tag{8.24}$$

The radiation is strong in the orbital plane for $\gamma\gg 1$. It is useful to estimate the angular distribution (8.21) at $\psi=0$:

$$\left.\frac{dI(\omega)}{d\omega}\right|_{\psi=0}\simeq\begin{cases}\dfrac{e^2}{c}\left(\dfrac{\Gamma(2/3)}{\pi}\right)^2\left(\dfrac{3}{4}\right)^{1/3}\left(\dfrac{\omega\rho}{c}\right)^{2/3}, & \text{for } \omega\ll\omega_c.\\[2ex] \dfrac{3}{2\pi}\dfrac{e^2}{c}\dfrac{\omega}{\omega_c}\gamma^2\mathrm{e}^{-2\omega/\omega_c}, & \text{for } \omega\gg\omega_c.\end{cases} \tag{8.25}$$

The spectrum initially increases as $\omega^{2/3}$, has a maximum near ω_c, and then drops exponentially to zero for $\omega\gg\omega_c$. These results have been compared with experiment [8.13].

8.3 Vacuum Spectrograph

From (3.44, 59), we can express the critical angle of reflection as

$$\sin\theta_c=\left(\frac{e^2 n}{\pi mc^2}\right)^{1/2}\lambda, \tag{8.26}$$

where θ_c is the grazing angle of incidence, and n is the number of electrons per unit volume of the medium. Thus, for a given λ, total reflection occurs at all grazing angles less than and up to θ_c, at which point the reflectance decreases rapidly. For a given grazing angle θ, all wavelengths longer than

$$\lambda_{\min}[\text{Å}]=(3.33\times 10^{14})n^{-1/2}\sin\theta, \tag{8.27}$$

are totally reflected. For a glass (or Al) grating $n^{1/2}=8.8\times 10^{11}$, and so $\lambda_{\min}[\text{Å}]=379\sin\theta$, or $\lambda_{\min}[\text{Å}]=6.6\,\theta^\circ$ for small θ. For $\theta=5^\circ$ this gives $\lambda_{\min}=39.6$ Å, as the order of magnitude to be expected in the experiment. For Pt, $n^{1/2}=22.7\times 10^{11}$ and $\lambda_{\min}[\text{Å}]=147\sin\theta$.

The decrease of reflectance with decreasing wavelength, of all grating materials (glass; Al, Au, Pt coatings) necessitates the use of grazing-incidence ($\theta\sim 5^\circ$) spectrographs for SXS (~ 300 Å). If a concave grating is used, it serves as a focusing as well as a dispersing element.

Figure 8.7 is a simplified diagram of the *concave-grating vacuum spectrograph*. The simple grating equation is

$$d(\sin\phi-\sin\phi_n')=n\lambda, \qquad (\phi=90^\circ-\theta), \tag{8.28}$$

where n is the spectral order, and $\phi(\phi_n')$ is the angle of incidence (diffraction). The zero order or the direct image is formed at $\phi=\phi_n'$. If ρ is the diameter of the Rowland circle, the angle $\phi-\phi_n'$ is simply related to the distance x along the plate from the zero order to the spectral line as

$$\phi_n'=\phi-x/\rho. \tag{8.29}$$

The radius of the grating is ρ. We can use (8.28) with (8.29) for the numerical calculation of λ from the measured values of x.

A convenient choice for the region ~ 300 Å is: $\rho=2$ m, $d=8.47\times 10^{-5}$ cm (the reciprocal of 30 000 lines per inch), $\phi=85^\circ$ (grazing angle $\theta=5^\circ$), $n=1$. The Al-coated grating becomes more transparent (less reflecting) as λ decreases below ~ 100 Å. The efficiency of concave gratings for SXS has been discussed by *Speer* [8.21], and *Morse* and *Weissler* [8.22].

For $\lambda>500$ Å, it is possible to use the normal-incidence vacuum spectrograph with ϕ close to zero. Many other mountings are also used [8.3]. Adjustments of grating spectrographs have been discussed by *Harrison* et al. [8.23]. *MacAdam* [8.24], and *Sawyer* [8.25] have discussed the optics of small displacements from the Rowland circle.

Synthetic crystals (organic esters such as octadecyl hydrogen maleate, $2d\sim 64$ Å; dioctadecyl adipate, $2d\sim 94$ Å; octadecyl hydrogen succinate, $2d\sim 97$ Å) with large interplanar spacings are available, which are useful for SXS

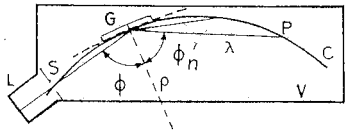

Fig. 8.7. Concave grating grazing incidence vacuum spectrograph. The slit S, the grating G and the plate P, all lie on the Rowland circle C of radius $\rho/2$. L is the source, and V the vacuum chamber

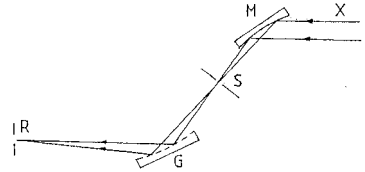

Fig. 8.8. Optical system for a conventional spectrometer. X: radiation from the synchrotron; M: fixed toroidal mirror; S: fixed entrance slit; G: fixed spherical grating; R: exit slit that moves on a Rowland circle

in the region $25<\lambda<100$ Å. The synthetic crystal of potassium acid phthalate ($2d=26$ Å) is convenient for $\lambda\sim25$ Å [8.26].

Spectrometer optical systems have been developed for use with synchrotron radiation. For good intensity a condenser mirror is used at grazing incidence [8.27] before the entrance slit (Fig. 8.8).

8.4 Detectors

In the soft X-ray region, the energy of the photons (25–250 eV) is so low that they are easily absorbed by the protective gelatin layer of ordinary photographic emulsions. Special emulsions, on thin backing plates that may be bent along the Rowland circle, are therefore needed. In early days, Schumann plates were used. Eastman Short-Wave-Range (SWR) plates and Ilford Q-emulsion plates are found to be very suitable. In these emulsions, the density of silver bromide grains is high and the gelatin layer is very thin (less than 1000 Å).

In the range 100–800 Å, *Piore* et al. [8.28] used a Be–Cu *photoelectron multiplier* as a detector that moves along the Rowland circle. It is 1000-fold more sensitive than the photographic plate. *Rogers* and *Chalkin* [8.29] used a *Geiger counter*, with 500 Å thick collodion window, in the range of about 20–200 Å. *Ederer* and *Tomboulian* [8.30] used a Geiger counter between 100 and 300 Å to measure absolute intensities. A silicon photodiode can also be used [8.31] in the range 580 to ~1600 Å. For energy-dispersive detectors over a wide range of X-ray energies see Sect. 9.9.

8.5 Emission Spectra

A large body of data exists on soft X-ray emission and absorption spectra. Soft X-ray emission bands are produced when an electron is ejected from an inner shell of an atom and the resulting hole is filled by a transition from the band of

valence electrons. The intensity is given by

$$I(E)=\nu^3 P(E)N(E), \quad P(E)\propto\sum_i|\int\psi_f^* x_i\psi_k\,d_\tau|^2, \tag{8.30}$$

for $E\leq E_F$ and $I(E)=0$ for $E>E_F$. In terms of a one-electron model the emission spectra give direct information about the occupied valence band $N_{oc}(E)$.

From (6.57), for the free-electron model,

$$E_F=\frac{\hbar^2}{2m}\left(\frac{3\pi^2 N}{V_a}\right)^{2/3}. \tag{8.31}$$

The corresponding density of orbitals at the Fermi energy is

$$N(E_F)=\frac{dN}{dE_F}=\frac{V_a}{2\pi^2}\left(\frac{2m}{\hbar^2}\right)^{3/2}E_F^{1/2}=\frac{3N}{2E_F}. \tag{8.32}$$

Thus, the number of orbitals per unit energy range at the Fermi energy is determined by the total number of conduction electrons divided by the Fermi energy.

We can use (8.32) for the number of orbitals per unit energy range, $N(E)$, or the density of states, for $E<E_F$,

$$N(E)=\frac{dN}{dE}=\frac{V_a}{2\pi^2}\left(\frac{2m}{\hbar^2}\right)^{3/2}E^{1/2}. \tag{8.33}$$

The density of single-particle states $f(E,T)N(E)$ is plotted in Fig. 8.9 as a function of E, where $f(E,T)$ is given by (6.1). The average energy is increased when the temperature is increased from 0 to T, because electrons are thermally excited from region 1 to region 2. If spin is included, the electron density, that is the number of electrons per unit volume per unit energy, becomes

$$N_e(E)=2N(E)f(E,T). \tag{8.34}$$

We can find a general expression for $N(E)$. From (6.53), the number of allowed values of k for which the energy is between E and $E+dE$, $E=\hbar^2k^2/2m$, is

$$N(E)dE=\frac{V_a}{(2\pi)^3}\int_{\text{shell}}d^3k, \tag{8.35}$$

where the integration is over the volume of the shell in $\boldsymbol{k}$ space lying between two surfaces, one of energy E and the other of energy $E+dE$. Consider a volume element $dS_E dk_\perp$, where dS_E is the cross-sectional area and $dk_\perp$ is the perpendicular distance between these two surfaces, so that

$$\int_{\text{shell}}d^3k=\int dS_E dk_\perp.$$

The gradient of E, $\nabla_k E$, is also normal to the surface on which E is constant; also, obviously the quantity $|\nabla_k E|dk_\perp=dE$. Thus, $dS_E dk_\perp=dS_E(dE/\nabla_k E)$, and

$$N(E)=\frac{V_a}{(2\pi)^3}\int\frac{dS_E}{|\nabla_k E|}, \tag{8.36}$$

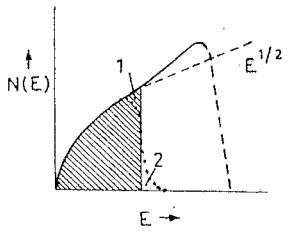

Fig. 8.9. $N(E)$ vs E curve for a free-electron gas in three dimensions. The dotted curve represents the density $f(E, T)N(E)$ of occupied orbitals at a finite temperature T. The hatched area represents the occupied orbitals at $T=0$. $N(E)$ drops to zero at the Brillouin-zone boundary (dashed curve)

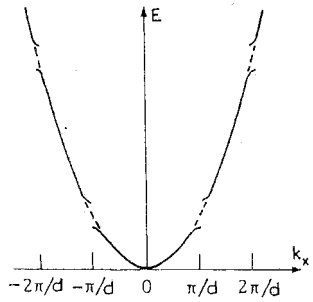

Fig. 8.10. E vs k plot for almost-free electrons in a simple lattice. The discontinuities occur at values of k for which Bragg's law is satisfied

where the integration is on the surface S_E of constant energy E. *Van Hove singularities* are associated with points in the $\boldsymbol{k}$ space for which $V_k E$ vanishes.

When the free motion of the electron in the valence band is assumed to be modulated by the periodic potential provided by the lattice, energy discontinuities occur for certain values of k (see, for example, [8.32]). For the simple case of a cubic lattice, they occur at

$$\pi(\alpha^2+\beta^2+\gamma^2)d^{-1}+\alpha k_x+\beta k_y+\gamma k_z=0. \tag{8.37}$$

Because $E=\hbar^2k^2/2m$, these discontinuities occur precisely where Kronig's formula for the Bragg reflection by (α, β, γ) planes holds. At these discontinuities, $N(E)$ drops to zero (Fig. 8.9) and ceases to be parabolic. This defines the boundary of the first Brillouin zone. Half of this zone would be filled for a monovalent metal, because $N_e=2N(E)$ at absolute zero (Fig. 8.9). Thus, the electrons in the first zone are those of lower kinetic energy and their de Broglie wavelengths are greater than the values required for Bragg diffraction at the lattice planes. In an actual crystal, the evaluation of $N(E)$ is quite complicated.

The zone boundaries are determined by $n\lambda_B=2\pi n/k=2d\sin 90°$, that is

$$k=(n\pi/d), \quad n=1, 2, \ldots . \tag{8.38}$$

In the simplest case, the energy discontinuities occur for these values of k (Fig. 8.10). Qualitatively, as the zone boundaries are approached, $N(E)$ increases more rapidly than the free-electron $E^{1/2}$ behaviour (as k approaches π/d, a small increase of E leads to a large increase of the number of k states, Fig. 8.10), leading to a cusp (Fig. 8.11). $N(E)$ then drops to zero if there is no energy overlap between the first and second zones. The level density is zero over the region of

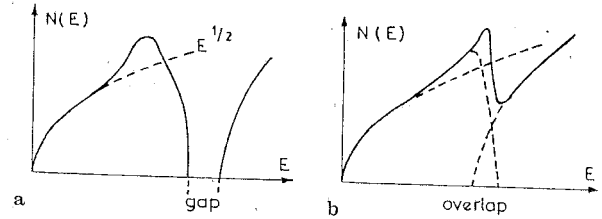

Fig. 8.11a, b. $N(E)$ curves for **a** non-overlapping bands, and **b** overlapping bands

forbidden energies, beyond which it begins to rise as energies that correspond to the second zone are reached (Fig. 8.11a). In case of overlap (like s–p hybridization), the levels in the second zone beging to contribute before the end of the first zone is reached (Fig. 8.11b). A theoretical $N(E)$ curve for overlapping bands was drawn in Fig. 7.6 for ^{29}Cu metal.

In (8.30), $I(E)$ depends on both $P(E)$ and $N(E)$. In general,

$$I(E)\propto \nu^3 \int \frac{|M_{f,i}|^2}{V_k(E)} dS_E.$$

If the matrix element $|M_{f,i}|$ were independent of $\boldsymbol{k}$,

$$I(E)\propto \nu^3 |M_{f,i}|^2 N(E), \quad \text{for } E\leq E_F.$$

For K spectra, the final state is a 1s atomic level, and for $L_{II,III}$ spectra it is a $2p$ level. The ψ_k may be represented by $\exp(i\boldsymbol{k}\cdot\boldsymbol{r})$. The matrix element can then be evaluated for small $k(E\sim 0)$. It turns out[1] that for K spectra $P(E)\sim E$, and for L

[1] The spontaneous-emission matrix element has the form

$$\langle\psi_{core}|\boldsymbol{p}\cdot\boldsymbol{A}|\psi_k\rangle=-i\hbar\,\boldsymbol{A}\cdot\left(\langle\psi_{core}|\nabla|\boldsymbol{k}\rangle-\sum_\alpha\langle\psi_{core}|\nabla|\alpha\rangle\langle\alpha|\boldsymbol{k}\rangle\right),$$

because there are two terms in the single orthogonalized plane wave, the plane wave $|\boldsymbol{k}\rangle$ and the orthogonalization term. We can write $\langle\psi_{core}|\nabla|\boldsymbol{k}\rangle=i\boldsymbol{k}\langle\psi_{core}|\boldsymbol{k}\rangle$. For a core S state (K spectra), the overlap $\langle\psi_{core}|\boldsymbol{k}\rangle$ is nearly independent of $\boldsymbol{k}$; therefore, the first term on the right is proportional to k. In the second term, there are matrix elements $\langle\psi_{core}|\nabla|\alpha\rangle$, only for α corresponding to a p state. This matrix element is constant, but the overlap $\langle\alpha|\boldsymbol{k}\rangle\propto k$ for a p state. Thus, both of the terms are proportional to k, or $P(E)\sim E$, for the K spectra. For the L spectra, $\langle\psi_{core}|\nabla|\boldsymbol{k}\rangle$ contains a factor k from the gradient and a second factor of k from the overlap of the core p state with the plane wave. If this were the only term (a free-electron approximation), we would get $P(E)\propto E^2$ and $I(E)\sim E^{5/2}$. However, the second term gives matrix elements with α corresponding to a core s state; the corresponding overlap is constant; therefore, this term gives a nearly constant contribution. This leads to $I(E)\sim E^{1/2}$ for L bands.

spectra $P(E) \sim$ constant. Therefore, with $N(E) \propto E^{1/2}$ for small E, for K bands

$$I(E) \propto \nu^3 |M_{K,k}|^2 N_p(E) \propto \nu^3 E^{3/2}, \tag{8.39}$$

where $N_p(E)$ is the partial density of states of p symmetry. For L bands

$$I(E) \propto \nu^3 |M_{L,k}|^2 N_{s,d}(E) \propto \nu^3 E^{1/2}, \tag{8.40}$$

where $|M_{f,i}|$ is the matrix element between the initial and final states.

To obtain the intensity curve, an emission band is photographed twice, using two different exposure times. A calibration curve of the emulsion is thus obtained. By its use and the known instrumental dispersion, the spectrogram can be reduced so as to yield relative intensities within the band, as a function of E. For the Li K band, the result is shown in Fig. 8.12a; the result for the Na $L_{II,III}$ band is shown in Fig. 8.12b.

Let us now compare the simple theory, based on the one-electron approximation, with experiments [8.1, 33–35]. The electronic configuration of the Li atom is $1s^2 2s^1$. Because the inner level can be only a K state, solid Li has one of the simplest energy level diagrams. The distribution within the observed band is quite smooth (Fig. 8.12a) and should roughly represent the $N_p(E)$ curve or the $\nu^3 E^{3/2}$ law, (8.39). A relation of this form fits the observations quite well. It has a *low-energy tail* because of the Auger broadening. At E_F, the intensity decreases to only about 0.75 of its peak; we expect an abrupt drop, not a broad edge, in the simple model. This anomaly has attracted considerable attention. The band calculations [8.36] show that there is no contact of the Fermi surface with the Brillouin zone and that the $N(E)$ curve increases near the Fermi surface. *Goodings* [8.37] ascribed this decrease of intensity to a change of $N(E)$ in the presence of the 1s hole. He showed that the wave functions at the perturbed atom acquire more localized character at the expense of the band wave functions, resulting in a decrease of N(E) near E_F. A detailed discussion has beem given by *Ausman* and *Glick* [8.38]. The situation is not yet clear, because recent optical data support a connected Fermi surface [8.39].

The $L_{II,III}$ emission band of Na is shown in Fig. 8.12b. The L_{II} band is considerably weakened by Auger decay, so the spectrum is almost pure L_{III}. The L_{III} emission spectra of Na, Mg, Al show a peak at the threshold. These peaks are probably caused by the X-ray edge singularity, given by the threshold

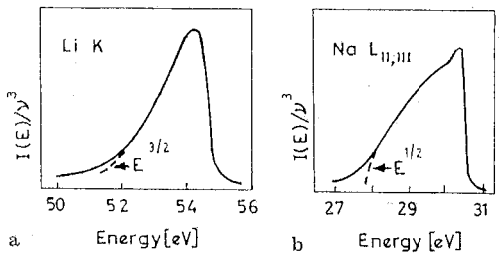

Fig. 8.12. a The K emission band of Li, and **b** the $L_{II,III}$ band of Na

converging factor $(\omega - \omega_T)^{-\alpha_0}$. A p-state hole excites electrons into the conduction band with mostly s-wave symmetry. The exponent α_0 is positive and gives a power-law divergence at threshold [8.40]. The earlier explanations depend on density-of-states arguments. The band structure of Na is similar to Li (alkali metal), and has the same density-of-states curve (Fig. 8.13). If the Fermi energy were at the peak E_1 of the $N(E)$ curve, or just below it, the observed peak (Fig. 8.12b) in Na near the X-ray threshold could be explained on this simple theory. However, the optical measurements show that E_F is considerably below E_1 [8.41]. Therefore, the idea that the Na L_{III} emission-band peak is caused by the band-structure effect must be discarded.

Thus, the explanation based on the one-electron model gives only limited information about the valence band. It has now been recognized that the transition probability, electron interactions and many-particle effects play an important role [8.42–47]. The proper treatment of these effects remains an open question.

K bands of ^{11}Na, ^{12}Mg, ^{13}Al, have been carefully observed [8.1, 48–50] and compared with the corresponding $N(E)$ curves. For recent reviews on K and L emission soft X-ray spectra see *Tomboulian* [8.2], *Appleton* [8.51], *Rooke* [8.52] and *Sénémaud* [8.53].

We summarize in Fig. 8.14 the various typical features of the observed $L_{II,III}$ soft X-ray emission spectra. From such features, we can understand several aspects of the behaviour of electrons in solids in the one-electron model. We briefly mention these aspects here.

1) The absence of a sharp edge on the high-energy side of the band in nonmetals (like S, Si) enables us to distinguish them from metals (like Na, Al). (Fig. 8.15).

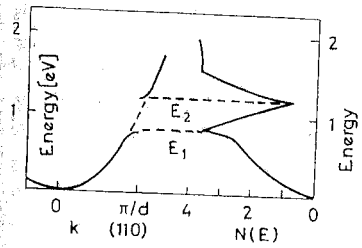

Fig. 8.13. Band structure of an alkali metal in the (110) direction

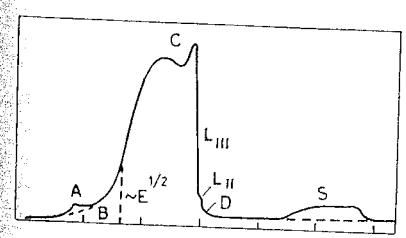

Fig. 8.14. A qualitative picture of Mg $L_{II,III}$ emission spectrum. A: plasmon satellite $L_I \rightarrow L_{III}$, B: low-energy tail, C: edge anomaly due to cascade effect of electron-hole pairs, D: high-energy tail, S: satellite band $L_{III} L_{II} \rightarrow L_{II} V$

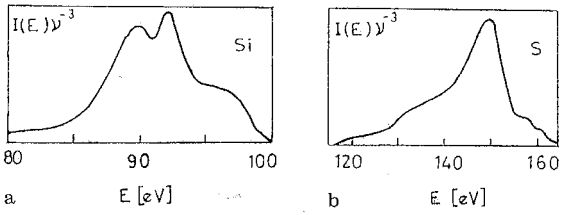

Fig. 8.15a, b. $L_{II,III}$ emission bands of **a** Si, and **b** *S*

2) The same material in two different crystalline forms (such as graphite and diamond) gives rise to emission bands of varying shapes.

3) The effect of the Fermi function $f(E, T)$ on (8.34), and therefore on (8.30), can be directly seen by changing the temperature, T. As shown in Fig. 8.9, the high-energy edge of the observed band should get broadened as the temperature is increased from absolute zero. This effect has been observed [8.1] (Fig. 8.16) and is in agreement with the distribution given by (6.1). Thus, SXS provides a direct verification of the Fermi distribution that plays an important role in electronic processes in solids.

4) The low-energy tail B (Fig. 8.14) is associated with the radiationless transitions of electrons within the valence band. The transition of a valence electron to an L level creates a hole in the valence band. An electron from a level higher in the valence band makes a radiationless transition into this vacant level; as a result another electron is ejected into an empty band level (Fig. 8.17). The effect of the radiationless transition is to reduce the lifetime Δt of the initial valence-band state that participated in the soft X-ray radiative process. Therefore, this state acquires a width $\Delta E \sim \hbar/\Delta t$. This argument holds for all the levels of the valence band, except that Δt for a state near the bottom of the valence band is shorter than that for a state near E_F. Thus, the levels near the bottom of the valence band become broader and $N(E)$ no longer drops to zero at the bottom of the band, but extends toward lower energies. This gives a gradual

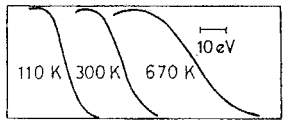

Fig. 8.16. Temperature broadening of emission edges on the high-energy side of the Al L_{III} band

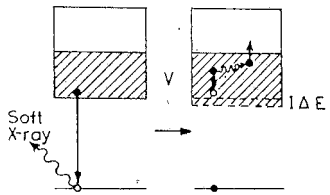

Fig. 8.17. Intra-band Auger transitions for the low-energy tail. The wiggly line in the shaded band represents non-radiative screened interaction

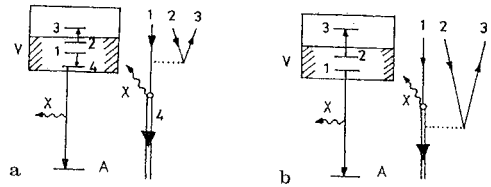

Fig. 8.18. a Internal Auger conversion; **b** shake-up process. The double line is for He atom and the dotted line for the screened Coulomb potential

decline in $I(E)$ toward the low-energy region of the emission band, that is, a *low-energy tail.*

Landsberg [8.54] gave a quantitative treatment of the low-energy tail in soft X-ray emission, based on the many-body approach. He used a screened Coulomb potential $r^{-1}\exp(-r/\lambda)$, shown as a dotted line in Fig. 8.18a (internal Auger conversion of Fig. 8.17). The unscreened potential r^{-1} gave a divergence. The screening length λ of this static electron-electron interaction is an adjustable parameter. A larger and correct value of λ was proposed later in the Bohm–Pines theory [8.55]. This situation was upset when *Pirenne* and *Longe* [8.56] considered the double (or multiple) transitions of a shake-up process (Fig. 8.18b) along with the Auger process. An electron near the top of the filled band jumps above the Fermi level, during the X-ray transition, and takes up a part of the photon energy. It is due to a scattering by the core hole potential switched off at the time of the transition. The situation was rescued by *Longe* and *Glick* [8.57] who noted that as these processes have the same final states, a final-state interaction occurs. It gives a negative interference term which compensates the large positive contributions of the two processes. The theory then yields a correct tailing effect.

5) *Intensity anomalies* caused by other Auger processes are observed in SXS (Chap. 4). For example, in light elements the $L_I(j=1/2)$ and $M_I(j=1/2)$ emission bands have not been observed. Also, $L_{II}(j=1/2)$ is much weaker and $L_{III}(j=3/2)$ is much stronger than would be expected from the statistical weight ratios determined by $(2j+1)$. Thus, theoretically $L_I:L_{II}:L_{III}=1:1:2$, whereas we observe approximately 0:1:10 for Na. Consider the partial energy-level diagram for Al (Fig. 8.19). Let a hole be created in L_I. A radiationless transition transfers the hole to L_{II} and simultaneously ejects an electron from the valence band with energy $(117.7-72.9)-12=32.8$ eV, which is sufficient to eject the electron from the metal. Auger electrons of this type have been detected [8.58]. The energy distribution of such Auger electrons, like the soft X-ray emission band, gives information about the density of states in the valence band. The second electron that participates in the Auger process (marked 2 in Fig. 8.19) merely excites a valence-band electron near E_F to the vacant states (marked 2'). Auger transitions of the type $L_I \rightarrow L_{II,III}$ shorten the lifetime of the L_I excited state and give it a width of about 2 eV. In addition, this reduces the probability of a radiative transition $V \rightarrow L_I$, as confirmed by experiments. Similarly, the Auger transfer $L_{III} \rightarrow L_{II}$ reduces the probability of the radiative transition $V \rightarrow L_{II}$ and increases that of $V \rightarrow L_{III}$. This explains why the L_{III} band occurs

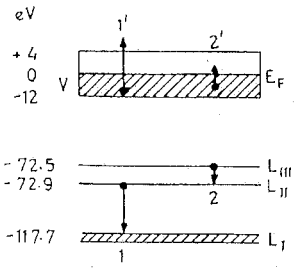

Fig. 8.19. Auger process for the intensity anomaly in Al L-emission spectra

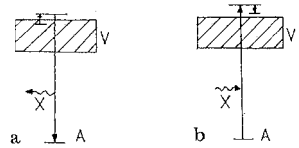

Fig. 8.20a,-b. Lowest order contributions to the replacement effect: **a** emission; **b** absorption

with an enhanced intensity, L_{II} with reduced intensity, and L_I with near-zero intensity.

6) Plasmon satellite A (Fig. 8.14) was first observed by *Rooke* [8.59] in soft X-ray emission. Its shake and intensity were estimated by *Brouers* [8.60], using the collective variables of Bohm–Pines theory, and by *Glick* and *Longe* [8.61], using the dielectric function formalism [8.57].

7) The anomaly D (Fig. 8.14) due to electron-hole cascades, has been discussed independently by *Mahan* [8.42] and *Anderson* [8.62] in a many-body theory. The band shake near the emission (or absorption) edge is given by a power low $(\xi/\omega)^\alpha$ where ξ is a constant with the dimensions of energy and ω is the frequency distance from the edge. *Nozières* and *de Dominicis* [8.44] calculated the exponent α using

$$\alpha = \alpha_1 + \alpha_2,$$

$$\alpha_1 = -2\sum_l (2l+1)(\delta_l/\pi)^2,$$

$$\alpha_2 = 2\delta_l/\pi, \tag{8.41}$$

where δ_l are the phase shifts of the Fermi level electrons scattered by the initial (final) core hole for emission (absorption) process. The α_1 is related to a shake-up effect and is always negative. Many weak energy pairs are excited at the moment of the X-ray transition (the lowest-order one-pair case contributing to α_1 is the same as Fig. 8.18b with 1, 2, 3 states close to the Fermi level). This produces a sudden change in the core potential. The α_2 is positive and related to a replacement effect (Fig. 8.20). For L bands $l=0$, and for K bands $l=1$. Because $\delta_0 > \delta_1 > \delta_2 > \ldots$, α is positive and gives a peak structure only for the L bands ($l=0$).

8) *Skinner* [8.1] assumes that the high-energy tail D (Fig. 8.14) is a satellite of the type $L_{II}V \rightarrow VV$. He attributed the satellite bands to the transition $L_{III}L_{II} \rightarrow L_{II}V$.

The L and M emission bands of heavier elements and compounds have also been studied [8.63–66].

8.6 Absorption-Spectra Recording

The absorber is prepared by evaporating the metal (~100 Å thick) onto a substrate. The substrate is usually a Zapon (cellulose acetate, collodion), Mylar (polyethylene tetraphthalate), or Formvar (polyvinyl formal) film of about 300 Å thickness, to avoid excessive absorption [8.67] of soft X-rays. Cellulose compounds can be dissolved in amyl acetate and Mylar in ethylene bromide. To prepare a collodion film, a drop of 10% solution is allowed to spread on the surface of distilled water in a tray. When dry, this surface film can be lifted on a small metal frame. Two absorbers of thicknesses x_1 and $x_2 > x_1$ are prepared.

The Lyman discharge tube gives a line spectrum. When the absorber is present, the lines in the wavelength region of absorption are reduced in intensity. Four exposures of the photographic plate are made, two through x_1 differing by a factor of two in the number of sparks (exposure). two through x_2 also differing from each other by a factor of two in exposure, but increased by a factor R so that the radiation reaching the plate through thin (x_1) and thick (x_2) absorbers is nearly the same.

A microphotometer trace is made of each spectrum. The deflections d_E for one exposure and twice that exposure, d_{2E}, are read and plotted as in Fig. 8.21a. This is done for both thin and thick absorbers and the average of all the points is taken. This curve is used to plot a relative-exposure versus deflection curve (Fig. 8.21b). First, some arbitrary point d_a is taken on the first curve in the region of small deflection. This gives the relative exposure 1 and is plotted. For twice that exposure, at the corresponding point on the second curve, the deflection is d_{2a}. This is a relative exposure of 2. For deflection $d_b = d_{2a}$ on the first curve there is a corresponding d_{2b} on the second curve for which the exposure is 2×2 or 4. This process, carried out for the available values of d, yields a response curve.

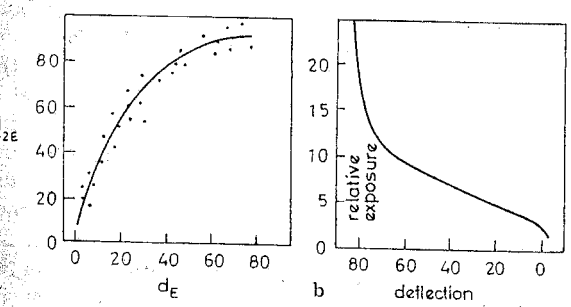

Fig. 8.21. **a** d_E vs d_{2E} plot. The solid curve is the average of the points from x_1 and x_2 absorbers. **b** Response curve

Intermediate points can be determined by taking other starting points on the first relative-exposure curve (Fig. 8.21) and repeating the process. This curve (Fig. 8.21b) is the *response curve* of the photographic emulsion used. It is based on the assumption that for the wavelength region covered on a plate, the response curve is independent of wavelength [8.68].

The response curve is used to determine the exposure for the deflection corresponding to each spectral line λ_i through both thick and thin samples. At any λ_i, the ratio of these exposures, thick to thin, divided by R, the ratio of the number of sparks through thick and thin absorbers, gives the transmittance T_i for the thickness $\Delta x = x_2 - x_1$. Then the absorption coefficient $\mu(\lambda_i)$ is found from the equation $T_i = \exp[-\mu(\lambda_i)\Delta x]$, for each λ_i in the region of interest. The points so obtained are plotted on a μ vs λ graph. These points are connected with a smooth curve to give the required absorption curve. When synchrotron continuous soft X-rays are used as source radiation the method of analysis is the same as for the hard X-ray region described earlier.

8.7 Interpretation of Absorption Spectra

The absorption coefficient $\mu(E)$ is given by

$$\mu(E) = 0, \quad E \leq E_F,$$
$$\propto P(E)N(E), \quad E > E_F. \tag{8.42}$$

The K and $L_{II,III}$ absorption spectra of the lighter elements have been measured with the synchrotron source and reviewed by *Brown* [8.6]. The earlier data from conventional sources have been reviewed by *Tomboulian* [8.2]. In Fig. 8.22, we show the general structure of $L_{II,III}$ absorption curves of Na, Mg, and Al. The absorption rises from a spike or line at the edge to a broad maximum 30 eV or more above threshold. The general rise from threshold is a matrix-element effect associated with transitions from the initial p state to the continuum d states [8.69], the transitions to continuum s states being very weak.

The characteristic sharp spikes or X-ray singularities close to the threshold for metals have been explained as a final many-body-state effect. The formation of a "core hole" in a metal during an X-ray absorption process gives rise to the sudden creation of a long-range hole (Coulomb) potential. This potential is screened in some way by the conduction electrons in the final state of the process. The deep hole being localized on the core level ψ_i of a definite atom, the screening resembles that around an excess nuclear charge and leads to the formation of an exciton [8.70]. There is not a one-to-one correspondence between the Wannier excitons (hole in the valence band and electron in the conduction band that forms a bound state) and the X-ray excitons (hole in the core state and electron in the bound state), but both lead to an enhanced transition probability, because the electron prefers to spend some time near the hole before moving away. *Mahan* [8.42] originally derived this enhancement

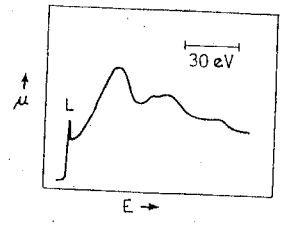

Fig. 8.22. Qualitative $L_{II,III}$-absorption shape for metals such as Na, Mg, Al. The spike is marked L

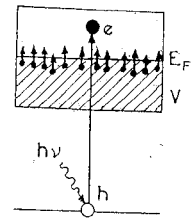

Fig. 8.23. Shielding of a suddenly created core hole in an energy picture for the absorption process. h: core hole; e: extra electron in the empty band due to the absorption transition

of threshold of the absorption (X-ray edge singularity) from exciton theory. *Nozières* and *De Dominicis* [8.44] assumed that in the final state, all of the conduction states ψ'_k are scattered by the screened potential V_j (hole) of the core hole and therefore differ from the corresponding unperturbed states ψ_k. Consequently, the transition probability $\langle\psi_i|\nabla|\psi'_k\rangle$ is modified.

As a reaction to the sudden creation of a hole potential, the conduction electrons rush in, so as to shield this potential. *Mahan* [8.42] regarded this many-body effect as the plasmon excitation. *Nozières* and *De Dominicis* [8.44] think of it as a scattering effect characterized by phase shifts δ_l in a partial wave analysis.

The theory of the X-ray edge singularity is very complicated [8.40]. In a pedestrian way, we can say that in the ordinary picture of scattering in space, the conduction electrons are scattered by a spherically symmetric potential

$$V_j^{\text{hole}}(r) = \int \frac{\rho_j(r')}{|r-r'|} d^3r', \quad \rho_j(r') = e^2|\psi_j(r')|^2, \tag{8.43}$$

where ψ_j is the hole wave function. A theorem by *Anderson* [8.62] states that the many-body ground state in the presence of a localized potential well is orthogonal to the many-body state in the absence of the potential well, because an infinite number of electrons undergo an infinitesimal change of their states to produce the adjustment to the localized potential. This is the starting point of the X-ray edge theory. In the energy picture, this change of conduction-electron states can be thought of as an infinite number of transitions near the Fermi surface excited by a V_j^{hole} (Fig. 8.23). (The corresponding lowest order diagram for emission will look like Fig. 8.18b.) Thus, the final-state effect is an assembly of many Auger processes, which gives rise to a large number of electron-hole pairs at E_F that accompany core excitation. We expect that the transition rate for these Auger-like processes would be maximum for the smallest excitation energy E measured above threshold E_T,

$$w(E) \propto \frac{1}{(E-E_T)^\alpha} \xi^\alpha (E-E_T). \tag{8.44}$$

The critical exponent α (related to phase shift δ_l) for a $p \rightarrow s$ transition is positive, so that an enhancement occurs for L shell absorption (Fig. 8.22) at the threshold in Na, Mg, and Al. These spikes have been called excitons in a metal, although they differ from the usual excitons in an insulator (Fig. 7.4b). *Combescot* and *Nozières* [8.71] have given a theory for excitons in which the transition from insulator to metal behaviour can be followed. For a clear discussion of many-body effects in metals and the Anderson orthogonality theorem, see [8.72].

Like the emission plasmon satellite A (Fig. 8.14), an absorption plasmon satellite edge is theoretically expected at frequency $\varepsilon + \omega_p(0)$ where ε is the main edge frequency. However, being weak, it has not been detected: what has been predicted and detected is an absorption plasmon resonant structure at a slightly higher frequency [8.73, 74]. We have already discussed resonance lines in the soft X-ray emission spectra (Sect. 6.4). The absorption structure occurs as a small *dip* at a frequency of $\varepsilon + \omega_p(q_c)$, where q_c is the plasmon cutoff wave-numbers. This structure estimates the frequency range of plasmon dispersion in metals. Usually $\omega_p(q_c) = \frac{3}{2}\omega_p(0)$. The relevant diagram is shown in Fig. 8.24. The process is virtual for the $\omega_p(0)$ plasmon.

The soft X-ray M-absorption spectra of transition metals and oxides have been measured by several workers (for example [8.6, 75–80]). Comparison with the theoretical $N(E)$ curve has led *Agarwal* and *Givens* [8.77] to conclude that the antiferromagnetic nature of Cr can be directly demonstrated by the study of soft X-ray absorption and emission spectra (Fig. 8.25). This kind of interpretation has been further elaborated by *Mott* and *Stevens* [8.81]. The $M_{II,III}$ absorption spectra of Cr differ in high-energy details when studied with a conventional soft-ray source [8.77] and by the synchrotron source [8.76], although the position and slope of the X-ray edge is nearly the same in both cases. *Sonntag* and *Brown* [8.82] have recently studied the soft X-ray absorption spectra of transition-metal layer compounds.

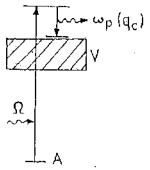

Fig. 8.24. Transitions for the absorption plasmon resonant structure. $\Omega = \varepsilon + \omega_p(q_c)$, and the link line is a plasmon

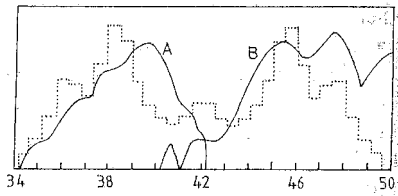

Fig. 8.25. The Cr $M_{II,III}$ soft X-ray emission band A [8.65], absorption band B [8.77] and the calculated density of states curve C for the $3d$ band. The dip in the middle indicates antiferromagnetism. Five electrons per atom occupy the lower half of the band with a like number of empty states above. The sixth valence electron is in the $4s$ band with the Fermi level at the dip

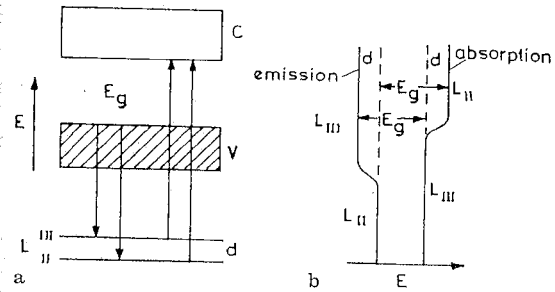

Fig. 8.26. **a** L_{II} and L_{III} emission and absorption transitions. **b** Estimation of E_g and L_{II}–L_{III} level separation in an idealized situation

In a light element, such as ^{15}P, the L emission spectrum consists of two superimposed bands whose edges are separated by the energy difference between the L_{II} and L_{III} levels. The L absorption spectrum also gives two edges separated by the same amount (Fig. 8.26a). The separation of L_{III} emission and L_{III} absorption should correspond to the energy gap E_g between the valence-band edge and the conduction-band edge. The idealized situation is shown in Fig. 8.26b. Although the observed edges are not so sharp as shown, they can give a reasonable estimate of E_g and L_{II}–L_{III} level separation. The SXS thus gives information about inner-level separations, band gaps, the entire valence-band (in emission), and the conduction-band (in absorption) density of states, in the first approximation. In contrast, most other solid-state studies give information only about states near E_F.

9. Experimental Methods

The essential instrumentation required for X-ray spectroscopy consists of (a) the primary X-ray source unit, (b) the spectral analyzer, and (c) the detector. We describe the elements of these units in this chapter.

9.1 X-Ray Tubes

X-ray tubes are mainly of two kinds: 1) gas tubes, and 2) filament tubes. In gas tubes the electrons that strike the target are produced by ionization of the gas atoms; in filament tubes they are produced by heating the filament by passing an electric current through it. Filament tubes are further divided into two types: 1) sealed or Coolidge tubes, and 2) demountable tubes.

Gas tubes. The original tubes used by Röntgen consisted of a glass bulb evacuated to a pressure of 10^{-4} mm Hg. When a high voltage is applied between the cathode and anode, the residual air becomes partially ionized. The positive ions and free electrons are accelerated to the cathode and target (anode), respectively. The positive ions knock out some electrons on striking the cathode. (Metals of low Z disintegrate less under bombardment by positive ions, so Al is usually used as the cathode material). The electrons, or cathode rays, tend to collide with the gas ions on their way to the anode. In this way, the ionization builds up. The final tube current is determined by the gas pressure, the applied voltage and the tube geometry. In Fig. 9.1a we show the general structure of a gas tube with a glass envelope, and with a metal body [9.1]. The concave cathode produces an electrostatic focusing effect that gives a sharp focal spot on the target. In the Hadding tube (Fig. 9.1b), gas is continuously leaked in through a needle valve and evacuated by a diffusion pump, to give the desired low pressure.

Coolidge tubes. W.D. Coolidge replaced the Al cathode with a tungsten filament in a sealed glass tube evacuated to less than 10^{-5} mm Hg (Fig. 9.2a). When the filament is heated to a temperature $T[K]$ by passing a current through it, it emits electrons according to the Richardson–Dushman equation (see, for example [9.2]),

$$I = ze = AT^2 \exp(-B/T),$$

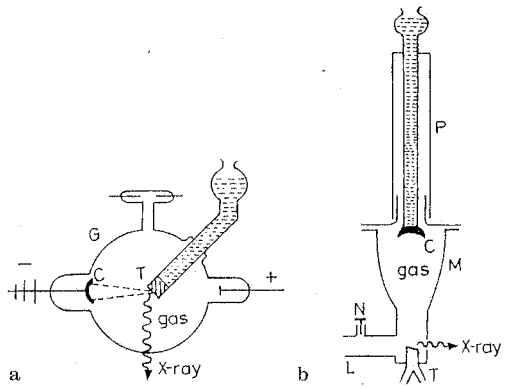

Fig. 9.1. **a** Gas X-ray tube with glass envelope. **b** Hadding tube. *C*: Al cathode, *T*: water-cooled target, *G*: glass bulb, *M*: metal body, *P*: porcelain cathode assembly, *N*: needle value to introduce air, *L*: to diffusion pump backed by rotary pump

where A, B are constants and the current I is the product of the number z of electrons that leave unit area of the surface per second and the electronic charge e. The thermionically emitted electrons are accelerated toward the target to produce X-rays. For a given voltage V on the tube, the tube current depends on the temperature of the filament. The advantage of Coolidge tubes, over gas tubes, is that the tube current i and the voltage V can be varied independently. This advantage would be lost, and the efficiency reduced, if the electrons from

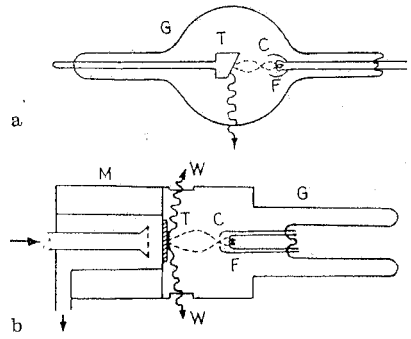

Fig. 9.2a, b. Schematic cross section, of (top, **a**) Coolidge sealed-off tube, (bottom, **b**) commercial X-ray tube. *T*: water-cooled target, *M*: metal housing, *W*: beryllium window, *F*: fil ament, *C*: focusing hood, *G*: glass envelope

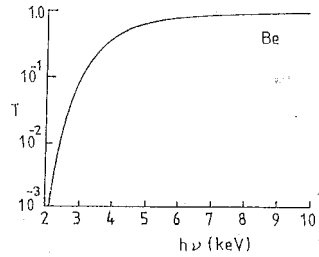

Fig. 9.3. Transmission coefficient of beryllium window (25 mil thick), *T*, as a function of photon energy

the filament could collide with gas atoms and produce extra electrons. Therefore, high vacuum is maintained inside the tube.

In Fig. 9.2b, we show a typical sealed tube, of the Coolidge type, that is now commercially available. A metal focusing hood, at the same potential as the filament, helps to focus the thermionically emitted electrons to a small area (*focal spot*) of the target. Non-porous beryllium is used as window material. Because of its low atomic number, it is transparent to hard X-rays and does not produce secondary X-rays in this region. The transmission curve for the beryllium window is shown in Fig. 9.3. Beryllium thinner than 25 μm is likely to have pinholes.

Table 9.1. Some radioisotope sources for X-ray work[a]

Source	Main decay	Half-life [y]	Radiation		Typical activity [Ci]	Excited X-rays
			Type	Energy [keV]		
$^{109}_{48}$Cd	Cap[b]	1.3	Ag *K*	22.2	0.005	Ca-Tc *K*
			γ	88		
$^{57}_{27}$Co	Cap	0.74	Fe *K*	6.4	0.5	≤Cr *K*
			γ	14, 122, 136		
$^{55}_{26}$Fe	Cap	2.7	Mn *K*	5.9	0.05	Al-Cr *K*
$^{153}_{64}$Gd	Cap	0.65	Eu *K*	42	0.01	Mo-Ce *K*
			γ	97, 103		
$^{3}_{1}$H-Ti	β^-	12.3	Wr[c]	3–10	5	Na-Cu *K*
			Ti *K*	4–5		
$^{125}_{53}$I	Cap	0.16	Te *K*	27		≤Xe *K*
			γ	35		
$^{210}_{82}$Pb	β^-	22	Bi L	11	0.01	≤Sm *K*
			γ	47		
$^{238}_{94}$Pu	α	89.6	U *L*	15–17	0.03	Ca-Br *K*

[a] For sources giving 10^7 photons/s the radiation hazard is small from unshielded sources.
[b] Cap: electron capture.
[c] Wr: white radiation.

Demountable (filament) tubes. For X-ray spectroscopic work, we often need long exposures and different target materials, either for emission studies or for suitable reference lines. With a demountable tube, we can dismantle the (porcelain) cathode and (metal) anode assemblies to replace the burnt-out filament and to change the target layer. An oil-diffusion vacuum pump, backed by a rotary pump, is used to produce the necessary vacuum (10^{-5} mm Hg) in the tube. The demountable tube has virtually an infinite lifetime.

The conventional X-ray tubes have been replaced, wherever facilities exist, by synchrotrons and storage rings as sources. High-brilliance X-ray sources have been described by *Yoshimatsu* and *Kozaki* [9.3].

Commonly used radioisotope sources for X-ray spectrometric excitation are given in Table 9.1. The activity of a radioactive source is measured in curies ($1\text{Ci} \equiv 3.7 \times 10^{10}$ transformations/s. A 0.1 Ci source gives 3.7×10^9 photons/s, whereas an X-ray tube at 100 μA tube current gives about 10^{12} photons/s.

9.2 Line-Focus Filament

Large energy input in a tube with a small focal spot is not possible because it leads to excessive heating and melting of the target. Increase of the area of the focal spot in all directions causes bad geometry and loss of sharpness in photographs. The focus area should be increased in such a way that the cross-section through the emitted X-ray beam at the focal spot is as small as possible.

The *line-focus filament* of Goetze provides a satisfactory solution. A long cylindrical spiral (obtained, say, by winding tungsten wire on a pin) of very small diameter gives a line focal spot (area $\sim 1\text{ mm} \times 10\text{ mm}$) on the target that by virtue of its length can dissipate considerable energy without damage to the target. In the sealed-off tubes, the target is normal to the incident electron beam. When the line-shaped focal spot is viewed from one of its ends, the focal spot becomes foreshortened. By choosing the takeoff angle properly ($\sim 6°$, $\sin 6° \simeq 0.1$), the effective focal spot can be made to look like a small square (1 mm × 1 mm) (Fig. 9.4a). Thus, the intensity of the X-ray beam is increased whereas the effective size of the focal spot remains small, to give sharp images.

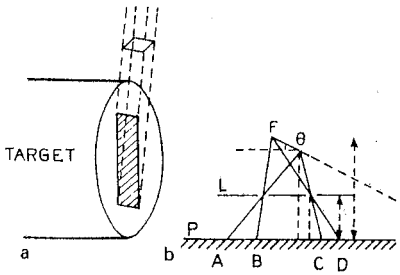

Fig. 9.4. a Line-focus of a filament. **b** Two-pinhole method for determining the angle of the focal spot. *F*: focal spot, *L*: lead sheet, *P*: film

The angle of the line-focus spot can be determined by photographing it through two pinholes in a lead sheet as shown in Fig. 9.4b.

Even with a line-focus spot, the heating of the target is great. For example, a tube run at 50 kV, 20 mA, or at 10^3 W, all confined to a focal spot of area $1 \times 10\text{ mm}^2$, has a specific loading of $100\text{ W/mm}^2 \simeq 25\text{ cal s}^{-1}\text{ mm}^{-2}$. The efficiency of an X-ray tube is about 1% or less at 50 kV (Chap. 2). Therefore, virtually all of this energy is used up in heating the target. It is enough to heat 100 cm^3 of water from 25°C to the boiling point in about 5 min; it is essential to remove this heat as rapidly as possible, by cooling the target. If the target is earthed, it can be connected directly with the water mains and a flow of one or more litres per minute is enough to cool the target, under normal conditions. A water-circulation pump with a reservoir can also be used to supply this flow rate.

Copper is a good conductor of heat. Therefore, the anode assembly in X-ray tubes is usually made of copper, and the desired target metals are either plated onto its surface or mechanically fitted into it. After long use, the focal spot gets broadened and stray cathode electrons begin to strike the copper studs or the frame that holds the target material. This gives rise to Cu, Ni and Fe emission lines in old Mo or W target X-ray tubes.

The electrons penetrate the target by about a micrometre only, so the X-ray source remains a thin, almost transparent, layer even for a small takeoff angle.

9.3 High-Tension Circuits

A filament X-ray tube has the structure of a diode rectifier or a kenotron. Therefore, it gives half-wave *self-rectification* when alternating high volage is directly applied from a transformer. For continuous operation, this is not recommended, because the target may get heated enough to produce thermionic electrons and therefore a reverse current. This can seriously damage the filament.

The recommended circuit for *half-wave rectification* involves a kenotron (Fig. 9.5). To avoid production of X-rays by the kenotron, its voltage current characteristics are kept different from that of the X-ray tube. Both of them have diode-like characteristic curves. For a given tube current, the voltage drop across the kenotron is much smaller (about 200 V) than across the X-ray tube (about 20 000 V) (Fig. 9.6). These days solid-state high-potential rectifiers (diodes made of silicon) are being used in place of kenotrons. No X-rays are generated by such rectifiers themselves.

The *Gratz circuit* uses four kenotrons for *full-wave rectification* (Fig. 9.7). When *B*, one end of the secondary winding, is negative and *A* is positive, electrons flow from *B* through kenotron 3, the X-ray tube, and then through kenotron 4 to *A*. When *A* is negative the flow is $1 \rightarrow X \rightarrow 2 \rightarrow B$. Thus, in the X-ray tube the current always flows in one direction.

To minimize the voltage changes on the anode, a capacitor *C* is introduced into the circuit (Fig. 9.8). It draws current from the high-tension transformers

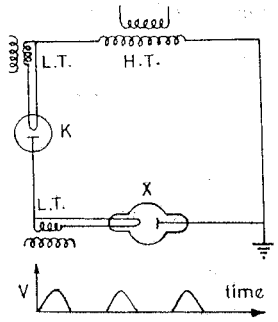

Fig. 9.5. Half-wave-rectifier circuit. *H.T.*: high-tension transformer, *L.T.*: low-tension transformer for the filament current. *K*: kenotron, *X*: X-ray tube *V*: voltage

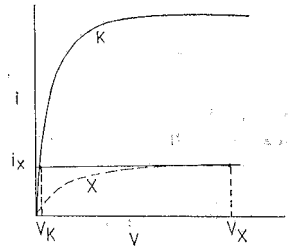

Fig. 9.6. Voltage-current characteristic curves *X* for the *X*-ray tube and *K* for the kenotron. For the same tube current i_x, $V_x \gg V_K$

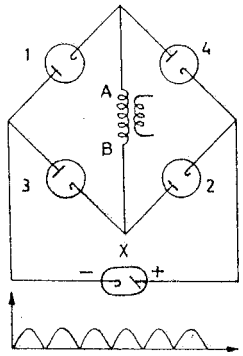

Fig. 9.7. Full-wave-rectifier circuit

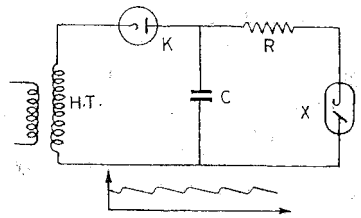

Fig. 9.8. Constant-voltage circuit. *C*: condenser, *K*: kenotron, *X*: X-ray tube, *R*: surge-limiting resistor

when the transfer voltage happens to be higher than the capacitor voltage; this may happen only over a small fraction of the total period of the cycle. Its capacity should be such that the decrease of the capacitor voltage is small during the discharge part of the cycle.

9.4 Wavelength Units

The *unit cell* of rock salt (NaCl) is shown in Fig. 9.9. The location of the atoms can be formally described as follows:

4 Na atoms at	0 0 0	$\frac{1}{2}\ \frac{1}{2}\ 0$	$0\ \frac{1}{2}\ \frac{1}{2}$	$\frac{1}{2}\ 0\ \frac{1}{2}$
4 Cl atoms at	$\frac{1}{2}\ \frac{1}{2}\ \frac{1}{2}$	$\frac{1}{2}\ 0\ 0$	$0\ \frac{1}{2}\ 0$	$0\ 0\ \frac{1}{2}$

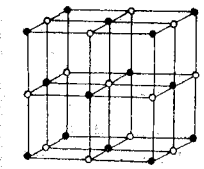

Fig. 9.9. Unit cell of rock salt: • Na, ○ Cl

We can determine the interplanar distance d (distance between planes of identical atomic population) as follows:

Molecular weight of NaCl = M = 23.00 + 35.46 = 58.46,

No. of atoms in 58.46 g NaCl = $2N_A = 2 \times 6.064 \times 10^{23}$,

Density of rock salt = $\rho = 2.163\ \mathrm{g\,cm^{-3}}$,

No. of atoms in 1 $\mathrm{cm^3} = n = 2N_A\rho/M$,

Distance between Na and Cl along cube edge = d,

No. of atoms in a row 1 cm long = $1/d$,

No. of atoms in 1 $\mathrm{cm^3} = n = 1/d^3$.

Equating the two expressions for n, we obtain

$$d^{-3} = 2 \times 6.064 \times 10^{23} \times 2.163/58.46,$$

$$d = 2.81400 \times 10^{-8}\ \mathrm{cm}. \tag{9.1}$$

The crystal-grating spacing of the calcite ($CaCO_3$) crystal can be evaluated from the Bragg equation,

$$n\lambda = 2d_{\mathrm{NaCl}} \sin\theta_{\mathrm{NaCl}} = 2\mathrm{d}_{\mathrm{CaCO_3}} \sin\theta_{\mathrm{CaCO_3}}. \tag{9.2}$$

Siegbahn in this way found the calcite-cleavage spacing to be 3.02945×10^{-8} cm. He recognized the uncertainty of the values of N_A and ρ used in his calculation and proposed a new unit called the X unit (XU) in which the d values were arbitrarily set as (for $n = 1$)

$$d_{\mathrm{NaCl}} = 2814.00\ \mathrm{XU} = 2.81400\ \mathrm{kXU}, \quad (\text{at } 18^\circ\mathrm{C}),$$

$$d_{\mathrm{CaCO_3}} = 3.02904\ \mathrm{kXU}, \quad (\text{at } 18^\circ\mathrm{C}). \tag{9.3}$$

Thus, 1 kXU is approximately equal to 10^{-8} cm or 1 Å [9.4].

When ruled gratings became available for X-ray measurements, it was found that the wavelength values of the well-known lines were always about 0.2% higher than those obtained by use of the Siegbahn value of d for calcite. The ruled-grating measurements of λ of well-known lines made in 1935 by *Bearden* were free from the uncertainty involved in the values of ρ and N_A, and gave the corresponding value of d for calcite as 3.03560 Å. Bragg's conversion factor [9.5] is 1.00202 Å = 1 kXU. *Bearden* [9.6] took the W $K\alpha_1$ to define the X-ray

wavelength standard as

$$\lambda_{W\,K\alpha_1} = 0.2090100\ \text{A}^*. \tag{9.4}$$

This relation defines a new unit A*. It approximates more closely to Å than to XU. To indicate the similarity to Å and yet distinguish the new unit as an independent entity, *Bearden* denoted it by A*. The above choice makes Å/A* very close to unit, but the conversion factor remains an experimentally determined quantity, subject to revision by future measurements.

The Bragg law is $n\lambda = 2d_n \sin\theta_n$, where d_n is the crystal grating constant for the nth order of diffraction (the small dependence on n is due to the index of refraction μ). We can write (3.54) in this form if the true grating constant $d \equiv d_\infty$ (so written because $d_n \to d_\infty$ as $n \to \infty$) is defined as

$$d_n = d_\infty\left(1 - \frac{\delta}{\sin^2\theta_n}\right) = d_\infty\left(1 - \frac{4d_\infty^2}{n^2}\frac{\delta}{\lambda^2}\right). \tag{9.5}$$

For most crystals δ/λ^2 is nearly independent of λ, away from the absorption edge. Then the small correction to the grating constant is proportional to n^{-2}. For calcite (211): $d_1(\text{A}^*) = 3.03553$, $d_2(\text{A}^*) = 3.03584$, $d_\infty^{(\text{A}^*)} = 3.03594$.

In precision work, it is necessary to consider thermal expansion of the crystal by using

$$d_\infty = d_{0\infty}(1 + \alpha \Delta t),$$

where α is the linear coefficient of expansion, $d_{0\infty}$ is the grating constant at a reference temperature (18°C), and Δt is the temperature rise above the reference value. In Table 9.2 we give the data on the crystals normally used in X-ray spectroscopy.

From the Bragg law, with $n\lambda$ constant,

$$0 = 2d[\delta(\sin\theta)/dt] + 2(\delta d/\partial t)\sin\theta,$$

$$0 = d(\cos\theta)\Delta\theta/\Delta t + (\Delta d/\Delta t)\sin\theta,$$

$$-\Delta\theta = [1/d\Delta d/\Delta t](\tan\theta)\Delta t = (\alpha\tan\theta)\Delta t.$$

Table 9.2. Useful data on crystals

Crystal	d at 18°C [kXU]	[Å]	$\alpha(°C)^{-1}$
Rock salt, NaCl (200)	2.81400	2.81971	4.0×10^{-5}
Calcite, $CaCO_3$ (211)	3.02945	3.03560	1.02
Quartz, SiO_2 (1010)	4.24602	4.25465	1.04
Gypsum, $CaSO_4.2H_2O$ (020)	7.56470	7.6001	3.78
Mica, $KAl_2[AlSi_3O_{10}]\cdot[OH]_2$ (001)	9.94272	9.9629	0.15

Lee and *Campbell* [9.7] measured $\Delta\theta$ as a shift in the peak intensity of known λ for a given Δt. This gave α.

Extensive lists of crystals and their properties are now available. See Appendix I. The atomic positions in the unit cell of calcite are [9.8]

2Ca $\frac{1}{4}\frac{1}{4}\frac{1}{4}$ $\frac{3}{4}\frac{3}{4}\frac{3}{4}$

2C 0 0 0 $\frac{1}{2}\frac{1}{2}\frac{1}{2}$

6O $\frac{1}{4}\frac{3}{4}0$ $\frac{3}{4}0\frac{1}{4}$ $0\frac{1}{4}\frac{3}{4}$ $\frac{1}{4}\frac{3}{4}\frac{1}{2}$ $\frac{3}{4}\frac{1}{2}\frac{1}{4}$ $\frac{1}{2}\frac{1}{4}\frac{3}{4}$

Thus, the unit cell does not have faces parallel to the cleavage planes of calcite; therefore, the indices of these planes are not (100) in terms of this unit cell, but are (211). The smallest *rhombohedron* of calcite that has faces parallel to the cleavage planes, and that contains an integral number of $CaCO_3$ molecules, has four molecules. It is not the true unit cell of calcite. The true unit has two molecules and does not have faces parallel to the cleavage planes.

9.5 Plane-Crystal Spectrograph

A simple arrangement [9.9] for absolute measurement (without using reference lines) of an unknown wavelength by use of a plane-crystal spectrograph is shown in Fig. 9.10a. It is called the *method of displacement* [9.10–12]. The line of wavelength λ under study is photographed on the same film at two positions, P and P', of the plate holder held normal to the incident ray I. If the displacement of the plate holder is l and the distance between the recorded line images is x, then λ can be estimated under normal setting of the spectrograph by using the relations

$$2d\sin\theta = n\lambda, \quad \tan 2\theta = x/l. \tag{9.6}$$

It can happen that the plate holder is not normal to I. Suppose it is tilted by a small angle ψ (Fig. 9.10b). From the triangle BB′C,

$$\frac{x}{\sin 2\theta} = \frac{l}{\cos(2\theta \pm \psi)}. \tag{9.7}$$

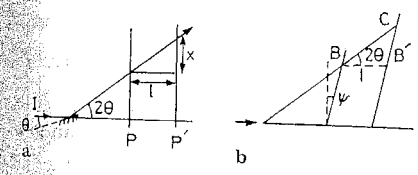

Fig. 9.10. a Absolute measurement of λ by a plane-crystal spectrograph. **b** Correction for the tilt of the plate holder

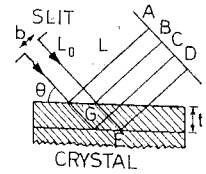

Fig. 9.11. Resolving power

From (9.6),

$$\psi=\cos^{-1}\left[\frac{\ln\lambda}{xd}\left(1-\frac{n^2\lambda^2}{4d^2}\right)^{1/2}\right]\pm 2\sin^{-1}(n\lambda/2d). \tag{9.8}$$

By recording a line of known wavelength λ, the angle ψ, a constant of the instrument can be determined, and then (9.7) can be used to find θ for the unknown λ [9.13]. Another method is to record the line λ on both sides of the incident beam. If the image is displaced by x on one side and by y on the other, then

$$\tan 2\theta=\frac{2xy}{l(x+y)}\cos\psi,\quad \sin\psi=\frac{l(x-y)}{2xy}.$$

The *angular dispersion*, $D=d\theta/d\lambda$, defines the ability of the crystal to separate two wavelengths, λ_1 and λ_2. It represents the angular difference $d\theta$ (in radians) corresponding to the wavelength difference $d\lambda$ (in Å). From (9.6)

$$D=\frac{d\theta}{d\lambda}=\frac{n}{2d}\frac{1}{\cos\theta}=\frac{\tan\theta}{\lambda}. \tag{9.9}$$

D increases with order, n, and becomes large near 90°. The angular dispersion is different from the *resolving power*, $\lambda/d\lambda$, or *resolution*. The definition of resolution is somewhat arbitrary. *Allison* [9.14] assumed that two lines are just resolved if their separation is equal to the full width of the instrumental window. The expression for the resolution then follows by putting $d\theta=\sigma=b/L_0$ where b is the effective width of the instrumental window (Fig. 9.11),

$$\frac{\lambda}{d\lambda}=\frac{\tan\theta}{d\theta}=\frac{\tan\theta}{\sigma}. \tag{9.10}$$

Thus, the resolving power is large if σ is small. Note that $\lambda/d\lambda=E/|dE|$.

To see the effect of other parameters, consider the situation where the lines are recorded at a distance L from the crystal, and the X-rays penetrate a small distance t in the crystal (Fig. 9.11). From the diagram,

$$AD=AB+BD=b+EG\sin 2\theta=b+2t\cos\theta.$$

Suppose that we wish to resolve λ and $\lambda+\Delta\lambda$. When the crystal is rotated $\Delta\theta$, the beam is rotated $2\Delta\theta$. From (9.6), we have $2D\cos\theta\,\Delta\theta=n\Delta\lambda$. The two images will not overlap; they will be just resolved, if $L\,2\Delta\theta>b+2t\cos\theta$, or

$$\Delta\lambda>(d/nL)\cos\theta\,(b+2t\cos\theta). \tag{9.11}$$

Clearly, the resolving power is large when $\Delta\lambda$ is small, or when L is large, b is small, and t is small. The effect of geometrical factors on Bragg-spectrometer measurements has been fully discussed by *Thomsen* [9.15].

The plane crystal is made to oscillate so that several wavelengths of interest present in the divergent X-ray beam can be simultaneously recorded. Another advantage is that the effect of lattice defects is partly obliterated because the

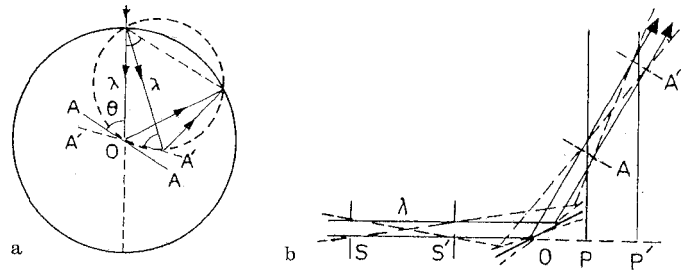

Fig. 9.12. a Parafocusing. **b** Parafocusing in the method of displacement. S and S' are collimating slits which are given the same width and the crystal oscillates about O. Distances are such that $OA=OS'$, $OA'=OS$, $SS'=AA'$, $OP=OS'\cos 2\theta$, and $PP'=AA'\cos 2\theta$, where θ is the Bragg angle for λ. The two lines of a given λ are recorded with identical widths

whole crystal surface participates in the reflection of a line. The rays of wavelength λ that enter through the slit in a divergent beam strike the rotating crystal at the Bragg angle θ. The reflected rays will cross the circle through the slit at one and the same point regardless of the position of the crystal at the moment of reflection (Fig. 9.12a). This is called *Bragg–Brentano parafocusing*. The term parafocusing was used by *Brentano* [9.16] to distinguish it from true optical focusing, which can be obtained only by bending the crystal. Here we get successive, rather than simultaneous, diffraction of a number of rays to one place, and there is no gain in the instantaneous measured intensity.

Parafocusing can be used with advantage in the method of displacement (Fig. 9.12b).

Two slits, each of width $b=0.1$ mm, separated by $l=1000$ mm, give an angular width of about $b/(\frac{1}{2}l)\simeq 40''$. This provides enough resolution for separating the Cu $K\alpha_1\alpha_2$ doublet ($\Delta\lambda\sim 4$XU at $\lambda\simeq 1540$XU). The slits S and S' must be made vertical and the centres aligned on a straight line passing through the spectrometer axis. The crystal surface must also be made vertical and brought on the axis [9.15].

The Bragg equation in terms of the photon energy $h\nu$ is

$$h\nu=hcn/(2d\sin\theta)=(6119.3\text{ eV})\,n/(d\sin\theta), \tag{9.12}$$

where d is in angstroms.

9.5.1 Soller Slit

Consider the diffraction of X-rays from a point source by a large crystal (Fig. 9.13a). The Bragg reflection will occur for all wavelengths between λ_1 and λ_3 as X-rays fall at all angles between θ_1 and θ_3. A slit at A (or B) will collimate the beam and select the desired wavelengths. The beam from a broad sample (Fig. 9.13b) shows divergence both on the θ-plane (also called the horizontal

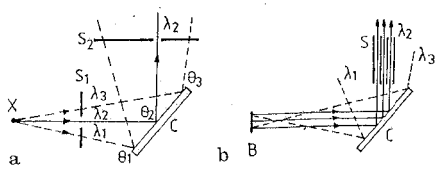

Fig. 9.13a, b. Diffraction of X-rays coming from **a** a point source X (*C*: crystal; S_1, S_2: alternative slit positions), **b** a broad sample *B* (*C*: crystal; *S*: Soller slit system)

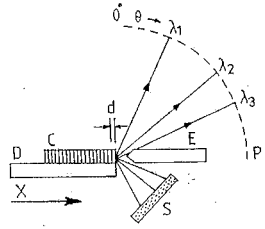

Fig. 9.14. Edge-crystal spectrograph. *X*: radiation, *S*: sample, *P*: photographic film, *E*: limiting edge, *C*: thin crystal (~ 0.1 mm), *D*: shield

plane) and in the perpendicular plane. The latter divergence is tolerated. A *Soller* [9.17] slit reduces the θ-plane divergence. It is a stack of thin parallel plates forming a series of extended slits, in the beam direction, intersecting the θ-plane (Fig. 9.13b). For a 4 in (10 cm) long Soller collimator, consisting of 1 mil (25 μm) thick sheets spaced by 10 mil (250 μm), the divergence is $2(\Delta\theta)=0.3°$, where $\Delta\theta=\arctan(0.01/4)=0.15°$.

9.5.2 Edge-Crystal Spectrograph

The edge-crystal spectrograph is shown in Fig. 9.14 [9.18]. For each secondary wavelength emitted by the sample Bragg reflection occurs from planes parallel to the edge of a thin crystal (~0.1 mm). The width of each spectral line is the projected width of the edge. Each recorded line comes from a different part of the sample.

9.6 Curved-Crystal Spectrograph

Consider a thin crystal section of mica (or quartz) bent so that it becomes part of a cylindrical surface MN of radius of curvature *R* (Fig. 9.15). The figure shows a cross-section of this cylinder perpendicular to its axis. A divergent beam of X-rays from a broad focal spot (for example, a line focus looked at from a side rather than from an end) is incident from above. The radiation is transmitted through the thin bent crystal and diffracted by prominent transverse crystal planes. For simplicity, let us assume that these crystal planes are normal to the surface. This gives the basic geometry of the Cauchois spectrograph. The curved-crystal spectrograph acquired importance and maturity in the research of Professor Mlle Cauchois [9.19].

Consider a wavelength λ in the incident beam, for which the Bragg angle is θ. A ray of this wavelength is incident at point N ($R\cos\phi$, $R\sin\phi$) with polar angle ϕ, and the diffracted ray is NA. Then the equation of the straight line NA that makes an angle $\theta+\phi$ with x axis is given by

$$y=\tan(\theta+\phi)x+c. \tag{9.13}$$

The constant c is determined by the fact that the line passes through the point N ($R\cos\phi$, $R\sin\phi$). The resulting equation of NA is

$$y-\tan(\theta+\phi)(x-R\cos\phi)-R\sin\phi=0. \tag{9.14}$$

As the point of incidence N moves along the arc NM, the angle ϕ varies; the envelope of the diffracted rays is obtained by differentiating (9.14) with respect to ϕ,

$$\cos^{-2}(\theta+\phi)(x-R\cos\phi)+\tan(\theta+\phi)R\sin\phi+R\cos\phi=0. \tag{9.15}$$

This can be solved for x to give

$$x=R\sin\theta\sin(\theta+\phi). \tag{9.16}$$

From (9.16, 14),

$$y=-R\sin\theta\cos(\theta+\phi). \tag{9.17}$$

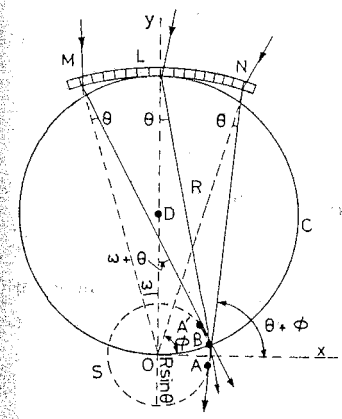

Fig. 9.15. Transmission-type curved-crystal Cauchois spectrograph. *C*: focal circle, *S*: caustic circle, *MLN*: crystal bent to radius *R*

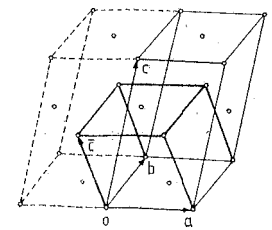

Fig. 9.16. Unit cell of mica. Larger cell ($a=5.18$ Å, $b=9.02$ Å, $c=20.02$ Å, $\widehat{ac}=95°30'$, $\widehat{bc}=\widehat{ab}=90°$) is due to Tschermak. Smaller cell ($c=10.10$ Å, $\widehat{ac}=99°17'$, $\widehat{bc}=\widehat{ab}=90°$) is due to Mauguin and used here. The cleavage face (100) is *ab*

We can combine (9.16, 17) to get

$$x^2+y^2=(R\sin\theta)^2. \tag{9.18}$$

This represents a circle S with centre O and radius $R\sin\theta$. It is called the *caustic circle*.

In practice, the segment MN is small (~ 1 cm) and $R\sim 40$ cm. Therefore, $\phi\sim 90°$ and all of the diffracted rays that correspond to the incident angle θ pass in the immediate neighbourhood (A to A') of point B (Fig. 9.15),

$$x=R\sin\theta\cos\theta, \quad y=R\sin^2\theta. \tag{9.19}$$

There is no sharp focus at B, but the finite angular width of the diffracted rays that overlap here will produce a very great intensity (about a hundred times more than in a plane-crystal spectrograph). This is a great advantage.

We would now like to find the locus of points, defined by (9.19), as the wavelength varies, that is, as θ varies. From (9.19), this locus is found by eliminating θ. It is a circle of radius $R/2$,

$$x^2+(y-\tfrac{1}{2}R)^2=\tfrac{1}{4}R^2, \tag{9.20}$$

whose centre D is given by $x=0$, $y=R/2$. This is the *focal circle* C. If a photographic film is wrapped along this circle, the various wavelengths will be simultaneously focused upon it in an inexact sense. Thus, a wide range of spectrum is recorded without any oscillation or rotation of the crystal. The line would be sharp on the edge at B and somewhat diffuse on the far edge.

Let 2ω be the angular width of the crystal at 0. Coordinates of A are

$$x=R\sin\theta\cos(\theta-\omega), \quad y=R\sin\theta\sin(\theta-\omega), \tag{9.21}$$

and those of A' are

$$x'=R\sin\theta\cos(\theta+\omega), \quad y'=R\sin\theta\sin(\theta+\omega). \tag{9.22}$$

The concentration of rays occurs along the arc AA'. The distance over which we can displace the photographic plate (*depth of focus*) parallel to the y axis is

$$y'-y=R\sin 2\theta\sin\omega. \tag{9.23}$$

Two spectral lines that correspond to the Bragg angles θ_1 and θ_2 subtend an angle $\theta_2-\theta_1$ at L. The linear separation s between them is $s=R(\theta_2-\theta_1)$. Using (9.10), $d\lambda/\lambda=\cot\theta\, d\theta$,

$$ds=Rd\theta, \quad d\lambda/\lambda=(ds/R)\cot\theta,$$

$$ds/d\lambda=(R/\lambda)\tan\theta=nR/(2d\cos\theta). \tag{9.24}$$

For $ds=1$ mm, $d\lambda$ can be calculated in the XU region from this formula.

In Fig. 9.15, the low λ end of the recorded line is at B. The ray MA' hits the film (or C) farthest away from B (towards the right). From (9.19, 22), the horizontal distance between A' and B is

$$x-x'\simeq R\omega\sin^2\theta, \quad (\omega \text{ small}). \tag{9.25}$$

The line is narrow if $x-x'$ is small (that is, ω and θ are small). From geometrical considerations, the line width l (arc length from B to where MA' hits C) is

$$l=\Delta\sin\theta/\cos(\theta+\omega), \tag{9.26}$$

where $\Delta=2R\sin^2(\omega/2)$ is the small radial distance of the bent crystal at N from the focal circle C. It is less than

$$l=2R\sin^2(\omega/2)\tan(\theta+\omega)$$
$$\simeq(\Omega^2/8R)\tan\theta, \tag{9.27}$$

where Ω is the total linear aperture of the crystal.

A sheet of muscovite mica, $(OH)_2KAl_2(Si_3Al)O_{10}$, is easily bent. Its structure (Fig. 9.16) has been discussed by *Clark* [9.20]. The cleavage plane of mica is (001). Planes normally used in curved-crystal spectrographs are listed in Table 9.3. The planes that belong to a zone can be selected by taking a Laue photograph of the mica sheet, aligned with the photographic film (Fig. 9.17). The mica sheet can then be cut with edges perpendicular to the zone axis drawn with the help of Laue spots. These edges are bent along the cylinder of radius R to form the curved crystal. The zone axis is then parallel to the generators of the cylinder defined by the curbed crystal. The various planes (hkl) that belong to the zone axis with indices $[uvw]$ are related by the equation

$$uh+vk+wl=0. \tag{9.28}$$

All of these various (hkl) planes intersect each other on lines parallel to the zone

Table 9.3. Data on muscovite (monoclinic) crystal. F is the structure factor

Zone	hkl	α	d[Å]	F
[010]	$\bar{2}01$	$-5°30'$	2.578	182
[010]	100	$9°17'$	2.556	155
[110]	$\bar{3}31$	$-0°29'$	1.498	276

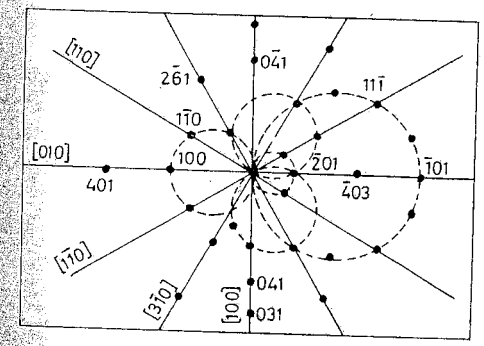

Fig. 9.17. Laue spots of mica obtained by placing the sheet normal to the incident beam. To use, say, (100) planes, cut the aligned mica sheet edges along the line marked [010], which is obtained by joining the (100) spot to the centre. These cut edges are bent to form area of the cylinder

axis and are inclined at different angles α_{hkl} to the planes normal to the surface. The theory given here holds for these planes as well, except that θ must be replaced by $\theta \pm \alpha_{hkl}$. In practice, the crystal holder is rotated an angle $\theta \pm \alpha_{hkl}$ so that the (hkl) plane at L (Fig. 9.15) makes Bragg angle θ with the incident beam. One such setting is shown in Fig. 9.18.

DuMond [9.21] used the Cauchois spectrograph in reverse, with a point source placed on the focal circle. The beam falls on the concave side of the crystal and the transmitted resolved radiation is detected by a Geiger counter, after it passes through a multiplate diaphragm.

In the Johann-type curved-crystal spectrograph [9.22] the divergent X-ray beam is reflected by a system of atomic planes parallel to the curved surface of radius R. The X-rays from a line-focus spot placed on the circle of radius $R/2$ are reflected so as to give a fairly sharp line on the same circle (Fig. 9.19). The principle of this spectrograph easily follows from that of the transmission-type instrument. The crystal-source and crystal detector distances L are the same, $L = n\lambda R/2d = R \sin\theta$. To improve the focusing [9.23], the crystal is ground to a radius of R and then bent to $R/2$. It makes no practical difference if the crystal is first bent to a radius of R and then ground to $R/2$.

Gilberg [9.24] has described a device for bending a thin crystal into a cylindrical form with the curvature of a circle of a logarithimic spiral. The latter gives ideal focusing for one wavelength. *Ehrhardt* et al. [9.25] and *Parker* [9.26] have used a spherically curved crystal. It is produced by placing it on an o-ring at the end of a cylinder and creating a vacuum in the cylinder.

Berreman [9.27] has given a simple dynamical theory of X-ray diffraction in curved crystals. He has also discussed [9.28] the reflectance and efficiency of such crystals.

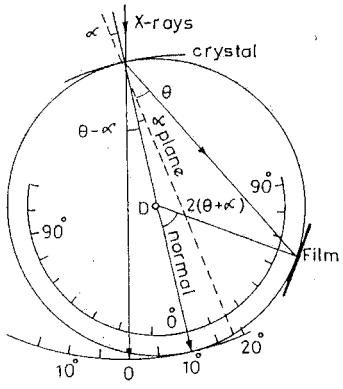

Fig. 9.18. The $(\theta-\alpha)$ setting of the Cauchois spectrograph for the case $\theta > \alpha$

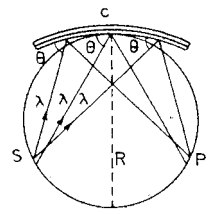

Fig. 9.19. Johann spectrograph. *S*: source, *C*: crystal, *P*: film

9.7 Double-Crystal Spectrometer

The double-crystal spectrometer is an ionization spectrometer in which the incident beam first falls on the crystal A, and then on the crystal B. The theory has been developed by *Schwarzschild* [9.29], *Spencer* [9.30] *Laue* [9.31], and *Smith* [9.32]. It has been reviewed by *Compton* and *Allison* [9.33], *Thomsen* [9.15], *Schnopper* [9.34] and *Drahokoupil* and *Fingerland* [9.35] present here only a simple treatment of the basic results. We assume that the effects of tilt of the slit and vertical divergence are negligible.

The two possible settings, *plus position* $(1,1)$ and *minus position* $(1,-1)$ are shown in Fig. 9.20, for the first-order reflections from A and B. In the $(1, 1)$ setting the incident ray and the ray reflected from B lie on the same side of the ray between A and B, whereas in the $(1, -1)$ setting they lie on opposite sides and A is paralle to B for $\beta = 0$.

Consider a characteristic wavelength λ_0 corresponding to the peak position of a line in the incident radiation. Let $J(\lambda-\lambda_0)d\lambda$ be proportional to the intensity of X-rays between λ and $\lambda+d\lambda$. The function J thus gives the distribution of energy in the incident spectrum; for a line it can be approximated by the classic Lorentz form

$$J(\lambda-\lambda_0) = \frac{A}{1+[2(\lambda-\lambda_0)/\Gamma)]^2}, \tag{9.29}$$

where Γ is the linewidth. J is great only in the neighbourhood of λ_0. Let a function $G(\alpha)$ describe the geometry of the instrument, that is, the slit size, the distribution of intensity in the focal spot, etc. Then,

$$\iint G(\alpha) J(\lambda-\lambda_0) d\alpha \, d\lambda \tag{9.30}$$

gives the total power in the incident beam.

Let a cenral ray λ_0 make the correct Bragg angle θ_0 with the first crystal A and the neighbouring wavelength λ make an angle $\theta_0+\alpha$ with the face of the

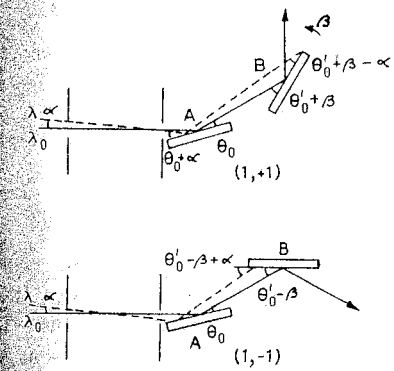

Fig. 9.20. The double-crystal spectrometer settings

crystal A. The correct Bragg angle for λ according to the Bragg law $2d \sin\theta_0 = \lambda_0$, is $\theta_0 + \Delta\theta_0$ where

$$\Delta\theta_0 = (\lambda - \lambda_0) d\theta_0/d\lambda_0 = [(\lambda - \lambda_0)/\lambda_0] \tan\theta_0 . \tag{9.31}$$

The power reflected from the crystal A will be given by a function $R(\delta\theta)$ of the deviation $\delta\theta$ of the actual angle $\theta_0 + \alpha$ from the correct Bragg angle $\theta_0 + \Delta\theta_0$, for the wavelength λ; $\delta\theta = (\theta_0 + \alpha) - (\theta_0 + \Delta\theta_0) = \alpha - \Delta\theta_0$. The *single-crystal diffraction-pattern function* $R(\delta\theta)$ would have its maximum value for $\delta\theta = 0$. The total power in the beam after diffraction from the first crystal A is

$$\iint G(\alpha) J(\lambda - \lambda_0) R(\alpha - \Lambda_0 \tan\theta_0) d\alpha \, d\lambda , \tag{9.32}$$

where $\Lambda_0 = (\lambda - \lambda_0)/\lambda_0$. This result is also applicable to a single-crystal Bragg spectrometer.

Let the ray λ_0 make the correct Bragg angle θ_0' with the second crystal B in the original position (1, 1) or (1, −1), where the prime indicates the angles at the second crystal B; $\theta_0' = \theta_0$. The deviation $\delta\theta'$ of the ray λ for the two settings can be calculated when the second crystal B has been rotated by an angle β (taken positive when counterclockwise) (Fig. 9.20):

(1, 1) *position*

glancing angle of ray $\lambda_0 = \theta_0' + \beta$,

glancing angle of ray $\lambda = \theta_0' + \beta - \alpha$,

$$\delta\theta_+' = (\theta_0' + \beta - \alpha) - (\theta_0' + \Delta\theta_0') = \beta - \alpha - \Lambda_0 \tan\theta_0' . \tag{9.33}$$

(1, −1) *position*

glancing angle of ray $\lambda_0 = \theta_0' - \beta$,

glancing angle of ray $\lambda = \theta_0' - \beta + \alpha$,

$$\delta\theta_-' = -\beta + \alpha - \Lambda_0 \tan\theta_0' . \tag{9.34}$$

We can combine the two results as

$$\delta\theta_\pm' = \pm\beta \mp \alpha - \Lambda_0 \tan\theta_0' , \tag{9.35}$$

where the upper sign is for the plus position and the lower sign is for the negative position.

The power reflected by the second crystal B can now be written as

$$P(\beta) = \int_{\lambda_{\min}}^{\lambda_{\max}} \int_{-\alpha_m}^{\alpha_m} G(\alpha) J(\lambda - \lambda_0) R(\alpha - \Lambda_0 \tan\theta_0) \times R'(\pm\beta_+^- \alpha - \Lambda_0 \tan\theta_0') d\alpha \, d\lambda , \tag{9.36}$$

where the limits of λ are determined by the limits of wavelengths reflected by A, which depend on the horizontal divergence of the incident beam. If the limiting slits are rectangular apertures of equal width w separated by the distance L, then $\alpha_m = w/L$. Equation (9.36) is the general equation of the instrument. We can

deduce from it the properties of different types of *rocking curves* under suitable assumptions. A rocking curve is an ionization-versus-position curve obtained by rotating the second crystal B about its own axis. We shall assume the reflection coefficient R to be the same function of the angle of reflection for each crystal, $R = R'$.

An expression for the *dispersion* can be obtained by assuming that a perfectly discrete Bragg angle θ exists for any incident wavelength λ. Then the contribution to $P'(\beta)$ would occur from only that portion of the beam that has zero deviation from the correct Bragg angle, $\delta\theta = 0$. Thus,

$$\alpha - \Lambda_0 \tan\theta_0 = 0, \quad \text{(for } A\text{)}, \tag{9.37}$$

$$\pm\beta \mp \alpha - \Lambda_0 \tan\theta_0' = 0, \quad \text{(for } B\text{)}. \tag{9.38}$$

Eliminating α,

$$\beta - \Lambda_0 (\tan\theta_0 \pm \tan\theta_0') = 0. \tag{9.39}$$

The dispersion D of the double-crystal spectrometer when crystal B alone is rotated is defined as $d\beta/d\lambda$,

$$D_\pm = \frac{d\beta}{d\lambda} = \lambda_0^{-1} (\tan\theta_0 \pm \tan\theta_0') . \tag{9.40}$$

Obviously, $D_+ \neq 0$ and $D_- = 0$, and therefore the minus position is a case of zero dispersion. For the Mo $K\alpha_1$ line $D_+ \simeq 68.57$ (angle in s/XU), which is twice the value for a single-crystal spectrometer. $D_- = 0$ is a useful property.

9.7.1 The Case of Zero Dispersion (Minus Position)

In (9.36), $R(\alpha - \Lambda_0 \tan\theta_0)$ is large when the deviation from the Bragg angle is negligible, $\alpha - \Lambda_0 \tan\theta_0 \simeq 0$. Thus, the action of A is to separate the beam into monochromatic parallel bundles (Fig. 9.21a). Similarly, $R(-\beta + \alpha - \Lambda_0 \tan\theta_0')$ is large when $\beta \simeq \alpha - \Lambda_0 \tan\theta_0'$ for the crystal B. From the condition on A, we conclude that $\beta \simeq 0$, for the (1, −1) setting, for a large value of $P(\beta)$. Thus, the effective range of β is very small. The limits of λ integration are determined by $\lambda_\pm = \lambda \pm \alpha_m \, d\lambda_0/d\theta_0 = \lambda_0 \pm \alpha_m \lambda_0 \cot\theta_0$.

From the condition on A, we can write $G(\alpha) = G(\Lambda_0 \tan\theta_0)$. Also, because the important values of α lie very close to $\Lambda_0 \tan\theta_0$, that is, in a range that is too

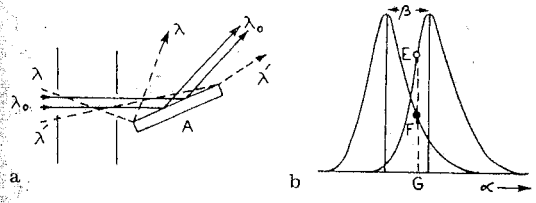

Fig. 9.21. **a** Action of crystal A. **b** Overlap of $R(l)$ and $R(l - \beta)$

small compared to the range $2\alpha_m = 2w/L$, we can extend the limit of α integration to $\pm\infty$ without affecting the value of the integral. For the minus (parallel) setting $R = R'$ and $\theta_0 = \theta_0' = \theta$. Therefore, (8.25) becomes

$$P(\beta) = \int_{\lambda_-}^{\lambda_+} G(\Lambda_0 \tan\theta) J(\lambda-\lambda_0) d\lambda \int_{-\infty}^{+\infty} R(l) R(l-\beta) dl$$

$$= K \int_{-\infty}^{+\infty} R(1) R(l-\beta) dl, \tag{9.41}$$

where K is a number, $\lambda_\pm = \lambda_0 \pm \alpha_m \lambda_0 \cot\theta$, and we have replaced the variable α by the new variable $l = \alpha - \Lambda_0 \tan\theta$, $dl = d\alpha$.

The properties of the overlap integral (9.41) can be studied graphically. In Fig. 9.21 we show plots of $R(l)$ and $R(l-\beta)$ as functions of 1 for a given β. The two curves have the same shape but $R(l-\beta)$ is displaced relative to $R(l)$. The integrand for any given l is given by the product of the ordinates of the two curves, for example, GF and GE. If a series of these products is plotted against the corresponding values of α, the area under the resulting curve would give the value of the integral for the given β. Clearly, it has a peak at $\beta = 0$ (the two curves coincide) and falls off *symmetrically* as $|\beta|$ increases, $P(\beta) = P(-\beta)$. This is an important property of the rocking curve and can be verified from consideration of Fig. 9.21 or by use of the theorem

$$\int_{-\infty}^{+\infty} F(x) dx = \int_{-\infty}^{+\infty} F(x-a) dx, \quad a = \text{const.} \tag{9.42}$$

for F finite and continuous everywhere. Thus,

$$P(\beta) = K \int_{-\infty}^{+\infty} R(l) R(l-\beta) dl = K \int_{-\infty}^{+\infty} R(l+\beta) R(l) dl = P(-\beta). \tag{9.43}$$

The power incident on the second crystal B can be written as

$$K \int_{-\infty}^{\infty} R(l) dl. \tag{9.44}$$

We use this as a normalization factor, and write

$$P(\beta) = \int_{-\infty}^{\infty} R(l) R(l-\beta) dl \Big/ \int_{-\infty}^{\infty} R(l) dl. \tag{9.45}$$

The intensity of an unpolarized X-ray beam can be considered as the sum of two equal parts of the independent components in the two directions of polarization. For unpolarized incident radiation, therefore, (9.45) becomes

$$P(\beta) = \frac{\int_{-\infty}^{\infty} [R_\sigma(l) R_\sigma(l-\beta) + R_\pi(l) R_\pi(l-\beta)] dl}{\int_{-\infty}^{\infty} [R_\sigma(l) + R_\pi(l)] dl}. \tag{9.46}$$

where the suffix $\sigma(\pi)$ indicates that the electric vector is perpendicular (parallel) to the plane of incidence.

For a perfect crystal with negligible absorption, Darwin found that the angular widths of R curves, and so the areas under them, are related as [8.28]

$$\int_{-\infty}^{\infty} R_\pi(l) dl = \cos 2\theta \int_{-\infty}^{\infty} R_\sigma(l) dl. \tag{9.47}$$

We shall now consider how the area of the double-reflection curve, the integral of $P(\beta)$ with respect to β, written as $P_D = \int P(\beta) d\beta$, is related to the integrated reflection from the single crystal. Let us introduce a new variable γ such that $\beta = l - \gamma$, $d\beta = -d\gamma$. Then for either integral in the numerator of (9.46),

$$\int_{-\infty}^{\infty} \int_{-\infty}^{\infty} R(l) R(l-\beta) dl\, d\beta = \int_{-\infty}^{\infty} \int_{\infty}^{-\infty} R(l) R(\gamma) dl (-d\gamma)$$

$$= \int_{-\infty}^{\infty} \int_{-\infty}^{\infty} R(l) R(\gamma) dl\, d\gamma = \left[\int_{-\infty}^{\infty} R(l) dl \right]^2.$$

Thus,

$$P_D = \int_{-\infty}^{\infty} P(\beta) d\beta = \frac{\rho_\sigma^2 + \rho_\pi^2}{\rho_\sigma + \rho_\pi} = \frac{1+\cos^2 2\theta}{1+\cos 2\theta} \rho_\sigma,$$

where

$$\rho_\sigma = \int_{-\infty}^{\infty} R_\sigma(l) dl, \quad \rho_\pi = \int_{-\infty}^{+\infty} R_\pi(l) dl = \cos 2\theta\, \rho_\sigma$$

are the integrated reflections from the single crystal for the respective polarizations, σ, π. For the unpolarized radiation, define $\rho_D = (\rho_\sigma \times \rho_\pi)/2 = (1 + \cos 2\theta)\, \rho_\sigma/2$, so that

$$P_D = \frac{2(1+\cos^2 2\theta)}{(1+\cos 2\theta)^2} \rho_D, \tag{9.48}$$

in Darwin's approximation. From (9.48), ρ_D can be calculated from the area of the observed rocking curve, and compared with Darwin's theory [9.36–38].

For $\beta = 0$, the numerator in (9.46) becomes $(1 + \cos 2\theta) \int [R_\sigma(l)]^2 dl$ and

$$P(\beta = 0) = \frac{\int_{-\infty}^{\infty} [R_\sigma(l)]^2\, dl}{\int_{-\infty}^{\infty} R_\sigma(l) dl} = \frac{32/15}{8/3} = \frac{4}{5}, \tag{9.49}$$

in Darwin's theory. Because $P(\beta = 0)$ is the peak value of the symmetrical rocking curve, it can be compared with the theoretical value 4/5.

The $(1, -1)$ setting is characterized by zero dispersion, and so by economy of X-ray energy. For illustration, we consider Cu $K\alpha_{1,2}$ lines. $K\alpha_2$ is at a slightly longer λ and has half the intensity of $K\alpha_1$. If α_1 has found a spot at which to

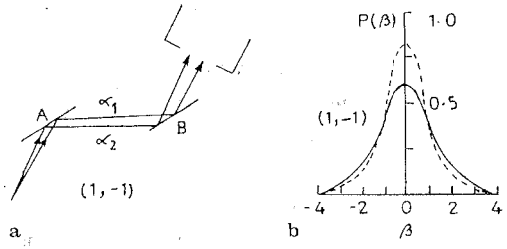

Fig. 9.22. **a** The (1, −1) position, $D = 0$. **b** A typical rocking curve (dotted: calculated, solid: observed)

reflect from A and therefore also from B (parallel to A), there is also a spot at which α_2 can reflect from A and B and enter the detector (Fig. 9.22a). Thus, α_1 and α_2 and all nearby wavelengths are simultaneously recorded by the detector. Consequently, a strong but single peak is obtained in the rocking curve (Fig. 9.22b). The observed peak shape and height can be made to approach the theoretical curve by polishing and etching the crystals A and B. A convenient graphical method due to *Du Mond* [9.39] can be used to analyze the problem without using the integrals.

9.7.2 The Case of Non-zero Dispersion (Plus Setting)

For the (1, 1) setting, we get from (9.36), with $\theta_0 = \theta_0' = \theta$ and $R = R'$,

$$P(\beta) = \int_{\lambda_{\min}}^{\lambda_{\max}} \int_{-\alpha_m}^{\alpha_m} G(\alpha)\, J(\lambda - \lambda_0)\, R(\alpha - \Lambda_0 \tan\theta)\, R(\beta - \alpha - \Lambda_0 \tan\theta)\, d\alpha\, d\lambda. \tag{9.50}$$

For the reflection to be strong, we must have

$$\alpha \simeq \Lambda_0 \tan\theta, \quad \text{(for } A\text{)}, \tag{9.51}$$

$$\beta \simeq \alpha + \Lambda_0 \tan\theta \simeq 2\Lambda_0 \tan\theta, \quad \text{(for } B\text{)}. \tag{9.52}$$

Thus, unlike the (1, −1) case, in this case β has a large effective range.

The assumption $\theta_0 = \theta_0' = \theta$ means that the crystal B is positioned so that $K\alpha_1$ from the crystal A strikes B at the proper Bragg angle for reflection. However, $K\alpha_2$ requires a larger angle than does $K\alpha_1$; it leaves A at a large angle, and arrives at B at a smaller angle than the correct Bragg angle for $K\alpha_2$ (Fig. 9.23). Consequently, we must rotate B from the $K\alpha_1$-reflection position to

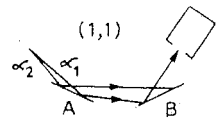

Fig. 9.23. The (1, 1) position, $D \neq 0$

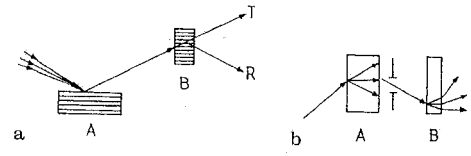

Fig. 9.24. **a** Bragg–Laue scheme. Symmetrical reflection with the same indices in crystal A (Bragg) and B (Laue). **b** Laue–Laue scheme. Crystal A is thick, with anomalous transmission of X-rays (Borrmann effect)

find the $K\alpha_2$-reflection position. (In the minus setting the conditions for α_1 and α_2 reflections were simultaneously satisfied.) The resulting high resolution of the double-crystal spectrometer makes it a very useful instrument.

The spectrometer was improved as follows:

(1) Use of the Bragg–Laue scheme (Fig. 9.24a) and Laue–Laue scheme [9.40, 41].

(2) Three-crystal spectrometer suggested by *Du Mond* [9.39] and developed by *Renninger* [9.42] and *Bubakova* et al. [9.43].

(3) Use of asymmetrical arrangement in different schemes [9.44].

(4) Double-crystal spectrometer in the Laue–Laue scheme with the use of the Borrmann effect in the first crystal (Fig. 9.24b) [9.45] *Borrmann* [9.46] has shown that a perfect crystal can provide anomalously high transmission for a portion of the internally reflected beam. All these cases have been discussed by *Pinsker* [9.47].

9.8 Use of Ruled Gratings

The discovery of total reflection of X-rays made it possible to measure wavelengths by use of ruled gratings provided that the glancing angle $\theta < \theta_c$. Such measurements are free from the uncertainties of determination of interplanar spacings in crystals. *Compton* and *Doan* [9.48] were the first to obtain a spectrum with a metal grating; it had 50 lines mm^{-1}. Gratings with 200 lines mm^{-1} gives improved results. *Thibaud* [9.49] obtained the K spectrum of Cu with a ruled grating.

If d is the grating constant (Fig. 9.25a), the grating equation is

$$n\lambda = d[\cos\theta - \cos(\theta + \alpha_n)] = 2d \sin\tfrac{1}{2}\alpha_n \sin\tfrac{1}{2}(2\theta + \alpha_n). \tag{9.53}$$

A grating with 1200 lines mm^{-1} has $d = 8333$ Å. For the carbon $K\alpha$ line (44.4 Å), $\theta = 0.75°$ and $\theta + \alpha_1 = 6.3°$. Here n can be negative, with the corresponding glancing angles of diffraction lying between the plane of the grating and the totally reflected ray. However, the negative-order spectra are weak. *Eckart* [9.50] has given a general derivation of the grating equation. Gratings may have symmetrical (V-shaped) grooves or grooves with a saw-tooth shape (blazed).

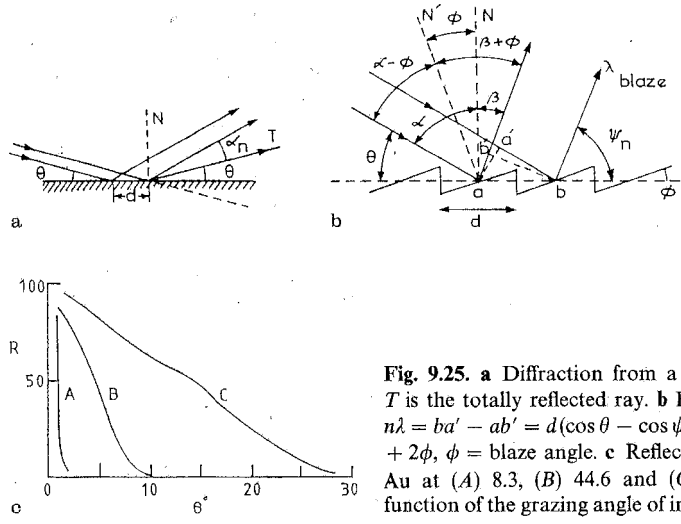

Fig. 9.25. a Diffraction from a ruled grating. T is the totally reflected ray. **b** Blazed grating: $n\lambda = ba' - ab' = d(\cos\theta - \cos\psi_n)$, $\psi_n = \theta + 2\phi$, ϕ = blaze angle. **c** Reflectance $R(\%)$ of Au at (A) 8.3, (B) 44.6 and (C) 114 Å as a function of the grazing angle of incidence [9.53]

Recently, blazed replica gratings have been widely used in the region 20 Å $< \lambda <$ 100 Å. Figure 9.25 shows the cross-section of a blazed grating. Let N be the normal to the macroscopic surface of the grating and N' to the groove face of blaze angle ϕ. The blaze angle is selected so that the wavelength of interest is diffracted in a direction that coincides with the direction of the specularly reflected beam from the surface of the facet, for greater intensity. The condition for this specular reflection is $\alpha - \phi = \beta + \phi$ (Fig. 9.25b), where $\alpha(\beta)$ is the angle of incidence (diffraction). Therefore, $\beta = \alpha - 2\phi$ and $n\lambda = d(\sin\alpha - \sin\beta) = d[\sin\alpha - \sin(\alpha - 2\phi)] = d(\cos\theta - \cos\psi_n)$, where $\psi_n = \theta + 2\phi$. The use of gratings in X-ray spectra has been discussed in detail by *Cuthill* [9.51]. A hard X-ray spectrometer has been discussed by *Franks* et al. [9.52].

From (3.44, 45, 50), for total reflection ($\theta' = 0$) case, we get $\cos\theta = 1 - (e^2 n\lambda^2/2\pi mc^2)$, or using $1 - \cos\theta = 2\sin^2(\theta/2)$ and $2\sin(\theta/2) \simeq \sin\theta$,

$$\sin\theta_c = (ne^2/\pi mc^2)^{1/2}\lambda, \tag{9.54}$$

where θ_c is the grazing angle of incidence and n the number of electrons per unit volume. For a given λ, total reflection occurs at all grazing angles up to a certain maximum θ_c at which the reflectance drops rapidly. Conversely, for a given grazing angle of incidence, λ in (9.54) gives the minimum totally reflected wavelength,

$$\lambda_{\min}[\text{Å}] = (3.33 \times 10^{14})\, n^{-1/2} \sin\theta.$$

For glass $n = 78 \times 10^{22}$, and so $\lambda_{\min}[\text{Å}] = 6.6\,\theta°$. For gold $n = 466 \times 10^{22}$ and $\lambda_{\min}[\text{Å}] = 154 \sin\theta$. Observed reflectance of Au [9.53] at 8.3, 44.6 and 114 Å as a function of grazing incidence angle is shown in Fig. 9.25c.

9.9 Detectors

In general, we have, in X-ray spectroscopy, *wavelength-dispersive* and *energy-dispersive* instruments. Former devices (spectrometer), even if equipped with a position-sensitive detector, only measure a small portion of the spectrum. The energy-dispersive detectors usually measure the whole X-ray spectrum simultaneously.

Röntgen detected X-ray for the first time with a fluorescent screen coated with barium platinocyanide. He also was the first to use photographic films for recording X-rays.

X-ray detectors are mainly of three kinds: 1) photographic films, 2) ionization detectors, and 3) solid-state detectors. We shall briefly discuss them here.

Detection can be made after the usual crystal dispersion, or the undispersed beam can be detected and electronic dispersion applied to the output of the detector. In the latter case, the detector itself takes part in the electronic dispersion. Electronic detectors are, these days, usually *digital* (photon counters). These energy-dispersive detectors come in three types: gas-filled counters, scintillation detectors and solid-state devices.

9.9.1 Photographic Films

Double-coated films, or single-emulsion films, can be used. When an X-ray beam is incident at an oblique angle on a double-coated film, two images, which are slightly displaced with respect to each other, are formed. Therefore, it is usual to remove the far-side emulsion before measuring lines.

Photographic emulsion is a colloidal suspension of small grains of silver bromide in gelatin. The emulsion layer is about 15 μm thick with a protective gelatin layer, about 1 μm thick, coated over it. The X-ray film base is about 200 μm thick.

The action of an X-ray photon is to free electrons from the bromide ions. These electrons tend to collect in regions of the crystals known as "electron traps". The excess negative charge in the traps neutralizes adjacent silver ions, which are thereby converted to uncharged silver atoms. Those atoms form a "latent image", which acts as a catalyst for development. The developer increases the size of such metallic-silver particles many millions of times. Overdevelopment produces "fog", because the developer tends to reduce unexposed silver bromide as well.

9.9.2 Gas-Filled Detectors

Usually, an argon-filled detector is ued to detect X-rays. It takes about 30 eV to create an electron-ion pair in Ar, $Ar + h\nu \rightarrow Ar^+ + e^-$. The theoretical ionization potential of Ar is 15.8 eV. Due to the finite range of particles the effective value is 26.4 eV for producing an ion pair ($Ar^+ + e^-$). The number n of primary ions

produced is given by

$$n = E_v / V_i , \tag{9.55}$$

where E_v is the X-ray photon energy and V_i the effective ionization potential. An X-ray photon of $\lambda = 1$ Å has an energy of 12,400 eV. Therefore, for each photon absorbed by the gas, about 400 electron-ion pairs are formed. If there is no applied voltage on the enclosed gas, the liberated electrons and ions tend to recombine. On the other hand, if a metal wire, centrally mounted in a metal cylinder (Fig. 9.26a), is made about 100 V positive relative to the cylinder, the electrons are rapidly swept toward the positive wire anode, whereas the heavy ions move slowly toward the negative envelope. This prevents recombinations, and an electric current, proportional to the number of photons absorbed, is produced in the recording circuit. The detector used in this way is said to be an *ionization chamber*. Argon gas at a pressure of about 75 cm Hg is used for $\lambda > 1$ Å. Other useful gases are CH_3I, CH_3Br and krypton at about 20 cm Hg or less for $\lambda < 1$ Å. When the photon energy is greater than absorption-edge energy of the counter gas, characteristic radiation will be produced from the gas, which will produce an additional "escape" peak that may interfere with measurements.

The number of electron-ion pairs can be increased by increasing the voltage on the wire. When the voltage exceeds approximtely 300 V, each electron liberated by the absorbed photon acquires enough kinetic energy by acceleration so as to be able to produce, in turn, new electron-ion pairs, by collision with gas atoms. This amplification factor or gas gain A is proportional to the applied voltage V in the range $300 < V < 900$ V. If n is the number of electron-ion pairs formed by each photon absorbed, then in the proportional region $N = An$ electrons reach the wire, such that

$$A = N/n = N(V_i/E_v). \tag{9.56}$$

Individual electrical pulses can be measured if the photons come at reasonable intervals. The ionization detector (Fig. 9.26) used in this voltage range is called a

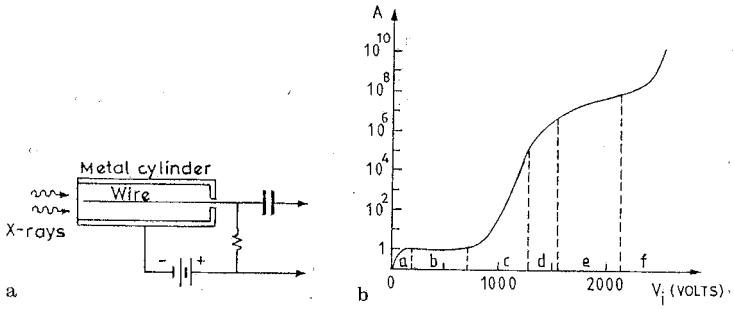

Fig. 9.26. **a** Ionization detector. **b** Plot of the gas gain factor A as a function of applied potential V_i for the gas-filled detector. The various regions are *a* (region of unsaturation), *b* (ionization chamber), *c* (proportional counter), *d* (limited proportionality), *e* (Geiger counter), *f* (discharge)

proportional counter, because the magnitude of the electrical pulses, detected for each X-ray photon absorbed, is proportional to the energy $h\nu$ of the X-ray photon. Gains up to 10^6 are achieved.

If the voltage is increased to about 1 kV or more, an "avalanche effect" is triggered which gives a much increased value of A. This avalanche spreads throughout the counter so rapidly (about 1 μs) that almost the same-size pulse is formed by any absorbed X-ray photon, regardless of its energy. It now works as a *Geiger–Müller counter*. A gain of 10^9 is possible in this region.

Figure 9.26b shows the gas gain as a function of detector potential. The various regions of operation are indicated. In the region *a* the potential difference is not enough to stop recombination of the ion pairs and the gain $A < 1$. In the ion chamber region *b* the V_i is just able to counteract recombination ($A = 1$). In the proportional region ($A \sim 10^6$) an upper limit is reached due to the space charge effect as the electrons are rapidly collected, the heavy positive ion space-charge sheath gets formed around the wire). In the region *d* of limited proportionality, the proportionality deteriorates. It is not useful for X-ray detection. Beyond the Geiger region ($A \sim 10 \sim 10^8$) continuous corona discharge occurs.

a) *Dead time.* The slow dissipation of the heavy positive ion sheath near the anode reduces the field and so prevents further pulses. There is a recovery time for the detector to reach equilibrium after a pulse is generated, which is called the *dead time* t_D of the counter. It is 1–2 μs for every event, and so reduces the count rate. The measured count rate, or intensity I_m, is lower than the true count rate I_T. The simple dead time equation is

$$I_T = I_m/(1 - I_m t_D). \tag{9.57}$$

It gives *coincidence loss* as X-ray photons are lost (not counted) when they arrive at the detector too soon after the preceding one. For $t_D = 2$ μs at $I_m = 10$ counts/s the loss is 20%. *Beaman* et al. [9.54] have treated the dead time correction in detail. For $I_m t_D < 0.1$, the term $(1 - I_m t_D)$ approximates the series expansion of Beaman's exponential term.

Various ways of measuring the dead time are known. The K_α/K_β ratio method of *Birks* [9.55] is simple. Conditions are set to give $K\alpha$ intensity of $I_\alpha \sim 1000$ counts/s. The intensity of $K\beta$ is then $I_\beta \sim 200$ counts/s. Dead time losses are negligible at these intensities. The X-ray excitation is now increased in the same element to give $I'_\beta \sim 1000$ counts/s and I'_α is also measured. The I'_β is still free of dead time loss, so that $I'_{\beta T} = I'_{\beta m}$. As I'_α is in the region of dead time loss, the true $K\alpha$ intensity is given by

$$I'_{\alpha T} = I_\alpha (I'_\beta / I_\beta). \tag{9.58}$$

The t_D is now given by (9.57), using the true and measured I'_α intensities.

b) *Counter resolution.* The pulse amplitude from the proportional counter shows a nearly Gaussian spread over energy [9.56, 57]. A Gaussian distribution is drawn for the frequency of occurrence of a quantity x with a peak at the mean

value $\bar{x}$ of x. The standard deviation σ is the rms deviation of a limited set of measurements n from $\bar{x}$, with FWHM $= 2\,(2\ln 2)^{1/2}\,\sigma = 2.35\,\sigma$. For a single measurement of n counts, $\sigma = \sqrt{n}$. The FWHM gives the resolution. In X-ray literature, a *relative resolution* R is defined by

$$R = [2.35\sqrt{n}/n] \times 100$$
$$= 235/\sqrt{E_v/V_i}\,(\%). \tag{9.59}$$

For an argon counter $V_i = 0.0264$ keV, and $R = (38.3/\sqrt{E_v})\%$. It is usually written as

$$R = 235\sqrt{FE_vV_i}/E_v\,(\%), \tag{9.60}$$

where F is the Fano factor [9.58], which corrects the theoretical σ to agree with measurements ($F \sim 0.125$). The term $\sqrt{E_vV_i}$ is the FWHM to be expected for a Gaussian distribution of E_v/V_i ion pairs. The Fano factor reduces this value. Experiments [9.59–61] agree with the $R \propto E_v^{-1/2}$ variation. Essentially $R = [\mathrm{FWHM}/E_v] \times 100$, where E_v corresponds to the voltage of the pulse amplitude maximum.

For two X-ray photon energies E'_v and E''_v

$$R'/R'' = (E''_v/E'_v)^{1/2} = (\lambda'/\lambda'')^{1/2}. \tag{9.61}$$

c) *Escape peak.* The general expression for the *amplitude* of a pulse V, corresponding to a photon of energy E_v (wavelength λ), is

$$V = (E_v/V_i)A_gA_eL^{-1}, \tag{9.62}$$

where $A_g(A_e)$ is the gas (electronic) amplification factor, and L is the sum of the attenuation stages introduced to bring the pulse size in the range of scaling circuits. Note that $V \propto E_v$.

When E_v is greater than the absorption edge energy of the counter gas, two pulses occur with

$$V \propto E_v,$$
$$V_{\mathrm{escape}} \propto E_v - E(\mathrm{Ar}\,K\alpha), \tag{9.63}$$

where $E(\mathrm{Ar}\,K\alpha)$ is the energy that has been lost if Ar is the ionizable gas (atoms have low absorption for their own characteristic radiation). The Ar $K\alpha$ radiation produced in the counter escapes without detection. Although $V_{\mathrm{escape}}/V < 1$, the escape peaks at $E_v - E_v(\mathrm{Ar}\,K\alpha)$ can interfere with measurements [9.62]. For example, interference occurs between P $K\alpha$ and the Ca $K\beta$ escape peak (Fig. 9.27). The photo-pulses from Ca $K\beta$ can be removed by the method of pulse height selection, but the escape pulses continue to interfere.

d) *Gas flow proportional counter.* For light elements the detector window material absorbs too much of the radiation. Therefore, a flow proportional counter [9.63] has been developed. Its principle is the same as that of the sealed

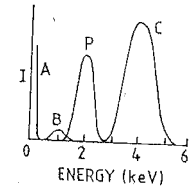

Fig. 9.27. Escape peak interference. *A*: Noise due to general electron vibration in the amplifier circuit; *B*: Ca escape peak; *P*: P $K\alpha$; *C*: Ca $K\beta$

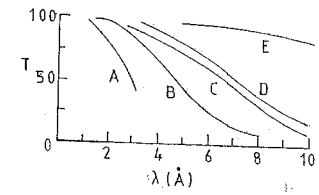

Fig. 9.28. Transmission T[%] of a few typical X-ray detector window materials. *A*: 12 μm mica *B*: 2.5 μm Al; *C*; 25 μm Be; *D*: 6 μm Mylar (polyethylene terephthalate); *E*: 1 μm propylene

counter, except that now it is fitted with a very thin entrance window. The usual gas mixture used is P.10 gas (90% Ar + 10% CH_4). As gas can leak through a thin window, the gas is allowed to flow through the detector. The relative transmission of different window material is shown in Fig. 9.28. For $\lambda > 20$ Å one can use collodion supported on a frame.

Consider a Xe-filled proportional counter. Suppose two X-ray lines reach it simultaneously. Let them be Sc $K\alpha$ (4.09 keV) and (Cu $K\alpha$ (8.04 keV). For Xe, $V_i \simeq 20$ eV, and so the number of ion pairs generated per photon is $n = E_v/V_i \simeq E_v/0.02$, that is, 200 for Sc and 400 for Cu. The statistical spread σ is $\sqrt{n}$, that is, 14 for Sc and 20 for Cu. The relative resolution (9.59) is $R = 235/\sqrt{n}$, that is, 17% for Sc and 12% for Cu. The height of each pulse is determined by (9.62). If all the variables except E_v are kept constant, the phonon energy determines the pulse height. Thus

$$V_{\mathrm{Sc}}/V_{\mathrm{Cu}} = E_v(\mathrm{Sc}\,K\alpha)/E_v(\mathrm{Cu}\,K\alpha).$$

All these features are displayed in Fig. 9.29. The number of pairs created (or the total charge released) is proportional to the energy of the detected photon.

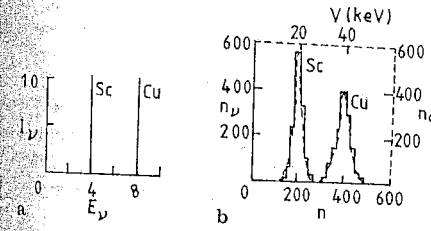

Fig. 9.29. a Incident intensity I_ν (photons/s) of X-ray lines at E_ν [keV] = 4.09 and 8.04. **b** Number of photons n_ν producing n ion pairs (s^{-1}) plotted against ion pairs n produced per photon (solid line); dashed scale and curves: distribution impulse amplitude after amplification, that is, number of pulses per second, n_c [counts/s] as a function of pulse height, V [volts]. The integrated intensities (areas under the peaks are essentially the same

9.9.3 Scintillation Counter

Phosphor-coated screens have been used since the early days to detect X-rays. The X-ray energy is converted into visible light by the process of fluorescence. Zinc calcium sulphide fluoresces at about 5300 Å, at which wavelength the eye has maximum sensitivity.

Pulses of visible light (scintillations) can be produced by X-rays in a single crystal (phosphor, *scintillator*) that is almost transparent to such light. The light pulses can then be amplified with the help of a *photomultiplier*. Such an assembly is called a *scintillation counter* [9.64, 65]. Its sensitivity range is 0.2–2 Å.

An ideal phosphor has high absorption for X-rays, has a visible fluorescence spectrum, and gives the same pulse energy (pulse height) for every quantum of incident monochromatic X-rays. A thallium activated NaI crystal, NaI(Tl), meets these requirements. It is almost exclusively used in scintillation counters. The decay time is $\sim 0.25\ \mu s$. The heavy iodine atoms give high X-ray absorption. The excitation potential of NaI(Tl) being near 3 V, it produces light of about 4100 Å (blue). A photomultiplier with a cesium-antimony photocathode responds well to this wavelength. The phosphor and photomultiplier are optically coupled (Fig. 9.30). Being hygroscopic, NaI(Tl) must be hermetically sealed.

The gain G of the photomultiplier is the number of electrons reaching the anode (collector) for each photoelectron arriving at the first dynode,

$$G = ks^n, \tag{9.64}$$

where k is the first dynode collection efficiency (~ 0.9), s is the secondary emission ratio (3–4), and n is the number of dynodes. A progressively increasing shower of secondary electrons cascades along the multiplier. For $s \approx 4$ and $n = 10$, the gain is 0.9×4^{10} or $\sim 10^6$.

The resolution is poor when compared to the proportional counter. For Fe Kα ($\lambda = 1.937$ Å), the NaI(Tl) phosphor emits photons ($\lambda = 4100$ Å) whose number is $4100/1.937 = 2117$. Assuming a crystal efficiency of 20% and a photomultiplier efficiency of 5%, the effective number of photons is $n = 21.2$. The resolution is $R = 2.35\sigma$ and $\sigma[\%] = 100/\sqrt{n}$, giving $R = 129/\sqrt{E_v}$ for Fe Kα, compared to $38.3/\sqrt{E_v}$ for the proportional counter. The main advantage is that the scintillation counter has almost constant spectral response over a large range. Escape peaks occur when the X-ray photon ejects a K or L iodine atom electron. The I K edge is at 0.37 Å and L_{III} edge at 2.7 Å. The former gives the escape peak for $K\alpha$ lines of elements with $Z > 57$ only.

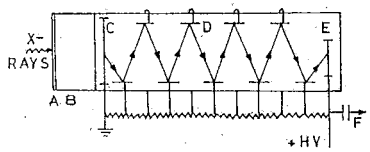

Fig. 9.30. Structure of a scintillation counter. *A*: Be window (0.2 mm thick) coated with Al (1 μm thick) to give opacity (only X-rays enter); *B*: NaI(Tl) crystal; *C*: photocathode (Cs–Sb) produces electrons on receiving blue light; *D*: dynodes, each acting in turn, collect and amplify the electron beam; *E*: anode, where a small current is produced and voltage pulses arise; *F*: signal to preamplifier. Each successive dynode (term for dual function of collection and secondary emission of electrons) is given a higher positive potential by a potential divider. The HV is 600–1000 V

The long wavelength limit (2 Å) of the scintillation counter overlaps with the short wavelength limit (1.5 Å) of the gas flow proportional counter. One can mount the two detectors in tandem (the X-rays pass first through the proportional counter and then through the scintillation counter), to cover the range 0.2–20 Å [9.66].

9.9.4 Semiconductor Detector

An important recent improvement in X-ray intensity measurement is the use of the lithium-drifted silicon, Si(Li), or germanium, Ge(Li), detector. It is a p-i-n type diode. The intrinsic region is formed by diffusion (drifting) of Li into a p-type Si (or Ge) single-crystal semiconductor. The Li compensates charge due to impurities present in any Si single crystal. This increases the intrinsic (sensitive) layer in which X-rays produce electron-hole pairs. It forms the depletion layer of a reversed bias p-i-n junction [9.67–69].

The Si(Li) detector and its operation are shown in Fig. 9.31. When a potential difference (reverse bias) is applied the Li ions penetrate inward. All charge carriers are swept out to the region thus penetrated. The resistivity therefore rises until it acquires pure semiconductor (intrinsic) value. The i region is the sensitive region of the detector over which the electric field strength is virtually constant (Fig. 9.31). When an X-ray quantum ($\lambda = 1$ Å) strikes this region, it creates about $12\,400/3.8 \simeq 3250$ electron-hole pairs in Si(Li), compared to about 400 ion peaks in a gas-filled detector, so the resolution of the Si(Li) detector is superior. These highly mobile charge carriers move rapidly to the electrodes (Fig. 9.31b). They are collected before recombination can take place. The detector is stored and operated at 77 K (liquid nitrogen temperature) to reduce the mobility of Li.

The discussion applies also to p-n junction photodiodes. Si(Li) and Ge(Li) are being replaced by hyperpure germanium, Ge(HP), diodes, which can be stored at room temperature.

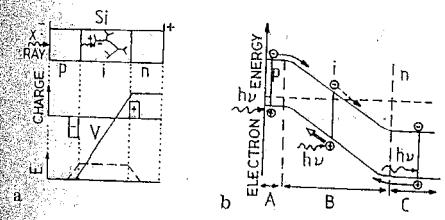

Fig. 9.31. a A p-i-n detector showing space charge, potential and electric field strength. The applied voltage gradient is about 1000 V/m. **b** Energy-band diagram under reverse bias. *A*: Electron diffusion; *B*: draft space; *C*: hole diffusion

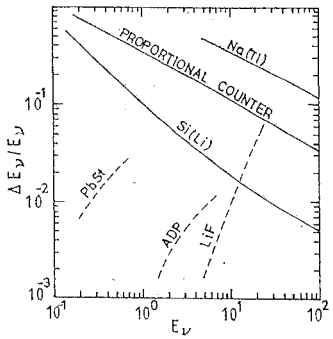

Fig. 9.32. Comparison of energy resolution ($\Delta E_\nu/E_\nu$) as a function of photon energy of various X-ray energy-dispersive detectors and a wavelength dispersive spectrometer with LiF, ammonium dihydrogen phosphate (ADP) and PbSt crystals (respective angular resolutions 1, 2, and 5 mrad). (After [9.70])

The preamplifier noise contributes significantly to the overall resolution of a Si(Li) or Ge(Li) detector,

$$\text{FWHM} = \{\sigma_{\text{noise}}^2 + [2.35(FE_\nu V_i)^{1/2}]^2\}^{1/2}. \tag{9.65}$$

For a small (10 mm^2) detector σ_{noise} is about 100 eV. The relative (energy) resolution is given by FWHM/E_ν or $\Delta E_\nu/E_\nu$. A typical value of the energy resolution is 150 eV at 6 keV X-ray energy (Fig. 9.32).

Recently *Dabrowski* et al. [9.71] have used a mercury-iodide device at room temperature to detect 30 keV X-rays with nearly 100% efficiency.

Quantum efficiency is the number of electron–hole pairs generated per incident photon:

$$\eta = (I_p/q_e)/P_X/E_\nu), \tag{9.66}$$

where I_p is the photogenerated current, q_e the charge, and P_X the absorbed X-ray power at the energy $E_\nu = h\nu$. The quantum efficiency, usually expressed as a percentage, gives the fraction of incident photons that produce pulses of countable pulses. It represents the countable output pulses divided by the number of incident photons, both in the same time interval. It is measured at counting rates at which dead-time (coincidence) loss is negligible. Typical η curves for some common detectors are shown in Fig. 9.33.

The fall in η of the Si(Li) detector at the long wavelength end of the range is due to several factors. The main factors are absorption by the Be window (10–50 μm) and the Si "dead" layer (0.1 μm) at the detector surface before reaching the active volume of the counter. For 20 Å X-rays a 0.1 μm layer of Si will attenuate the signal by a factor of 2. The fall in η at the short wavelength end is due to the finite thickness (3–5 mm) of the diode itself. It absorbs only about 15% of the radiation of $\lambda = 0.2$ Å. The required critical depth of about 8 cm is impracticable for the Li drift process.

A Si(Li) detector diode is made from a cylindrical section of a single crystal of p-type Si. The sensitive volume ranges from 4 to 16 mm in diameter, and 3 to 5 mm in thickness. A smaller diameter gives better energy resolution at low energies. A thicker detector has higher detection efficiency at $E_\nu > 20$ keV.

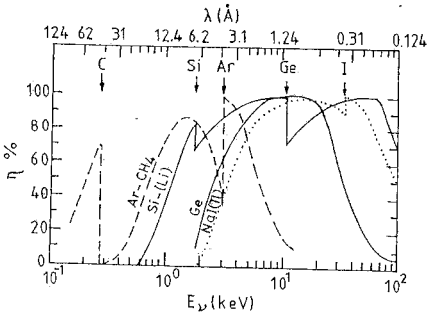

Fig. 9.33. Typical quantum efficiencies η of various X-ray detectors. Full curves: Si(Li) detector (5 mm thick, 7.5 μm Be window), Ge detector (5 mm thick, 127 μm Be window); dashed curve: Ar–CH_4 proportional counter (2 μm polypropylene window); dotted curve: NaI(Tl) scintillation detector (2.54 cm diameter × 0.1 cm deep, 0.005 in. Be window plays reflector). The K absorption edges are marked by arrows. The solid and dashed curves are after [9.70]. The photon energy is given by E_ν[keV] = 12.4/λ[Å]

The number of pairs produced is $n = E_\nu/V_i$, with $V_i = 3.8$ eV. The electrons drift to the positive terminal (Fig. 9.31) where the total charge collected is $Q = nq_e$, $q_e = 1.6 \times 10^{-19}$ C. This terminal is connected to the preamplifier input so that Q is stored in a capacitor C_f. It gives a pulse of amplitude.

$$V_0 = Q/C_f = q_e E_\nu/(V_i C_f). \tag{9.67}$$

The charge collection time is quite short ($\sim$25–100 ns).

Table 9.4. Comparison of X-ray detectors for Cu $K\alpha$ (8040 eV) radiation

Ar-*filled proportional counter*	
Effective ionization potential of Ar	26.4 eV
Number of pairs for Cu $K\alpha$ photon	8040/26.4 = 305
Deviation for Gaussian shape σ	$\sqrt{305} = 17.5$ pairs
FWHM	$2.35\sqrt{305} = 41.3$ pairs
Resolution R	(41.3/305) × 100 = 14%
NaI(Tl) *scintillation counter*	
NaI(Tl) phosphor efficiency	50 eV/(light) photon
Number of light photons per Cu $K\alpha$ photon	8040/50 = 161 photons
Number of photoelectrons emitted (efficiency of photocathode ~0.1)	0.1 × 161 ≃ 16
Deviation for Gaussian shape σ	$\sqrt{16} = 4$ photoelectrons
FWHM	$2.35\sqrt{16} \simeq 9$ photo electrons
Resolution R	(9/16) × 100 ≃ 56%
Si(Li) *detector*	
Energy to make one pair	3.8 eV
Number of pairs per Cu $K\alpha$ photon	8040/3.8 = 2116
Deviation for Gaussian shape σ	$\sqrt{2116} = 46$ pairs
FWHM	$2.35\sqrt{2116} = 108$ pairs
Resolution R	(108/2116) × 100 = 5%

A low-energy peak distortion occurs when a Si(Li) detector is used in X-ray spectrometry. It may be due to incomplete charge collection [9.72, 73]. *Heckel* and *Scholz* [9.74] have recently given a simple model to describe it.

Various X-ray detectors are compared in Table 9.4.

9.10 Energy-Dispersion Spectrometry

The Geiger–Müller counter is unable to distinguish the relative energies of X-rays and so is not of much use in X-ray spectroscopy. Proportional counters or solid-state detectors are commonly employed, because the magnitude of the pulse produced in them is proportional to the energy of the incident photon. This property enables us to use an electronic circuit that transmits only pulses greater than a certain magnitude or "height" and blocks lower-height pulses. Such a *pulse-height discriminator* can be combined with another circuit that transmits only those pulses that are smaller than a given height to form a *single-channel pulse-height analyzer*. In this way, it is possible to detect pulses that are formed by X-rays in a narrow range of energies. This is the principle of *energy-dispersion spectrometry*.

The pulse height selection isolates a moderately narrow range of incident wavelengths by using energy separation as opposed to wavelength separation in crystal dispersion.

Gilfrich et al. [9.75] have compared the wavelength- and energy-dispersive methods. The main advantage of the energy dispersive method is that a crystal is not required and therefore higher orders are absent. Another advantage is a greater economy of intensity by reduction of distance between detector and emitting specimen, increased solid angle of interception, and absence of collimators. The conservation of intensity makes it possible to use radioactive isotope excitation. However, for wavelengths longer than about 0.8 Å (15 keV) the resolution of a Si(Li) energy dispersive spectrometer is poorer than that of a crystal spectrometer. The resolution of an energy dispersive setup using a proportional or scintillation counter is poorer at all wavelengths.

9.10.1 Pulse-Height Selection

The gas-filled proportional counter, NaI(Tl) scintillation counter and Si(Li) solid-state detector are all proportional detectors. The energy E_ν of the incident X-ray photons determines the size of the voltage pulse generated by them. One can thus use the method of selecting only a narrow range of voltage pulses to eliminate unwanted radiation.

The simplified block diagram in Fig. 9.34 shows how the method of pulse height selection works for (say) pulses of three amplitudes. [In a wavelength-dispersive crystal spectrometer the wavelengths are separated prior to detection and so pulse selection is not usually required. It may be required if higher-order spectral lines interfere. For example, first order P $K\alpha$ (6.16 Å), second order

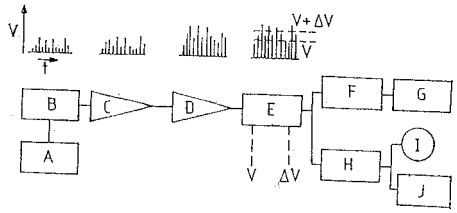

Fig. 9.34. Simplified block diagram of pulse-height selection method. *A*: Detector power supply (0–2 kV); *B*: detector; *C*: preamplifier; *D*: amplifier; *E*: pulse-height analyzer baseline ($V = 0$–100 V, window $\Delta V = 0$–30 V); *F*: scaler; *G*: timer; *H*: ratemeter; *I*: meter; *J*: recorder. The X-ray photons and so the pulses have a random distribution in time

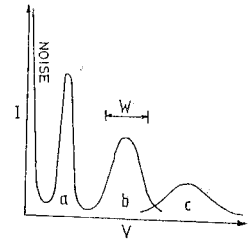

Fig. 9.35. Pulse-height distribution *a*, *b* and *c* for low, medium, and high X-ray photon energies, respectively. *W* is the window (or channel). *I* is intensity (counts/s) and *V* is pulse height

Ca $K\beta$ (3.09 Å) and third order Ga $L\alpha$ (2.05 Å) will satisfy the Bragg law for nearly the same angle θ.] Three different wavelengths will produce three different average voltage levels.

The detector output pulses for a given λ, or photon energy E_ν, are not all of exactly the same size. They show a Gaussian distribution with FWHM determined by the resolution of the detector. Simplified pictures of pulse height (V) versus time (t) are shown in Fig. 9.34. The low pulses represent noise. The medium and high pulses correspond to two X-ray wavelengths with medium and high photon energy, respectively. The pulses occur randomly in time and are independent of each other. This leads to a Poisson distribution which can be approximated by a Gaussian one. The mean height V of each pulse is proportional to the incident photon energy.

A *discriminator* passes all pulses of height greater than a given minimum and rejects all the lower pulses. It is used to exclude detector and amplifier noise pulses.

A *pulse-height selector* passes all pulses of height greater than one level V, but lower than a second level $V + \Delta V$, and rejects all pulses outside this.

The potential V (lower discriminator level) is called the *baseline* (or *window level* or *channel level*). The potential interval ΔV between the two levels is called the *window* (or *channel*).

Consider three pulse-height distributions of three X-ray lines having low, medium and high energy (Fig. 9.35). (They are of the form given in Fig. 9.29.) If the window is set as shown, the peak *b* is passed while *a* and *c* are excluded. This illustrates the *principle of pulse height selection*.

9.10.2 Pulse-Height Distribution Curves

Following *Bertin* [9.76] and *Kiley* [9.77], consider the problem of finding a 1% concentration of Si in Fe using an EDDT (ethylene diamine dextro-tartrate)

crystal ($2d = 8.08$ Å). The fourth-order Fe $K\beta$ (1.76 Å = 7.045 keV) overlaps a little with Si $K\alpha$ (7.13 Å = 1.739 keV), as $4\lambda(\text{Fe}\,K\beta) = 7.04$ Å. The two lines are separated only by 2° 2θ. The strong Fe line (~1600 counts/s) at 106° 2θ has a tail (~30 counts/s) contributing to the weak (~200 counts/s) Si line at 108° 2θ.

Let the crystal be set at 108° 2θ to measure the Si $K\alpha$ line. The Ar-filled proportional counter output will give five groups of pulses of various intensities and amplitudes: (i) Very low amplitude and very high intensity noise from detector and amplifier; (ii) continuous X-ray background (~160 counts/s); (iii) Si $K\alpha$ pulses of low amplitude and intensity ~200 counts/s; (iv) Fe $K\beta$ pulses of relatively high amplitude and intensity ~30 counts/s; and (v) Fe $K\beta$ escape peak pulses (not considered here). On the oscilloscope display the low amplitude Si $K\alpha$ pulses are more numerous (~200 counts/s) than the high amplitude Fe $K\beta$ pulses (~30 counts/s) (Fig. 9.36a). The high energy Fe $K\beta$ gives a higher pulse height than Si $K\alpha$, as $E_\nu \propto V$.

The *single-channel pulse-height analyzer* (SCA) is used to record the *differential pulse-height distribution curve* shown in Fig. 9.36b. The window is set at some small width $\Delta V \sim 1$ volt. The baseline is scanned by moving the baseline discriminator level V (and with it the window) from 0 to 100 volts as intensity is recorded. For any instantaneous baseline setting, the window passes only those pulses to the ratemeter that have a height between V and $V + \Delta V$. It gives the I versus V curve (Fig. 9.36b).

If a *multichannel pulse-height analyzer* (MCA) is used [9.78], the baseline (or pulse height) in Fig. 9.36a is divided effectively into 200, 400, 800, 1200 or more narrow equal windows. Each window is connected to its accumulator (or memory). The amplified detector output pulses reaching the MCA are sorted according to the height, directing each to its proper box along the baseline. The process continues until about 10^5 counts accumulate in the channel for the highest peak. The number of counts in each channel are then quickly recorded electronically and displayed on an X–Y recorder (or oscilloscope, or digital printer).

Use of the MCA is illustrated in Fig. 9.37 for the oversimplified case of 15 channels only. While the SCA scanned the baseline sequentially, the MCA scans it simultaneously by dividing the baseline into 15 equal pulse-height intervals (channels), each with its own accumulator. The pulses are accumulated in all

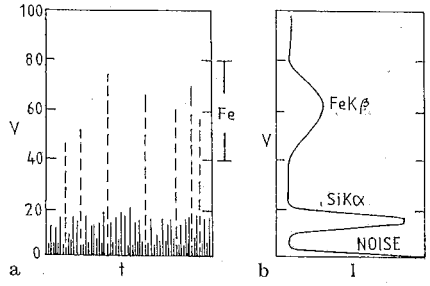

Fig. 9.36. a The cathode ray display of the counter output showing baseline or pulse height V [volts] vs time t. Besides noise, two groups of pulses, Si $K\alpha$ (solid) and Fe $K\beta$ (dotted), are shown for the Si line crystal setting. **b** Differential pulse-height distribution curve; it is aligned to permit correlation with **a**

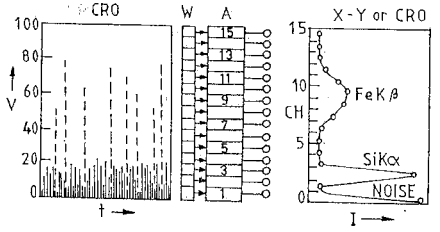

Fig. 9.37. Schematic illustration of the working of a multichannel analyzer with 15 channels. *V*: Baseline or pulse height; *W*: windows or channels; *A*: accumulators; *CH*: channel number ∝ pulse height

channels simultaneously. An MCA with 200 or more channels will give so many points that the display will appear essentially as in Fig. 9.36b.

The energy spectrum given in Fig. 9.37 is due to the multichannel analysis of the X-rays after Bragg diffraction from a crystal. More often, the MCA is used directly to energy disperse the X-rays emitted by a specimen. If a Si(Li) detector is used, instead of a proportional or a scintillation counter, the pulse distributions are much narrower (Table 9.4). The MCA is calibrated using known spectral lines from radioisotopes (Table 9.1). This relates the channel number to the X-ray photon energy. For use with the Si(Li) detector as an energy-dispersive spectrometer the MCA should have 1000 channels or more, and a count capacity of $\sim 10^6$ per channel. It is useful for a qualitative X-ray spectrometric analysis.

9.10.3 Automatic Pulse-Height Selection

For each λ, the pulse height $V \propto E_\nu$. This means that different settings for the detector potential and/or amplifier gain (or for the baseline and window) are needed. This is inconvenient for the 2θ scans. It is desirable to vary the pulse-selection conditions automatically with 2θ (that is, λ). Then the 2θ scan gives a pure first-order spectrum. One can attain the automation in several ways [9.79].

In the *method of variation of pulse amplitude*, all pulses are amplified by varying degrees to bring them within the range of a present channel width. This is achieved either by varying the detector voltage to change the gas gain A_g (or the photomultiplier gain for the scintillation counter), or by varying the electronic amplification $A_e L^{-1}$ in (9.62). The latter method is better as A_g strongly depends on counter characteristics. If A_g is kept constant, V is proportional to $E_\nu (A_e L^{-1})$, where $E_\nu \propto 1/\lambda = (2d \sin\theta)/n$, and so

$$A_e L^{-1} \propto V \sin\theta (2d/n). \tag{9.68}$$

For a given analyzer crystal reflecting in a certain order, if $A_e L^{-1}$ is varied sinusoidally with θ, *all* pulses will occur at V [9.80]. It is called a *sine-function amplifier*.

In the second method [9.81–83], $A_e L^{-1}$ is held constant, then for a specific detector and potential (A_g and V_i constant),

$$V \propto E_\nu \propto 1/\lambda \propto 1/\sin\theta. \tag{9.69}$$

As θ varies, the baseline is varied in proportion to $1/\sin\theta$. If E_v changes, the window width required to pass the pulse changes (Fig. 9.35). Therefore, the window width should also vary with θ for good results. Theoretically the width should change as $1/(\sin\theta)^{1/2}$. In practice, a linear change of width with θ is sufficient.

9.11 Non-Dispersive Analysis

In the *wavelength-dispersive* method the spectral lines are separated by a crystal according to their wavelength. In the *energy-dispersive* method the spectral lines entering the detector are dispersed on the basis of their pulse height and thereby their photon energies. In the *non-dispersive* method the spectral lines are not separated on the basis of either λ or E_v but by using selective excitation, selective filtration or selective detection.

9.11.1 Selective Excitation Method

Primary X-rays fall on a radiator (fluorescer) R which in turn gives strong spectral lines on the short-wavelength side of the absorption edge of the specimen (analyte) S. This excites the analyte line, which is detected. In a multielement specimen, this easily determines the presence of the analyte having the longest wavelength line (Fig. 9.38a). If X-rays first fall on S and the secondary radiation from it excites the R chosen to have an absorption edge that is excited only by the analyte line of shortest wavelength (Fig. 9.38b), then the analyte having line of shortest wavelength is detected. For an analyte having a line of intermediate wavelength, the first radiator R_1 is chosen to give a spectral line that excites only the analyte and elements in S with absorption edges at longer wavelength. The secondary emission from S falls on a second radiator R_2 (Fig. 9.38c) that is excited only by the line of the shortest λ present in the emission from S (that is, the analyte line). The intensity of the R_2 line detected is a measure of the intensity of the analyte line of intermediate wavelength [9.84].

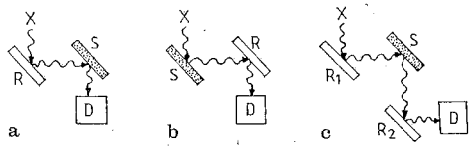

Fig. 9.38a–c. Method of selection excitation. **a** Primary X-rays first fall on R. Radiation R excites only specimen S elements having absorption edges at λ longer than its own line. **b** Primary X-rays first fall on S. R, placed after S, is excited only by specimen S emission having λ shorter than its own edge. **c** R_1 excites only S elements having edges at λ longer than its own line. R_2 is excited only by S emission having λ shorter than its own edge. X: Primary X-rays, D: detector

Suppose Cr($Z=24$), Fe(26) and Ni(28) are to be detected in a specimen of steel by *monochromatic* excitation. The wavelengths [Å] of $K\alpha$ lines and K edges are as follows:

	Cr	Fe	Ni
$\lambda(K_{ab})$[Å]	2.07	1.74	1.49
$\lambda(K\alpha)$[Å]	2.29	1.94	1.66

Cr is detected with Fe as R because Fe $K\alpha$ excites Cr but not Ni (Fig. 9.38a). Ni is also detected with Fe as R (placed after S, Fig. 9.38b) because Fe $K\alpha$ is excited by Ni $K\alpha$ from the specimen S but not by Cr $K\alpha$. Iron is detected with Ni as R_1 and Cr as R_2 in Fig. 9.38c. Ni $K\alpha$ from R_1 excites both Cr $K\alpha$ and Fe $K\alpha$ in S, but of these, only Fe $K\alpha$ excites Cr $K\alpha$ in R_2.

9.11.2 Selective Filtration Method

Filters can isolate a spectral line (Fig. 9.39). A *simple Hull filter* [9.85] is a thin foil (or layer) of an element with a K (or L_{III}) absorption edge at a wavelength λ just shorter than that of the analyte line λ'' (Fig. 9.39a). All lines of shorter wavelength (like λ') are strongly absorbed. For the brass sample (Cu–Zn alloy), a 25 μm thick Ni filter (K_{ab} 1.49 Å) suppresses the Zr $K\alpha$ line (1.44 Å) almost completely.

A *balanced Ross filter* [9.86, 87] has two thin foils of elements with atomic numbers Z and $Z-1$, selected to bracket the desired λ in the *pass band* between their absorption edges (Fig. 9.39b). For example, Ni(K_{ab} 1.49 Å) and Co(K_{ab} 1.16 Å) filters can measure the Cu $K\alpha$ line (1.54 Å).

A *Kustner filter* [9.88] is foil with a K (or L_{III}) edge at a wavelength just longer than that of the analyte line. It means the desired line is absorbed by the filter.

In the filter-scan method of *Dothie* [9.89], a series of filters (same mg/cm^2) of successive Z values are placed in turn in the secondary beam. The intensity transmitted through each is plotted. It is a filter scan of the spectrum, and can resolve lines of elements of adjacent Z values.

9.11.3 Other Methods

The selective detection method is based on *gas discrimination*, as the quantum efficiency η of the detector depends on λ (Fig. 9.33). It is useful only when one can realize high η for the analyte line.

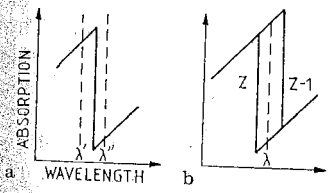

Fig. 9.39 a, b Use of filters. **a** Hull, **b** Ross

Another method is based on *modulated excitation* [9.90]. The dc potential V on the X-ray tube is modulated with a sinusoidal alternating potential V_f of frequency f. The V is set at the analyte excitation potential. The analyte is excited *only* during the positive half-cycle of the modulation. The analyte line emission occurs from the specimen in pulses at frequency f.

9.12 X-Ray Lasers

Light amplification by stimulated emission of radiation (*laser*) produces a highly coherent, collinear, monochromatic and intense beam of radiation.

Experiments to generate a laser action in the X-UV and X-ray wavelength region are rapidly developing. Several useful reviews exist [9.91–95].

The laser principle is as follows. A ground state electron in an atom is raised to a higher orbital on absorbing a photon of wavelength λ. Ordinarily, the excited electron returns to the ground state, spontaneously and almost instantly, emitting a photon of the same wavelength. However, it can happen that the electron falls into some intermediate level from which the probability of spontaneous transition to the ground state is very small. The electron is trapped there. The exciting radiation λ can then pump many electrons in this metastable state leading to a *population inversion* (more atoms in the metastable state than in the ground state). Note that only one specific electron in each atom undergoes this transition. The desired transition from metastable state to ground state corresponds to λ' ($>\lambda$). It can be tiggered (*stimulated*) by radiation of wavelength λ'. This radiation is not absorbed. When one metastable atom returns to the ground state, the emitted energy quantum promptly stimulates other metastable atoms to decay. A strong beam of λ' radiation is thus created.

A ruby rod (Al_2O_3 with Cr impurity), with both ends silvered (one end opaque, other $\sim 90\%$ transmittance) to form a resonator, forms a laser when placed along the axis of a helical, electronic pulsed flash lamp. The Cr atoms undergo a population inversion. The λ' photons are reflected by the ends to further stimulate the transitions. After all Cr atoms have returned to the ground state, another flash starts the pumping again.

It is difficult to produce an X-ray laser mainly because, as the energy of the metastable-to-ground interval increases (for λ' to be in the X-ray region), the lifetime of the state decreases. It becomes difficult to maintain the population inversion. Also, reflection of the laser X-ray from the ends is difficult to achieve.

The first attempt to obtain population inversion for X-rays was, as for the visible region, the optical pumping of neutral atoms [9.96]. *Waynant* [9.97] and *Hodgson* and *Dreyfus* [9.98] have used electron discharges to get lasing in the Lyman and Werner bands of H_2, without employing a resonant cavity. The shortest-wavelength lasing line is at 1161 Å (10.7 eV) for a transition in the Werner band. Coherent emissions at 532 Å (23.3 eV) and 380 Å (32.6 eV) are produced on using the 5th and 7th order nonlinear interactions in He excited by the 4th harmonic of a Nd laser [9.99, 100], by frequency upconversion (Fig. 9.40)

The reflection coefficient at 100 Å is $\sim 10^{-4}-10^{-3}$ only. This is too low for a resonator. Lasing action is possible without a resonator if the gain GL [G: negative absorption coefficient ($-\alpha$), L: length of active medium] is large (*superradiance*). It is not an actual laser action because the medium does not emit a coherent X-ray beam but merely acts as an amplifier.

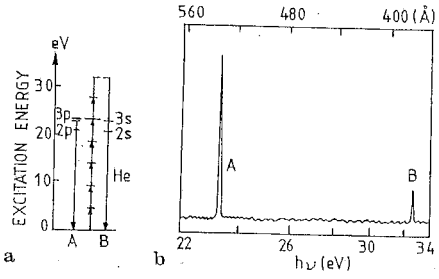

Fig. 9.40. a Energy levels of He and the relevant transitions. **b** Spectrum of coherent radiation. *A*: 23.3 eV; *B*: 32.6 eV

Plasma can provide an active medium for supporting superradiance. Dense hot plasma produced from laser-irradiated targets have a particle density of about 10^{22} cm^{-3} near the target surface. The ions in the plasma play the role of atoms involved in visible lasers, but their transitions occur in the soft X-ray region. Free electrons (10–1000 eV) surround the ions. Population inversion can occur not only from pumping mechanisms (say, electron ion collisions), but also due to recombination of multicharged ions in higher energy levels.

A plasma produced by an ordinary 1.06 μm laser pulse gives densities of 4×10^{15} cm^{-3} $Li^+(1s2s)$ metastable ions in a Li vapour of density 10^{17} cm^{-3}. An auxiliary visible laser can then be used to transfer the $1s2s$ population to the upper level of the lasing transition $1s2p-1s^2$ [9.101]. *Kepros* et al. [9.102] have also observed X-ray laser action using a Nd laser as a pump on gelatin in a copper(II) sulphate solution.

Dense plasma can be used as amplifying medium. Se^{24+} ions have been used for obtaining an amplification in the 200 Å region [9.103, 104].

Another idea is population inversion due to recombination in rapidly cooling plasma. It has been studied in H-like ions. Non-equilibrium in a fast cooling plasma results in three-body recombination, highly populating the excited levels of the recombined H-like ion. It is followed by a collisional radiative decay cascade. Plasma heated by Nd laser, focused on a carbon fibre, is cooled by adiabatic expansion of the plasma into the vacuum. A prepulse precedes the main pulse to create the plasma. The soft X-ray spectrum is recorded simultaneously [9.105, 106].

9.13 Intensity Measurement

The *intensity* I is the energy of X-rays that cross 1 cm^2 area/s perpendicular to the beam. If n photons of energy $h\nu$ in a monochromatic beam cross 1 cm^2 area/s, $I = nh\nu$. For the continuous spectrum of X-rays

$$I = \int_0^{\nu_{max}} (dn/d\nu)h\nu\, d\nu = \int_0^{\nu_{max}} I_\nu d\nu, \tag{9.70}$$

where dn/dv is the numerical density of photons per unit of frequency that pass through 1 cm^2 in 1 s. If I_j is the intensity of the separate lines present,

$$I = \int_0^{\nu_{max}} I_\nu d\nu + \Sigma_j I_j. \tag{9.71}$$

Rump [9.107] directly measured the energy of X-rays using a calorimeter.

9.13.1 Characteristic Line Intensity

Consider a detector with sensitive area A and detector efficiency $\eta(E)$ at energy E. Let dn photons cross an area ΔA in time Δt. Then I at the surface is

$$I = \frac{E\,\Delta n}{\Delta A\,\Delta t} \quad \text{J/m}^2\,\text{s}. \tag{9.72}$$

The *flux density* ϕ is the number of photons passing through unit area per unit time,

$$\phi = \Delta n/(\Delta A\,\Delta t) = I/E. \tag{9.73}$$

If the intensity is uniform over the entire area of the detector held normal to the incident beam, the number of photons falling on it in time t is

$$n = \phi A t = (I/E)At, \tag{9.74}$$

so the detected *counting rate* $\rho(E)$ for photons of energy E is

$$\rho(E) = \eta(E)A\phi = [\eta(E)A/E]I. \tag{9.75}$$

For a given detector and E, $\rho(E)$ is proportional to both ϕ and I. Therefore, in X-ray fluoroscence spectrometry *one often uses I for the photon counting rate at the detector*. This proportionality is lost when photons of more than one energy are present in the beam, because

$$n = n_1 + n_2 = (\phi_1 + \phi_2)At = [(I_1/E_1) + (I_2/E_2)]At, \tag{9.76}$$

where the subscripts refer to photons of energy E_1 and E_2. While n is proportional to the sum of flux densities, it is no longer proportional to the sum of intensities. Even this total-flux-density proportionality is lost for the total detected counting rate,

$$\begin{aligned} R &= \rho(E_1) + \rho(E_2) = [\phi_1\eta(E_1) + \phi_2\eta(E_2)]A \\ &= [(I_1/E_1)\eta(E_1) + (I_2/E_2)\eta(E_2)]A, \end{aligned} \tag{9.77}$$

unless η is same for all energies counted.

For the usual single-photon-counting X-ray spectrometers, one measures I loosely in terms of counts per second (counts/s). The response of source detectors is proportional to the detected intensity. In a Si(Li) detector one

measures the average current i produced,

$$\begin{aligned} i &= \rho(E_1)E_1(q_e/V_i) + \rho(E_2)E_2(q_e/V_i) \\ &= [\eta(E_1)I_1 + \eta(E_2)I_2](q_e/V_i), \end{aligned} \tag{9.78}$$

where q_e is electronic charge and V_i the average energy for producing one pair in the detector. If η is same over the detected range then $i \propto (I_1 + I_2)$. Most systems operate on this principle.

The background contribution needs to be subtracted to get the net peak intensity. If $n(n')$ counts are recorded in time $t(t')$ at the line (background near the line) position, then the net peak intensity of the line (λ) is

$$I_\lambda = I - I' = n/t - n'/t'. \tag{9.79}$$

This is the value used for quantitative analysis in wavelength-dispersive spectrometers.

In energy-dispersive fluorescence spectrometers, both n and n' are acquired simultaneously. It is not possible to divide time between peak and background counting, so the question is: How much of the available spectrum measures the net peak intensity? Or, how many channels within the peak are to be utilized?

A number of channels N is chosen to just cover the peak, and they give n_λ counts. The n_λ counts include the n' counts from the background under the peak. Therefore, the net counts n due to the peak alone are $n = n_\lambda - n'$. To estimate n', two background regions, one on each side of the peak (λ) are selected, each containing N' channels. Then

$$n' = (N/N')(n'_1 + n'_2), \tag{9.80}$$

where n'_1 is the total background counts in the $N'/2$ channels on the lower energy side of the peak, and n'_2 in the $N'/2$ channels on the high energy side of the peak. Therefore,

$$n = n_\lambda - (N/N')(n'_1 + n'_2). \tag{9.81}$$

for the net peak counts n.

The net intensity of emitted characteristic X-rays from one element in a *matrix* (mixture of elements) is related to the concentration C of that element (Fig. 9.41). The theoretical curve of the peak counting rate R_λ against C is a straight line $y = mx + c$, with $y = R_y$, $x = C$, $c = R'C$ (background rate) and the

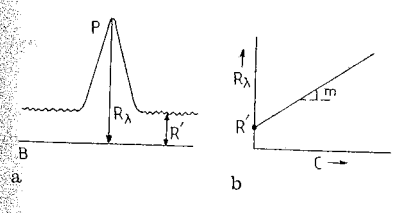

Fig. 9.41. a Peak P and background B of a characteristic line (λ). **b** Plot of R_λ against the concentration C

slope $m = (R_\lambda - R')/C$. In terms of the calibration factor (slope),

$$C = (R_\lambda - R')/m. \tag{9.82}$$

The value of m is found for a standard element in a matrix. Then the unknown concentration can be determined by substituting measured values of R_λ and R' in (9.82). Statistical estimates of several errors in R_λ and R' are needed for good accuracy. The absorption within the matrix is important as the characteristic radiation is always produced at a finite depth below the sample surface [see Fig. 4.20 and eq. (4.72)]. For more details see [9.66, 108].

Shiraiwa and *Fujino* [9.109] have given theoretical expression for the fluorescent intensity in terms of concentrations. *Criss* and *Birks* [9.110] and *Mainardi* et al. [9.111] have developed empirical models for concentration determinations. Recently *Tartari* et al. [9.112] have used K_β/K_α ratios of *Scofield* [9.113] in Fig. 2.17 for elemental analysis of thick samples. X-ray spectrometry is used for both the qualitative and quantitative analysis of samples.

9.13.2 X-Ray Dose

In considering radiation health and safety, X-ray are measured in terms of *dose* D (unit Röntgen R). The R unit is the quantity of X-radiation that produces in 1 cm^3 (0.001293 g) of dry air at 0°C and 760 torr, ions carrying 1 esu of charge (regardless of sign).

The average energy required to ionize one molecule of air is 33.73 ± 0.15 eV. The dose produced by one photon/cm^2 in air can be approximated by [9.114]

$$d \approx (4.8 \times 10^{-10})\lambda^2 \text{ R photon}^{-1}\,\text{cm}^{-2}, \tag{9.83}$$

in the wavelength region $\lambda = 0.2 - 3$ Å. The number of photons per cm^2 in air required to produce a dose of 1 R is

$$n_R \approx 1/d \approx (2.1 \times 10^9)\lambda^{-2} \text{ photons cm}^{-2}\,\text{R}^{-1}. \tag{9.84}$$

If n is the total measured count of X-rays of wavelength λ in a detector of effective area A cm^2 and quantum efficiency η, expressed as a fraction, then the dose D in units of R is

$$\begin{aligned} D = K_1 n &= [1/(n_R A\eta)]n \\ &= [(4.8 \times 10^{-10})\lambda^2/A\eta]n. \end{aligned} \tag{9.85}$$

For the intensity I (counts/s), the *dose rate* D/T in R per hour is

$$\begin{aligned} D/t = K_2 I &= [3600/(n_R A\eta)]I \\ &= [(1.7 \times 10^{-6})\lambda^2/A\eta]I. \end{aligned} \tag{9.86}$$

The constants K_1 and K_2 are for a particular detector at a given λ.

Appendix A
Rutherford Scattering for an Attractive Field

A.1 Equation of Hyperbola

In Fig. A.1 establish at 0 the origin (inner focus) of polar coordinates r, ϕ. Now establish a point (external focus) 0′ at $\phi = \pi$, $r = 2a\varepsilon$. The perihelion $OB = a\varepsilon - a$, with $2a$ as the distance between the vertices of the two branches of the hyperbola that can be drawn between 0 and 0′ with *eccentricity* ε.

The hyperbola is the locus of all points whose distances r and r', from the foci 0 and 0′, have a constant difference $2a$, that is

$$r' - r = 2a, \quad r'^2 = r^2 + 4ar + 4a^2. \tag{A.1}$$

From the triangle $00'A$,

$$r'^2 = r^2 + (2a\varepsilon)^2 - 2r(2a\varepsilon)\cos(180 - \phi).$$

Equating these values of r'^2,

$$r = \frac{a(\varepsilon^2 - 1)}{1 - \varepsilon\cos\phi}. \tag{A.2}$$

The *asymptotes* correspond to $r = \infty$ and make angles $\pm\phi_0$, such that $1 = \varepsilon\cos\phi_0$. If θ is the angle of deflection, then

$$\theta = \pi - 2\phi_0, \quad \cos\phi_0 = \sin\frac{1}{2}\theta = \frac{1}{\varepsilon}, \quad \varepsilon^2 - 1 = \cot^2\frac{1}{2}\theta.$$

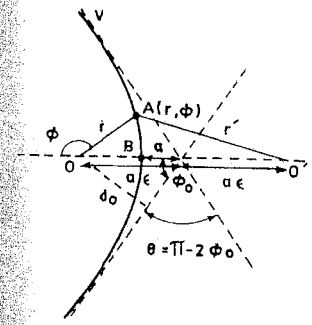

Fig. A.1. Hyperbolic orbit, which is characteristic of the Coulomb attractive force

The minimum positive value of r (vertex) is for $\phi = 180°$, $\cos\phi = \cos\pi = -1$, and locates the vertex at $r_{0B} = a(\varepsilon - 1)$, $\phi = \pi$. Because the impact parameter is given by $\sin\phi_0 = d_0/a\varepsilon$ (Fig. A.1) we can eliminate a from (A.2), to get

$$r = \frac{d_0 \tan\phi_0}{1 - \varepsilon\cos\phi}. \tag{A.3}$$

A.2 Rutherford Scattering

An electron of mass m, charge $-e$ and velocity v moves along the hyperbola if a heavy nucleus of charge $+Ze$ is at the focus 0. We have, at the vertex B, by conservation of energy.

$$\frac{1}{2}mv^2 = \frac{1}{2}mv_B^2 - \frac{Ze^2}{a(\varepsilon - 1)},$$

or, because $a = d_0/\varepsilon\sin\phi_0 = d_0/\tan\phi_0$,

$$\frac{v_B^2}{v^2} = 1 + \frac{2k}{d_0}\frac{\sin\phi_0}{1 - \cos\phi_0}, \quad k = \frac{Ze^2}{mv^2}. \tag{A.4}$$

The conservation of angular momentum gives $mvd_0 = mv_B a(\varepsilon - 1)$, or

$$\frac{v_B}{v} = \frac{d_0}{a(\varepsilon - 1)} = \frac{\sin\phi_0}{1 - \cos\phi_0}. \tag{A.5}$$

From (A.4, 5),

$$\tan\phi_0 = \frac{d_0}{k} = \frac{md_0v^2}{Ze^2}. \tag{A.6}$$

Appendix B
Bohr's Formula for Energy Loss

In 1913 *Bohr* [A.1] derived a classical expression for the space rate of energy loss for a heavy charged particle of charge ze, mass m_z and velocity v, passing an atomic electron of mass m at a distance d_0 (impact parameter), see Fig. B.1. There is always a force in the y direction. The associated impulse I_y and energy acquired by the electron are

$$I_y = \int_{-\infty}^{+\infty} F_y\,dt = \int_{-\infty}^{+\infty} \frac{ze^2\sin\theta\,dx}{r^2\quad v} = \int_0^{\pi} \frac{ze^2\sin\theta\,d\theta}{d_0 v} = \frac{2ze^2}{d_0 v}, \tag{B.1}$$

$$E(d_0) = \frac{I_y^2}{2m} = \frac{2z^2e^4}{mv^2}\frac{1}{d_0^2}. \tag{B.2}$$

A particle passing through matter see electrons at various distances from its path. If L is the number of target atoms per cm^3, the number of electrons located at impact parameters between d_0 and $d + dd_0$ in a thickness dx of target is $L\,2\pi d_0\,dd_0\,dx$. Therefore, the energy loss is

$$-\frac{dE}{dx} = 2\pi L\int E(d_0)d_0\,dd_0 = 4\pi L\frac{z^2e^4}{mv^2}\int_{\min}^{\max}\frac{1}{d_0^2}d_0\,dd_0 = 4\pi L\frac{z^2e^4}{mv^4}\ln\frac{d_{\max}}{d_{\min}}. \tag{B.3}$$

The integral over dd_0 is not taken from 0 to ∞ because then dE/dx would be infinite.

We have now to select values for $d_{\min}$ and $d_{\max}$. The maximum change of kinetic energy possible in an elastic collision is $m/2$ (change of velocity)^2 =

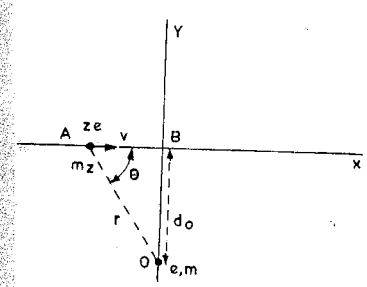

Fig. B.1. A heavy particle of charge ze and mass m_z passing an electron at distance d_0

$m(2v)^2/2 = 2mv^2$. If we insert this value of $E_{max}(d_0)$ in (B.2),

$$d_{min} = \frac{ze^2}{mv^2}. \tag{B.4}$$

The time during which energy transfer takes place is of the order of $d_0/v = \tau \approx \hbar/(E_n - E_0) = 1/\omega$, where E_n and E_0 are atomic energy levels. We can write

$$d_{max} \simeq v/2\pi\nu_j, \tag{B.5}$$

$$-\frac{dE}{dx} = 4\pi L \frac{z^2e^4}{mv^2} \ln\frac{mv^3}{2\pi\nu_j e^2 z}. \tag{B.6}$$

Taking the sum over all frequencies ν_j of electrons,

$$\sum_{j=1}^{Z} \ln\frac{mv^3}{2\pi\nu_j e^2 z} = Z \ln\frac{mv^3}{2\pi\bar{\nu}_j z e^2} = Zl, \tag{B.7}$$

where $\bar{\nu}_j$ is some average value. The quantity l takes an average value of 6. Because $dv^4/dx = (8E/m^2)dE/dx = (4v^2/m)dE/dx$, we finally get

$$\frac{dv^4}{dx} = -bZ, \quad b = 16\pi L \frac{z^2e^4}{m^2} l. \tag{B.8}$$

Kramers has used this formula for the passage of electrons through a target. For fast electrons, it overestimates the energy loss.

Appendix C
X-Ray Atomic Energy Levels

Siegbahn [A.2] first evaluated the atomic energy levels from X-ray absorption edges and emission lines. K edges were used for low Z and L_{III} edges for the rest, as reference levels. Other levels were determined on a relative scale from the emission lines. The principles involved in evaluating atomic energy levels are shown in Fig. C.1. Usually, the energy difference between two levels can be obtained in two or more ways. For example, the L_{II} and L_{III} difference can be found from $k\alpha_1 - k\alpha_2$, or from $L\beta_1(L_{II} \rightarrow M_{IV}) - L\beta_2(L_{III} \rightarrow M_{IV})$. The number of available lines is usually much greater than the number of levels involved. In place of the X-ray absorption edge, photoelectron measurement values can be used, if available [A.3], as they establish the absolute scale. For thorium, as many as ninety-nine equations (including sixteen photoelectric measurements) can be set up to determine only twenty-five unknown levels. A least-square solution of this set gives the required energy levels.

As improved X-ray and photoelectron data have become available, several reviews have appeared [A.3–11]. The K atomic energy levels are given in Appendix D. E_K is the energy difference between the Fermi level (zero energy) and the K state.

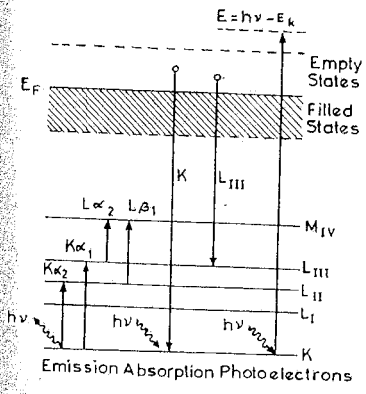

Fig. C.1. Principles involves in evaluating atomic energy levels from measurements in solids. E_F is the Fermi energy

Appendix D
Electron Distribution Among the Levels of Free Atoms

K Binding energies [eV]	Element		Level											
			1*s*	2*s*	2*p*	3*s*	3*p*	3*d*	4*s*	4*p*	4*d*	4*f*	5*s*	5*p*	5*d*
13.6	1 H	Hydrogen	1												
24.6	2 He	Helium	2												
55	3 Li	Lithium	*K*	1											
111	4 Be	Beryllium	*K*	2											
188	5 *B*	Boron	*K*	2	1										
284	6 C	Carbon	*K*	2	2										
402	7 N	Nitrogen	*K*	2	3										
532	8 O	Oxygen	*K*	2	4										
685	9 F	Fluorine	*K*	2	5										
867	10 Ne	Neon	*K*	2	6										
1072	11 Na	Sodium	*KL*			1									
1305	12 Mg	Magnesium	*KL*			2									
1560	13 Al	Aluminium	*KL*			2	1								
1839	14 Si	Silicon	*KL*			2	2								
2146	15 P	Phosphorus	*KL*			2	3								
2472	16 S	Sulphur	*KL*			2	4								
2822	17 Cl	Chlorine	*KL*			2	5								
3203	18 Ar	Argon	*KL*			2	6								
3607	19 K	Potassium	*KL*			2	6		1						
4038	20 Ca	Calcium	*KL*			2	6		2						
4493	21 Sc	Scandium	*KL*			2	6	1	2						
4966	22 Ti	Titanium	*KL*			2	6	2	2						
5465	23 V	Vanadium	*KL*			2	6	3	2						
5989	24 Cr	Chromium	*KL*			2	6	5	1						
6539	25 Mn	Manganese	*KL*			2	6	5	2						
7112	26 Fe	Iron	*KL*			2	6	6	2						
7709	27 Co	Cobalt	*KL*			2	6	7	2						
8333	28 Ni	Nickel	*KL*			2	6	8	2						
8979	29 Cu	Copper	*KL*			2	6	10	1						
9659	30 Zn	Zinc	*KL*			2	6	10	2						
10367	31 Ga	Gallium	*KLM*						2	1					
11103	32 Ge	Germanium	*KLM*						2	2					

K binding energies [eV]	Element		1*s*	Level 2*s*	2*p*	3*s*	3*p*	3*d*	4*s*	4*p*	4*d*	4*f*	5*s*	5*p*	5*d*
11867	33 As	Arsenic	*KLM*				2	3							
12658	34 Se	Selenium	*KLM*				2	4							
13474	35 Br	Bromine	*KLM*				2	5							
14326	36 Kr	Krypton	*KLM*				2	6							
15200	37 Rb	Rubidium	*KLM*				2	6				1			
16105	38 Sr	Strontium	*KLM*				2	6				2			
17038	39 Y	Yttrium	*KLM*				2	6	1			2			

K binding energies [eV]	Element		1*s*	Level 4*s*	4*p*	4*d*	4*f*	5*s*	5*p*	5*d*	5*f*	6*s*	6*p*	6*d*	7*s*
17998	40 Zr	Zirconium	*KLM*	2	6	2		2							
18986	41 Nb	Niobium	*KLM*	2	6	4		1							
20000	42 Mo	Molybdenum	*KLM*	2	6	5		1							
21044	43 Tc	Technetium	*KLM*	2	6	6		1							
22117	44 Ru	Ruthenium	*KLM*	2	6	7		1							
23220	45 Rh	Rhodium	*KLM*	2	6	8		1							
24350	46 Pd	Palladium	*KLM*	2	6	10		1							
25514	47 Ag	Silver	*KLM*	2	6	10		1							
26711	48 Cd	Cadmium	*KLM*	2	6	10		2							
27940	49 In	Indium	*KLM*	2	6	10		2	1						
29200	50 Sn	Tin	*KLM*	2	6	10		2	2						
30491	51 Sb	Antimony	*KLM*	2	6	10		2	3						
31814	52 Te	Tellurium	*KLM*	2	6	10		2	4						
33169	53 I	Iodine	*KLM*	2	6	10		2	5						
34561	54 Xe	Xenon	*KLM*	2	6	10		2	6						
35985	55 Cs	Cesium	*KLM*	2	6	10		2	6			1			
37441	56 Ba	Barium	*KLM*	2	6	10		2	6			2			
38925	57 La	Lanthanum	*KLM*	2	6	10		2	6	1		2			
40443	58 Ce	Cerium	*KLM*	2	6	10	2	2	6			2			
41991	59 Pr	Praseodymium	*KLM*	2	6	10	3	2	6			2			
43569	60 Nd	Neodymium	*KLM*	2	6	10	4	2	6			2			
45184	61 Pm	Promethium	*KLM*	2	6	10	5	2	6			2			
46834	62 Sm	Samarium	*KLM*	2	6	10	6	2	6			2			
48519	63 Eu	Europium	*KLM*	2	6	10	7	2	6			2			
50239	64 Gd	Gadolinium	*KLM*	2	6	10	7	2	6	1		2			
51996	65 Tb	Terbium	*KLM*	2	6	10	9	2	6			2			
53789	66 Dy	Dysprosium	*KLM*	2	6	10	10	2	6			2			
55618	67 Ho	Holmium	*KLM*	2	6	10	11	2	6			2			
57486	68 Er	Erbium	*KLM*	2	6	10	12	2	6			2			
59390	69 Tm	Thulium	*KLM*	2	6	10	13	2	6			2			

K binding energies [eV]	Element		1*s*	Level 4*s*	4*p*	4*d*	4*f*	5*s*	5*p*	5*d*	5*f*	6*s*	6*p*	6*d*	7*s*
61332	70 Yb	Ytterbium	*KLM*	2	6	10	14	2	6			2			
63314	71 Lu	Lutetium	*KLMN*					2	6	1		2			
65351	72 Hf	Hafnium	*KLMN*					2	6	2		2			
67416	73 Ta	Tantalum	*KLMN*					2	6	3		2			
69525	74 W	Tungsten	*KLMN*					2	6	4		2			
71676	75 Re	Rhenium	*KLMN*					2	6	5		2			
73871	76 Os	Osmium	*KLMN*					2	6	6		2			
76111	77 Ir	Iridium	*KLMN*					2	6	7		2			
78395	78 Pt	Platinum	*KLMN*					2	6	8		2			
80725	79 Au	Gold	*KLMN*					2	6	10		1			
83102	80 Hg	Mercury	*KLMN*					2	6	10		2			
85530	81 Tl	Thallium	*KLMN*					2	6	10		2	1		
88005	82 Pb	Lead	*KLMN*					2	6	10		2	2		
90526	83 Bi	Bismuth	*KLMN*					2	6	10		2	3		
93105	84 Po	Polonium	*KLMN*					2	6	10		2	4		
95730	85 At	Astatine	*KLMN*					2	6	10		2	5		
98404	86 Rn	Radon	*KLMN*					2	6	10		2	6		
101137	87 Fr	Francium	*KLMN*					2	6	10		2	6		1
103921	88 Ra	Radium	*KLMN*					2	6	10		2	6		2
106755	89 Ac	Actinium	*KLMN*					2	6	10		2	6	1	2
109651	90 Th	Thorium	*KLMN*					2	6	10		2	6	2	2
112601	91 Pa	Protactinium	*KLMN*					2	6	10	2	2	6	1	2
115606	92 U	Uranium	*KLMN*					2	6	10	3	2	6	1	2
118678	93 Np	Neptunium	*KLMN*					2	6	10	4	2	6	1	2

K binding energies [eV]	Element			Level 5*s*	5*p*	5*d*	5*f*	6*s*	6*p*	6*d*	7*s*
121818	94 Pu	Plutonium	*KLMN*	2	6	10	5	2	6	1	2
125027	95 Am	Americium	*KLMN*	2	6	10	6	2	6	1	2
128220	96 Cm	Curium	*KLMN*	2	6	10	7	2	6	1	2
131590	97 Bk	Berkelium	*KLMN*	2	6	10	8	2	6	1	2
135960	98 Cf	Californium	*KLMN*	2	6	10	10	2	6		2
139490	99 Es	Einsteinium	*KLMN*	2	6	10	11	2	6		2
143090	100 Fm	Fermium	*KLMN*	2	6	10	12	2	6		2
146780	101 Md	Mendelevium	*KLMN*	2	6	10	13	2	6		2
150540	102 No	Nobelium	*KLMN*	2	6	10	14	2	6		2
154380	103 Lw	Lawrencium	*KLMN*	2	6	10	14	2	6	1	2

Appendix E
Curves Representing Values of Electron Energies

Curves representing values of electron energies, as a function of atomic number Z (compare with Appendix D for the filling of shells), are given in Fig. E.1. They have been calculated by the Thomas–Fermi method.

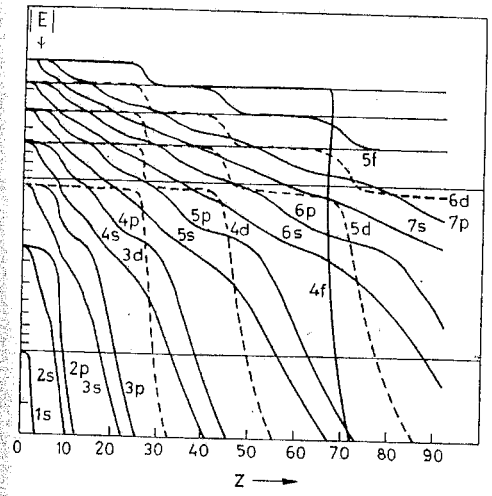

Fig. E.1. Electron energies as a function of Z

Appendix F
Dipole Sum Rule

Consider the commutation relation $xp - px = i\hbar$. Its matrix element between the normalized states $|a\rangle$ is

$$\langle a|xp - px|a\rangle = i\hbar\langle a|a\rangle = i\hbar. \tag{F.1}$$

If we have a complete set of normalized states $|b\rangle$, then we can apply the closure property, $\sum_b |b\rangle\langle b| = 1$, to write (F.1) as

$$\sum_b (\langle a|x|b\rangle\langle b|p|a\rangle - \langle a|p|b\rangle\langle b|x|a\rangle) = i\hbar. \tag{F.2}$$

We can now use the equation of motion $\dot{A} = [A, H]/i\hbar$, to write

$$\begin{aligned}\langle a|p|b\rangle &= \langle a|m\dot{x}|b\rangle = (m/i\hbar)\langle a|[x, H]|b\rangle \\ &= (m/i\hbar)\langle a|xH - Hx|b\rangle = (m/i\hbar)(E_b - E_a)\langle a|x|b\rangle.\end{aligned} \tag{F.3}$$

From (F.2, 3)

$$\sum_b (E_b - E_a)|\langle b|x|a\rangle|^2 = \hbar^2/(2m). \tag{F.4}$$

This is called the dipole sum rule or Thomas–Reiche–Kuhn sum rule.

Note that for the dipole moment

$$\sum_b |x_{ba}|^2 = \sum_b x_{ab}x_{ba} = (x^2)_{aa} = \int |\psi_a|^2 x^2\, dx. \tag{F.5}$$

If the state a is isotropic,

$$\sum_b |x_{ba}|^2 = \tfrac{1}{3}(r^2)_{aa}. \tag{F.6}$$

Appendix G
Screening Effect, According to Slater

The ionization energy for one inner electron in a hydrogen-like atom is given approximately by

$$E_i = hc\tilde{\nu}_i = R_\infty hc(Z/n)^2. \tag{G.1}$$

In a many-electron atom, all of the energies result from attractive interactions of electrons with positive-ion cores and repulsive interactions of electrons among themselves. Therefore, for better agreement with experimental results, we can write

$$\tilde{\nu}_i/R_\infty = [(Z-\sigma_i)/n_i^*]^2, \tag{G.2}$$

where σ_i is the internal screening constant, and n_i^* is the effective principal quantum number for the i level. The energy of the normal atom can be expressed in Rydbergs as

$$\tilde{\nu}/R_\infty = \sum_i z_i(\tilde{\nu}_i/R_\infty) = \sum_i z_i[(Z-\sigma_i)/n_i^*]^2, \tag{G.3}$$

where z_i is the number of electrons in the level i. A similar equation will hold for an ion with energy denoted by $(\tilde{\nu}/R_\infty)_q$.

For an atom with one electron removed from the q level to a final level,

$$\tilde{\nu}_q/R_\infty = (\tilde{\nu}/R_\infty)_q - \tilde{\nu}/R_\infty, \tag{G.4}$$

where $\tilde{\nu}_q/R_\infty$ gives the energy of the q level or of the q absorption edge.

Slater (1930) gives the following values for n_i^*:

n_i:	1	2	3	4	5	6
n_i^*:	1	2	3	4.7	4.0	4.2

Further, he assigns a certain fraction $\Delta\sigma_j$ (Table G.1) of the internal screening constant to each electron, such that

$$\sigma_i = \sum_{j=1}^{i-1} z_j \Delta\sigma_j + (z_i - 1)\Delta\sigma_i = \left(\sum_{j=1}^{i} z_j \Delta\sigma_j\right) - \Delta\sigma_i. \tag{G.5}$$

Here j is the order number of the electron groups into which Slater distributes all of the electron shells of the atom,

$$1s;\ 2s, p;\ 3s, p;\ 3d;\ 4s, p;\ 4d;\ 4f;\ 5, sp;\ 5d; \ldots .$$

Table G.1. The fractions $\Delta\sigma_j$ of the inner screening constants σ_i of electrons of the i level

Electrons of group i		Electrons of internal level		$j\,(n_j \leqq n_i)$
$i = 1s$	$i * 1s$	$i = s, p$		$i = d, f$
$n_j = n_i$	$n_j = n_i$	$n_j = n_i - 1$	$n_j \leqq n_i - 2$	$n_j \leqq n_i - 1$
$\Delta\sigma_j = 0.30$	0.35	0.85	1.00	1.00

Thus, *ns* and *np* valence electrons are treated on the same footing, independent of n, except that $1s$ electrons interact with each other more strongly (Table G.1). The *nd* electrons are found to lie outside the *ns* and *np* ones, or more precisely between *ns*, *np* and $(n+1)s, (n+1)p$.

Consider the tin atom (^{50}Sn). Slater's groups are

$$1s^2 2(s,p)^8 3(s,p)^8 3d^{10} 4(s,p)^8 4d^{10} 5(s,p)^4.$$

The screening constants for these groups are

$$\sigma_{1s} = 1 \times 0.30 = 0.30,$$

$$\sigma_{2s,p} = 7 \times 0.35 + 2 \times 0.85 = 4.15,$$

$$\sigma_{3s,p} = 7 \times 0.35 + 8 \times 0.85 + 2 \times 1.00 = 11.25,$$

$$\sigma_{3d} = 9 \times 0.35 + 18 \times 1.00 = 21.15,$$

$$\sigma_{4s,p} = 7 \times 0.35 + 18 \times 0.85 + 10 \times 1.00 = 27.75,$$

$$\sigma_{4d} = 9 \times 0.35 + 36 \times 1.00 = 39.15,$$

$$\sigma_{5s,p} = 3 \times 0.35 + 18 \times 0.85 + 28 \times 1.00 = 44.35.$$

Table G.2. Calculation of the energy of the tin atom

Group	$Z - \sigma_i$	n_i^*	z_i	$z_i(\tilde{\nu}_i/R_\infty)$
$1s$	49.70	1	2	4940
$2s, p$	45.85	2	8	4200
$3s, p$	38.75	3	8	1336
$3d$	28.85	3	10	925
$4s, p$	22.25	3.7	8	289
$4d$	10.85	3.7	10	86
$5s, p$	5.65	4.0	4	8
$\tilde{\nu}/R_\infty = \sum_i z_i(\tilde{\nu}_i/R_\infty) = 11784$				

The calculation of $\tilde{\nu}/R_\infty$, (I.3), is shown in Table G.2. For an application of Slater's rule, see [A.12].

Slater takes into account only the inner screening effect. To improve agreement with the observed values,

$$E_{nl} = -R_\infty hc[(Z-\sigma)/n^*]^2 + V_0$$

is usually used. The difference $n - n^*$ is called the *quantum defect* [A.13]; V_0 takes care of the *outer* screening effect *after an absorption process*. As the ejected electron moves outward through the region occupied by the outer electrons, it is repelled by them and consequently gains energy V_0. The outer screening potential V_0 depends on the number and radial distribution of electrons and ranges up to $\sim$20 keV near the nucleus of heavy atoms [A.14].

Appendix H
Electronegativity Scale

The electronegativity scale of *Pauling* [A.15] is given below:

Li	Be	B												C	N	O	F
1.0	1.5	2.0												2.5	3.0	3.5	4.0
Na	Mg	Al												Si	P	S	Cl
0.9	1.2	1.5												1.8	2.1	2.5	3.0
K	Ca	Sc	Ti	V	Cr	Mn	Fe	Co	Ni	Cu	Zn	Ga	Ge	As	Se	Br	
0.8	1.0	1.3	1.5	1.6	1.6	1.5	1.8	1.8	1.8	1.9	1.6	1.6	1.8	2.0	2.4	2.8	
Rb	Sr	Y	Zr	Nb	Mo	Te	Ru	Rh	Pd	Ag	Cd	In	Sn	Sb	Te	I	
0.8	1.0	1.2	1.4	1.6	1.8	1.9	2.2	2.2	2.2	1.9	1.7	1.7	1.8	1.9	2.1	2.5	
Cs	Ba	La–Lu	Hf	Ta	W	Re	Os	Ir	Pt	Au	Hg	Tl	Pb	Bi	Po	At	
0.7	0.9	1.1–1.2	1.3	1.5	1.7	1.9	2.2	2.2	2.2	2.4	1.9	1.8	1.8	1.9	2.0	2.2	
Fr	Ra	Ac	Th	Pa	U	Np–No											
0.7	0.9	1.1	1.3	1.5	1.7	1.3											

These values are for the common oxidation states (see also [A.16])

Appendix I
Common Analyzing Crystals

	Crystal	*hkl*, *hkil* $[i = -(h + k)]$	$2d$ [Å]	Crystal system
1	Quartz Silicon dioxide SiO_2	$50\bar{5}2$ $20\bar{2}3$ $21\bar{3}1$ $11\bar{2}2$ $10\bar{1}2$ $10\bar{1}1$ $10\bar{1}0$	1.624 2.749 3.082 3.636 4.564 6.687 8.52	Hexagonal
2	Lithium fluoride LiF	422 420 220 200	1.652 1.80 2.848 4.027	Cubic
3	Topaz Hydrated aluminium fluoro-silicate $Al_2(F, OH)_2SiO_4$	303 006 200 002	2.712 2.795 4.64 8.374	Orthorhombic
4	Mica Mica, muscovite $K_2O, 3Al_2O_3 \cdot 6SiO_2 \cdot 2H_2O$	$33\bar{1}$ 100 $\bar{2}01$ 010 002	3.0 5.11 5.16 9.02 19.84	Monoclinic
5	Silicon Si	220 111	3.84 6.27	Cubic
6	Fluorite Calcium fluoride CaF_2	220 111	3.862 6.306	Cubic
7	Germanium Ge	220 111	4.00 6.532	Cubic

Common Analyzing Crystals

	Crystal	*hkl*, *hkil* [$i = -(h + k)$]	$2d$ [Å]	Crystal system
8	Aluminium Al	200 111	4.048 4.676	Cubic
9	Gypsum Calcium sulphate dihydrate $CaSO_4 \cdot 2H_2O$	002 020	4.99 15.19	Monoclinic
10	Rock salt Sodium chloride NaCl	200	5.641	Cubic
11	Calcite Calcium carbonate $CaCO_3$	200 ($20\bar{2}0$) 211 cleavage	6.071	Hexagonal
12	ADP Ammonium dihydrogen phosphate $NH_4H_2PO_4$	112 200 101	6.14 7.50 10.64	Tetragonal
13	Graphite Carbon C	002 (0002)	6.708	Hexagonal
14	PET Pentaerythritol $C(CH_2OH)_4$	002	8.742	Tetragonal
15	EDDT Ethylenediamine-dextro-tartrate $C_6H_{14}N_2O_6$	020	8.808	Monoclinic
16	SHA Sorbitol hexaacetate $C_6H_8O_6(COCH_3)_6$	110	13.98	Monoclinic
17	Lead stearate Lead octadecannoate $[CH_3(CH_2)_{16}COO]_2Pb$	LBF	100.4	

Appendix J
Wavelength Tables

Table J.1. *K* absorption edges in the region 2 kXU to 0.5 kXU in pure elements. The *K*1 (longer wavelength) edge is given (marked *) where the main edge shows clear split structure. The values are based on those of *Cauchois* and *Hulubei*[a], *Sandström*[b], and *Bearden*[c]. The conversion factor used is E[keV] = 12372.42/λ [XU][c]

Element	Absorption edge [XU]	[keV]	Element	Absorption edge [XU]	[keV]
24 Cr	2065.91	5.9888	36 Kr	863.73	14.3244
25 Mn	1892.50	6.5376	37 Rb*	814.39[f]	15.1923
26 Fe	1739.85	7.1112	38 Sr	768.35[g]	16.1026
27 Co*	1604.8(2)[d]	7.7095	39 Y	726.15	17.0388
28 Ni	1484.99	8.3317	40 Zr*	687.57[h]	17.9944
29 Cu*	1377.79[e]	8.9799	41 Nb	651.63	18.9869
30 Zn	1280.7	9.6607	42 Mo	618.50	20.0039
31 Ga	1193.3	10.3682	43 Te	587.84	21.0473
32 Ge	1114.27	11.1036	44 Ru	559.35	22.1193
33 As	1042.8	11.8646	45 Rh	532.84	23.2198
34 Se	977.71	12.6545	46 Pd	508.15	24.348
35 Br (gas)	918.5	13.4702			
(KBr)	918.09	13.4763			

[a] Y. Cauchois, H. Hulubei: *Longueurs d'Onde des Emissions* X *et des Discontinuités d'Absorption* X (Hermann, Paris 1947)
[b] A. E. Sandström: Handbuch der Physik, Vol. 30, ed. by S. Flügge (Berlin Springer 1957)
[c] J. A. Bearden: "X-Ray Wavelengths"; Tech. Rep. NYO-10586, US Atomic Energy Commission, Oak Ridge, Tenn. (1964)
[d] A. K. Dey, B. K. Agarwal: J. Chem. Phys. **59**, 1397 (1973)
[e] B. K. Agarwal, C. B. Bhargava, A. N. Vishnoi, V. P. Seth: J. Phys. Chem. Solids **37**, 725 (1976)
[f] B. K. Agarwal, R. K. Johri: J. Phys. F **7**, 1607 (1977)
[g] V. B. Singh, B. K. Agarwal: J. Phys. Chem. Solids **35**, 465 (1974); interpolated value.
[h] B. K. Agarwal, R. K. Johri: Phys. Status Solidi B **88**, 309 (1978)

Table J.2. L absorption edges in the wavelength region 2 kXU to 0.75 kXU. Measuremets made on compounds are marked (+) [A.4]

Element	L_I [XU]	L_{II} [XU]	L_{III} [XU]
57 La	1973.9+	2100.9+	2256+
58 Ce	1889.5+	2008.2+	2162+
59 Pr	1810.3+	1921.5+	2074.8+
60 Nd	1735.4+	1840.2+	1992.6+
61 Pm	1663.9	1763.9	1915.1
62 Sm	1596.9+	1691.8+	1841.9+
63 Eu	1534.9+	1623.7+	1772.4+
64 Gd	1475.3+	1561.44[a]	1708.66[b, c]
65 Tb	1419.4+	1499.2+	1646.3+
66 Dy	1366.4+	1442.18[a]	1588.41[b]
67 Ho	1316.3+	1388.02[b]	1533.9[d]
68 Er	1268.0+	1337.09[a]	1480.4+
69 Tm	1222.5+	1286.5+	1430.4+
70 Yb	1179.4+	1240.2+	1384.54[e]
71 Lu	1137.8+	1196.0+	1337.7+
72 Hf	1097.4	1152.4	1294.5+
73 Ta	1059.1	1111.4	1252.7
74 W	1022.55	1072.3	1213.0
75 Re	987.4	1035.0	1174.9
76 Os	953.8	999.3	1138.4
77 Ir	921.7	965.1	1103.5
78 Pt	891.2	932.2	1070.1
79 Au	861.97	900.72	1037.85
80 Hg	833.6	870.4	1006.8[f]
81 Tl	806.4	841.7	977.16[g]
82 Pb	780.34	813.69	948.78[g]
83 Bi	755.5	787.1	921.49[g]

[a] B. K. Agarwal, B. R. K. Agarwal: X-Ray Spectrom. **7**, 12 (1978)
[b] B. R. K. Agarwal, L. P. Verma, B. K. Agarwal: Nuovo Cimento Lett. **2**, 581 (1971)
[c] P. Deshmukh, P. Deshmukh, C. Mande: J. Phys. C **10**, 3421 (1977) give for Gd L_{III} edge 1709.04 XU
[d] B. R. K. Agarwal, L. P. Verma, B. K. Agarwal: Nuovo Cimento Lett. **1**, 781 (1971)
[e] P. Deshmukh, C. Mande: Pramana **2**, 138 (1974)
[f] B. K. Agarwal, L. P. Verma: J. Phys. C **2**, 104 (1969)
[g] A. N. Vishnoi, B. K. Agarwal: Nuovo Cimento Lett. **4**, 771 (1970)

Table J.3. Some useful reference lines[1] [A.4]

Element	λ [XU]	Element	λ [XU]	
24 Cr	$K\alpha_2$ 2288.854	47 Ag	$K\alpha_2$ 562.630	
	α_1 2284.96		α_1 558.2486	
25 Mn	α_2 2101.42	50 Sn	α_2 494.027	
	α_1 2097.466		α_1 489.583	
26 Fe	α_2 1935.961	74 W	$L\beta_4(L_I M_{II})$	1298.92
	α_1 1932.031		$\beta_3(L_I M_{III})$	1260.07
27 Co	α_2 1789.136		$\gamma_2(L_I N_{II})$	1065.85
	α_1 1785.259		$\gamma_3(L_I N_{III})$	1059.80
			$\eta(L_{II} M_I)$	1418.16
28 Ni	α_2 1658.304		$\beta_1(L_{II} M_{IV})$	1279.153
	α_1 1654.475		$\gamma_5(L_{II} N_I)$	1130.00
29 Cu	α_2 1541.198		$\gamma_1(L_{II} N_{IV})$	1096.27
	α_1 1537.370		$l(L_{II} M_I)$	1674.7
	$\beta_{1,3}$ 1389.334		$\alpha_2(L_{III} M_{IV})$	1484.35
	β_2 1378.23		$\alpha_1(L_{III} M_V)$	1473.33
	β_5 1378.7		$\beta_6(L_{III} N_I)$	1287.22
30 Zn	α_2 1436.019		$\beta_{15}(L_{III} N_{IV})$	1243.73
	α_1 1432.182		$\beta_2(L_{III} N_V)$	1242.02
42 Mo	α_2 712.112			
	α_1 707.831			
	β_3 631.55			
	β_1 630.978			
	β_2 619.70			
	$\beta_5^{II}(KM_{IV})$ 625.78			
	$\beta_5^{I}(KM_V)$ 625.62			
	$\beta_4^{II}(KN_{IV})$ 618.95			
	$\beta_4^{I}(KN_V)$ 618.73			

[1] National Bureau of Standards Special Publication 398 (issued August 1974) gives the kXU to Å ratio as 1.0020772 based on $\lambda(\text{Cu } K\alpha_1) \equiv 1.537400$ kXU. In [A.17] the conversion factors used are $\Lambda = (\lambda/\text{Å})/(\lambda/\text{kXU}) = 1.0021017$ based on $\lambda(\text{Mo } K\alpha_1) \equiv 0.707831$ kXU. Also, $\lambda/\text{Å} \times E/\text{eV} = 12398.52$, which gives $\lambda/\text{XU} \times E/\text{keV} = 12372.52$.

1.34 C.J. Ulrey: Phys. Rev. **11**, 401 (1918)
1.35 H. Kulenkampff, L.S. Schmidt: Ann. Phys. **43**, 494 (1943)
1.36 D.L. Webster: Phys. Rev. **9**, 220 (1917)
1.37 W. Rump: Z. Phys. **43**, 254 (1927)
1.38 N.A. Dyson: Proc. Phys. Soc. London **73**, 924 (1959)
1.39 M. Green: Ph.D. Thesis, University of Cambridge (1962)
1.40 N.A. Dyson: *X-Rays in Atomic and Nuclear Physics* (Longman, London 1978)
1.41 A. Sommerfeld: Ann. Phys. **11**, 257 (1931); see also *Atomic Structures and Spectral Lines*, English ed. (Methuen, London 1923)
1.42 R. Weinstock: Phys. Rev. **61**, 584 (1942)
1.43 P. Kirkpatrick, L.Wiedmann: Phys. Rev. **67**, 321 (1945)
1.44 V.B. Berestetskii, E.M. Lifshitz, L.P. Pitaevaskii: *Relativistic Quantum Theory* (Pergamon, Oxford 1971)
1.45 W. Heitler: *The Quantum Theory of Radiation*, 3rd ed. (Clarendon, Oxford 1954) p. 248
1.46 B.K. Agarwal: *Quantum Mechanics and Field Theory*, 2nd ed. (Lokbharti, Allahabad 1983) p. 128
1.47 L.I. Schiff: *Quantum Mechanics*, 3rd ed. (McGraw-Hill, New York 1968) p. 140
1.48 H.S.W. Massey: *Electronic and Ionic Impact Phenomena*, Vol. II (Clarendon, Oxford 1969) p. 1180
1.49 A. Sommerfeld, A. W. Maue: Ann. Phys. **23**, 589 (1935)
1.50 T.S. Rao-Sahib, D.B. Wittry: J. Appl. Phys. **45**, 5060 (1974)
1.51 H.A. Bethe: Handb. Phys. **24**, 273 (1933)
1.52 F. Sauter: Ann. Phys. **18**, 486 (1933); ibid. **20**, 404 (1934)
1.53 R.H. Pratt: In *Fundamental Processes in Energetic Atomic Collisions*, ed. by H.O. Lutz, J.S. Briggs, H. Kleinpoppen (Plenum, New York 1983) p. 145
1.54 C.M. Lee, L. Kissel, R.H. Pratt, H.K. Tseng: Phys. Rev. A **13**, 1714 (1976)
1.55 R.H. Pratt, C.M. Lee: Phys. Rev. A **16**, 1733 (1977)
1.56 L. Kim, R.H. Pratt: Phys. Rev. A **36**, 45 (1987)
1.57 R. Hippler, K. Saeed, I. McGregor, H. Kleinpoppen: Phys. Rev. Lett. **46**, 1622 (1981)
1.58 H.K. Tseng, R.H. Pratt, C.M. Lee: Phys. Rev. A **19**, 187 (1979)
1.59 C.A. Quarles, D.B. Heroy: Phys. Rev. A **24**, 48 (1981)
1.60 H.W. Koch, J.W. Motz: Rev. Mod. Phys. **31**, 920 (1959)
1.61 R. Hippler: In *Radiation Physics*, ed. by E. Casnati, C. Baraldi, A. Tartari (North-Holland, Amsterdam 1987) p. 17
1.62 H.A. Bethe, L.C. Maximon: Phys. Rev. **93**, 768 (1954)
1.63 G. Elwert, E. Haug: Phys. Rev. **183**, 90 (1969)
1.64 R.H. Pratt: In *Advances in X-Ray Spectroscopy*, ed. by C. Bonnelle, C. Mande (Pergamon, New York 1982) p. 411
1.65 G. Elwert: Ann. Phys. (Leipzig) **34**, 178 (1939)
1.66 H. Banerjee: Phys. Rev. **111**, 532 (1958)
1.67 C. Fronsdal, H. Überall: Phys. Rev. **111**, 580 (1958)
1.68 W.H. McMaster: Rev. Mod. Phys. **33**, 8 (1961)
1.69 J.W. Motz, R.C. Placious: Phys. Rev. **109**, 235 (1958)
1.70 H. Kulenkampff, S. Leisegang, M. Scheer: Z. Phys. **137**, 435 (1954)
1.71 H. Kulenkampff, W. Zinn: Z. Phys. **161**, 428 (1961)
1.72 H. Kulenkampff, M. Scheer, E. Zeitler: Z. Phys. **157**, 275 (1959)
1.73 R.L. Gluckstern, M.H. Hull: Phys. Rev. **90**, 1030 (1953)

1.74 J.W. Motz, R.C. Placious: Nuovo Cimento **15**, 571 (1960)
1.75 H.A. Bethe, W. Heitler: Proc. R. Soc. London A **146**, 83 (1934)
1.76 U. Fano, K.W. McVoy, J.R. Albers: Phys. Rev. **116**, 1159 (1959)
1.77 J.D. Rozics, W.R. Johnson: Phys. Rev. **135**, B56 (1964)
1.78 K.W. McVoy, F.J. Dyson: Phys. Rev. **106**, 1360 (1957)
1.79 A. Bisi, L. Zappa: Nucl. Phys. **10**, 331 (1959)
1.80 B. Neumcke: Phys. Lett. **23**, 382 (1966)
1.81 M. Goldhaber, L. Gradzins, A.W. Sunyar: Phys. Rev. **106**, 826 (1957)
1.82 K. Güthner: Z. Phys. **182**, 278 (1965)
1.83 L. Kaufman, D.C. Camp: Adv. X-Ray Anal. **18**, 2 (1975)
1.84 R.H. Howell, W.L. Pickles, J.L. Cate Jr.: Adv. X-Ray Anal. **18**, 265 (1975)
1.85 J.D. Jackson: *Classical Electrodynamics*, 2nd ed. (Wiley, New York 1975) p. 717
1.86 J. Reinhardt, G. Soff, W. Greiner: Z. Phys. A **276**, 285 (1976)
1.87 D.H. Jakubassa, M. Kleber: Z. Phys. A **273**, 23 (1975)
1.88 K. Adler, A. Bohr, T. Huus, B. Mottelson, A. Winther: Rev. Mod. Phys. **28**, 432 (1956)
1.89 H.P. Trautvetter, J.S. Greenberg, P. Vincent: Phys. Rev. Lett. **37**, 202 (1976)
1.90 T.C. Chu, K. Ishii, A. Yamadera, M. Sebata, S. Morita: Phys. Rev. A **24**, 1720 (1981)
1.91 E. Merzbacher, H.W. Lewis: Handb. Phys. **34**, 166 (1958)
1.92 F. Folkmann, C. Gaarde, T. Huus, K. Kemp: Nucl. Instrum. Methods **116**, 487 (1974)
1.93 K. Ishii, S. Morita, H. Tawara: Phys Rev. A **13**, 131 (1976)
1.94 M. Ya, Amusia: Comments At. Mol. Phys. **11**, 123 (1982)
1.95 K. Ishii, S. Morita: In *X84: X-Ray and Inner-Shell Processes in Atoms, Molecules and Solids*, ed. by A. Meisel, J. Finster (Karl-Marx-Universität, Leipzig 1984) p. 135
1.96 R.L. Walter, R.D. Willis: In *X-Ray Spectrometry*, ed. by H.K. Herglotz, L.S. Birks (Dekker, New York 1978)
1.97 R. Anholt: Rev. Mod. Phys. **57**, 995 (1985)
1.98 W. Nakel, E. Pankau: Z. Phys. A **274**, 319 (1975)
1.99 M. Komma, W. Nakel: J. Phys. B **15**, 1433 (1982)
1.100 L.S. Birks, J.V. Gilfrich: Anal. Chem. **46**, 360R (1974)
1.101 D.J. Nagel: Adv. X-Ray Anal. **18**, 1 (1975)
1.102 O. Theimer: Ann. Phys. **22**, 102 (1963)

Chapter 2

2.1 D.L. Webster: Phys. Rev. **7**, 599 (1916)
2.2 H.G. Moseley: Philos. Mag. **27**, 703 (1914)
2.3 A.J.C. Wilson: Nature **151**, 562 (1943)
2.4 J.A. Bearden: "*X-Ray Wavelengths*"; Tech. Rep. NYO-10586, US Atomic Energy Commission, Oak Ridge, Tenn. (1964)
2.5 W. Heitler: *The Quantum Theory of Radiation*, 3rd ed. (Oxford University Press, Oxford 1954) p. 179
2.6 B.K. Agarwal: *Quantum Mechanics and Field Theory*, 2nd ed. (Lokbharti, Allahabad 1983) p. 127
2.7 E. Merzbacher, H.W. Lewis: Handb. Phys. **34**, 166 (1958)
2.8 G.N. Ogurtsov: Rev. Mod. Phys. **44**, 1 (1972)

References

Chapter 1

1.1 H.C. Ohanian: Am. J. Phys. **48**, 170 (1980)
1.2 C.G. Barkla: Philos. Trans. R. Soc. London **204**, 467 (1905)
1.3 H. Kulenkampff: Ann. Phys. **87**, 597 (1928)
1.4 B. Dasannacharya: Phys. Rev. **35**, 129 (1930)
1.5 G. Stokes: Proc. Manchester Lit. Philos. Soc. (1898)
1.6 J.J. Thomson: Philos. Mag. **45**, 172 (1898)
1.7 A. Sommerfeld: Phys. Z. **10**, 969 (1909)
1.8 R. Weinstock: Phys. Rev. **64**, 276 (1943); ibid. **65**, 1 (1944)
1.9 M. Scheer, E. Zeitler: Z. Phys. **140**, 642 (1955)
1.10 H. Kulenkampff: Z. Phys. **157**, 282 (1959)
1.11 A. Sommerfeld: Frank. Inst. J. **208**, 571 (1929)
1.12 G. Sesemann: Ann. Phys. **40**, 66 (1941)
1.13 W.W. Nicholas: US Bur. Stand. J. Res. **2**, 837 (1929)
1.14 K. Bohm: Ann. Phys. **33**, 315 (1938)
1.15 R. Honerjäger: Ann. Phys. **38**, 33 (1940)
1.16 K. Harworth, P. Kirkpatrick: Phys. Rev. **60**, 163 (1941); ibid. **62**, 334 (1942)
1.17 R. Kerscher, H. Kulenkampff: Z. Phys. **140**, 632 (1955)
1.18 H. Boersch, P. Dobberstein, D. Fritzsche, G. Sauerbrey: Z. Phys. **187**, 97 (1965)
1.19 S. Thordarson: Ann. Phys. **35**, 135 (1939)
1.20 H. Determann: Ann. Phys. **30**, 481 (1937)
1.21 H.P. Hanson, S.I. Salem: Phys. Rev. **124**, 16 (1961)
1.22 H.A. Kramers: Philos. Mag. **46**, 836 (1923)
1.23 G. Wentzel: Z. Phys. **27**, 257 (1924)
1.24 E.T. Whittaker, G.N. Watson: *A Course of Modern Analysis*, 3rd ed. (Cambridge University Press, Cambridge 1948) p. 381
1.25 L.D. Landau, E.M. Lifshitz: *The Classical Theory of Fields*, 4th ed. (Pergamon, New York 1985) p. 181
1.26 W. Duane, F.L. Hunt: Phys. Rev. **6**, 166 (1915)
1.27 P. Ohlin: Nature **152**, 392 (1943); Ark. Fys. **4**, 387 (1952)
1.28 J.A. Bearden, F.T. Johnson, H.M. Watts: Phys. Rev. **81**, 70 (1951)
1.29 G.L. Felt, J.N. Harris, J.W.M. Dumond: Phys. Rev. **92**, 1160 (1953)
1.30 H. Amrehn, H. Kulenkampff: Z. Phys. **140**, 452 (1955)
1.31 R. Whiddington: Proc. R. Soc. London A **86**, 360 (1912); ibid **89**, 554 (1914)
1.32 N. Bohr: Philos. Mag. **25**, 10 (1913)
1.33 H. Kulenkampff: Ann. Phys. **69**, 548 (1922)

2.9 U. Wille, R. Hippler: Phys. Rep. **132**, 129 (1986)
2.10 B. Davis: Phys. Rev. **11**, 433 (1918)
2.11 J. Hill, H. Terrey: Philos. Mag. **23**, 339 (1937)
2.12 G.H. Wannier: Phys. Rev. **90**, 817 (1953); ibid. **100**, 480 (1955)
2.13 H.A. Bethe: Ann. Phys. **5**, 325 (1930)
2.14 N.F. Mott, H.S.W. Massey: *The Theory of Atomic Collisions*, 3rd ed. (Clarendon, Oxford 1965) p. 497
2.15 H.S.W. Massey, E.H.S. Burhop: *Electronic and Ionic Impact Phenomena*, Vol. I (Clarendon, Oxford 1969) p. 438
2.16 M. Inokuti: Rev. Mod. Phys. **43**, 297 (1971)
2.17 E.H.S. Burhop: Proc. Cambridge Philos Soc., Math. Phys. Sci. **36**, 43 (1940)
2.18 E.J. McGuire: Phys. Rev. A **16**, 73 (1977)
2.19 C.R. Worthington, S.G. Tomlin: Proc. Phys. Soc. A **69**, 401 (1956)
2.20 R. Hippler, W. Jitschin: Z. Phys. A **307**, 287 (1982)
2.21 H.S. Perlman: Proc. Phys. Soc. **76**, 623 (1960)
2.22 J.H. Scofield: Phys. Rev. A **18**, 963 (1978)
2.23 P. Eschwey, P. Manakos: Z. Phys. A **308**, 199 (1982)
2.24 A.R. Zander, M.C. Andrews: Phys. Rev. A **20**, 1484 (1979)
2.25 R.K. Rice, F.D. McDaniel, G. Basbas, J.L. Duggan: Phys. Rev. A **24**, 758 (1981)
2.26 R. Hippler: In *Radiation Physics*, ed. by E. Casnati, C. Baraldi, A. Tartari (North-Holland, Amsterdam 1987) p. 17
2.27 L. Katz, A.S. Penfold: Rev. Mod. Phys. **24**, 28 (1952)
2.28 p. 516 of [2.14]
2.29 J.J.L. Chen, S.D. Warshaw: Phys. Rev. **80**, 97 (1950); ibid. **84**, 355 (1951)
2.30 A.T. Nelms: Circ. NBS, No. 577 (1956)
2.31 M. Green, V.E. Cosslett: Proc. Phys. Soc. **78**, 1206 (1961)
2.32 D.L. Webster, W.W. Hansen, F.B. Duveneck: Phys. Rev. **44**, 258 (1933)
2.33 J.A.J. Campbell: Proc. R. Soc. London **274**, 319 (1963)
2.34 G.D. Archard: J. Appl. Phys. **32**, 1505 (1961)
2.35 B.K. Agarwal, J.H. Sparrow: J. Phys. F **11**, 1303 (1981)
2.36 R.M. Dolby: Br. J. Appl. Phys. **11**, 64 (1960)
2.37 G.A. Bissinger, J.M. Joyce, E.J. Ludwig, W.S. McEver, S.M. Shafroth: Phys. Rev. A **1**, 841 (1970)
2.38 J.D. Garcia: Phys. Rev. A**1**, 280, 1402 (1970)
2.39 J.M. Kahn, D.L. Potter: Phys. Rev. A **133**, 890 (1964)
2.40 M. Geretschläger, O. Benka: Phys. Rev. A **34**, 866 (1986)
2.41 J.L. Price, J.L Duggan, F.D. McDaniel, G. Lipicki, R. Mehta: Phys. Rev. A **34**, 2830 (1986)
2.42 J.S. Briggs: J. Phys. B **7**, 47 (1974)
2.43 R. Anholt: Rev. Mod. Phys. **57**, 995 (1985)
2.44 H. Schmidt-Böcking, W. Lichtenberg, R. Schuch, J. Volpp, I. Iserruya: Phys. Rev. Lett. **41**, 859 (1978)
2.45 P. Tothill: Br. J. Appl. Phys. (J. Phys. D) **1**, 1093 (1968)
2.46 W. Pauli: Z. Phys. **31**, 778 (1925)
2.47 P.S. Bagus: Phys. Rev. A **139**, 619 (1965) see also T. Åberg: Phys. Rev. **162**, 5 (1967)
2.48 T. Koopmans: Physica **1**, 104 (1934)
2.49 R. Manne, T. Åberg: Chem. Phys. Lett. **7**, 282 (1970)
2.50 K.N. Huang, M. Aoyagi, M.H. Chen, B. Crasemann, H. Mark: At. Data Nucl. Data Tables **18**, 243 (1976)

2.51 R.D. Deslattes, E.G. Kessler, Jr., L. Jacobs, W. Schwitz: Phys. Lett. **71A**, 411 (1979)
2.52 E.G. Kessler, Jr., R.D. Deslattes, D. Girard, W. Schwitz, L. Jacobs, O. Renner: Phys. Rev. A **26**, 2696 (1982)
2.53 R.D. Deslattes, E.G. Kessler: In **X84**: *X-Ray and Inner-Shell Processes in Atoms, Molecules and Solids*, ed. by A Meisel, J. Finster (Karl-Marx-Universität, Leipzig 1984) p. 165
2.54 H.C. Burger, H.B. Dorgelo: Z. Phys. **23**, 258 (1924)
2.55 L.S. Ornstein, H.C. Burger: Z. Phys. **24**, 41 (1924)
2.56 E.U. Condon, G.H. Shortley: *The Theory of Atomic Spectra* (Cambridge University Press, Cambridge 1935)
2.57 J.H. Williams: Phys. Rev. **44**, 146 (1933)
2.58 J.H. Scofield: Phys. Rev. **179**, 9 (1969); ibid. A **9**, 1041 (1974); ibid. A **10**, 1507 (1974); ibid A **12**, 345 (1975)
2.59 A. Jönsson: Z. Phys. **36**, 426 (1926); ibid **43**, 845 (1927); ibid. **46**, 383 (1928)
2.60 H.S.W. Massey, E.H.S. Burhop: Proc. Cambridge Philos. Soc. **32**, 461 (1936)
2.61 H.R. Rosner, C.P. Bhalla: Z. Phys. **231**, 347 (1970)
2.62 R.K. Smither, M.S. Freedman, F.T. Porter: Phys. Lett. A **32**, 405 (1970)
2.63 P.V. Rao, J.M. Palms, R.E. Wood: Phys. Rev. A **3**, 1568 (1971)
2.64 J.L. Campbell, A. Perujo, W.J. Teesdale, B.M. Millman: Phys. Rev. A **33**, 2410 (1986)
2.65 N. Bohr, D. Coster: Z. Phys. **12**, 342 (1923)
2.66 G. Hertz: Z. Phys. **3**, 19 (1920)
2.67 A.E. Sandström: In *Handbuch der Physik*, Vol. 30, ed. by S. Flügge (Springer, Berlin, Heidelberg 1957)
2.68 A. Sommerfeld: Ann. Phys. **11**, 257 (1931); see also *Atomic Structures and Spectral Lines*, English ed. (Methuen, London 1923)
2.69 A.F. Burr, J.K. Carson: J. Phys. B **7**, 451 (1974)
2.70 B.G. Gokhale, U.C. Misra: J. Phys. B **10**, 3599 (1977); ibid. **11**, 2077 (1978)
2.71 U.D. Misra, R.N. Singh, B.G. Gokhale: J. Phys. B **12**, 1775 (1979)
2.72 W.J. Veigele, D.E. Stevenson, E.M. Henry: J. Chem. Phys. **50**, 5404 (1969)
2.73 S. Goudsmit: Phys. Rev. **31**, 946 (1928)
2.74 A.H. Compton, S.K. Allison: *X-Rays in Theory and Experiment*, 2nd ed. (Van Nostrand, Princeton, NJ 1935) p. 614
2.75 W. Duane: Phys. Rev. **37**, 1017 (1931)
2.76 P.A. Ross: Phys. Rev. **39**, 536, 748 (1932); ibid. **43**, 1036 (1933)
2.77 E. Carlsson: Z. Phys. **80**, 640 (1933)
2.78 J.A. Leiro: X-Ray Spectrom **16**, 177 (1987)
2.79 H. Hulubei: C. R. Acad. Sci. **201**, 1356 (1935)
2.80 Y. Cauchois, C. Sénémaud: *Selected Constants: Wavelengths of X-Ray Emission Lines and Absorption Edges* (Pergamon, Oxford 1978)
2.81 O. Beckman: Ark. Fys. **9**, 495 (1955)
2.82 S.K. Allison, A. Armstrong: Phys. Rev. **26**, 714 (1925)
2.83 H.T. Meyer: Wiss. Veröff. Siemens-Konzern **7**, 108 (1929)
2.84 A.L. Catz: Phys. Rev. Lett. **24**, 127 (1970)
2.85 J.H. Scofield: In *Atomic Inner Shell Processes*, ed. by B. Crasemann, Vol. I (Academic, New York 1975) p. 265
2.86 W.R. Johnson: Phys. Rev. Lett. **29**, 1123 (1972)
2.87 R. Anholt, J.O. Rasmussen: Phys. Rev. A **9**, 585 (1974)
2.88 R. Marrus, R.W. Schmieder: Phys. Rev. A **5**, 1160 (1972)

2.89 C.G. Barkla: Philos. Mag. **22**, 406 (1911)
2.90 M. Siegbahn: *Spektroskopie der Röntgenstrahlen*, 2nd ed. (Springer, Berlin 1931)
2.91 S. Idei: Sci. Rep. Tohoku Imp. Univ., Ser. 1: **19**, 559, 641(1930)
2.92 W. Kossel: Z. Phys. **1**, 119 (1920); ibid. **2**, 470 (1920)
2.93 A. Sandström: Z. Phys. **66**, 784 (1930)
2.94 S.K Allison: Phys. Rev. **34**, 7 (1929)
2.95 M.R. Khan, M. Karimi: X-Ray Spectrom. **9**, 32 (1980)
2.96 V.W. Slivinsky, P.J. Ebert: Phys. Rev. A **5**, 1581 (1972)
2.97 J.S. Hansen, H.U. Freund, R.W. Fink: Nucl. Phys. A **153**, 465 (1970)
2.98 A.G. dePinho: Phys. Rev. A **3**, 905 (1971)
2.99 O.W.B. Schult: Z. Naturforsch, A **26**, 368 (1971)
2.100 V.D. Mistry, C.A. Quarles: Phys. Lett. A **36**, 221 (1971)
2.101 J.H. McCrary, L.V. Singman, L.H. Zeigler, L.D. Looney, C.M. Edmonds, Carolyn E. Harris: Phys. Rev. A **4**, 1745 (1971)
2.102 B.K. Agarwal: Sci. Cult. **17**, 479 (1952)
2.103 A.J.C. Wilson: Phys. Abstr. **55**, 932 (1952)
2.104 J.A. Bearden: Rev. Mod. Phys. **39**, 78 (1967)

Chapter 3

3.1 H.A. Lorentz: *The Theory of Electrons* (G.E. Stechert, New York 1923)
3.2 J.S. Thomsen: J. Phys. B **16**, 1171 (1983)
3.3 B.G. Gokhale: Ann. Phys. (Paris) **7**, 852 (1952)
3.4 A. Larsson: Thesis, Uppsala (1929)
3.5 W.L. Bragg: Proc. Cambridge Philos. Soc. **17**, 43 (1913)
3.6 P.P. Ewald: In *Advances in X-Ray Spectroscopy*, ed. by C. Bonnelle, C. Mande (Pergamon, New York 1982)
3.7 A.H. Compton: Philos. Mag. **45**, 1121 (1923)
3.8 S.W. Smith: Phys. Rev. **40**, 156 (1932)
3.9 W. Stenström: Thesis, Lund (1919)
3.10 C.C. Hatley, B. Davis: Phys. Rev. **23**, 290 (1924)
3.11 C.C. Hatley: Phys. Rev. **24**, 486 (1924)
3.12 B. Davis, R. Von Nardoff: Phys. Rev. **23**, 291 (1924)
3.13 R. von Nardoff: Phys. Rev. **24**, 143 (1924)
3.14 A. Larsson, M. Siegbahn, I. Waller: Naturwissenschaften **12**, 1212 (1924)
3.15 B. Davis, C.M. Slack: Phys. Rev. **25**, 881 (1925); ibid. **27**, 18 (1926)
3.16 C.M. Slack: Phys. Rev. **27**, 691 (1926)
3.17 R. Ladenburg: Z. Phys. **4**, 451 (1921)
3.18 G.E.M. Jauncey: Philos. Mag. **48**, 81 (1924)
3.19 R. de L. Kronig: J. Opt. Soc. Am: **12**, 547 (1926)
3.20 H. Kallman, H. Mark: Naturwissenschaften **14**, 648 (1926); Ann. Phys. **82**, 585 (1927)
3.21 W. Bothe: Z. Phys. **40**, 653 (1927)
3.22 J.A. Prins: Z. Phys. **47**, 479 (1928)
3.23 H. Föll, K. Ulmer: Phys. Status Solidi A **41**, 113 (1977)
3.24 W. Kuhn: Z. Phys. **33**, 408 (1925)
3.25 W. Thomas: Naturwissenschaften **13**, 627 (1925)
3.26 H.A. Bethe, E.E. Salpeter: In *Handbuch der Physik*, Vol. 35, ed. by S. Flügge (Springer, Berlin, Heidelberg 1957) p. 88

3.27 S.T. Manson, J.W. Cooper: Phys. Rev. **165**, 126 (1968)
3.28 E.J. McGuire: Phys. Rev. **175**, 20 (1968)
3.29 U. Fano, J.W. Cooper: Rev. Mod. Phys. **40**, 441 (1968)
3.30 Y. Sugiura: J. de Phys. **8**, 113 (1927)
3.31 R. de L. Kronig. H.A. Kramers: Z. Phys. **48**, 174 (1928)
3.32 M. Wolf: Ann. Phys. **10**, 973 (1933)
3.33 H. Hönl: Z. Phys. **84**, 1 (1933); Ann. Phys. **18**, 625 (1933)
3.34 J.A. Wheeler, J.A. Bearden: Phys. Rev. **46**, 755 (1934)
3.35 F. Herman, S. Skillman: *Atomic Structure Calculations* (Prentice-Hall, Englewood Cliffs, NJ 1963)
3.36 E.N. Lassettre, S.A. Francis: J. Chem. Phys. **40**, 1208 (1964)
3.37 L.G. Parratt, C.F. Hempstead: Phys. Rev. **94**, 1593 (1954)
3.38 D.T. Cromer, D. Liberman: J. Chem. Phys. **53**, 1891 (1970); Acta Crystallogr. **A37**, 267 (1981)
3.39 R. Glocker, K. Schäfer: Z. Phys **73**, 289 (1931); see also K. Schäfer: Z. Phys. **86**, 739 (1933)
3.40 T. Fukamachi, S. Hosoya, T. Kawamura, J. Hastings: J. Appl. Crystallogr. **10**, 321 (1977)
3.41 T. Fukamuchi, S. Hosoya, T. Kawamura, S. Hunter, Y. Nakano: J. Appl. Phys. **17-2**, 326 (1978)
3.42 G. Martens, P. Rabe: Phys. Status Solidi A **58**, 415 (1980)
3.43 M. Hart, D.P. Siddons: Proc. R. Soc. London, A **376**, 465 (1981); see also D.P. Siddons, M. Hart: In *EXAFS and Near Edge Structure*, ed. by A. Bianconi, L. Incoccia, S. Stipcich, Springer Ser. Chem. Phys., Vol. 27 (Springer, Berlin, Heidelberg 1983)
3.44 U. Bonse, G. Materlik: Z. Phys. B **24**, 186 (1976)
U. Bonse, I. Hartmann-Lotsch, H. Lotsch: Nucl. Instrum. Methods **208**, 603 (1983); in *EXAFS and Near Edge Structure*, ed. by A. Bianconi, L. Incoccia, S. Stipcich, Springer Ser. Chem. Phys., Vol. 27 (Springer, Berlin, Heidelberg 1983)
3.45 P. Dreier, P. Rabe, W. Malzfeldt, W. Niemann: J. Phys. C **17**, 3123 (1984)
3.46 T. Kawamura, T. Fukumachi: Jpn. J. Appl. Phys. **17**, Suppl. 17-2, 224-226 (1978)
3.47 B.K. Agarwal: *Quantum Mechanics and Field Theory*, 2nd ed. (Lokbharti, Allahabad 1983) p. 494
3.48 V. Weisskopf, E. Wigner: Z. Phys. **63**, 54 (1980)
3.49 F.K. Richtmyer, S.W. Barnes, E. Ramberg: Phys. Rev. **46**, 843 (1934)
3.50 A. Beer: Ann. Phys. **86**, 78 (1952)
3.51 E.P. Bertin: *Principles and Practice of X-Ray Spectrometric Analysis* (Plenum, New York 1975)
3.52 B.L. Henke, R.L. Elgin: Adv. X-Ray Anal. **13**, 639 (1970)
B.L. Henke, P.A. Lee, T.J. Tanaka, R.L. Shimabukuro, B.K. Fujikawa: At. Data Nucl. Data Tables **27**, 1 (1982)
3.53 J.H. Hubbell: "Photon Cross Sections, Attenuation Coefficients and Energy Absorption Coefficients from 10 keV to 100 GeV"; Report NSRDS-NBS 29 (1969)
J.H. Hubbell, H.A. Gimm, I. overbo: J. Phys. Chem. Ref. Data **9**, 1023 (1980)
J.H. Hubbell: Int. J. Appl. Radiat. Isot. **33**, 1269 (1982)
E.B. Salmon, J.H. Hubbell: "X-ray Attenuation Coefficients (Total Cross Sections): Comparison of the Experimental Data Base with the Recommended Values of Henke and the Theoretical Values of Scofield for Energies between 0.1 and 100 keV"; National Bureau of Standards Internal Report NBSIR-86-3431 (1986)

3.54 J.H. Scofield: "Theoretical Photoionization Cross Sections from 1 to 1500 keV"; Lawrence Livermore Nat. Lab. Rep. UCRL-51326 (1973)
3.55 D.C. Creagh: In *Radiation Physics*, ed. by E. Casnati, C. Baraldi, A. Tartari (North-Holland, Amsterdam 1987) p. 1; see also D.F. Jackson, D.J. Hawkes: Phys. Rep. **70**, 169 (1981)
3.56 K. Lonsdale (ed.): *International Tables for X-Ray Crystallography* (Kynoch, Birmingham, England 1962) Sect. 3.2
3.57 B.A. Cooke, E.A. Stewardson: Br. J. Appl. Phys. **15**, 1315 (1964)
3.58 A.T. Nelms: Circ. Nat. Bur. Stand. No.577 (1956)
3.59 M.Stobbe: Ann. Phys. **7**, 661 (1930)
3.60 H. Wagenfeld: Phys. Rev. **144**, 216 (1966); see also G. Hildebrandt, J.D. Stephenson, H. Wagenfeld: Z. Naturforsch. **28a**, 588 (1973)
3.61 J.C. Slater: Phys. Rev. **36**, 57 (1930)
3.62 Z.G. Pinsker: *Dynamical Scattering of X-Rays in Crystals*, Springer Ser. Solid-State Sci., Vol. 3 (Springer, Berlin, Heidelberg 1978) pp. 82,359
3.63 R.T. Berger: Radiat. Phys. **15**, 1 (1961)
3.64 J.W. Allison: Aust. J. Phys. **14**, 443 (1961)
3.65 J.H. Hubbell: Radiat. Res. **70**, 58 (1977)
3.66 E. Jönsson: Thesis, Uppsala (1928)
3.67 H. Rindfleisch: Ann. Phys. **28**, 409 (1937)
3.68 S. Laubert: Ann. Phys. **40**, 553 (1941)
3.69 H. Tellez-Plasencia: J. Phys. Radium **10**, 14 (1949)
3.70 B. Walter: Fortschr. Geb. Röntgenstr. **35**, 929, 1308 (1927)
3.71 B.K. Agarwal: Curr. Sci. **23**, 357 (1954)
3.72 R. Böklen, S. Geiling: Z. Metallkd. **40**, 157 (1949)
3.73 J.A. Prins: Z. Phys. **47**, 479 (1928)
3.74 J.P. Thibaud: Phys. Rev. **35**, 1452 (1930)
3.75 H. Kiessig: Ann. Phys. **10**, 715, 769 (1931)
3.76 U. Bonse, M. Hart: Appl. Phys. Lett. **6**, 155 (1965); ibid. **7**, 99, 239 (1965); Z. Phy. **190**, 455 (1966)
3.77 M. Hart, U. Bonse: Phys. Today **23**, 26 (1970)
3.78 R.D. Deslattes: Proc. Intl. Conf. On Precision Measurement and Fundamental Constants, Aug. 1970 (Govt. Printing Office, Washington, DC 1971)
3.79 P.L. Cowan, J.A. Golovchenko, M.F. Robbins: Phys. Rev. Lett. **44**, 1680 (1980)
3.80 M.J. Bedzyk, G. Materlik: Phys. Rev. B **31**, 4110 (1985)
3.81 A. Frahm, M.J. Bedzyk: Phys. Rev. Lett. **52**, 441 (1984)

Chapter 4

4.1 K. Siegbhan, C. Nordling, A. Fahlman, R. Nordberg, K. Hamrin, J. Hedman, G. Johansson, T. Bergmark, S.E. Karlsson, I. Lindgren: Nova Acta Regiae Soc. Sci. Ups. **20**, 1 (1967)
See also I. Lindgren, J. Morrison: *Atomic Many-Body Theory*, 2nd ed., Springer Ser. Atoms Plasmas, Vol. 3 (Springer, Berlin, Heidelberg 1986)
S. Svanberg: *Atomic and Molecular Spectroscopy*, Springer Ser. Atoms Plasmas, Vol. 6 (Springer, Berlin, Heidelberg 1991)
4.2 M. Stobbe: Ann. Phys. **7**, 661 (1930)
4.3 F. Sauter: Ann. Phys. **11**, 454 (1931); see also R.H. Pratt, A. Ron, H.K. Tseng: Rev. Mod. Phys. **45**, 273, 663 (1973)

4.4 G. Schur: Ann. Phys. **4**, 433 (1930)
4.5 J. Cooper, R.N. Zare: J. Chem. Phys. **48**, 942 (1968)
4.6 W.J. Carter, G.K. Schweitzer, T.A. Carlson: J. Electron Spectrosc. **5**, 827 (1975); see also J.T.J. Huang, J.W. Rabalais: In *Electron Spectroscopy*, Vol. 2, ed. by C.R. Brundle, A.D. Baker (Academic, New York 1978)
4.7 J.H. Scofield: Lawrence Livermore Laboratory Report No. UCRL-51326 (1973)
4.8 J.J. Quinn: Phys. Rev. **126**, 1453 (1962)
4.9 C.N. Yang: Phys. Rev. **74**, 764 (1948); see also [4.4]
4.10 V.L. Jacobs: J. Phys. **B5**, 2257 (1972)
4.11 S.T. Manson, D. Dill: In *Electron Spectroscopy*, Vol. 2, ed. by C.R. Brundle, A.D. Baker (Academic, New York 1978)
4.12 S.T. Manson: In *Photoemission in Solids I*, ed. by M. Cardona, L. Ley, Topics Appl. Phys., Vol. 26 (Springer, Berlin, Heidelberg 1978)
4.13 R.J.W. Henry, L. Lipsky: Phys. Rev. **153**, 51 (1967)
4.14 H. Basch: J. Electron Spectrosc. **5**, 463 (1975)
4.15 L. Ley, S.P. Kowalczyk, F.R. McFeely, R.A. Pollak, D.H. Shirley: Phys. Rev. **B8**, 2392 (1973)
J.W. Gadzuk: Phys. Rev. B **14**, 2267 (1976)
4.16 C.S. Fadley: In *Electron Spectroscopy*, ed. by C.R. Brundle, A.D. Baker (Academic, New York 1978)
4.17 M.A. Brisk, A.D. Baker: J. Electron Spectrosc. **7**, 197 (1975)
4.18 D.A. Shirley: In *Photoemission in Solids I*, ed. by M. Cardona, L. Ley, Topics Appl. Phys., Vol. 26 (Springer, Berlin, Heidelberg 1978)
4.19 U. Fano: Phys. Rev. **124**, 1866 (1961)
4.20 U. Fano, J.W. Cooper: Rev. Mod. Phys. **40**, 441 (1968)
4.21 L.I. Johansson, J.W. Allen, I. Lindau, M.H. Hecht, S.B.M. Hagström: Phys. Rev. B **21**, 1408 (1980)
4.22 M.H. Hecht, I. Lindau: Phys. Rev. Lett. **47**, 821 (1981)
4.23 A.F. Starace: In *Handbuch der Physik*, Vol. 31, ed. by W. Mehlorn (Springer, Berlin, Heidelberg 1982)
4.24 B.L. Henke: Adv. X-Ray Anal. **5**, 285 (1962)
4.25 M.O. Krause: Chem. Phys. Lett. **10**, 65 (1971)
4.26 C.T. Hovland: Appl. Phys. Lett. **30**, 274 (1977)
4.27 M. Blume, D.E. Moncton: Phys. Today **38**, 69 (1985)
4.28 H. Robinson, W.F. Rawlinson: Philos. Mag. **28**, 277 (1914); ibid. **50**, 241 (1925)
4.29 E.M. Purcell: Phys. Rev. **54**, 818 (1938)
4.30 K.D. Sevier: *Low Energy Electron Spectrometry* (Wiley Interscience, New York 1972)
4.31 H.Z. Sar-El: Rev. Sci. Instrum. **38**, 1210 (1969)
4.32 S. Aksela: Rev. Sci. Instrum. **42**, 810 (1971)
4.33 K. Maeda, T. Ihara: Rev. Sci. Instrum. **42**, 1480 (1971); see also [4.30]
4.34 J.L. Gardner, J.A.R. Samson: J. Electron Spectrosc. **6**, 53 (1975)
4.35 C.S. Fadley, R.N. Healey, J.M. Hollander, C.E. Miner; J. Appl. Phys. **43**, 1085 (1972)
4.36 C.S. Fadley: Prog. Solid State Chem. **11**, 265 (1976)
4.37 E.C. Watson: Phys. Rev. **30**, 479 (1927)
4.38 H. Niehus, E. Bauer: Rev. Sci. Instrum. **46**, 1275 (1976)
4.39 N.V. Smith: In *Photoemission in Solids I*, ed. by M. Cardona, L. Ley, Topics Appl. Phys., Vol. 26 (Springer, Berlin, Heidelberg 1978)
4.40 C. Nordling: Ark. Fys. **15**, 397 (1959)

4.41 V. Dose: Prog. Surf. Sci. **13**, 225 (1983); see also F.J. Himpsel, N.V. Smith: Phys. Today **38**, 60 (1985)
4.42 P. Auger: C.R. Acad. Sci. **178**, 929 (1924); ibid. **180**, 65 (1925); ibid. **182**, 773, 1215 (1926)
4.43 E.H.S. Burhop, W.N. Asaad: In *Advance in Atomic and Molecular Physics*, Vol. 8, ed. by D.R. Bates (Academic, New York 1972)
4.44 W. Bambynek, B. Crasemann, R.W. Fink, H.U. Freund, H. Mark, C.D. Swift, R.E. Price, P.V. Rao: Rev. Mod. Phys. **44**, 716 (1972)
4.45 D. Chattarji: *The Theory of Auger Transitions* (Academic, New York, 1976)
4.46 G.E. McGuire, P.H. Holloway: In *Electron Spectroscopy*, Vol. 4, ed. by C.R. Brundle, A.D. Baker (Academic, New York 1981)
4.47 J.C. Fuggle: In *Electron Spectroscopy*, Vol. 4, ed. by C.R. Brundle, A.D. Baker (Academic, New York 1981)
4.48 E.H.S. Burhop: *The Auger Effect* (Cambridge University Press, Cambridge 1952)
4.49 H.A. Kramers: Z. Phys. **39**, 828 (1926)
4.50 D. Coster, R.L. Kronig: Physica **2**, 13 (1935)
4.51 H.S.W. Massey, E.H.S. Burhop: Proc. Cambridge Philos. Soc. **32**, 461 (1936)
4.52 J.N. Cooper: Phys. Rev. **65**, 155 (1944)
4.53 Y. Cauchois: J. Phys. Radium **5**, 1 (1944)
4.54 L. Asplund: Phys. Scr. **16**, 268 (1977)
4.55 F.K. Richtmyer, S.W. Barnes, E.G. Ramberg: Phys. Rev. **46**, 843 (1934)
4.56 J. Cooper: Phys. Rev. **61**, 234 (1942)
4.57 A. Bril: Physica **13**, 481 (1947)
4.58 E.G. Ramberg, F.K. Richtmyer: Phys. Rev. **51**, 913 (1937)
4.59 L. Pincherle: Physica **2**, 596 (1935)
4.60 G. Brogren: Ark. Fys. **23**, 219 (1963)
4.61 D. Coster, A. Bril: Physica **9**, 84 (1942)
4.62 E.J. McGuire: Phys. Rev. A **2**, 273 (1970); ibid. A**3**, 1801 (1971)
4.63 D.L. Walters and C.P. Bhalla: Phys. Rev. A**3**, 1919 (1971)
4.64 L.A. Harris: J. Appl. Phys. **39**, 1419 (1968)
4.65 J.F. McGilp, P. Weightman, E.J. McGuire: J. Phys. C **10**, 3445 (1977)
4.66 R. Nyholm, N. Martensson: Chem. Phys. Lett. **74**, 337 (1980)
4.67 G.L. Borchert, P.G. Hansen, B. Jonson, H.L. Ravn, O.W.B. Schult, P. Tidemand-Petersson, and the ISOLDE Collaboration: Phys. Lett. **63A**, 15 (1977)
4.68 J.H. Scofield: Phys. Rev. **179**, 9(1969); ibid. A**9**, 1041 (1974); ibid. A **10**, 1507 (1974); ibid. A **12**, 345 (1975)
4.69 M.H. Chen, B. Crasemann, H. Mark: Phys. Rev. A **21**, 436, 442, 449 (1980); ibid A **24**, 177 (1981)
4.70 B.G. Gokhale: C.R. Acad. Sci.: **233**, 937 (1951); Ann. Phys. (Paris) **7**, 852 (1952); see also B.G. Gokhale, S.N. Shukla, R.N. Srivastava: Phys. Rev. A **28**, 858 (1983); ibid. A **31**, 2715 (1985)
4.71 P. Amorim, L. Salgueiro, F. Parente, J.G. Ferreira: In *Radiation Physics*, ed. by E. Casnati, C. Baraldi, A. Tartari, (North-Holland, Amsterdam 1987)
4.72 S.I. Salem, P.L. Lee: Phys. Rev. A **10**, 2033 (1974): see also J.S. Thomsen: J. Phys. B **16**, 1171 (1983)
4.73 M. Siegbahn, W. Stenström: Phys. Z. **17**, 318 (1916)
4.74 G. Wentzel: Ann. Phys. **66**, 437 (1921); Z. Phys. **31**, 445 (1925)
4.75 M.J. Druyvesteyn: Z. Phys. **43**, 707 (1928)
4.76 Z. Horák; Proc. Phys. Soc. London **77**, 980 (1961)
4.77 T. Åberg, G. Graeffe, J. Utriainen, M. Linkoaho: J. Phys. C **3**, 1112 (1970)

4.78 A.N. Nigam, S.N. Soni: Physica **132**C, 407 (1985)
4.79 V.F. Demekhin, V.P. Sachenko: Bull. Acad. Sci. USSR, Phys. Ser. **31**(6), 913 (1967)
4.80 E.U. Condon, G.H. Shortley: *The Theory of Atomic Spectra* (Cambridge University Press, Cambridge 1935)
4.81 R.E. Lavilla: Phys. Rev. A **4**, 476 (1971)
4.82 G.R. Babu, V. Gopalakrishna, M.L.N. Raju, K. Parthasarathi, V.R.K. Murty, M.V.R. Murti, K.S. Rao: Phys. Rev. A **36**, 386 (1987)
4.83 M. Sawada, K. Tsutsumi, T. Shiraiwa, T. Ishimura, M. Obashi: Ann. Rep. Sci. Works, Osaka Univ. **7**, 1 (1959)
4.84 R.D. Deslattes: Phys. Rev. **133**, 4, 399 (1964)
4.85 T.A. Carlson, M.O. Krause: Phys. Rev. **140**, A 1057 (1965)
4.86 T. Åberg: Phys. Rev. **156**, 35 (1967)
4.87 A.N. Nigam, S. Arora: Physica **141C**, 115 (1986)
4.88 F.R. Hirsh: Phys. Rev. **50**, 191 (1936); Rev. Mod. Phys. **14**, 45 (1942)
4.89 L.G. Parratt: Phys. Rev. **54**, 99 (1938)
4.90 F.K. Richtmyer, E.G. Ramberg: Phys. Rev. **51**, 925 (1937)
4.91 L. Pincherle: Phys. Rev. **61**, 225 (1942)
4.92 Y. Cauchois: J. Phys. Radium **1**, 1 (1944)
4.93 M.O. Krause, F. Wuilleumier, C.W. Nestor: Phys. Rev. A **6**, 871 (1972)
4.94 Y. Cauchois, C. Sénémaud (eds.): *Wavelengths of X-Ray Emission Lines and Absorption Edges* (Pergamon, Oxford 1978)
4.95 H. Beuthe: Z. Phys. **60**, 603 (1930)
4.96 O.R. Ford: Phys. Rev. **41**, 577 (1932)
4.97 J. Valasek: Phys. Rev. **53**, 274 (1938)
4.98 M.A. Blokhin: Sov. Phys.—JETP **9**, 1515 (1939)
4.99 M. Sawada, K. Tsutsumi, T. Shiraiwa, M. Obashi: J. Phys. Soc. Jpn. **10**, 647 (1955)
4.100 H. Hulubei: C.R. Acad. Sci. **224**, 770 (1947)
4.101 H. Hulubei, Y. Cauchois, J. Manoscu: C.R. Acad. Sci. **226**, 764 (1948)
4.102 T. Åberg, J. Utriainen: Phys. Rev. Lett. **22**, 1346 (1969); J. de Phys. **32**, 295 (1971)
4.103 J. Utriainen, T. Åberg: J. Phys. C **4**, 1105 (1971)
4.104 T. Åberg: Phys. Rev. A **4**, 1735 (1971)
4.105 G.A. Rooke: Phys. Lett. **3**, 234 (1963)
4.106 D.S. Urch: J. Phys. C **3**, 1275 (1970)
4.107 J.P. Briand, P. Chevallier, M. Tavernier, J.P. Rozet: Phys. Rev. Lett. **27**, 777 (1971)
4.108 J.P. Briand, A. Touati, M. Frilley, P. Chevallier, A. Johnson, J.P. Rozet, M. Tavernier, S. Shafroth, M.O. Krause: J. Phys. B **9**, 1055 (1976)
4.109 T. Sagawa: J. de Phys. **32**, 186 (1971)
4.110 P. Richard, W. Hodge, C.F. Moore: Phys. Rev. Lett. **29**, 393 (1972); see also P. Richard, D.K. Olsen, R. Kauffman, C.F. Moore: Phys. Rev. A **7**, 1437 (1973)
4.111 J.P. Desclaux, C. Briancon, J.P. Thibaud, R.J. Walen: Phys. Rev. Lett. **32**, 447 (1974)
4.112 C.W.E. van Eijk, J. Winjhorst: Phys. Rev. A **15**, 1794 (1977)
4.113 W.F. Hanson, E.T. Arakawa: Z. Phys. **251**, 271 (1972)
4.114 M. Uda, A. Koyama, K. Maeda, Y. Sasa: In *X84: X-Ray and Inner-Shell Processes in Atoms, Molecules and Solids*, ed. by A. Maisel, J. Finster (Karl-Marx-Universität, Leipzig 1984) p. 307
4.115 I. Bergström, R.D. Hill: Ark. Fys. **8**, 21 (1954)
4.116 S.J. Edwards: Contemp. Phys. **11**, 195 (1970)
4.117 T.Åberg: In *Advance in X-Ray Spectroscopy*, ed. by C. Bonnelle, C. Mande (Pergamon, New York 1982)
4.118 E.H.S. Burhop: Proc. R. Soc. London A **198**, 272 (1935)

4.119 L. Pincherle: Nuovo Cimento **12**, 81, 122 (1935)
4.120 H.S.W. Massey, E.H.S. Burhop: Proc. R. Soc. London A **153**, 661 (1936)
4.121 H.J. Leisi, J.H. Brunner, C.F. Perdrisat, P. Scherrer: Helv. Phys. Acta **34**, 161 (1961)
4.122 W.Laskar: J. Phys. Radium **16**, 644 (1955)
4.123 V.O. Kostroun, M.H. Chen, B. Crasemann: Phys. Rev. A **3**, 533 (1971)
4.124 J.W. Colby: Adv. X-Ray Anal. **11**, 287 (1968)
4.125 R.W. Fink, R.C. Jopson, H. Mark, C.D. Swift: Rev. Mod. Phys. **38**, 513 (1966)
4.126 J.C. Bower: Proc. R. Soc. London A **157**, 662 (1936)
4.127 L.H. Martin, F.H. Eggleston: Proc. R. Soc. London A **158**, 46 (1937)
4.128 P.A. Ross: Phys. Rev. **28**, 425 (1926)
4.129 A.H. Compton: Philos. Mag. **8**, 961 (1921)
4.130 R.J. Stephenson: Phys. Rev. **51**, 637 (1937)
4.131 W.J. Campbell, J.V. Gilfrich: Anal. Chem. **42**, 248R (1970)
4.132 P. Natalis, J. Delwiche, J.E. Collin: Chem. Phys. Lett. **13**, 491 (1972)
4.133 C.D. Ellis, B.A. Skinner: Proc. R. Soc. London A **105**, 185 (1924)
4.134 V.L. Fitch, J. Rainwater: Phys. Rev. **92**, 789 (1953)
4.135 D. Kessler, H.L. Anderson, M.S. Dixit, H.J. Evans, R.J. McKee, C.K. Hargrove, R.D. Barton, E.P. Hincks, J.D. McAndrew: Phys. Rev. Lett. **18**, 1179 (1967)
4.136 C.S. Wu, L. Willets: Annu. Rev. Nucl. Sci. **19**, 527 (1969)
4.137 K.W. Ford, D.L. Hill: Annu. Rev. Nucl. Sci. **5**, 25 (1955)
4.138 E.H.S. Burhop: Contemp. Phys. **11**, 335 (1970)
4.139 G.R. Burleson, D. Cohen, R.C. Lamb, D.N. Michael, R.A. Schluter, J.O. White: Phys. Rev. Lett. **15**, 70 (1965)
4.140 C.E. Wiegand, D.A. Mack: Phys. Rev. Lett. **18**, 685 (1967)

Chapter 5

5.1 A.H. Compton, C.F. Hagenow: J. Opt. Soc. Am., Rev. Sci. Instrum. 487 (1924)
5.2 R.W. James: *The Optical Principles of the Diffraction of X-Rays* (Bell, East Brunswick, NJ 1967)
5.3 A.H. Compton: Phys. Rev. **21**, 207A (1923); ibid **22**, 409 (1923)
5.4 C.T.R. Wilson: Proc. R. Soc. London A **104**, 1 (1923)
5.5 A.A. Bless: Phys. Rev. **30**, 871 (1927)
5.6 R. Hofstadter, J.A. McIntyre: Phys. Rev. **78**, 24 (1950)
5.7 O. Klein, Y. Nishina: Z. Phys. **52**, 853 (1929)
5.8 B.K. Agarwal: *Quantum Mechanics and Field Theory*, 2nd ed. (Lokbharti, Allahabad 1983) p. 248
5.9 R.P. Singhal, A.J. Burns: Am. J. Phys. **46**, 646 (1978)
5.10 R.D. Evans: *Handbuch der Physik*, Vol. 34, ed. by S. Flügge (Springer, Berlin, Heidelberg 1958)
5.11 C.V. Raman: Indian J. Phys. **2**, 387 (1928)
5.12 A. Smekal: Naturwissenschaften: **11**, 873 (1923)
5.13 J.W.M. Dumond: Rev. Mod. Phys. **5**, 11 (1933)
5.14 A. Sommerfeld: Phys. Rev. **50**, 38 (1936)
5.15 K. Das Gupta: Phys. Rev. Lett. **3**, 38 (1959); ibid **13**, 338 (1964)
5.16 A. Faessler, P. Muhle: Phys. Rev. Lett. **17**, 4 (1966)
5.17 T. Suzuki: J. Phys. Soc. Jpn. **22**, 1139 (1967)
5.18 G.D. Priftis: Phys. Lett. **49** A, 281 (1974)

5.19 C.J. Sparks, Jr.: Phys. Rev. Lett. **33**, 262 (1974)
5.20 G.S. Brown, M.H. Chen, B. Crasemann, G.E. Ice: Phys. Rev. Lett. **45**, 1937 (1980)
5.21 Y.B. Bannett, I. Freund: Phys. Rev. Lett. **34**, 372 (1975)
5.22 D. Pines: *Elementary Excitations in Solids* (Benjamin, New York 1963) pp. 204-207
5.23 G.D. Priftis, A. Theodossion, K. Alexopoulos: Phys. Lett. **27**A, 577 (1968)
5.24 T. Suzuki, A. Tanokura: J. Phys. Soc. Jpn. **29**, 972 (1970)
5.25 G.G. Cohen, N.G. Alexandropoulos: Solid State Commun. **10**, 95 (1972)
5.26 R.H. Ritchie: Phys. Rev. **106**, 874 (1957)
5.27 A. Otto: Z. Phys. **224**, 65 (1969)
5.28 O.K. Harsh, B.K. Agarwal: Physica **144B**, 114 (1987); ibid 150*B*, 378 (1988)
5.29 R.H. Ritchie, R.E. Wilems: Phys. Rev. **178**, 372 (1969)
5.30 C. Kunz: Z. Phys. **196**, 311 (1966)
5.31 E.T. Arakawa, M.W. Williams, R.N. Hamm, R.H. Ritchie: Phys. Rev. Lett. **31**, 1127 (1973)
5.32 L. Ley, F.R. McFeely, S.P. Kowalczyk, J.G. Jenkin, D.A. Shirley: Phys. Rev. B **11**, 600 (1975)
5.33 G.D. Mahan: Phys. Rev. B **2**, 4334 (1970)
5.34 F.J. Feibelman, D.E. Eastman: Phys. Rev. B **10**, 4932 (1974)
5.35 P.H. Citrin, G.K. Wertheim, Y. Baer: Phys. Rev. B **16**, 425 (1977)
5.36 H. Raether: In *Springer Tracts in Modern Physics*, Vol. 38, ed. by G. Höhler (Springer, Berlin, Heidelberg 1965) p. 84
5.37 L.H. Jenkins, M.F. Chunz: Surf. Sci. **26**, 151 (1971)
5.38 M.O. Krause, J.G. Ferreira: J. Phys. B **89**, 2007 (1975)
5.39 O.K. Harsh, B.K. Agarwal: Physica **145B**, 45 (1987)
5.40 B.K. Agarwal, O.K. Harsh: Physica **151B**, 509 (1988)

Chapter 6

6.1 F. Hullinger, E. Mooser: "The Bond Description of Semiconductors: Polycompounds", in *Progress in Solid State Chemistry*, ed. by H. Reiss (Pergamon, Oxford 1965)
6.2 D.J. Nagel: In 18th ACAXA, Denver 1969: Advances in X-Rays, Vol. 13, ed. by B.L. Henke, J.B. Newkirk, G.R. Mallett (Plenum, New York 1970) p. 182
6.3 J.C. Phillips: Rev. Mod. Phys. **42**, 317 (1970)
6.4 J.C. Phillips: *Bonds and Bands in Semiconductors* (Academic, New York 1973)
6.5 C.A. Coulson, L.R. Redei, D. Stocker: Proc.R. Soc London **270**, 357 (1962)
6.6 L. Pauling: *The Nature of the Chemical Bond* (Cornell University Press, Ithaca, NY 1960)
6.7 A.L. Allred, E.G. Rochow: J. Inorg. Nucl. Chem. **5**, 264 (1958)
6.8 J.A. Van Vechten: Phys. Rev. **182**, 891 (1969): ibid **187**, 1007 (1969); ibid B 7, 1479 (1973); see also V.K. Srivastava: Phys. Rev. B **29**, 6993 (1984)
6.9 J.C. Phillips: Phys. Rev. Lett. **20**, 550 (1968)
6.10 J.P. Suchet: J. Phys. Chem. Sol. **21**, 156 (1961)
6.11 R.T. Sanders: *Inorganic Chemistry* (Van Nostrand Reinhold, New York 1967)
6.12 N.F. Mott, H. Jones: *Theory of the Properties of Metals and Alloys* (Dover, New York 1958)
6.13 D.R. Penn: Phys. Rev. **128**, 2093 (1962)
6.14 H.R. Phillips, M. Ehrenreich: Phys. Rev. **129**, 1550 (1963)

6.15 B.F. Levine: J. Chem. Phys. **59**, 1463 (1973); Phys. Rev. B **7**, 2591, 2600 (1973); ibid. B **10**, 1655 (1974)
6.16 B. Szigeti: Proc. R. Soc. London A **204**, 51 (1950)
6.17 E. Mooser, W.B. Pearson: Nature **190**, 406 (1961); ibid **192**, 335 (1961)
6.18 K. Siegbahn, C. Nordling, A. Fahlman, R. Nordberg, K. Hamrin, J. Hedman, G. Johansson, T. Bergmark, S.-E. Karlsson, I. Lindgren, B. Lindberg: *ESCA Atomic Molecular and Solid State Structure Studied by Means of Electron Spectroscopy* (Almqvist and Wiksell, Stockholm 1967)
6.19 K. Siegbahn: Philos. Trans. R. Soc. London A **268,** 33 (1970)
6.20 W.L. Jolly: J. Am. Chem. Soc. **92**, 3360 (1970)
6.21 M.E. Schwartz, J.D. Switalski, R.E. Stronski: In *Electron Spectroscopy*, ed. by D. A. Shirley (North-Holland, Amsterdam 1972)
6.22 J.P. Suchet: *Chemical Physics of Semiconductors* (Van Nostrand, London 1965)
6.23 Y.K. Syrkin, M.E. Dyatkina: *Structure of Molecules* (Butterworths, London 1950)
6.24 S.S. Batsanov, I.A. Ovsyannikova: In *Chemical Bonds in Semiconductors and Thermodynamics*, ed. by N.N. Sirota (Consultants Bureau, New York 1968) p.65
6.25 A.E. Lindh, O. Lundquist: Ark. Mat. Astron Fys. **18**, Nos. 14, 34, 35 (1924)
6.26 B.B. Ray: Philos Mag. **49**, 168 (1925)
6.27 E. Bäcklin: Z. Phys. **33**, 547 (1925); ibid **38**, 215 (1926)
6.28 G.B. Deodhar: Proc. R. Soc. London **A 131**, 647 (1931)
6.29 F.A. Gianturco, C.A. Coulson: Mol. Phys. **14**, 223 (1968)
6.30 C.R. Brundle, M.B. Robin, H. Basch: J. Chem. Phys. **53**, 2196 (1971).
6.31 A. Fahlman, K. Hamrin, J. Hedman, R. Nordberg, C. Nordling, K. Siegbahn: Nature **210**, 4 (1966)
6.32 A. Faessler, M. Goehring: Naturwissenschaften **39**, 1969 (1952); Z. Phys. **142**, 558 (1952)
6.33 E. Gilberg, B. Kern: Z. Phys. **174**, 372 (1963)
6.34 A. Faessler: "X-Ray Emission Spectra and Chemical Bonds" in Proc. of the Xth Colloquium Spectroscopium Internationale (University of Maryland 1963) p.307
6.35 R. Jenkins: *An Introduction to X-Ray Spectrometry* (Heyden, London 1976)
6.36 B.G. Gokhale, R.B. Chesler, F. Boehm: Phys. Rev. Lett. **18**, 957 (1967)
6.37 E.V. Petrovich, Yu. P. Smirnov, V.S. Zykov, A.I. Grushko, O.I. Sumbayev, I.M. Band, M.B. Trzhaskovskaya: Sov. Phys.—JETP **34**, 935 (1972)
6.38 M.A. Coulthard: J. Phys. B **7**, 440 (1974)
6.39 A.S. Koster, H. Mendel: J. Phys. Chem. Solids **31**, 2511, 2523 (1970)
6.40 S. Hagström, S.E. Karlsson: Ark. Fys. **26**, 451 (1964)
6.41 D.W. Fischer: J. Chem. Phys. **42**, 3814 (1965)
6.42 A. Fahlman, K. Hamrin, R. Nordberg, C. Nordling, K. Siegbahn: Phys. Rev. Lett. **14**, 127 (1965)
6.43 Landolt-Börnstein: *Zahlenwerte und Funktionen*, Vol. I (Springer, Berlin, Heidelberg 1955) p. 4
6.44 D.W. Fischer: Adv. X-Ray Anal. **13**, 173 (1969)
6.45 J.H.O. Varley: Nature **178**, 939 (1956)
6.46 A.T. Shubaev: Bull. Acad. Sci. USSR, Phys. Ser. **24**, 434 (1960)
6.47 W.J. Veigele, D.E. Stevenson, E.M. Henry: J. Chem. Phys. **50**, 5404 (1969)
6.48 U. Gelius: Phys. Scr. **9**, 133 (1974)
6.49 K. Siegbahn, C. Nordling, G. Johansson, J. Hedman, P.E. Hadén, K. Hamrin, U. Gelius, T. Bergmark, L.O. Werme, R. Manne, Y. Bear: *ESCA Applied to Free Molecules* (North-Holland, Amsterdam 1969)

6.50 K. Siegbahn, C. Nordling, A. Fahlman, R. Nordberg, K. Hamrin, J. Hedman, G. Johansson, T. Bergmark, S.-E. Karlsson, I. Lindgren, B. Lindberg: *ESCA, Atomic, Molecular and Solid State Structure by Means of Electron Spectroscopy*: Nova Acta Regiae Soc. Sci. Ups., Ser IV, **20** (1967)
6.51 D.A. Shirley: In *Advances in Chemical Physics*,Vol. XXIII, ed. by I. Prigogine, S.A. Rice (Wiley, New York 1973) p. 85
6.52 G. Hollinger, P. Kumurdijan, J.M. Mackowski, P. Pertosa, L. Porte, T.M. Duc; J. Electron Spectrosc. **5**, 237 (1974)
6.53 A. Rosén, I. Lindgren: Phys. Rev. **176**, 114 (1968)
6.54 R.E. Watson, J.F. Herbst, J.W. Wilkins: Phys. Rev. B **14**, 18 (1976)
6.55 L. Ley, S.P. Kowalczyk, F.R. McFeely, R.A. Pollak, D. A. Shirley: Phys. Rev. B **8**, 2392 (1973)
6.56 D.A. Shirley, R.L. Martin, S.P. Kowalczyk, F.R. McFeely, L. Ley: Phys. Rev. B **15**, 544 (1977)
6.57 N. Mårtensson, B. Johansson Solid State Commun. **32**, 791 (1979); see also B. Johansson, N. Mårtensson: Phys. Rev. B **21**, 4427 (1980)
6.58 V.I. Nefedov: J. Struct. Chem. (USSR) **7**, 518 (1966)
6.59 A.T. Shubaev; Bull. Acad. Sci. USSR, Phys. Ser. **25**, 998 (1961)
6.60 V.I. Nefedov: Phys. Status Solidi **2**, 904 (1962)
6.61 E. Clementi: IBM J. Res. Dev. Suppl. **9**, 2 (1965)
6.62 A.T. Shubaev: Bull. Acad. Sci. USSR, Phys. Ser. **27**, 6667 (1963)
6.63 G.L. Leonhardt, A. Meisel: J. Chem. Phys. **52**, 6189 (1970)
A. Meisel, G.L. Leonhardt, R. Szargan: *X-Ray Spectra and Chemical Binding*, Springer Ser. Chem. Phys., Vol. 37 (Springer, Berlin, Heidelberg 1989)
6.64 O.I. Sumbaev: Sov. Phys.—JETP **30**, 927 (1970)
6.65 J. Tilgner, I. Topol, G. Leonhardt, A. Meisel: J. Phys. Chem. Solids **30**, 27 (1975)
6.66 S.M. Karalnik: Bull. Acad. Sci. USSR, Phys. Ser. **20**, 739 (1956); ibid **21**, 1432 (1957)
6.67 C.A. Coulson, C. Zauli: Mol. Phys. **6**, 525 (1963)
6.68 V.F. Demekhin, V.P. Sachenko: Bull. Acad. Sci. USSR. Phys. Ser. **31**(6), 913 (1967)
6.69 B. Nordfors: Ark. Fys.**10**, 279 (1956)
6.70 G. Graeffe, H. Juslen, M. Karras: J. Phys. B **10**, 3219 (1977)
6.71 U.D. Misra, L.M. Watson: Phys. Scr. **36**, 673 (1987)
6.72 O. Benka, M. Uda: Phys. Rev. Lett. **56**, 54 (1986)
6.73 R.L. Park, J.E. Houston, D.G. Schreiner: Rev. Sci. Instrum. **41**, 1810 (1970)
6.74 R.L. Park, J.E. Houston: J. Vac. Sci. Technol. **11**, 1 (1974)
6.75 J.E. Houston, R.L. Park: J. Chem. Phys. **55**, 4601 (1971)
6.76 C. Bonnelle, R.C. Karnatak: C.R. Acad. Sci., Ser. B **258**, 494 (1969)
6.77 R.E. LaVilla: J. Chem. Phys. **56**, 2345 (1972); ibid **57**, 899 (1972)
6.78 L.E. Werme, B. Grennberg, J. Nordgren, C. Nordling, K. Siegbahn: Nature **242**, 453 (1973)
J. Nordgren, H. Ågren, C. Nordling, K. Siegbahn: J. Phys. B **10**, L511 (1977)
6.79 J.A. Bearden, H. Friedman: Phys. Rev. **58**, 387 (1940)
6.80 W.W. Beeman, H. Friedman: Phys. Rev. **56**, 392 (1939)
6.81 J. Farineau: Ann. Phys. **10**, 20 (1938)
6.82 H.W.B. Skinner: Philos. Trans. R. Soc. A **239**, 95 (1940)
6.83 R.H. Kingston; Phys. Rev. **84**, 944 (1951)
6.84 H.W.B. Skinner, T.G. Bullen, J.E. Johnston: Philos. Mag. **45**, 1070 (1954)
6.85 L.G. Parratt: Rev. Mod. Phys. **31**, 616 (1959)
6.86 C.G. Dodd, G.L. Glen: J. Appl Phys. **39**, 5377 (1968)

6.87 D.S. Urch: J. Phys. C **3**, 1275 (1970); Q. Rev. Chem. Soc. **25**, 343 (1971); In *Electron Spectroscopy—Theory, Techniques and Applications*, ed. by G.R. Brundle, A.D. Baker (Academic, London 1979) p. 1
6.88 L.A. Grunes: Phys. Rev. B **27**, 2111 (1983)
6.89 C.J. Ballhausen, H.B. Gray: *Molecular Orbital Theory* (Benjamin, New York 1964)
6.90 J. Müller, K. Feser, G. Wiech, A. Faessler: Phys. Lett. A **44**, 263 (1973)
6.91 J. Kieser: Z. phys. B **26**, 1 (1977)
6.92 G.Dräger, O. Brümmer: Phys. Status Solidi B **124**, 11 (1984)
6.93 T.E. Tegeler, N. Kosuch, G. Wiech, A. Faessler: Phys. Status Solidi B **84**, 561 (1977); B **91**, 223 (1979)
6.94 T.E. Tegeler, N. Kosuch, G. Wiech, A. Faessler: J. Electron Spectrosc. Relat. Phenom. **18**, 23 (1980)
6.95 E.C. Seltzer: Phys. Rev. **188**, 1916 (1969)
6.96 R.C. Barrett: Phys. Lett B **33**, 388 (1970)
6.97 R.T. Brockmeir. F. Boehm, E.N. Hatch: Phys. Rev. Lett. **15**, 132 (1965)
6.98 O.I. Sumbaev, A.F. Mezentsev: Zh. Eksp. Teor. Fiz. **49**, 459 (1965) [English transl. Sov. Phys.—JETP **22**, 323 (1966)]
6.99 R.B. Chesler, F. Boehm: Phys. Rev. **166**, 1202 (1968)
6.100 P.L. Lee, F. Boehm, A.A. Hahn: Phys. Rev. C **17**, 1859 (1978)

Chapter 7

7.1 A. Sandström: Z. Phys. **65**, 632 (1930)
7.2 C. Kurylenko: Thesis, Paris (1939)
7.3 T.V. Krishnan, A.N. Nigam: Proc. Indian Acad. Sci. **65**, 45 (1967)
7.4 L.G. Parratt, C.F. Hempstead, E.L. Jossem: Phys. Rev. **105**, 1228 (1957)
7.5 T. Magnusson: Thesis, Uppsala (1938)
7.6 B.K. Agarwal: Z. Phys. **142**, 161 (1955)
7.7 W.W. Beeman, H. Friedman: Phys. Rev. **56**, 392 (1939)
7.8 B.K. Agarwal: X-Ray Spectrom. **16**, 187 (1987)
7.9 A.E. Sandström: In *Handbuch der Physik*, ed. by S. Flügge, Vol. 30 (Springer, Berlin Heidelberg 1957)
7.10 W.F. Peed, L.E. Burkhart, R.A. Staniforth, L.G. Fable: Phys. Rev. **105**, 588 (1957)
7.11 G.D. Matthews: Master's Essay, Johns Hopkins University (1964)
7.12 O. Beckman, B. Axelsson, P. Bergvall: Ark. Fys. **15**, 567 (1959)
7.13 B.K. Agarwal, C.B. Bhargava, A.N. Vishnoi, V.P. Seth: J. Phys. Chem. Solids **37**, 725 (1976)
7.14 See, for example, J.E. Müller, J.W. Wilkins: Phys. Rev. B **29**, 4331 (1984)
7.15 J.E. Müller: In *EXAFS and Near Edge Structure III*, ed. by K.O. Hodgson, B. Hedman, J.E. Penner-Hahn, Springer Proc. Phys., Vol.2 (Springer, Berlin, Heidelberg 1984) p. 7
7.16 K. Schnopper: Phys. Rev. **131**, 2558 (1963); see also L.G. Parratt: Phys. Rev. **56**, 295 (1939)
7.17 L.G. Parratt: Rev. Mod. Phys. **31**, 616 (1959)
7.18 D. Coster: Z. Phys. **25**, 83 (1924)
7.19 L. Fonda, R.G. Newton: Ann. Phys. (NY) **9**, 416 (1960)
7.20 T. Watanabe: Phys. Rev. A **139**, 1747 (1965)
7.21 P.S. Bagus: Phys. Rev. A **139**, 619 (1965)
7.22 G.R. Mitchell: Dev. Appl. Spectrosc. **4**, 109 (1965)

7.23 E.E. Vainshtein, K.I. Narbutt: Izv. Akad. Nauk SSSR **1**, 71 (1945)
7.24 R.L. Barinskii, E.G. Nadzhakov: Bull. Acad. Sci. USSR, Phys. Ser. **24**, 419 (1960)
7.25 R.L. Barinskii: Bull. Acad. Sci. USSR, Phys. Ser. **25**, 958 (1961)
7.26 B.K. Agarwal, B.R.K. Agarwal: X-Ray Spectrom. **7**, 12 (1978); J. Phys. C **20**, 4223 (1978)
7.27 M. Croft, R. Neifeld, C.U. Segre, S. Raaen, R.D. Parks:Phys. Rev. B **30**, 4164 (1984)
7.28 Y. Cauchois, N. F. Mott: Philos. Mag. **40**, 1260 (1949)
7.29 D. Coster, H. DeLang: Physica **15**, 351 (1949)
7.30 Y. Cauchois, C. Bonnelle: C.R. Acad. Sci. **245**, 1230 (1957)
7.31 M.A. Blokhin, V.F. Demekhin, I.G. Shveitser: Bull. Acad. Sci. USSR **28**, 742 (1964)
7.32 S. Kawata, K. Maeda: J. Phys. Soc. Jpn. **32**, 778 (1972)
7.33 S. Kawata: J. Phys. F **5**, 324 (1975)
7.34 B.K. Agarwal, L.P. Verma: J Phys. C **1**, 208 (1968)
7.35 M. Brown, R.E. Peierls, E.A. Stern: Phys. Rev. B **15**, 738 (1977)
7.36 D.W. Fischer, W.L. Baun: J. Appl. Phys. **39**, 4757 (1968)
7.37 N.F. Mott: Proc. R. Soc. London **62**, 416 (1949)
7.38 T.K. Sham: In *EXAFS and Near Edge Structure*, ed. by A. Bianconi, L. Incoccia, S. Stipcich , Springer Ser. Chem. Phys., Vol. 27 (Springer, Berlin, Heidelberg 1983) p. 165
7.39 R.C. Lye, J.C. Phillips, D. Kaplan, S. Doniach, K.O. Hodgson: Proc. Natl. Acad. Sci. USA **77**, 5884 (1980)
7.40 P. Sakellaridis: C.R. Acad, Sci. **236**, 1014 (1953), and private communication (1971)
7.41 L.P. Verma, B.K. Agarwal: J. Phys. C **1**, 1658 (1968)
7.42 W. Seka, H.P. Hanson: J. Chem. Phys. **50**, 344 (1969)
7.43 A.K. Dey, B.K. Agarwal: J. Chem. Phys. **59**, 1397 (1973)
7.44 K.J. Rao, J. Wong, M.J. Weber: J. Chem. Phys. **28**, 6228 (1983)
7.45 J. Wong, S.H. Lamson, K.J. Rao: In *EXAFS and Near Edge Structure III*, ed. by K.O. Hodgson, B. Hedman, J.E. Penner–Hahn, Springer Proc. Phys., Vol. 2 (Springer, Berlin, Heidelberg 1984) p. 49
7.46 B.R.K. Agarwal, L.P. Verma, B.K. Agarwal: Nuovo Cimento Lett. **1**, 581 (1971)
7.47 D.M. Pease: Appl. Spectrosc. **30**, 405 (1976); see also E.A. Stern, K. Kim: Phys.Rev B **23**, 3781 (1981)
7.48 N.F. Mott, K.W.H. Stevens: Philos. Mag. **2**, 1364 (1957); see also R.D. Leapman, L.A. Grunes, P.L. Fejes: Phys. Rev. B **26**, 614 (1982)
7.49 B. Hedman, J.E. Penner-Hahn, K.O. Hodgson: In *EXAFS and Near Edge Structure III*, ed. by K.O. Hodgson, B. Hedman, J.E. Penner-Hahn Springer Proc. Phys., Vol.2 (Springer, Berlin, Heidelberg 1984) p.64
7.50 V.G. Bhide, N.V. Bhat: J. Chem. Phys. **48**, 3103 (1968); see also W.W. Beeman, J.A. Bearden: Phys. Rev. **61**, 455 (1942)
7.51 V.B. Singh, B.K. Agarwal: J. Phys. C **7**, 831 (1974)
7.52 B.K. Agarwal, R.K. Johri: J. Phys. F **7**, 1607 (1977)
7.53 A.N. Nigam, O.P. Rajput, B.D. Srivastava: X-Ray Spectrom. **13**, 156 (1984); ibid **15**, 111 (1986)
7.54 H.C. Yeh, L.V. Azaroff: J. Appl. Phys. **38**, 4034 (1967)
7.55 J.O. Dimmock: Solid State Phys. **26**, 103 (1971)
7.56 G.A. Burdick: Phys. Rev. **129**, 138 (1963)
7.57 L.V. Azaroff, D.M. Pease: In *X-Ray Spectroscopy*, ed. by L.V. Azaroff (McGraw-Hill, New York 1974) p. 284; also in *Advances in X-Ray Spectroscopy*, ed. by C. Bonnelle, C. Mande (Pergamon, New York 1982) p. 36
7.58 F.Szmulowicz, D.M. Pease: Phys. Rev. B **17**, 3341 (1978)

7.59 E.O. Kane: Phys. Rev. **159**, 624 (1967)
7.60 D.A. Goodings, R. Harris: J. Phys. C **2**, 1808 (1969)
7.61 D.J. Nagel: In *Band Structure Spectroscopy of Metals and Alloys*, ed. by D.J. Fabian, L.M. Watson (Academic, London 1973) p. 457
7.62 J.E. Muller, O. Jepsen, J.W. Wilkins: Solid State Commun. **42**, 365 (1982)
7.63 B.K. Agarwal, V.B. Singh: Nuovo Cimento Lett. **4**, 765 (1972)
7.64 V.G. Bhide, S.K. Kaicker: J. Phys. Chem. Solids **35**, 695 (1974)
7.65 V.O. Kostroun, R.W. Fairchild, C.A. Kukkonen, J.W. Wilkins: Phys. Rev. B **13**, 3268 (1976)
7.66 B.K. Agarwal, R.K. Johri: Phys. Status Solidi B **88**, 309 (1978)
7.67 J.E. Muller, O. Jepsen, O.K. Andersen, J.W. Wilkins: Phys. Rev. Lett. **40**, 720 (1978)
7.68 A. Kotani, Y. Toyozawa: J. Phys. Soc. Jpn. **35**, 1073, 1082 (1973)
J. Kanamori, A. Kotani (eds.): *Core-Level Spectroscopy in Condensed Systems*, Springer Ser. Solid-State Sci., Vol. 81 (Springer, Berlin, Heidelberg 1988)
7.69 B.K. Agarwal, V. Balakrishnan: Phys. Rev. B **28**, 2852 (1983)
7.70 J.L. Dehmer, A.F. Starace, U. Fano, J. Sugar, J.W. Cooper: Phys. Rev. Lett. **26**, 1521 (1971)
7.71 A. Bianconi, M. Campagna, S. Stizza: Phys. Rev. B **25**, 2477 (1982)
7.72 S.C. Moss, H. Metzger, E. Eisner, H.W. Huang, S.H. Hunter: Rev. Sci. Instrum. **49**, 1559 (1978)
7.73 H.W. Huang, S.H. Hunter, W.K. Warburton, S.C. Moss: Science **204**, 191 (1979)
7.74 J. Bergengren: Z. Phys. **3**, 247 (1920)
7.75 A.E. Lindh: Z. Phys. **6**, 303 (1921)
7.76 Y. Cauchois: *Les Spectres de Rayons X et la Structure Electronique de la Matière* (Gauthier-Villars, Paris 1948)
7.77 A. Meisel: Phys. Status Solidi **10**, 365 (1965)
A. Meisel, G. Leonhardt, R. Szargan: *X-Ray Spectra and Chemical Binding*, Springer Ser. Chem. Phys., Vol. 37 (Springer, Berlin, Heidelberg 1989)
7.78 D.J. Nagel, W.L. Baun: In *X-Ray Spectroscopy*, ed. by A. Azaroff (McGraw-Hill, New York 1974)
7.79 A.J. McAlister, R.C. Dobbyn, J.R. Cuthill, M.L. Williams: J. Phys. Chem. Ref. Data **2**, 411 (1973)
7.80 C.K. Jørgensen: In *Advances in X-Ray Spectroscopy*, ed. by C. Bonnelle, C. Mande (Pergamon, New York 1982) p. 225
7.81 C. Mande, V.B. Sapre: In *Advances in X-Ray Spectroscopy*, ed. by C. Bonnelle, C. Mande (Pergamon Press, New York 1982) p. 287
7.82 G. Wiech: Z. Phys. **207**, 428 (1967); ibid **216**, 472 (1968)
7.83 B.K. Agarwal, L.P. Verma: J. Phys. C **3**, 535 (1970)
7.84 V. Kunzl: Coll. Trav. Chim. Tchécoslovaquie **4**, 213 (1932)
7.85 G. Boehm, A. Faessler, G. Rittmayer: Z. Naturforsch. **9**, (b), 509 (1954)
7.86 E.E. Vainshtein: Sov. Phys.—Solid State **5**, 2150 (1964)
7.87 A. Miller: J. Phys. Chem. Solids **29**, 633 (1968)
7.88 V.B. Sapre, C. Mande: J. Phys. C **5**, 793 (1972)
7.89 B.K. Agarwal, V. Balakrishnan: J. Phys. F **12**, 1519 (1982)
7.90 I.A. Ovsyannikova, S.S. Batsanov, L.I. Nanonova, L.R. Batsanova, E.A. Nekrasova: Bull. Acad. Sci. USSR, Phys. Ser. **31**, 936 (1967)
7.91 A.K. Dey, B.K. Agarwal: Nuovo Cimento Lett. **1**, 803 (1971)
7.92 S.V. Adhyapak, A.S. Nigavekar: J. Phys. Chem. Solids **37**, 1037 (1976); ibid **39**, 171 (1978)
7.93 M.M. Ballal, C. Mande: J. Phys. Chem. Solids **38**, 843, 1383 (1977)

7.94 A.N. Vishnoi, B.K. Agarwal: Phys. Lett. **29A**, 105 (1969)
7.95 R.K. Johri, B.K. Agarwal: J. Phys. F **8**, 555 (1978)
7.96 M.N. Ghatikar, B.D. Padalia: J. Phys. C **11**, 1941 (1978)
7.97 G.L. Glen, C.G. Dodd: J. Appl. Phys. **39**, 5372 (1968)
7.98 R.G. Shulman, Y. Yafet, P. Eisenberger, N. E. Blumberg: Proc. Natl. Acad. Sci. USA **73**, 1384 (1976)
7.99 S.P. Cramer, W.O. Gillum, K.O. Hodgson, L.E. Mortenson, E.I. Steifel, J.R. Chisnell, W.J. Brill, V.K. Shah: J. Am. Chem. Soc. **100**, 3814 (1978)
7.100 F.W. Lytle, P.S.P. Wei, R.B. Gregor, G.H. Via, J.H. Sinfelt: J. Chem. Phys. **70**, 4849 (1979)
7.101 A. Bianconi: Appl. Surf. Sci. **6**, 392 (1980); also in *EXAFS and Near Edge Structure*, ed. by A. Bianconi, L. Incoccia, S. Stipcich, Springer Ser. Chem. Phys., Vol. 27 (Springer, Berlin, Heidelberg 1983)
7.102 W. Kossel: Z. Phys. **1**, 119 (1920); ibid **2**, 470 (1920)
7.103 A. Bianconi: In *EXAFS and Near Edge Structure III*, ed. by K.O. Hodgson, B. Hedman, J.E. Penner-Hahn, Springer Proc. Phys., Vol.2 (Springer, Berlin, Heidelberg 1984) p. 167
7.104 V.I. Nefedov: J. Struct. Chem. **11**, 277 (1970)
7.105 J.L. Dehmer: J. Chem. Phys. **56**, 4496 (1972); ibid **65**, 5327 (1976)
7.106 C.R. Natoli: In *EXAFS and Near Edge Structure*, ed. by A. Bianconi, L. Incoccia, S. Stipcich, Springer, Ser. Chem. Phys., Vol. 27 (Springer, Berlin, Heidelberg 1988) p.43
7.107 G.N. Greaves, P.J. Durham, G. Diakun, P. Quinn: Nature **294**, 139 (1981)
7.108 A. Bianconi, M. Dell' Ariccia, P.J. Durham, J.B. Pendry: Phys. Rev. B **26**, 6502 (1982)
7.109 J.C. Slater: *Quantum Theory of Molecules and Solids*, Vol. 4 (McGraw-Hill, New York 1974)
7.110 C.R. Natoli, D.K. Misemer, S. Doniach, F.W. Kutzler: Phys. Rev. A **22**, 1104 (1980)
7.111 F.W. Kutzler, D.E. Ellis, T.I. Morrison, G.K. Shenoy P.J. Viccaro, P.A. Montano, E.H. Appelman, L. Stein, M.J. Pellin, D.M. Gruen: Solid State Commun. **46**, 803 (1983)
7.112 G. Bunker, E. Stern: Phys. Rev. Lett. **52**, 1990 (1984)
7.113 N. Kosugi, T. Yokoyama, H. Kunoda: *In EXAFS and Near Edge Structure III*, ed. by K.O. Hodgson, B. Hedman, J.E. Penner-Hahn Springer Proc. Phys., Vol. 2 (Springer , Berlin, Heidelberg 1984) p. 55
T.A. Smith, J.E. Penner-Hahn, K.O. Hodgson, M.A. Berding, S. Doniach: ibid. p. 58
7.114 H. Fricke: Phys. Rev. **16**, 202 (1920)
7.115 G. Hertz: Z. Phys. **3**, 19 (1920)
7.116 D. Coster: Z. Phys. **25**, 83 (1924)
7.117 A.E. Lindh: Z. Phys. **6**, 303 (1921); ibid **31**, 210 (1925)
7.118 G.A. Lindsay: C.R. Acad. Sci. **175**, 150 (1922)
7.119 B.B. Ray: Z. Phys. **55**, 119 (1929)
7.120 B. Kievit, G.A. Lindsay: Phys. Rev. **36**, 648 (1930)
7.121 D. Coster, J. Veldkamp: Z. Phys. **70**, 306 (1931); ibid **74**, 191 (1932)
7.122 J.D. Hanawalt: Z. Phys. **70**, 20 (1931)
7.123 R. de L. Kronig: Z. Phys. **70**, 317 (1931)
7.124 L.V. Azaroff: Rev. Mod. Phys. **35**, 1012 (1963)
7.125 J.D. Hanawalt: Phys. Rev. **37**, 715 (1931)
7.126 R. de L. Kronig: Z. Phys **75**, 468 (1932)
7.127 H. Petersen: Z. Phys. **76**, 768 (1932); ibid **80**, 258 (1933); ibid **98**, 569 (1936)
7.128 D.R. Hartree, R. de L. Kronig, H. Petersen: Physica **1**, 895 (1934)

7.129 A.I. Kostarev: Zh. Eksp. Teor. Fiz. **11**, 60 (1941); ibid **19**, 413 (1949); ibid **21**, 917 (1951)
7.130 T. Hayasi: Sci. Rep. Tohoku Univ., Ser. 1. **33**, 123 (1949)
7.131 W.M. Weber: Phys. Rev. B **11**, 2744 (1975)
7.132 T. Shiraiwa, T. Ishimura, M. Sawada: Phys. Soc. Jpn. **12**, 788 (1957); ibid **13**, 847 (1958)
7.133 A.I. Kozlenkov: Bull. Acad. Sci. USSR, Phys. Ser. **25**, 968 (1961)
7.134 A.N. Vishnoi B.K. Agarwal: Proc. Phys. Soc. London **89**, 799 (1966)
7.135 V.V. Shmidt: Bull. Acad. Sci. USSR, Ser. Phys. **25**, 988 (1961); ibid. **27**, 392 (1963)
7.136 J.A. Jope: J. Phys. C **2**, 1817 (1969)
7.137 R.M. Levy: J. Chem. Phys. **43**, 1846 (1965)
7.138 F.W. Lytle: Adv. X-Ray Anal. **9**, 398 (1966)
7.139 B.K. Agarwal, R.K. Johri: J. Phys. C **10**, 3213 (1977)
7.140 D.E. Sayers, F.W. Lytle, E.A. Stern: Adv. X-Ray Anal. **43**, 248 (1970)
7.141 J. Perel, R.D. Deslattes: Phys. Rev. B **2**, 1317 (1970)
7.142 D.E. Sayers, E.A. Stern, F.W. Lytle: Phys. Rev. Lett. **27**, 1204 (1971)
7.143 E.A. Stern: Phys. Rev. B **10**, 3027 (1974)
7.144 F.W. Lytle, D.E. Sayers, E.A. Stern: Phys. Rev. B **11**, 4825 (1975)
7.145 E.A. Stern, D.E. Sayers, F.W. Lytle: Phys. Rev. B **11**, 4836 (1975)
7.146 B.M. Kincaid, P. Eisenberger: Phys. Rev. Lett. **34**, 1361 (1975)
7.147 C.A. Ashley, S. Doniach: Phys. Rev. B **11**, 1279 (1975)
7.148 P.A. Lee, J.B. Pendry: Phys. Rev. B **11**, 2795 (1975)
7.149 P.A. Lee, G. Beni: Phys. Rev. B **15**, 2862 (1977)
7.150 B.K. Teo, P.A. Lee: J. Am. Chem. Soc. **101**, 2815 (1979)
7.151 P.A. Lee, P.H. Citrin, P. Eisenberger, B.M. Kincaid: Rev. Mod. Phys. **53**, 769 (1981)
7.152 T.M. Hayes, J.B. Boyce: Solid State Phys. **37**, 173 (1982)
7.153 P.A. Lee: Phys. Rev. B **13**, 5261 (1976)
7.154 G. Beni, P.M. Platzman; Phys. Rev. B **14**, 9514 (1976)
7.155 D. Berreman: Phys. Rev. B **19**, 560 (1979)
7.156 K. Lonsdale (ed): International Tables for X-Ray Crystallography (Kynoch, Birmingham, England 1962)
7.157 J. Stöhr: Stanford Synchrotron Radiation Laboratory Report 80/70 (1980)
7.158 J. Waser, V. Shomaker: Rev. Mod. Phys. **25**, 671 (1953)
7.159 F.G. Halaka, J.D. Baldeschwieler, J.J. Boland: In *EXAFS and Near Edge Structure III*, ed. by K.O. Hodgson, B. Hedman, J.E. Penner-Hahn, Springer Proc. Phys., Vol. 2 (Springer, Berlin, Heidelberg 1984) p. 80
7.160 P. Mahto, A.R. Chetal: Phys. Rev. Lett. **58**, 889 (1987)
7.161 J.M. Tranquada, R. Ingalls: Phys. Rev. B **28**, 3520 (1983)
7.162 R.G. Shulman, P. Eisenberger, W.E. Blumberg, N.A. Stombaugh: Proc. Natl. Acad. Sci. USA **72**, 4003 (1975); see also S.J. Gurman, R.F. Pettifer: Philos. Mag. **40**, 345 (1979)
7.163 S.P. Cramer, T.K. Eccles, F.W. Kutzler, K.O. Hodgson, S. Doniach: J. Am. Chem. Soc. **98**, 8059 (1976)
7.164 M.B. Stearns: Phys. Rev. B **25**, 2382 (1982)
7.165 E.D. Crozier, A.J. Seary: Can. J. Phys. **58**, 3027 (1979)
7.166 J.Wong, H. Liebermann: Phys. Rev. B **29**, 651 (1984)
7.167 J. Stöhr, R. Jaeger, S. Brennen: Surf. Sci. **117**, 503 (1982)
7.168 P. Roubin, D. Chandesria, G. Rossi, J. Lecante, M.C. Desjonqueres, G. Treglia: Phys. Rev. Lett. **56**, 1272 (1986)

7.169 F. Comin, J.E. Rowe, P.H. Citrin: Phys. Rev. Lett. **56**, 2402 (1983)
7.170 R. Ingalls, E.D. Crozier, J.E. Whitmor, A.J. Seary, J.M. Tranquada: J. Appl. Phys. **51**, 3158 (1980)
7.171 J.M. Tranquada, R. Ingalls: Phys. Rev. B **28**, 3520 (1983)
7.172 H.W. Huang, W.H. Lin, T.Y. Teng, X.F. Wang: Rev. Sci. Instrum. **54**, 1488 (1983)
7.173 B. Chance, R. Fischetti, L. Powers: Biochemistry **22**, 3820 (1983)
7.174 J.G. Bednorz, K.A. Müller: Z. Phys. B **64**, 189 (1986)
7.175 J.B. Boyce, F. Bridges, T. Claeson, T.H. Geballe, C.W. Chu, J.M. Tarascon: Phy. Rev. B **35**, 7203 (1987)
7.176 D.C. Konisberger, R. Prins (eds.): *X-Ray Absorption: Principles, Applications and Techniques of EXAFS, SEXAFS, and XANES* (Wiley, New York 1988)
7.177 J.W.M. Du Mond, V.L. Bollman: Phys. Rev. **51**, 400 (1937)
7.178 P. Ohlin: Ark. Fys. **4**, 387 (1952)
7.179 A. Nilsson: Ark. Fys. **6**, 513 (1953)
7.180 P. Johansson: Ark. Fys. **18**, 329 (1960)
7.181 J.J. Spijkerman, J.A. Bearden: Phys. Rev. A **134**, 871 (1964)
7.182 B.R.A. Nijboer: Physica **12**, 461 (1946)
7.183 K. Ulmer: Z. Phys. **162**, 254 (1961)
7.184 G. Böhm, K. Ulmer: J. de Phys. **32**, C4-241 (1971)
7.185 J.S. Bergwoll, R.K. Tyagi: Ark. Fys. **29**, 439 (1965)
7.186 R.R. Turtle, R.J. Liefeld: Phys. Rev. B **7**, 3411 (1973)
7.187 H. Rempp: Z. Phys. **267**, 181, 187 (1974)
7.188 V. Dose: Appl. Phys. **14**, 117 (1977)
7.189 W.Speier, J.C. Fuggle, R. Zeller, M. Campagna: In *EXAFS and Near Edge Structure III*, ed. by K.O. Hedgson, B. Hedman, J.E. Penner-Hahn, Springer Proc. Phys., Vol. 2 (Springer, Berlin, Heidelberg 1984) p. 496

Chapter 8

8.1 H.W.B. Skinner: Philos. Trans. Soc. London A **239**, 95 (1940)
8.2 D.H. Tomboulian: In *Handbuch der Physik*, Vol. 30, ed. by S. Flügge (Springer, Berlin, Heidelberg 1957)
8.3 J.A.R. Samson: *Techniques of Vacuum Ultraviolet Spectroscopy* (Wiley, New York 1967)
8.4 D.J. Fabian: Crit. Rev. Solid State Sci. **2**, 255 (1971); see also in *X*84: *X-ray and Inner-Shell Processes in Atoms, Molecules and Solids*, ed. by A. Meisel, J. Finster (Karl-Marx-Universität, Leipzig 1984) p. 385
8.5 D.J. Fabian, L.M. Watson, C.A.W. Marshall: Rep. Prog. Phys. **34**, 601 (1971)
8.6 F.C. Brown: Solid State Phys. **29**, 1 (1974)
8.7 V. Schumann: Akad. Wiss. Wien **102** (2A), 625 (1893)
8.8 M. Plato: Z. Naturforsch. **19a**, 1324 (1964)
8.9 W.R.S. Garton, M.S.W. Webb, P.C. Wildy: J. Sci. Instrum. **34**, 496 (1957)
8.10 P.G. Wilkinson: J. Opt. Soc. Am. **45**, 1044 (1955)
8.11 N.N. Axelrod: J. Opt. Soc. Am. **53**, 297 (1963)
8.12 F.C. Fehsenfeld, K.M. Evenson, H.P. Broida: Rev. Sci. Instrum. **36**, 294 (1965)
8.13 D.H. Tomboulian, P.L. Hartman: Phys. Rev. **102**, 1423 (1956)
8.14 R.P. Godwin: Springer Tracts in Modern Physics, Vol. 51 (Springer, Berlin, Heidelberg 1969)

8.15 K. Feser, J. Müller, G. Wiech, A. Faessler: J. de Phys. **32**, C4–333 (1971)
8.16 W. Hayes: Contemp. Phys. **13**, 441 (1972)
8.17 K. Codling: Rep. Prog. Phys. **36**, 541 (1973)
8.18 J.D. Jackson: *Classical Electrodynamics*, 2nd ed. (Wiley, New York, 1975)
8.19 J. Schwinger: Phys. Rev. **70**, 798 (1946); ibid. **75**, 1912 (1949)
8.20 Y. Cauchois, Y. Heno: *Le Cheminement des Particules Chargées* (Gauthier-Villars, Paris 1964) p. 170
8.21 R.J. Speer: Space Sci. Instrum. **2**, 463 (1976); see also A. Franks, K. Lindsey, J.M. Bennett, R.J. Speer, D. Turner, D.J. Hunt: Philos. Trans. R. Soc. London **277**, 503 (1975)
8.22 A.L. Morse, G.L. Weissler: Sci. Light **15**, 22 (1966)
8.23 G.R. Harrison, R.C. Lord, J.R. Loofbourow: *Practical Spectroscopy* (Prentice Hall, Englewood Cliffs, NJ 1948)
8.24 D.L. MacAdam: J. Opt. Soc. Am. **23**, 178 (1933)
8.25 R.A. Sawyer: *Experimental Spectroscopy* (Dover, New York 1963)
8.26 G.A. Sawyer, A.J. Bearden, I. Henins, F.C. Jahoda, F.L. Ribe: Phys. Rev. **131**, 1891 (1963)
8.27 R.P. Madden, D.L. Ederer, K. Codling: Appl. Opt. **6**, 31 (1967); see also R.P. Madden: In *X-Ray Spectroscopy*, ed. by L.V. Azaroff (McGraw-Hill, New York 1974) p. 338
8.28 E.R. Piore, G.G. Harvey, E.M. Gyorgy, R.H. Kingston: Rev. Sci. Instrum. **23**, 8 (1952)
8.29 J.L. Rogers, F.C. Chalkin: Proc. Phys. Soc. London B **67**, 348 (1954)
8.30 D.L. Ederer, D.H. Tomboulian: Appl. Opt. **3**, 1073 (1964)
8.31 A.J. Tuzzolino: Rev. Sci. Instrum. **35**, 1332 (1964); Phys. Rev. **A 134**, 205 (1964)
8.32 B.K. Agarwal: *Quantum Mechanics and Field Theory*, 2nd ed. (Lokbharti, Allahabad 1983) p. 48
8.33 D.E. Bedo, D.H. Tomboulian: Phys. Rev. **109**, 35 (1958)
8.34 J.A. Catterall, J.A. Trotter: Philos. Mag. **4**, 1164 (1959)
8.35 R.S. Crisp, S.E. Williams: Philos. Mag. **5**, 525 (1960)
8.36 F.S. Ham: Phys. Rev. **128**, 82, 2524 (1962)
8.37 D.A. Goodings: Proc. Phys. Soc. London **86**, 75 (1965)
8.38 G.A. Ausman, A.J. Glick: Phys. Rev. **183**, 687 (1969)
8.39 A.G. Mathewson, H.P. Myers: Philos. Mag. **25**, 853 (1972)
8.40 G.D. Mahan: Solid State Phys. **29**, 75 (1974)
8.41 N.V. Smith: Phys. Rev. **183**, 634 (1969)
8.42 G.D. Mahan: Phys. Rev. **163**, 612 (1967)
8.43 Y. Mizuno, K. Ishikawa: J. Phys. Soc. Jpn. **25**, 627 (1968)
8.44 P. Nozières, C.T. de Dominicis: Phys. Rev. **178**, 1097 (1969)
8.45 B. Roulet, J. Gavoret, P. Nozières: Phys. Rev. **178**, 1072 (1969)
8.46 L. Hedin: In *X-Ray Spectroscopy*, ed. by L.V. Azaroff (McGraw-Hill, New York 1974) p. 226
8.47 P. Longe: In *Advances in X-Ray Spectroscopy*, ed. by C. Bonnelle, C. Mande (Pergamon, New York 1982) p. 254
8.48 W.L. Baun, D.W. Fischer: Adv. X-Ray Anal. **8**, 371 (1965)
8.49 H. Neddermeyer: Z. Phys. **271**, 329 (1974)
8.50 K. Läuger: In *Soft X-Ray Band Spectra and Electronic Structure of Metals and Materials*, Part I, ed. by D.J. Fabian (Academic, New York 1969)
8.51 A. Appleton: Contemp. Phys. **6**, 50 (1964)

8.52 G.A. Rooke: In *X-Ray Spectroscopy*, ed. by L.V. Azaroff (McGraw-Hill, New York 1974) p. 173
8.53 C. Senemaud: In *Advances in X-Ray Spectroscopy*, ed. by C. Bonnelle, C. Mande (Pergamon, New York 1982) p. 423
8.54 P.T. Landsberg: Proc. Phys. Soc. London **A 62**, 806 (1949)
8.55 D. Bohm, D. Pines: Phys. Rev. **92**, 609 (1953)
8.56 J. Pirenne, P. Longe: Physica **30**, 277 (1964)
8.57 P. Longe, A.J. Glick: Phys. Rev. **177**, 526 (1969)
8.58 J.J. Lander: Phys. Rev. **91**, 1382 (1953)
8.59 G.A. Rooke: Phys. Lett. **3**, 234 (1963)
8.60 F. Brouers: Phys. Lett. **11**, 297 (1964); Phys. Status Solidi **22**, 213 (1967)
8.61 A.J. Glick, P. Longe: Phys. Rev. Lett. **15**, 589 (1965)
8.62 P.W. Anderson: Phys. Rev. Lett. **18**, 1049 (1967)
8.63 Y. Cauchois: Philos. Mag. **44**, 173 (1953)
8.64 H.W.B. Skinner, T.G. Bullen, J.E. Johnston: Philos. Mag. **45**, 1070 (1954)
8.65 E.M. Gyorgy, G.G. Harvey: Phys. Rev. **87**, 861 (1952); ibid. **93**, 365 (1954)
8.66 D.J. Fabian (ed.): *Soft X-Ray Band Spectra* (Academic, New York 1968) and references therein
8.67 D.H. Tomboulian, D.E. Bedo: Rev. Sci. Instrum. **26**, 747 (1955)
8.68 M.P. Givens, W.P. Siegmund: Phys. Rev. **85**, 313 (1952)
8.69 J.W. Cooper: Phys. Rev. **128**, 681 (1962)
8.70 J. Friedel: Philos. Mag **43**, 153, 1115 (1952); Comments Solid State Phys. **2**, 21 (1969)
8.71 M. Combescot, P. Nozières: J. de Phys. **32**, 913 (1971)
8.72 A. Kotani, Y. Toyozawa: In *Synchrotron Radiation*, ed. by C. Kunz, Topics Curr. Phys. Vol. 10 (Springer, Berlin, Heidelberg 1979)
8.73 S.M. Bose, P. Longe: Phys. Rev. B **18**, 3921 (1978)
8.74 C. Sénémaud: Phys. Rev. B **18**, 3929 (1978)
8.75 H.W.B. Skinner, J.E. Johnston: Proc. Soc. London A **161**, 420 (1937)
8.76 K. Tsutsumi, Y. Iwasaki, O. Aita, K. Ishikawa, T. Watanabe: J. Phys. Soc. Jpn. **47**, 1920 (1979)
8.77 B.K. Agarwal, M.P. Givens: Phys. Rev. **107**, 62 (1957)
8.78 B.K. Agarwal, M.P. Givens: Phys. Rev. **108**, 658 (1957); J. Phys. Chem. Solids **6**, 178 (1958)
8.79 B. Sonntag: DESY-F41/1 Rep. (Hamburg 1969); see also B. Sonntag, R. Haensel, C. Kunz: Solid State Commun. **7**, 597 (1969)
8.80 F.C. Brown, C. Gähwiller, A.B. Kunz: Solid State Commun. **9**, 487 (1971), W. Gudat, C. Kunz: Phys. Status Solidi B **52**, 433 (1972)
8.81 N.F. Mott, K.W.H. Stevens: Philos. Mag. **2**, 1364 (1957)
8.82 B. Sonntag, F.C. Brown: Phys. Rev. B **10**, 2300 (1974)

Chapter 9

9.1 A. Hadding: Z. Phys. **3**, 369 (1920)
9.2 B.K. Agarwal, M. Eisner: *Statistical Mechanics* (Wiley Eastern, New Delhi 1988) p. 159
9.3 M. Yoshimatsu, S. Kozaki: In *X-Ray Optics*, ed. by H.J. Queisser, Topics Appl. Phys., Vol. 22, (Springer, Berlin, Heidelberg 1977)
9.4 J.S. Thomsen, A.F. Burr: Am. J. Phys. **36**, 803 (1968)

9.5 W.L. Bragg: J. Sci. Instrum. **24**, 27 (1947)
9.6 J.A. Bearden: Phys. Rev. B **137**, 455 (1965)
9.7 F.S. Lee, W.J. Campbell: Adv. X-Ray Anal. **8**, 431 (1965)
9.8 R.W.G. Wycoff: *The Structure of Crystals* (Chemical Catalog Co., New York 1931) p. 981
9.9 M. Siegbahn: *Spektroskopie der Röntgenstrahlung* (Springer, Berlin 1931)
9.10 H.S. Uhler, C.D. Cooksey: Phys. Rev. **10**, 645 (1917)
9.11 H.S. Uhler: Phys. Rev. **11**, 1 (1918)
9.12 C.D. Cooksey, D. Cooksey: Phys. Rev. **36**, 85 (1930)
9.13 B.K. Agarwal, A.N. Vishnoi: Naturwissenschaften **49**, 178 (1962)
9.14 S.K. Allison: Phys. Rev. **38**, 203 (1931)
9.15 J.S. Thomsen: In *X-Ray Spectroscopy*, ed. by L.V. Azaroff (McGraw-Hill, New York 1974) p. 26
9.16 J.C.M. Brentano: J. Appl. Phys. **17**, 420 (1946)
9.17 W. Soller: Phys. Rev. **24**, 158 (1924)
9.18 L.S. Birks, E.J. Brooks: Anal. Chem. **27**, 1147 (1955)
9.19 Y. Cauchois: J. Phys. Radium **3**, 320 (1932); ibid. **4**, 61 (1933); C.R. Acad. Sci. **194**, 1479 (1932); ibid. **223**, 82 (1946); Rev. Opt. Theor. Instrum. **29**, 151 (1950)
9.20 G.L. Clark: *Applied X-Rays* (McGraw-Hill, New York 1955) p. 544; see also W.W. Jackson, J. West: Z. Kristallogr. **85**, 160 (1933); E.W. Radoslovich: Acta Crystallogr. **13**, 919 (1960)
9.21 J.W.M. DuMond: Rev. Sci. Instrum. **18**, 626 (1947); see also G.L. Borchert, P.G. Hansen, B. Jonson, H.L. Ravn, O.W.B. Schult, P. Tidemand-Petersson: Nucl. Instrum. Methods **178**, 209 (1980)
9.22 H. Johann: Z. Phys. **69**, 185 (1931)
9.23 T. Johansson: Z. Phys. **82**, 507 (1933)
9.24 E. Gilberg: Rev. Sci. Instrum. **42**, 1189 (1971)
9.25 C.H. Ehrhardt, E.M. Banas, J.L. Janik: Appl. Spectrosc. **22**, 730 (1968)
9.26 D.L. Parker: Adv. X-Ray Anal. **17**, 521 (1974)
9.27 D.W. Berreman: Phys. Rev. B **14**, 4313 (1976)
9.28 D.W. Berreman: Phys. Rev. B **19**, 560 (1979)
9.29 M.M. Schwarzschild: Phys. Rev. **32**, 162 (1928)
9.30 R.C. Spencer: Phys. Rev. **38**, 618 (1931)
9.31 A. von Laue: Z. Phys. **72**, 472 (1931)
9.32 L.P. Smith: Phys. Rev. **46**, 343 (1934)
9.33 A.H. Compton, S.K. Allison: *X-Rays in Theory and Experiment* (Van Nostrand, New York 1935)
9.34 H.W. Schnopper: J. Appl. Phys. **36**, 1415, 1423, 3692 (1965)
9.35 J. Drahokoupil, A. Fingerland: In *Advances in X-Ray Spectroscopy*, ed. by C. Bonnelle, C. Mande (Pergamon, New York 1982) p. 167
9.36 B. Davis, W. Stempel: Phys. Rev. **17**, 608 (1921); ibid. **19**, 504 (1922)
9.37 S.K. Allison: Phys. Rev. **41**, 1 (1932)
9.38 L.G. Parratt: Phys. Rev. **41**, 561 (1932)
9.39 J.W.M. DuMond: Phys. Rev. **52**, 872 (1937)
9.40 G. Brogren: Ark. Fys. **8**, 391 (1954)
9.41 G. Brogren, Ö. Adell: Ark. Fys. **8**, 97 (1954)
9.42 M. Renninger: Acta Crystallogr. **8**, 597 (1955)
9.43 R. Bubakova, J. Drahokoupil, A. Fingerland: Czech. J. Phys. B **11**, 205 (1961)
9.44 K. Kohra: J. Phys. Soc. Jpn. **17**, 589 (1962)

9.45 A. Authier: Bull. Soc. Fr. Mineral. **84**, 51 (1961); see also C. Malgrange, A. Authier: C.R. Acad. Sci. **261**, 3774 (1965)
9.46 G. Borrmann: Phys. Z. **42**, 157 (1941); Z. Phys. **127**, 297 (1950)
9.47 Z.G. Pinsker: *Dynamical Scattering of X-Rays in Crystals*, Springer Ser. Solid-State Sci., Vol. 3 (Springer, Berlin, Heidelberg 1978) p. 302
9.48 A.H. Compton, R.L. Doan: Proc. Natl. Acad. Sci. **11**, 598 (1926)
9.49 J.P. Thibaud: J. de Phys. **8**, 13 (1927)
9.50 C. Eckart: Phys. Rev. **44**, 12 (1933)
9.51 J.R. Cuthill: In *X-Ray Spectroscopy*, ed. by L.V. Azaroff (McGraw-Hill, New York 1974)
9.52 A. Franks, K. Lindsey, J.M. Bennett, R.J. Speer, D. Turner, D.J. Hunt: Philos. Trans. R. Soc. London A **277**, 503 (1975)
9.53 R.W. Hendrick: J. Opt. Soc. Am. **47**, 165 (1957)
G.L. Johnson, R.F. Wuerker: In *X-Ray Optics and Microanalysis*, ed. by H.H. Pattee, V.E. Cosslett, A. Engström (Academic, New York 1963) p. 229
9.54 D.R. Beaman, J.A. Isari, H.K. Birnbaum, R. Lewis: J. Phys. E **5**, 767 (1972)
9.55 L.S. Birks: *X-Ray Spectrochemical Analysis*, 2nd ed. (Interscience, New York 1969) p. 63
9.56 S.C. Curran, A.L. Cockroft, J. Angus: Philos. Mag. **40**, 929 (1949)
9.57 A.J. Campbell, K.W.O. Ledingham: Br. J. Appl. Phys. **17**, 769 (1966)
9.58 U. Fano: Phys. Rev. **70**, 44 (1946)
9.59 U.W. Arndt, W.A. Coates, A.R. Crathorn: Proc. Phys. Soc., London B **67**, 357 (1954)
9.60 A. Bisi, L. Zappa: Nuovo Cim. **2**, 988 (1955)
9.61 J.L. Culhane, J. Herring, P.W. Sanford, G. O'Shea, R.D. Phillips: J. Sci. Instrum. **43**, 908 (1966)
9.62 R. Jenkins, P.W. Hurley: Can. Spectrosc. **13**, 35 (1968)
9.63 C.F. Hendee, S. Fine, W.B. Brown: Rev. Sci. Instrum. **27**, 531 (1956)
9.64 J.T. Nelson, R.T. Ellickson: J. Opt. Soc. Am. **45**, 984 (1955)
9.65 H.I. West, Jr. W.E. Meyerhof, R. Hofstadter: Phys. Rev. **81**, 141 (1951)
9.66 R. Jenkins, J.L. de Vries: *Practical X-Ray Spectroscopy*, 2nd ed. (Springer, New York 1975)
9.67 H.R. Bowman, E.K. Hyde, S.G. Thomson, R.C. Jared: Science **151**, 562 (1966)
9.68 D.A. Gedke: X-Ray Spectrom. **1**, 129 (1972)
9.69 R.L. Health: Advan. X-Ray Anal. **15**, (1972)
9.70 U. Wille, R. Hippler: Phys. Rep. **132**, 129 (1986)
9.71 A.J. Dabrowski, M. Singh, G.B. Huth: In *Energy Dispersive X-Ray Spectroscopy*, ed. by K.F.J. Heinrich et al., NBS Special Publication 604 (1981) p. 45
9.72 E. Marageter, W. Wegscheider, K. Mueller: Nucl. Instrum. Methods B **1**, 137 (1984)
9.73 J.L. Campbell, B.M. Hillman, J.A. Maxwell, A. Perujo, W.J. Teesdale: Nucl. Instrum. Methods B **9**, 71 (1985)
9.74 J. Heckel, W. Scholz: X-Ray Spectrom. **16**, 181 (1987)
9.75 J.V. Gilfrich, P.G. Burkhalter, L.S. Birks: Anal. Chem. **45**, 2002 (1973)
9.76 E.P. Bertin: *Principles and Practice of X-Ray Spectrometric Analysis* (Plenum, New York 1975) p. 320
9.77 W.R. Kiley: Norelco Rep. **7**, 143 (1960)
9.78 A.B. van Rennes: Nucleonics **10**, 32 (1952); **10**, 50 (1952)
9.79 K.F.J. Heinrich: Adv. X-Ray Anal. **4**, 370 (1961)
9.80 S.A. Wytzes: Philips Tech. Rev. **27**, 300 (1966)

9.81 F.B. Riggs: Rev. Sci. Instrum. **34**, 312 (1963)
9.82 J. Marchal, K. Weber: J. Sci. Instrum. **41**, 15 (1964)
9.83 M.L. Salmon: Adv. X-Ray Anal. **7**, 604 (1964)
9.84 L.S. Birks: *X-Ray Spectrochemical Analysis*, (Interscience, New York 1969) p. 63
9.85 M.L. Salmon: Adv. X-Ray Anal. **6**, 301 (1963)
9.86 P. Kirkpatrick: Rev. Sci. Instrum. **15**, 223 (1944)
9.87 T. Tanemura: Rev. Sci. Instrum. **32**, 364 (1961)
9.88 H. Kustner: Z. Phys. **70**, 324 (1931); ibid. **77**, 52 (1932)
9.89 H.J. Dothie: Nature **196**, 984 (1962); see also H.J. Dothie, B. Gale: Spectrochim. Acta **20**, 1735 (1964)
9.90 R. Voparil: J. Sci. Instrum. [2] **3**, 798 (1970)
9.91 R.W. Waynant, R.C. Elton: Proc. IEEE **64**, 1059 (1976)
9.92 R.C. Elton: Adv. X-Ray Anal. **21**, 1 (1978)
9.93 D.J. Nagel: In *Advances in X-Ray Spectroscopy*, edited by C. Bonnelle, C. Mande (Pergamon, New York 1982) p. 371
9.94 G. Jamelot: In *Radiation Physics*, ed. by E. Casnati, C. Baraldi, A. Tartari (North-Holland, Amsterdam 1987) p. 169
9.95 C. Yamanaka (ed.): *Short-Wavelength Lasers and Their Applications*, Springer Proc. Phys. Vol. 30 (Springer, Berlin, Heidelberg 1988)
9.96 M.A. Duguay, P.M. Rentzenpis: Appl. Phys. Lett. **10**, 530 (1967)
9.97 R.W. Waynant: Phys. Rev. Lett. **28**, 533 (1971)
9.98 R.T. Hodgson, R.W. Dreyfus: Phys. Rev. Lett. **28**, 536 (1979)
9.99 J. Reintjes, R.C. Eckardt, C.Y. She, N.E. Karangelen, R.C. Elton, R.A. Andrews: Phys. Rev. Lett. **37**, 1540 (1976)
9.100 J. Reintjes, C.Y. She, R.C. Eckardt: IEEE J. QE-14(8), 581 (1978)
9.101 R.G. Caro, J.C. Wang, J.F. Young, S.E. Harris: Phys. Rev. A **30**, 1470 (1984)
9.102 J.G. Kepros, E.M. Eyring, F.W. Cagle Jr.: Phys. Today 25(10), 18 (1972)
9.103 M.D. Rosen P.L. Hagelstein, D.L. Matthews, E.M. Campbell, A.U. Hazi, B.L. Whitten, B.J. MacGowan, R.E. Turner, P.D. Rookett et al.: Phys. Rev. Lett. **54**, 106 (1985)
9.104 D.L. Matthews, P.L. Hagelstein, M.D. Rosen, M.J. Eckart, N.M. Ceglio, A.U. Hazi, H. Medecki, B.J. MacGowan, T.A. Weaver et al.: Phys. Rev. Lett. **54**, 110 (1985)
9.105 D. Jacoby, G.J. Pert, S.A. Ramsden, L.D. Shorrock, G.J. Tallents: Opt. Commun. **37**, 193 (1981)
9.106 D. Jacoby, G.J. Pert, L.D. Shorrock, G.J. Tallents: J. Phys. B **15**, 3557 (1982)
9.107 W. Rump: Z. Phys. **43**, 254 (1927)
9.108 R. Jenkins: *An Introduction to X-Ray Spectrometry* (Heyden, London 1976); see also R. Jenkins, R.W. Gould, D. Gedeke: *Quantitative X-Ray Spectrometry* (Dekker, New York 1981)
9.109 T. Shiraiwa, N. Fujino: J. Appl. Phys. Jpn. **5**, 886 (1966); Bull. Chem. Soc. Jpn. **40**, 2289 (1967)
9.110 J.W. Criss, L.S. Birks: Anal. Chem. **40**, 1080 (1968)
9.111 R.T. Mainardi, M. Rubio, J. Meda: X-Ray Spectrom. **11**, 66 (1982)
9.112 A. Tartari, E. Casnati, C. Baraldi, G. Napoli: In *Radiation Physics* ed. by E. Casnati, C. Baraldi, A. Tartari (North-Holland, Amsterdam 1987)
9.113 J.H. Scofield: Phys. Rev. **179**, 9 (1969); ibid. **A9**, 1041 (1974); ibid. **A 10**, 1507 (1974); ibid. A **12**, 345 (1975)
9.114 T.R. Kohler, W. Parrish: Rev. Sci. Instrum. **27**, 705 (1956)

Appendix

A.1 N. Bohr: Philos. Mag. **25**, 10 (1913)
A.2 M. Siegbahn: *Spektroskopie der Röntgenstrahlen*, 2nd ed. (Springer, Berlin 1931)
A.3 S. Hagström, C. Nordling, K. Siegbahn: α-, β-, and γ-Ray Spectroscopy, Vol. 1, ed. by K. Siegbahn (North-Holland, Amsterdam 1965)
A.4 J.A. Bearden: "*X-Ray Wavelengths*"; Tech. Rep. NYO-10586, US Atomic Energy Commission, Oak Ridge, Tenn. (1964)
A.5 A.E. Sandström: *Handbuch der Physik*, Vol. 30, ed. by S. Flügge (Springer, Berlin, Heidelberg 1957)
A.6 J.A. Bearden: Rev. Mod. Phys. **39**, 78 (1967)
A.7 E. Saurl: *Landolt-Börnstein*, Vol. 1, ed. by A. Eucken (Springer, Berlin, Heidelberg 1950)
A.8 Y. Cauchois: J. Phys. Radium **13**, 113 (1952)
A.9 Y. Cauchois: J. Phys. Radium **16**, 253 (1955)
A.10 R.D. Hill, E.L. Church, J.W. Mihelich: Rev. Sci. Instrum. **23**, 523 (1952)
A.11 J.C. Slater: Phys. Rev. **98**, 1039 (1955)
A.12 L.C. Snyder: J. Chem. Phys. **55**, 95 (1971)
A.13 E.J. McGuire: Phys. Rev. **161**, 51 (1967)
A.14 A.R.P. Rau, U. Fano: Phys. Rev. **167**, 7(1968)
A.15 L. Pauling: *The Nature of the Chemical Bond* (Cornell University Press, Ithaca, NY 1960)
A.16 W. Gordy, W.J.O. Thomas: J. Chem. Phys. **24**, 439 (1956)
A.17 Y. Cauchois, C. Sénémaud (eds.) *Wavelengths of X-Ray Emission Lines and Absorption Edges* (Pergamon, New York 1978)

Author Index

Subject Index